ORNL/TM-2020/1612
Revision 0

Destructive PIE and Safety Testing of Six AGR-2 UO_2 Capsule 3 Compacts

John D. Hunn
Tyler J. Gerczak
Robert N. Morris
Fred C. Montgomery
Darren J. Skitt
Grant W. Helmreich
Brian D. Eckhart
Charles A. Baldwin

September 2020

OAK RIDGE NATIONAL LABORATORY
MANAGED BY UT-BATTELLE FOR THE US DEPARTMENT OF ENERGY

ORNL/TM-2020/1612

Reactor and Nuclear Systems Division

DESTRUCTIVE PIE AND SAFETY TESTING OF SIX AGR-2 UO_2 CAPSULE 3 COMPACTS

John D. Hunn
Tyler J. Gerczak
Robert N. Morris
Fred C. Montgomery
Darren J. Skitt
Grant W. Helmreich
Brian D. Eckhart
Charles A. Baldwin

Revision 0

Date Published: September 2020

Work sponsored by
US DEPARTMENT OF ENERGY
Office of Nuclear Energy—Advanced Reactor Technologies
under the
Advanced Gas Reactor Fuel Development and Qualification Program

Prepared by
OAK RIDGE NATIONAL LABORATORY
Oak Ridge, TN 37831-6283
managed by
UT-BATTELLE, LLC
for the
US DEPARTMENT OF ENERGY
under contract DE-AC05-00OR22725

CONTENTS

LIST OF FIGURES

LIST OF TABLES

ABBREVIATIONS

3D	three-dimensional (imaging)
AGR	Advanced Gas Reactor (Fuel Development and Qualification Program)
AGR-1	first AGR program irradiation experiment
AGR-2	second AGR program irradiation experiment
ATR	Advanced Test Reactor
BEC	backscattered electron composition
CCCTF	Core Conduction Cooldown Test Facility
CO	carbon monoxide
DLBL	deconsolidation leach-burn-leach
EDS	energy-dispersive x-ray spectroscopy
EOL	end of life
FB-CVD	fluidized-bed chemical vapor deposition (coating furnace)
FIMA	fissions per initial metal atom
HTGR	high-temperature gas-cooled reactor
ID	identification
IFEL	Irradiated Fuels Examination Laboratory
INL	Idaho National Laboratory
IMGA	Irradiated Microsphere Gamma Analyzer
IPyC	inner pyrolytic carbon (TRISO layer)
JMOCUP	Jim Sterbentz's MCNP-ORIGEN2 coupled utility program
M/A	measured vs. average
M/C	measured vs. calculated
MCNP	Monte Carlo N-Particle Transport code
MDL	minimum detection limit
OPyC	outer pyrolytic carbon (TRISO layer)
ORIGEN	Oak Ridge Isotope Generation and Depletion code
ORNL	Oak Ridge National Laboratory
PGS	Precision Gamma Scanner
PIE	post-irradiation examination
RS	randomly-selected (particles)
SD	standard deviation
SEI	secondary electron imaging
SEM	scanning electron microscope
SiC	silicon carbide (TRISO layer)
SP	special particle (abnormal particles typically identified with IMGA)
TA_{max}	time-average maximum (temperature)
TA_{min}	time-average minimum (temperature)
TAVA	time-average, volume-average (temperature)
TRISO	tristructural isotropic (coated particles)
UCO	uranium carbide and uranium oxide (fuel kernels)
UO_2	uranium oxide (fuel kernels)
XCT	computed x-ray tomography
Z	atomic number

ACKNOWLEDGMENTS

This work was sponsored by the US Department of Energy Office of Nuclear Energy Advanced Reactor Technologies as part of the Advanced Gas Reactor Fuel Development and Qualification Program. Analysis of leach solutions and Core Conduction Cooldown Test Facility furnace components was conducted by the Oak Ridge National Laboratory (ORNL) Nuclear Analytical Chemistry and Isotopics Laboratory. Hot cell activities were supported by ORNL Irradiated Fuels Examination Laboratory staff.

1. INTRODUCTION AND BACKGROUND

The Advanced Gas Reactor (AGR) Fuel Development and Qualification Program's second irradiation experiment (AGR-2) was irradiated in the Advanced Test Reactor (ATR) at Idaho National Laboratory (INL) from June 2010 to October 2013 (Collin 2014). The fuel compacts in this experiment held either tristructural isotropic (TRISO)-coated spherical kernels of uranium oxide (UO_2) or TRISO-coated kernels containing both uranium carbide and uranium oxide phases (UCO). There were six separately monitored and controlled capsules in the AGR-2 test train. Capsule 3 held twelve compacts containing UO_2-TRISO particles fabricated by BWX Technologies Nuclear Operations Group. The AGR-2 TRISO particles were fabricated in a pilot-scale fluidized-bed chemical vapor deposition (FB-CVD) furnace with a coating chamber inner diameter of 150 mm (Phillips, Barnes, and Hunn 2010), which was a change from the first irradiation experiment (AGR-1) particles that had been coated in a lab-scale FB-CVD coating system with a chamber inner diameter of 50 mm (Lowden 2006). The TRISO particles were overcoated with resinated graphite flake at Oak Ridge National Laboratory (ORNL), and the overcoated particles were pressed into one-inch-long, half-inch-diameter cylinders (Hunn, Montgomery, and Pappano 2010). Each cylindrical compact held an average of 1,543 TRISO particles with 9.6% enriched UO_2 kernels that had a nominal diameter of 500 µm (Hunn, Savage, and Silva 2012). Capsule 3 compacts were irradiated to average calculated burnups of 9.01–10.69% fissions per initial metal atom (FIMA), and the average calculated fluences of fast neutrons with energies $E_n > 0.18$ MeV were $3.05–3.53\times10^{25}$ n/m^2 (Sterbentz 2014). The calculated time-average, volume-average Capsule 3 compact temperatures were 996–1,062°C. However, Capsule 3 compact temperatures varied several hundred degrees across each compact, and the time-average minimum (TA_{min}) and time-average maximum (TA_{max}) temperatures were between 889–999°C and 1,072–1,105°C, respectively (Hawkes 2014).

After irradiation, the AGR-2 test train was transferred from ATR to the INL Materials and Fuels Complex for inspection and disassembly (Ploger, Demkowicz, and Harp 2015). The initial inspection included dimensional metrology of the compacts and graphite fuel holders. Like all the AGR-2 compacts, the compacts in Capsule 3 shrank slightly during irradiation, as expected, with an average length reduction of 1.07–1.24% and an average diameter reduction of 0.13–0.41%. Post-irradiation examination (PIE) of the capsule components was completed to measure select fission products (^{90}Sr, ^{110m}Ag, ^{134}Cs, ^{137}Cs, ^{144}Ce, and ^{154}Eu) outside the compacts (Stempien and Demkowicz 2020). This involved gamma counting of the graphite and graphoil spacers at the top and bottom of each capsule, acid leaching for radiochemical analysis of fission products on the metallic capsule components, and burn-leach analysis of the graphite holders. The total amount of ^{110m}Ag measured on the Capsule 3 components was 13% of the calculated capsule inventory. This was significantly lower than the amount of ^{110m}Ag measured on the three UCO capsule components, which ranged from 32–70%. The lower ^{110m}Ag release in Capsule 3 was likely due to lower peak temperatures compared with the UCO fuel capsules (Hawkes 2014). Measured inventories of the other select fission products were also lower in Capsule 3.

Prior to any destructive analysis, the compacts and graphite fuel holders were gamma scanned with the INL Precision Gamma Scanner (PGS), which provided information on fission product retention and burnup (Harp, Demkowicz, and Stempien 2016). Burnup determined by PGS agreed well with the predicted burnup values determined via physics calculations (Sterbentz 2014). The ^{110m}Ag retention, as measured with the PGS, ranged from 85–117% of the calculated inventory, in which values greater than 100% indicate that at least some of the calculated inventories underpredict the actual inventories. Cesium hot spots were observed in the graphite holders from the three AGR-2 UCO capsules, and adjacent compacts were inspected due to experience from AGR-1 PIE, in which similar cesium hot spots were correlated to the presence of failed particles (Hunn et al. 2014a). Failed particles were recovered from some of the suspect AGR-2 UCO compacts (Hunn et al. 2016), while other showed evidence for exposed kernels in the deconsolidation and acid leaching solutions (Hunn et al. 2018a). No cesium hot spots were observed in the Capsule 3 graphite holder, so there were no as-irradiated compacts from Capsule 3 specifically selected for failed particle analysis.

Polished compact sections from Compact 3-2-3 were examined with emphasis on cataloging general structural changes in the kernel and buffer caused by kernel swelling, pore formation, and buffer densification, in which buffer densification almost always led to detachment of the bulk of the buffer from the inner pyrolytic carbon (IPyC) layer (Rice, Stempien, and Demkowicz 2016). The UO_2 kernel pores appeared to be generally smaller and more evenly dispersed than in the UCO kernels. Buffer fracture in the radial direction was only observed in 3 out of 102 catalogued Compact 3-2-3 particles, and this fracture only left a narrow radial gap, in contrast to the wider gaps often accompanied by kernel extrusion sometimes observed in UCO TRISO particles. One Compact 3-2-3 particle exhibited a gap between the IPyC and silicon carbide (SiC) layer, which allowed the IPyC layer to move inward and remain in contact with the buffer as it densified. Because there was no apparent damage on the outer surface of the IPyC, the irradiated structure in this abnormal particle was almost certainly related to a coating defect at the IPyC/SiC interface, as there is normally a strong bond between these two layers. Inspection of general structural changes in the IPyC, SiC, and outer pyrolytic carbon (OPyC) involved looking for fracture or tears in these layers. A few IPyC tears that were apparently related to the buffer detachment were noted, while no fractures or other unusual features were evident in the SiC or OPyC. Additional information on the irradiation behavior of the TRISO coatings was obtained by performing serial sectioning of individual particles from (Stempien, Plummer, and Schulthess 2019). Four parallel sections were observed in 200 particles randomly selected from Compact 3-3-1, and spherical fits based on the observed circumferences of kernel, buffer, IPyC, and SiC in 175 particles with structures and images viable for analysis were used to compute volumes for comparison to as-fabricated averages. The average UO_2 kernel swelling in the Compact 3-3-1 particles was 10 ± 10%, which was measurably less than what was observed in the UCO kernels, regardless of relative burnup, fast neutron fluence, or temperature. Average buffer shrinkage in the Compact 3-3-1 particles (28 ± 24%) and the resultant gaps between the buffer and IPyC (22 ± 6 μm) were similar to what were observed in the UCO particles. No significant dimensional changes could be measured in the IPyC or SiC layers.

Six of the AGR-2 Capsule 3 UO_2 compacts were shipped to ORNL for as-irradiated PIE or safety testing followed by post-safety test examination, and results are reported herein. The individual identities and key irradiation and safety test parameters for these six compacts are listed in Table 1-1. Compacts with the same capsule and level number that were adjacently located in Stacks 1 and 2 were considered "sister compacts" due to similar irradiation conditions.

Table 1-1. Irradiation and safety test parameters for AGR-2 UO_2 Capsule 3 compacts analyzed in this study

Compact ID [a]	Fabrication ID [b]	Safety test (°C)	Burnup [c] (% FIMA)	Fast fluence [c] (n/m^2)	Temperature [d] (°C)		
					TAVA	TA_{min}	TA_{max}
AGR-2 3-1-2	LEU11-OP2-Z098	none	10.66	3.45×10^{25}	1,012	903	1,084
AGR-2 3-3-1	LEU11-OP2-Z106	none	10.46	3.49×10^{25}	1,062	997	1,104
AGR-2 3-1-1	LEU11-OP2-Z029	1,500	10.60	3.41×10^{25}	1,011	900	1,083
AGR-2 3-3-2	LEU11-OP2-Z034	1,600	10.54	3.53×10^{25}	1,062	999	1,105
AGR-2 3-4-2	LEU11-OP2-Z150	1,600	10.69	3.50×10^{25}	1,013	904	1,085
AGR-2 3-4-1	LEU11-OP2-Z188	1,700	10.62	3.47×10^{25}	1,013	901	1,085

[a] The compact identification (ID) denotes the compact's location in the irradiation test train: *capsule-level-stack* (Collin 2014).
[b] Data for individual compacts are available and referenced by fabrication ID (Hunn, Montgomery, and Pappano 2010).
[c] Compact average burnups and fast neutron fluences (E_n > 0.18 MeV) are based on physics calculations (Sterbentz 2014).
[d] Compact temperatures are based on thermal calculations (Hawkes 2014).

2. EXPERIMENTAL METHODS*

2.1 SAFETY TESTING METHODS

Safety testing in the ORNL Core Conduction Cooldown Test Facility (CCCTF) furnace (Figure 2-1) was accomplished using the same methods that were used for AGR-1 safety testing (Baldwin et al. 2012). A compact was placed in a graphite holder that positions the compact in the furnace and simulates the graphite that surrounds the compacts in a prismatic block reactor. A water-cooled deposition cup located near the top of the tantalum-lined furnace chamber collected vaporized metallic elements that escaped from the compact and the encompassing graphite holder. Deposition cups were periodically removed and replaced with new cups using a maximum exchange interval of ~24 h. Shorter exchange intervals were used for the first few cups removed after heating up to the test temperature to better track higher rate changes during this period. The cups were monitored with gamma spectrometry to track safety test progress, with particular emphasis on the collected cesium inventory, which would indicate retention failure in the SiC layer because cesium is well retained by a normal SiC layer but not by the IPyC or OPyC layers (Hunn et al. 2014a). Gaseous fission products were collected from the helium sweep gas as it passed through a trap cooled with liquid nitrogen. The trap was monitored for ^{85}Kr, because significant krypton release would indicate failure of the gaseous fission product retention of a normal TRISO coating (Morris et al. 2014). Particles that release a significant fraction of their cesium inventory are classified as having *failed SiC* if they do not also release a significant fraction of krypton gas, which would indicate the SiC failure was accompanied by gas retention failure in the IPyC and OPyC. Particles that exhibit significant release of both cesium and krypton are classified as having *failed TRISO*. After each safety test was completed, additional analysis was performed to measure actinides and fission products on the deposition cups and other CCCTF furnace internals (graphite fuel holder, tantalum furnace liner, and tantalum gas inlet line). These data were used to determine the cumulative release from the compact of each detected isotope.

Actinide and fission product measurements were converted to fractions of the total compact inventory, or *compact fraction*, using the standard ORNL AGR PIE approach (Hunn et al. 2013). This method used the total compact inventory of each isotope estimated from physics calculations (Sterbentz 2014) to determine the inventory at three specific times after the end of the irradiation, also called the *end of life* (EOL): namely, one day after EOL, one year after EOL, and two years after EOL. Radioisotope quantities measured by gamma spectrometry (e.g., ^{85}Kr, ^{110m}Ag, ^{134}Cs, ^{137}Cs, ^{154}Eu, and ^{155}Eu) or chemical separation and beta spectrometry, in the special case of ^{90}Sr, were decay-corrected to one day after EOL and divided by the calculated total inventory at that time to determine the total inventory fraction. For stable isotopes such as ^{104}Pd and for actinides (e.g., ^{235}U, ^{236}U, ^{238}U, ^{239}Pu, and ^{240}Pu), the measured quantity was divided by the calculated total inventory at one year after EOL. This was done because many stable isotope inventories increased significantly over the first year after the compacts were removed from the reactor, while any further increase in the calculated inventories after one year was typically negligible. The mass spectrometry analysis was almost always performed after one year based on the time required for the test train to cool down and be disassembled. Results were also calculated and are often presented in terms of the equivalent particle inventory, or the number of *particle equivalents*, which is defined as the total compact inventory fraction multiplied by the average number of particles per compact: 1,543 for AGR-2 UO_2 compacts (Hunn, Montgomery, and Pappano 2010).

The efficiency of fission product collection on the deposition cups varied for different elements due to the variability in transport of these elements out of the graphite holder and onto the water-cooled cups. The cumulative fraction of each fission product measured on the deposition cups—relative to the total released from the compact and measured on the cups, tantalum internals, and graphite holder at the end of each safety test—provided a value for the average effective deposition cup collection efficiency for that fission

* This experimental methods section is a revised version of a similar section in a previous AGR-2 PIE report (Hunn et al. 2019), and is included herein for contextual information and definition of common terminology used throughout this report.

product. The compact release during each deposition cup residence period was estimated by multiplying the amount of each fission product measured on the cup by the average effective collection efficiency for that fission product, and this estimated compact release during each deposition cup residence period was plotted to illustrate the time-dependent release from the compact. The accuracy of this method for estimating time-dependent fission product release from the compact is usually good for fission products like silver and cesium, whose transport time to the cup is relatively short compared with the deposition cup residence period. Silver and cesium typically exhibit a high deposition cup collection efficiency that does not vary significantly after the furnace reaches the safety test temperature. Some fission products (e.g., strontium and europium) are held up in the graphite holder and transport relatively slowly to the deposition cups. For these fission products, the time-dependent plots of the fractional releases during safety testing are often not representative of the time-dependent release from the compact, especially during the early stages of the safety test when an apparent increase in the release rate may be dominated by the changing concentration profile in the graphite holder. However, because the average effective deposition cup collection efficiencies are based on the cumulative release from the compact to all of the internal furnace components where fission products primarily accumulate, the values plotted for the final deposition cup accurately represent the total compact release fractions.

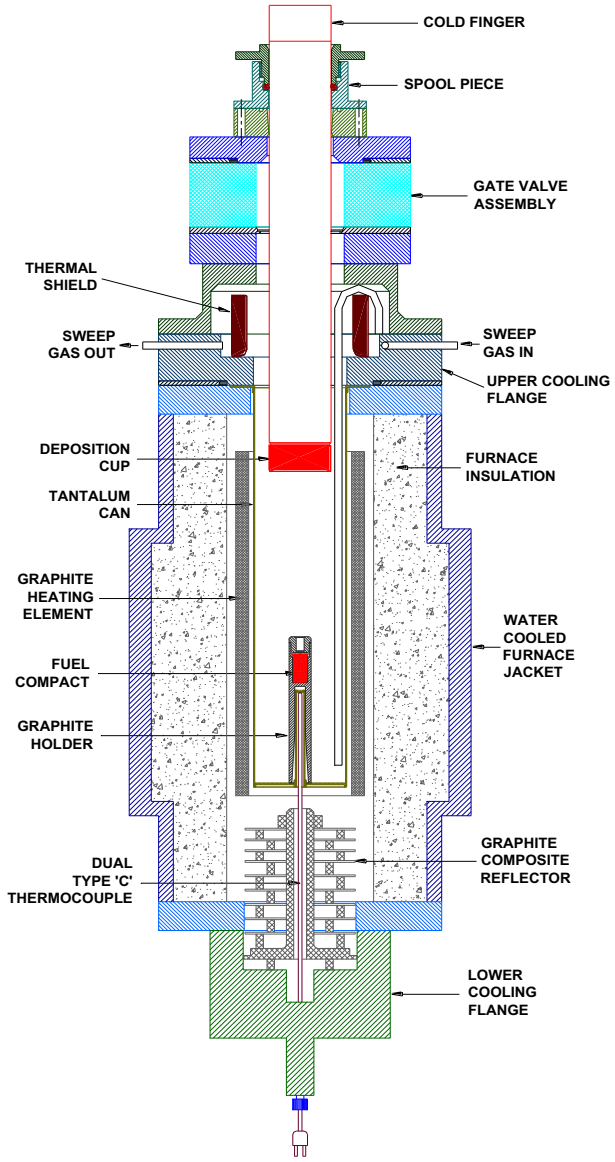

Figure 2-1. Schematic of the CCCTF safety test furnace.

2.2 DLBL AND IMGA METHODS

Post-safety test destructive examination was performed using the same methods that were developed for destructive PIE of as-irradiated AGR-1 compacts, and the details of the equipment and methods have been previously reported (Hunn et al. 2013). Figure 2-2 is a flow diagram of the typical process for compact deconsolidation and leach-burn leach (DLBL) integrated with gamma survey of the particle inventory using the ORNL Irradiated Microsphere Gamma Analyzer (IMGA). Deconsolidation and leach solutions were analyzed by gamma and mass spectrometry, providing information about actinides and fission products that were not sealed inside retentive SiC layers. Actinides and fission products leached in the deconsolidation acid, pre-burn Soxhlet extractions of the particles and matrix, pot boil of the particles and matrix, and postburn pot leaches of the matrix may have come from (1) uranium contamination outside the SiC in the as-fabricated compacts, (2) diffusion through the SiC during irradiation or safety testing, and/or (3) exposed kernels in particles with failed TRISO. Actinides and fission products leached in the postburn Soxhlet extractions of the particles may have come from (1) exposed kernels in particles with failed SiC and/or (2) diffusively-released actinides and fission products that were not leached prior to the burn because they were previously sequestered in the OPyC layer or in an insoluble chemical form.

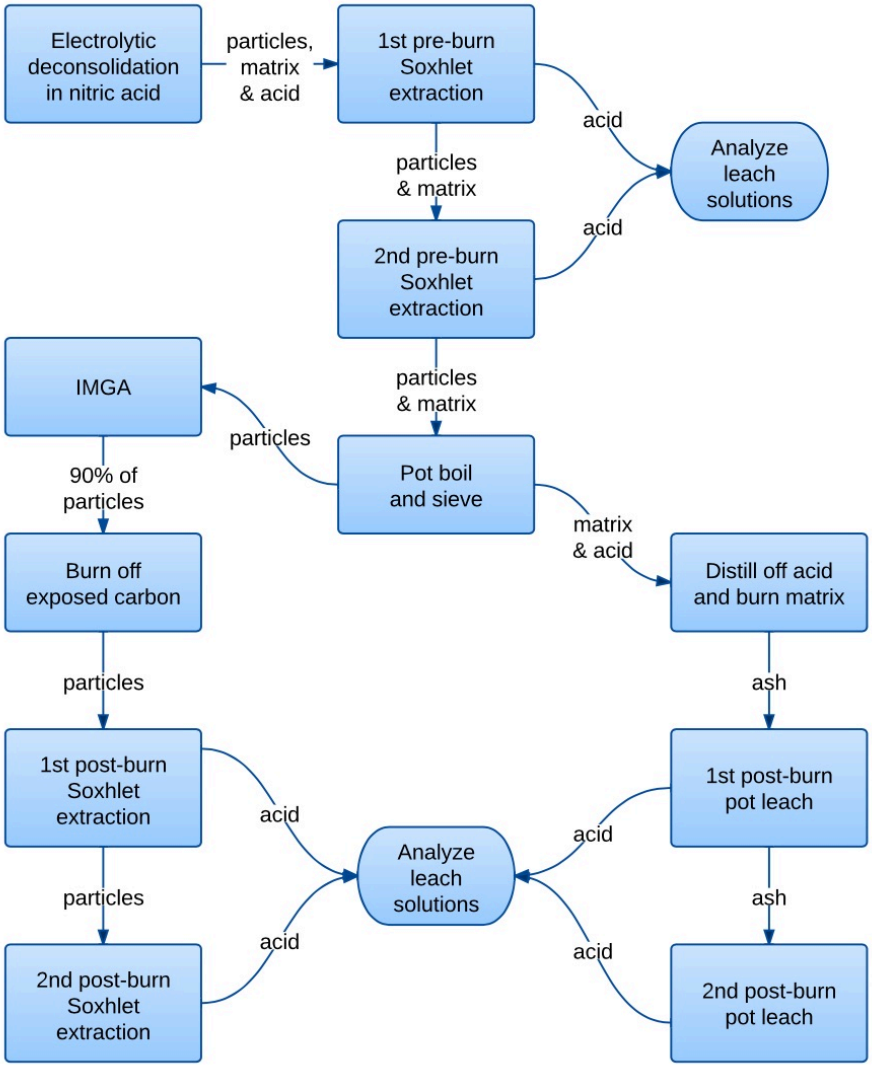

Figure 2-2. Process flow for DLBL and IMGA.

The DLBL data were decay-corrected and converted to compact inventory fraction and particle equivalent values using the same protocol applied to the safety test data. The IMGA data are reported herein as activities in Bq/particle that were decay-corrected to one day after EOL or various unitless ratios that communicate the retained fraction of each isotope. The simplest ratio was the measured activity of a particle, A_i, normalized to the average measured activity for all particles in a sample of n particles, reported herein as the measured vs. average (M/A) value. For example,

$$\frac{A_i(^{144}Ce)}{\sum_{i=1}^{n}\left(\frac{1}{n}\right)A_i(^{144}Ce)} \tag{2.1}$$

is the ^{144}Ce M/A value for Particle i (i.e., the measured ^{144}Ce activity of Particle i, normalized to the average ^{144}Ce activity). The ratio form in Equation 2.1 was used to generate ^{137}Cs, ^{144}Ce, and ^{106}Ru histograms of the IMGA survey results, which were centered on unity and had a distribution that resulted from measurement uncertainty and real particle-to-particle variation in isotopic content. For particles with negligible radioisotope release, this real particle-to-particle variation was related to variation in fissionable material and burnup, which might occur due to variation in kernel size and local neutron fluence.

A calculated value for the expected activity of a given isotope in each particle was estimated from the average calculated activity for that isotope, A_{calc}, predicted by physics simulations (Sterbentz 2014) multiplied by the normalized activity of a different and preferably well-retained isotope to adjust for particle-to-particle variation in fissionable material and burnup. For instance,

$$A_{calc}(^{137}Cs)\frac{A_i(^{144}Ce)}{\sum_{i=1}^{n}\left(\frac{1}{n}\right)A_i(^{144}Ce)} \tag{2.2}$$

is the calculated ^{137}Cs activity of Particle i after adjusting for particle-to-particle variation in fissionable material and burnup using the normalized ^{144}Ce activity of Particle i. The normalized ^{144}Ce activity was typically used for making the adjustment to the average calculated ^{137}Cs activity to account for the variation in fissionable material and burnup in each particle. However, the normalized ^{106}Ru activity was used if it could be measured with greater accuracy, which was the case for later PIE due to quicker decay of the ^{144}Ce activity and the lower energy of the ^{144}Ce gamma emission.

The ratio of the measured activity in Particle i vs. the calculated activity of Particle i is reported herein as the measured vs. calculated (M/C) value. For example,

$$\frac{A_i(^{137}Cs)}{A_{calc}(^{137}Cs)\frac{A_i(^{144}Ce)}{\sum_{i=1}^{n}\left(\frac{1}{n}\right)A_i(^{144}Ce)}} \tag{2.3}$$

is the ^{137}Cs M/C value for Particle i adjusted for particle-to-particle variation in fissionable material and burnup using the normalized ^{144}Ce activity of Particle i. The ratio form in Equation 2.3 was used to generate a ^{137}Cs M/C histogram from the IMGA survey data that illustrated the cesium retention in each particle, in which particles with low cesium retention could be identified as discrete values below the main distribution. These low cesium particles were sorted out during the IMGA survey and labeled as special particles (SP) using the compact number and a sequential ID (e.g., Particle 312-SP01, Particle 312-SP02, etc.). Special particles were typically analyzed with computed x-ray tomography (XCT) for signs of localized SiC failure, and targeted materialography was accomplished using this three-dimensional (3D) imaging to guide the generation of a polished planar section that revealed microstructure related to the cesium release (Hunn et al. 2014a).

After IMGA survey, special particles and a randomly riffled subsample of about 45 randomly-selected (RS) particles were subjected to longer gamma counting to obtain the better counting statistics needed for measurement of ^{110m}Ag and ^{154}Eu. The M/C values were calculated from the long-count IMGA data for isotopes other than ^{137}Cs using the ratio form in Equation 2.3, but rather than ^{144}Ce, the normalized ^{137}Cs activity was used for making the adjustment to the average calculated isotope activities. For example,

$$\frac{A_i(^{110m}Ag)}{A_{calc}(^{110m}Ag)\frac{A_i(^{137}Cs)}{\sum_{i=1}^{n}(\frac{1}{n})A_i(^{137}Cs)}} \tag{2.4}$$

is the ^{110m}Ag M/C value for Particle *i* adjusted for particle-to-particle variation in fissionable material and burnup using the normalized ^{137}Cs activity of Particle *i*. The ^{137}Cs isotope was chosen for the adjustment over ^{144}Ce based on comparisons that showed that ^{137}Cs was a better choice for the inventory adjustment (Hunn et al. 2012). In the absence of SiC failure, cesium is retained well by the SiC coating, sometimes better than cerium. Furthermore, the buildup of ^{137}Cs was much more linear than ^{144}Ce as a function of burnup throughout the course of the AGR-1 and AGR-2 irradiations because the irradiation tests extended over several ^{144}Ce half-lives. The average M/C for well-retained isotopes was not always close to unity, because error in the calculated inventory sometimes resulted in an offset which could be significant. The offset was substantial for the isotopes of europium and antimony as a result of large errors in the calculated values.

Another calculated ratio, reported herein as the measured vs. adjusted average (M/AA) value, was determined in a manner similar to that used to determine M/C, except the offset in the calculated activity was mostly removed by replacing the average calculated activity, A_{calc}, predicted by physics simulations and used in Equation 2.3 and Equation 2.4 with the average measured activity. For instance,

$$\frac{A_i(^{110m}Ag)}{\sum_{i=1}^{n}(\frac{1}{n})A_i(^{110m}Ag)\frac{A_i(^{137}Cs)}{\sum_{i=1}^{n}(\frac{1}{n})A_i(^{137}Cs)}} \tag{2.5}$$

is the ^{110m}Ag M/AA value for Particle *i* adjusted for particle-to-particle variation in fissionable material and burnup using the normalized ^{137}Cs activity of Particle *i*. This ratio form is useful for identifying particles with average retention.

2.3 MATERIALOGRAPHY AND XCT METHODS

Select special particles and RS particles that had been gamma counted with IMGA were examined by XCT and/or cross sectioned for materialography. For materialography, particles were embedded in epoxy in small aluminum holders and polished to near midplane with a Buehler Minimet 1000 grinder/polisher using the methods developed for AGR-1 PIE (Hunn et al. 2013). Final polish was typically achieved with a 0.5 µm diamond film. Polished cross sections were imaged with a Leica DMI5000 optical microscope.

Particles designated for XCT were embedded in epoxy in a Lucite holder (Figure 2-3a), which was removed from the hot cell and loaded into a tungsten shielded enclosure (Figure 2-3b) designed for use in an Xradia MicroXCT-400 (Figure 2-3c), which had been custom-designed by ORNL and Xradia for imaging TRISO fuel particles. A particle was rotated perpendicular to the x-ray beam, and radiographs were obtained at multiple angles of rotation. Tomographic reconstruction was performed to determine the relative x-ray density of each minimum resolvable volume element (voxel) in the cylindrical volume of rotation. From this data, two-dimensional tomograms could be produced for any planar section. In addition to these tomograms, three-dimensional representations were produced using various software packages for three-dimensional visualization of tomographic data sets. Details of the XCT methods were discussed by Hunn et al. in the AGR-1 Irradiated Compact 4-4-2 PIE Report (Hunn et al. 2013).

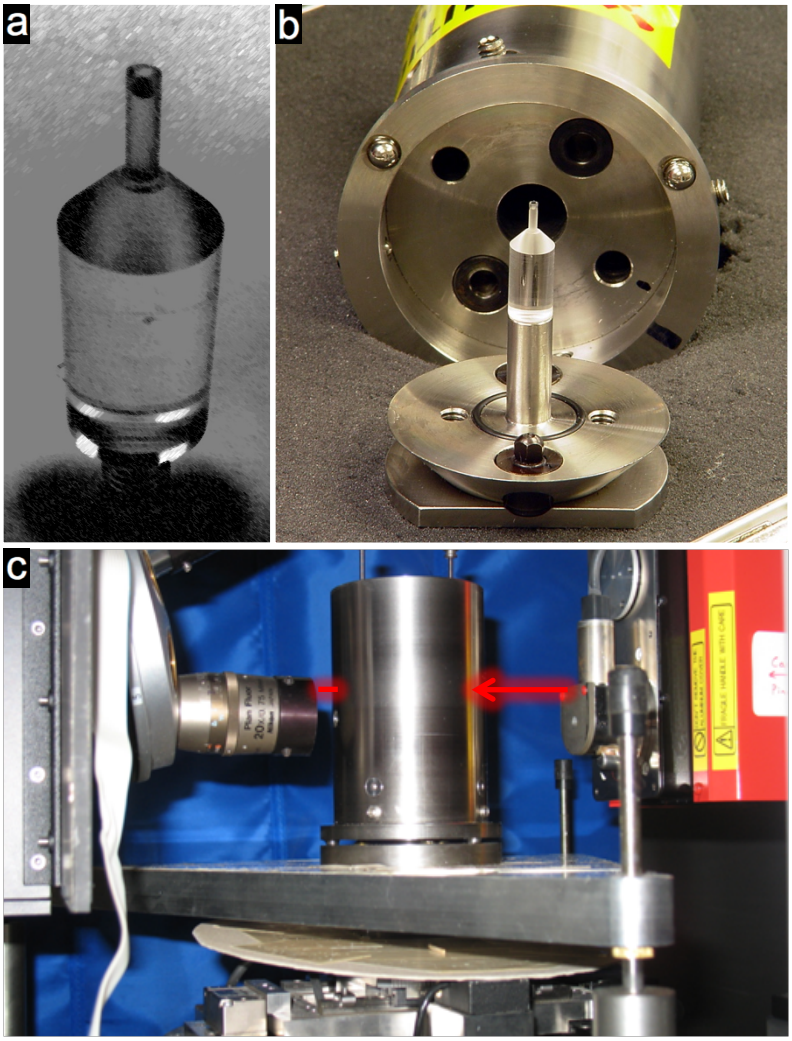

Figure 2-3. (a) Lucite holder, (b) shielded enclosure, and (c) XCT system used for non-destructive 3D imaging of irradiated fuel particles.

2.4 SEM AND EDS METHODS

Analysis was performed with a JEOL JSM-6390L scanning electron microscope (SEM) equipped with an Oxford X-Max 50 silicon drift detector for energy-dispersive x-ray spectroscopy (EDS) using the Oxford AZtec analysis software suite. The SEM was located in a contamination control area in Room 120 of the ORNL Irradiated Fuels Examination Laboratory (IFEL). The SEM analysis was performed on the mounts previously imaged by optical microscopy. To facilitate analysis, the mounts were transferred out of the IFEL hot cell to the charging area, where initial decontamination was performed to reduce radiological contamination. The mounts were then transferred to a hood located in Room 120 for final radiological decontamination and surface cleaning. The mounts underwent ultrasonic cleaning in deionized water, were rinsed with isopropyl alcohol, and were wiped with a cotton swab. These cleaning processes were repeated three times. Following cleaning, the samples were smeared and surveyed prior to being released from the hood. After the samples were released, their surfaces were checked with an optical microscope located in the contamination control area. If the sample surfaces were free of significant debris, then they were secured onto an aluminum SEM stub using conductive carbon tape and colloidal graphite to facilitate SEM analysis. Special particles previously encased in nonconducting epoxy from XCT analysis were coated with a thin layer of carbon (5–10 nm) using a Cressington Series 108 sputter coater to create a conductive surface to mitigate charging effects.

Two complementary SEM imaging modes—secondary electron imaging (SEI) and backscattered electron composition (BEC)—were performed, as they provide different and complementary information on particle cross sections. The secondary electron signal was surface sensitive, which allowed for identification of surface features and any irregularities. The SEI micrographs were obtained using a 3 kV accelerating voltage with a spot size setting of 40 (a unitless value) and a working distance of 8 mm. The backscattered electron signal was dependent on the atomic number (Z) of the elements near the surface. Because they appeared as bright spots, the high-Z actinides and fission products embedded in the relatively low-Z TRISO layers could be readily identified. The BEC micrographs were obtained using a 20 kV accelerating voltage with a spot size setting of 64 and a working distance of 10 mm. Image pairs of the same areas were acquired using both imaging modes to ensure that surface features (such as loose debris) were not misinterpreted as embedded features. A general image set was taken for each particle cross section. The image set typically consisted of particle overview images, low magnification (500×) images of the TRISO layers in four cardinal directions, and higher magnification (1,500×) images of the SiC and IPyC/SiC interface in four cardinal and four intercardinal directions around the circumference of the particle. Additional images of selected areas of interest were also acquired when necessary.

Two or more locations were chosen on each particle cross section for EDS analysis to gain an understanding of the distribution of actinides and fission products in the TRISO layers after irradiation and safety testing. Point-ID analysis was used to identify local compositions in high-Z features. The Point-ID analysis was acquired under the same conditions as images acquired in the BEC mode, which resulted in a sufficient count rate. The general acquisition parameters used for Point-ID analysis were to collect spectra within an energy range of 0–20 keV with 10 eV/channel, 4,096 channels, a unitless process time of 2, and a live time of 30 s. Data acquired by Point-ID analysis were processed using standardless analysis, and significant contributions from the surrounding matrix were included in the data due to the submicron size of the analyzed features; therefore, information on feature composition was not quantitative. In addition, minor constituents present in the high-Z actinide and fission product features may not be observed. However, the Point-ID analysis information on feature composition was useful for qualitative classification of the features, which supported identification of general trends and comparison of the features observed in different locations in the TRISO layers.

3. SAFETY TEST RESULTS

Isothermal safety tests on four Capsule 3 were conducted in the CCCTF by heating the compacts in flowing helium to a target temperature and holding at this temperature for an extended soak time to observe fission product release and possible particle failure that could occur during a high-temperature excursion resulting from an abnormal reactor condition. Compacts were first heated from room temperature to 1,250°C at a ramp rate of 120°C/h, with a 2 h soak at 400°C to drive off any retained moisture. The compacts were held at 1,250°C for 12 h to allow them to stabilize, and then heated to the planned safety test temperature at a ramp rate of 50°C/h. Table 3-1 lists the safety test temperatures and the soak times the compacts were held at these temperatures. Also listed in Table 3-1 are references to summary reports that provide additional detail for each safety test and a more thorough presentation and discussion of the test results than the summary herein. The 1,600°C test temperature represents the standard AGR program safety test temperature and is based on expected peak temperature that may be experienced by the fuel compacts during an accidental depressurization conduction cooldown event in a typical high-temperature gas-cooled reactor (HTGR). One compact was tested at 1,700°C to explore the safety test performance margin. Margin testing for the AGR-2 UCO compacts was performed at 1,800°C based on previously observed low failure rates at 1,700 and 1,800°C during AGR-1 safety testing and continuing observation of low failure rates at 1,800°C in the AGR-2 irradiation test fuel (Hunn et al. 2018a, Hunn et al. 2018b). However, higher failure rates were anticipated for the UO_2 fuel, so 1,800°C testing was avoided. The 1,500°C safety test was performed because the SiC failure fraction at 1,600°C already significantly exceeded that of the AGR UCO fuel, and the lower test temperature could provide more information on the thresholds for lower failure rates.

The soak time for all four tests was originally planned to be ~300 h. The Compact 3-1-1 safety test was extended to 400 h because there was no indication for failure until after 258 h at 1,500°C, when an uptick in the cesium release rate indicated a particle was beginning to fail. Extending the soak time to 400 h allowed for the observation of cesium release from this failed particle. The Compact 3-4-1 safety test was prematurely terminated after holding at 1,700°C for 164 h because escalating cesium release (approaching 9% of the total inventory) might otherwise have resulted in dose rates from fission products on the furnace internals exceeding standard operating limits adhered to for safe hands-on maintenance of the furnace.

Table 3-1. AGR-2 UO_2 Capsule 3 compacts subjected to safety testing

Compact ID	Safety test temperature (°C)	Soak time (h)	Safety test summary report	Reference
AGR-2 3-1-1	1,500	400	ORNL/TM-2020/1451	Hunn et al. 2020
AGR-2 3-3-2	1,600	288	ORNL/TM-2015/388	Hunn et al. 2015a
AGR-2 3-4-2	1,600	305	ORNL/TM-2015/388	Hunn et al. 2015a
AGR-2 3-4-1	1,700	164	ORNL/TM-2018/956	Hunn et al. 2018b

3.1 KRYPTON RELEASE DURING SAFETY TESTING

Table 3-2 lists the cumulative releases of typically tracked fission products at the end of each AGR-2 UO_2 Capsule 3 safety test. Krypton releases were negligible at 1,500 and 1,600°C, clearly indicating there were no particles in these three tests with failed TRISO. The ^{85}Kr release from the 1,700°C safety test was somewhat elevated, with a cumulative release of 0.067 particle equivalents. However, it did not show the expected magnitude and temporal profile of ^{85}Kr release from a failed-TRISO particle. A classic example of safety test release resulting from SiC failure and TRISO failure was seen in an 1,800°C safety test of

AGR-1 UCO Compact 4-3-2 (Demkowicz et al. 2015a). Cesium release from a particle with failed SiC was followed after a short break-through period by a gradual release of 0.085 particle equivalents of ^{85}Kr over about 80 h (Figure 3-1). This gradual krypton release at 1,800°C indicated transport through intact pyrocarbon in the particle with failed SiC. After about 80 h of gradual release, there was a rapid release of ^{85}Kr that brought the cumulative release to ~0.92 particle equivalents of ^{85}Kr. This rapid release indicated a particle with failed TRISO. A second example of the same type of stepwise failure in a second particle was observed later in the same test.

Table 3-2. Cumulative releases of radioactive isotopes from safety-tested AGR-2 UO_2 Capsule 3 compacts

Fission product	Compact 3-1-1 1,500°C safety test	Compact 3-3-2 1,600°C safety test	Compact 3-4-2 1,600°C safety test	Compact 3-4-1 1,700°C safety test
^{85}Kr	~6.2×10^{-6} (~0.01)	<1×10^{-6} (<0.002)	<1×10^{-6} (<0.002)	4.33×10^{-5} (0.067)
^{90}Sr	3.35×10^{-5} (0.052)	1.44×10^{-3} (2.23)	2.70×10^{-3} (4.16)	4.47×10^{-2} (68.9)
^{110m}Ag	6.37×10^{-3} (9.83)	1.73×10^{-2} (26.6)	1.13×10^{-2} (17.5)	8.92×10^{-2} (138)
^{134}Cs	3.62×10^{-4} (0.56)	2.11×10^{-3} (3.26)	9.29×10^{-3} (14.3)	8.72×10^{-2} (135)
^{137}Cs	3.90×10^{-4} (0.60)	2.05×10^{-3} (3.16)	9.21×10^{-3} (14.2)	8.21×10^{-2} (127)
^{154}Eu	2.90×10^{-5} (0.045)	3.76×10^{-4} (0.58)	3.15×10^{-4} (0.49)	3.05×10^{-3} (4.70)

Values are reported as compact fractions and particle-equivalents (in parentheses).

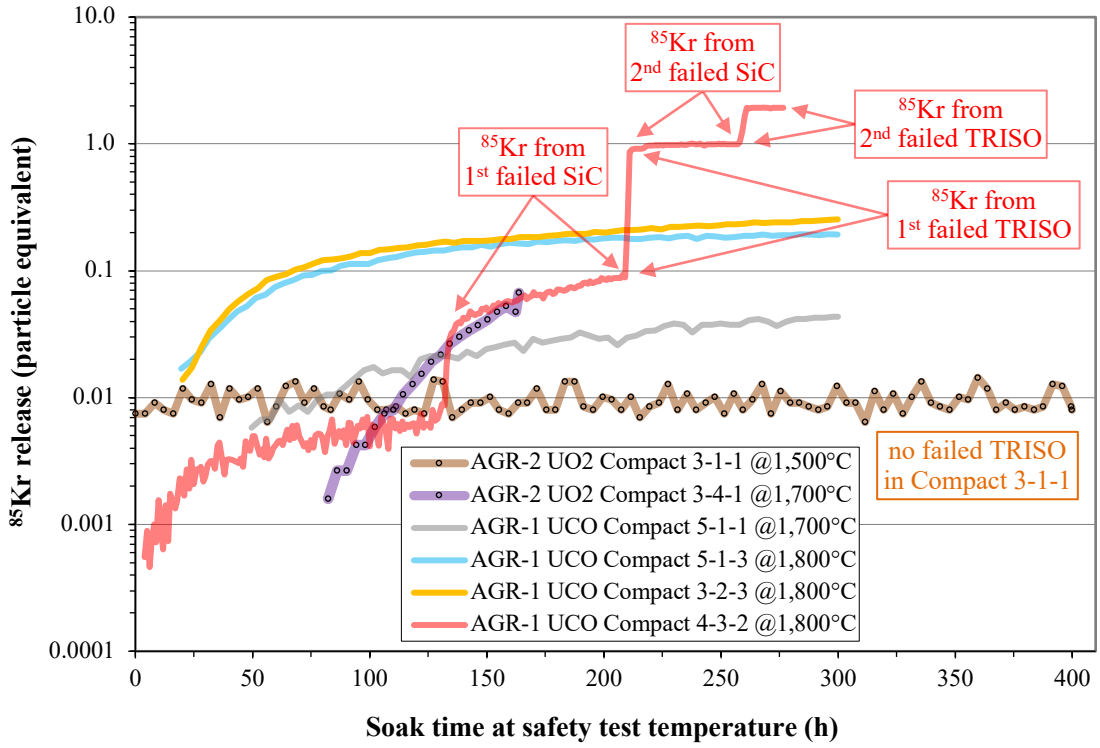

Figure 3-1. ^{85}Kr release during safety testing of AGR-2 UO_2 Compacts 3-1-1 and 3-4-1 compared with AGR-2 UCO compacts (labels refer to ^{85}Kr release from AGR-2 UCO Compact 4-3-2).

Observations of gradual release of small amounts of ^{85}Kr from particles with failed SiC, without subsequent TRISO failure, were observed during the 1,800°C safety testing of AGR-1 Compacts 5-1-3 and 3-2-3 (Hunn et al. 2014b). In those tests, the cumulative ^{85}Kr release was 0.20 particle equivalents from six or seven Compact 5-1-3 particles with failed SiC and 0.25 particle equivalents from eleven Compact 3-2-3 particles with failed SiC. Low levels of uranium in the initial DLBL leachates from these two compacts confirmed that there were no particles with failed TRISO. Evidence for the transport rate of krypton through intact pyrocarbon has also been observed at 1,700°C. Gradual ^{85}Kr release was observed in conjunction with three failed-SiC particles in the 1,700°C safety test of AGR-1 Compacts 5-1-1 (Hunn et al. 2015b); the cumulative ^{85}Kr release during this test was 0.04 particle equivalents. Figure 3-1 shows the similarity of the ^{85}Kr release during the AGR-2 UO_2 Compact 3-4-1 safety test to the gradual release of low levels of krypton from particles with failed SiC in the AGR-1 UCO compacts. Given the similarity to previous observations of krypton release from particles with failed SiC and the extent of SiC failure in Compact 3-4-1 as discussed in Section 3.2, the gradual release of ^{85}Kr measured in the latter half of the 1,700°C safety test of AGR-2 Compact 3-4-1 can be explained by very small releases from numerous particles with failed SiC (Hunn et al. 2018b).

3.2 CESIUM RELEASE AND SIC FAILURE DURING SAFETY TESTING

Figure 3-2 shows the estimated time-dependent fractional releases of typically tracked fission products during the 1,500°C safety test of Compact 3-1-1, and Figure 3-3 shows the time-dependence of the average rate for fractional release of cesium to each cup. As previously mentioned, the Compact 3-1-1 safety test soak time was extended to 400 h because an uptick in the cesium release rate after 258 h at 1,500°C indicated a particle was beginning to fail. As discussed in more detail in the safety test summary report (Hunn et al. 2020), the amount of cesium that was released during the Compact 3-1-1 safety test and the time dependence of the cesium release rate were consistent with the presence of one particle with failed SiC (a compact fractional release of 6.5×10^{-4} corresponds to the average inventory in one particle). During the first two-thirds of this test, cesium levels on the deposition cups were slightly elevated in comparison to the 1,600°C safety tests of Compacts 3-3-2 and 3-4-2 and other AGR-2 UCO compacts. These elevated levels could be related to contamination in the furnace or incipient SiC failure in the particle that released higher levels of cesium later in the test (Hunn et al. 2020).

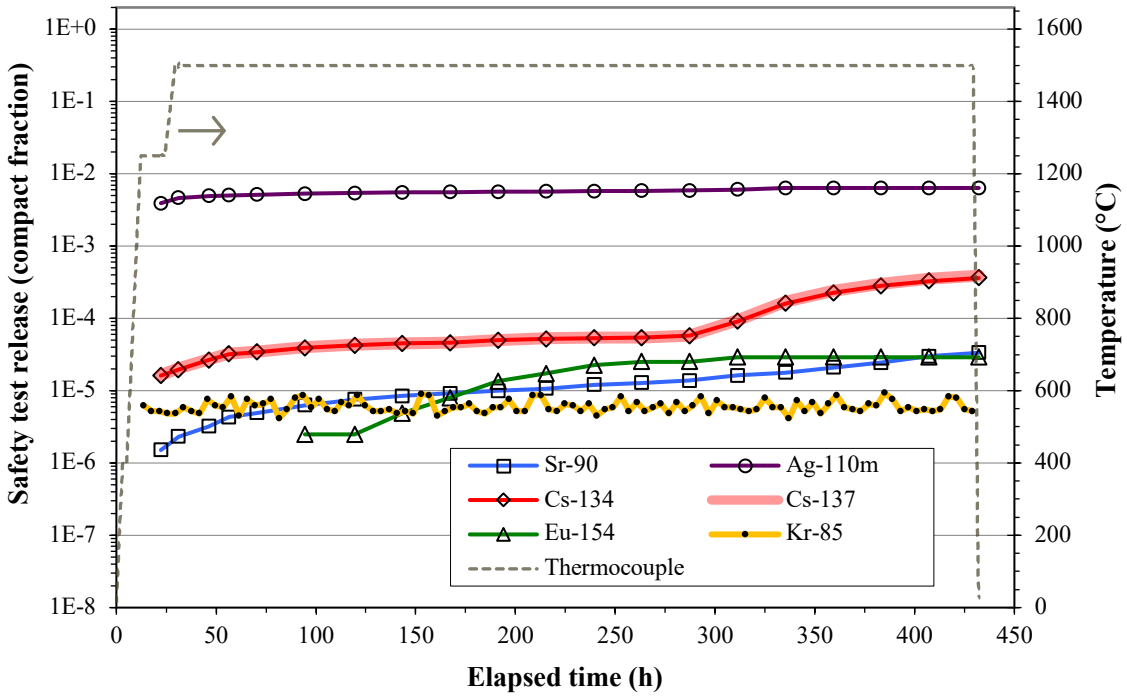

Figure 3-2. Release of fission products from Compact 3-1-1 during a 1,500°C safety test.

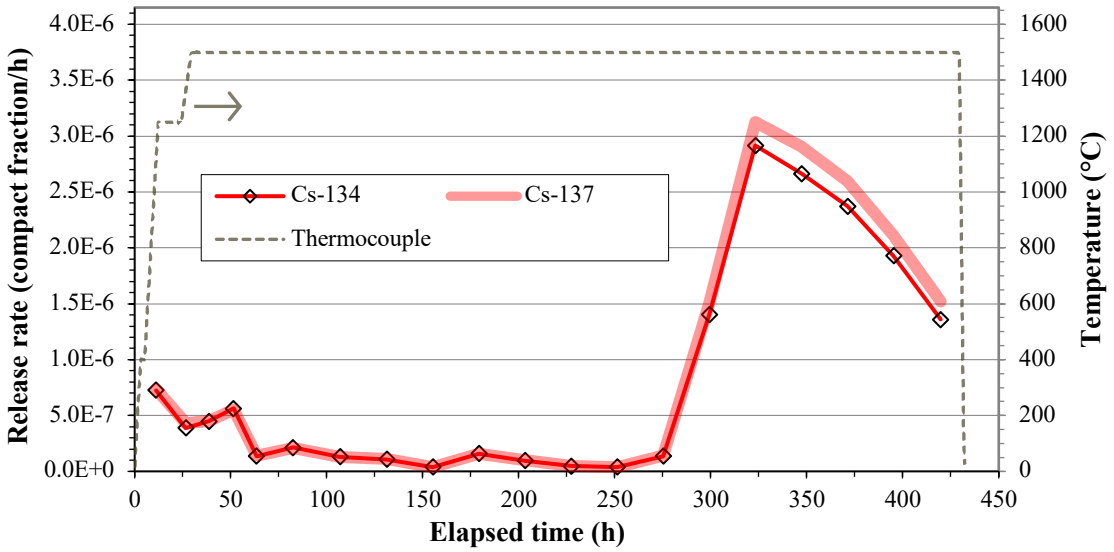

Figure 3-3. Cesium release rate from Compact 3-1-1 during a 1,500°C safety test.

The values for the cumulative ^{134}Cs and ^{137}Cs release in Table 3-2 show that there was roughly an order of magnitude increase in the total safety test release for each 100°C increase in the safety test temperature from 1,500°C to 1,700°C. Figure 3-4 illustrates how the cesium release from SiC failure varied not only in magnitude but also as a function of time. At 1,500°C, significant cesium from SiC failure was not observed until after a soak time of 258 h. Shorter periods before the obvious onset of SiC failure were observed at 1,600°C (after 39 h for Compact 3-3-2 and after 87 h for Compact 3-4-2). Significant cesium release occurred in the first 13 h at 1,700°C. After the onset of significant release from one particle with failed SiC in the 1,500°C safety test of Compact 3-1-1, the cesium release rate increased over a period of about 48 h and then gradually decreased, but remained significant over the next 94 h. This illustrates the fact that cesium release from particles with failed SiC occurred gradually over a time scale of days, likely related to the time required for cesium to diffuse through intact pyrocarbon. Cesium release was similarly drawn out at 1,700°C, in which it took ~1.5 days to reach a release of one particle equivalent.

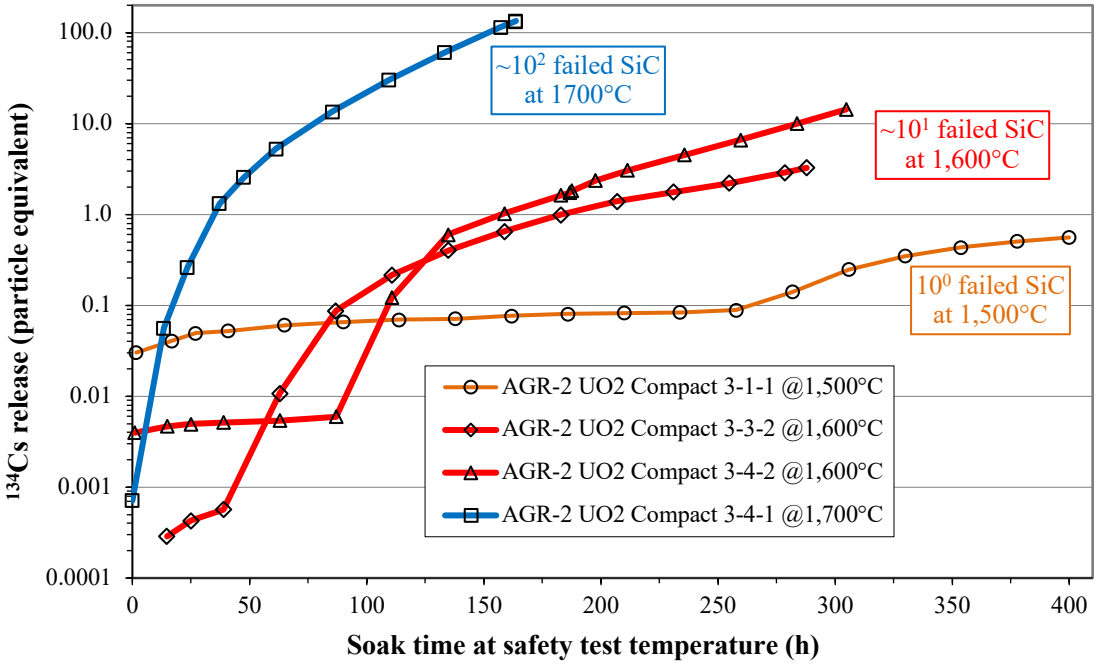

Figure 3-4. ^{134}Cs release during safety testing of four AGR-2 UO_2 compacts (^{137}Cs release was similar).

Figure 3-5 is a plot of the ^{134}Cs release rates in particle equivalents per hour with the time for each data set shifted to roughly align the data to the onset of significant cesium release from SiC failure. This graph illuminates the similarities and differences in the release behavior. The initial 50 h of significant cesium release from Compact 3-3-2 at 1,600°C was similar to that from Compact 3-1-1 at 1,500°C, which suggests that the release from Compact 3-3-2 during most of this period was from a single particle with failed SiC. The higher slopes of the release rate trendlines for Compacts 3-4-1 and 3-4-2 suggest release from more than one particle soon after onset of SiC failure. While the release rate from Compact 3-3-2 overlaid that from Compact 3-1-1 for the first 50 h after onset, it did not drop off afterward like it did in Compact 3-1-1 as available cesium in the one particle with failed SiC was depleted. The gradual increase in the Compact 3-3-2 ^{134}Cs release rate after 50 h indicates that more and more particles with failed SiC were contributing as time progressed. Compacts 3-4-1 and 3-4-2 showed even greater escalating release rates consistent with their higher populations of particles with failed SiC. Additional insight regarding particle failure was provided by the DLBL analysis (Section 4), the IMGA survey of particles recovered from each compact (Section 5), and the microstructural analysis of individual special particles (Section 8).

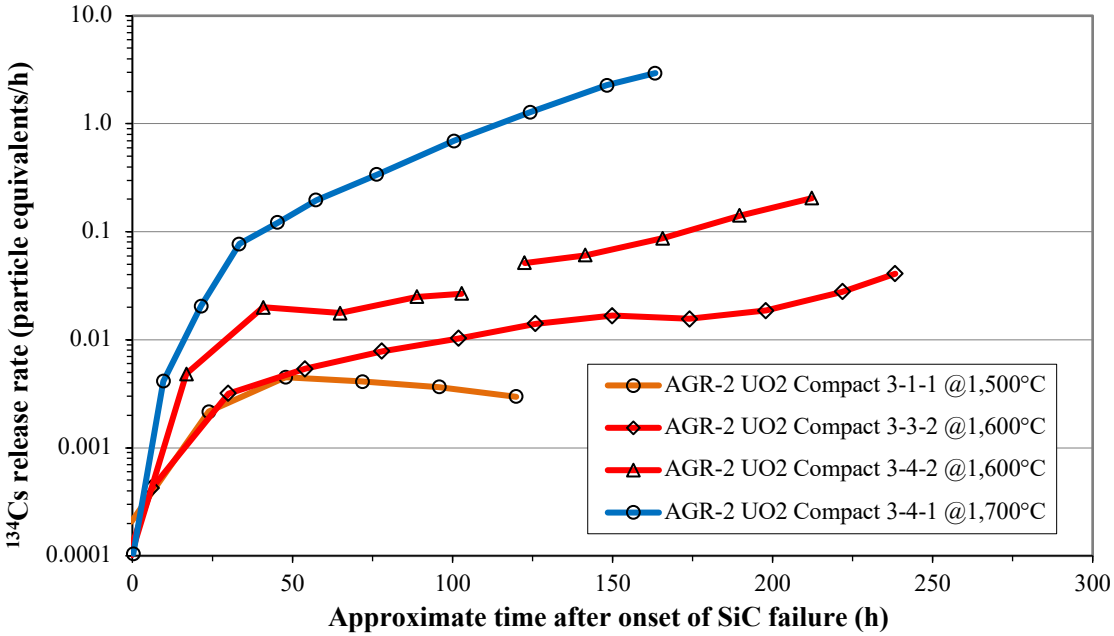

Figure 3-5. Rate of ^{134}Cs release during safety testing of four AGR-2 UO_2 compacts.

3.3 SILVER RELEASE DURING SAFETY TESTING

Significant fractions of the silver generated in each fuel kernel during TRISO fuel irradiation are released through normal SiC layers throughout the irradiation (Nabielek, Brown, and Offermann 1977; Amian and Stöver 1983). In the AGR-1 irradiation experiment, it was commonly observed that some of this silver exited the compacts and deposited on the capsule components, while the remainder was sequestered in the OPyC and graphitic matrix (Demkowicz et al. 2015b). Most of this sequestered silver is released when compacts are heated above the irradiation test temperature at the beginning of a safety test, and additional release through intact SiC during the several hundred hours of safety testing is negligible at 1,600°C and 1,700°C (Morris et al. 2014). The AGR-2 UO_2 compacts exhibited the expected release of sequestered silver when heated to 1,500, 1,600, and 1,700°C. Initial ^{110m}Ag releases were 0.5–1.4% of the compact inventory. The variation between compacts can be assumed to be due to the amount sequestered in the OPyC and graphitic matrix of each compact, rather than the safety test temperature. Similar initial ^{110m}Ag compact fractions of 0.7–2.1% were released from the AGR-2 Capsule 2 and Capsule 5 UCO compacts, while the lower burnup AGR-2 Capsule 6 UCO compacts released 0.14–0.30%. Additional ^{110m}Ag release observed later in each AGR-2 UO_2 compact safety test was mostly related to particle failure.

Figure 3-6 shows the fractional release of ^{110m}Ag from Compact 3-1-1, and Figure 3-7 shows the same data in terms of the fractional release rate. After the initial release of ^{110m}Ag sequestered in the OPyC and matrix when the compact was heated to 1,500°C, the ^{110m}Ag release rate dropped but was still sufficient to produce a measurable accumulation as the safety test progressed. There was a spike in the ^{110m}Ag release rate after 258 h at 1,500°C that corresponded with the spike in the cesium release rate (Figure 3-3). No ^{110m}Ag was measured on the last four cups, which is why the ^{110m}Ag release rate was zero later in the test. However, this may be an analysis artifact related to the relatively higher cesium activity. Nevertheless, 0.77 particle equivalents of ^{110m}Ag were measured after the uptick in the release rate. The timing of this uptick in ^{110m}Ag release and the amount of the release indicates that it was associated with the particle with SiC failure (Hunn et al. 2020).

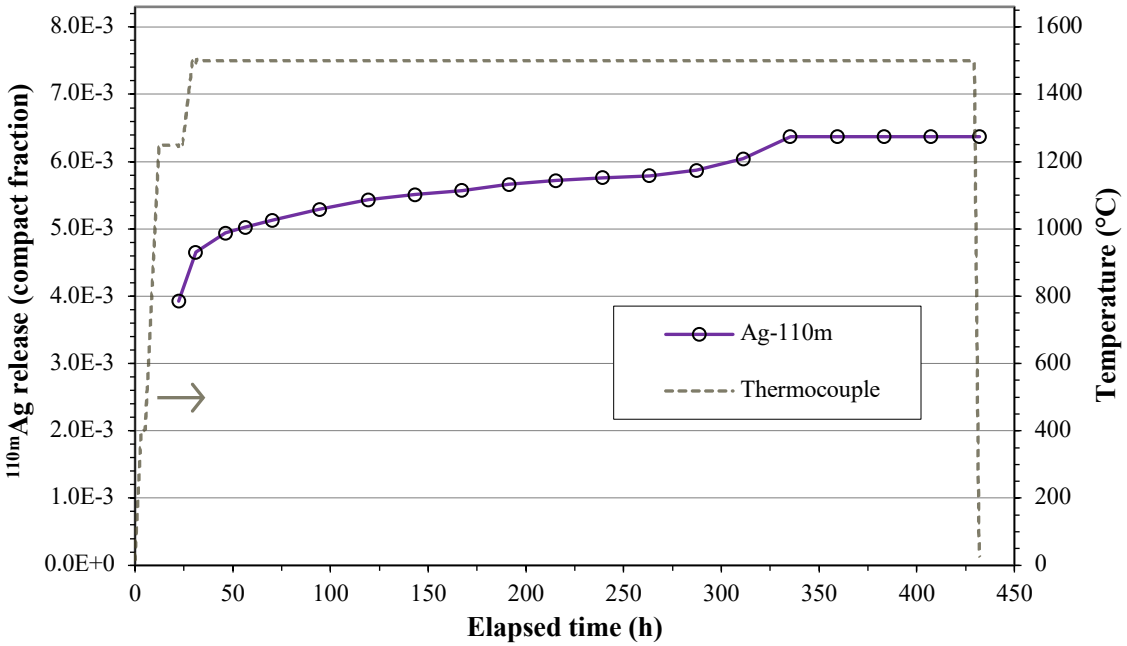

Figure 3-6. Fractional release of ^{110m}Ag from Compact 3-1-1 during a 1,500°C safety test.

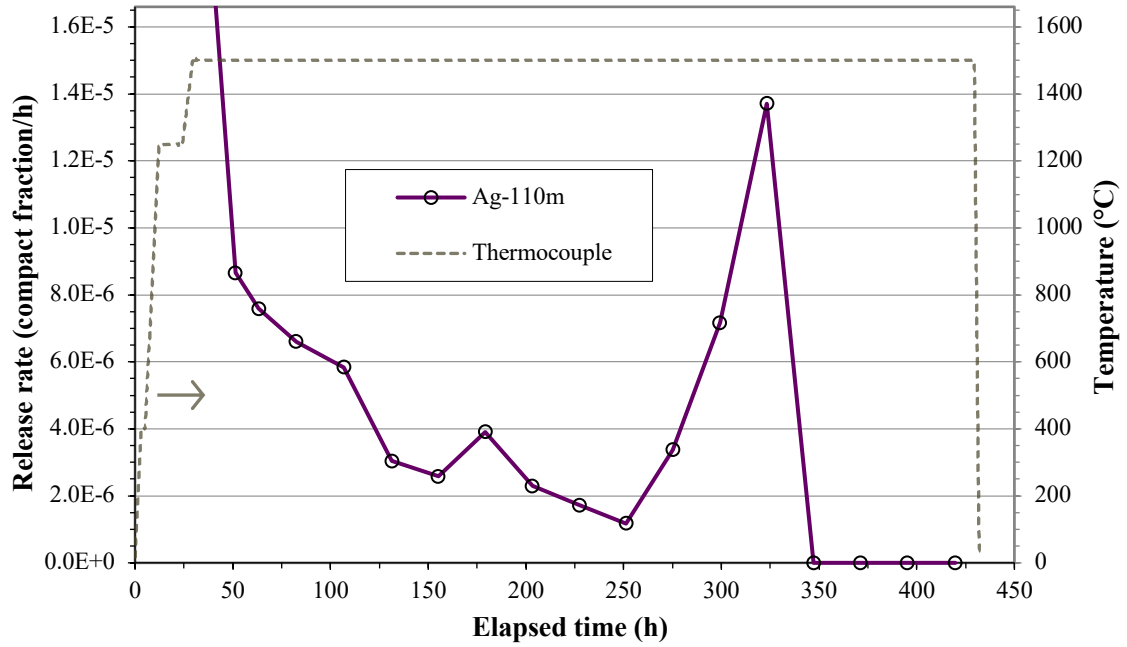

Figure 3-7. Silver release rate from Compact 3-1-1 during a 1,500°C safety test.

Figure 3-8 and Figure 3-9 show the ^{110m}Ag, ^{134}Cs, ^{137}Cs, and ^{90}Sr release rates during the 1,600°C safety tests of Compact 3-3-2 and 3-4-2, respectively, and Figure 3-10 shows the release rates for these isotopes during the 1,700°C safety test of Compact 3-4-1. An interruption in the Compact 3-4-2 safety test is indicated in Figure 3-9 by a temporary drop in temperature from 1,600°C to room temperature. This was the result of a furnace shutdown when the water-cooled power line clogged (Hunn et al. 2015a). As was observed during the Compact 3-1-1 safety test at 1,500°C, there was a decrease in the ^{110m}Ag release rates after the start of the 1,600°C and 1,700°C safety tests that indicated a depletion of the ^{110m}Ag sequestered in the OPyC and graphitic matrix, then the rates increased concurrently with the cesium release. It can be presumed that this latter increase in the ^{110m}Ag release rate was dominated by ^{110m}Ag coming out of the particles with failed SiC. Table 3-3 shows the particle equivalents of ^{110m}Ag that were released before and after the onset of SiC failure. The relative amounts of ^{110m}Ag released after onset of SiC failure were consistent with the relative number of particles with failed SiC in each compact.

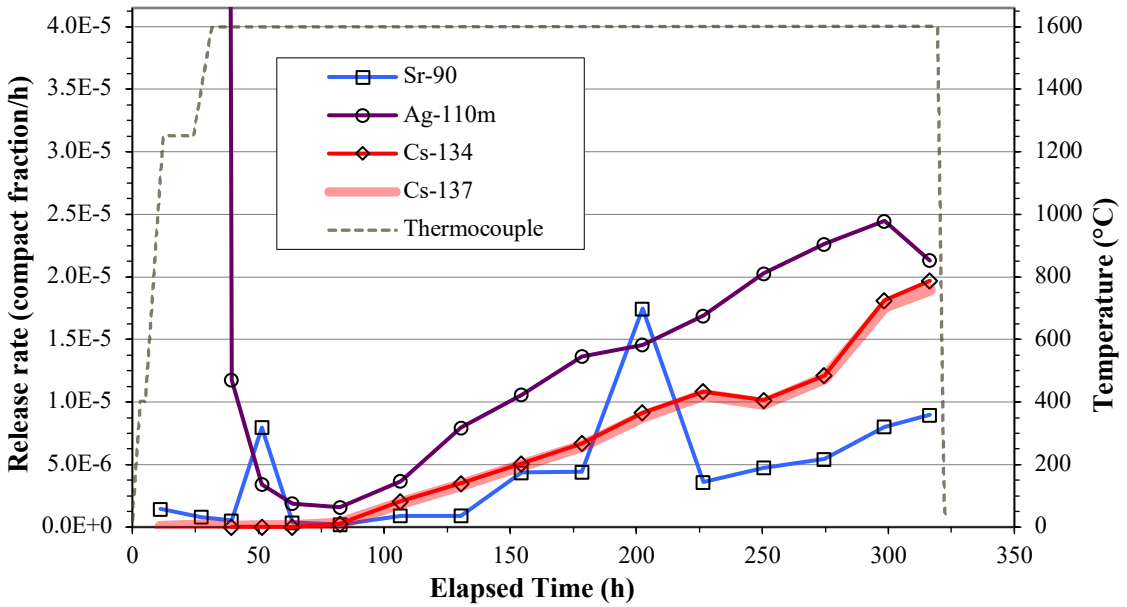

Figure 3-8. Silver, cesium, and strontium release rates from Compact 3-3-2 during a 1,600°C safety test.

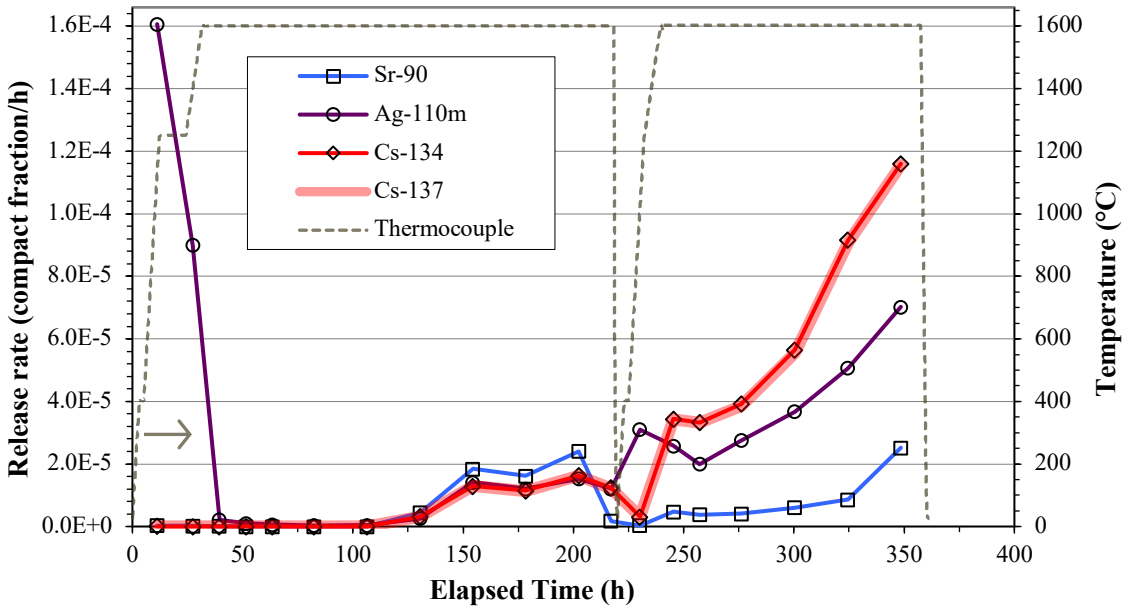

Figure 3-9. Silver, cesium, and strontium release rates from Compact 3-4-2 during a 1,600°C safety test.

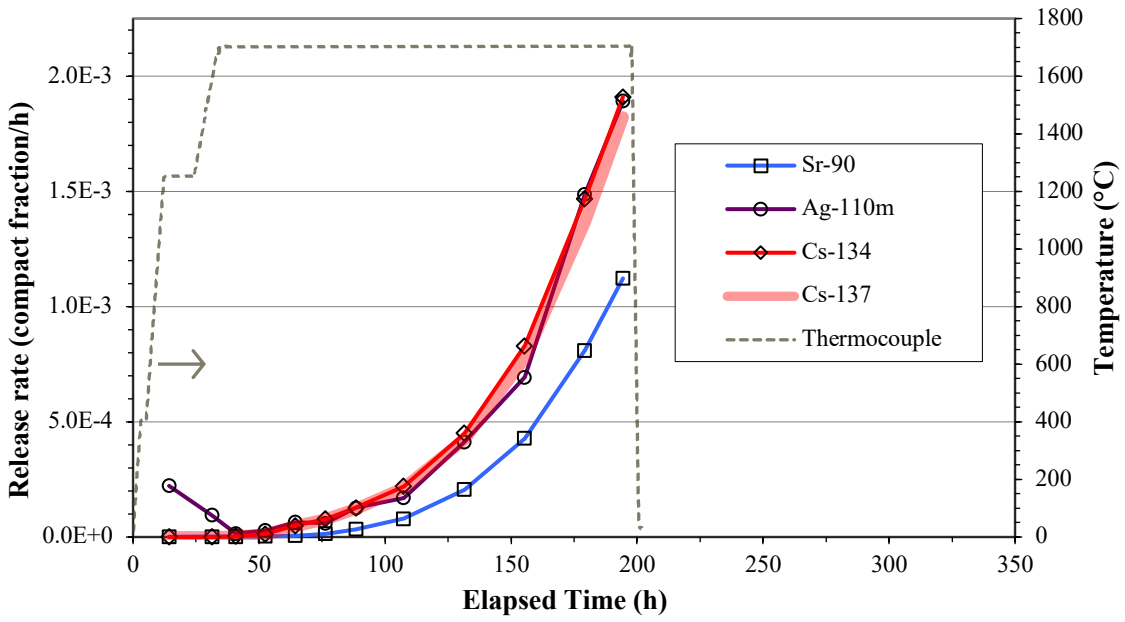

Figure 3-10. Silver, cesium, and strontium release rates from Compact 3-4-1 during a 1,700°C safety test.

Table 3-3. Particle equivalents of ^{110m}Ag released before and after onset of SiC failure

Safety Test	^{110m}Ag released before onset of SiC failure	^{110m}Ag released after onset of SiC failure
Compact 3-1-1 at 1,500°C	9.06	0.77
Compact 3-3-2 at 1,600°C	21.2	5.4
Compact 3-4-2 at 1,600°C	7.1	10.4
Compact 3-4-1 at 1,700°C	10.6	127.1

3.4 STRONTIUM AND EUROPIUM RELEASE DURING SAFETY TESTING

The cumulative ^{154}Eu releases from the four safety tested AGR-2 UO_2 compacts were relatively low (Table 3-2), and time dependent estimates based on activity on the deposition cups had little meaning due to the low fraction of released europium that accumulated on the cups (Table 3-4). Most of the europium released from each compact during safety testing was trapped in the graphite holder, which was analyzed at the end of the test. The relative amounts of ^{154}Eu from each test (Table 3-2) were consistent with the relative number of particles in each compact that experienced SiC failure, but the magnitude of ^{154}Eu releases indicated only a small fraction of the europium inventory in the particles with failed SiC was released. High retention of europium in UO_2 TRISO particles with failed SiC is not unexpected given that europium is expected to form a stable oxide in the UO_2 kernel (Homan et al. 1977).

Table 3-4. Cumulative fractions of radioactive isotopes collected on deposition cups

Safety Test	^{90}Sr	^{110m}Ag	^{134}Cs	^{137}Cs	^{154}Eu
Compact 3-1-1 at 1,500°C	12.4%	~100%	98.3%	89.6%	6.5%
Compact 3-3-2 at 1,600°C	2.8%	32.2%	19.9%	19.7%	1.5%
Compact 3-4-2 at 1,600°C	4.2%	35.7%	18.9%	18.7%	0.1%
Compact 3-4-1 at 1,700°C	29.4%	100%	98.6%	98.4%	6.5%

Note: The fractions collected on the cups during the 1,600°C safety tests were particularly low due to an inadvertently reversed helium sweep gas flow.

The cumulative release of ^{90}Sr during the 1,500°C safety test of Compact 3-1-1 was low (Table 3-2). There was a barely discernable increase in the ^{90}Sr release rate after the onset of SiC failure, as shown in Figure 3-11. This increase may have been related to the particle failure but could also be explained by slow transport of strontium through the graphite holder. The cumulative releases of ^{90}Sr during the 1,600°C and 1,700°C safety tests of the AGR-2 UO_2 compacts were notably higher than what was observed at 1,500°C (Table 3-2), and the rate plots in Figure 3-8, Figure 3-9, and Figure 3-10 show that the ^{90}Sr release tended to track with the releases of ^{134}Cs, ^{137}Cs, and ^{110m}Ag from particles with failed SiC. This was especially evident for the 1,700°C safety test, in which the number of particles with failed SiC was the highest. The apparent lag in the ^{90}Sr release vs. the ^{134}Cs, ^{137}Cs, and ^{110m}Ag, as plotted in Figure 3-10, may be due to a combination of factors including the slower transport of strontium to the deposition cups and a higher retention in the UO_2 kernel. However, it is clear that any impact of kernel retention of strontium was much less effective than for europium. The relative behavior of strontium and europium in the AGR-2 UO_2 safety tests was significantly different than that observed in AGR-2 UCO safety tests, in which strontium release typically tracked with europium and was slightly lower (e.g., Figure 3-12).

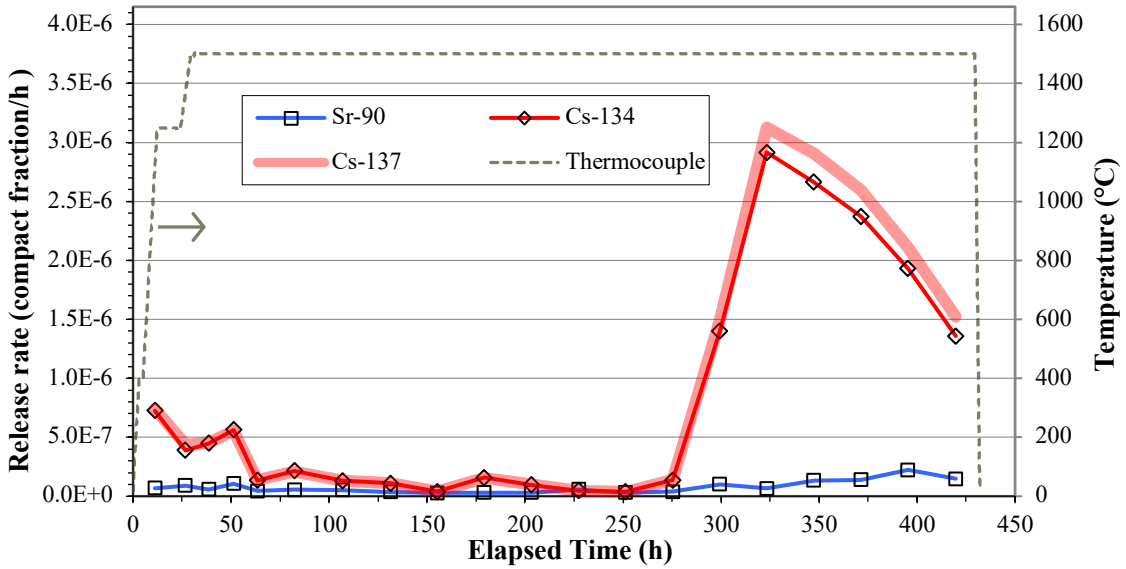

Figure 3-11. Strontium and cesium release rates from Compact 3-1-1 during a 1,500°C safety test.

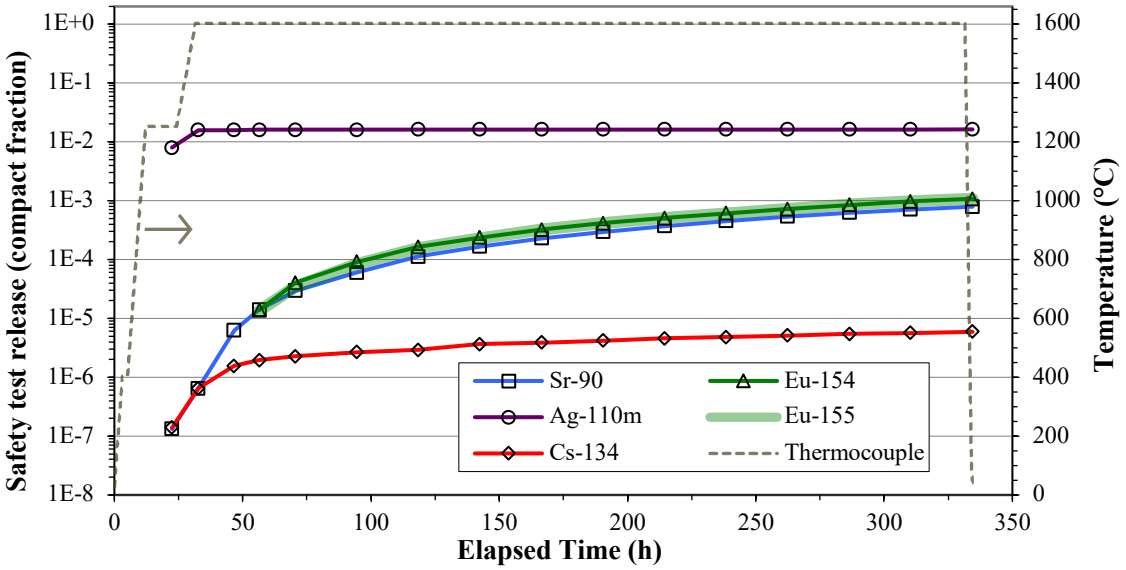

Figure 3-12. Release of fission products from AGR-2 UCO Compact 5-2-2 during a 1,600°C safety test.

4. DECONSOLIDATION AND LEACH-BURN-LEACH ANALYSIS

The AGR-2 UO_2 compacts were deconsolidated and subjected to the standard DLBL procedure described in Section 2.2 (with noted exceptions) to recover the TRISO particles for survey with the IMGA and to measure the amount of exposed actinides and fission products remaining in the compact. Appendix A contains tabulated data for each compact in three general groupings of selected isotopes: (1) some of the more abundant uranium and plutonium isotopes, (2) various radioactive isotopes that are typically measured and tracked during AGR PIE, and (3) several stable isotopes that may be of interest. The ^{238}U isotope is a useful indicator for exposed kernels due to its abundance in the kernel, relatively low release through intact SiC layers during irradiation and safety testing, and relatively high solubility in nitric acid. Table 4-1 is a compilation of the ^{238}U detected in each leach solution during the DLBL analysis of the six AGR-2 UO_2 compacts. While the ^{238}U values in Table 4-1 are used in this section's discussions regarding the kernels exposed during the DLBL analyses, it is worth noting that the observations are also supported by the measured values for ^{235}U, ^{236}U, and ^{144}Ce reported in Appendix A, which correlated well with the ^{238}U. Although less abundant than ^{238}U and hampered by a relatively short half-life (285 d) when PIE is performed several years after EOL, the ^{144}Ce isotope, in particular, is a useful secondary indicator for exposed kernels because its analysis is independent of the mass spectrometry used to measure uranium. Table 4-1 is duplicated at the end of Appendix A, and a similar table for ^{144}Ce is provided for easy comparison.

Table 4-1. ^{238}U detected in DLBL solutions

DLBL Step	3-1-2	3-3-1	3-1-1	3-3-2	3-4-2	3-4-1
Deconsolidation acid [a]		8.18E-6 (0.013)	3.75E-6 (0.0058)	2.24E-6 (0.0035)	1.93E-6 (0.0030)	
Preburn leach 1	2.82E-5 (0.043)	4.68E-6 (0.0072)	1.17E-6 (0.0018)	1.38E-3 (2.137)	4.49E-4 (0.692)	
Preburn leach 2 [b]	7.34E-5 (0.113)	2.93E-6 (0.0045)	6.72E-6 (0.010)	8.00E-4 (1.235)	1.26E-3 (1.938)	
Postburn matrix leach 1 [c]	6.55E-4 (1.011)	5.52E-5 (0.085)	6.85E-4 (1.058)	4.15E-4 (0.640)	1.41E-3 (2.170)	2.96E-3 (4.562)
Postburn matrix leach 2	3.77E-6 (0.0058)	2.40E-6 (0.0037)	6.68E-6 (0.010)	1.15E-5 (0.018)	1.01E-4 (0.156)	1.78E-6 (0.0027)
Postburn particle leach 1	2.89E-3 (4.466)	6.37E-6 (0.0098)	1.49E-5 (0.023)	6.74E-6 (0.010)	4.74E-3 (7.314)	1.47E-3 (2.263)
Postburn particle leach 2	1.06E-5 (0.016)	1.87E-6 (0.0029)	4.62E-6 (0.0071)	1.89E-6 (0.0029)	4.56E-6 (0.0070)	4.96E-6 (0.0077)
Subtotal of ^{238}U removed before IMGA survey	7.61E-4 (1.174)	7.34E-5 (0.113)	7.04E-4 (1.086)	2.61E-3 (4.032)	3.21E-3 (4.960)	2.96E-3 (4.565)
Total	3.67E-3 (5.656)	8.17E-5 (0.126)	7.23E-4 (1.116)	2.62E-3 (4.046)	7.96E-3 (12.281)	4.43E-3 (6.835)

Note: Values are reported as compact inventory fractions and particle equivalents (in parentheses).
[a] The deconsolidation acid from Compact 3-1-2 was combined with the first preburn leach acid.
[b] The second preburn leach values for Compacts 3-3-2 and 3-4-2 include analyses of a subsequent water rinse.
[c] The first postburn matrix leach values for Compact 3-4-1 include analyses of prior leach solutions.

There were <0.13 particle equivalents of ^{238}U detected during DLBL of as-irradiated Compact 3-3-1. This indicated that no kernels were exposed in this compact, neither because of particles with failed TRISO in the preburn leaches nor because of particles with failed SiC in the postburn particle leaches. The relative amounts of ^{238}U in each leach solution indicated that the uranium was primarily in the matrix. There were 0.013 particle equivalents of ^{238}U, about 10% of the total, in the room temperature deconsolidation acid.

The two subsequent hot leaches of the deconsolidated particles and matrix debris removed progressively less ^{238}U, and together accounted for 9% of the total leached ^{238}U. The progressive reduction in the quantity leached indicates that the uranium available at that stage of the process was being reduced and no additional sources were being made available. After the second preburn leach, the particles and matrix debris were boiled in acid to further digest the matrix and remove residual matrix from the surface of the TRISO particles before sieving to separate the particles from the digestion acid and matrix debris (Figure 2-2). There were 0.048 particle equivalents of ^{238}U in the digestion acid, which was 10× more than what was leached in the second preburn leach. This increase indicated that uranium in the undigested matrix was previously inaccessible to the hot acid in the two 24 h hot acid extractions in the Soxhlet device. The digestion acid values are not included in Table 4-1 because the dissolved actinides and fission products in that acid remained with the matrix debris in the quartz vessel when the digestion acid was distilled off before the burn (Hunn and Montgomery 2020). There were 0.089 particle equivalents of ^{238}U detected in the postburn matrix leaches, which was about 71% of the total ^{238}U detected during DLBL. The increase in this value over the digestion acid further indicated that some uranium in the matrix debris remained inaccessible by the hot acid until the matrix was fully disassociated by the burn. There were 0.012 particle equivalents of ^{238}U, about 10% of the total, detected during the particle burn-leach. This came from chunks of undeconsolidated matrix picked out of the particle sample before IMGA survey, residual matrix on the TRISO particles, and any uranium in the OPyC. The source of most of the exposed uranium in Compact 3-3-1 was probably minor diffusive release from the TRISO particles during irradiation, as the observed fraction was significantly higher than the average fraction of uranium contamination in the as-fabricated AGR-2 UO_2 compacts, which was determined to be $\sim 1 \times 10^{-6}$ via DLBL analysis of 75 compacts that contained no particles with defective SiC or defective TRISO (Hunn, Savage, and Silva 2010).

The acid from the deconsolidation of as-irradiated Compact 3-1-2 was included in the first preburn leach acid. There were 0.043 particle equivalents of ^{238}U in the first preburn leach acid, which was about double what was detected during the deconsolidation and first preburn leach of Compact 3-3-1, but still low enough to rule out the presence of particles with failed TRISO. However, the of ^{238}U in the second preburn leach was higher (0.113 particle equivalents), which suggested that a kernel may have been exposed at some point during that stage. During the pot boil to further digest the matrix debris before sieving out the particles, 1.05 particle equivalents of ^{238}U were detected, indicating at least one kernel was exposed and leached prior to sieving. As discussed in Section 5.2, one particle with a leached kernel (Particle 312-SP02) was recovered during the IMGA survey and imaged with XCT. Particle 312-SP02 is discussed further in Sections 5.2 and 8.1. There were 1.02 particle equivalents of ^{238}U detected in the postburn matrix leaches, which was consistent with the value measured in the digestion acid and related to the same exposed kernel. There were 4.466 particle equivalents of ^{238}U in the first postburn particle leach, and 0.016 particle equivalents of ^{238}U in the second postburn particle leach, which indicated that the exposed uranium had been effectively dissolved in the first leach. The uranium detected in the postburn particle leaches was likely related to exposed kernels and kernel fragments from particles fractured during IMGA. As discussed in Section 5.2, there were observations of fragments from broken particles during IMGA survey of the Compact 3-1-2 particles that were probably caused by operational problems with the IMGA.

The amounts of ^{238}U in the deconsolidation acid and first preburn leach of the particles and matrix debris from 1,500°C safety-tested Compact 3-1-1 were both <0.01 particle equivalents. This confirmed that no kernels were exposed, as expected from the low ^{85}Kr release during safety testing, which had already indicated there were no particles with failed TRISO. The amount of ^{238}U in the second preburn leach was 0.010 particle equivalents. While this was a small amount, the fact that the second leach was not lower than the first indicated conditions may have changed. The first postburn leach of the matrix debris contained 1.06 particle equivalents of ^{238}U, and this level of uranium was also detected in the digestion acid prior to sieving. This level of uranium in the deconsolidation acid indicated a kernel was exposed during or just before that step in the procedure. As discussed in Section 5.3, no particles with low cesium were identified and separated out during the IMGA survey. Therefore, the one exposed kernel detected during DLBL was likely from the particle with failed SiC that released cesium during safety testing. The

kernels in particles with failed SiC are sometimes leached during the preburn DLBL stages as a result of fracture of the intact pyrocarbon layer, usually the OPyC, which would have previously prevented release of fission gases. These particles are sometimes recovered for analysis (see Figure 5-26 for an example), but it is not unusual for the particle coatings to fragment into pieces, which is apparently what happened in this case. The small uptick of ^{238}U observed in the second preburn leach suggests that the kernel was exposed at the end of the second preburn leach, perhaps when the particles and matrix debris in the Soxhlet thimble were rinsed to collect residual acid after removing the thimble from the Soxhlet extraction apparatus. This would have resulted in a small amount of uranium dissolving in the rinse solution. The total amount of ^{238}U in the postburn particle leaches was 0.03 particle equivalents, which indicated that no particles with failed SiC were missed during the IMGA survey and included in the particle burn-leach.

The deconsolidation acids from 1,600°C safety-tested Compacts 3-3-2 and 3-4-2 showed negligible concentrations of ^{238}U. This supported the safety test conclusions that there were no particles with failed TRISO in these compacts. However, subsequent leaching of the particles from these two compacts indicated kernels were exposed at various stages of the DLBL. There were 4.03 particle equivalents of ^{238}U detected in the DLBL analysis of the particles and matrix debris before the IMGA survey of the Compact 3-3-2 particles (i.e. the total in all DLBL solutions except from the two postburn particle leaches). As discussed in Section 5.4, four particles associated with this dissolved uranium were found during the IMGA survey and XCT showed that most of their kernel material was absent. These particles had fractured IPyC and failed SiC as a result of safety testing, and cracks in the OPyC layer that presumably occurred during the DLBL. There were 4.96 particle equivalents of ^{238}U detected in the pre-IMGA DLBL analysis of the particles and matrix debris from Compact 3-4-2. IMGA survey found four particles whose kernel material had been mostly removed and one particle (Particle 342-SP06) that had partial kernel leaching (Section 5.5). This left ~1 particle equivalent of uranium unaccounted for, and it is possible that there was a Compacts 3-4-2 particle with failed SiC that was broken during DLBL and not recovered. There were no indications in the postburn leaches of the particles from Compact 3-3-2 for the presence of particles with failed SiC or particles damaged by the analysis. However, 7.32 particle equivalents of ^{238}U were dissolved during the postburn leaches of the particles from Compact 3-4-2. As discussed in Section 5.5, this uranium may have been from particles with failed SiC that were not sorted out by the IMGA survey because their cesium release was not high enough to segregate them from the normal particles.

Because of the number of expected particles with failed SiC in the 1,700°C safety-tested Compact 3-4-1, the standard DLBL procedure was modified to minimize the steps before sieving out particles for IMGA survey. The two preburn leaches of particles and matrix debris in the Soxhlet extractor shown in Figure 2-2 were skipped. After compact deconsolidation, the particles and matrix debris were digested by boiling in acid and then the mixture was poured through a sieve stack to collect the particles and larger pieces. The acid slurry with the matrix fines was decanted for analysis, but only about two thirds of the acid could be decanted without including too much of the matrix debris. Two additional preburn leaches of the matrix debris were performed after adding fresh acid to maximize uranium recovery prior to the matrix burn. The ^{238}U measured in the three preburn solutions is included in the first matrix postburn leach value of 4.56 particle equivalents reported in Table 4-1; most of this was in the acid used for deconsolidation and digestion. Five particles with obviously missing kernel material were found with the IMGA, but more than these five particles may have been associated with the ^{238}U detected in the DLBL analysis of the particles prior to IMGA survey. Post-IMGA DLBL of the particles from Compact 3-4-1 resulted in the leaching of 2.27 particle equivalents of ^{238}U, which may have come from particles with failed SiC. However, many more particles with failed SiC were expected in the postburn particle leaches based on the cesium release in the CCCTF and the cesium retained in the particles surveyed with the IMGA, as discussed in Section 5.6. Particles that released a significant fraction of their cesium inventory were classified as having *failed SiC* in Section 2.1. However, some particles with degraded SiC that released cesium may not have had damage structures that were susceptible to oxidation during the burn. This appeared to be the case for many low-cesium particles analyzed from Compact 3-4-1.

5. IMGA SURVEY AND XCT OF SPECIAL PARTICLES

Additional insights regarding particle performance during irradiation and safety testing were provided by measuring the inventory of key gamma-emitting fission products with the IMGA. A survey of all particles recovered from each compact was performed using a short counting time, which was initially 100 s, and progressively increased up to 300 s as radioactive inventory decayed over the five-year time span between survey of Compact 3-3-2 and Compact 3-1-2. After IMGA survey, special particles and a subset of ~45 randomly-selected particles were counted for 6 h each. Results of the IMGA surveys are presented in this section and the 6 h data are provided in Appendix B.

5.1 AS-IRRADIATED COMPACT 3-3-1

Figure 5-1 and Figure 5-2 show the normalized activities of ^{144}Ce and ^{137}Cs in 1462 particles from as-irradiated Compact 3-3-1, respectively. One particle had very low ^{144}Ce M/A and ^{137}Cs M/A, so this particle was labeled Particle 331-SP01 and designated for microstructural analysis. Figure 5-3 shows the ^{137}Cs M/C of Particle 331-SP01 as off-scale because the very low ^{144}Ce activity resulted in a ratio of 4.2. The other particles from Compact 3-3-1 exhibited a normal ^{137}Cs M/C distribution with no outliers.

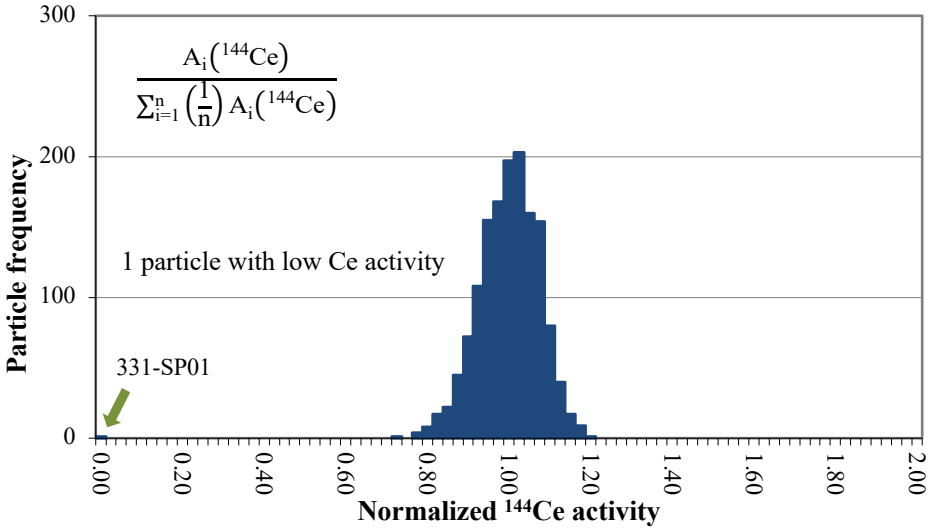

Figure 5-1. Normalized ^{144}Ce activity in 1462 particles from Compact 3-3-1.

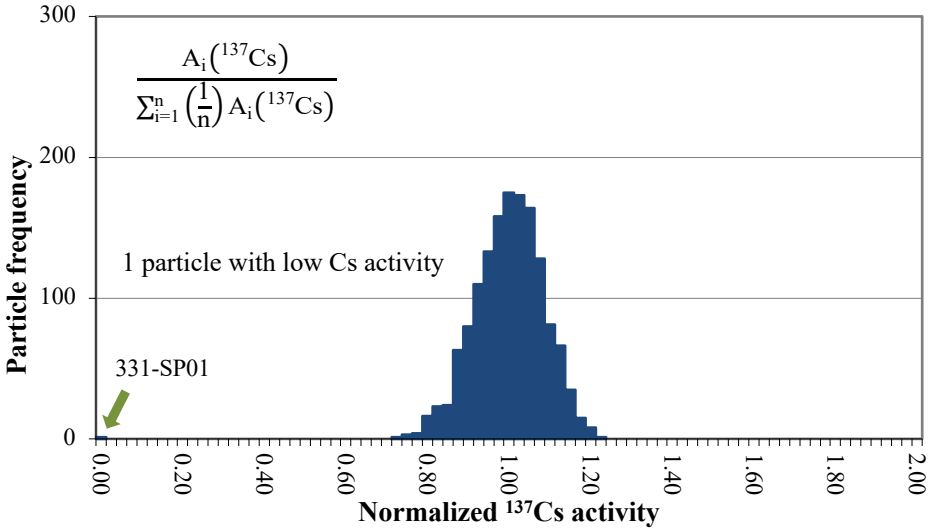

Figure 5-2. Normalized ^{137}Cs activity in 1462 particles from Compact 3-3-1.

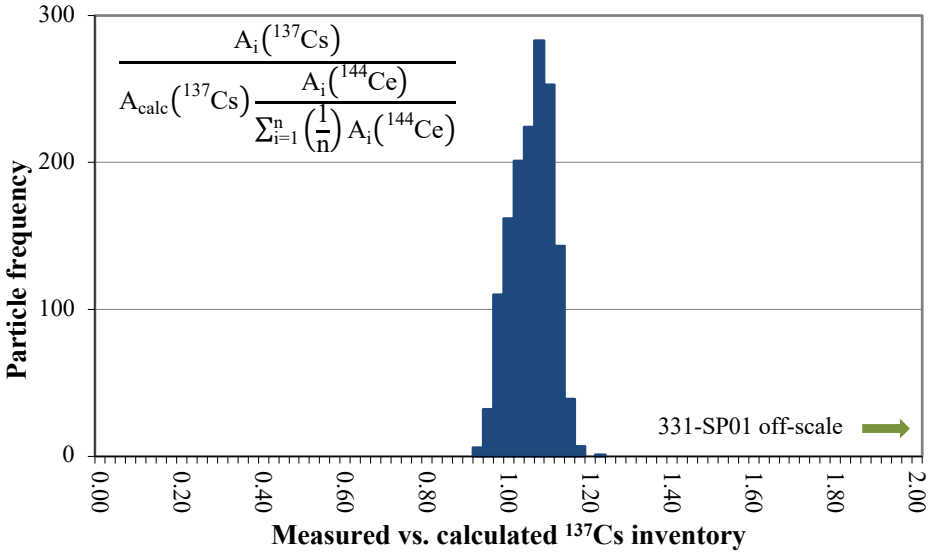

Figure 5-3. Measured vs. calculated ^{137}Cs inventory in 1462 particles from Compact 3-3-1.

Figure 5-4a shows a representative x-ray tomogram of a random midplane through Particle 331-SP01. There were no indications of damage to the three outer coating layers, the buffer exhibited typical densification and resultant detachment of the bulk of the buffer layer from the buffer/IPyC interface, and there was no indication of missing kernel material to explain the low activity. Figure 5-4b shows an optical micrograph taken after grinding and polishing to near midplane. The kernel is a ZrO_2 ceramic sphere with a diameter of ~520 µm. After fabrication of the AGR-2 UCO TRISO particles, seven surrogate particle coating runs (93077–93083) were performed using the BWXT pilot-scale FB-CVD coating furnace (Barnes and Marshall 2009). Four of these runs deposited TRISO coatings on 520 µm diameter ZrO_2 kernels. The AGR-2 UO_2 TRISO particles were coated in run number 93085, shortly after completion of the ZrO_2 runs. Particle 331-SP01 should have buffer and IPyC deposition conditions essentially identical to the AGR-2 UO_2 TRISO particles, and it has experienced the same irradiation conditions without interaction from a fissioning kernel. Study of this particle may provide valuable information on radiation-induced changes in the buffer layer separate from the effects of kernel swelling, fission product recoil, and chemical reaction with the UO_2 kernel and its fission products.

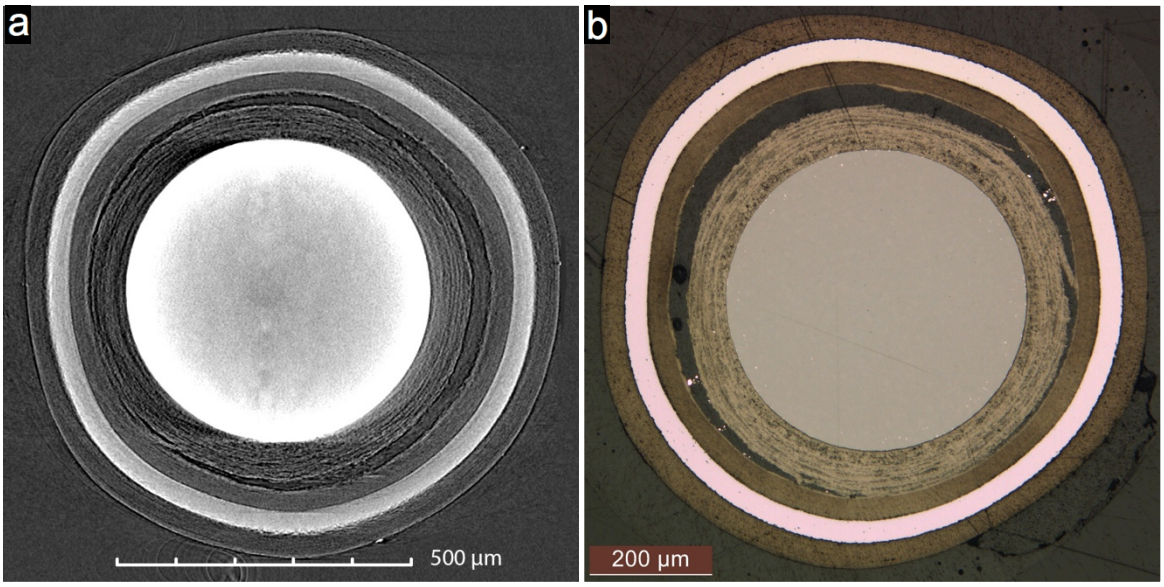

Figure 5-4. (a) X-ray tomogram through the center of Particle 331-SP01, and (b) optical micrograph of a polished section near midplane showing ZrO_2 kernel.

Particle 331-SP04 was a special particle picked out prior to the IMGA survey because of its dimpled geometry, as shown in Figure 5-5a. This geometry has been observed in as-fabricated fuel particles and multiple studies have shown it to often be the result of fragmentation of the kernel prior to coating. Prior to compacting at ORNL, the AGR-2 UO_2 TRISO particle batch was sorted using a rollermicrometer (Hunn, Montgomery, and Pappano 2010). Six uncoated kernels and several broken TRISO coating fragments were removed, as were 18 small or highly aspherical particles segregated to the 825–850 µm bin. There were numerous dimpled particles observed among several thousand particles (~0.8% of the total population) in the 850–875 µm rollermicrometer bin. These particles were retained in the compacted batch, based on a program decision to not upgrade the fuel batch beyond what would be representative of the pilot-scale process employed by BWXT. The XCT image in Figure 5-5b shows the kernel fragment and the resultant coating structure in Particle 331-SP04. The particle was gamma counted for 6 h and results are shown in Appendix Table B-2. Ignoring ^{110m}Ag for the moment, the particle M/A values showed that Particle 331-SP04 had 88–91% of the activity in an average particle, due to the missing kernel material at the start of the irradiation; however, the M/AA values were close to unity, which indicated normal fission product retention. There were also no obvious cracks or degraded regions in the layers that would be expected if this particle had failed SiC. For comparison, a particle in AGR-1 Compact 4-1-2 had a dimpled shape due to soot inclusions between the buffer and IPyC. This particle also survived irradiation without failure but experienced SiC failure during 1,600°C safety testing when the SiC cracked along the rim of the dimple where stress was concentrated by the high curvature (Hunn et al. 2014a). Particle 331-SP04 was not the only Compact 3-3-1 particle with reduced M/A values but M/AA values near unity. Particles 331-RS26 and 331-RS30 also had M/A values below 0.9 but M/AA values near unity, which indicated these particles probably contained undersized or fragmented kernels as well. Visual inspection of these particles revealed faceted coatings consistent with fragmented kernels.

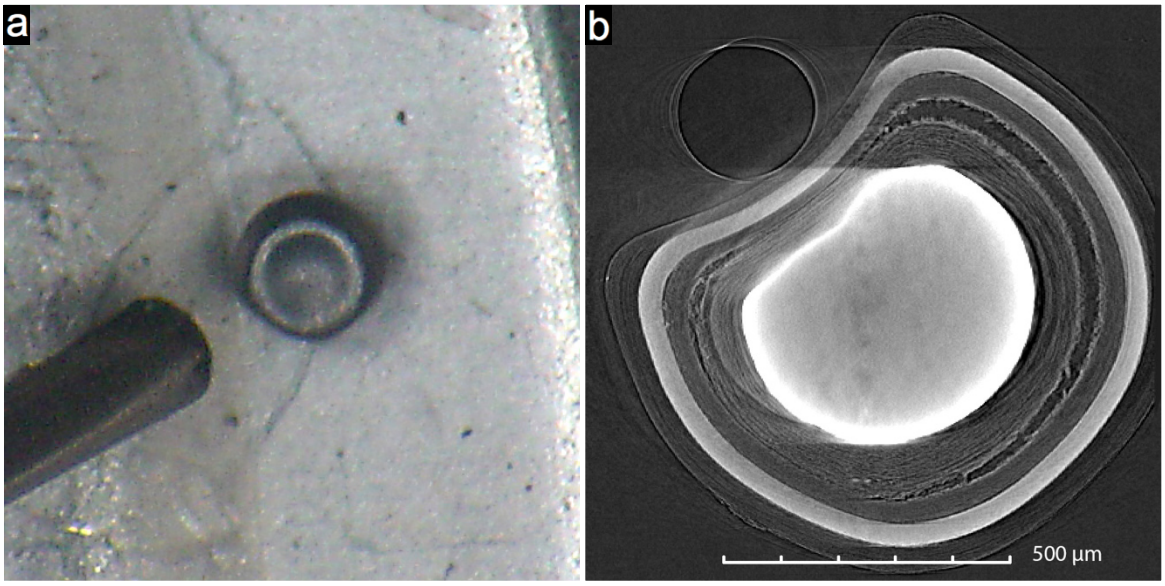

Figure 5-5. (a) Photograph of dimpled Particle 331-SP04 isolated during pre-IMGA inspection, and (b) x-ray tomogram through the center showing the responsible aspherical kernel fragment.

Figure 5-6 is a histogram of the Compact 3-3-1 ^{154}Eu M/C data in Appendix Table B-2. As discussed in Appendix B, the offset from unity for the mean ^{154}Eu M/C value does not indicate europium release. This mean value was typical for the AGR-1 and AGR-2 irradiations, and the offset was due to a systematic error in the predicted inventory value determined via the physics calculations (Sterbentz 2014). The DLBL analysis of Compact 3-3-1 (Appendix Table A-8), PGS scans of the Capsule 3 compact and holder (Harp, Demkowicz, and Stempien 2016), and mass balance analysis for Capsule 3 (Stempien and Demkowicz 2020) together indicated very little ^{154}Eu release from Compact 3-3-1 particles. The 3.1% standard deviation (SD) in the ^{154}Eu M/C values indicated minimal particle-to-particle variability in the ^{154}Eu inventory, and there were no outliers in the random sample of 36 particles.

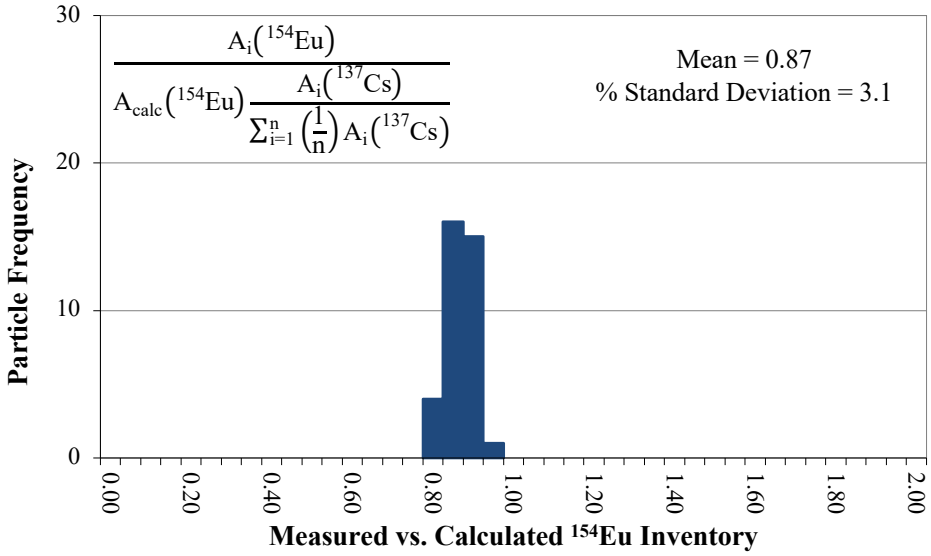

Figure 5-6. Measured vs. calculated ^{154}Eu inventory in 36 particles from Compact 3-3-1.

The ^{110m}Ag capsule fraction measured on the Capsule 3 components was 0.13 (Stempien and Demkowicz 2020), in which capsule fraction was defined similarly to compact fraction as the measured activity divided by the calculated activity for the whole capsule (Section 2.1). Figure 5-7 is a histogram of the Compact 3-3-1 ^{110m}Ag M/C data tabulated in Appendix Table B-2. The 36 RS particles measured with IMGA exhibited a very broad distribution centered at a ^{110m}Ag M/C value of 0.90. The shift in the distribution to a mean value less than unity was consistent with the expectation from the Capsule 3 analysis of a measurable average ^{110m}Ag release, and the magnitude of the shift was consistent with the compact fraction of ^{110m}Ag measured in Compact 3-3-1 by PGS of 0.94±0.01 (Harp, Demkowicz, and Stempien 2016). The exposed ^{110m}Ag compact fraction of 1.8E-3 measured by DLBL was relatively low (Appendix Table A-8), suggesting that what was released by the particles was not retained well in the matrix. While it is clear that silver was released by at least some of the particles in Compact 3-3-1, it is difficult to determine based on the individual ^{110m}Ag M/C values how much each particle released. The fact that about one-third of the RS particles exhibited values above unity, with one as high as 1.39, indicated that there was considerable uncertainty in the ^{110m}Ag M/C values. This uncertainty included both measurement uncertainties and uncertainty in the ^{110m}Ag inventory generated in each particle by the irradiation.

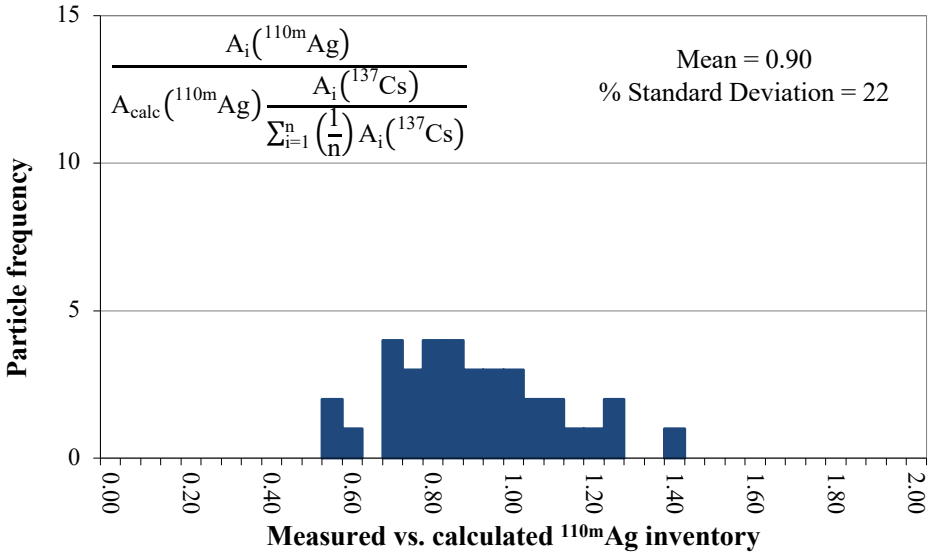

Figure 5-7. Measured vs. calculated ^{110m}Ag inventory in 36 particles from Compact 3-3-1.

5.2 AS-IRRADIATED COMPACT 3-1-2

IMGA survey of Compact 3-1-2 was performed about six years after EOL. While the ^{144}Ce activity was calculated to be 2.16× that of ^{106}Ru at EOL (Sterbentz 2014), the ^{106}Ru activity became higher about four years after EOL because of the difference in half-lives (372 d for ^{106}Ru vs. 285 d for ^{144}Ce). At the time the IMGA survey was performed, the ^{106}Ru activity was ~1.6× that of ^{144}Ce. The higher ^{106}Ru activity, coupled with a higher energy primary gamma peak (511.9 keV for ^{106}Ru vs. 133.5 keV for ^{144}Ce), made the ^{106}Ru a better candidate for sorting during the survey. Comparison of the histograms in Figure 5-8 and Figure 5-9 illustrates the advantage of using ^{106}Ru rather than ^{144}Ce for adjusting for particle-to-particle variation in fissionable material and burnup when calculating the ^{137}Cs M/C values using the equations described in Section 2.2. The narrower distribution in Figure 5-8 is the result of a better correlation between the measured activities of ^{137}Cs and ^{106}Ru, compared with Figure 5-9, in which the greater uncertainty in the measurement of the ^{144}Ce activity resulted in a broader ^{137}Cs M/C distribution.

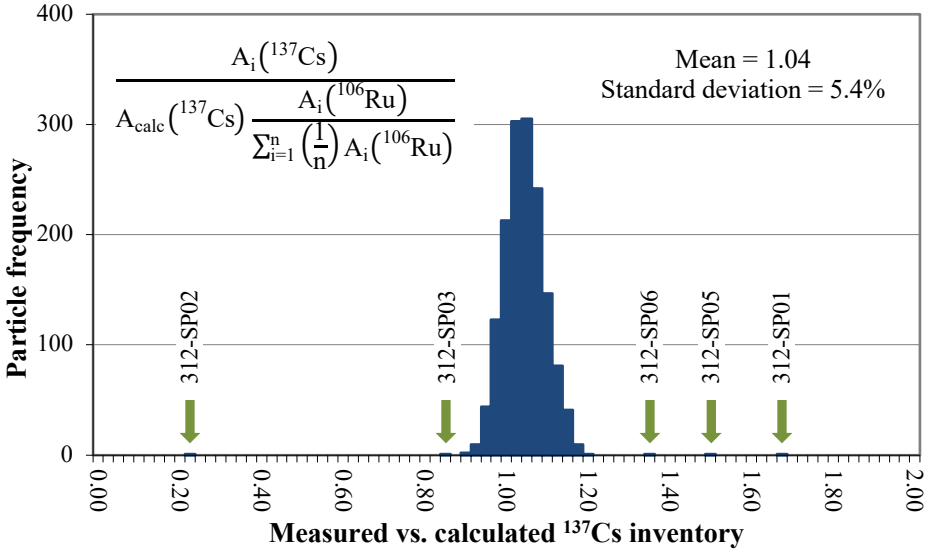

Figure 5-8. Measured vs. calculated ^{137}Cs inventory in 1527 particles from Compact 3-1-2, adjusted for particle variability using ^{106}Ru.

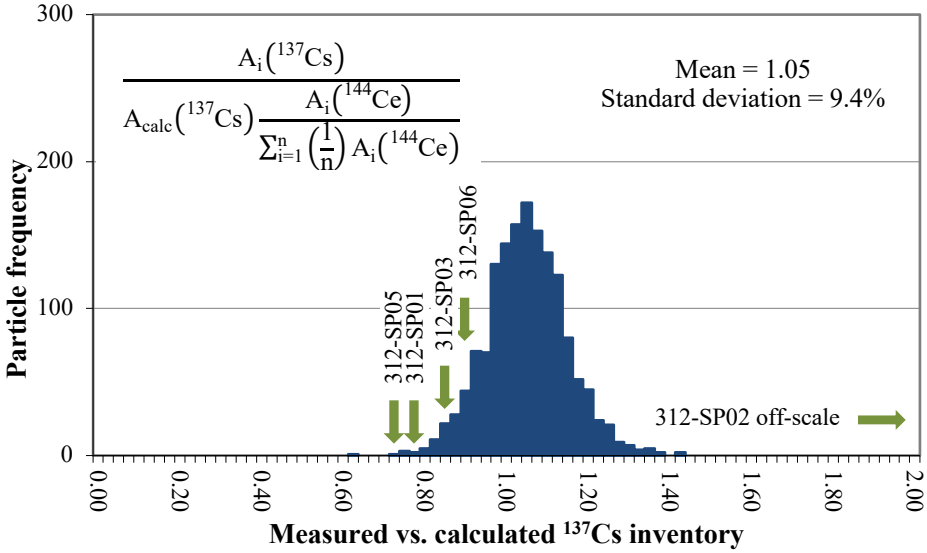

Figure 5-9. Measured vs. calculated ^{137}Cs inventory in 1527 particles from Compact 3-1-2, adjusted for particle variability using ^{144}Ce.

There were six particles with abnormal inventories identified during the IMGA survey of the particles from Compact 3-1-2. Particle 312-SP04 was picked out prior to IMGA survey because of its small size and gamma counted for 6 h. Its M/A values (Appendix Table B-1) reflected its smaller size, but its M/AA and M/C values showed that it had normal retention. Particle 312-SP03 had a slightly reduced ^{137}Cs M/C that allowed it to be distinguished from the main distribution (Figure 5-8). It was automatically sorted out during the IMGA survey based on its ^{137}Cs/^{106}Ru ratio. The particle was imaged with XCT and found to be missing its three outer layers (Figure 5-11). The Particle 312-SP03 ^{106}Ru M/A was 1.00 (Figure 5-11) and the ^{144}Ce M/A was 1.00 (Figure 5-12), but the ^{137}Cs M/A was 0.82 (Figure 5-13).The reduced cesium inventory can be explained by the fact that some of the cesium resided in the IPyC layer at the end of the irradiation, while the ruthenium and cerium were in the kernel. The coatings most likely broke off during the IMGA survey. There were numerous broken coating fragments observed in the particle hopper during the IMGA survey, and this was probably related to a problem with the IMGA operation during this run. When the IMGA picks up a particle in the hopper, it records the needle position and returns to a set distance above that position to initiate the next particle acquisition. If a funnel shape forms in the needle bed and the funnel collapses between acquisition cycles, the needle may drive down into the particle bed. This can sometimes break particles. Hopper agitation and increasing the needle back off distance between particle acquisitions are used to minimize the likelihood of particle damage. As discussed in Section 4, exposed kernels leached during the postburn particle leaches (Table 4-1) were probably related to TRISO coatings being damaged during the IMGA survey.

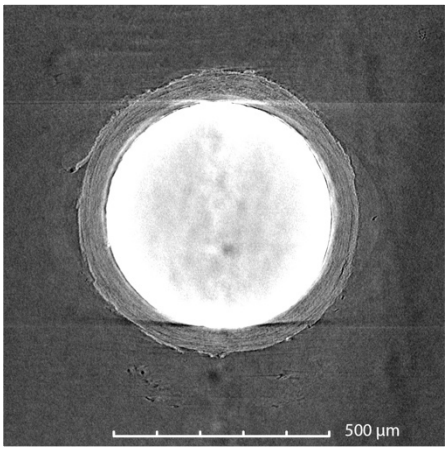

Figure 5-10. X-ray tomogram through the center of Particle 312-SP03.

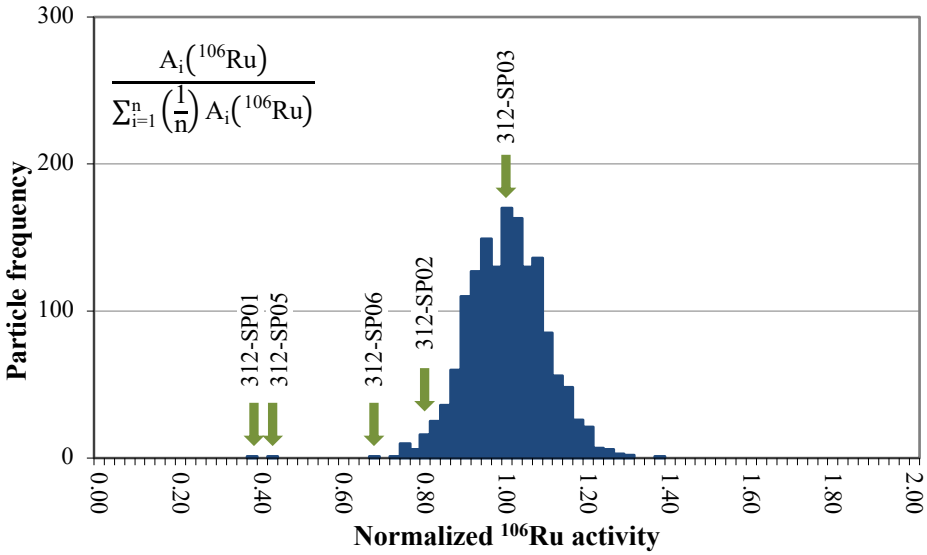

Figure 5-11. Normalized ^{106}Ru activity in 1527 particles from Compact 3-1-2.

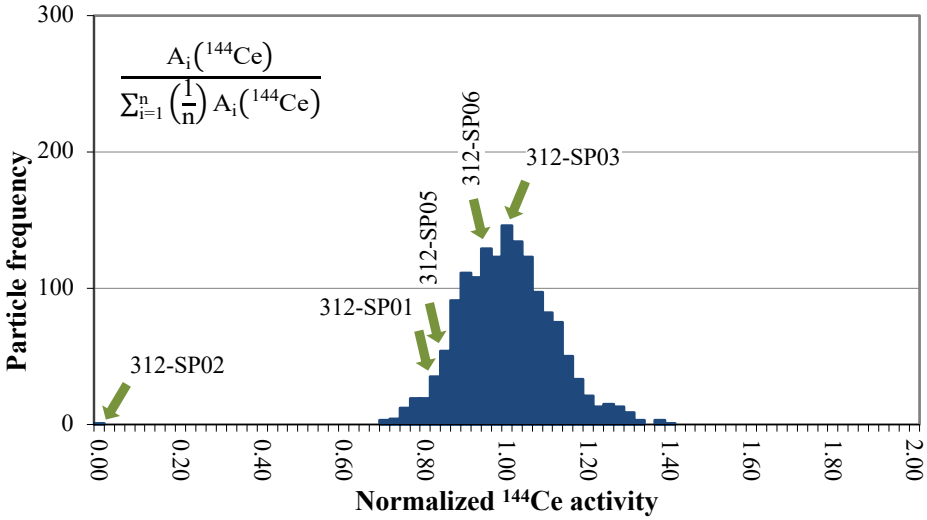

Figure 5-12. Normalized ^{144}Ce activity in 1527 particles from Compact 3-1-2.

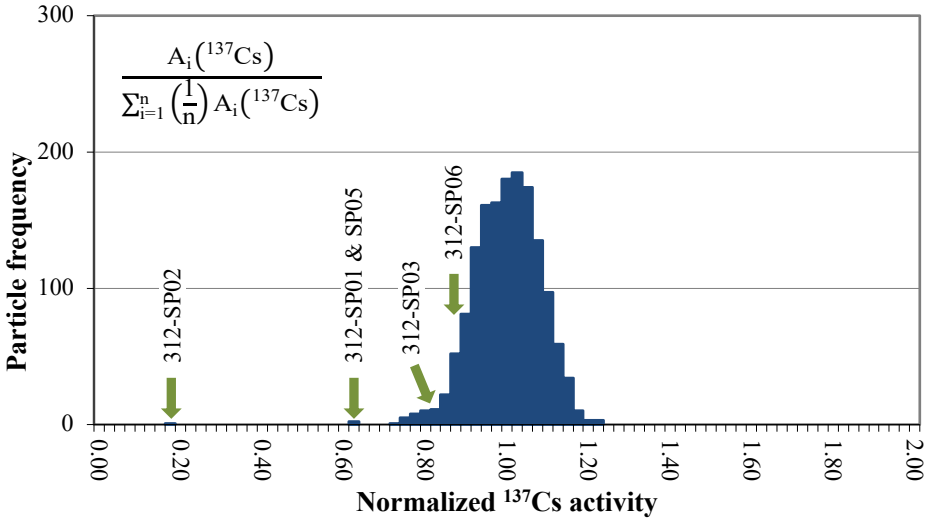

Figure 5-13. Normalized ^{137}Cs activity in 1527 particles from Compact 3-1-2.

Particle 312-SP02 had a ^{137}Cs M/C value of 0.16, which indicated preferential release of cesium compared with ruthenium (Figure 5-8), and resulted in it being automatically sorted out during the IMGA survey based on its ^{137}Cs/^{106}Ru ratio. Figure 5-11 shows that the ^{106}Ru activity in Particle 312-SP02 was below average, but the M/A value was not nearly as low as the ^{144}Ce (Figure 5-12) or ^{137}Cs (Figure 5-13). Figure 5-14 shows thats Particle 312-SP02 was missing most of its kernel material, as expected from the amount of kernel material leached during the pre-IMGA DLBL (Section 4). The larger fractures in the buffer and IPyC evident in the two XCT images were related and part of one connected crack. The buffer and IPyC fractures aligned where the two layers were still attached on one side of the fracture, and the fracture was presumably related to the stress along this line of detachment. At these locations, the IPyC was detached from the SiC and the connected buffer/IPyC structure was curled inward. This type of behavior has been observed in other AGR particles and indicated that the fracture probably occurred during irradiation and was followed by additional radiation induced dimensional changes. Partial fractures in the SiC were evident along the boundary of where the IPyC layer had pulled away from the SiC, which would have been a location of elevated stress on the SiC. At one location along this boundary, there was a circumferential fracture in the SiC. This fracture had not propagated more than about 5 µm from the IPyC/SiC interface. There were also two radial cracks through the SiC layer. One of these was located in the region of the circumferential crack and was aligned with a crack through the OPyC. The radial cracks in the SiC and OPyC probably occurred at the same time, namely, after irradiation and sometime at the

end of the second preburn leach or digestion step, when kernel leaching initiated during DLBL. Particle 312-SP02 was analyzed in the SEM and is discussed further in Section 8.1.

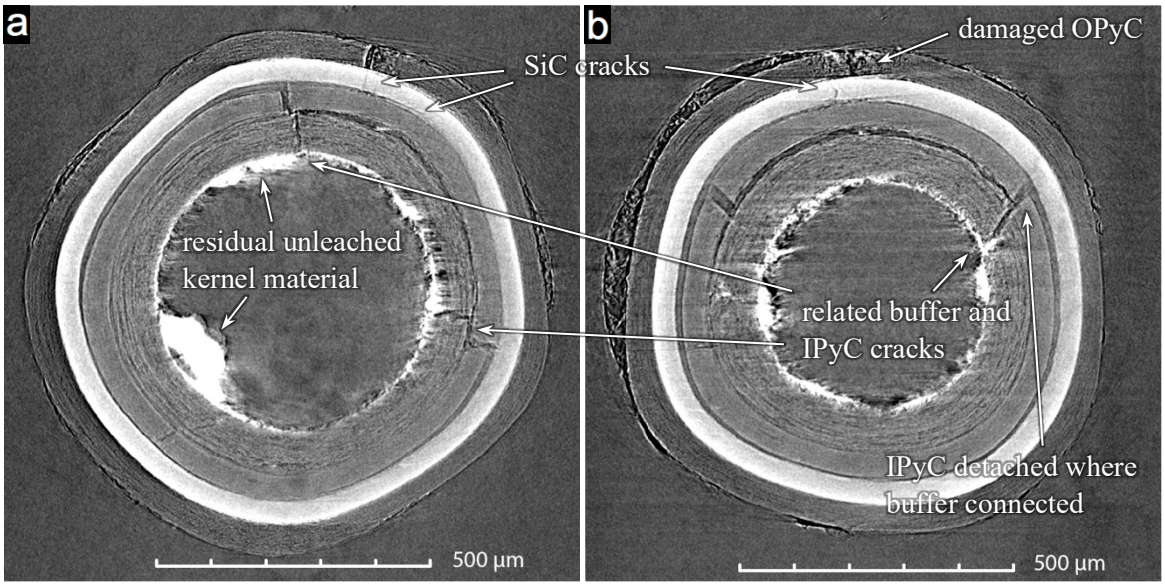

Figure 5-14. (a) X-ray tomogram through the center of Particle 312-SP02 and (b) off-midplane x-ray tomogram showing plane orthogonal to Figure 5-14.

As listed in Appendix Table B-1, Particles 312-SP01 and 312-SP05 had ~37% of the normal ^{106}Ru activity (Figure 5-11), ~60–61% of the normal ^{137}Cs activity (Figure 5-13), and ~82–86% of the normal ^{144}Ce activity (Figure 5-12). Imaging with XCT (Figure 5-15) revealed no evidence of degradation in the outer three retentive TRISO layers to explain the low ^{106}Ru and ^{137}Cs activities. However, these two particles had two unusual features for AGR-2 UO_2 particles: (1) both particles had extensive buffer fracture with kernel material protruding into the gaps between the buffer fragments, which was abnormal for AGR-2 UO_2 TRISO (Section 6), and (2) the SiC layer diameters indicated initial kernel diameters were typical of the nominally 425 µm AGR-2 UCO kernels. Figure 5-16a shows a polished section of Particle 312-SP01. The kernel of Particle 312-SP01 did not resemble any of the AGR-2 UO_2 kernels shown in Appendix C. However, its appearance was similar to many of the UCO kernels in the particles from 1,800°C safety-tested AGR-2 UCO Compact 6-2-1 (Figure 5-16b).

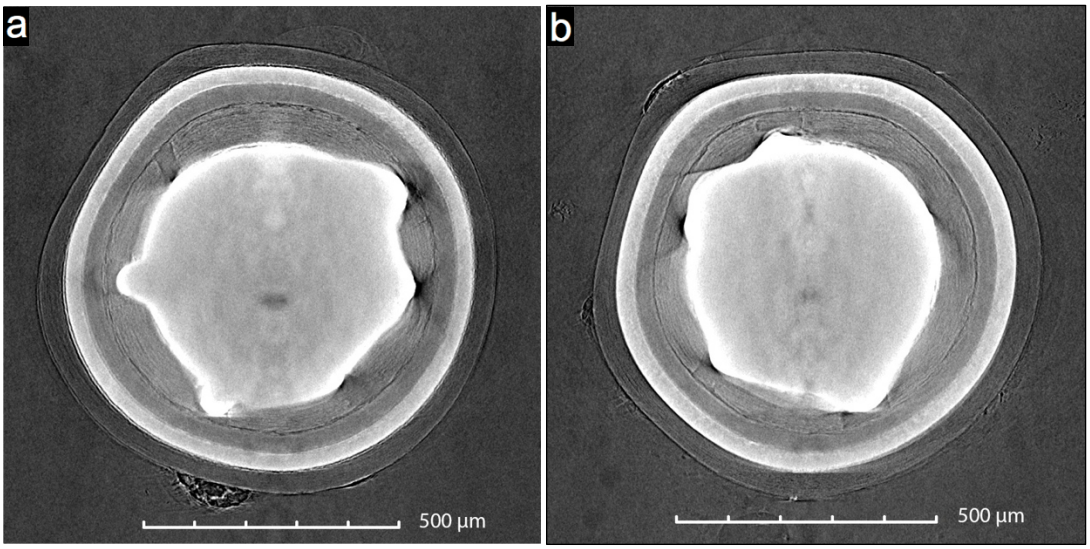

Figure 5-15. X-ray tomograms through the center of (a) Particle 312-SP01 and (b) Particle 312-SP05.

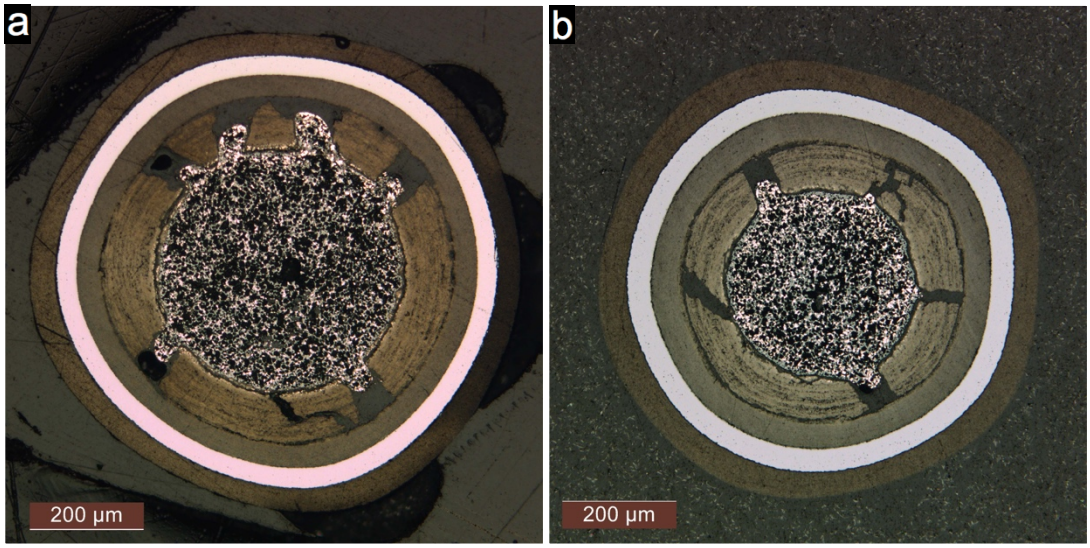

Figure 5-16. Optical micrographs of off-midplane polished sections of (a) Particle 312-SP01 and (b) a similar UCO TRISO particle from 1,800°C safety-tested AGR-2 Compact 6-2-1.

Table 5-1 shows the measured activities and 312-M/A values of Particles 312-SP01 and 312-SP05 from Appendix Table B-1, in which the 312-M/A values were calculated by dividing the measured activities of each particle by the mean activities of the Compact 3-1-2 RS particles. The measured activities of Particles 312-SP01 and 312-SP05 were below the minimum activities measured in the 312-RS particles, and the ratio of the ^{137}Cs 312-M/A vs. the ^{134}Cs 312-M/A was greater than 1.5 for these two particles, while the ratios for the RS particles were 0.93–1.08. Low retention or undersized kernels should produce essentially the same change in M/A for both cesium isotopes, so this ratio should only vary from unity as a function of the measurement uncertainty. Table 5-1 also shows 612-M/A values for Particles 312-SP01 and 312-SP05, which were calculated by dividing the measured activities of each particle by the mean activities of the 621-RS particles. Processing the measured activities for Particles 312-SP01 and 312-SP05 with the assumption that they were actually particles from AGR-2 UCO Compact 6-2-1 removed the discrepancy between the two cesium isotopes and resulted in 612-M/A values that were typical for particles with normal fission product retention. In addition, the measured activities for Particles 312-SP01 and 312-SP05 fell within the range of measured activities for the RS particles from Compact 6-2-1. Therefore, Particles 312-SP01 and 312-SP05 were probably from AGR-2 UCO Compact 6-2-1, which had been measured with IMGA one month before the Compact 3-1-2 particles.

Table 5-1. Recalculation of M/A for Particles 312-SP01 and 312-SP05

Particle	Value	^{106}Ru	^{125}Sb	^{134}Cs	^{137}Cs	^{144}Ce	^{154}Eu
312-SP01	Bq	1.18E+7	2.35E+5	3.93E+6	4.83E+6	5.21E+7	1.32E+5
312-SP01	312-M/A	0.37	0.53	0.39	0.60	0.82	0.41
312-SP01	621-M/A	1.04	1.07	1.13	1.07	1.10	1.09
312-SP05	Bq	1.19E+7	2.44E+5	3.80E+6	4.89E+6	5.48E+7	1.27E+5
312-SP05	312-M/A	0.37	0.55	0.38	0.61	0.86	0.39
312-SP05	621-M/A	1.06	1.11	1.09	1.08	1.16	1.04
312-RS Minimum	Bq	2.56E+7	3.63E+5	8.04E+6	6.59E+6	5.51E+7	2.58E+5
312-RS Mean	Bq	3.20E+7	4.45E+5	9.97E+6	8.03E+6	6.36E+7	3.21E+5
312-RS Maximum	Bq	3.73E+7	5.09E+5	1.18E+7	9.19E+6	7.05E+7	3.88E+5
621-RS Minimum	Bq	1.38E+7	2.54E+5	4.01E+6	5.17E+6	5.47E+7	1.62E+5
621-RS Mean	Bq	1.13E+7	2.20E+5	3.48E+6	4.52E+6	4.72E+7	1.22E+5
621-RS Maximum	Bq	9.55E+6	1.96E+5	2.94E+6	4.02E+6	4.25E+7	1.00E+5

As listed in Appendix Table B-1, Particle 312-SP06 had ~65% of the normal ^{106}Ru activity (Figure 5-11), ~84% of the normal ^{137}Cs activity (Figure 5-13), and ~96% of the normal ^{144}Ce activity (Figure 5-12). Imaging with XCT revealed no evidence of degradation in the outer three retentive TRISO layers to help explain the low ^{106}Ru and ^{137}Cs activities. In addition, a relatively higher fractional release of ^{106}Ru compared with ^{137}Cs is unexpected for particles with SiC or TRISO failure, as ruthenium is better retained in all cases. Similar to what was observed for Particles 312-SP01 and 312-SP05, Particle 312-SP06 exhibited features typical for AGR-2 UCO TRISO, namely, buffer fracture with kernel protrusion and layer diameters that indicated an initial kernel diameters around 425 µm (Figure 5-17). Figure 5-18 shows two optical micrographs comparing a polished cross section of Particle 312-SP06 with a similar appearing AGR-2 UCO TRISO particle from Compact 5-4-2. In addition to similar porosity and kernel material, both kernels possessed a dense outer layer thought to be a residual structure related to the carbide skin that forms on UCO kernels during coating and compact heat treatment (Hunn et al. 2012), which differentiated them from the UO_2 kernels shown in Appendix C. While it appears that this particle had a UCO kernel, and Compact 5-4-2 particles were handled in the IMGA cubicle prior to the IMGA survey of particles from Compact 3-1-2, the ^{137}Cs/^{134}Cs ratio was consistent with the expected ratio for UO_2 Compact 3-1-2, and no recalculation like that in Table 5-1 could match the measured activities to the expected inventories of any AGR-2 particles. Therefore, there is currently no available explanation for the measured isotopic inventories in Particle 312-SP06.

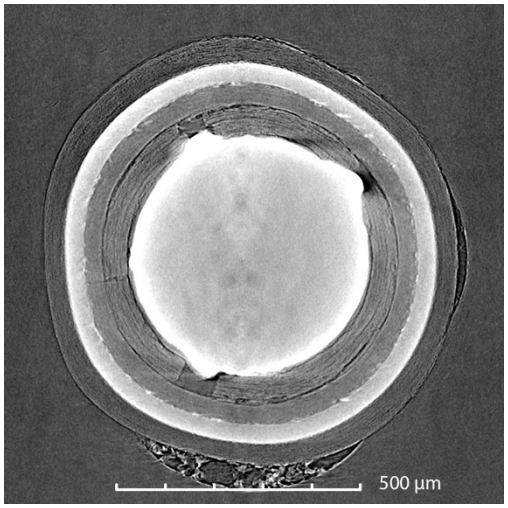

Figure 5-17. X-ray tomogram through the center of Particle 312-SP06.

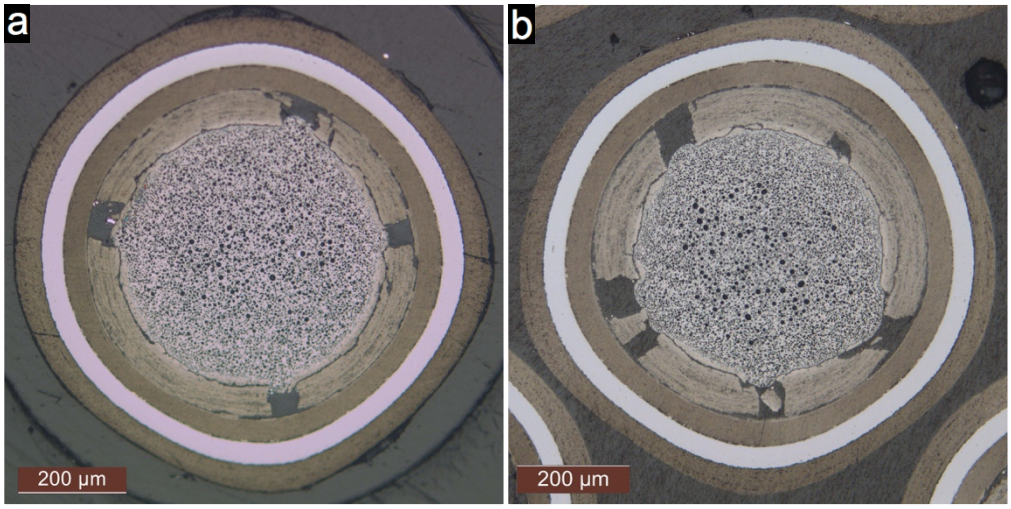

Figure 5-18. Optical micrographs of off-midplane polished sections of (a) Particle 312-SP06 and (b) a similar UCO TRISO particle from Compact 5-4-2.

As discussed above, IMGA survey of Compact 3-1-2 was performed about six years after EOL. The ^{110m}Ag M/C had a high minimum detection limit (MDL) of <65–72% because there was only 0.22–0.23% of the EOL activity remaining after 8.7–8.8 half-lives. The histogram of the Compact 3-1-2 ^{110m}Ag M/C is shown in Figure 5-19 and has 13 out of 45 measured particles plotted in the zero bin because they were below the MDL (MDL values are listed in Appendix Table B-1). The estimated measurement uncertainty for the ^{110m}Ag gamma peaks above the MDL was 23–58%, but this cannot fully explain the range in measured ^{110m}Ag M/C values, which were as high as 1.73.

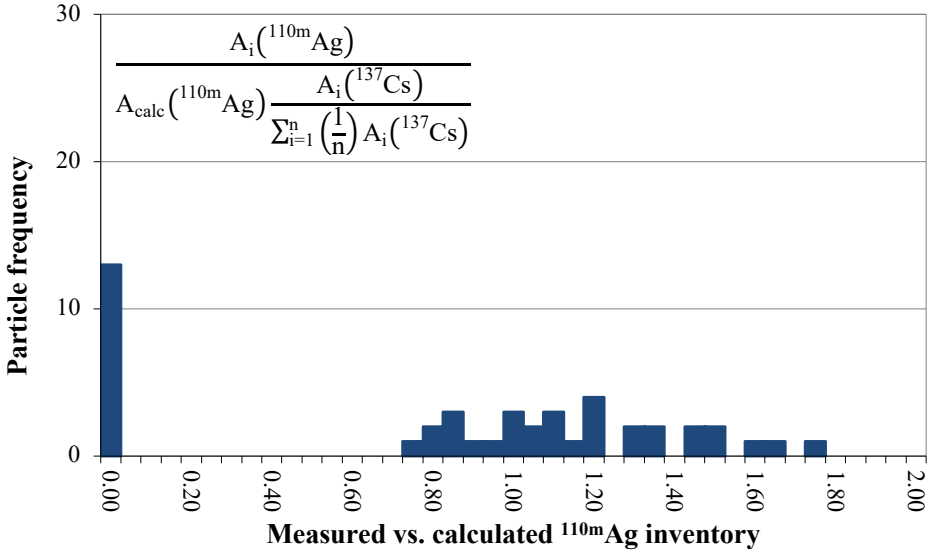

Figure 5-19. Measured vs. calculated ^{110m}Ag inventory in 45 particles from Compact 3-1-2 (particles plotted as "zero" were below a detection limit of ^{110m}Ag M/C <65–72%).

5.3 1,500°C SAFETY-TESTED COMPACT 3-1-1

As shown in Figure 5-20, no abnormally low cesium particles from Compact 3-1-1 were detected with IMGA (Hunn et al. 2020). The one particle with failed SiC, expected on account of the cesium release during safety testing, was apparently leached during DLBL analysis. Presumably, this particle had a failed SiC layer and an intact OPyC layer at the conclusion of the safety test, and the OPyC broke at the end of the second preburn leach, as discussed in Section 4.

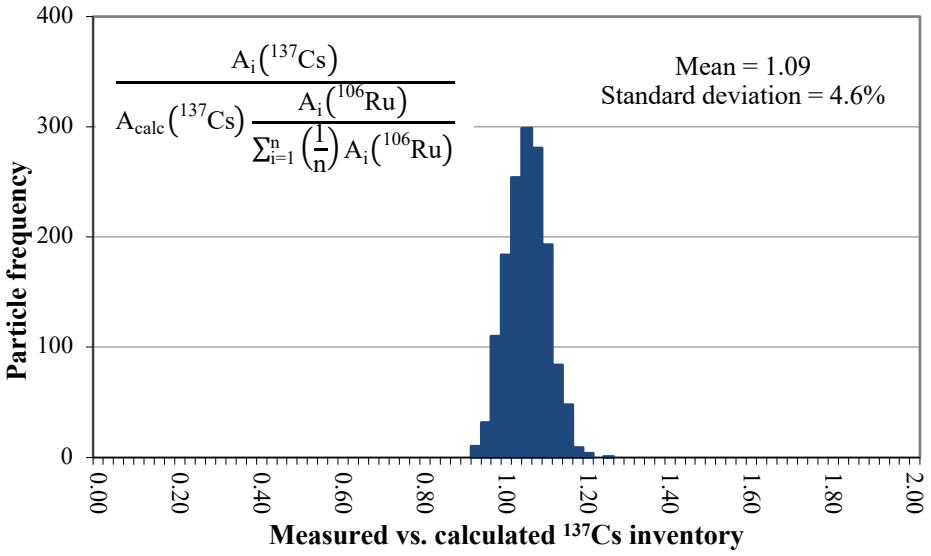

Figure 5-20. Measured vs. calculated ^{137}Cs inventory in 1509 particles from Compact 3-1-1.

IMGA survey of 1,500°C safety-tested Compact 3-1-1 was performed about six years after EOL. The ^{110m}Ag M/C had a high minimum detection limit (MDL) of <59–67% because there was only 0.23–0.26% of the EOL activity remaining after 8.6– 8.8 half-lives. The histogram of the Compact 3-1-2 ^{110m}Ag M/C data is shown in Figure 5-19 and has 14 out of 45 measured particles plotted in the zero bin because they were below the MDL (MDL values are listed in Appendix Table B-1). The estimated measurement uncertainty for the ^{110m}Ag gamma peaks above the MDL was 16–54%, but this cannot fully explain the range in measured ^{110m}Ag M/C values, which were as high as 1.53.

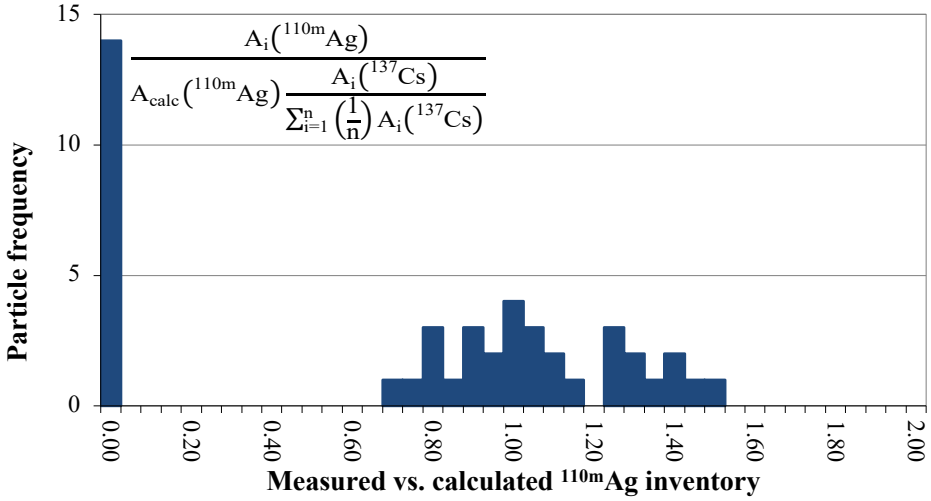

Figure 5-21. Measured vs. calculated ^{110m}Ag inventory in 45 particles from Compact 3-1-1.

5.4 1,600°C SAFETY-TESTED COMPACT 3-3-2

Figure 5-22 shows the normalized activity of ^{144}Ce from the IMGA survey of particles recovered from 1,600°C safety-tested Compact 3-3-2, and Figure 5-23 shows the normalized ^{137}Cs activity. Four particles had very low ^{144}Ce and ^{137}Cs inventories. All four particles were imaged with XCT and determined to have missing kernel material, as shown in Figure 5-24–Figure 5-27, which was consistent with the 4.0 particle equivalents of ^{238}U leached during pre-IMGA DLBL. Particle 332-SP01 had extensive fracturing in the pyrocarbon and SiC layers. The other three particles had circular, low-density regions penetrating the SiC where local IPyC fracture had exposed the SiC to carbon monoxide (CO) corrosion, as discussed in Section 8.2. The evident cracks in the OPyC presumably occurred during the DLBL, given the absence of significant ^{85}Kr release during safety testing.

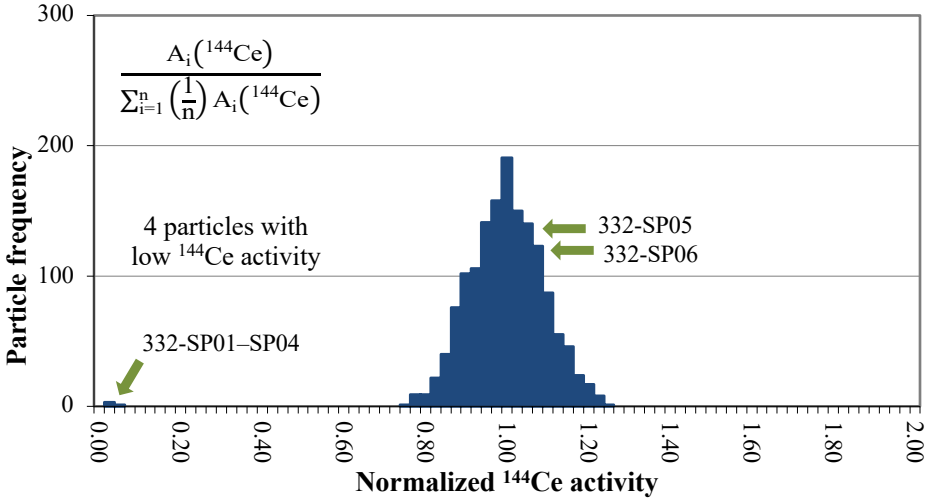

Figure 5-22. Normalized ^{144}Ce activity in 1510 particles from Compact 3-3-2.

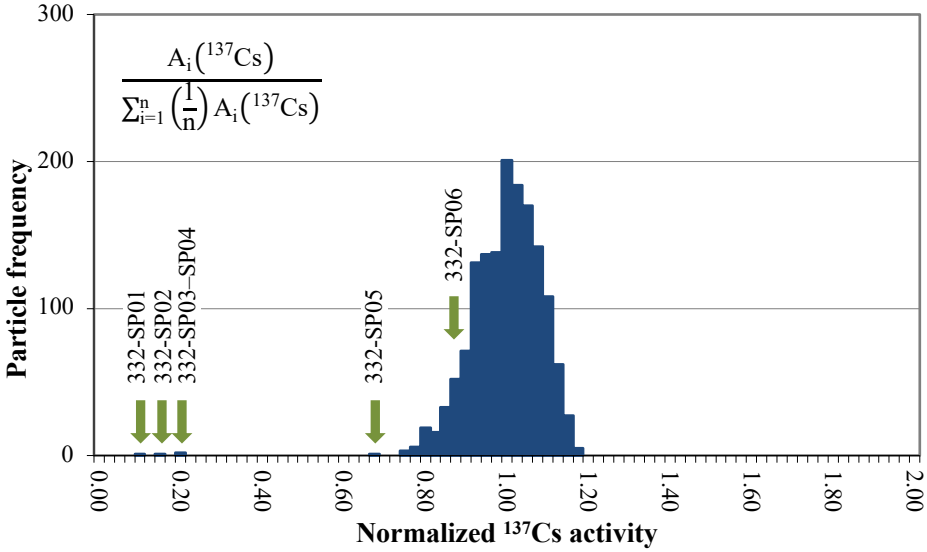

Figure 5-23. Normalized ^{137}Cs activity in 1510 particles from Compact 3-3-2.

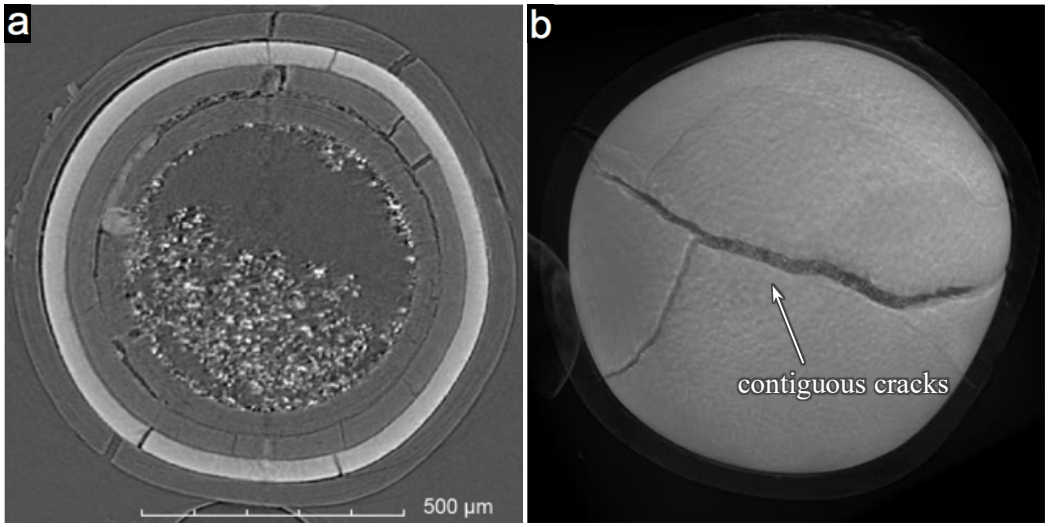

Figure 5-24. (a) X-ray tomogram of Particle 332-SP01 and (b) 3D representation of the SiC surface.

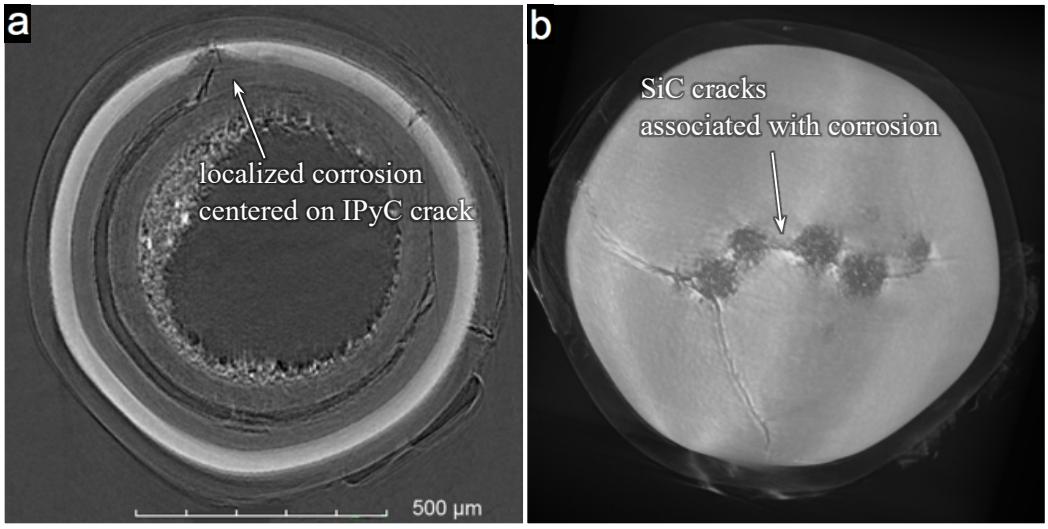

Figure 5-25. (a) X-ray tomogram of Particle 332-SP02 and (b) 3D representation of the SiC surface.

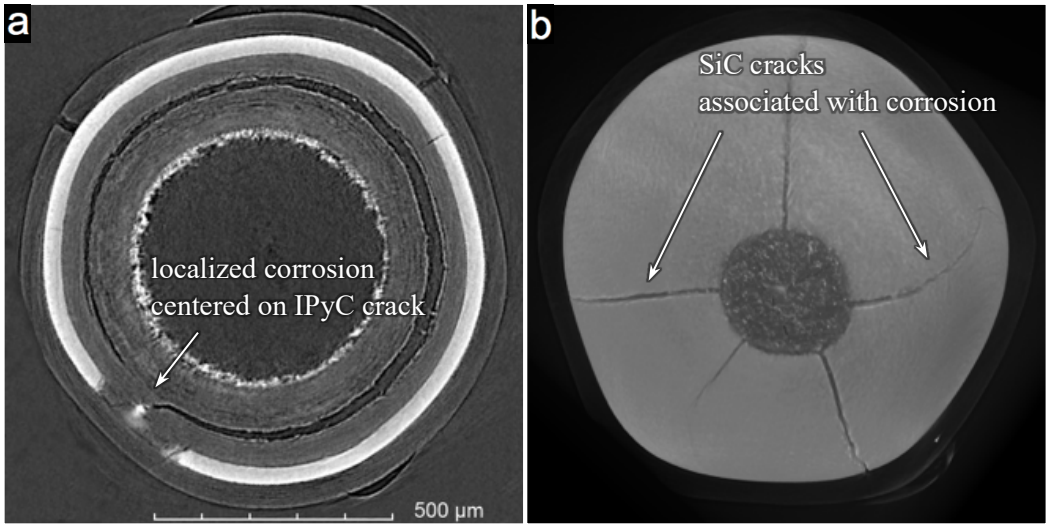

Figure 5-26. (a) X-ray tomogram of Particle 332-SP03 and (b) 3D representation of the SiC surface.

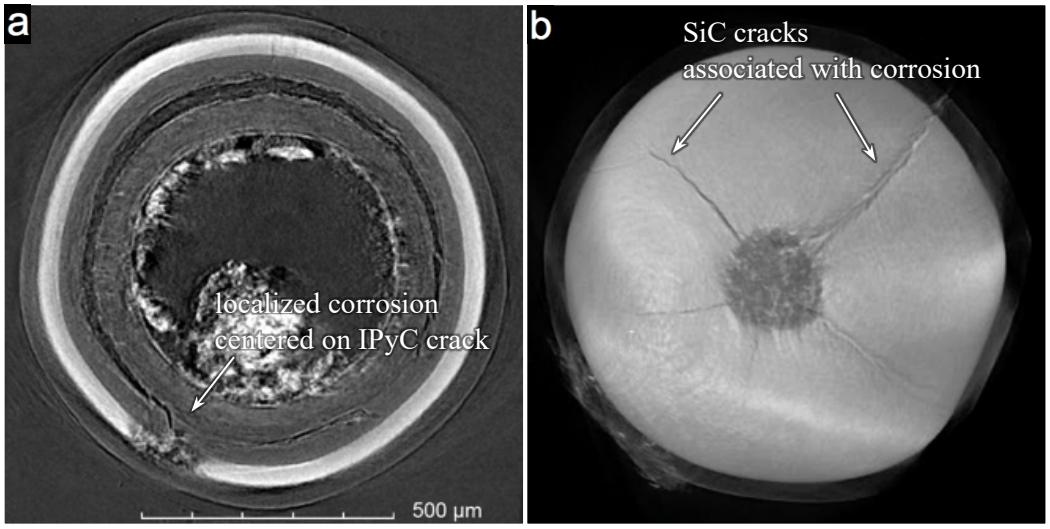

Figure 5-27. (a) X-ray tomogram of Particle 332-SP04 and (b) 3D representation of the SiC surface.

The x-ray tomograms in Figure 5-25–Figure 5-27 show that the IPyC fracture was located at a boundary between attached and detached buffer, and the buffer detachment appeared to divert to the IPyC fracture. Presumably, the same forces generated by the radiation-induced shrinkage of the buffer, which caused it to detach from the IPyC, were also responsible for the IPyC fracture. This was observed to be the primary cause of IPyC fracture in AGR-1 test fuel (Ploger et al. 2012). Observations of AGR-1 UCO TRISO particles with failed SiC found that IPyC fracture was the primary cause for the SiC failure, in which exposure of the inside surface of the SiC allowed concentrated degradation by mobile fission products, primarily palladium (Hunn et al. 2014a). The combination of effects leading to SiC failure in the AGR-2 UO_2 TRISO appear to be similar to the AGR-1 UCO TRISO, with the exception of the primary agent chemically attacking the SiC changing from palladium to CO and the prevalence of associated cracking of the SiC, which may also be related to the CO. In UO_2 TRISO particles, oxygen released by uranium fission reacts with the buffer carbon to form CO. Excess CO leads to various irradiation performance issues under certain operating conditions, such as pressure-induced fracture, kernel migration, and CO corrosion of the SiC (Petti et al. 2002, Minato et al. 1991). In UCO TRISO particles, CO formation is reduced because the chemical potential for oxidation of uranium carbide is lower than for oxidation of carbon, hence the reason for including uranium carbide in the UCO kernel design (Homan et al. 1977).

Figure 5-28 shows the ^{137}Cs M/C histogram for Compact 3-3-2. Particles 332-SP01–SP04 are off-scale because the ^{144}Ce activities were reduced relatively more than the ^{137}Cs activities. This is understandable, as some cesium typically resides in the pyrocarbon, where it is less susceptible to dissolution in the leach acid. Particles 332-SP05 and 332-SP06 had distinctly reduced ^{137}Cs M/C values, while their ^{144}Ce inventories were in the normal range (Figure 5-22). Figure 5-29 shows a soot inclusion in the SiC layer of Particle 332-SP05. Soot inclusions can occur when individual particles within the coating furnace are ejected above the fluidized particle bed as the result of non-optimal fluidization. These particles can pick up carbon soot if they strike the upper coating chamber wall. When this carbon soot is overcoated with SiC, a raised lump enclosing a lower-density region is formed. There was a crack at the edge of the soot inclusion that presumably formed during safety testing and resulted in the observed cesium release, whereas the soot inclusion was present throughout the irradiation test with no negative result. Particles with failed SiC as a result of soot inclusions were observed in AGR-1 UCO particles after safety testing at 1,600°C (Hunn et al. 2014a) and 1,800°C (Hunn et al. 2015b).

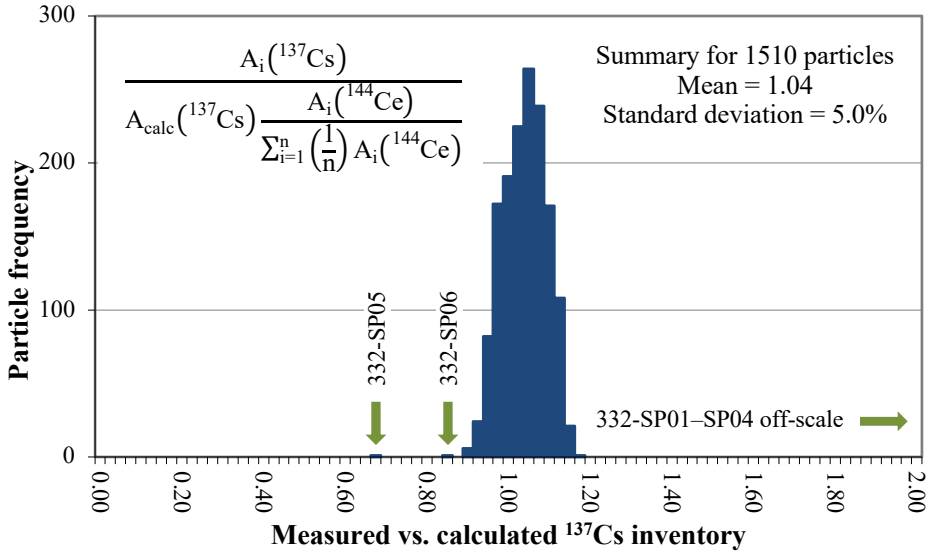

Figure 5-28. Measured vs. calculated ^{137}Cs inventory in 1510 particles from Compact 3-3-2.

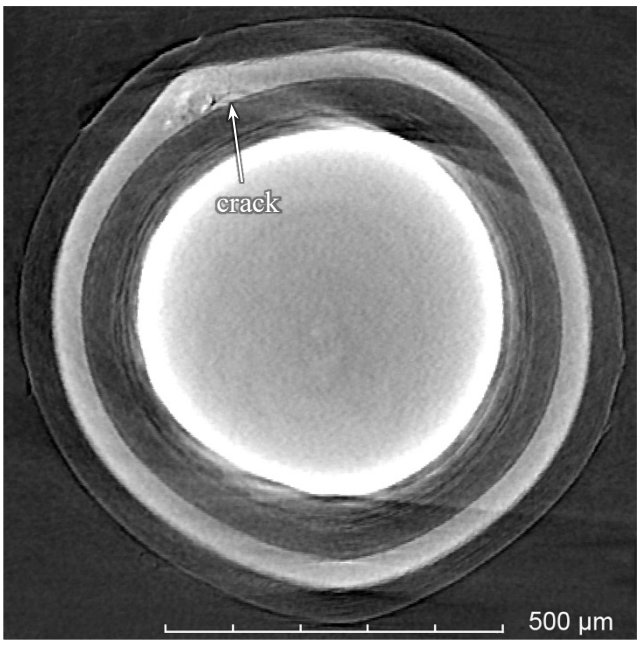

Figure 5-29. X-ray tomogram through the center of Particle 332-SP05.

Figure 5-30 is an x-ray tomogram showing a plane through Particle 332-SP06 where a faint crack is visible that traversed the buffer and IPyC layers. A faint line can be seen radiating from the IPyC crack into the SiC layer that suggests the crack may have extended through the SiC layer, but this feature was below the capability for the x-ray imaging to resolve with confidence.

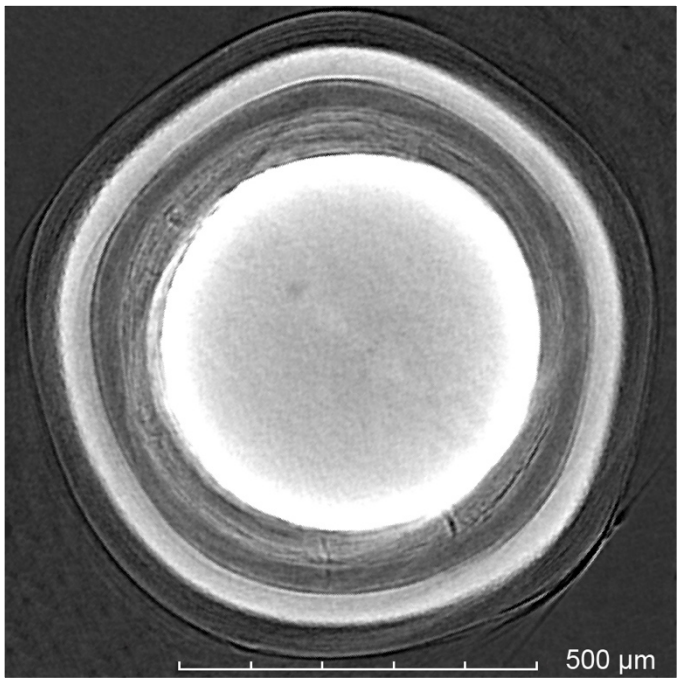

Figure 5-30. X-ray tomogram through the center of Particle 332-SP06.

There was a total of 4.9–5.5 particle equivalents of ^{134}Cs released from Compact 3-3-2 and measured either on the CCCTF components (Table 3-2) or in the pre-IMGA DLBL solutions (Appendix Table A-10), in which the upper value includes indication from the digestion acid of 0.6 particle equivalents of ^{134}Cs lost during the matrix burn. There were 2.1 particle equivalents of ^{134}Cs retained in the six special particles that were found with IMGA and analyzed for SiC failure. If all six particles had SiC failures and had average ^{134}Cs inventories at the start of the safety test, then there were 3.9 particle equivalents of ^{134}Cs released from these six particles, which leaves 1–1.6 particle equivalents of released ^{134}Cs not accounted for. Not counting Particle 332-SP06 as a SiC failure leaves 1.2–1.8 particle equivalents of released ^{134}Cs unaccounted for. This suggests there were at least 1–2 additional particles with failed SiC that were perhaps broken and lost during the IMGA survey. Therefore, it is reasonable to assume that there were at least 7±1 particles with failed SiC in 1,600°C safety-tested Compact 3-3-2.

5.5 1,600°C SAFETY-TESTED COMPACT 3-4-2

Figure 5-31 and Figure 5-32 show that there were five particles recovered from 1,600°C safety-tested Compact 3-4-2 with very low ^{144}Ce and ^{137}Cs activities (Particles 342-SP01–342-SP05), and a sixth particle, Particle 342-SP06, had significantly reduced ^{144}Ce and ^{137}Cs activities, relative to the norm. The normalized activities (M/A values) for these particles are shown in Table 5-2. Particles 342-SP01, 342-SP02, 342-SP04, and 342-SP05 had M/A values similar to the four particles from Compact 3-3-2 that had leached kernels (also shown in Table 5-2). Kernel leaching removed the majority of the silver, cerium, and europium. Ten to twenty percent of the cesium was left in the particles with leached kernels, probably sequestered in the pyrocarbon, while ruthenium and antimony appeared to be in relatively insoluble forms. Particle 342-SP03 had measured activities similar to Particle 331-SP01, which had a ZrO_2 kernel. The fact that Particle 342-SP03 had very low ^{106}Ru and ^{125}Sb activities made it unlikely that this particle's low activities were due to a leached kernel. Examination with XCT confirmed that this particle had normal coating structure (Figure 5-33), and cross sectioning verified the kernel was ZrO_2.

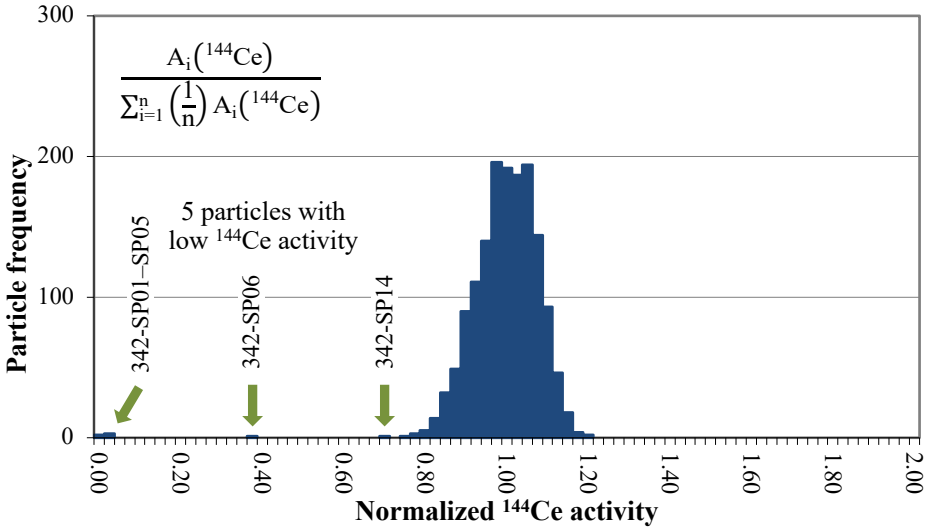

Figure 5-31. Normalized ^{144}Ce activity in 1528 particles from Compact 3-4-2.

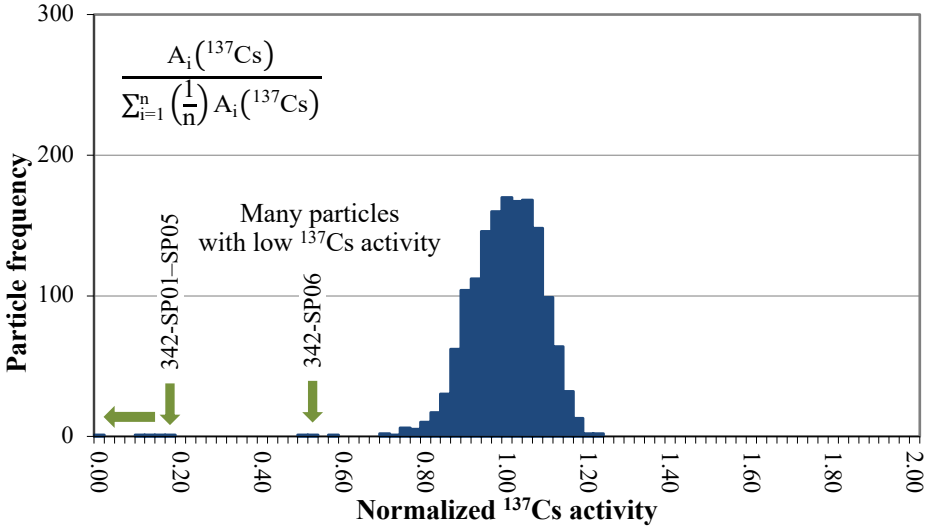

Figure 5-32. Normalized ^{137}Cs activity in 1528 particles from Compact 3-4-2.

Table 5-2. M/A values of Compact 3-4-2 particles with low activity, compared with similar particles

Particle	Value	^{106}Ru	^{110m}Ag	^{125}Sb	^{134}Cs	^{137}Cs	^{144}Ce	^{154}Eu
342-SP01	M/A	0.78	0.01	1.06	0.09	0.09	0.03	0.01
342-SP02	M/A	0.59	<0.02	1.10	0.13	0.13	0.00	0.01
342-SP04	M/A	0.54	<0.02	0.89	0.14	0.14	0.02	0.01
342-SP05	M/A	0.65	<0.02	1.03	0.17	0.17	0.03	0.02
332-SP01	M/A	0.85	0.02	0.82	0.08	0.09	0.04	0.02
332-SP02	M/A	0.61	<0.02	0.92	0.14	0.15	0.02	0.05
332-SP03	M/A	0.74	<0.02	1.05	0.19	0.20	0.02	0.07
332-SP04	M/A	0.72	<0.02	1.05	0.19	0.20	0.02	0.06
342-SP03	M/A	0.00	<0.01	0.00	0.00	0.01	0.01	0.00
331-SP01	M/A	0.00	<0.03	0.00	0.00	0.01	0.00	0.01
342-SP06	M/A	0.89	0.42	1.02	0.53	0.53	0.37	0.25

Note: Particles 342-SP03 and 331-SP01 had ZrO_2 kernels.

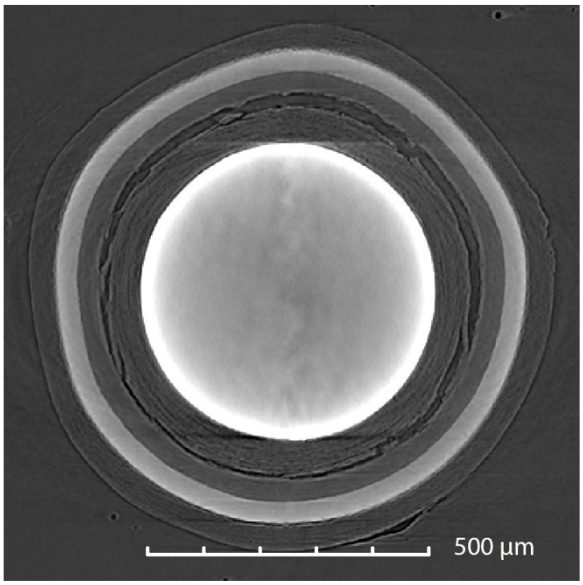

Figure 5-33. X-ray tomogram through the center of Particle 342-SP03.

Figure 5-34 shows that Particle 342-SP01 was missing most of its kernel material, as expected. There were two localized corrosion sites in the SiC layer, and both appeared to penetrate about halfway through the SiC layer. Both sites were centered on visible cracks through the IPyC layer which were located at a boundary between a detached and connected buffer/IPyC interface. One of the corrosion sites had a crack through the SiC layer that was aligned with the IPyC crack; this was probably the cause of the cesium release from this particle during safety testing. A second crack seen in the tomogram in Figure 5-34a was determined to be connected with the crack at the corrosion site. Figure 5-35 is a 3D XCT representation of the SiC surface that shows this crack in the SiC, which extended around about half the circumference of the particle and had a shorter branching crack. The presence of solid material in the buffer/IPyC gap, opposite from the corrosion site in Figure 5-34a, was determined by EDS analysis to be an SiO_2 precipitate. This SiO_2 precipitate contained reaction product from the CO corrosion, as discussed in Section 8.3.

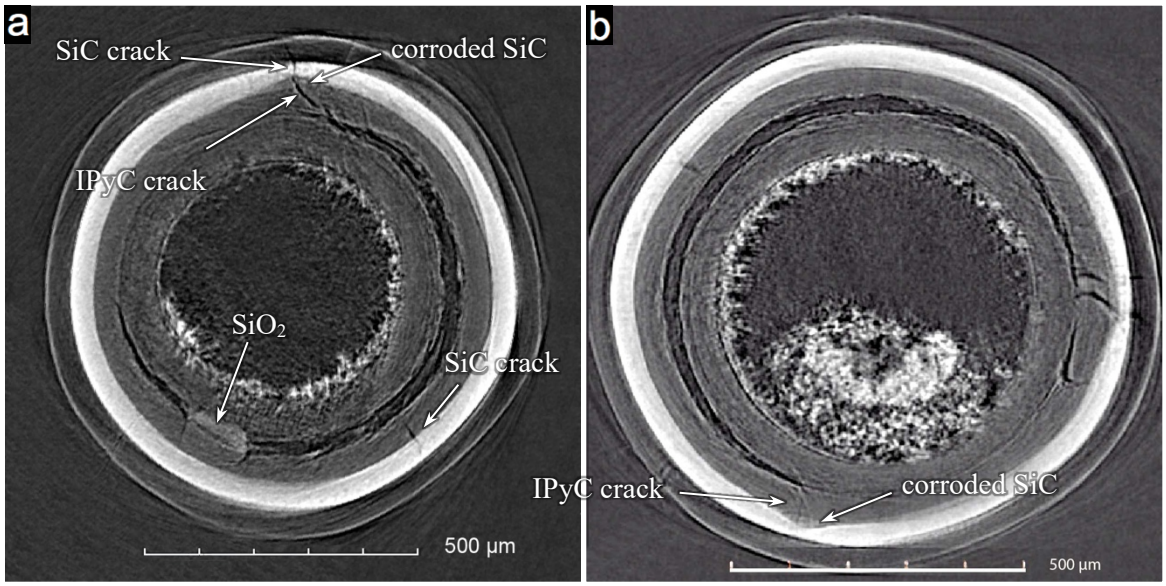

Figure 5-34. X-ray tomograms of Particle 342-SP01 showing two corrosion sites.

Figure 5-35. 3D representation of SiC surface of Particle 342-SP01.

Particle 342-SP02 (Figure 5-36) did not show a localized region of corroded SiC. All layers were fractured, and at many locations the fractures in the IPyC, SiC, and OPyC were aligned. The SiC fractures were all connected, with one main fracture circling about 60% of the particle and multiple branching cracks. Unlike Particle 332-SP01, in which fracture was also the primary failure mode, Particle 342-SP02 did not show significant separation between the IPyC and SiC layers, and there were no visible precipitates of SiO_2 to indicate significant corrosion. As expected from the gamma analysis (Table 5-2), most of the kernel material was missing.

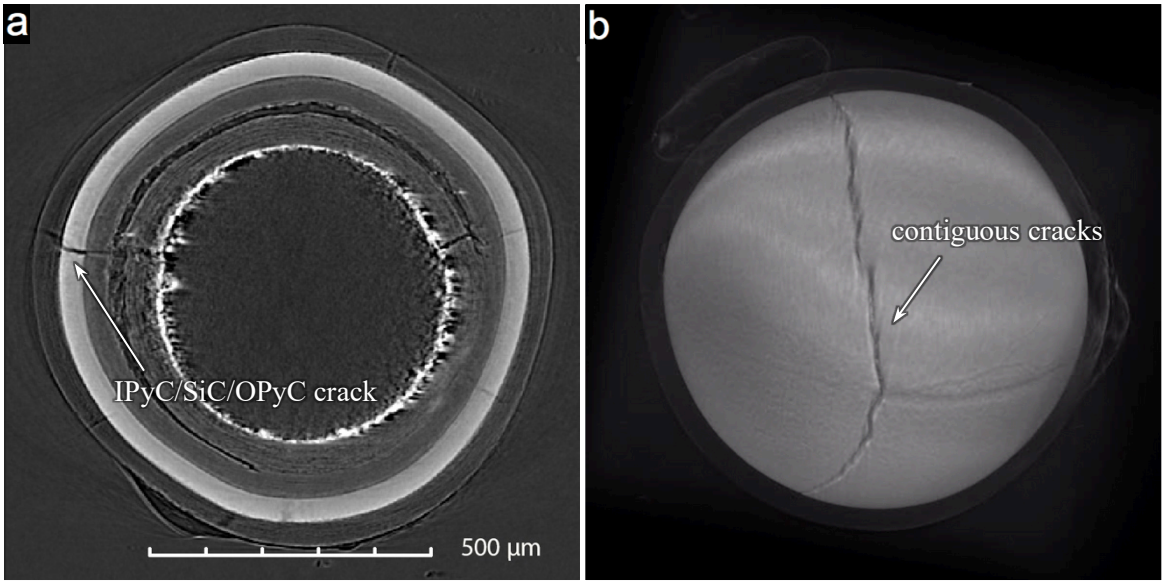

Figure 5-36. (a) X-ray tomogram of Particle 342-SP02 and (b) 3D representation of the SiC surface.

Particle 342-SP04 (Figure 5-37) and Particle 342-SP05 (Figure 5-38) each showed a large region of localized corrosion through the SiC layer, with associated cracks radiating out from the corrosion site. Examination of the XCT images showed all the standard trends for SiC failure, in which IPyC fracture was instigated by buffer detachment and CO corrosion occurred where the IPyC fracture exposed the SiC. As expected from the gamma analysis (Table 5-2), most of the kernel material was missing from Particles 342-SP04 and 342-SP04. Cracks in the OPyC were remote from the microstructure related to SiC failure,

and these cracks presumably occurred during DLBL concurrent with the onset of kernel leaching. These particles were very similar to Particle 332-SP03 (Figure 5-26) and Particle 332-SP04 (Figure 5-27). Large-scale Si-O precipitates, as discussed in Section 8.2 with regard to the Compact 3-3-2 particles, were visible in the buffer/IPyC gap of Particle 342-SP05 (Figure 5-38a), but were not visible in Particle 342-SP04.

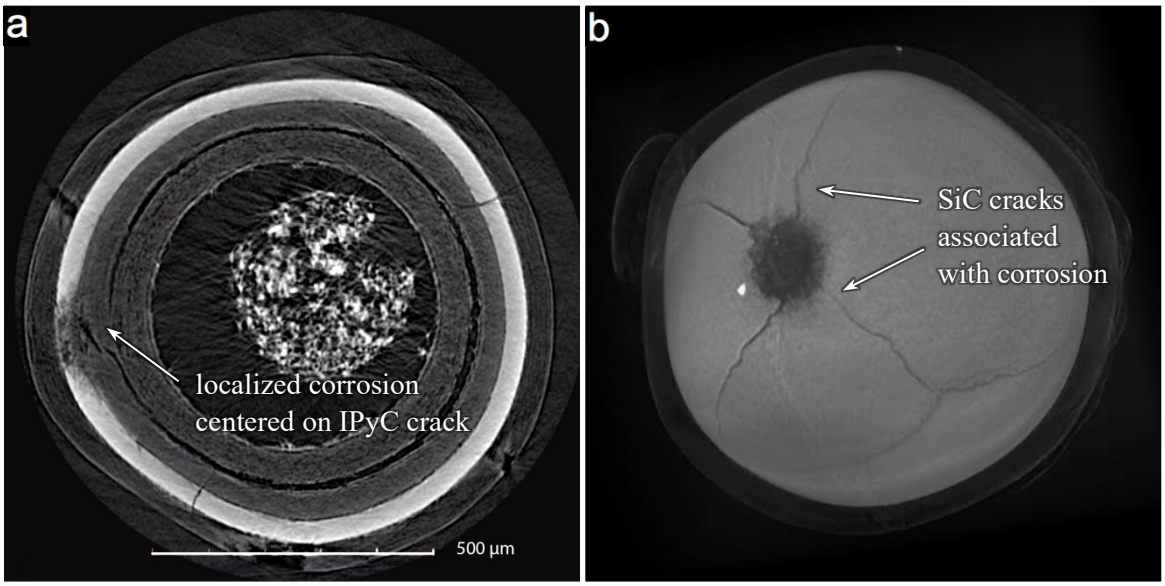

Figure 5-37. (a) X-ray tomogram of Particle 342-SP04 and (b) 3D representation of the SiC surface.

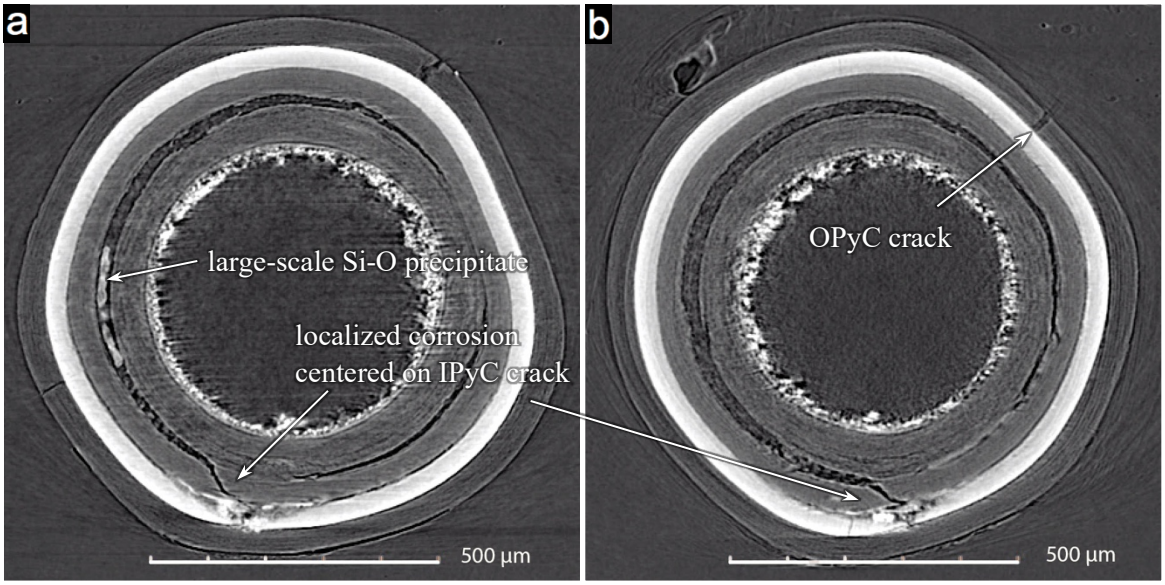

Figure 5-38. X-ray tomograms of Particle 342-SP05.

Figure 5-39 shows a tomographic cross section and 3D representation of Particle 342-SP06. Partial penetration of x-rays around the perimeter of the kernel indicated partial kernel leaching, as expected from the measured M/A values (Table 5-2). Cracks were observed in all layers. Like Particle 332-SP01, in which SiC failure was related to layer fracture, Particle 342-SP06 had detached areas at all TRISO coating interfaces. Examination with SEM and EDS, as discussed in Section 8.3, revealed CO corrosion around the IPyC/SiC interface, but no direct evidence that the corrosion caused localized weakening of the SiC layer.

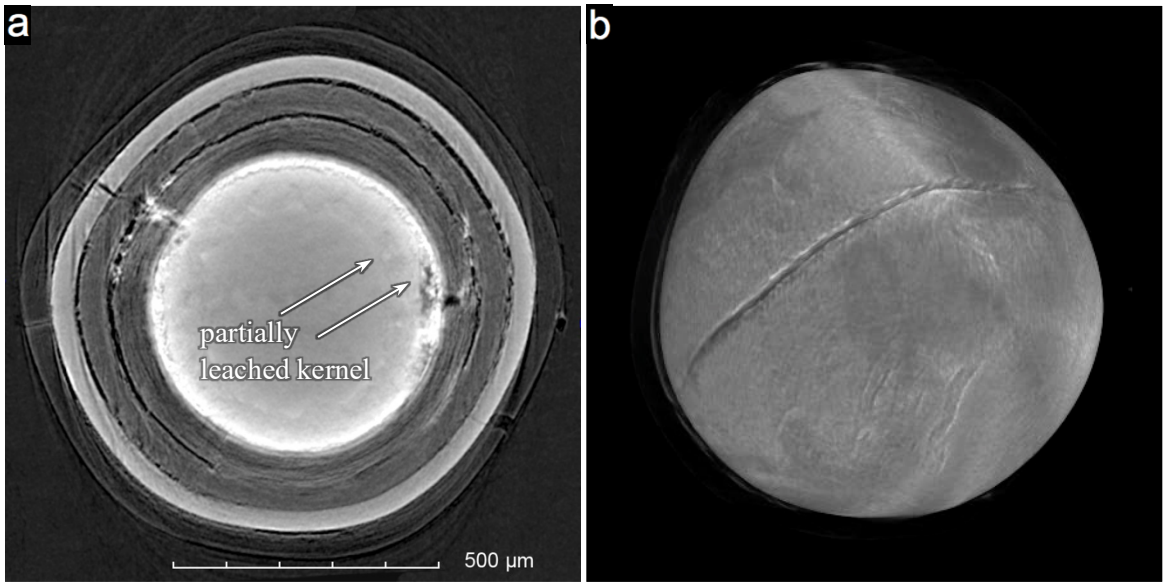

Figure 5-39. (a) X-ray tomogram of Particle 342-SP06 and (b) 3D representation of the SiC surface.

Figure 5-40 shows a histogram of the ^{137}Cs M/C values for the particles recovered from Compact 3-4-2. Numerous particles had preferentially reduced ^{137}Cs inventories suggesting some degree of SiC failure in each. It was not feasible to fully investigate every particle with suspected SiC failure. The special particles identified in Figure 5-40 were gamma counted for 6 h each. Results are tabulated in Appendix Table B-5, and M/A values are listed in Table 5-3. All particles had relatively low cesium activities. Particles 342-SP07, 342-SP15, 342-SP18, and 342-SP22 had ^{137}Cs M/A values close to unity, but were still relatively low in cesium and appeared in the low cesium tail in Figure 5-40 because of over-sized kernels, as indicated by high M/A values for ^{106}Ru, ^{125}Sb, ^{144}Ce, and ^{154}Eu. Particles 342-SP09 and 342-SP24 had uniformly low M/A values for ^{106}Ru, ^{125}Sb, ^{144}Ce, and ^{154}Eu, which indicated under-sized kernels rather than material loss. Particle 342-SP10 had preferentially low M/A values for ^{154}Eu and ^{110m}Ag, and Particle 342-SP14 had preferentially low M/A values for ^{154}Eu, ^{110m}Ag, and ^{144}Ce, indicating possible loss of these isotopes during safety testing. The other eleven particles had relatively normal activities for ^{106}Ru, ^{125}Sb, ^{144}Ce, and ^{154}Eu, with all but Particles 342-SP08 and 342-SP11 also having relatively normal activities for ^{110m}Ag.

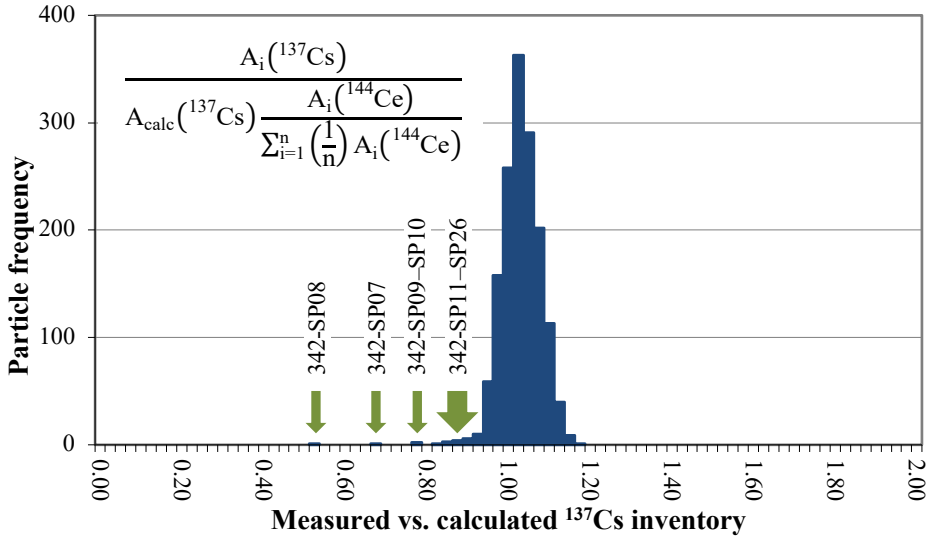

Figure 5-40. Measured vs. calculated ^{137}Cs inventory in 1528 particles from Compact 3-4-2.

Table 5-3. M/A values of Compact 3-4-2 special particles identified in Figure 5-40 with low ^{137}Cs M/C.

Particle	Characteristic	^{106}Ru	^{110m}Ag	^{125}Sb	^{134}Cs	^{137}Cs	^{144}Ce	^{154}Eu
342-SP07	large kernel	1.13	0.80	1.14	0.72	0.71	1.07	1.18
342-SP08	low Ag	1.00	0.64	1.01	0.48	0.50	1.00	1.04
342-SP09	small kernel	0.86	0.71	0.86	0.66	0.68	0.90	0.82
342-SP10	low Eu, Ag	1.04	0.71	1.06	0.71	0.72	0.96	0.25
342-SP11	low Ag	1.05	0.16	1.02	0.89	0.85	1.02	1.05
342-SP13	only low Cs	1.04	1.02	1.03	0.84	0.81	0.97	1.09
342-SP14	low Eu, Ce, Ag	0.93	0.57	1.01	0.57	0.57	0.70	0.13
342-SP15	large kernel	1.20	1.20	1.19	1.00	0.98	1.13	1.15
342-SP16	only low Cs	1.08	1.02	1.09	0.85	0.83	0.99	1.13
342-SP17	only low Cs	1.01	1.02	1.02	0.92	0.91	1.03	1.03
342-SP18	large kernel	1.11	0.98	1.10	0.99	0.98	1.10	1.09
342-SP19	only low Cs	1.03	1.03	1.03	0.90	0.88	1.00	1.04
342-SP20	only low Cs	1.00	1.02	0.97	0.85	0.82	0.94	0.96
342-SP21	only low Cs	1.04	1.10	1.03	0.91	0.87	1.00	1.08
342-SP22	large kernel	1.13	1.15	1.13	1.00	0.96	1.05	1.13
342-SP23	only low Cs	1.09	1.16	1.05	0.87	0.86	1.01	1.07
342-SP24	small kernel	0.90	0.78	0.87	0.73	0.77	0.92	0.81
342-SP25	only low Cs	1.06	1.04	1.09	0.89	0.87	1.02	1.11
342-SP26	only low Cs	1.11	0.92	1.07	0.94	0.93	1.05	1.05

Seven of the particles in Table 5-3 were examined with XCT. Figure 5-41 shows Particle 342-SP07. This particle had fractured buffer that was separated from the IPyC except in two regions. There was a thicker than average portion of residual buffer attached to the IPyC layer where the buffer had detached, which suggested that this detachment required more force than usual. The XCT imaging showed an atypically large amount of high-Z material in the buffer/IPyC gap of Particle 342-SP07. Two small tears in the IPyC layer were observed at the boundary between detached and connected buffer, but these tears did not appear to go through the layer. The IPyC was separated from the SiC over most, if not all of the particle. This separation may have been related to higher stress on the IPyC/SiC interface before detachment of the buffer. No other structural damage in the outer three TRISO layers was observed that would explain the low cesium activity. Cracks in the SiC after cross sectioning were not seen in the XCT images and are assumed to be grinding artifacts. Further SEM examination of this particle is discussed in Section 8.3.

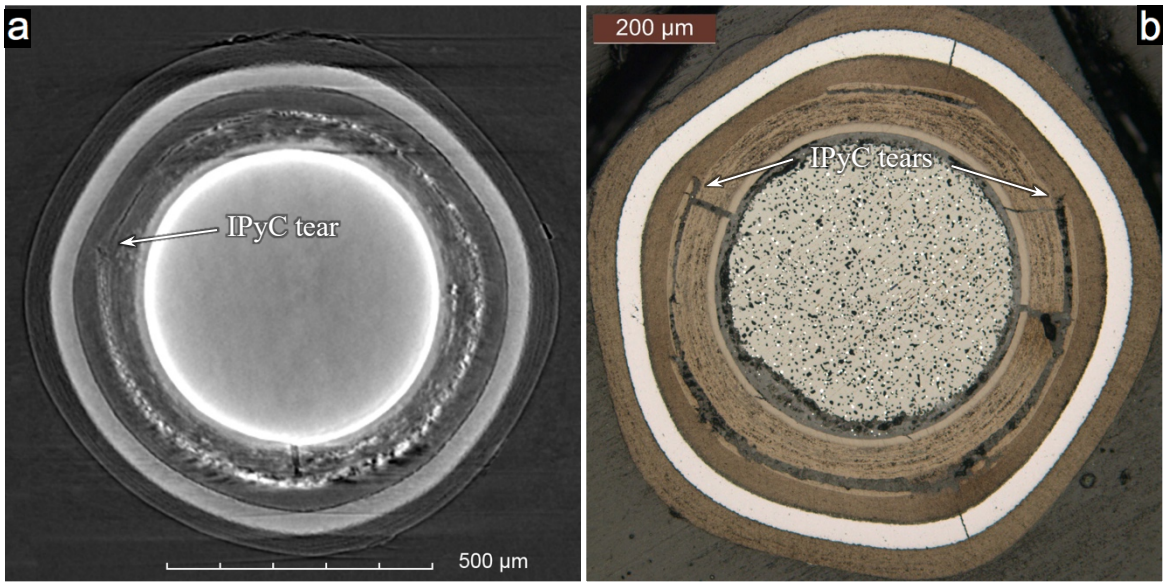

Figure 5-41. (a) X-ray tomogram and (b) optical micrograph of Particle 342-SP07.

Figure 5-42 shows x-ray tomograms of Particles 342-SP08 and 342-SP09. Particle 342-SP08 apparently released half of its cesium inventory, as well as more silver than was typical (Table 5-3). However, the XCT examination revealed nothing about this particle that could be directly related to preferential cesium and silver release. The particle exhibited limited buffer fracture and separation at the buffer/IPyC interface, except for one small region that was possibly still connected. The buffer/IPyC gap was almost non-existent. There appeared to be a barely discernible separation between the IPyC and SiC, which was at the limit of the XCT resolution. No further analysis was performed on this particle.

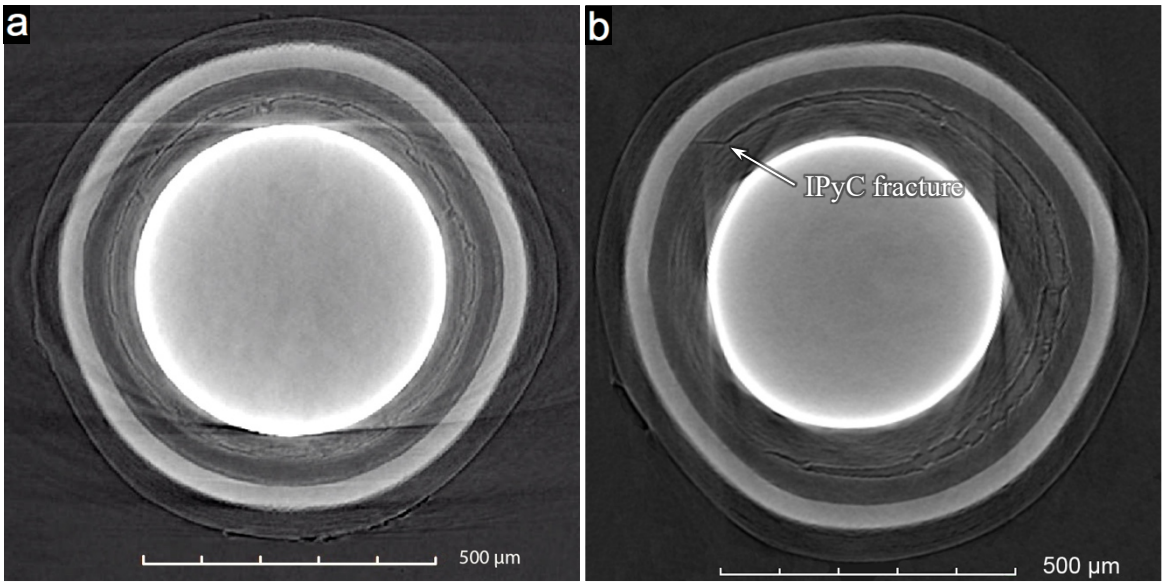

Figure 5-42. X-ray tomograms of (a) Particle 342-SP08 and (b) Particle 342-SP09.

The low M/A values for ^{106}Ru, ^{125}Sb, ^{144}Ce, and ^{154}Eu in Particle 342-SP09 could be explained by a kernel diameter ~20–30 µm below average. The average particle size estimated from the XCT imaging was consistent with an initial kernel diameter in this range. Particle 342-SP09 had a normal appearing microstructure, with the exception of a through-layer IPyC fracture at the boundary between detached and connected buffer and a small region of IPyC/SiC separation at the outer edge of this fracture. Additional SEM examination of this particle is discussed in Section 8.3.

Particles 342-SP10 and 342-SP14 are shown in Figure 5-43. Table 5-3 shows that both these particles had low europium inventories, in addition to indications of significantly below average retained inventories of cesium and silver, as well as reduced cerium in the case of Particle 342-SP14. Both particles had intact buffer layers that were detached from the IPyC except for one region of residual connection. Particle 342-SP10 had a crack through the IPyC at the boundary of this residual buffer/IPyC connection, and this crack was filled with high-Z material. Below average resolution in the XCT image data hampered clear identification of IPyC fracture in Particle 342-SP14. Separation at the IPyC/SiC interface was also observed in both particles. There was an obvious gap extending over about 50% of the interface in Particle 342-SP14, while the IPyC/SiC separation was nearly complete in Particle 342-SP10. A large fraction of the IPyC/SiC gap in Particle 342-SP10 was filled with high-Z material. Particle 342-SP14 had moderately less high-Z material in the IPyC/SiC gap, but significantly more high-Z material in the buffer/IPyC gap. Particles 342-SP10 and 342-SP14 were sectioned and examined further in the SEM (Section 8.3).

Particles 342-SP16 and 342-SP17 are shown in Figure 5-44. These particles had slightly below average cesium activities, with all other measured isotopic activities close to the norm. Both particle looked like normal particles with typical buffer behavior (i.e., no buffer fracture and buffer/IPyC detachment except for one small area). No damage to the three outer layers was observed except for a few minor tears in the IPyC as a result of the buffer detachment.

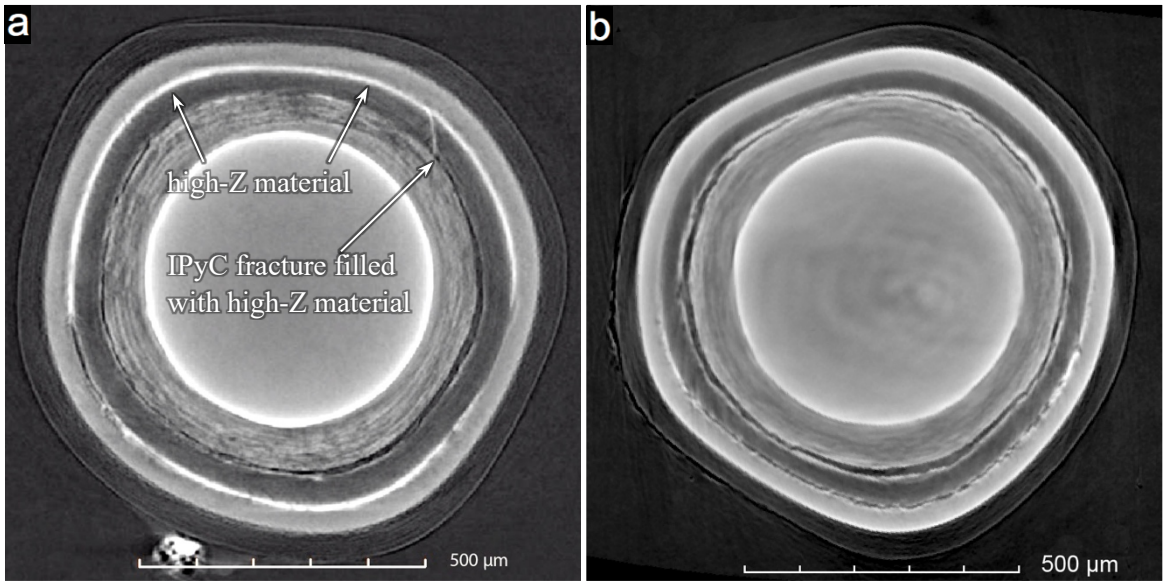

Figure 5-43. X-ray tomograms of (a) Particle 342-SP10 and (b) Particle 342-SP14.

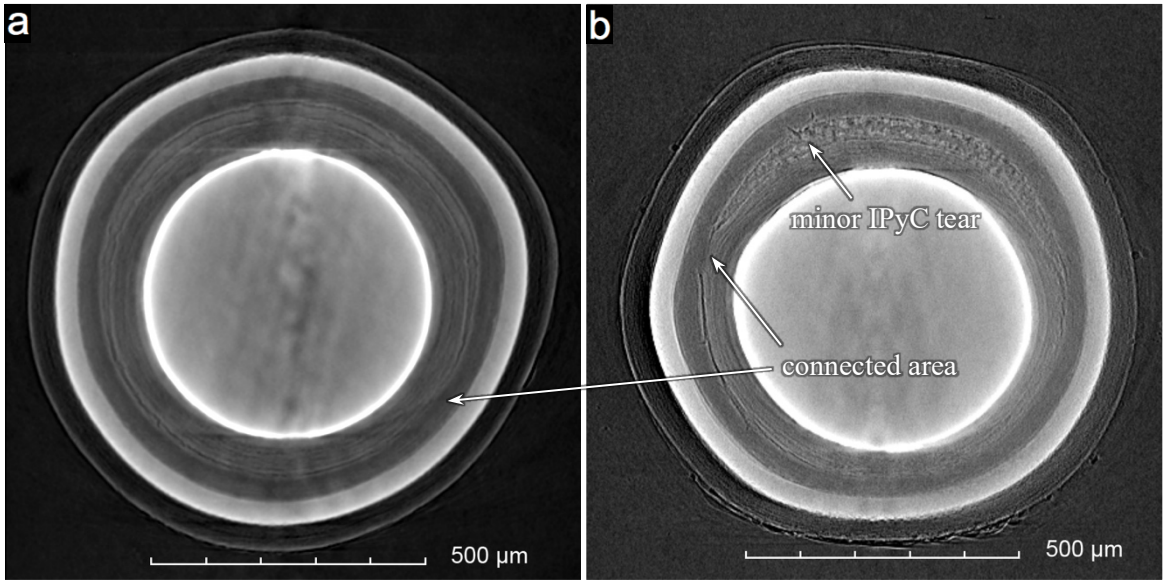

Figure 5-44. X-ray tomograms of (a) Particle 342-SP16 and (b) Particle 342-SP17.

There was a total of 18.6–18.8 particle equivalents of ^{134}Cs released from Compact 3-4-2 and measured either on the CCCTF components (Table 3-2) or in the pre-IMGA DLBL solutions (Appendix Table A-11), in which the upper value includes indication from the digestion acid of 0.2 particle equivalents of ^{134}Cs lost during the matrix burn. The amount of ^{134}Cs released from the special particles listed in Table 5-2 and Table 5-3 with either verified or suspected SiC failure can only account for about half of the ^{134}Cs released during safety testing and DLBL. Only one particle is suspected of being lost during DLBL, based on the exposed uranium analysis discussed in Section 4. It is doubtful that the other missing particles were all lost during the IMGA survey. There may have been numerous unidentified particles with failed SiC that released quantities of cesium that were too small to differentiate them from the main ^{137}Cs M/C distribution (Figure 5-40). As discussed in Section 4, 7.32 particle equivalents of ^{238}U were dissolved during the postburn leaches of the particles from Compact 3-4-2. This suggested at least seven particles with failed SiC were included in those subjected to burn leach after the IMGA survey. While the PIE could not determine the number of failed particles with much certainty, it clearly showed there was an unacceptably high SiC failure fraction (>1%) during the Compact 3-4-2 safety test.

5.6 1,700°C SAFETY-TESTED COMPACT 3-4-1

Figure 5-45 shows that there were five particles recovered from Compact 3-4-1 with ^{144}Ce activities distinctly below the main distribution, and Figure 5-46 shows numerous particles with below average ^{137}Cs activities. Particles 341-SP01, 341-SP02, and 341-SP03 were automatically culled out by the IMGA subroutines. Particle 341-SPX1 apparently dropped off the IMGA vacuum needle between the gamma counting position and the low-cerium particle collector vial and was lost. Particle 341-SPX2 was above the threshold for sorting by ^{144}Ce activity (^{144}Ce M/A < 0.40), so its identity was not maintained during the IMGA survey.

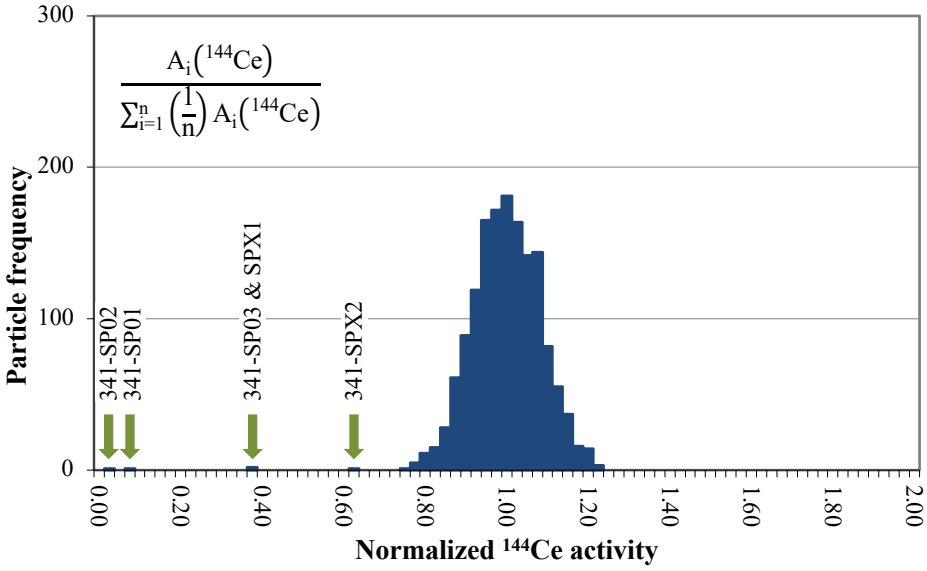

Figure 5-45. Normalized ^{144}Ce activity in 1509 particles from Compact 3-4-1.

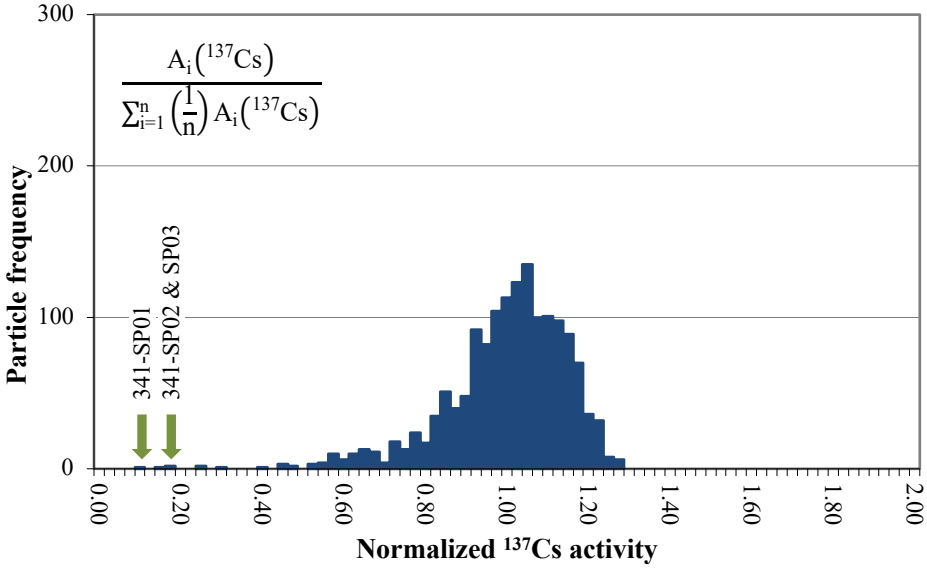

Figure 5-46. Normalized ^{137}Cs activity in 1509 particles from Compact 3-4-1.

Particles 341-SP01, 341-SP02, and 341-SP03 had M/A values (Table 5-4) similar to particles from Compacts 3-3-2 and 3-4-2 that had kernel material leached during DLBL (Table 5-2). As with those particles, most of the ruthenium and antimony remained in the particle, while the inventories of the other measured isotopes were reduced by varying degrees.

Table 5-4. M/A values of Compact 3-4-1 particles with low ^{144}Ce activity

Particle	Value	^{106}Ru	^{110m}Ag	^{125}Sb	^{134}Cs	^{137}Cs	^{144}Ce	^{154}Eu
341-SP01	M/A	0.90	<0.06	1.10	0.08	0.08	0.08	0.01
341-SP02	M/A	0.85	<0.06	1.02	0.15	0.15	0.04	0.01
342-SP03	M/A	1.03	<0.07	1.05	0.17	0.17	0.39	0.05

Figure 5-47 shows two XCT tomograms of Particle 341-SP01. This particle had an unusual buffer morphology, in which it remained attached to the IPyC. As discussed in Section 6, only one out of a sampling of 209 particles from AGR-2 Capsule 3 exhibited this behavior. That particle also showed complete separation between the IPyC and SiC in the plane of inspection (Rice, Stempien, and Demkowicz 2016). These two behaviors were likely related and suggest that the IPyC/SiC interface in the as-fabricated particle was abnormally weak. The Particle 341-SP01 IPyC/SiC interface was similarly detached, either completely or almost completely, and the buffer and IPyC had fractured as a unit into roughly two halves. Figure 5-47b shows that the buffer and the IPyC were curled in along the fracture surface, as has often been observed when these two layer were connected and separated from the SiC. Multiple localized corrosion sites were observed around the inside surface of the SiC layer, and the SEM/EDS analysis discussed in Section 8.4 showed that the large deposits in the gaps between the two buffer/IPyC fragments were SiO_2 from the corrosion reaction. The through-layer pathway through the outer half of the SiC layer shown in Figure 5-47a was not an extended crack like those associated with corrosion sites in other particles with failed SiC (e.g., Particle 342-SP01 in Figure 5-34a and Figure 5-35). This was a "hole" that had similar dimension in the plane perpendicular to that shown in Figure 5-47a. Although the XCT resolution was above average in the images obtained of Particle 341-SP01, due to the missing kernel material, there was no visible through-layer hole or crack in the OPyC. This suggested that the observed kernel reduction may have occurred during safety testing, rather than as a result of acid infiltration during DLBL.

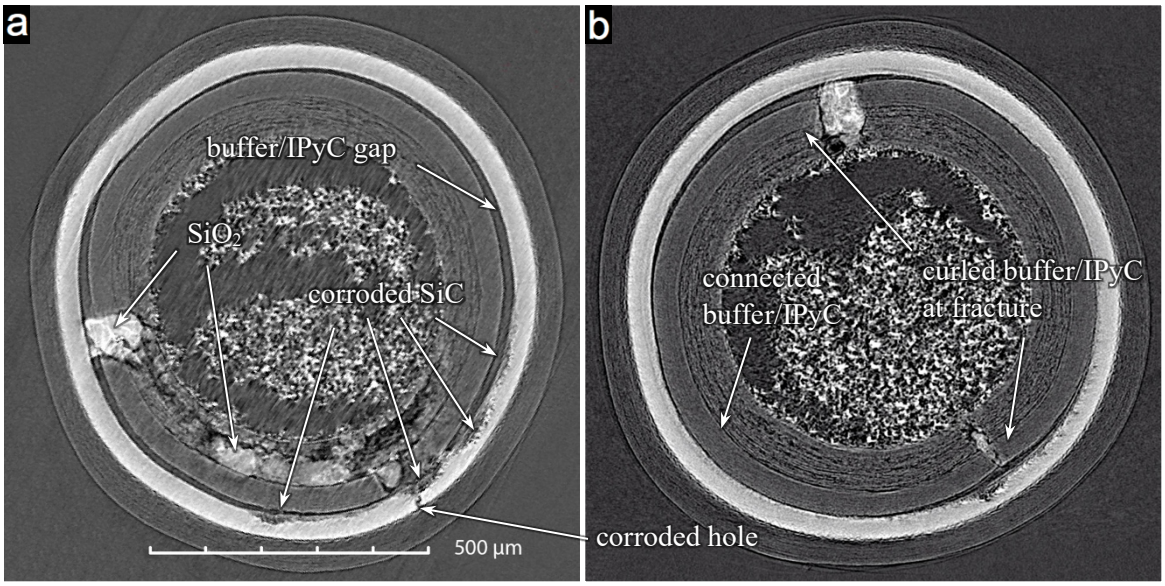

Figure 5-47. X-ray tomograms of Particle 341-SP01.

Figure 5-48a shows Particle 341-SP02. As expected, most of the kernel material was missing. However, like Particle 341-SP01, no obvious flaw in the OPyC was observed. Particle 341-SP02 showed all the common structures associated with SiC failure. The IPyC layer was fractured along the boundary between detached and connected buffer. There was a crack in the buffer, but that did not appear related with the IPyC fracture. Localized corrosion of the SiC was most prominent adjacent to the IPyC crack, and the corrosion penetrated about 10 µm into the SiC layer. A hairline crack through the SiC layer ran along most of the corroded SiC region. There appeared to be a gap that extended around the majority of the

IPyC/SiC interface, but corrosion was not visible in the XCT images more than about 200 μm from the IPyC crack. Deposits in the gap between the buffer and IPyC were likely SiO_2 precipitates, but SEM/EDS was not performed on this particles to confirm this.

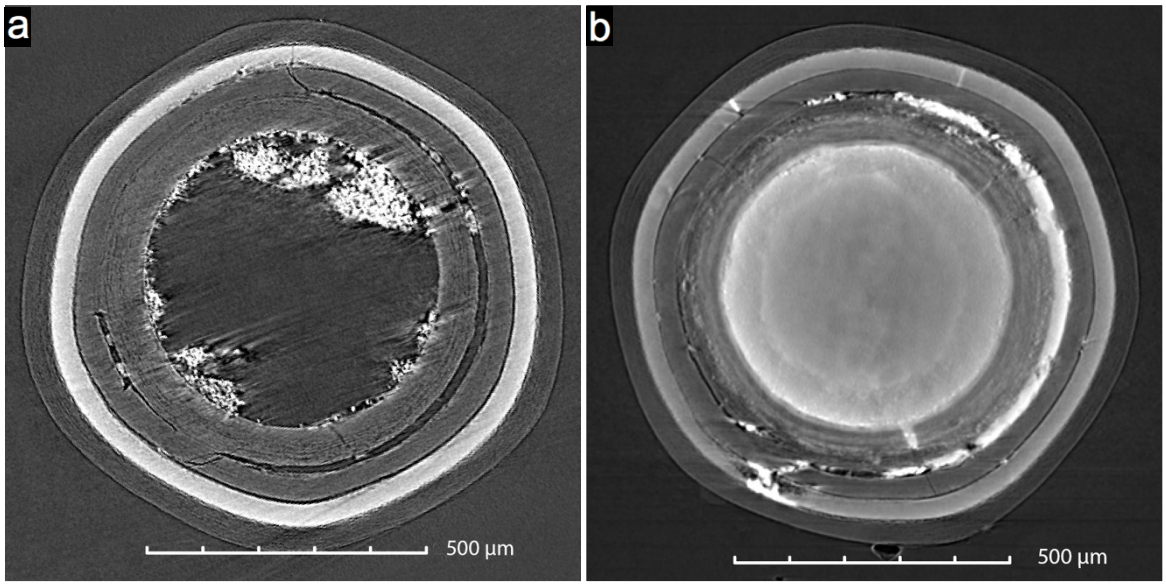

Figure 5-48. X-ray tomograms of (a) Particle 341-SP02 and (b) Particle 341-SP03.

The XCT images of Particle 341-SP03 (Figure 5-48b) showed x-ray penetration around the perimeter of the kernel indicative of a partially leached kernel, similar to Particle 342-SP06. This particle had a fractured buffer that was separated from the IPyC except for two areas. At the edge of one of these connected areas, there was an IPyC crack that led to a through-layer corroded region in the SiC layer. Significant high-Z deposits in the buffer and many of the open regions were observed with SEM/EDS, as discussed in Section 8.4. Figure 5-49 shows some of this high-Z material resided in the SiC cracks, which radiated from the primary corrosion site. The visualization in Figure 5-49a used a threshold equivalent to the x-ray density of SiC, while the visualization in Figure 5-49b used a threshold equivalent to the x-ray density of the higher-Z material (making the SiC semitransparent). Figure 5-49b also shows the high-Z material in the buffer/IPyC gap and remaining kernel material.

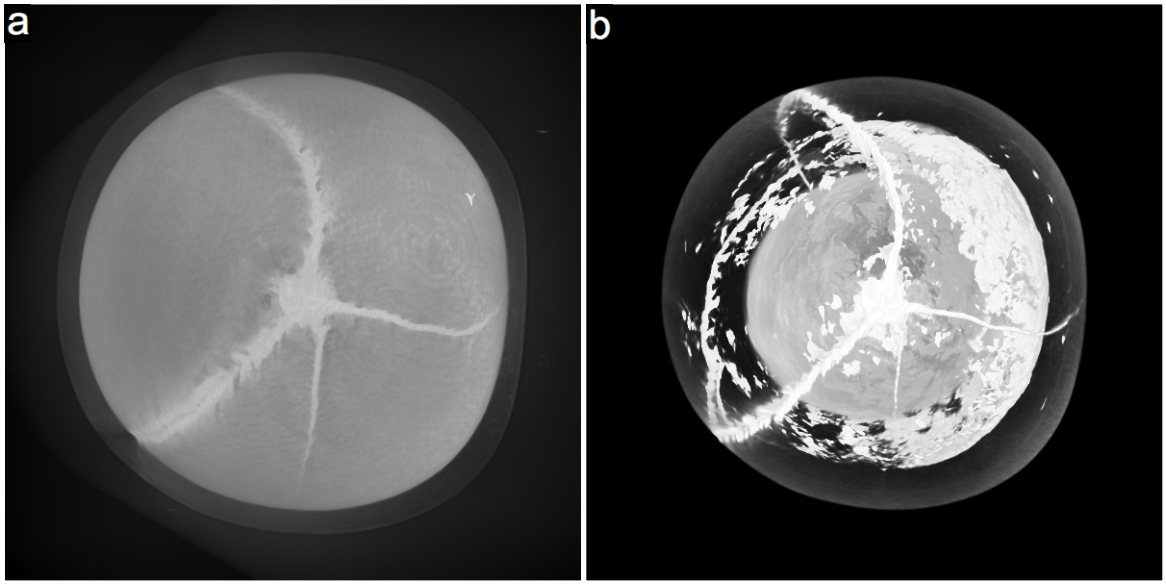

Figure 5-49. 3D representations of Particle 341-SP03.

Figure 5-40 shows a histogram of the ^{137}Cs M/C values for the particles recovered from Compact 3-4-1. There were over 150 particles with a ^{137}Cs M/C ≤ 0.80, and it can be presumed with high confidence that almost all these particles released some cesium. These particles were separated from the main population by the IMGA sorting process, which binned particles according to their ^{137}Cs M/AA ratio (Section 2.2). However, the total estimated ^{137}Cs release from these 150+ particles only accounted for roughly half of the ^{137}Cs measured on the CCCTF deposition cups and furnace internals (Hunn et al. 2018b). Therefore, there were numerous particles that released cesium with ^{137}Cs M/AA > 0.80 that were not separated out from the main distribution, which may have also contained particles that did not release cesium. A rough accounting for the ^{137}Cs released in the CCCTF using the IMGA-measured amount of ^{137}Cs retained in the recovered Compact 3-4-1 particles and summing all particles starting from the left side of Figure 5-40, with the assumption that particles started with an average ^{137}Cs M/C = 1.05–1.10, yielded an estimate of 400–800 particles with failed SiC (i.e., up to half of the particles in the compact). The exact number is somewhat irrelevant, as this failure fraction is so far beyond a typical safety basis that use of an oxygen-gettered kernel design, such as UCO, for fuel intended for this level of burnup is clearly recommended if accident conditions might reach 1,700°C.

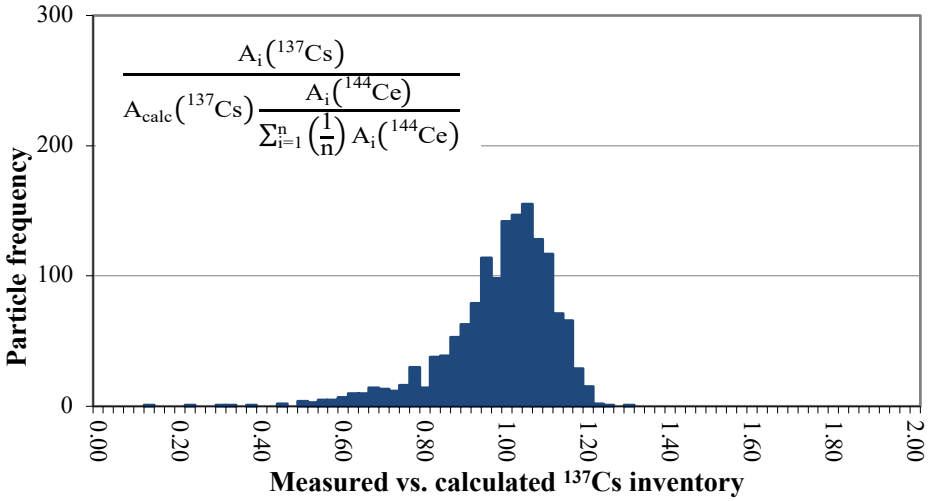

Figure 5-50. Measured vs. calculated ^{137}Cs inventory in 1509 particles from Compact 3-4-1.

Table 5-5 lists the ^{137}Cs M/A values for the other Compact 3-4-1 special particles imaged with XCT. Particles 341-SP04, 341-SP05, 341-SP06, and 341-SP07 were selected from the 28 particles in Bin 6, which collected particles with ^{137}Cs M/AA < 0.60 and ^{144}Ce M/A > 0.40. Figure 5-51 shows XCT tomograms of these four particles. All four particles had detached buffer and IPyC fracture along the boundary where the buffer remained attached. Particles 341-SP04 and 341-SP06 had no other visible irregularities other than some barely-resolvable indications of IPyC/SiC separation, nevertheless, their low cesium inventories indicated these particles were most likely among the many 1,700°C safety-tested particles with failed SiC. Particle 341-SP05 had fractured buffer, a large gap at the IPyC/SiC interface, general corrosion of the inner surface of the exposed SiC, and high–Z material throughout the buffer, buffer fragment gaps, buffer/IPyC gap, and in the IPyC crack. Particle 341-SP07 also had high-Z in the buffer and buffer/IPyC gap, as well as a narrow IPyC/SiC gap. In addition, there was a clearly resolvable crack extended around half the SiC layer of Particle 341-SP07.

Table 5-5. M/A values of Compact 3-4-1 special particles with low ^{137}Cs M/C imaged with XCT.

Particle	Characteristic	^{106}Ru	^{110m}Ag	^{125}Sb	^{134}Cs	^{137}Cs	^{144}Ce	^{154}Eu
341-SP04	M/A	1.17	0.75	1.14	0.55	0.54	1.13	1.08
341-SP05	M/A	0.94	0.36	0.96	0.49	0.51	1.01	0.51
341-SP06	M/A	0.98	0.75	0.99	0.55	0.55	0.92	0.95
341-SP07	M/A	0.95	0.40	0.97	0.43	0.44	1.02	0.92
341-SP15	M/A	0.96	0.89	0.99	0.76	0.74	0.95	1.02

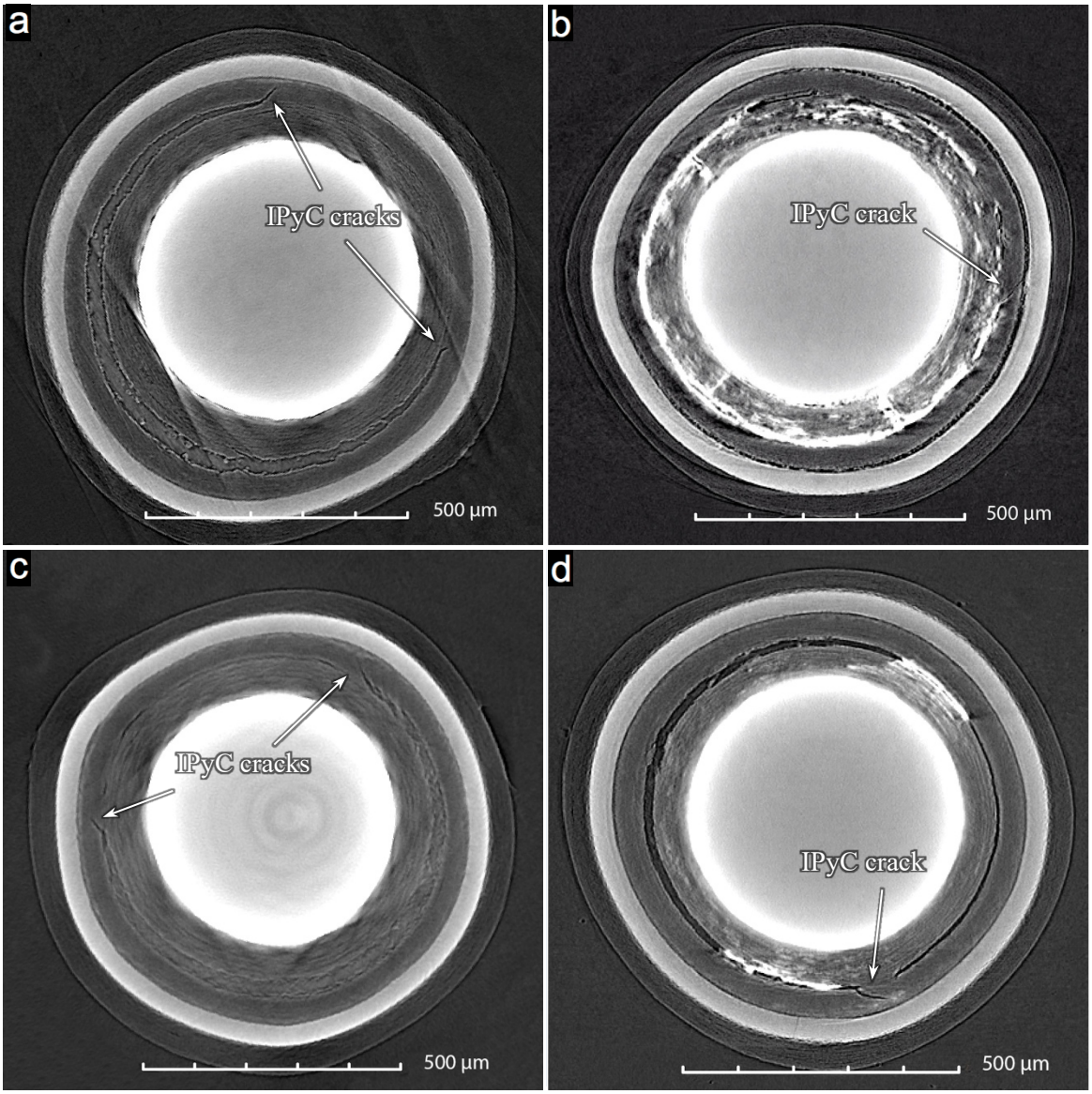

Figure 5-51. X-ray tomograms of (a) Particle 341-SP04, (b) Particle 341-SP05, (c) Particle 341-SP06, (d) Particle 341-SP07.

There were 46 particles in IMGA Bin 7, which collected particles with $0.60 < {}^{137}Cs\ M/AA < 0.70$ and ${}^{144}Ce\ M/A > 0.40$; and there were 80 particles in IMGA Bin 8, which collected particles with $0.60 < {}^{137}Cs\ M/AA < 0.70$ and ${}^{144}Ce\ M/A > 0.40$. It was not feasible to examine all these low-cesium particles, so Particle 341-SP15 was chosen from Bin 8 for XCT and SEM analysis to provide a look at particles with marginal cesium release. Particle 341-SP15 had no significant buffer separation (Figure 5-52), which would be unusual if it were a normal particle, as discussed above with regard to Particle 341-SP01. This particle is discussed further in Section 8.4. Section 6 explains that larger materialographic mounts were used to cross section about 30 particles at one time for inspection with optical microscopy. All the remaining particles from Bins 6 and 32 particles from Bin 8 were mounted, and images are in Appendix C. These particles showed more abnormal features than the as-irradiated particles discussed in Section 6. These differences were due to both the 1,700°C thermal exposure during safety testing and the nonrandom sampling, in which some of the worst performing particles were inspected. For example, there were 9 out of 55 particles with connected or mostly connected buffer/IPyC interfaces (Figure 5-53) vs. only 1 out of 209 in the random sampling of as-irradiated particles (Section 6). This buffer morphology did not change during safety testing, so the higher fraction in the Bin 6 and Bin 8 nonrandom samples was

due to these morphologies having a tendency to result in poorer cesium retention. There were also particles like those in Figure 5-54 with obvious SiC failure and many of the related features observed in the special particles with failed SiC, such as fractured IPyC, separated IPyC/SiC interfaces, corroded SiC, and eroded kernels. These features were related to radiation-induced changes, such as IPyC fracture, that made the particles more susceptible to failure, as well as changes that occurred during the safety test.

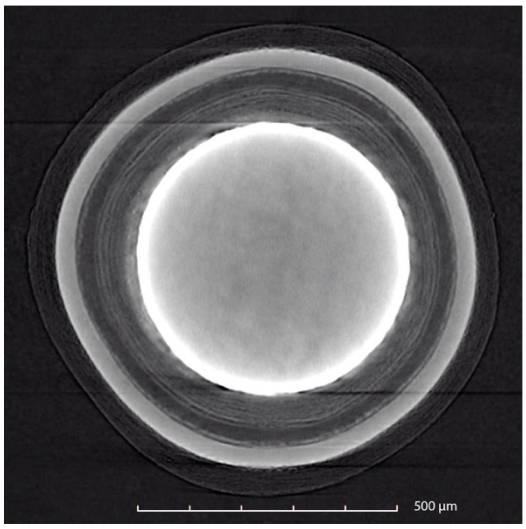

Figure 5-52. X-ray tomogram of Particle 341-SP15.

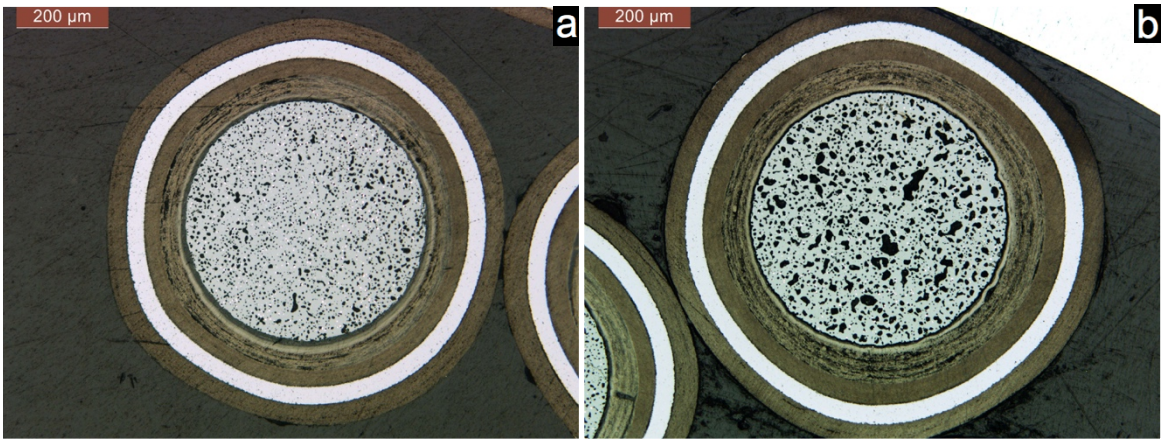

Figure 5-53. Compact 3-4-1 particles with connected buffer/IPyC interfaces from (a) Bin 6 and (b) Bin 8.

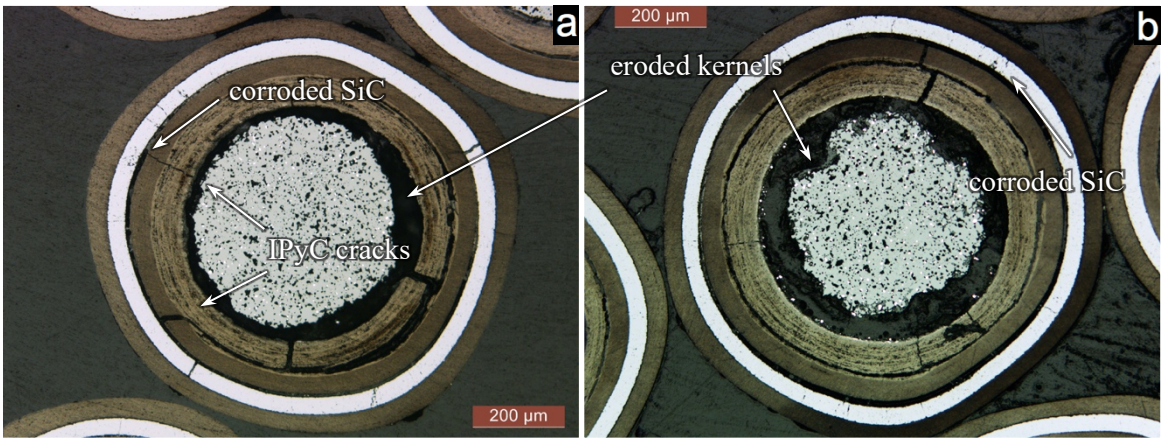

Figure 5-54. Compact 3-4-1 particles with obvious SiC failure from (a) Bin 6 and (b) Bin 8.

6. BUFFER AND KERNEL EVOLUTION UNDER IRRADIATION

In addition to the materialography described in Section 2.3, which was performed on individual particles selected from the special particles and RS particles measured with IMGA, several random samples were riffled from the available as-irradiated particles deconsolidated from Compacts 3-1-2 and 3-3-1 and polished in larger mounts designed to hold ~30 AGR-2 UO_2 TRISO particles to provide a general overview of the irradiated particle microstructures (Figure 6-1). Individual optical micrographs of these particles are provided in Appendix C.

Figure 6-1. Multiparticle mount of 31 random particles from Compact 3-3-1.

Of particular interest was the behavior of the buffer and kernel, which are the components in a TRISO particle that normally undergo the most noticeable microstructural change as a result of the neutron irradiation (Stempien, Plummer, and Schulthess 2019). Study of buffer behavior in UCO TRISO particles has shown that neutron irradiation caused densification and volume reduction of the buffer layer. Typical

and probably preferred behavior involved detachment of the buffer from the inner pyrocarbon in such a way that the IPyC layer was not damaged. This allowed the buffer layer to freely shrink in outer diameter. Fissions from neutron irradiation of the kernel caused chemical and physical changes in the kernel that included generation of porosity due to gaseous fission products, which produced kernel swelling. Kernel swelling was restrained when the buffer was detached from the IPyC and not fractured. Fractured buffer allowed some asymmetric swelling of the kernel. When the buffer was not detached from the IPyC, kernel swelling was less restrained.

A total of 35 particles from Compact 3-3-1 were examined: 31 particles were prepared in the multiparticle mount shown in Figure 6-1, and 4 RS particles were cross sectioned for SEM analysis, as discussed in Section 7.1. All 35 Compact 3-3-1 particles had detached buffer with no signs of buffer fracture or IPyC tearing. In most cases, a residual area of connected buffer/IPyC could be seen in the polished cross section. The connected area was expected because the forces involved in causing the buffer detachment were reduced as a function of the fraction of buffer already detached. The connected area can be small enough to not be included in the plane of polish, so conclusions regarding buffer that appeared completely detached in a single observation plane may not be meaningful. As observed early in AGR-1 PIE (Hunn et al. 2012), buffer detachment was not like delamination observed in some coated materials. It was actually a mechanical tearing apart of the buffer material, which usually occurred close to the buffer/IPyC interface. This was evidenced by the presence of buffer material that remained at the buffer/IPyC interface and by tendrils of incompletely detached buffer material that spanned the gap (Figure 6-2).

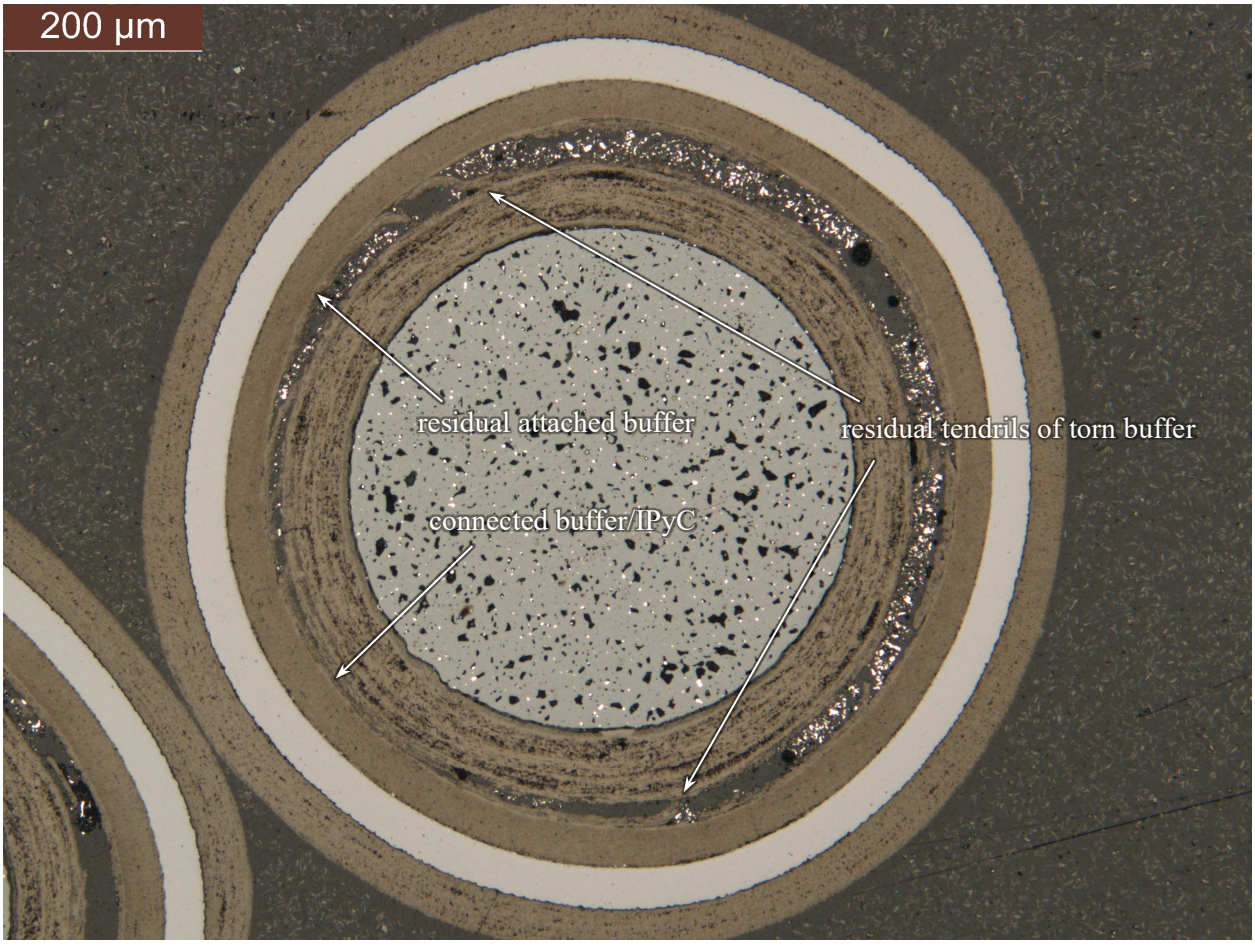

Figure 6-2. Typical particle from Compact 3-3-1 showing common features of buffer detachment.

A total of 72 random particles from Compact 3-1-2 were examined: 66 particles were sectioned in two multiparticle mounts and are shown in Appendix C, and 6 RS particles were cross sectioned for SEM

analysis, as discussed in Section 7.1. All 72 Compact 3-1-2 particles had detached buffer and 68 particles showed no signs of buffer fracture or IPyC tears. Three particles had gaps in the buffer that did not go through the whole layer (Figure 6-3a–c). These gaps appeared to be caused by buffer fracture, but had a different appearance from what has been typically observed in UCO TRISO. The gaps in the buffer terminated at a dense buffer region located at the kernel/buffer interface. This dense buffer region was a common feature in many Capsule 3 particles and was also see in UCO TRISO particles (e.g., Hunn et al. 2018c). Analysis of the dense buffer region with EDS, as discussed in Section 7, showed the presence of uranium and several fission products. This portion of the buffer may have been modified by some combination of chemical reaction with the kernel, fission product recoil, and kernel swelling. Figure 6-3d shows an as-irradiated AGR-2 UCO Compact 5-4-2 particle with buffer fracture. In different locations around the UCO kernel/buffer interface, the dense region was sometimes connected to the kernel, sometimes connected to the buffer, and sometimes fractured down the middle with portions remaining attached to both the buffer and the kernel. In addition, the dense region remained continuous across the buffer gaps, not completely unlike what was observed in the UO_2 TRISO. The different behavior of this region in the UCO TRISO may be related to the carbide skin the forms on UCO kernels when they are heated during coating and heat treatment after compacting (Hunn et al. 2012).

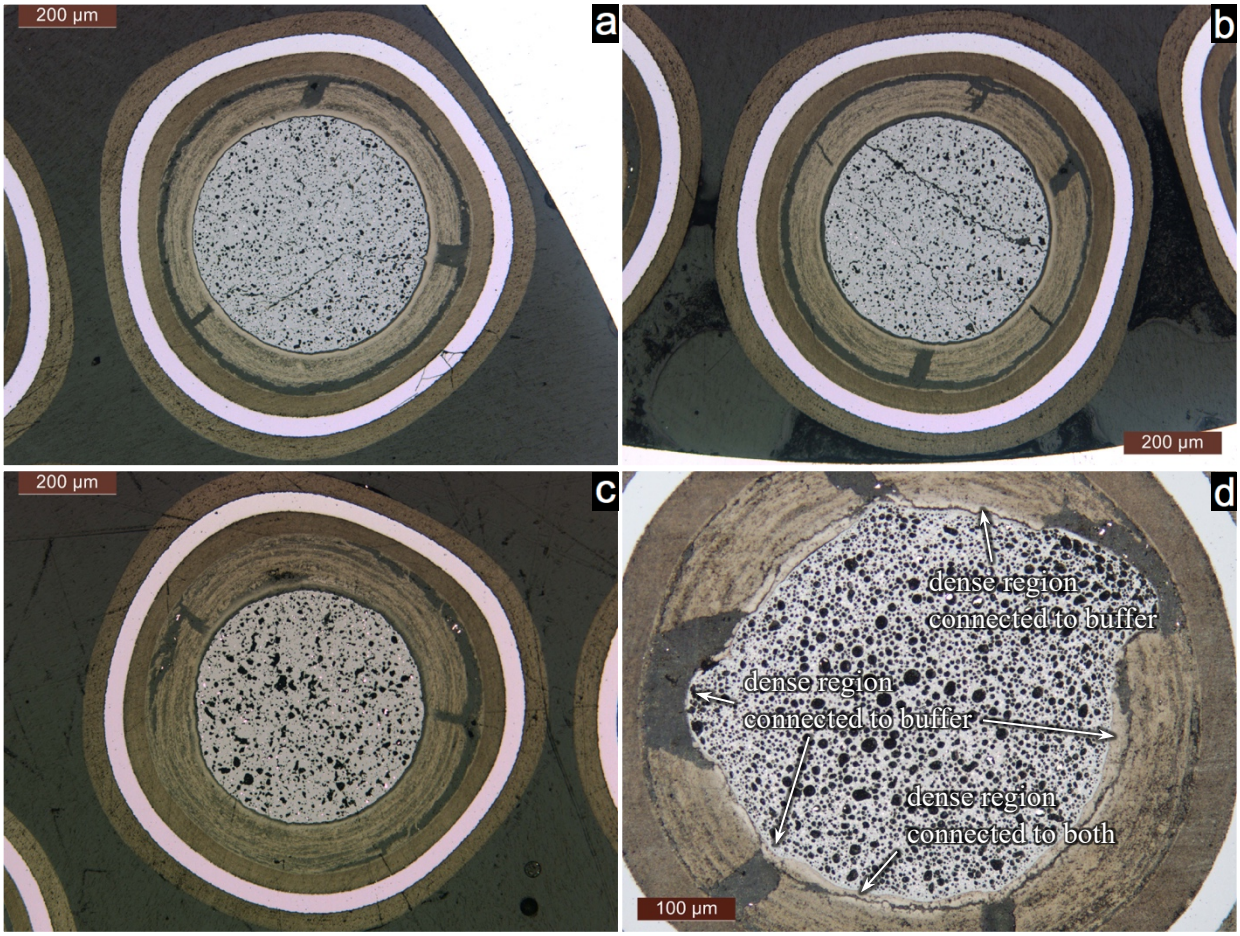

Figure 6-3. (a–c) Particles from AGR-2 UO_2 Compact 3-1-2 with gaps in buffer, and (d) a particle from AGR-2 UCO Compact 5-4-2 for comparison.

Figure 6-4 shows an abnormal particle from Compact 3-1-2. This particle exhibited unusual buffer detachment, with the circumferential tearing apart of the buffer material occurring further from the interface than normal at some locations. This was the only random particle observed with IPyC tears. These tears were evident on both sides of the connected buffer/IPyC region. There also appeared to be an inclusion at the buffer/IPyC interface that very likely played a role in the adjacent IPyC tear.

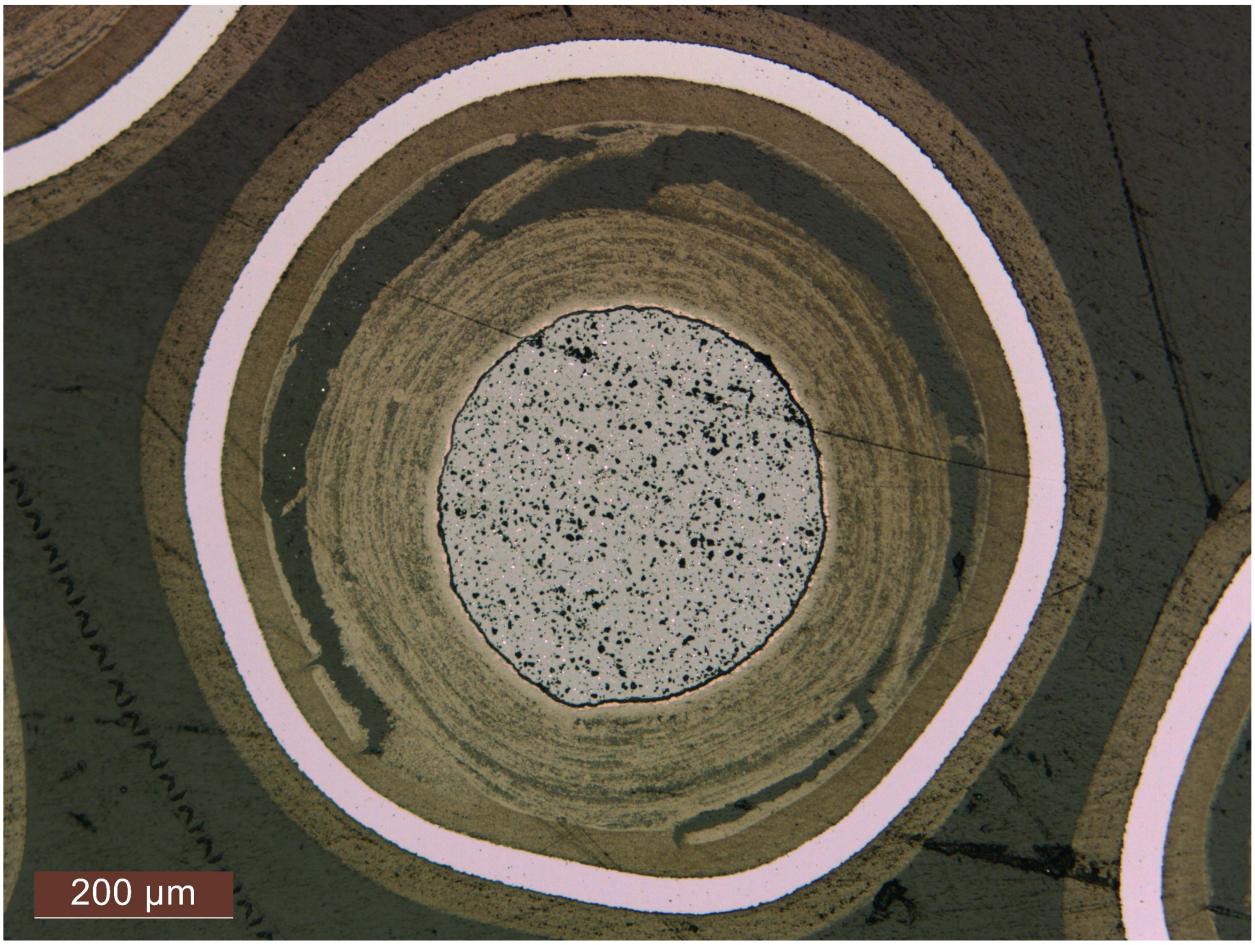

Figure 6-4. Abnormal particle from Compact 3-3-1 with IPyC tears.

Results from the survey of as-irradiated particles deconsolidated from AGR-2 UO_2 Compacts 3-1-2 and 3-3-1 were consistent with a similar study of particles from AGR-2 UO_2 Compact 3-2-3 (Rice, Stempien, and Demkowicz 2016). In that study, particles sufficiently revealed in polished sections taken from whole compacts were catalogued for the various common morphologies. Out of 102 particles catalogued from AGR-2 UO_2 Compact 3-2-3, 98 had detached buffer with no apparent fracture, 3 had detached buffer with visible fracture, and 1 had a buffer layer that was not detached. Particle morphologies were also studied in AGR-2 UCO Compact 5-1-3 (Rice, Stempien, and Demkowicz 2016) and deconsolidated particles from Compact 5-2-3 (Hunn et al. 2016). Buffer fracture was prevalent in Compact 5-1-3 (70 out of 181) and Compact 5-2-3 (76 out of 88). In contrast, particles from AGR-2 high-temperature Capsule 2 were shown to have lower incidents of buffer fracture in those two studies, similar to the AGR-2 UO_2 TRISO. Some of the factors contributing to these differences were discussed by Rice, Stempien, and Demkowicz (2016), and may include not only differences in irradiation conditions, but also factors related with difference in kernel swelling.

7. SEM ANALYSIS OF RANDOMLY SELECTED PARTICLES

Table 7-1 lists the RS particles from Appendix B subjected to SEM image analysis, and Appendix X provides comprehensive image sets from each particle. Particle selection was based on the M/AA values, as defined in Section 2.2. An isotopic M/AA value close to unity represents average retention for that isotope in a particular compact. One or two particles with M/AA values close to unity for all measured isotopes were selected to represent average particles from each compact. In addition to average particles, particles were selected, if available, that represented the lowest below average and highest above average silver retention, with an additional criterion that all other isotopes exhibited average retention to rule out abnormal particles. Silver inventory was targeted because the silver release from a compact has been shown to vary with the TAVA compact irradiation temperature (Harp et al. 2016) and variation in silver release for normal particles from the same compact is thought be impacted by the spatial variation in temperature across the compact (Demkowicz et al. 2015b; Gerczak et al. 2018). While silver and silver retention were not specifically studied as part of the SEM analysis presented herein, ^{110m}Ag M/AA served as a convenient indicator of what particles may have experienced different irradiation temperatures, with significantly lower silver retention indicating particles irradiated at generally higher temperature.

Table 7-1. M/AA values of RS particles subjected to SEM analysis

Particle Value	**^{106}Ru** M/AA	**^{110m}Ag** M/AA	**^{110m}Ag** M/C	**^{125}Sb** M/AA	**^{134}Cs** M/AA	**^{137}Cs** M/AA	**^{144}Ce** M/AA	**^{154}Eu** M/AA
312-RS06	0.98	<0.67	<0.69	0.98	1.04	1.00	0.98	1.02
312-RS32	0.98	<0.68	<0.69	0.99	0.99	1.00	0.97	0.98
312-RS05	1.02	1.06	1.08	1.00	1.04	1.00	0.97	1.01
312-RS34	0.96	1.18	1.21	0.99	1.00	1.00	1.01	0.98
312-RS02	0.99	1.54	1.58	1.01	0.96	1.00	1.04	0.95
312-RS11	1.01	1.60	1.64	1.01	0.93	1.00	1.06	0.95
331-RS04	0.96	0.62	0.56	1.00	0.97	1.00	1.00	1.00
331-RS19	0.98	0.61	0.56	0.98	0.97	1.00	0.97	1.02
331-RS03	0.95	1.02	0.92	0.97	1.00	1.00	0.98	1.01
331-RS12	0.98	0.95	0.86	0.99	1.00	1.00	1.00	0.99
311-RS07	1.02	<0.64	<0.60	1.01	1.03	1.00	1.04	0.98
311-RS29	0.95	<0.70	<0.66	0.97	1.04	1.00	1.00	0.98
311-RS08	1.05	1.03	0.96	1.00	1.12	1.00	0.94	1.05
311-RS32	1.05	1.05	0.98	1.02	1.08	1.00	0.99	1.02
311-RS18	0.98	1.58	1.47	0.99	0.97	1.00	1.07	0.94
311-RS36	1.04	1.51	1.41	1.02	1.09	1.00	0.97	1.03
332-RS12	0.97	0.64	0.60	1.01	1.01	1.00	0.93	1.02
332-RS18	0.99	0.65	0.61	1.01	1.01	1.00	1.00	1.00
332-RS22	0.99	1.00	0.94	1.00	0.98	1.00	0.97	1.03
332-RS43	1.01	1.00	0.94	0.96	1.00	1.00	1.00	1.01
332-RS26	1.09	1.31	1.23	1.06	1.01	1.00	1.07	1.03
332-RS31	1.09	1.29	1.21	1.05	1.00	1.00	1.10	0.99
342-RS17	0.96	0.77	0.86	0.98	0.96	1.00	1.02	0.95
342-RS29	0.96	0.81	0.90	0.97	0.99	1.00	1.02	0.96
342-RS07	0.97	0.99	1.09	0.97	1.02	1.00	0.97	0.96
342-RS21	0.98	1.01	1.11	0.97	1.00	1.00	1.00	1.00
342-RS03	1.05	1.20	1.33	1.02	1.08	1.00	0.90	1.08
342-RS15	1.12	1.17	1.30	1.07	1.04	1.00	1.04	1.08
341-RS21	0.94	0.70	0.74	0.94	0.92	1.00	1.05	0.90
341-RS36	1.00	0.89	0.94	0.99	1.02	1.00	1.03	0.99
341-RS01	0.96	1.01	1.07	1.00	0.97	1.00	1.04	0.98

Note: Highlighted particles are representative of average retention of all measured isotopes for their particular compact.

7.1 AS-IRRADIATED COMPACTS 3-1-2 AND 3-3-1 RS PARTICLES

SEM analysis of particles from as-irradiated compacts focused on evaluation of the structure of the buffer, IPyC, SiC, and OPyC layers and their respective interfaces. A primary focus of AGR-2 PIE has been the identification of the actinides and fission products released from the kernel and interacting within the various layers of the TRISO particle. This analysis provided a general understating of how fission products and actinides were redistributed during operation and the role of the different layers on accommodating the fission products. Analysis of the as-irradiated particles also established a baseline for the particle behavior prior to safety-testing. As-irradiated Compacts 3-1-2 and 3-3-1 were explored, as they were sister compacts to safety-tested Compacts 3-1-1 and 3-3-2, respectively.

Select SEI images are shown in Figure 7-1 and Figure 7-2 to highlight the structural variation in the IPyC/SiC/OPyC layers. The SEI imaging highlighted the structural variation across particles. Features that were common across all particles were low-Z inclusions or material pullout caused by sample preparation. Compositional EDS analysis indicated a higher carbon composition in these features suggesting they were carbon inclusions. The *IPyC/SiC interface region* was defined by the dense SiC boundary surface and the adjacent region of the IPyC layer, which had variable porosity and SiC penetration. Considerable structural variation was observed in this region. In particular, the degree of PyC inclusion in the first few microns of the SiC layer varied from location-to-location in a single particle and across different particles. Similarly, the IPyC showed variable porosity around the circumference of the IPyC/SiC interface that sometimes formed low-density banded structures. Some of the observed porosity may have been a sample preparation artifact; however, the porosity that appeared at discrete distances from the dense SiC boundary was likely a processing feature from the FB-CVD deposition.

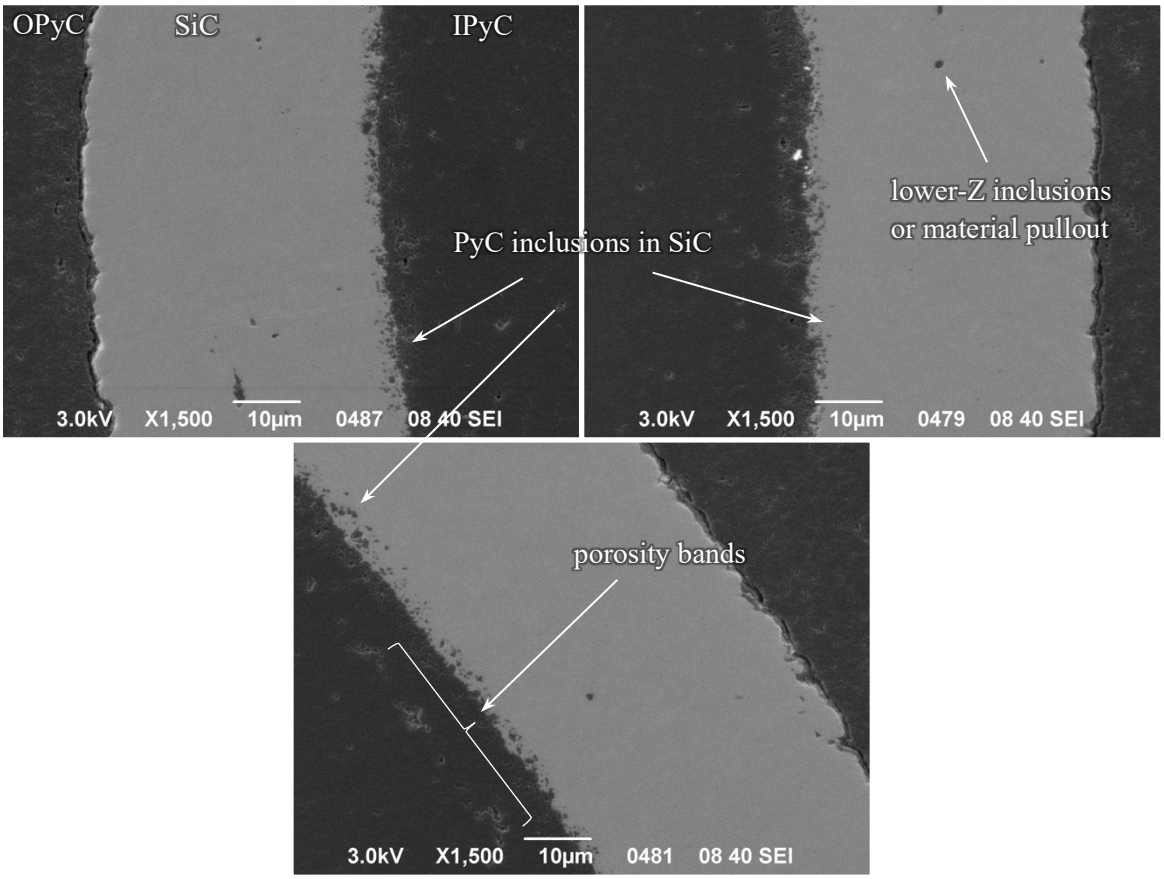

Figure 7-1. Example SEI micrographs of the IPyC/SiC/OPyC layers in Particle 312-RS34.

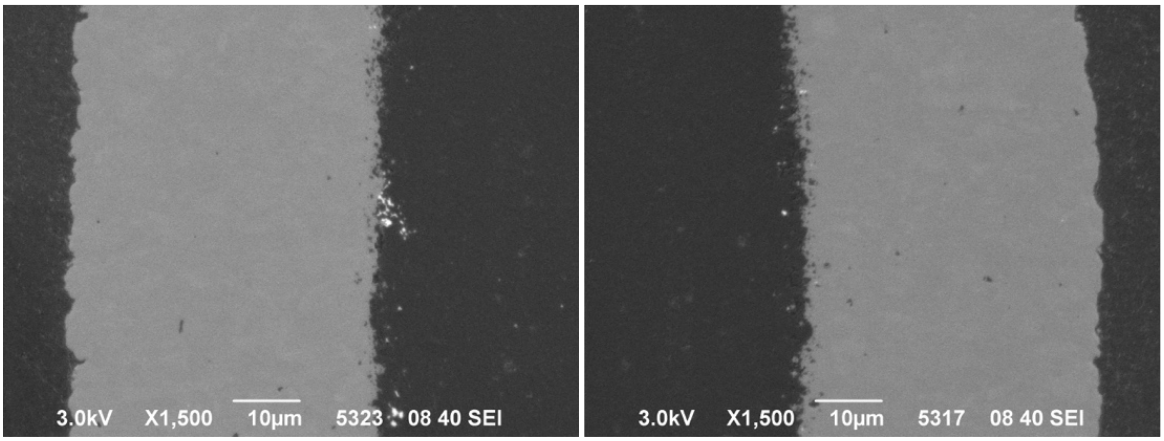

Figure 7-2. Example SEI micrographs of the IPyC/SiC/OPyC layers in Particle 331-RS19.

High-Z features were observed in variable distributions in the IPyC/SiC/OPyC layers. Four general classes of high-Z features were defined for the IPyC and SiC layers to delineate between high-Z agglomerates in the IPyC/SiC interface region and those in the IPyC and SiC away from that region: a *high-Z SiC feature* is an agglomerate inside the dense SiC layer; a *high-Z boundary feature* is an agglomerate at the IPyC/SiC boundary; a *high-Z interface feature* is an agglomerate located in the IPyC less than 10 µm from the SiC boundary; and a *high-Z IPyC feature* is an agglomerate located in the IPyC more than 10 µm away from the SiC boundary. Observations of these feature types in the AGR-2 UO_2 TRISO were consistent with observations in AGR-1 and AGR-2 UCO TRISO (Gerczak et al. 2018). Examples of all four feature types are shown in Figure 7-3.

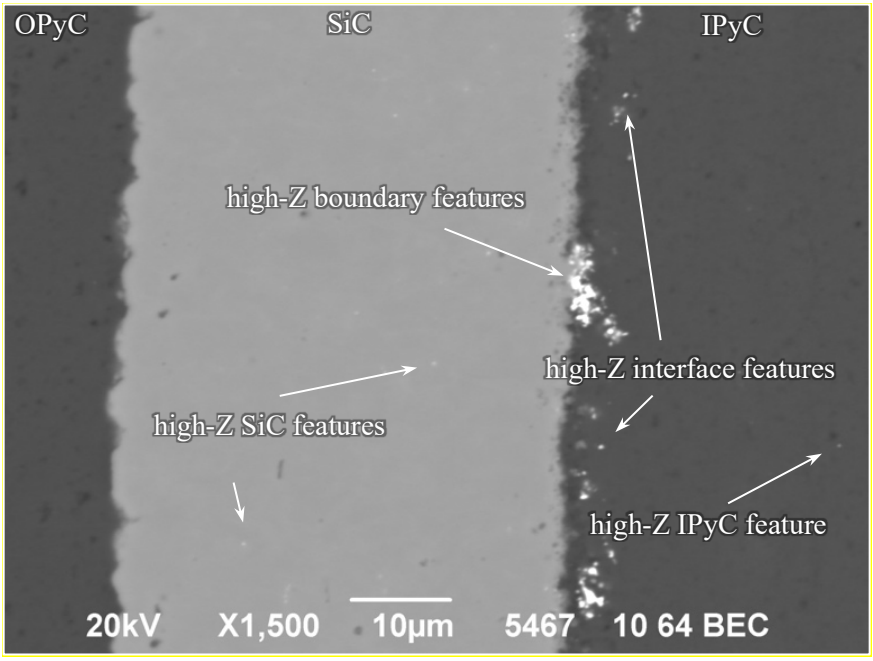

Figure 7-3. Examples of different feature types in Particle 331-RS19.

Examples of the feature distributions in Compact 3-1-2 particles are shown in Figure 7-4–Figure 7-6. Analysis of Compact 3-1-2 particles did not reveal any high-Z SiC features in the SiC layer. Micron-scale high-Z features were observed in the IPyC/SiC interface region. The features were almost exclusively high-Z boundary features, with few high-Z interface features observed. The size and frequency of the high-Z boundary and interface features varied from location to location within the particle. This is shown in the comparison of locations within Particle 312-RS34 (Figure 7-5 and Figure 7-6), in which one side of

the particle had a lower frequency of high-Z features. All Compact 3-1-2 particle cross sections analyzed with SEM showed the typical buffer microstructure, as described in Section 6, in which the buffer was detached from the IPyC except for one region. No obvious correlations between the frequency and distribution of high-Z features at the IPyC/SiC interface were observed for the Compact 3-1-2 particles.

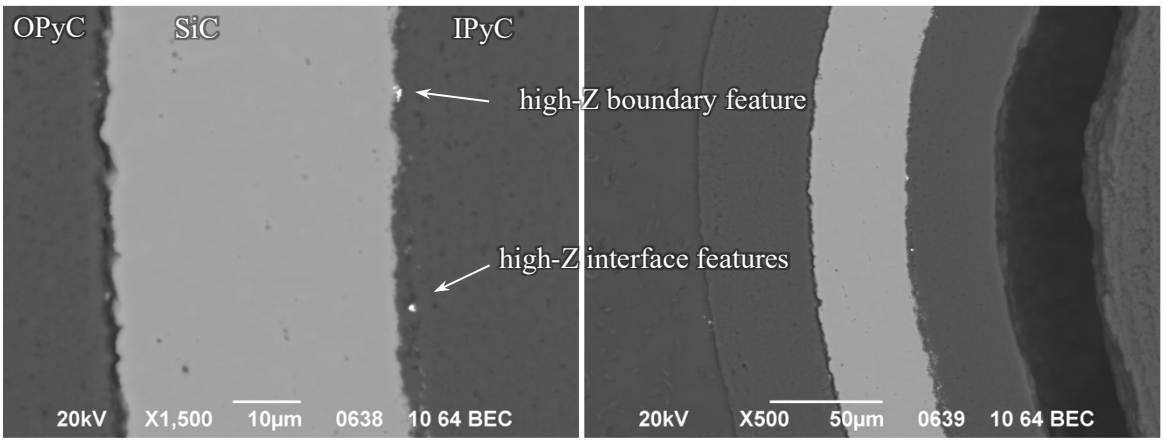

Figure 7-4. Example BEC images of the TRISO layers in Particle 312-RS11.

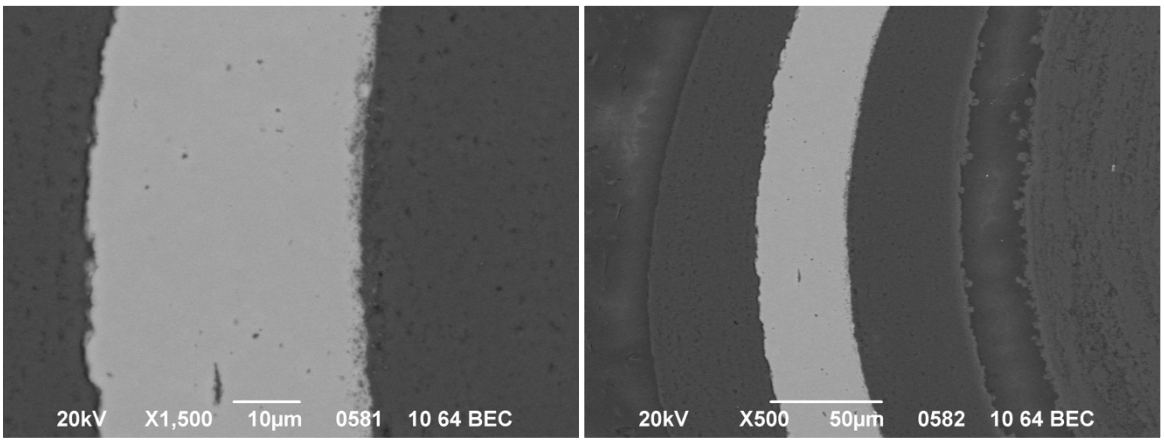

Figure 7-5. Example BEC images of the TRISO layers in Particle 312-RS34.

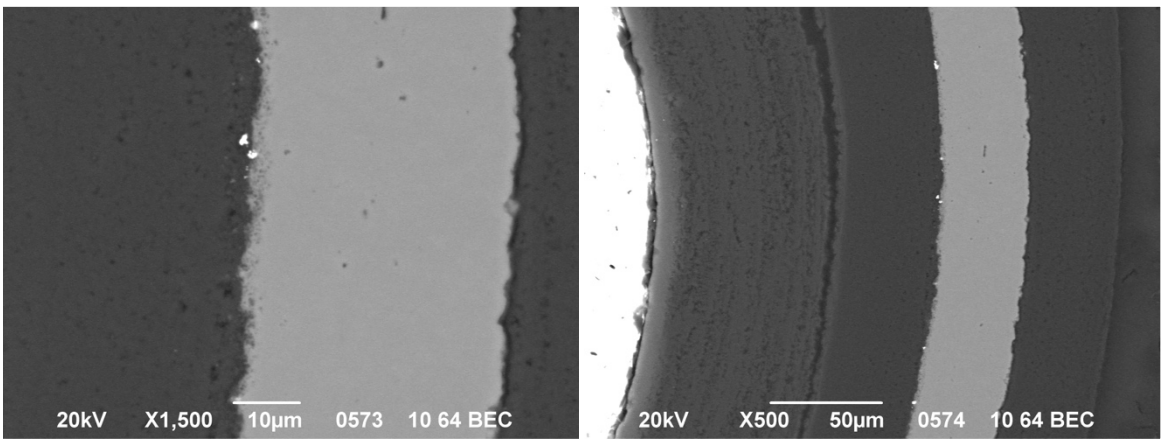

Figure 7-6. Example BEC images of the TRISO layers in Particle 312-RS34.

Example BEC images of the feature distributions in Compact 3-3-1 particles are shown in Figure 7-7 and Figure 7-8. Initial Compact 3-3-1 observations have been discussed by Gerczak et al. (2018). Particle

331-RS03 was missing its OPyC layer, which was lost during DLBL or IMGA survey. Fine-scale, high-Z SiC features were observed in all Compact 3-3-1 particles except Particle 331-RS03. The high-Z SiC features extended across the entire thickness of the SiC layer (Figure 7-3 and Figure 7-7). All the Compact 3-3-1 particle cross sections examined with SEM showed detached buffer layers, and only Particle 331-RS04 did not show a remaining connected region. Particles 331-RS03 and 331-RS19 exhibited a generally uniform distribution of features around the circumference of the IPyC/SiC interface. In contrast, Particle 331-RS12 showed preferential segregation of high-Z boundary and interface features to the IPyC/SiC interface adjacent to the connected buffer/IPyC region, as well as local variations in the size of the features around the circumference of the IPyC/SiC interface. High-Z interface features were the dominant feature type in the IPyC/SiC interface region of Particles 331-RS03, 331-RS04, and 331-RS19. Particle 331-RS12 showed a predominance of high-Z boundary features. The high-Z interface features appeared to be segregated to distinct bands ~5–10 μm from the SiC boundary surface.

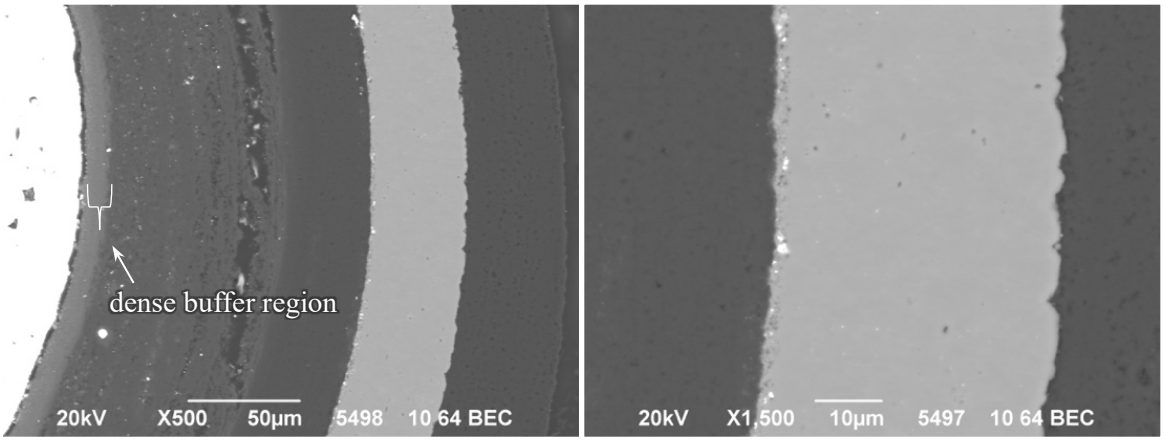

Figure 7-7. Example BEC images of the TRISO layers in Particle 331-RS12.

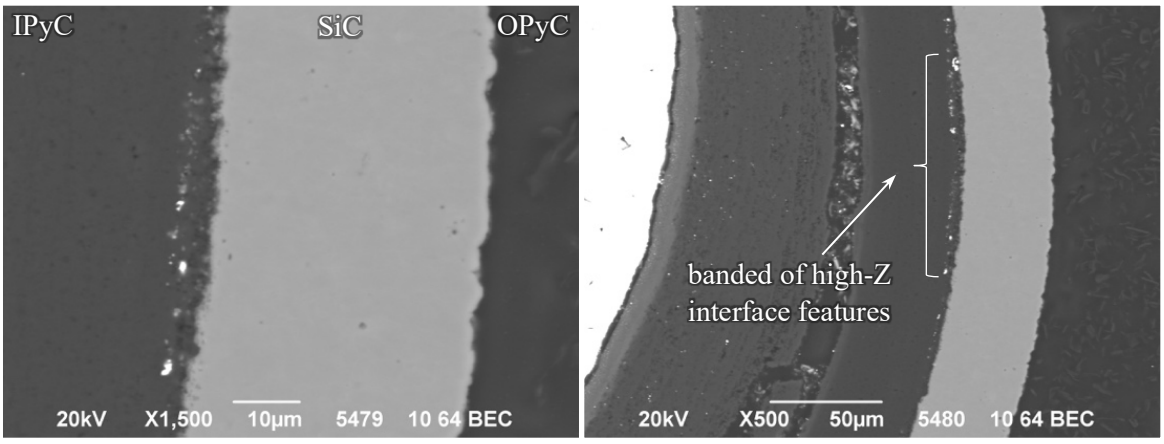

Figure 7-8. Example BEC images of the TRISO layers in Particle 331-RS03.

Elemental analysis via EDS was performed on examples of all observed high-Z feature types. The high-Z features observed in the IPyC/SiC interface region and in the SiC layer were dominated by the presence of palladium. All fine-scale, high-Z SiC features were classified as *Pd-only*, meaning palladium was the only measurable fission product or actinide species in the feature (Gerczak et al. 2018). The features were likely silicides based on the increased silicon to carbon concentration ratio relative to the reference spectra of the surrounding SiC layer, which was determined using the standardless AZtec software processing routine. The features were also expected to be silicides based on analysis of similar features in AGR-1 UCO TRISO fuel using scanning transmission electron microscopy (van Rooyen et al. 2012). Limited diversity was observed in the high-Z features observed in the IPyC/SiC interface region. Example

EDS spectra of high-Z boundary and high-Z interface features from Particle 331-RS19 are shown in Figure 7-9. All high-Z boundary features were Pd-only. A notable silicon intensity in the high-Z interface features, which were often located more than 5 µm from the SiC boundary, indicated these features were likely silicides. The high-Z interface features showed some diversity in composition, with features showing the presence of trace rhodium in Particles 331-RS04 and 331-RS19. The maximum palladium to rhodium concentration was 10:1. Trace cesium was also identified in all high-Z interface features, but not observed in the high-Z boundary features.

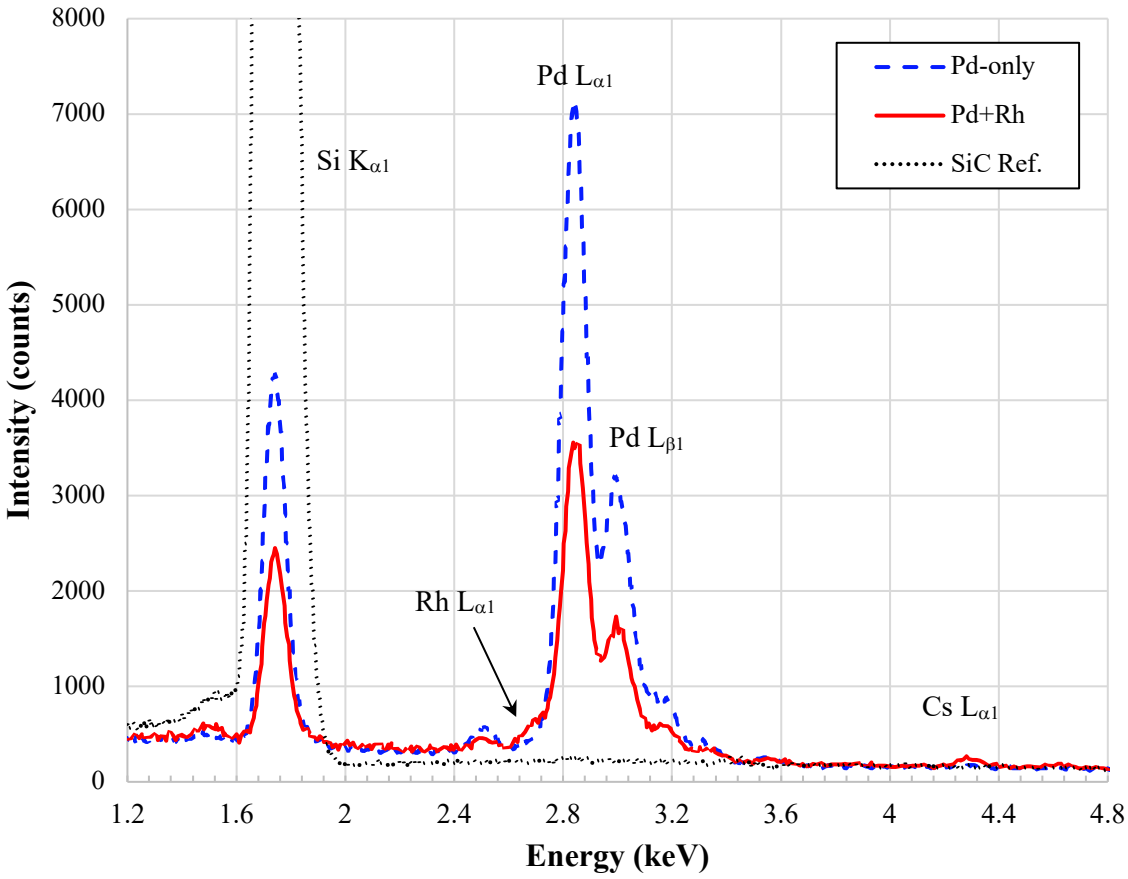

Figure 7-9. Example of Pd-only and Pd-Rh high-Z features in the IPyC/SiC interface region of Particle 331-RS19 (unlabeled peaks are lower order Pd lines).

Analysis of the buffer region adjacent to the kernel showed a local region of apparent higher density based on limited porosity relative to the remainder of the buffer region. The BEC image analysis indicated the region included diffuse higher-Z material. In some instances, small segregated features were observed in this dense, high-Z region. Example BEC images of the dense buffer region in particles from Compacts 3-1-2 and 3-3-1 are shown in Figure 7-6–Figure 7-8. Compositional analysis by EDS of the dense buffer region indicated the presence of cesium, iodine, zirconium, uranium, tellurium, ruthenium, rhodium, and molybdenum. The fine-scale, high-Z features in the dense buffer region were Ru-U rich. Representative EDS spectra of the diffuse high-Z and fine-scale, high-Z features in the dense buffer region are shown in Figure 7-10. The dense region was on the order of ~10 µm thick. This length scale suggested the region may have been formed by fission recoil damage and subsequent fission product implantation into the buffer adjacent to the kernel. The aluminum and silicon signals shown in the representative spectra were likely artifacts, in which aluminum was probably contamination from the aluminum stubs used for polishing samples (Hunn et all 2012) and the low silicon intensity was due to internal fluorescence from the Si drift detector (Gerczak et al. 2020a). The EDS analysis of the dense buffer region was only performed on Compact 3-3-1 particles.

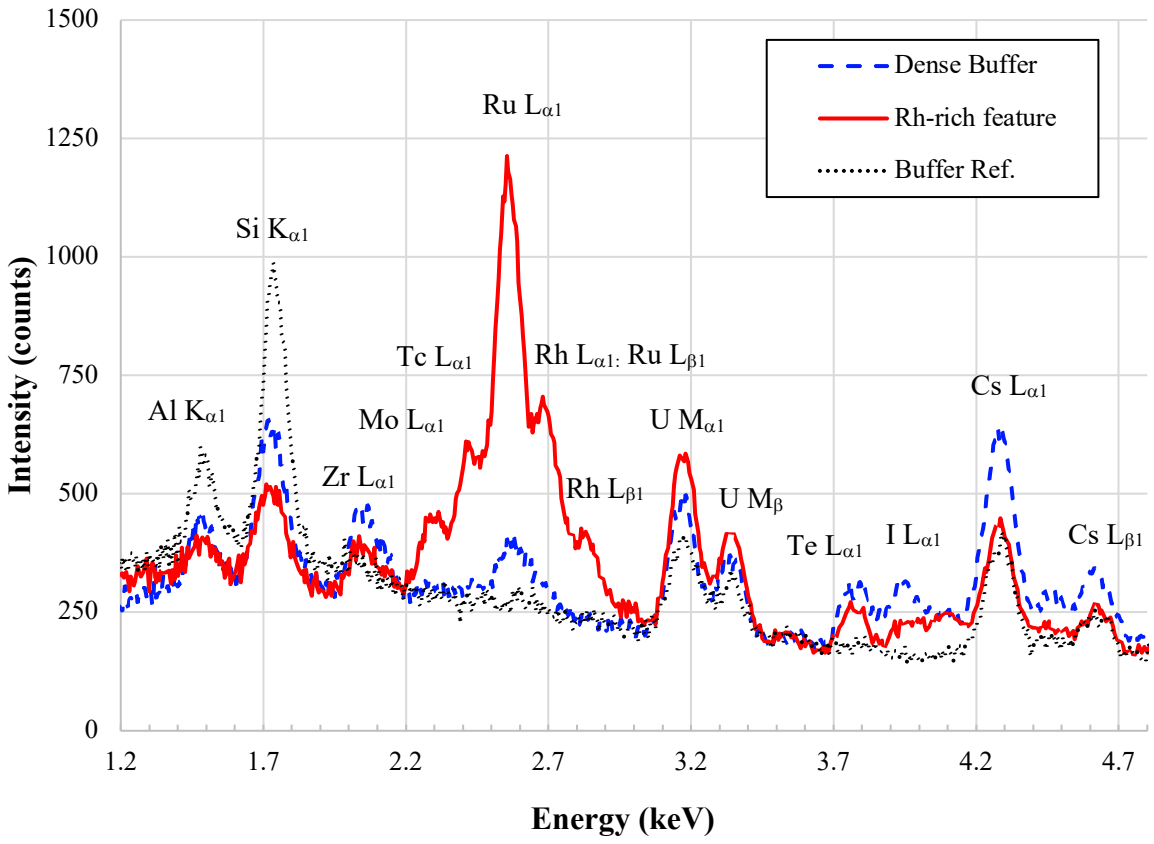

Figure 7-10. Representative EDS spectra of the diffuse high-Z material and fine-scale, high-Z features in the dense buffer region, with the most probable characteristic x-ray lines identified.

In general, the Compact 3-1-2 particles had limited fission product presence in the IPyC/SiC layers relative to the Compact 3-3-1 particles. This may have been due to the higher irradiation temperature for Compact 3-3-1. The particles from Compact 3-3-1 also showed a difference in fission product distribution and composition relative to their ^{110m}Ag M/AA values that was not observed for Compact 3-1-2. In AGR-1 and AGR-2 UCO TRISO particles, distinct variations in high-Z feature distribution within the IPyC/SiC layers were observed when comparing particles with the highest and lowest silver retention (Demkowicz et al. 2015; Gerczak et al. 2018). Particles 331-RS04 and 331-RS19, which had lower ^{110m}Ag M/AA values, showed a presence of rhodium in the high-Z interface features, while no clear indication of rhodium was observed in Particles 331-RS12 and 331-RS03, which had average ^{110m}Ag M/AA values (Table 7-1). In addition, Particles 331-RS04 and 331-RS19 showed high-Z SiC features in the SiC layer, while high-Z SiC features were noted in only one of the average ^{110m}Ag M/AA particles (Particle 331-RS12).

The observation of porosity in the IPyC near the IPyC/SiC boundary and the corresponding high-Z interface features appearing with a banded distribution at similar distances from the boundary suggested the extended structure of the IPyC/SiC interface influenced how fission products were accommodated in that region. However, the relationship between the observed porosity and fission product accommodation was not explicitly clear from the two-dimensional analysis discussed herein. AGR-2 particles are being examined with 3D SEM analysis that may better explore this hypothesis.

7.2 1,500°C SAFETY-TESTED COMPACT 3-1-1 RS PARTICLES

Compact 3-1-1 was a safety-tested sister compact to Compact 3-1-2 (Table 1-1). Six RS particles from Compact 3-1-1 were analyzed (Table 7-1). Representative SEI micrographs of select particles are shown in Figure 7-11 to demonstrate the variation in structural features observed in the IPyC/SiC/OPyC layers. Structural features that were observed in all particle included low-Z inclusions or material pullout from sample preparation, as well as a gap at the SiC/OPyC interface. The IPyC/SiC interface region was fairly consistent across all the particles analyzed except Particle 311-RS08 (Figure 7-11c), which showed pronounced PyC inclusions in the SiC layer near the SiC boundary similar to many of the Compact 3-1-2 particles (Figure 7-1). The SEI imaging showed porosity in the IPyC around the circumference of the IPyC/SiC interface, which varied in extent from particle to particle. Particles 311-RS29, 311-RS08, and 311-RS36 had regions of low-density bands around the entire circumference of the IPyC/SiC interface, with Particles 311-RS08 having the most pronounced low-density features. Particles 311-RS07, 311-RS32, and 311-RS18 showed some localized regions of low-density bands, but at a relatively lower frequency than the other particles. Similar to the as-irradiated Capsule 3 particles, the discreet locations of these bands suggested they may have been artifacts of the FB-CVD process. Similarly, the variable interface structures (e.g., PyC inclusions in the SiC) were also probably fabrication dependent.

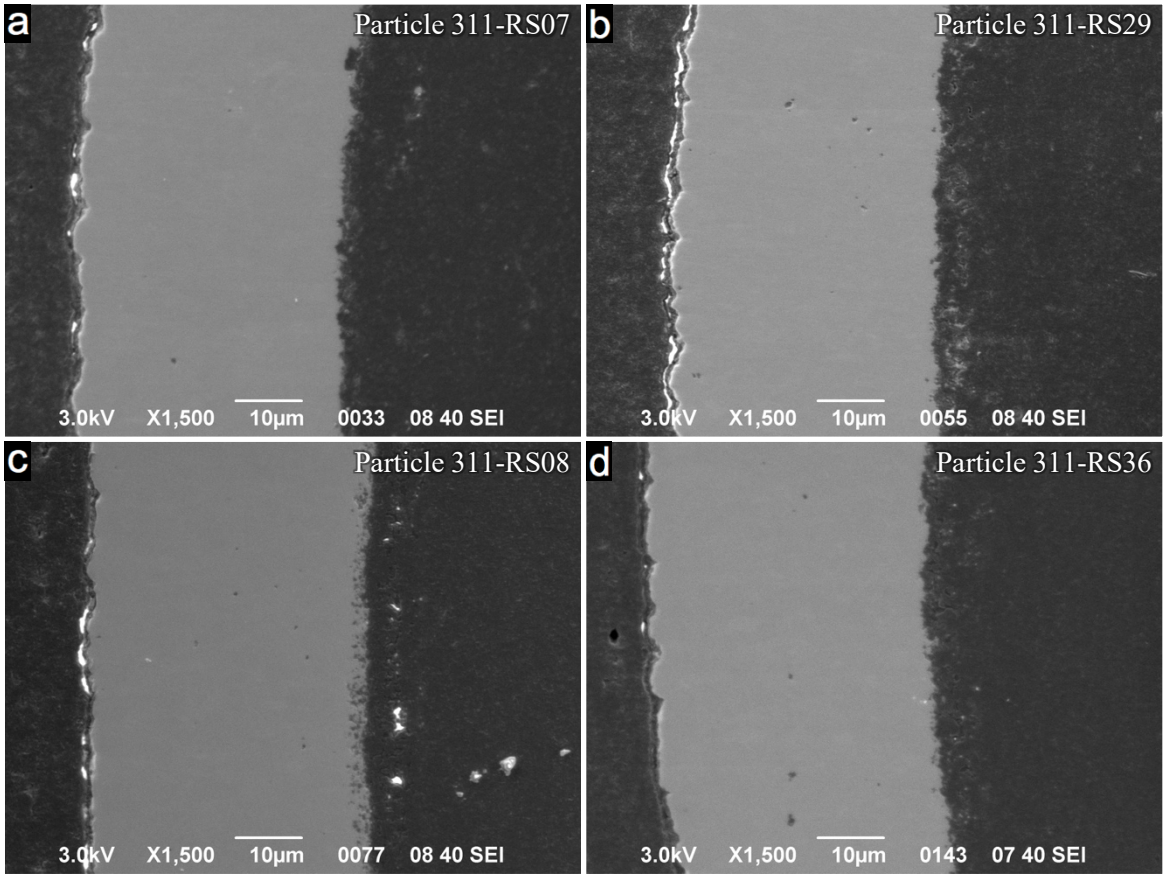

Figure 7-11. Example SEI micrographs of IPyC/SiC/OPyC layers in Compact 3-1-1 particles. Bright locations at SiC/OPyC gap and in the porosity of Particle 311-RS08 were from charging backfill epoxy.

High-Z features were observed with variable distributions in the IPyC/SiC/OPyC layers of the particles from Compact 3-1-1. All four general classes of high-Z features were identified. In the as-irradiated Compact 3-3-1 particles, high-Z SiC features appeared as faint, fine-scale features in the SiC layer. Similar fine-scale, high-Z SiC features were observed in five of six analyzed Compact 3-1-1 particles, with none observed in Particle 311-RS08 (Figure 7-12). In Particles 311-RS07, 311-RS29, 311-RS32, and 311-RS18, high-Z SiC features were observed across the entire thickness of the SiC layer, while in

Particle 311-RS36, these features were primarily observed in the SiC ≤10 μm from the IPyC. Examples of the distribution of fine-scale, high-Z SiC features are shown in Figure 7-13 and Figure 7-14. The presence of high-Z SiC features in Compact 3-1-1 particles varied from sister Compact 3-1-2, where no fine-scale, high-Z features were observed in the SiC layer (Figure 7-4–Figure 7-6). The presence of measurable high-Z SiC features in the Compact 3-1-1 particles may be due to heating during the safety test, in which additional diffusion into the SiC layer or coarsening of existing high-Z material in the SiC layer to observable sizes and concentrations may have occurred. Comparison with the high-Z SiC features in as-irradiated Compact 3-3-1 (Figure 7-3 and Figure 7-7) shows the features were qualitatively more pronounced in the safety tested Compact 3-1-1 particles.

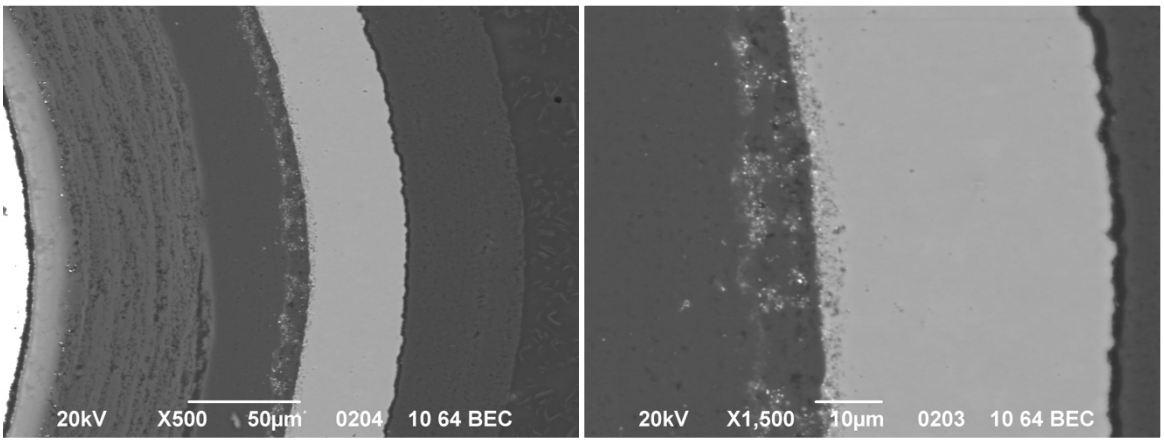

Figure 7-12. Example BEC images of the TRISO layers in Particle 311-RS08.

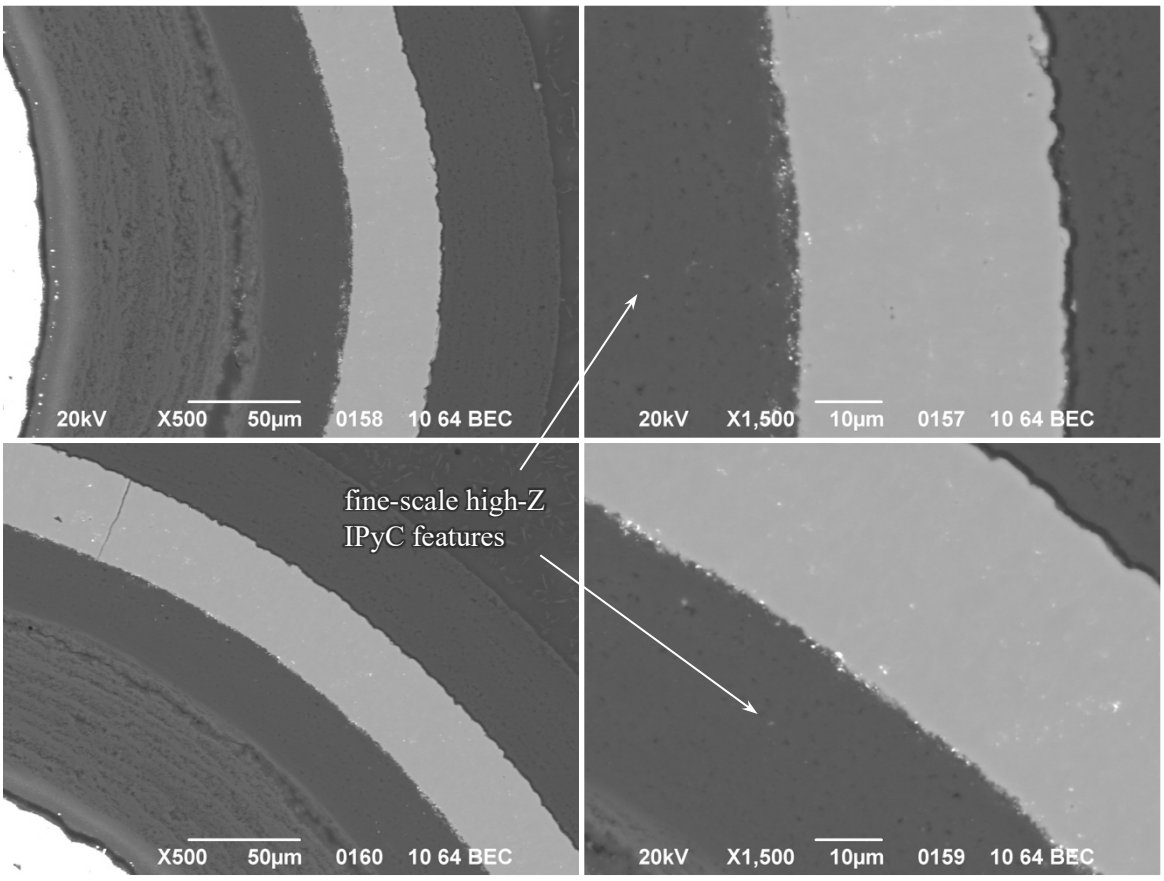

Figure 7-13. Example BEC images of the TRISO layers in Particle 311-RS07.

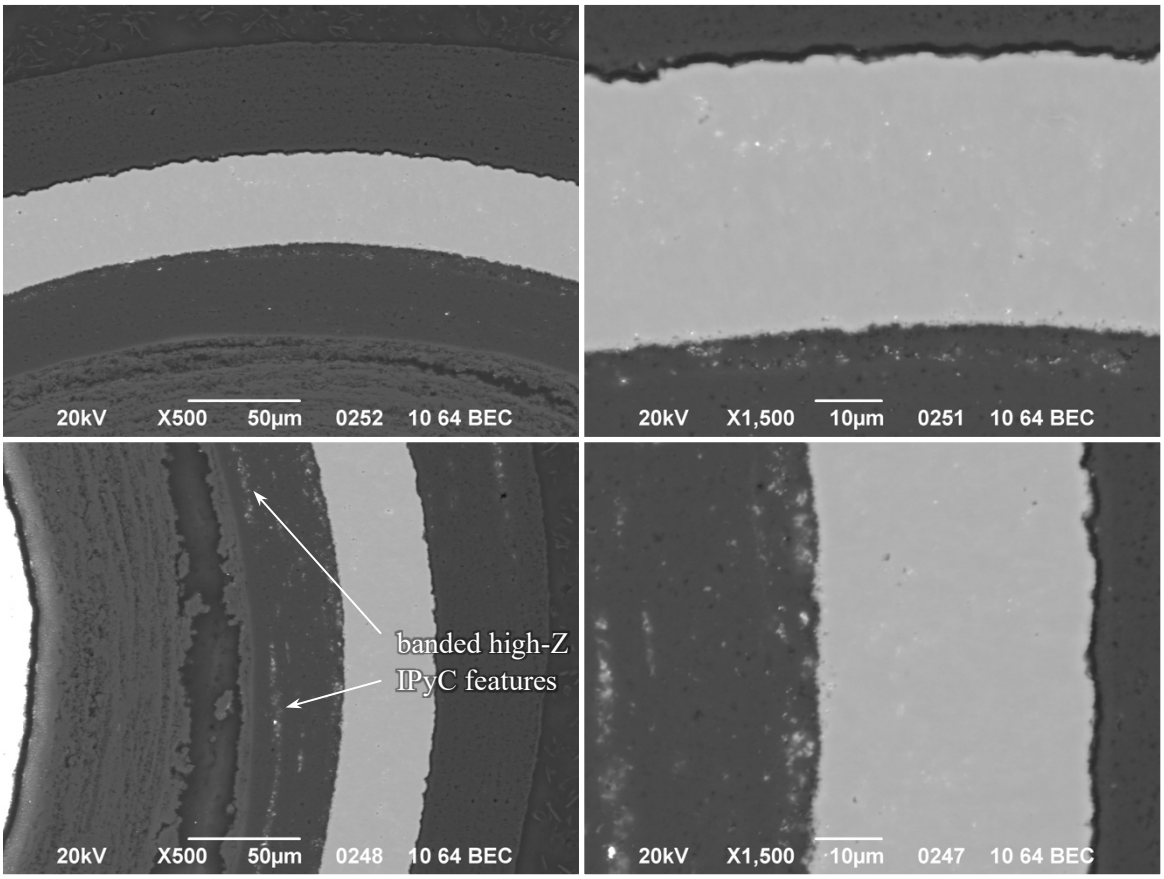

Figure 7-14. Example BEC images of the TRISO layers in Particle 311-RS18.

Both high-Z boundary features, and high-Z interface features were observed in the IPyC/SiC interface region of the Compact 3-1-1 particles. For most particles, the observed high-Z features were qualitatively uniform around the circumference of the interface. All six Compact 3-1-1 particles had detached buffer, with a residual connected buffer/IPyC region visible in Particles 311-RS07, 311-RS08, and 311-RS18. There were no obvious correlations of feature location in these three particles to the location of the connected buffer/IPyC interface. The Compact 3-1-1 particles showed relatively uniform distributions features around the circumference of the IPyC, with the exception of one area in Particle 311-RS18, where there were dense bands of high-Z IPyC features ~10 µm from the buffer (Figure 7-14). The distribution and predominance of specific feature types varied from particle to particle as shown in Figure 7-13, Figure 7-14, and Appendix D. Particle 311-RS07, which had limited low-density banded regions in the IPyC near the IPyC/SiC boundary (Figure 7-11a), had a higher frequency of high-Z boundary features relative to the other particles. Comparatively, particles with bands of porosity in the IPyC near the IPyC/SiC boundary showed a preference for high-Z interface features over high-Z boundary features. While both feature types were observed for all particles, the predominance of each feature type appeared to be directly related to the structure of the IPyC/SiC interface region. High-Z IPyC features were observed in all Compact 3-1-1 particles, either as fine-scale high-Z IPyC features scattered throughout the IPyC or in larger agglomerates of banded, high-Z IPyC features. Examples are shown in Figure 7-13 and Figure 7-14.

Elemental analysis of the various high-Z feature types was performed using EDS to determine their general compositions. High-Z SiC features were observed in Particles 311-RS07 and 311-RS18, with no obvious compositional difference between the features observed in these two particles. The compositions of the features in the SiC layer were predominately Pd-only, with ~20% of the total features being Pd-Rh. The Pd-Rh composition was exclusively observed in the high-Z SiC features near the IPyC/SiC boundary (<5 µm into the SiC), and only trace concentrations of rhodium were observed. These features were likely

silicides based on their increased silicon composition relative to the surrounding SiC matrix. Example spectra are shown in Figure 7-15.

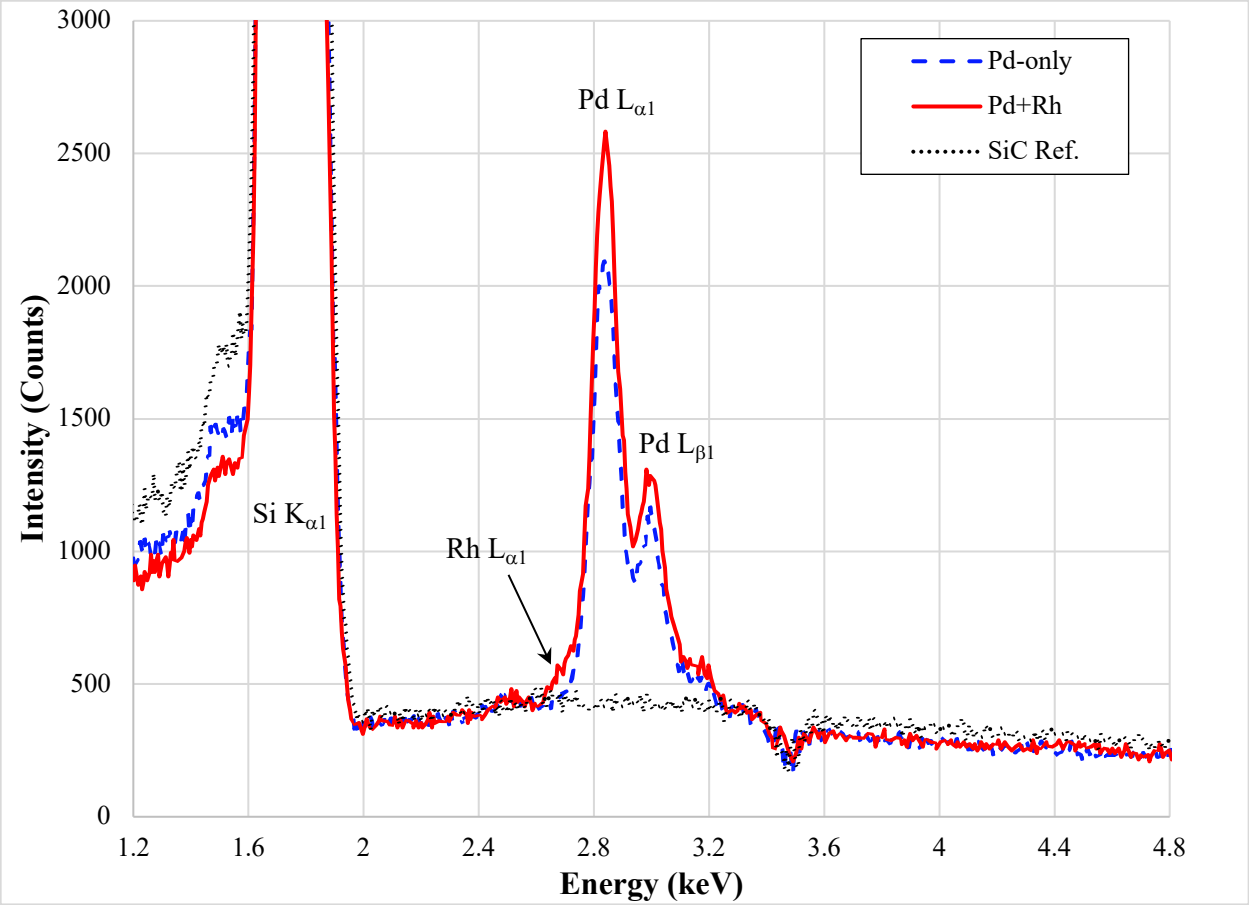

Figure 7-15. Reference Pd-only and Pd-Rh spectra for high-Z SiC features.

In the as-irradiated particles, Pd-Rh compositions were observed in the high-Z interface features, but not in the high-Z SiC or high-Z boundary features. The high-Z boundary and high-Z interface features in safety-tested Particles 311-RS07, 311-RS08, and 311-RS18 had almost exclusively Pd-Rh compositions for both feature types, with spectra similar to those shown in Figure 7-9 for the as-irradiated high-Z interface features. Particles 311-RS07 and 311-RS18 showed only Pd-Rh compositions in the high-Z interface features, while Particle 311-RS08 showed a population of 80% Pd-Rh high-Z interface features. For high-Z boundary features, Particle 311-RS07 showed exclusively Pd-Rh compositions, while Particles 311-RS08 and 311-RS18 had ~40–70% Pd-Rh high-Z boundary features. In a few features, trace ruthenium was observed along with palladium and rhodium. The elevated silicon signal, especially for features ~10 μm from the SiC boundary, suggested the features were predominantly silicides. Trace cesium and barium were observed along with the primary components in all the high-Z boundary and high-Z interface features.

The banded, high-Z IPyC features present across the thickness of the IPyC layer in Particle 311-RS18 (Figure 7-14) were analyzed by EDS. The features contained uranium, barium, and cesium, and had an elevated aluminum content. There were similar banded, high-Z interface features. The banded high-Z IPyC and banded high-Z interface features varied from the fine-scale, high-Z IPyC features in that they contained significantly higher uranium and aluminum concentrations. Example EDS spectra of these feature types are shown in Figure 7-16 along with their relevant locations in Figure 7-17. The significant aluminum content suggested the features were probably sample preparation artifacts due to material transfer from the SEM mount, and perhaps debris from the kernel was trapped in the soft aluminum.

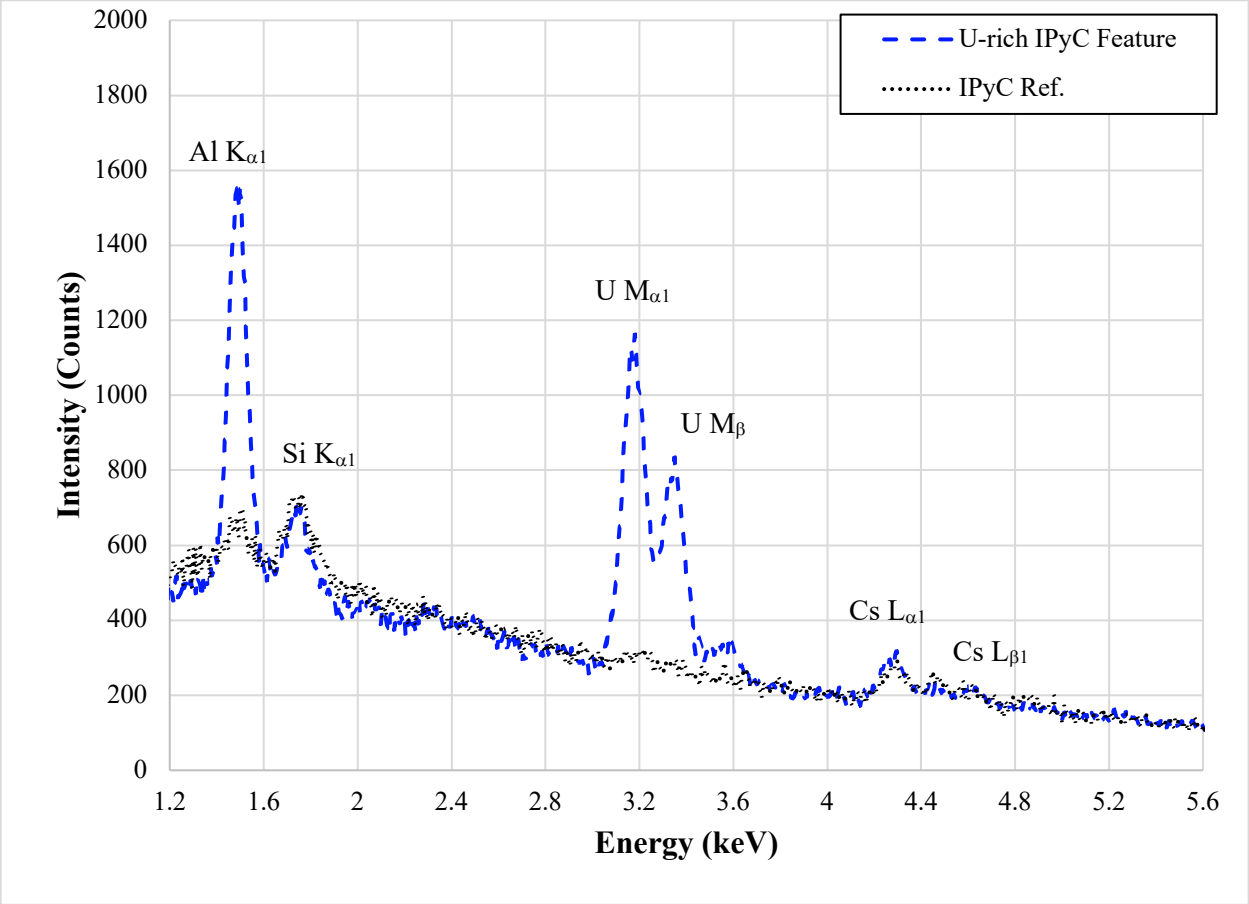

Figure 7-16. EDS analysis of the uranium-rich IPyC features in Particle 311-RS18.

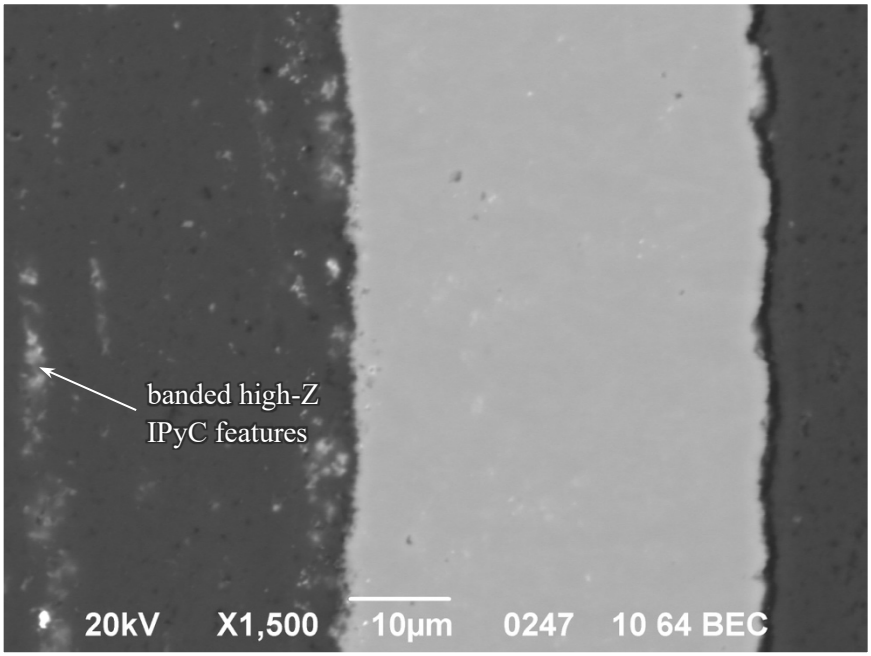

Figure 7-17. BEC image showing the location of the uranium-rich feature in Particle 311-RS18.

The fine-scale, high-Z IPyC features (Figure 7-13) showed elevated barium, silicon, and strontium relative to the reference IPyC spectra which also showed trace aluminum, cesium, and uranium (Figure

7-18). The presence of oxygen was also suggested. The low aluminum concentrations indicated these features were not artifacts from polishing as suggested for the banded high-Z IPyC features. The strontium intensity was difficult to isolate explicitly due to the overlap of the Sr $L_{\alpha 1}$ line (1.80 keV) with the Si $K_{\alpha 1}$ line (1.74 keV), but the skewness of the peak shape towards higher energy gave weight to identifying it as a strontium peak. Fine-scale, high-Z IPyC features have been observed in safety tested AGR-2 UCO TRISO particles (Gerczak et al. 2018); however, their compositions included significantly more diversity in included fission products (e.g., Zr and Ru) and higher relative uranium concentrations.

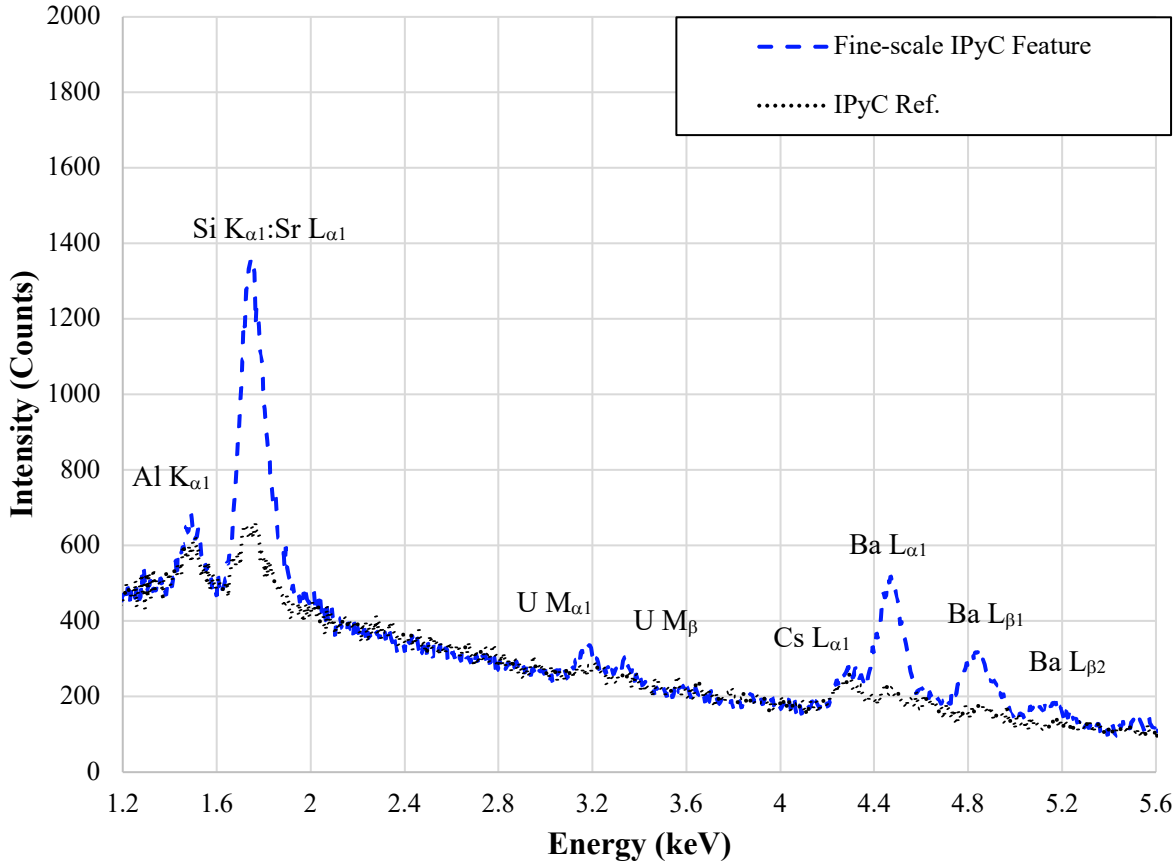

Figure 7-18. Reference fine-scale, high-Z IPyC feature.

Compact 3-1-1 analysis (Figure 7-12–Figure 7-14) showed a significant increase in high-Z features in the IPyC/SiC interface region relative to as-irradiated, sister Compact 3-1-2 (Figure 7-4–Figure 7-6). This was consistent with the observation of no fine-scale, high-Z SiC features in as-irradiated Compact 3-1-2 relative to Compact 3-3-1, which suggested a temperature effect. The features also showed a relative increase in palladium features containing rhodium, and in some cases ruthenium. This was especially evident in the high-Z SiC features, which contained trace rhodium for features near the SiC boundary. Both of these observations suggested additional release from the kernel and mobility in the TRISO layers of high-Z elements at 1,500°C during the 300 h soak, especially palladium and rhodium. The observation of uranium in one location of one specific particle would be of interest, except the isolated observation was likely due to sample preparation.

Similar to the as-irradiated particles, a dense buffer region adjacent to the kernel was noted for all Compact 3-1-1 particles examined. Examples can be seen in the BEC images in Figure 7-12–Figure 7-14. The nature of the interface appeared to vary from particle to particle without any clear trends. In some locations, segregated features were observed inside or adjacent to the dense region. Elemental analysis was performed on the dense buffer region and reference buffer ~40–50 µm from the dense buffer region.

Figure 7-19 shows an example spectrum from the two regions in Particle 311-RS18. The analysis indicated consistent features for all particles. Common features were cesium, xenon, uranium, rubidium, barium, and strontium in both the dense buffer region and reference buffer. The dense buffer region showed increased uranium, cesium, and xenon presence along with iodine, molybdenum, zirconium and trace ruthenium, technetium, and tellurium. The bright segregated features were predominantly uranium-rich with molybdenum and zirconium. The presence of xenon, the limited ruthenium presence, and no clear observation of rhodium in the dense buffer region differed from the as-irradiated particle behavior. The xenon may have been released from the kernel and accommodated in the buffer. Ruthenium and especially rhodium were probably actively diffusing in the system at 1,500°C during safety testing, as indicated by the increased rhodium and ruthenium presence in the IPyC/SiC interface region relative to the as-irradiated particles in both Compacts 3-1-2 and 3-3-1.

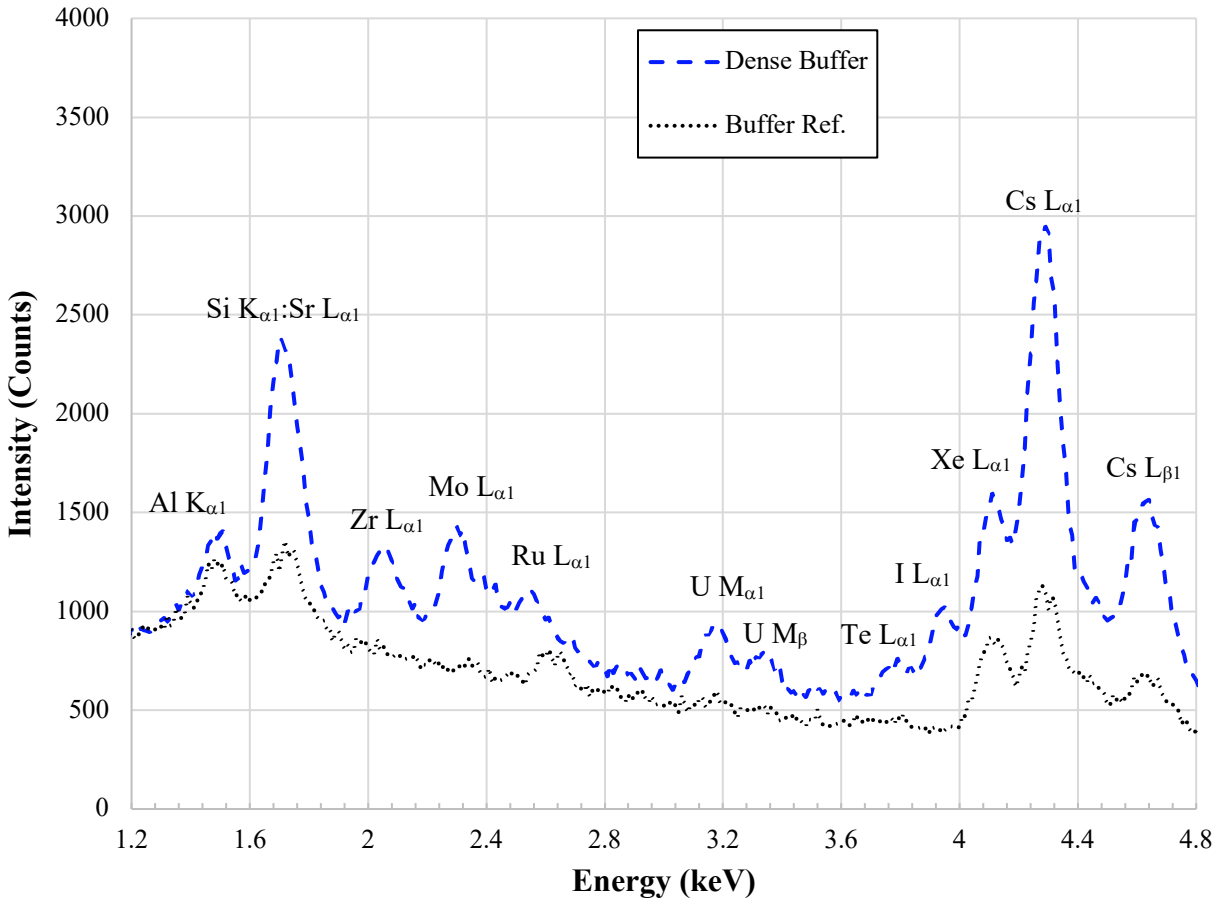

Figure 7-19. EDS spectra of dense buffer region and reference buffer from Particle 311-RS08.

7.3 1,600°C SAFETY-TESTED COMPACT 3-3-2 RS PARTICLES

Compact 3-3-2 was a safety-tested sister compact to Compact 3-3-1 (Table 1-1). Six RS particles were selected for comprehensive analysis, Table 7-1. Relevant SEI micrographs of select particles are shown in Figure 7-20–Figure 7-22. Structural features that were observed in all particles included low-Z inclusions or material pullout from sample preparation and a gap at the SiC/OPyC interface. The IPyC/SiC interface region was fairly consistent across all the particles analyzed with limited PyC inclusions at the SiC boundary for all particles. There were regions of porosity distributed parallel to the radius of the IPyC/SiC interface that were similar to other particles discussed above. These regions were predominantly located within the first ~10 µm of the IPyC/SiC interface region. The degree of porosity and PyC inclusions differed from what was observed in particles from as-irradiated sister Compact 3-3-1 (Figure 7-2), but this difference was likely related to the small statistical sampling, because the particles in these two compacts

came from the same coating batch. One particle to particle variation in the Compact 3-3-2 particles was the observed open gap at the IPyC/SiC interface for Particle 332-RS26 (Figure 7-22). However, there were no obvious indicators of CO corrosion or a fabrication defect to explain the separation of the IPyC from the SiC.

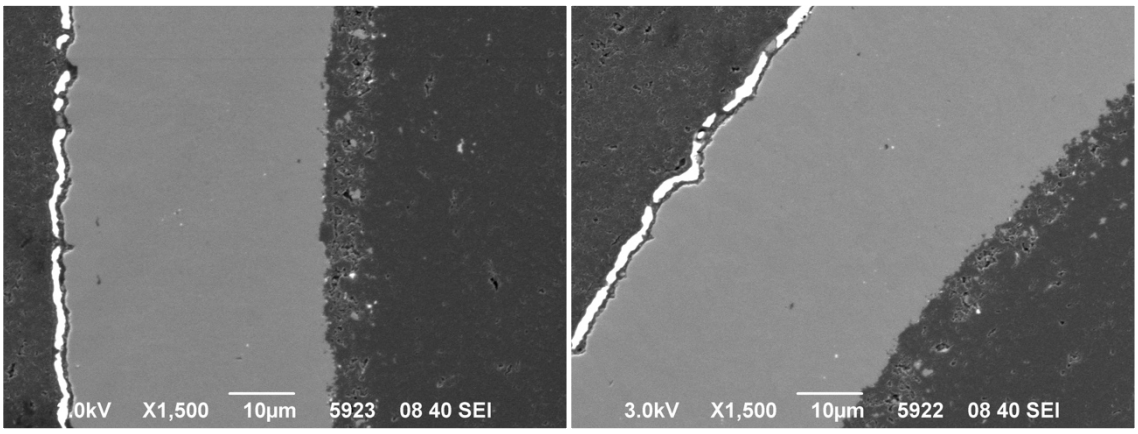

Figure 7-20. Example SEI micrographs of IPyC/SiC/OPyC layers in Particle 332-RS12. Bright locations at SiC/OPyC gap were from charging backfill epoxy.

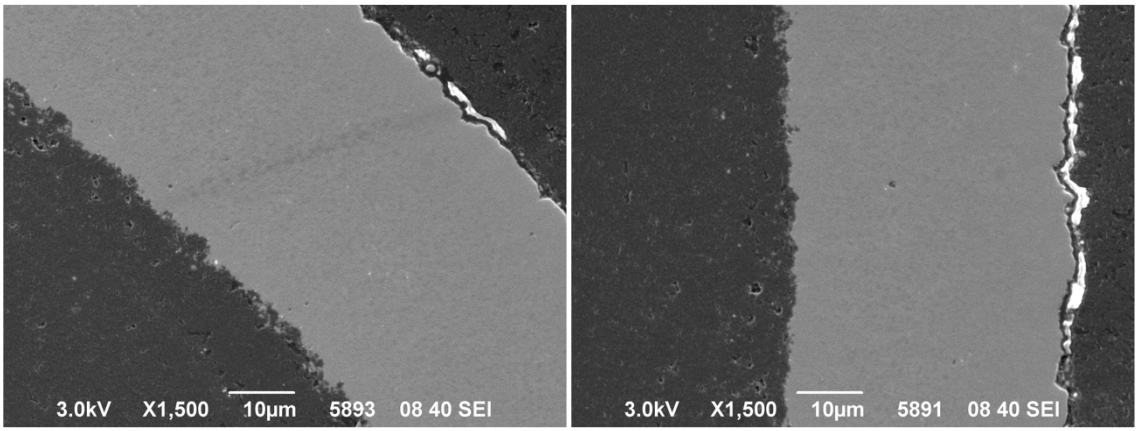

Figure 7-21. Example SEI micrographs of IPyC/SiC/OPyC layers in Particle 332-RS18. Bright locations at SiC/OPyC gap were from charging backfill epoxy.

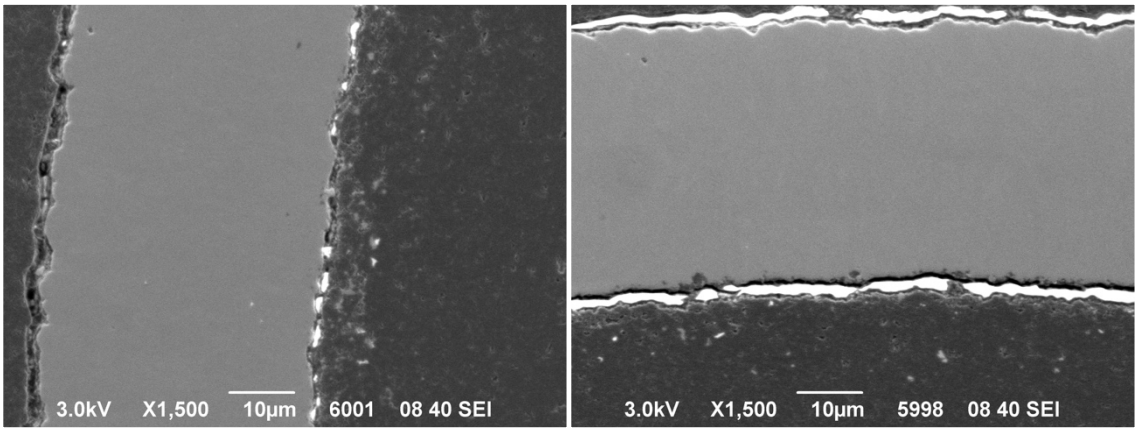

Figure 7-22. Example SEI micrographs of IPyC/SiC/OPyC layers in Particle 332-RS26. Bright locations at SiC/OPyC gap and IPyC/SiC gap were from charging backfill epoxy.

High-Z features were observed in variable distributions in the IPyC/SiC/OPyC layers of the analyzed Compact 3-3-2 particles, and all four general classes of high-Z features were identified. Examples of the distribution of fine-scale, high-Z SiC features in Compact 3-3-2 particles are shown in Figure 7-23–Figure 7-25. High-Z SiC features were observed in all particles analyzed, and they were generally more intense than the high-Z SiC features observed in particles from as-irradiated sister Compact 3-3-1 (Figure 7-7 and Figure 7-8). However, Particle 332-RS26 (Figure 7-24) showed fewer fine-scale, high-Z SiC features, with a population similar to what was observed in Compact 3-3-1, which suggests that the gap between the IPyC and SiC may have occurred prior to safety testing and reduced fission product transport to the SiC.

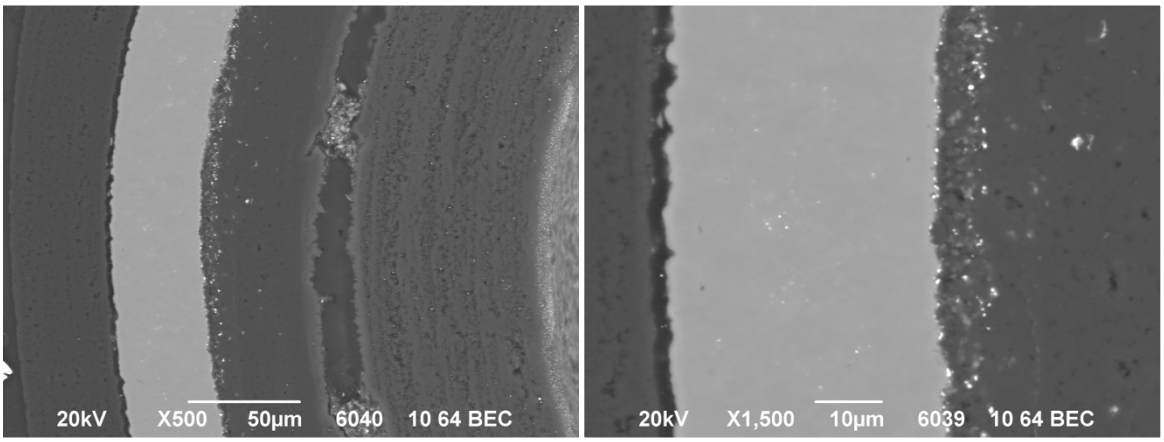

Figure 7-23. Example BEC images of the TRISO layers in Particle 332-RS12.

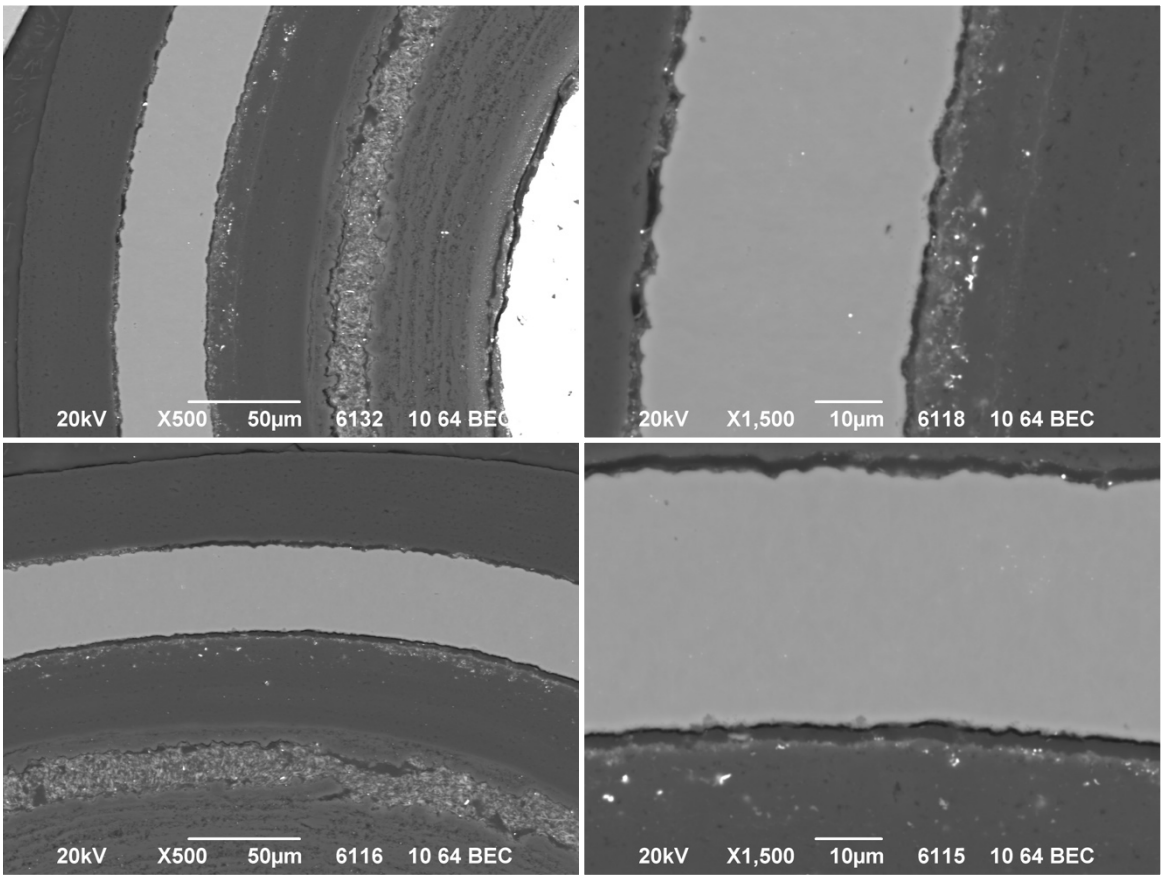

Figure 7-24. Example BEC images of the TRISO layers in Particle 332-RS26.

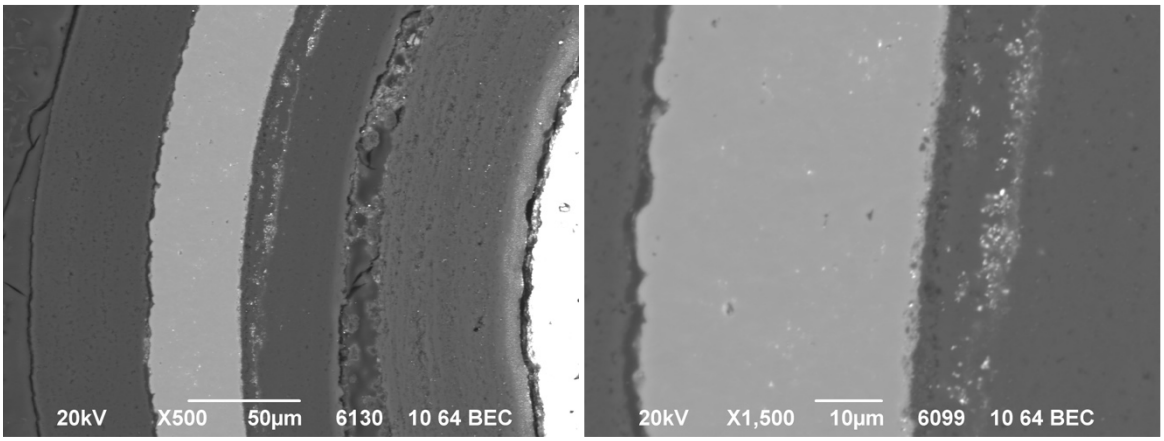

Figure 7-25. Example BEC images of the TRISO layers in Particle 332-RS31.

Both high-Z boundary features and high-Z interface features were observed in the IPyC/SiC interface region of Compact 3-3-2 particles. For most particles the observed high-Z features were qualitatively uniform around the entire circumference of the IPyC/SiC interface. All six particles from Compact 3-3-2 had detached buffer, with a residual connected buffer/IPyC region visible. However, no correlations of feature location with the connected buffer/IPyC regions were observed. High-Z interface features were predominant in all particles, and high-Z boundary features were observed in all particles except Particle 332-RS26. The absence of high-Z boundary features in Particle 332-RS26, like the absence of high-Z SiC features, was probably related to the separation between the IPyC and SiC. The qualitative predominance of high-Z boundary features varied somewhat in the other particles. Particles 332-RS12, 332-RS22, and 332-RS43 showed no preference for high-Z boundary features versus high-Z interface features while Particles 332-RS18 and 332-RS31 showed fewer high-Z boundary features relative to the observed high-Z interface features. Similar to other particles, the high-Z interface features were aligned in a banded structure replicating the low density, porous regions, suggesting these features correlated with the structure in the IPyC/SiC interface region. Common to all compacts, remaining porosity was observed in the IPyC/SiC interface region indicating high-Z material did not fill all free volume (Figure 7-25). Also similar to Compact 3-1-1 was the presence of fine-scale, high-Z IPyC features (Figure 7-23-Figure 7-25), although in some instances the features were more pronounced Figure 7-23.

Elemental analysis of the various feature types was performed to determine the general compositions of the various high-Z features observed in the TRISO layers. The compositions of the features in the SiC layer were Pd-only or Pd-Rh, similar to the compositions of Compact 3-1-1 high-Z SiC features (Figure 7-15). No Pd-Rh high-Z SiC features were observed in Particles 332-RS12, 332-RS18, and 332-RS26, while high-Z SiC features in Particles 332-RS22, 332-RS43 and 332-RS31 showed both Pd-only and Pd-Rh compositions. The Pd-Rh compositions were predominantly located in the first half of the SiC layer and ranged from 7–20% of the total analyzed high-Z SiC features. These features were different from the as-irradiated sister compact, Compact 3-3-1, in which no rhodium was observed in the SiC layer.

The high-Z boundary and high-Z interface features had either Pd-Rh-Ru or Pd-Rh compositions. The presence of ruthenium was more pronounced relative to the features with suggested ruthenium in Compact 3-1-1. Example spectra showing representative Pd-Rh-Ru and Pd-Rh compositions are shown in Figure 7-26. Most of the high-Z boundary features had Pd-Rh compositions. However, the frequency varied from particle to particle, with Particles 332-RS22 and 332-RS31 showing only Pd-Rh features, while Particles 332-RS12, 332-RS18, and 332-RS43 showed ~50–70% of the analyzed high-Z boundary features had a Pd-Rh composition, with the remainder being Pd-Rh-Ru. No features in the interface region were determined to be Pd-only. Particle 332-RS26 did not have any SiC boundary features for analysis. The high-Z interface features presented more diversity in composition compared with the high-Z boundary features. The compositions of higher intensity high-Z interface features were predominantly Pd-Rh-Ru with a small population of Pd-Rh composition types. Only Pd-Rh-Ru high-Z interface features

were observed in Particles 332-RS43 and 332-RS31, while the populations of high-Z interface features with Pd-Rh composition were ~10–30% for the other particles. Similar to the analysis of other particles, the elevated silicon signal, especially for the high-Z interface features ~10 µm from the SiC boundary suggested the features predominantly contained silicides. For all high-Z interface features trace cesium and barium were observed along with the primary components.

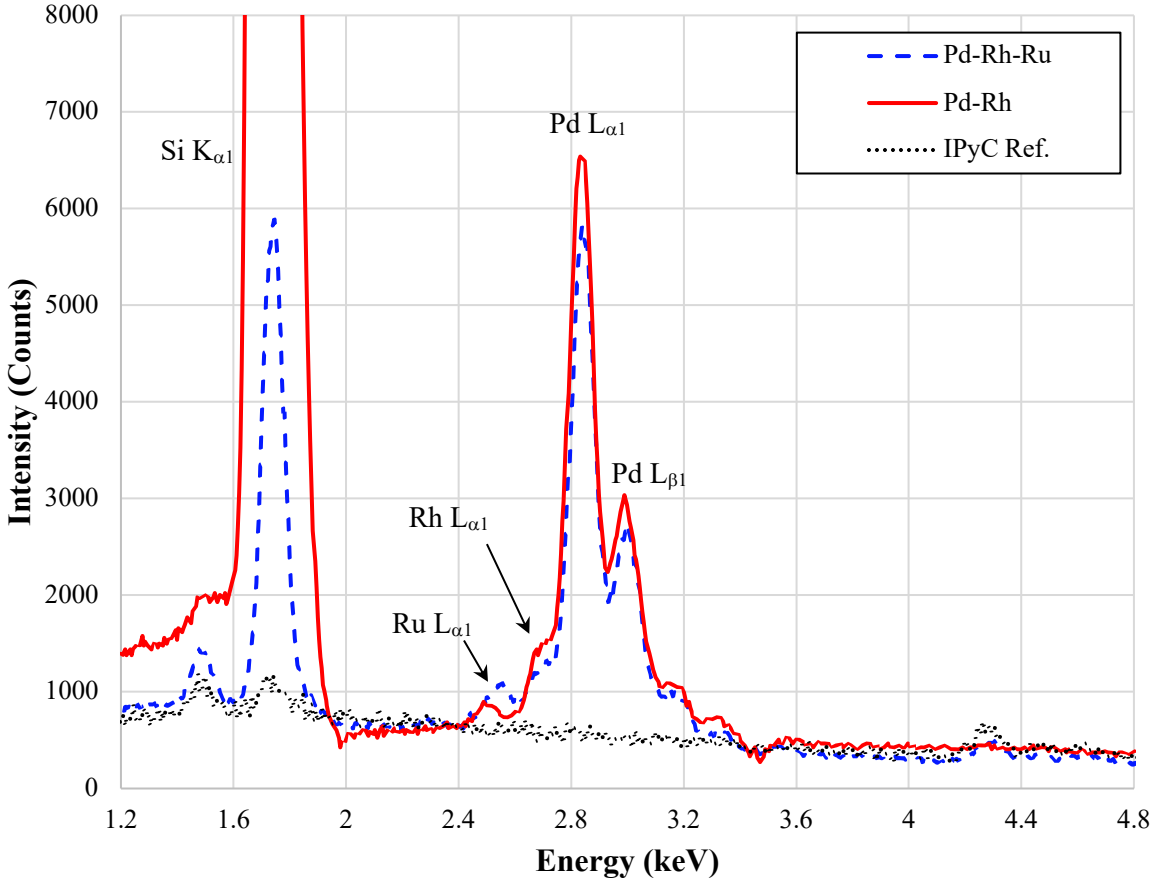

Figure 7-26. Example spectra of a Pd-Rh-Ru high-Z interface feature and a Pd-Rh high-Z boundary feature.

Also present in the IPyC/SiC interface region were diffuse banded structures Figure 7-23–Figure 7-25. These banded high-Z interface features were observed in all Compact 3-3-2 particles, and had a similar appearance to the uranium-rich, banded high-Z IPyC features in Particle 311-RS18 (Figure 7-14 and Figure 7-16). The presence of uranium and aluminum suggested the features in Particle 311-RS18 were artifacts of the polishing process. However, the compositions of the diffuse banded structures in the Compact 3-3-2 particles were different. The compositions of the Compact 3-3-2 banded high-Z interface features were dominated by barium, strontium, and silicon, with some indication for the presence of oxygen. The strontium intensity was difficult to isolate explicitly due to the overlap of the Sr $L_{\alpha 1}$ line (1.80 keV) with the Si $K_{\alpha 1}$ line (1.74 keV), but the skewness of the peak shape towards higher energy gives weight to identifying it as a strontium peak. Similar compositions were observed for some larger features in the IPyC layer typically segregated at the outer edge of the low-density IPyC/SiC interface region. This composition class was also observed in banded high-Z IPyC features beyond the IPyC/SiC interface region. Example spectra are shown in Figure 7-27 with analysis locations identified in Figure 7-28. These feature types were measured in all Compact 3-3-2 particles analyzed. Fine-scale, high-Z IPyC features were also observed in all Compact 3-3-2 particles, with similar compositions to those observed in Compact 3-1-1 (Figure 7-18), namely, C-Si-Ba-Sr-U with cesium and aluminum present in all spectra, including the reference spectra.

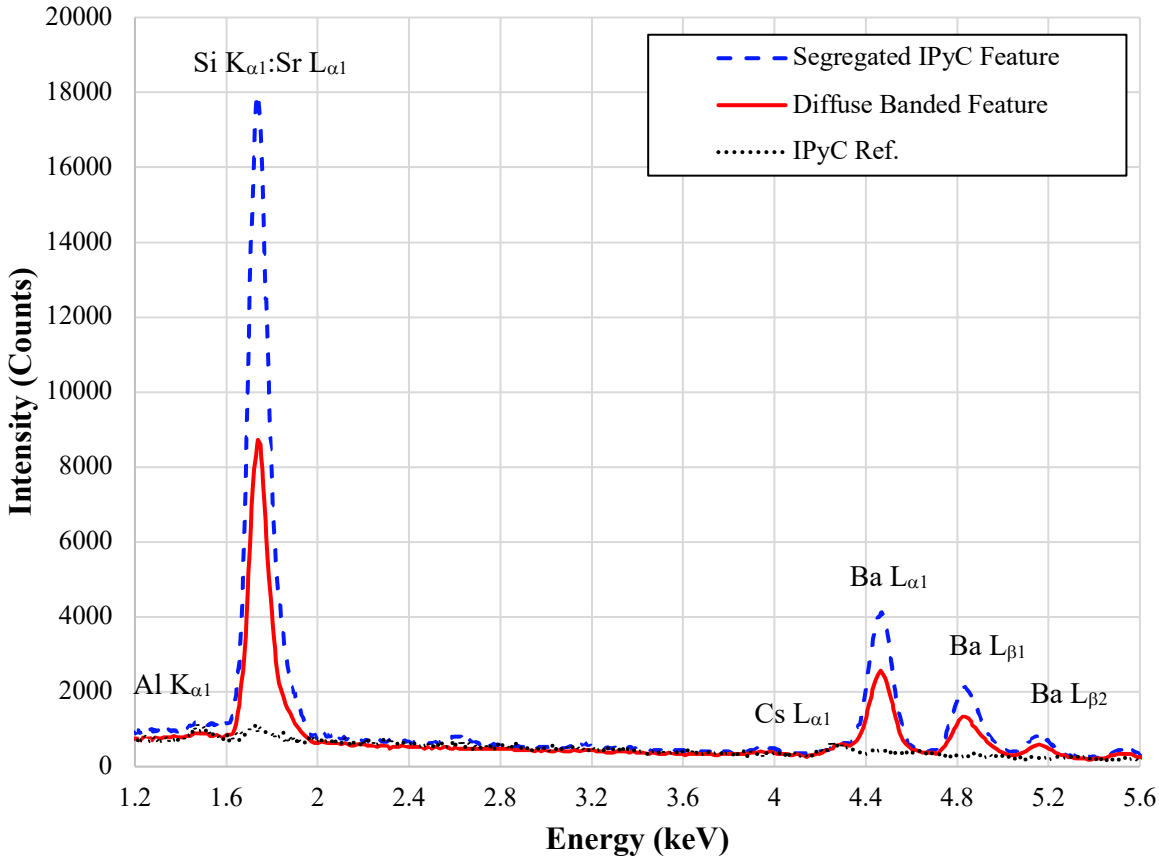

Figure 7-27. Example spectra of representative banded, high-Z interface features and segregated, high-Z IPyC features showing Ba-Sr-Si compositions.

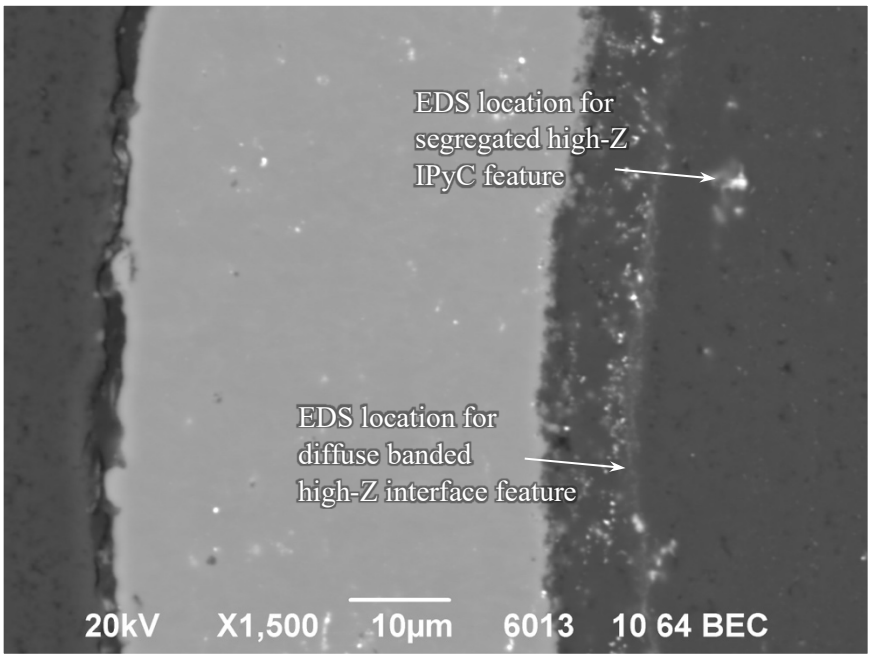

Figure 7-28. EDS locations in Particle 332-RS18 for spectra in Figure 7-29.

Dense buffer regions adjacent to the kernel were observed in all Compact 3-3-2 particles. These regions appeared with less contrast compared to the bands observed in particles from as-irradiated Compact 3-3-1 (Figure 7-7 and Figure 7-8), which suggested a lower concentration of the diffuse high-Z material in the Compact 3-3-2 particles. However, all analyzed Compact 3-3-2 particles had segregated deposits of high-Z material in higher concentrations throughout the dense buffer region that suggested the high-Z material had redistributed (Figure 7-23–Figure 7-25). Elemental analysis was performed to determine the composition of the dense buffer region. The fine-scale, segregated features were predominantly metallic fission products of zirconium, molybdenum, ruthenium, and technetium, while some features contained rhodium and palladium. The segregated features in the dense buffer region from Particles 332-RS12 and 332-RS26 showed elevated uranium and zirconium compositions relative to the segregated features in the other particles. Examples of the compositions of different segregated feature types are shown in Figure 7-29. While the segregated features showed increased intensity of metal fission product species, overall the dense buffer region was consistent with the Compact 3-1-1 analysis, which indicated increased presence of uranium, cesium, xenon, iodine, molybdenum, and zirconium, with trace ruthenium, technetium, and tellurium relative to the remainder of the buffer.

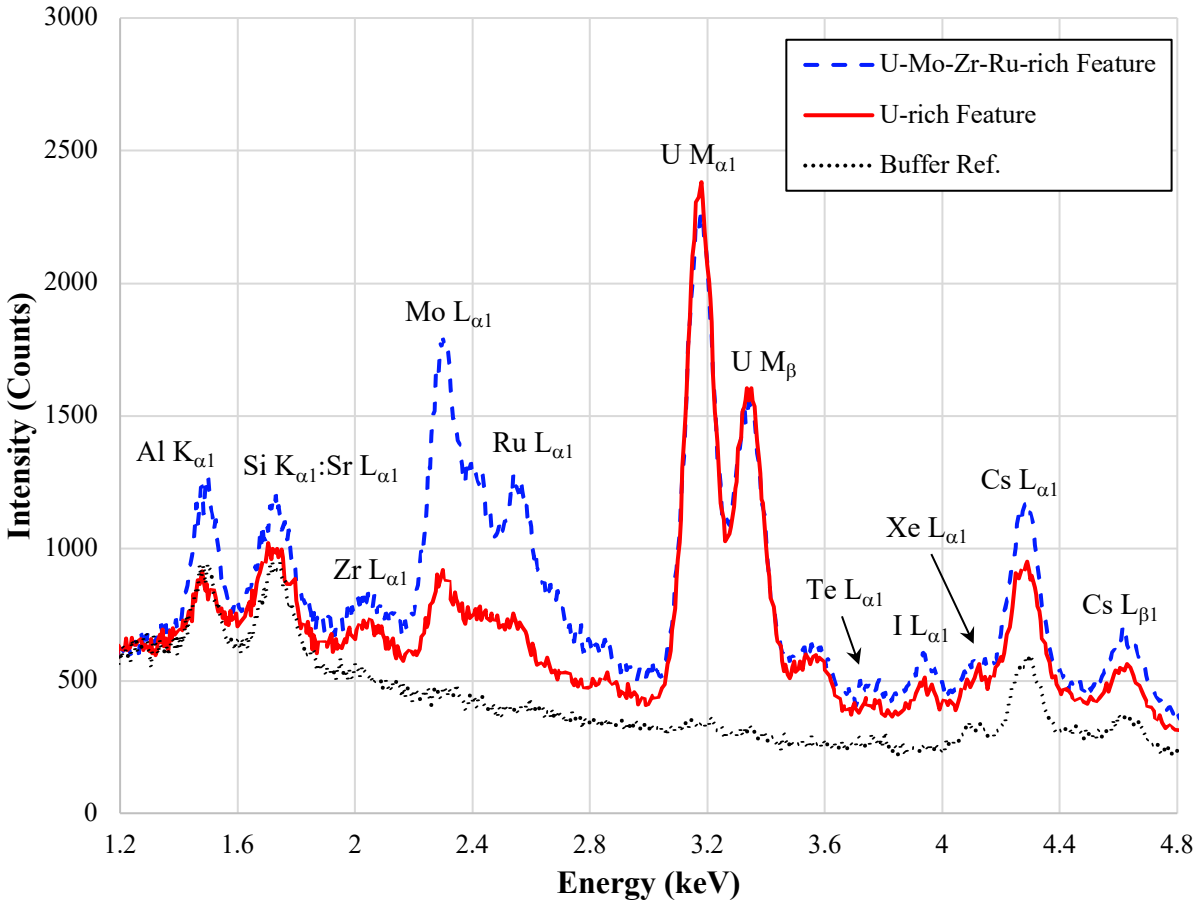

Figure 7-29. Examples of segregated features in the dense buffer region on Particle 332-RS12.

7.4 1,600°C SAFETY-TESTED COMPACT 3-4-2 RS PARTICLES

Compact 3-4-2 was a 1,600°C safety tested sister compact to 1,700°C safety-tested Compact 3-4-1, which is discussed in Section 7.5. Six RS particles were analyzed with SEM (Table 7-1), and representative SEI micrographs of select particles are shown in Figure 7-30 and Figure 7-31, which show some of the common structural features observed in the Compact 3-4-2 IPyC/SiC/OPyC layers. Structural features that were observed in all particles included low-Z inclusions or material pullout from sample preparation and a SiC/OPyC interface gap. The IPyC/SiC interface was fairly consistent across all the particles

analyzed, except Particle 342-RS07 (Figure 7-31), which showed pronounced PyC inclusions in the SiC at the IPyC/SiC boundary. The IPyC/SiC boundary in Particle 342-RS07 was similar to many of the Compact 3-1-2 particles (Figure 7-1). All other Compact 3-4-2 particles showed PyC inclusions at the IPyC/SiC boundary, but with a lower frequency. The SEI analysis indicated the presence of porosity in the IPyC/SiC interface region around the circumference, with the extent of the porosity varying from particle to particle. Figure 7-30a shows a region in Particle 342-RS17 with more porosity in the IPyC compared with the denser IPyC in Particle 342-RS29 (Figure 7-30b).

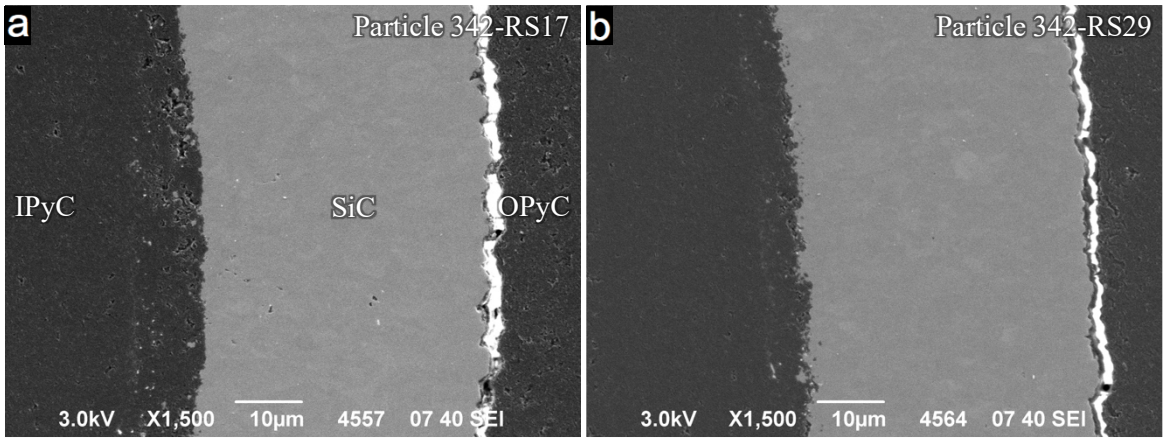

Figure 7-30. Example SEI micrographs of IPyC/SiC/OPyC layers in (a) Particle 342-RS17 and (b) Particle 342-RS29. Bright locations at SiC/OPyC gap were from charging backfill epoxy.

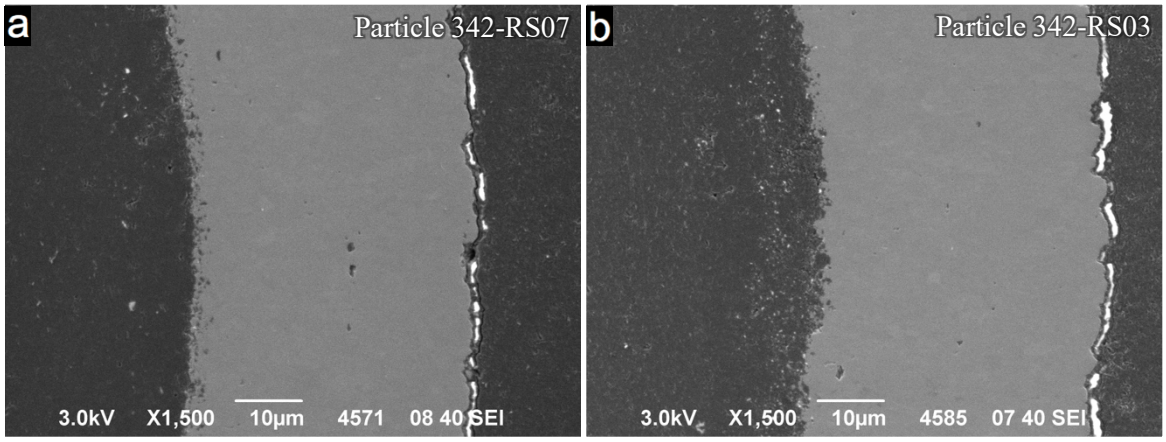

Figure 7-31. Example SEI micrographs of IPyC/SiC/OPyC layers in (a) Particle 342-RS07 and (b) Particle 342-RS03. Bright locations at SiC/OPyC gap were from charging backfill epoxy.

All four general classes of high-Z features in the IPyC and SiC layers were identified. The presence and distribution of high-Z SiC features varied from particle to particle. Representative examples of the distribution of fine-scale, high-Z SiC features in particles from Compact 3-4-2 are shown in Figure 7-32–Figure 7-35. High-Z SiC features were observed across the SiC layers of Particles 342-RS17 and 342-RS29 (Figure 7-32 and Figure 7-33). These features were more intense than those observed in the particles from as-irradiated Compact 3-3-1 (Figure 7-7 and Figure 7-8), and were similar to the features observed from 1,600°C safety-tested Compact 3-3-2 (Figure 7-25). Particle 342-RS07 showed faint high-Z features in the SiC layer predominantly in the first half of the SiC layer, though some features were observed in the second half of the SiC layer (Figure 7-34). Particles 342-RS21, 342-RS03, and 342-RS15 showed no obvious fine-scale features across the SiC layer, though some features were observed just within the SiC layer close to the IPyC/SiC interface (Figure 7-35). The extended presence of high-Z SiC features in Particles 342-RS17 and 342-RS29 was consistent with the expectation that these two particles experienced relatively higher temperatures based on their higher silver release.

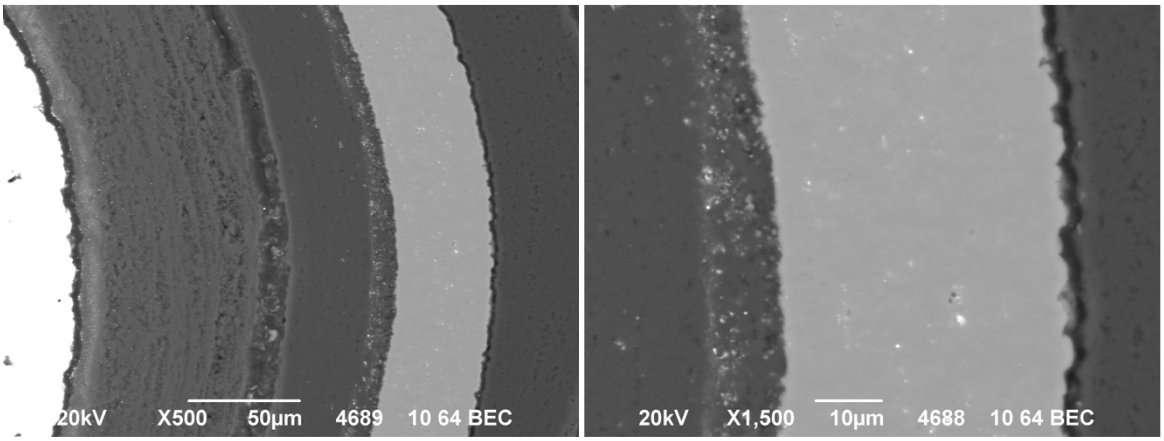

Figure 7-32. Example BEC images of the TRISO layers in Particle 342-RS17.

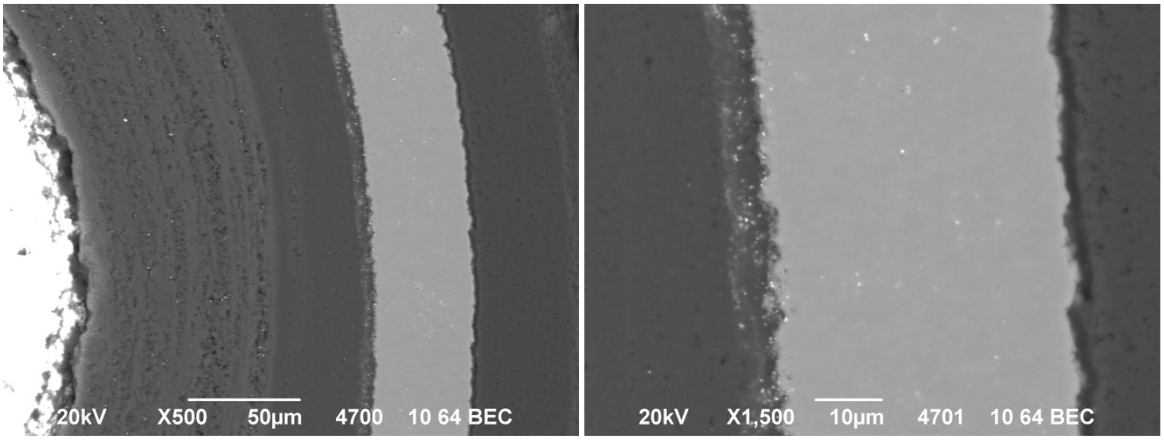

Figure 7-33. Example BEC images of the TRISO layers in Particle 342-RS29.

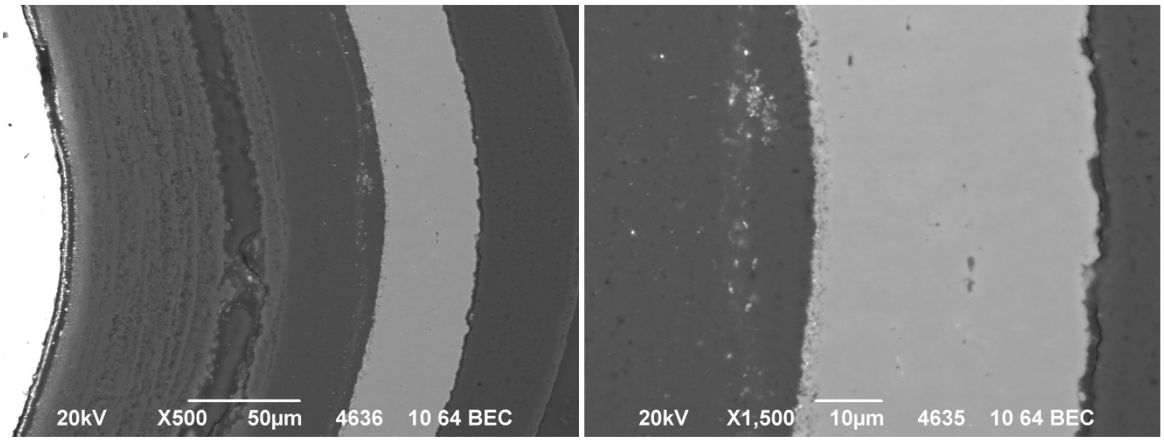

Figure 7-34. Example BEC images of the TRISO layers in Particle 342-RS07.

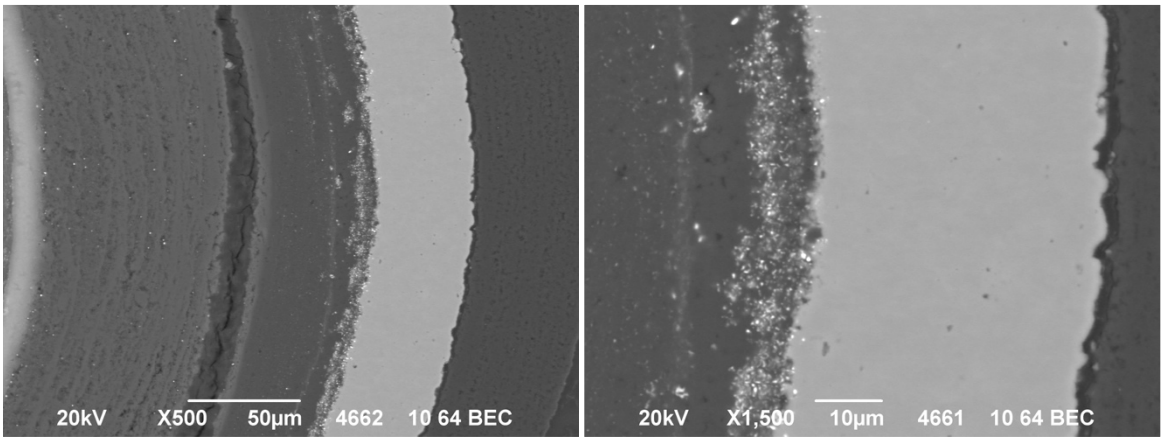

Figure 7-35. Example BEC images of the TRISO layers in Particle 342-RS03.

Both high-Z boundary features and high-Z interface features were observed in the IPyC/SiC interface region, and for the most part were qualitatively uniform around the entire circumference of the polished section. All six particles from Compact 3-4-2 had detached buffer, with a residual connected buffer/IPyC region visible; however, no correlations of feature location with the connected buffer/IPyC regions were observed. Frequency and intensity of the high-Z interface features varied from particle to particle. Figure 7-34 and Figure 7-35 provide examples of the bounding behaviors. Particles 342-RS07 and 342-RS29 showed a lower density of high-Z interface features compared with the other particles, with Particle 342-RS03 having a significantly higher density than all the other particles. Particle 342-RS03 also showed the highest concentration of high-Z boundary features (Figure 7-36). In general, the presence of high-Z boundary features scaled with the presence of high-Z interface features.

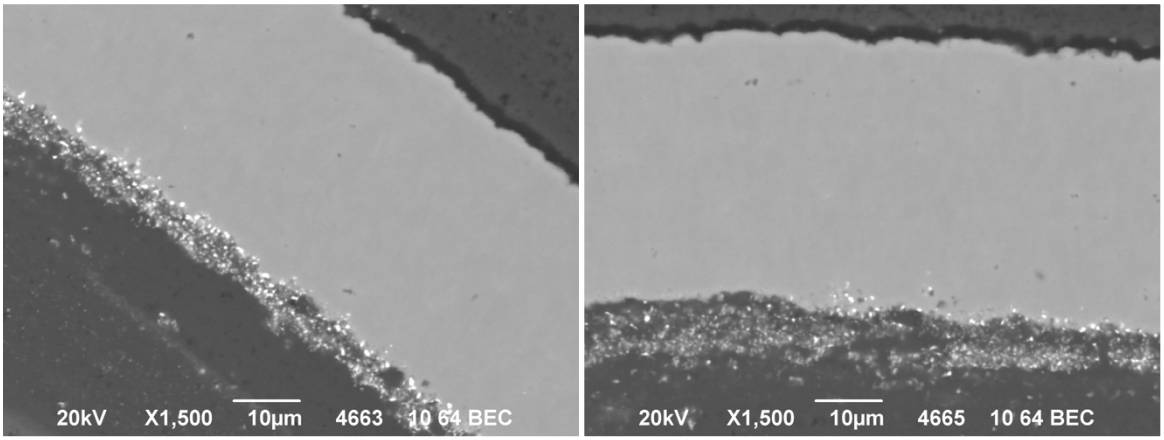

Figure 7-36. BEC images showing the predominance of high-Z boundary features in Particle 342-RS03.

Similar to the particles from the other UO_2 compacts, the high-Z interface features were aligned in a banded structure replicating the observed porosity, suggesting these features correlated with this aspect of the IPyC structure. Diffuse banded structures and fine-scale, high-Z IPyC features were observed in the IPyC layer of all particles, much like Compact 3-3-2, as can be seen in the BEC images in Figure 7-32–Figure 7-35 and Appendix D.

Elemental analysis was performed on Particles 342-RS17, 342-RS07, and 342-RS15. High-Z SiC features were predominate in Particle 342-RS17 and limited in Particle 342-RS07 while Particle 342-RS15 showed a few high-Z SiC features along the inside edge the SiC layer. The measured compositions were predominantly Pd-only. Analysis of the high-Z interface and high-Z boundary features showed feature compositions consistent with those in Compact 3-3-2. The high-Z interface features had Pd-Rh-Ru or Pd-Rh compositions. The compositions of the high-Z interface features in all analyzed particles were

predominantly Pd-Rh-Ru, with ~40% Pd-Rh high-Z interface features in Particle 342-RS17 and only ~20% Pd-Rh high-Z interface features in Particles 342-RS07 and 342-RS15. The diffuse banded features frequently observed in the IPyC/SiC region were identical to those found in Compact 3-3-2, which showed predominantly barium, strontium, and silicon, with some cesium, traces uranium and aluminum, and suggestions of oxygen presence (Figure 7-27).

Analysis of the high-Z boundary features showed both Pd-Rh and Pd-Rh-Ru compositions were present. In Particles 342-RS07 and 342-RS15, Pd-Rh compositions were observed in ~70% and ~50% of the high-Z boundary features, respectively. The analysis of Particle 342-RS17 revealed only high-Z boundary features with Pd-Rh composition; however, the sample size was very limited due to a low number of these features available for analysis. A unique high-Z boundary feature containing silver was observed in Particle 342-RS15. Compositional analysis of this feature revealed predominant peaks from cesium, rhodium, silver, and palladium with a balance of carbon, oxygen and silicon. A spectra is shown in Figure 7-37, and the feature location is shown in Figure 7-38. This feature clearly contained silver, as the Ag $L_{\alpha 1}$ line dominated and was not concealed by the Pd $L_{\beta 1}$ overlap, which has often presented a challenge for identifying silver presence in UCO TRISO particles (Hunn et al. 2012). The presence of silver was suggested by automated identification with the Aztec software in some palladium-rich features in almost all compacts analyzed, but confirmation could not be made with any confidence in those cases. The composition of this feature was unique compared to other silver observations in AGR UCO TRISO fuel, which showed silver to be collocated in fine-scale features along with radionuclides such as palladium and uranium (van Rooyen et al. 2014). The ration of the fission product species in atomic percent was roughly 5% Cs:3% Rh:3% Ag:1% Pd. This relatively large high-Z boundary feature was also an outlier compared to the smaller size of typically observed high-Z boundary features.

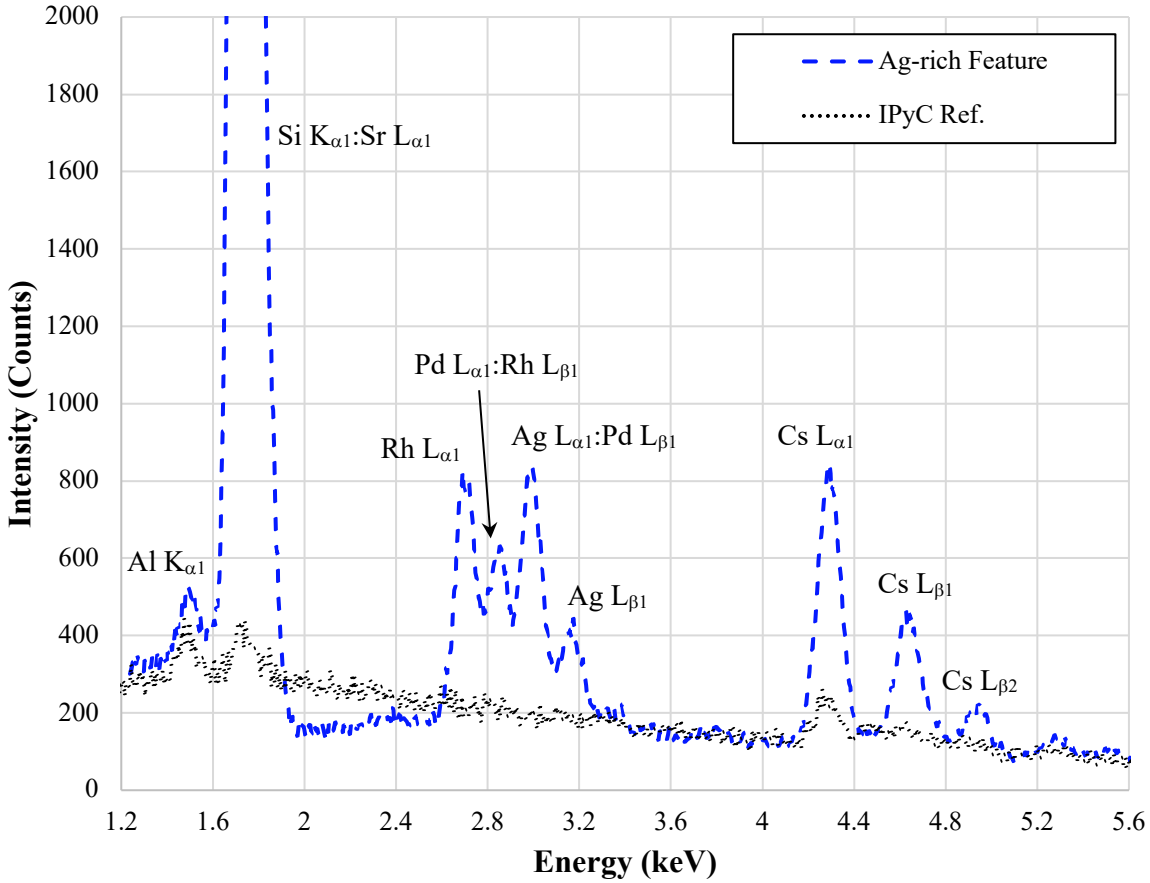

Figure 7-37. EDS spectra of Ag-rich feature in Compact 3-4-2.

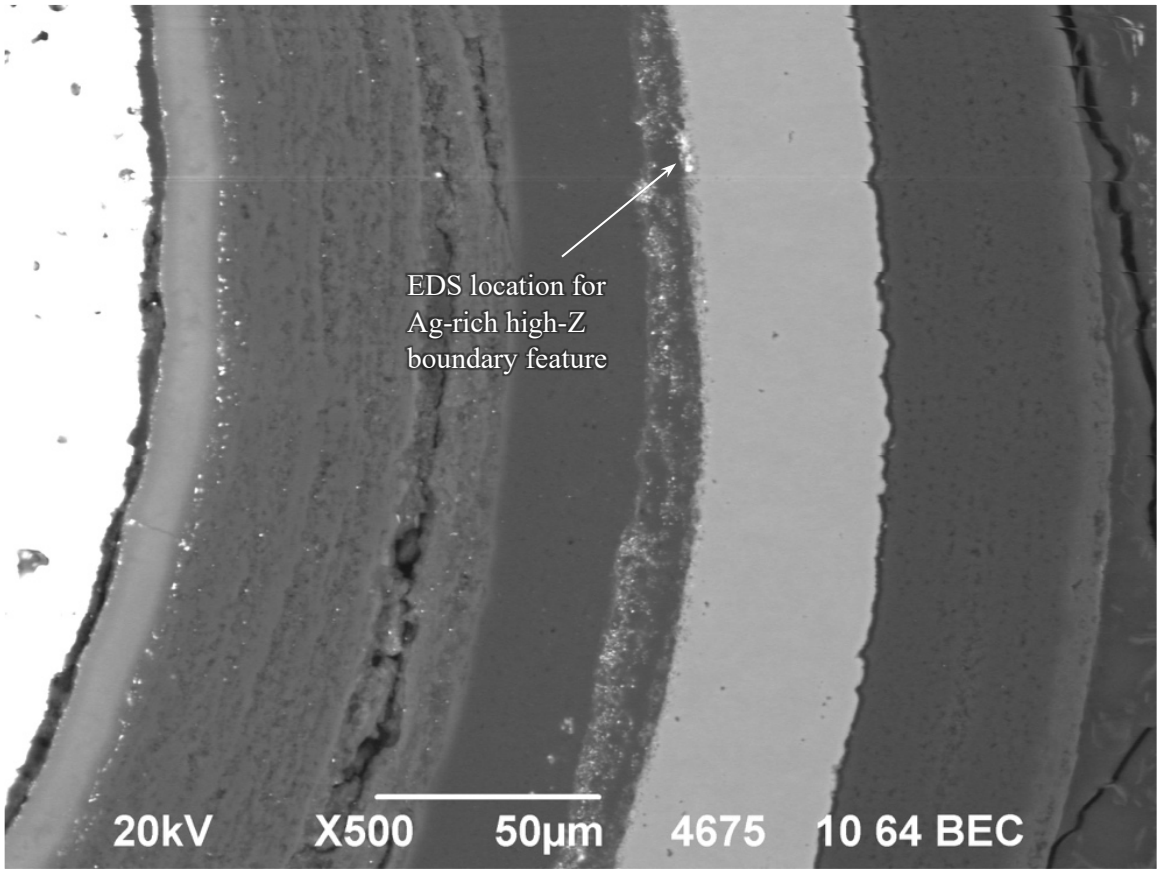

Figure 7-38. EDS location in Particle 342-RS15 for Ag-rich spectrum in Figure 7-37.

Like other compacts, dense buffer regions were observed in all particles. The nature of the dense buffer regions varied from particle to particle with Particles 342-RS03 and 342-RS15 having defined and pronounced regions showing a heavy but diffuse high-Z presence (Figure 7-35 and Figure 7-38). Localized concentrations of high-Z features were segregated in and adjacent to the dense buffer regions. Similar to what was observed in the EDS analysis of the dense buffer regions in Compact 3-3-2 (Figure 7-29), EDS analysis of the Compact 3-4-2 dense buffer regions showed higher concentrations of uranium, cesium, xenon, iodine, molybdenum, and zirconium, with trace ruthenium, technetium, and tellurium compared with the remainder of the buffer; although xenon, rubidium, and strontium were also observed elsewhere in the buffer. The fine-scale, segregated features in and around the dense buffer region were predominately molybdenum, zirconium, ruthenium, and uranium.

7.5 1,700°C SAFETY-TESTED COMPACT 3-4-1 RS PARTICLES

Compact 3-4-1 was exposed to a 1,700°C safety test soak time of 164 h and was a sister compact to Compact 3-4-2, which was expose to a 1,600°C soak time of 305 h. Three RS particles were analyzed (Table 7-1). Representative SEI micrographs of select particles are shown in Figure 7-39–Figure 7-41 and additional images are provided in Appendix D. Structural features that were observed in all particles included low-Z inclusions or material pullout from sample preparation. A gap at the SiC/OPyC interface was observed Particles 341-RS21 and 341-RS36, but not in Particle 341-RS01. The IPyC/SiC interface region was consistent in that all particles showed PyC inclusions in the SiC at the IPyC/SiC boundary around the entire circumference of the interface. The depth of the PyC inclusions in the SiC layer was typical, and not as pronounced as that observed in some Capsule 3 particles (Figure 7-1). The SEI imaging showed porosity around the circumference of the IPyC/SiC interface region. The extent of the porosity varied from particle to particle, in which Particle 341-RS21 showed a qualitatively denser interface region relative to Particles 341-RS01 and 341-RS36.

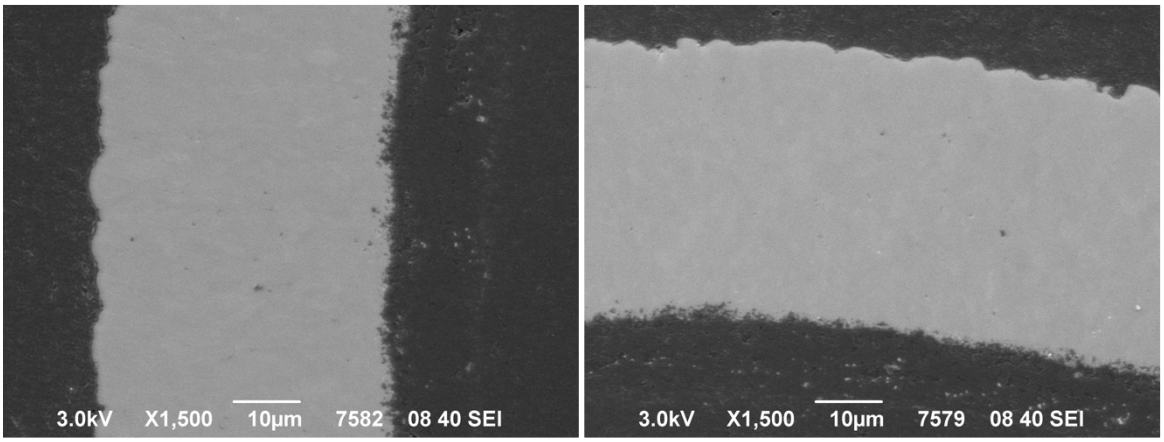

Figure 7-39. Example SEI micrograph of IPyC/SiC/OPyC layers in Particle 341-RS21.

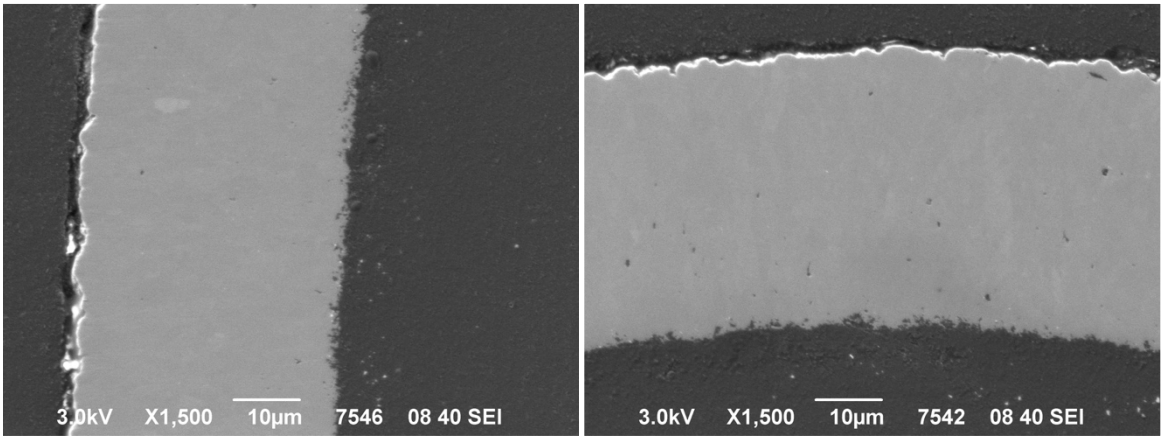

Figure 7-40. Example SEI micrograph of IPyC/SiC/OPyC layers in Particle 341-RS21. Bright locations at SiC/OPyC gap were from charging.

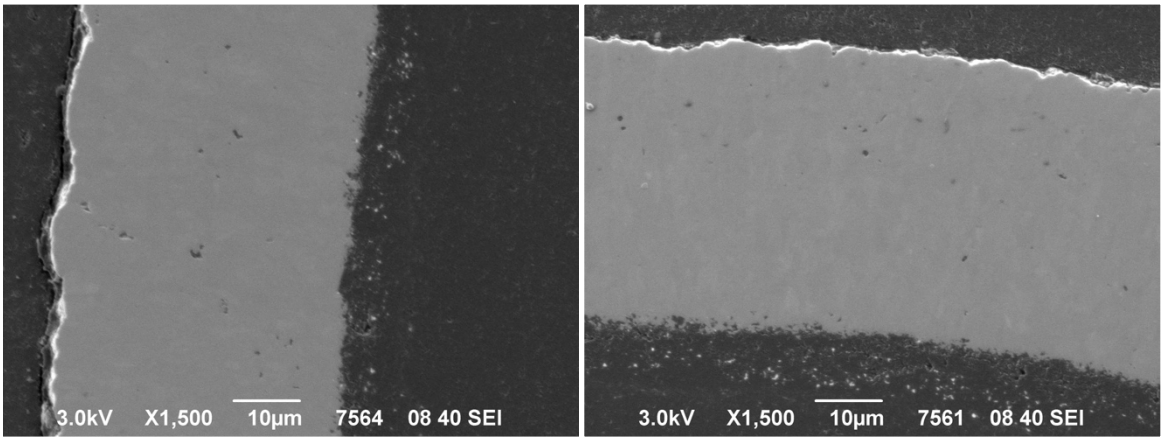

Figure 7-41. Example SEI micrograph of IPyC/SiC/OPyC layers in Particle 341-RS36. Bright locations at SiC/OPyC gap were from charging.

High-Z features were observed in variable distributions in the IPyC/SiC/OPyC layers. All four general classes of high-Z features were identified. The presence and distribution of high-Z SiC features varied from particle to particle. Representative examples of the distribution of fine-scale, high-Z SiC features in Compact 3-4-1 are shown in Figure 7-42–Figure 7-44. All three particles had detached buffer, with residual connected buffer/IPyC regions visible in Particles 341-RS01 and 341-RS21. No obvious high-Z

SiC features were observed in Particle 341-RS36, which had a detached buffer and no visible connected buffer/IPyC region (Figure 7-42). Particle 341-RS01 showed faint high-Z features in the SiC layer that were predominantly adjacent to the connected buffer/IPyC region. No high-Z SiC features were observed in the SiC layer opposite the attached buffer/IPyC region in this particle (Figure 7-43). Particle 341-RS21 had fine-scale, high-Z SiC features throughout the SiC layer (Figure 7-44). These features were more intense than those in the other two particles from Compact 3-4-1 and those observed in particles from as-irradiated Compact 3-3-1 (Figure 7-7 and Figure 7-8), and they were similar to the features observed in particles from the 1,600°C safety-tested compacts (Figure 7-25 and Figure 7-32). There features were slightly more concentrated near the connected buffer/IPyC region.

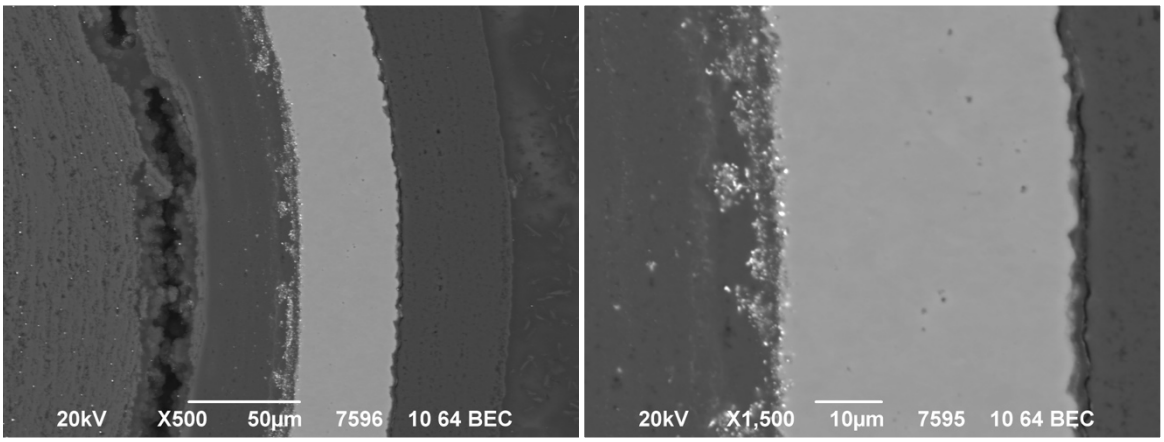

Figure 7-42. Example BEC images of the TRISO layers in Particle 341-RS36.

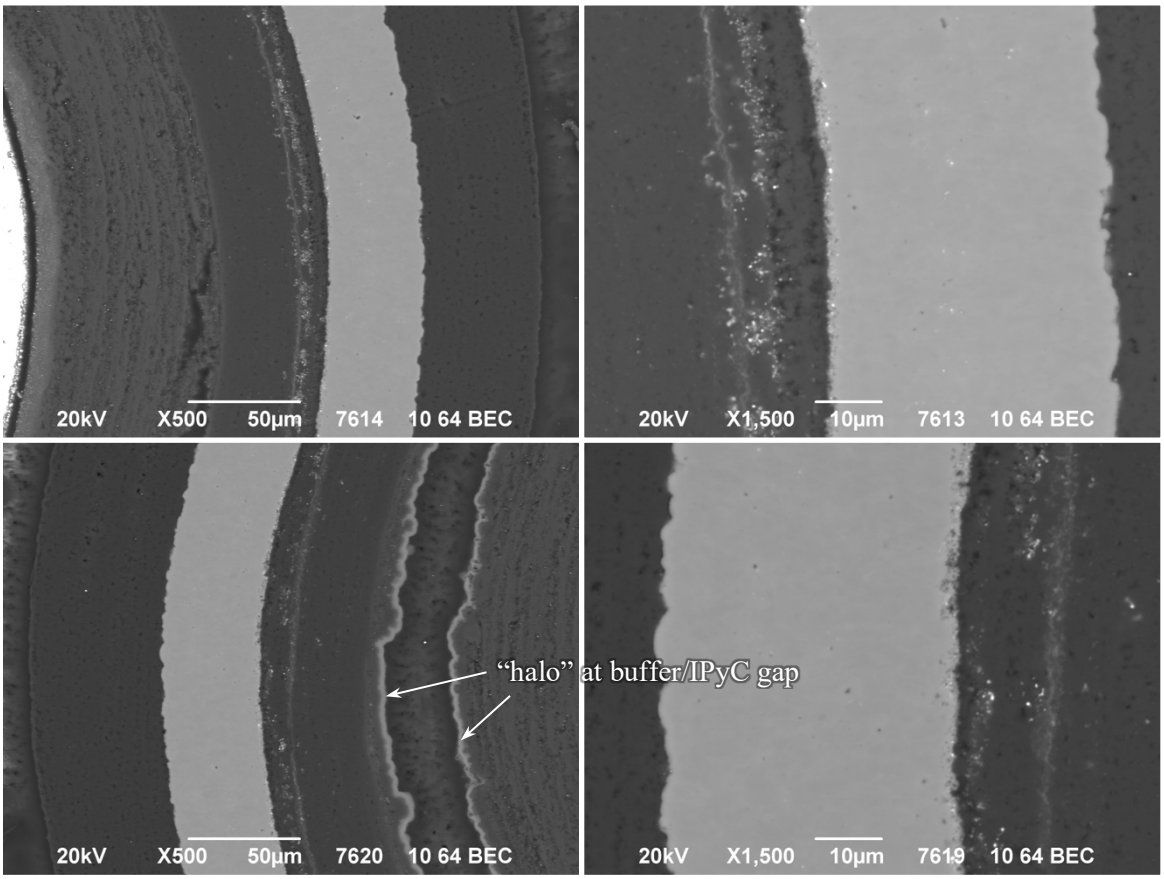

Figure 7-43. Example BEC images of the TRISO layers in Particle 341-RS01.

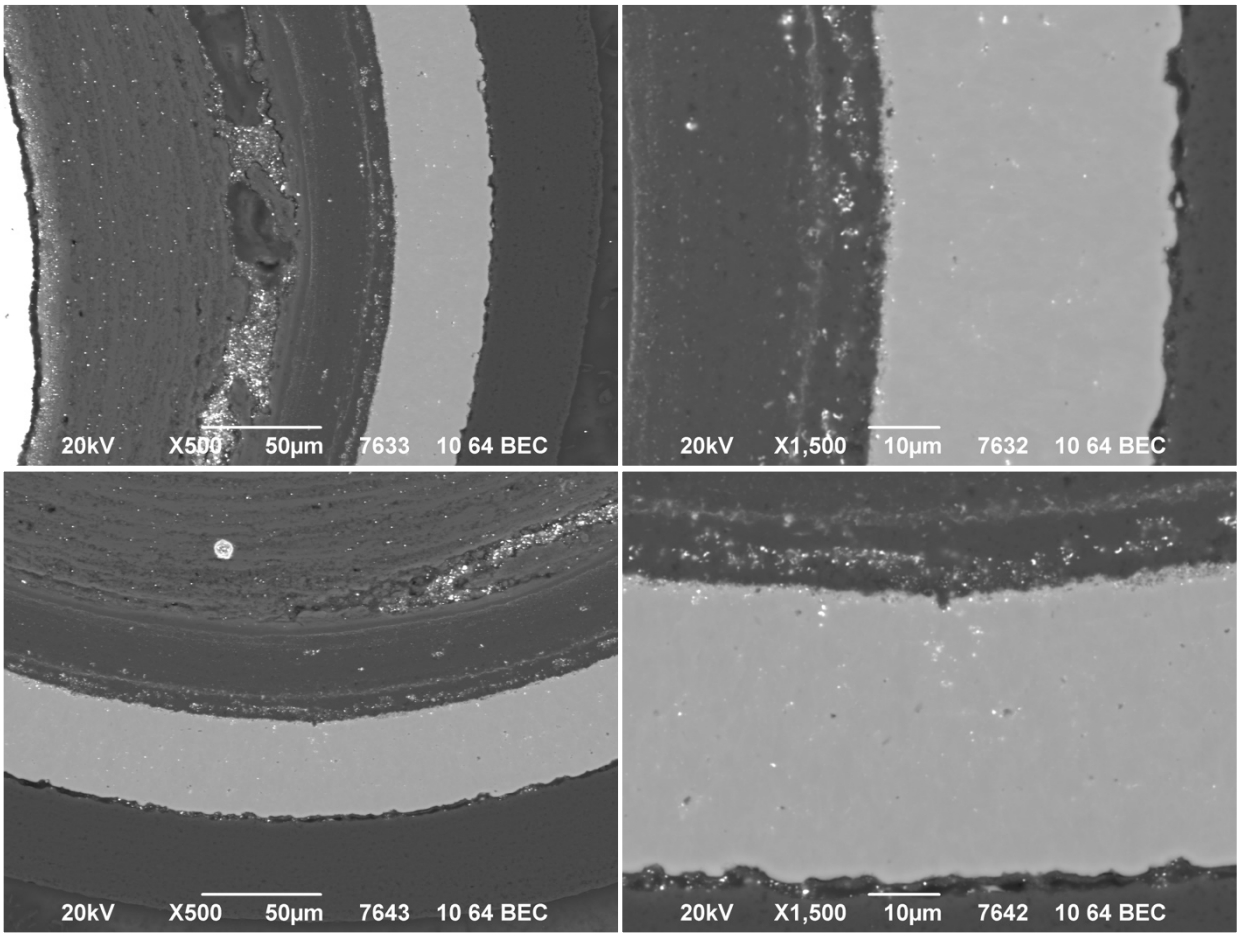

Figure 7-44. Example BEC images of the TRISO layers in Particle 341-RS21.

Much like Compact 3-4-2, both high-Z boundary features and high-Z interface features were observed in the IPyC/SiC interface region. For all particles the observed high-Z features were qualitatively uniform around the entire circumference of the IPyC/SiC interface. There did not appear to be any significant correlation of feature location with the connected buffer/IPyC regions. This suggests the apparent correlation of the high-Z SiC features with these regions for Particles 341-RS01 and 341-RS21 may not be significant. High-Z interface features were present in all three particles. No obvious differences in the distributions of high-Z interface features were observed between the three analyzed particles, though it could be argued that Particle 341-RS01 showed more dispersed high-Z interface features relative to Particles 341-RS21 and 341-RS36. High-Z boundary features were also observed in all three particles. The qualitative predominance of high-Z boundary features varied from particle to particle, namely, a lower frequency of high-Z boundary features were observed in Particle 341-RS01 relative to the other particles.

Similar to the other Capsule 3 particles analyzed with SEM, the high-Z interface features were aligned in a banded structure replicating the observed porosity, which suggested features were forming in the pore structures. Diffuse banded structures were also observed in the IPyC layer much like Compact 3-3-2 and Compact 3-4-2, these features can be seen in the BEC images in Figure 7-42–Figure 7-44, and they were observed in all three particles. Also similar to other safety-tested compacts was the presence of fine-scale high-Z IPyC features in all particles. Unique to Compact 3-4-1 analysis was the observation of a “halo” around the Buffer/IPyC gap in Particle 341-RS01 (Figure 7-43). Because the BEC contrast was sensitive to the atomic weight of the substrate, the observation of the “halo” indicated it was composed of high-Z elements.

The high-Z "halo" was analyzed by point-ID analysis to determine its composition. Representative spectra of the buffer/IPyC gap "halo" observed in Figure 7-43 is presented in Figure 7-45. The region appeared to have a higher relative concentration of cesium, xenon, and iodine relative to the reference spectra. It can be hypothesized that the resulting "halo" was due to gas phase interaction of these particular species with the buffer and IPyC adjacent to the gap. However, speculation as to why this was observed only in this particular particle is beyond the scope of this analysis.

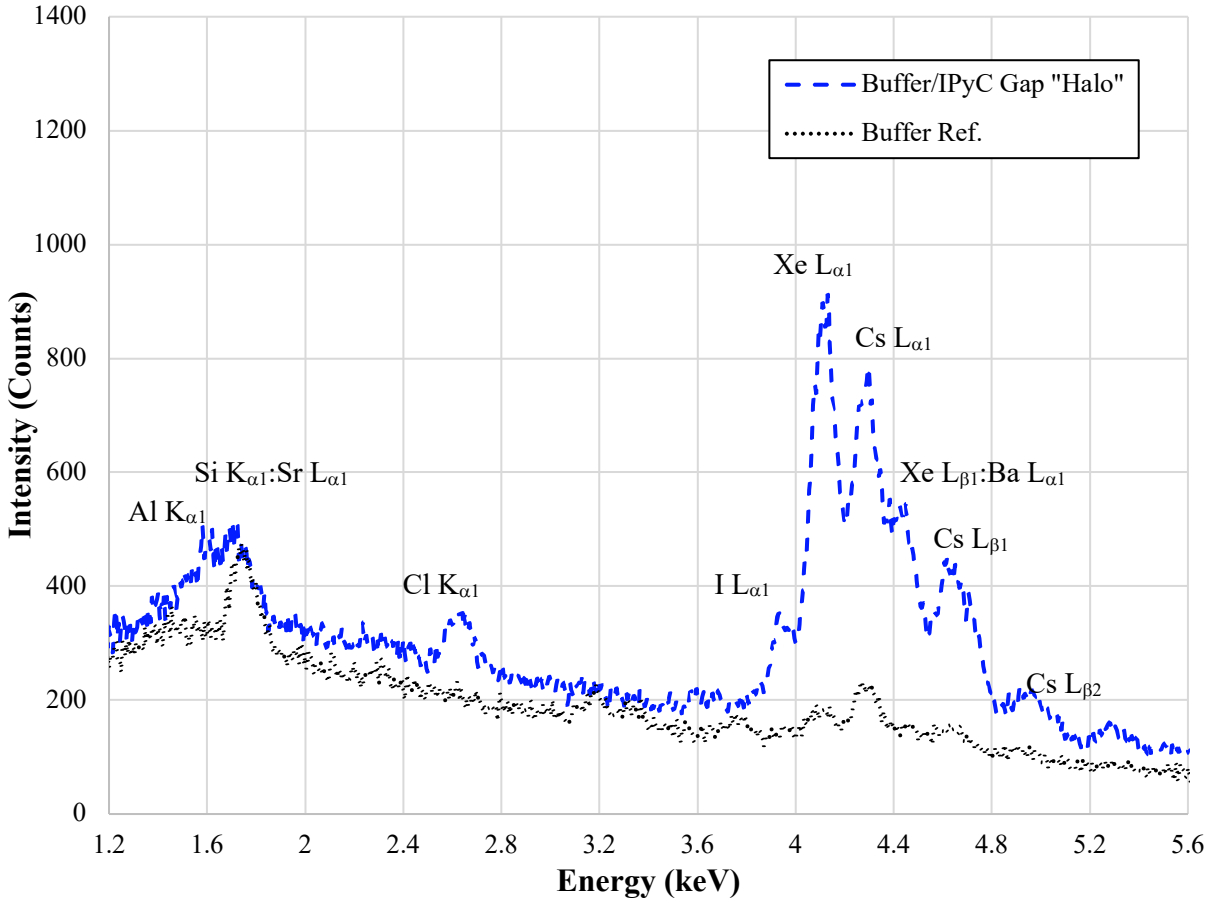

Figure 7-45. Representative EDS spectra of high-Z "halo" and buffer reference.

Elemental analysis was performed on all Compact 3-4-1 RS particles. High-Z SiC features were plentiful in Particle 341-RS21 and limited in Particle 341-RS01. The high-Z SiC features were predominantly Pd-only with a few Pd-Rh high-Z SiC features observed < 5 µm from the IPyC/SiC boundary. Analysis of the high-Z interface and high-Z boundary features showed consistent feature compositions with that of Compacts 3-3-2 and 3-4-2. The compositions of high-Z boundary features were of the Pd-Rh-Ru or Pd-Rh classes observed prior, though the ruthenium presence was elevated in some of the Compact 3-4-1 high-Z boundary features compared with what was observed in the other safety-tested compacts, in which the typical Pd:Ru ratio in atomic percent based on standardless analysis was <10% Pd:1% Ru. In the Compact 3-4-1 analysis relative Pd:Ru atomic concentrations of up to ~5% Pd:1% Ru were observed.

The high-Z interface features were exclusively Pd-Rh-Ru with no Pd-Rh compositions observed. This differed from Compact 3-4-2, in which ~20–40% of the high-Z interface features were Pd-Rh. The diffuse banded features frequently observed in the IPyC/SiC region were similar in composition to those found in Compacts 3-3-2 and 3-4-2, with elevated levels of barium, strontium, and silicon, some cesium, trace uranium and aluminum, and suggestions of oxygen presence. However, additional signals from uranium and possibly trace levels of ruthenium were observed in the diffuse banded high-Z IPyC features further from the IPyC/SIC boundary. This coincided with more pronounced uranium presence in the fine-scale,

IPyC features relative to Compacts 3-3-2 and 3-4-2. This variation in uranium signal across the IPyC layer, with more uranium near the buffer layer is shown in Figure 7-46, with the locations of each spectra shown in Figure 7-47. The elevated uranium signal in the absences of aluminum indicated these features were probably not artifacts and suggested uranium was moving out from the kernel at 1,700°C.

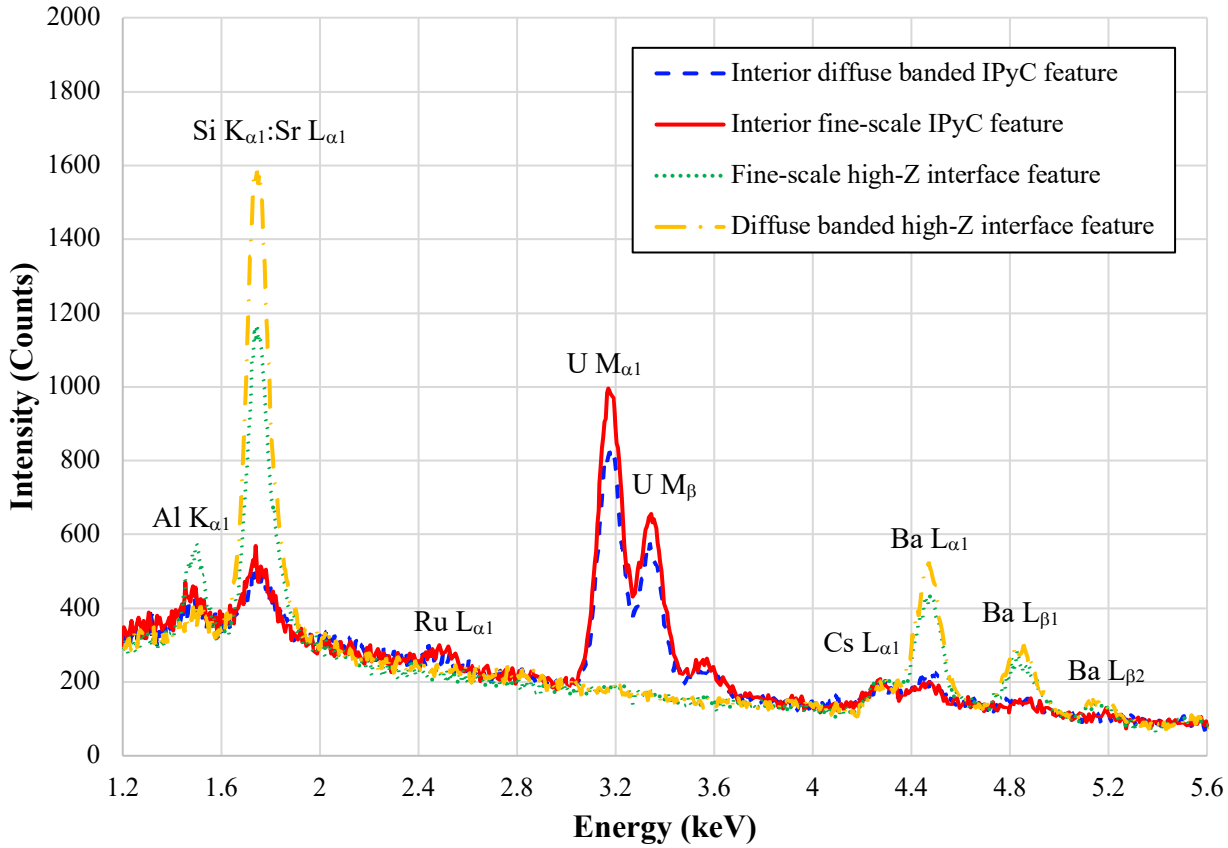

Figure 7-46. EDS spectra showing more uranium in the interior IPyC layer of Particle 341-RS21.

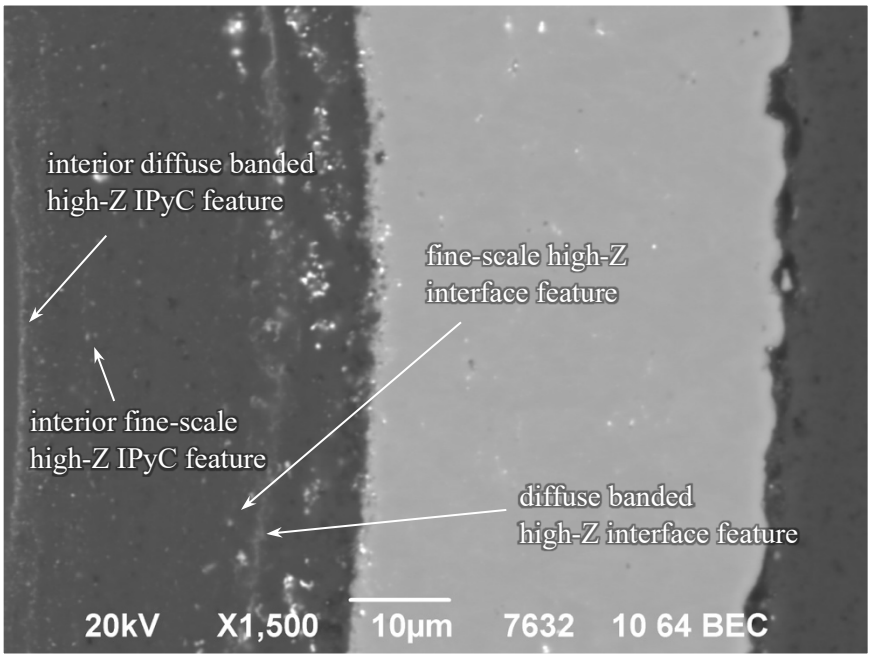

Figure 7-47. EDS locations in Particle 341-RS21 for spectra in Figure 7-46.

Dense buffer regions were observed in all particles from Compact 3-4-1. The nature of the dense buffer regions was similar to Compacts 3-3-2 and 3-4-2, with a diffuse dense region adjacent to the kernel and segregated fine scale high-Z features distributed throughout. Elemental analysis showed feature compositions in the dense buffer regions similar to the other safety-tested compacts, namely, high concentrations of uranium, cesium, xenon, iodine, molybdenum, and zirconium, with trace ruthenium, technetium, and tellurium, although some xenon, rubidium, and strontium were also observed elsewhere in the buffer. Also similar to Compact 3-4-2 was the observation that the fine-scale segregated features were predominately molybdenum, zirconium, ruthenium, and uranium.

7.6 DISCUSSION OF SEM ANALYSIS OF RS PARTICLES

The analysis of the RS particles indicated the structure of the IPyC/SiC interface influenced how actinides and fission products interacted with the layers of the UO_2 TRISO fuel. This was most apparent when considering the observation of banded high-Z features in the IPyC layer and IPyC/SiC interface region. The correlating observations of banded accumulations of high-Z material and bands of porosity suggested the IPyC structure influenced the accommodation of the high-Z material. The observation of pronounced PyC inclusions in the SiC layer in some particles with relatively minimal PyC inclusions in others suggests variable IPyC/SiC interfaces were present in particles from a single compact. However, the analysis as it stands, did not show any significant correlation between the PyC inclusions and fission product behavior.

A trend in mobility of actinides and fission products based on high-Z feature composition was observed when comparing as-irradiated compacts and those subjected to safety-testing temperatures up to 1,700°C. Specifically, higher rhodium and ruthenium intensities were observed in conjunction with higher safety test temperatures. Rhodium appeared to be more mobile than ruthenium as a function of temperature, as indicated by frequent rhodium observations beginning at 1,500°C and frequent ruthenium observations beginning at 1,600°C. Similarly, temperature-dependent mobility of uranium was observed. In the 1,600°C safety-tested samples, uranium appeared in the dense buffer region adjacent to the kernel, while in the 1,700°C safety-tested samples, uranium was observed further from the kernel in the IPyC layer near the buffer/IPyC interface. This suggested uranium diffusion was active at 1,700°C, although no obvious uranium was present in the IPyC/SiC interface region or in the SiC layer. This differed from the UCO TRISO fuel subjected to safety testing, which showed the presence of uranium in the SiC layer. In general, the diversity of radionuclides in observed accumulations within the SiC layer was much lower in UO_2 TRISO than in UCO TRISO. This was expected based on the elevated oxygen potential in the UO_2 kernels compared to the UCO kernel (Gerczak et al. 2018).

In UCO TRISO, the distribution of actinides and fission products typically followed a trend of greater penetration of high-Z features into the SiC layer and greater radionuclide diversity (particularly uranium presence) for particles whose higher silver release indicated exposure to higher temperature (Demkowicz et al. 2015; Gerczak et al. 2018, Gerczak et al. 2020a). Trends in fission product distribution relative to measured ^{110m}Ag content were not as obvious in most UO_2 TRISO particles analyzed herein, compared with previous studies of UCO TRISO particles. However, Compact 3-4-2 particles showed a distinct trend, in which the two particles with the lowest ^{110m}Ag content (^{110m}Ag M/A = 0.77–0.81) showed fine-scale high-Z SiC features throughout the SiC layer, while the two particles with the highest ^{110m}Ag content (^{110m}Ag M/A = 1.17–1.20) showed only a few high-Z SiC features, which were confined to the first few microns of the layer. A correlation of temperature, as indicated by ^{110m}Ag retention, to high-Z SiC feature behavior was further supported by a general trend in other compacts, in which the particles with the lowest ^{110m}Ag M/A were always among the particles with the most pronounced high-Z SiC features compared with other particles from the same compact. Although some particles with average or high ^{110m}Ag M/A also showed pronounced high-Z SiC features, such as particles from Compacts 3-3-2 and 3-4-1, this did not contradict the temperature dependent trend. No correlation of ^{110m}Ag M/A to rhodium or ruthenium presence in the IPyC/SiC interface region was observed, which suggested the presence of these elements was primarily only impacted by the higher safety test temperatures.

8. SEM ANALYSIS OF SPECIAL PARTICLES

Special particles identified during particle inspection and IMGA survey, as discussed in Section 5, were imaged in the SEM and subjected to EDS elemental analysis. These particles had abnormal inventories of one or more gamma-emitting isotopes, as shown in Table 8-1. Table 8-1 presents the M/A values from Appendix B, which best communicate the abnormal inventory for these particles. The M/AA and M/C values based on using ^{137}Cs to adjust for variation in initial fissile content and burnup are available in Appendix B, but interpretation of these values is more complicated due to the preferential loss of cesium in many cases. For some particles, the M/AA and M/C values can be recalculated using a better retained isotope, if available (e.g., ^{106}Ru for Particles 342-SP07, 341-SP03, and 341-SP15). However, the M/A values are sufficient for supporting the discussion herein. Typical PIE progression for special particles suspected of having failed SiC or failed TRISO involved following identification during IMGA survey with a series of examinations and sample preparation techniques designed to reveal what was usually a localized degradation of the TRISO coating microstructure. These steps included XCT, guided materialography, optical microscopy, and ultimately analysis with electron microscopy. The multiscale analysis provided a systematic way of determining or confirming the relevant failure mechanism responsible for release (Hunn et al. 2014a). Prior results of AGR-2 UO_2 TRISO particle failure and supporting SEM analysis have been reported previously, in which particle failures were primarily related to CO corrosion of the SiC layer (Morris et al. 2016; Gerczak et al 2020b).

Table 8-1. Special particles from Capsule 3 subjected to SEM analysis

Particle	**^{106}Ru**	**^{110m}Ag**	**^{125}Sb**	**^{134}Cs**	**^{137}Cs**	**^{144}Ce**	**^{154}Eu**
Value	M/A	M/A	M/A	M/A	M/A	M/A	M/A
312-SP02	0.75	<0.32	0.84	0.19	0.16	0.00	0.00
332-SP01	0.85	0.02	0.82	0.08	0.09	0.04	0.02
332-SP02	0.61	<0.02	0.92	0.14	0.15	0.02	0.05
332-SP03	0.74	<0.02	1.05	0.19	0.20	0.02	0.07
332-SP04	0.72	<0.02	1.05	0.19	0.20	0.02	0.06
342-SP01	0.78	0.01	1.06	0.09	0.09	0.03	0.01
342-SP06	0.89	0.42	1.02	0.53	0.53	0.37	0.25
342-SP07	1.13	0.80	1.14	0.72	0.71	1.07	1.18
342-SP09	0.86	0.71	0.86	0.66	0.68	0.90	0.82
341-SP01	0.90	<0.06	1.10	0.08	0.08	0.08	0.01
341-SP03	1.03	<0.07	1.05	0.17	0.17	0.39	0.05
341-SP15	0.96	0.89	0.99	0.76	0.74	0.95	1.02

8.1 AS-IRRADIATED COMPACT 3-1-2 SPECIAL PARTICLES

As-irradiated Particle 312-SP02 was missing most of its kernel material, indicating all three layers were permeable to the acid leach, and XCT clearly showed cracks through all coating layers (Figure 5-14). The general structure of the layers was discussed in Section 5.2. Table 8-1 shows that the acid removed almost all of the ^{144}Ce and ^{154}Eu. Minor retention of ^{134}Cs and ^{137}Cs can be explained by transport of cesium during irradiation into the carbon layers between the kernel and the SiC, making it was less accessible to the acid. The ^{106}Ru and ^{125}Sb inventories were mostly retained in the leached kernel, suggesting these isotopes were present in forms less soluble in nitric acid. The DLBL data in (Appendix Table A-7) agreed with this assessment, with <0.13 particles equivalents of ^{106}Ru and <0.11 particles equivalents of ^{125}Sb in the pre-IMGA leaches. The XCT imaging showed some residual high-Z material remained in the kernel location, and this probably included ruthenium and antimony. Representative BEC images of Particle 312-SP02 are shown in Figure 8-1. While the XCT imaging showed some sections of the IPyC were still attached to the SiC, a gap was observed around the entire IPyC/SiC interface in the polished cross section. The gap was more pronounced where the buffer was connected to the IPyC. The through-layer crack in

the SiC shown in Figure 8-1d and Figure 5-14b was adjacent to a through-layer damaged OPyC region. The damaged OPyC region was primarily open volume in the observed polished cross section, partly due to material pullout and EDS analysis showed significant aluminum and chlorine intensity suggesting the presence of sample preparation artifacts and epoxy from the backfill. However, based on the through layer nature and low density of the region, along with the XCT imaging, it is likely that this was part of the through-layer pathway that allowed acid infiltration during DLBL.

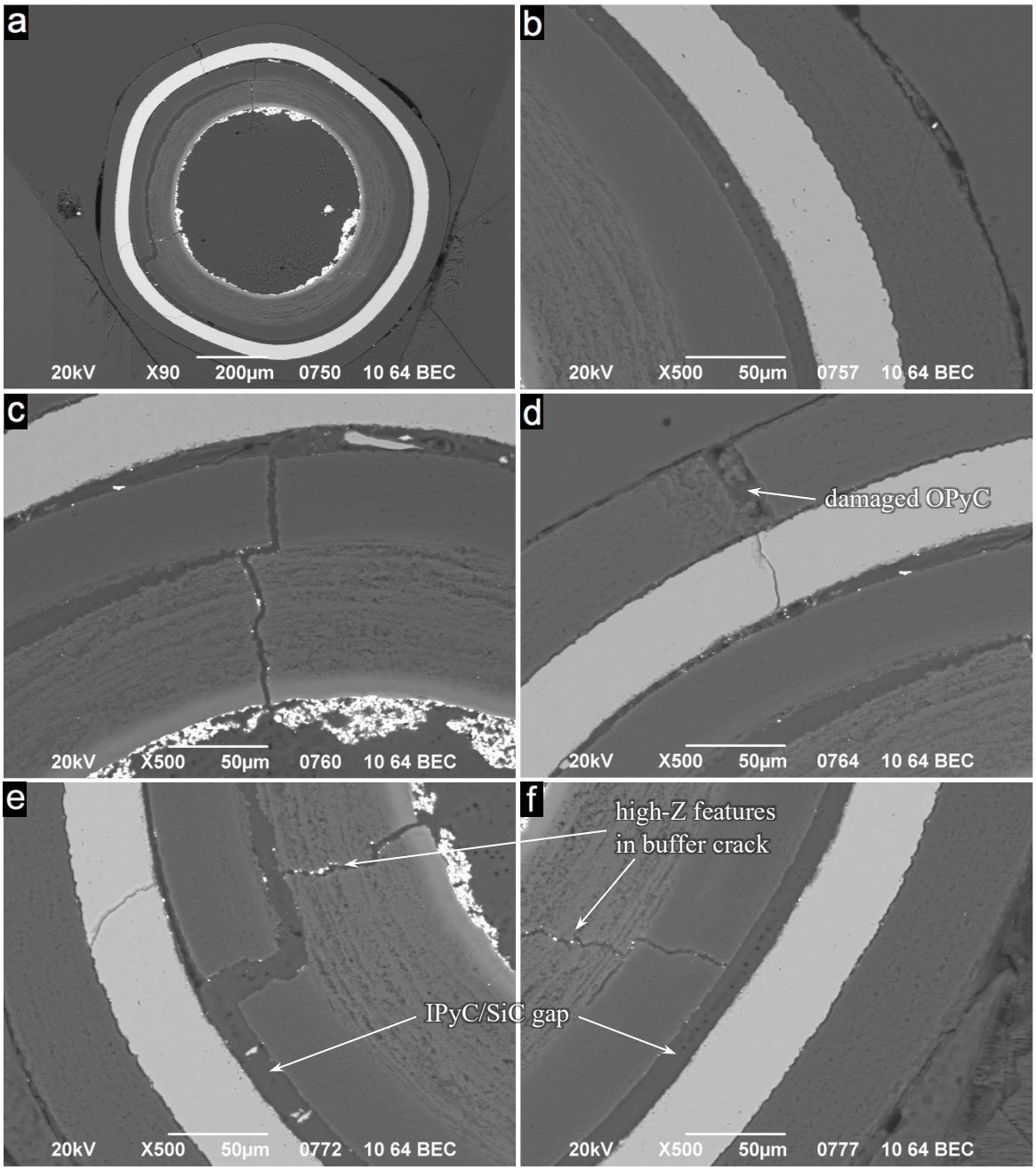

Figure 8-1. BEC images of regions of interest in Particle 312-SP02.

The exposure of the inner SiC surface could make the SiC susceptible to CO corrosion, which was shown to be the predominant mechanism for SiC degradation in UO_2 TRISO fuel (Minato et al. 1991). In that study, identifiers of CO corrosion included intergranular grain boundary corrosion of the SiC layer and the presence of Si-O features within the particle. Close up BEC/SEI image pairs of the SiC layer from Particle 312-SP02 are shown in Figure 8-2. No obvious indicators of extensive grain boundary corrosion

were observed at the inner surface of the SiC layer, based on comparison with the analysis of as-irradiated particles (Section 7.1). There were near-surface features which may be indicators of CO corrosion, but these could not be differentiated from PyC inclusions or residual IPyC left attached to the SiC after the formation of the IPyC/SiC gap. The formation of the IPyC/SiC gap suggested that CO corrosion was active, but evidence for this corrosion was below the resolution of the SEM system leveraged for this work. CO corrosion in particles from safety-tested AGR-2 UO_2 compacts was evidenced by the presence of Si-O precipitates in the open volumes of the coating structure, such as at the Buffer/IPyC gap (Gerczak et al. 2020b). Features with contrast similar to the SiC layer were observed in the IPyC/SiC gap in Particle 312-SP02 and were analyzed for the presence of Si-O compositions indicative of CO corrosion. However, EDS analysis indicated these features were SiC debris that was likely embedded in the epoxy during sample preparation.

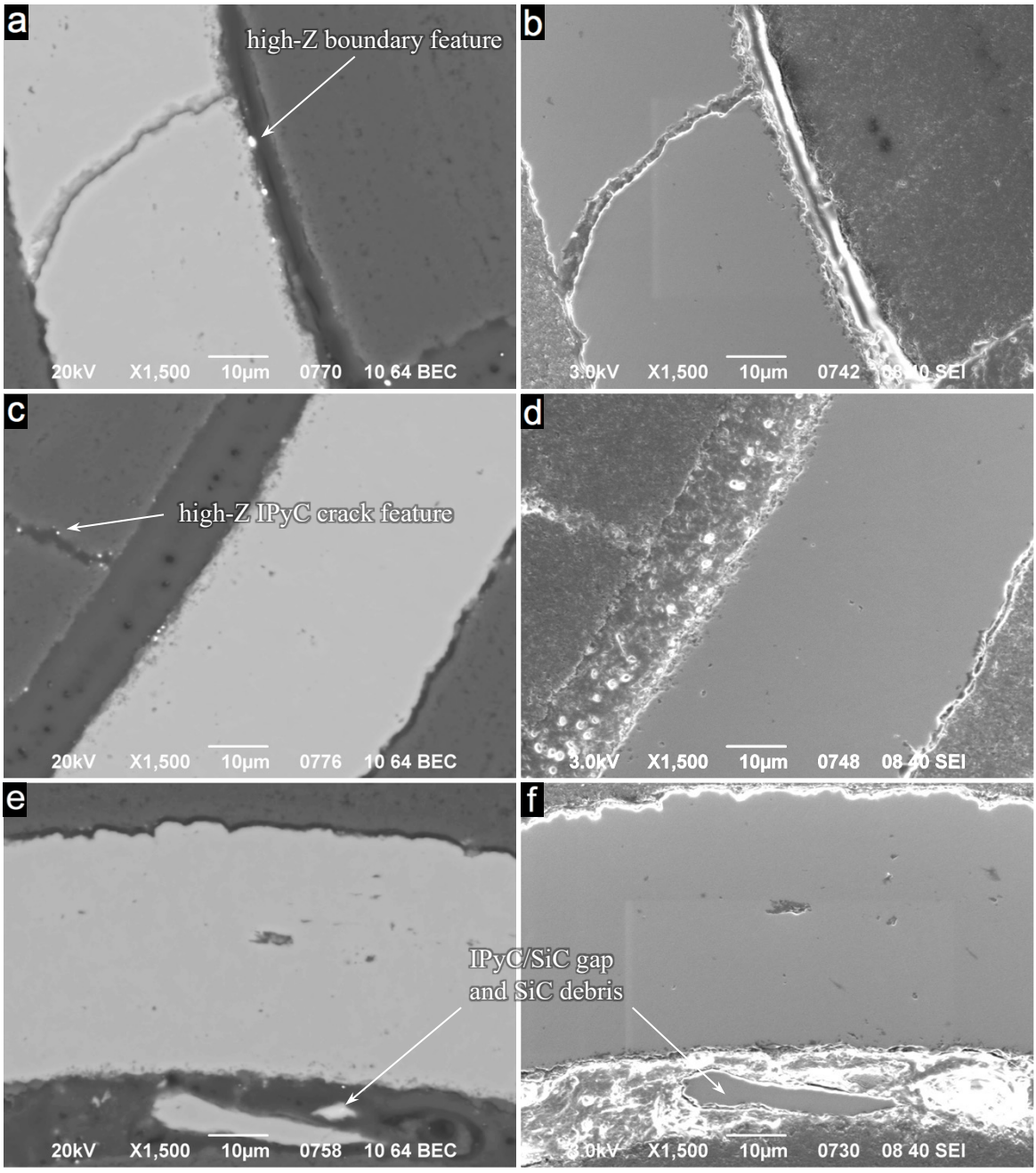

Figure 8-2. BEC/SEI image pairs of regions of interest in Particle 312-SP02.

High-Z features were observed decorating the buffer and IPyC cracks (e.g., Figure 8-1f and Figure 8-2c). High-Z boundary features were also observed (Figure 8-2a), while no high-Z interface features were observed. The lack of high-Z interface features was not unexpected as few high-Z interface features were observed in the random sample Compact 3-1-2 particles (Section 7.1). The high-Z features decorating the buffer and IPyC cracks were predominantly Mo-Ru-Tc-Pd-Ru in composition. Minato et al. observed these features in corroded UO_2 TRISO particles and identified them as silicides (Minato et al. 1991). An example spectrum of a high-Z feature in a buffer crack showing the Mo-Ru-Tc-Pd-Ru composition is compared with a buffer reference spectrum in Figure 8-3. The high-Z boundary features were almost exclusively Mo-Ru-Tc-Pd-Ru composition however, select features were observed to be Pd-only, similar to the Compact 3-1-2 as-irradiated particle analysis.

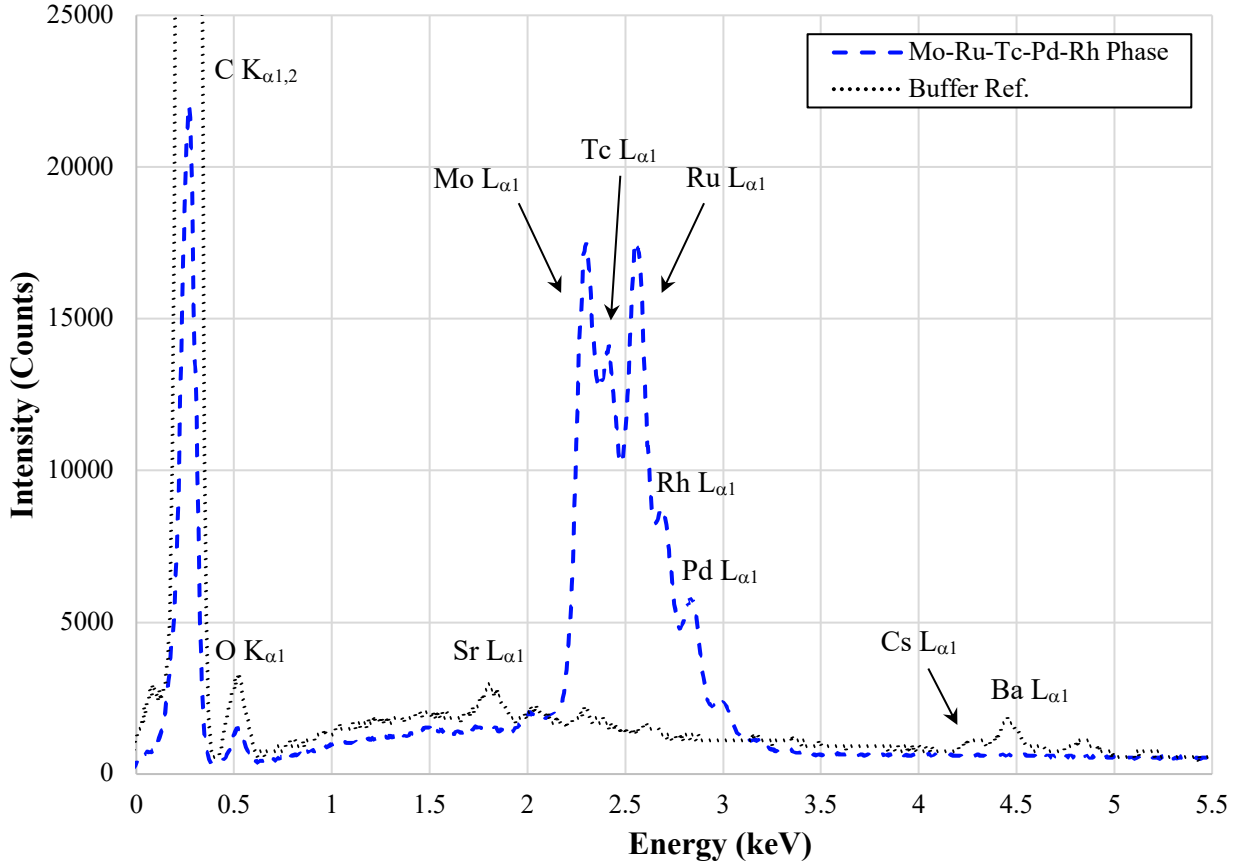

Figure 8-3. Example spectra of features with Mo-Ru-Tc-Pd-Rh composition present in the IPyC/SiC gap and TRISO cracks.

8.2 1,600°C SAFETY-TESTED COMPACT 3-3-2 SPECIAL PARTICLES

Four special particles from Compact 3-3-2 were examined in the SEM (Table 8-1). Three of the four particles showed localized regions in the SiC layer with advanced stages of corrosion, and these regions were located where IPyC cracks had exposed the SiC layer. Summary BEC images are shown for these three particles (Particles 332-SP04, 332-SP03, and 332-SP02) in Figure 8-4, Figure 8-5, and Figure 8-6, respectively. As discussed in Section 5.4, XCT imaging showed the IPyC cracks were all related to incomplete buffer/IPyC separation. This precursor to failure was similar to that observed in UCO TRISO particles where the exposed SiC layer was degraded by metallic fission products (Hunn et al. 2014a). In these three particles, the SiC degradation showed typical features associated with CO corrosion, namely, intergranular corrosion and deposits of SiO_2 (Minato et al. 1991). The intergranular corrosion was especially obvious in Particles 332-SP04 and 332-SP03 (Figure 8-4 and Figure 8-5, respectively). Grain boundary corrosion in Particle 332-SP04 was further explored with scanning transmission electron

microscopy and transmission Kikuchi diffraction analysis, which showed intragranular corrosion and preferential grain boundary attack as a function of grain boundary character (Gerczak et al. 2020b).

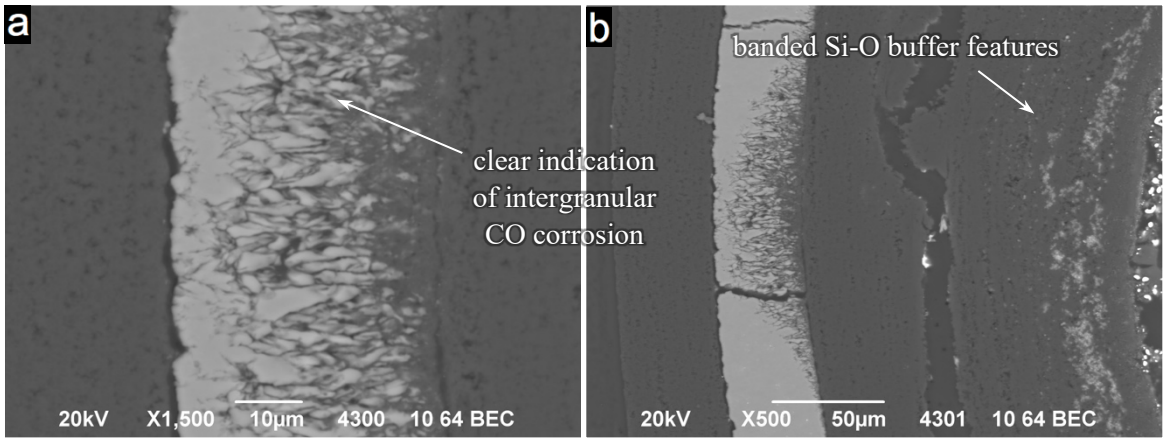

Figure 8-4. BEC images of corroded SiC in Particle 332-SP04.

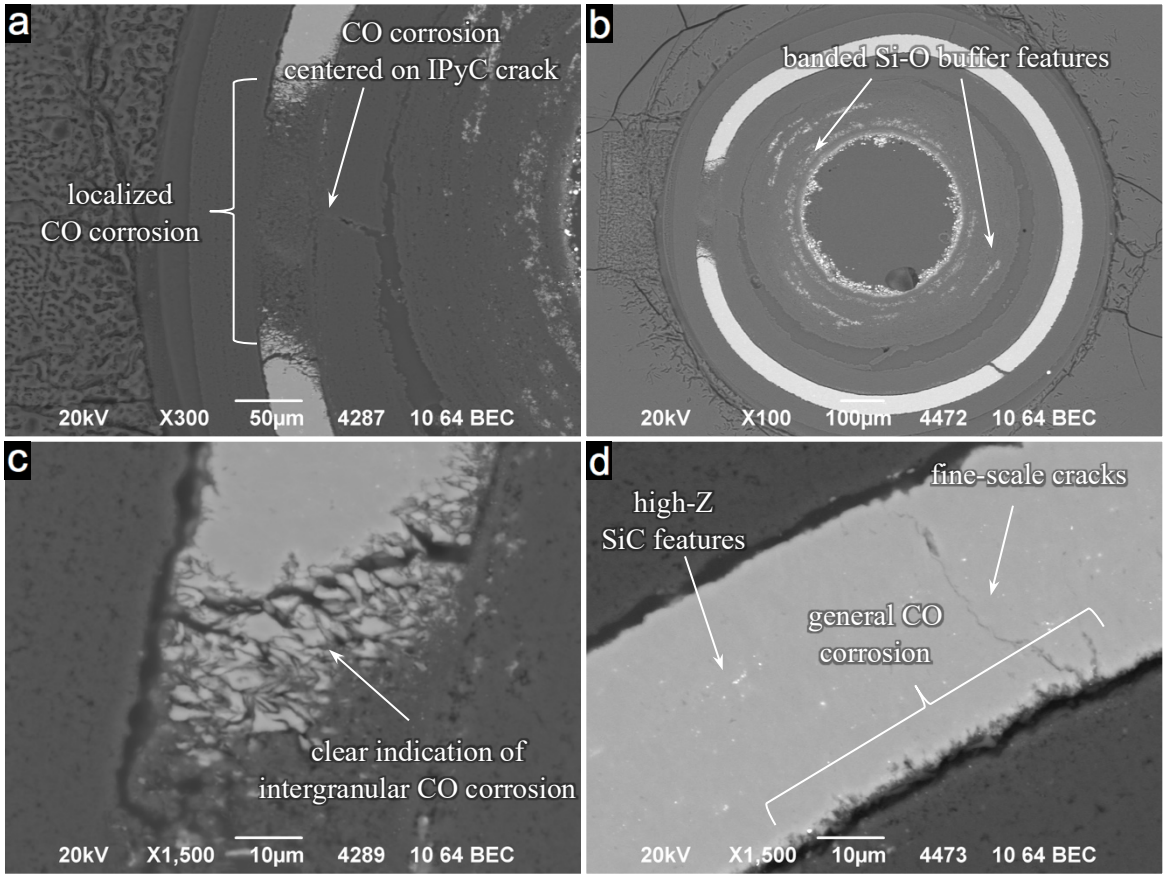

Figure 8-5. BEC images of regions of interest in Particle 332-SP03.

Significant cracking of the SiC was observed in and around the corroded regions, which implied the degradation and thinning of the SiC layer weakened the SiC in that area and led to fracture. In Figure 8-6c, the SiC fracture looks as if it were the final contributor to through-layer failure, but the corrosion in this region also penetrated the layer in a plane not imaged by SEM, as shown in the XCT image in Figure 8-7a. The XCT images in Section 5.4 (Figure 5-25–Figure 5-27) show extended cracks in the SiC associated with the corroded regions. At least some of these cracks may have occurred after safety testing,

especially those that did not show corrosion of the fracture surface. There were also fine-scale cracks remote from the corroded regions (Figure 8-5d), but XCT analysis showed these cracks were connected to cracks associated with the corroded regions elsewhere in the particle.

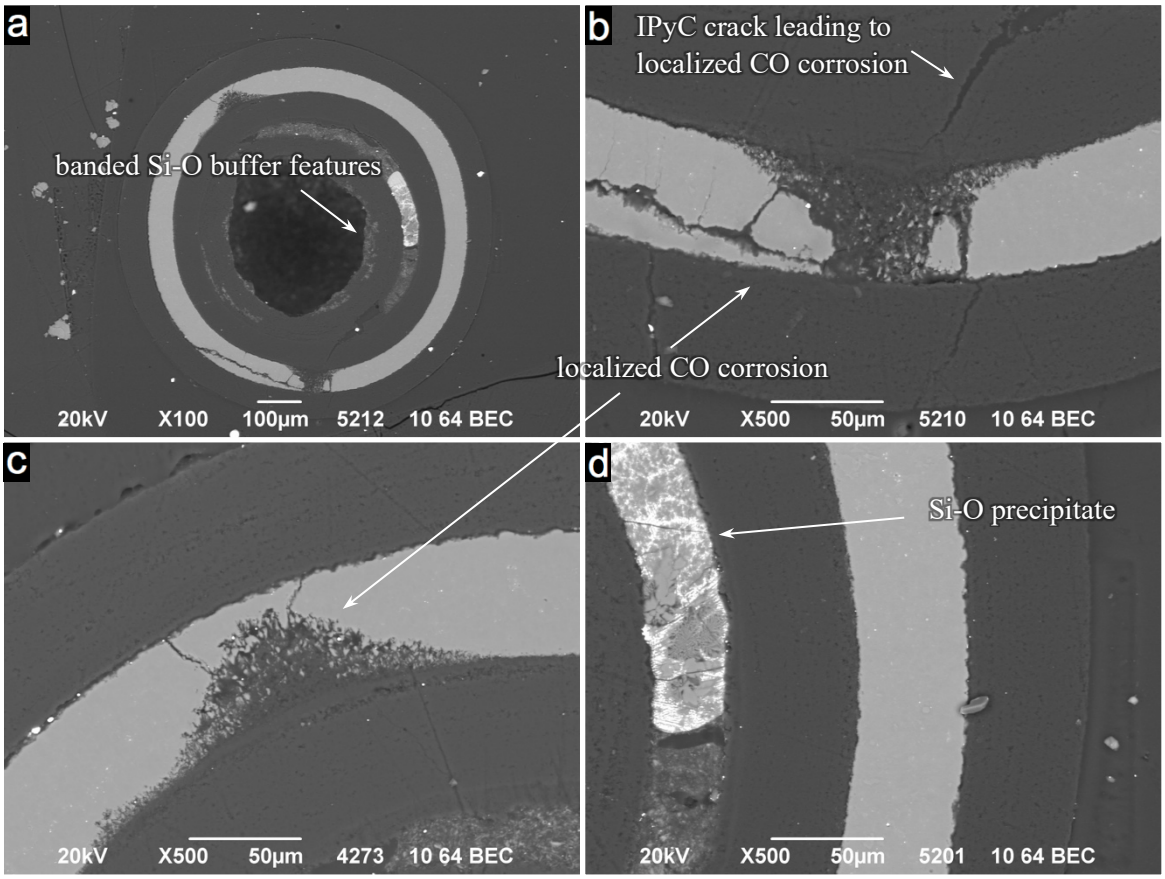

Figure 8-6. BEC images of regions of interest in Particle 332-SP02.

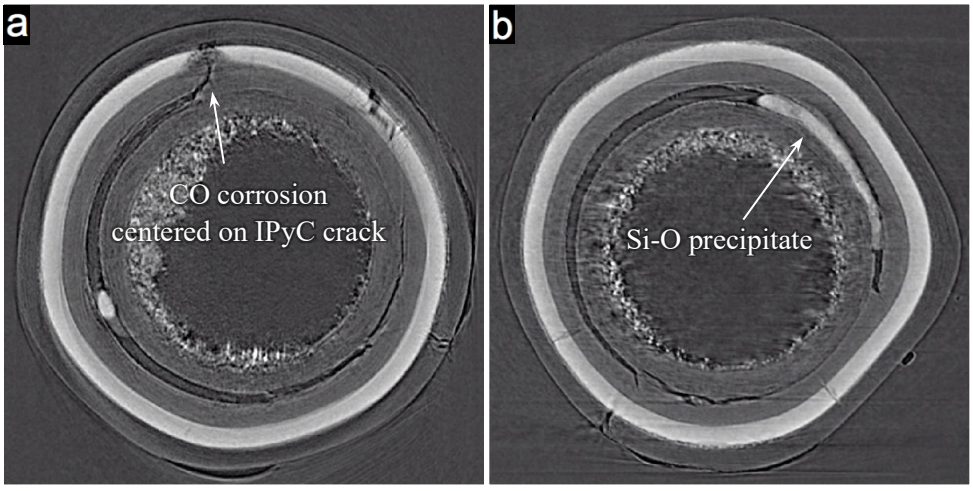

Figure 8-7. XCT images showing alternate cross sections of regions of interest shown in Figure 8-6.

The SEM imaging of the particles revealed the presence of dense features in the carbon layers remote from the localized CO corrosion sites in the SiC. EDS analysis identified these features as having an Si-O composition. Two types of observed Si-O features were large-scale Si-O precipitates and banded Si-O buffer features. The large-scale Si-O precipitates had formed in the open gaps generated by buffer

detachment and fracture. Figure 8-6d shows an example of a large-scale Si-O precipitate that filled a region of the buffer/IPyC gap in Particle 332-SP02, and Figure 8-7b shows the same precipitate from another angle that better shows its size. The XCT analysis showed similar large-scale precipitates in Particles 332-SP03 and 332-SP01, while Particle 332-SP04 XCT imaging only showed smaller high-Z agglomerates in the gaps. Banded Si-O buffer features were observed in the cross sections of Particle 332-SP02 (Figure 8-6a), Particle 332-SP03 (Figure 8-5b), and Particle 332-SP04 (Figure 8-4b). The banded nature of these features suggested that they were also formed by Si-O precipitates filling open volumes (in this case, the buffer pores). Standardless analysis indicated the large-scale Si-O precipitates were likely SiO_2 (Gerczak et al. 2020b). Analysis of the large-scale Si-O precipitate in Particle 332-SP01 is discussed below. A representative EDS spectrum showing the composition of a banded Si-O buffer feature is shown in Figure 8-8. The banded Si-O buffer features included elevated levels of zirconium and barium, and trace molybdenum, uranium, and cesium, relative to the reference buffer. As discussed by Minato et al., thermodynamic analysis shows that SiO has a high vapor pressure at safety testing temperatures and SiO formation is expected to dominate and transport the Si-O reaction product away from the CO corrosion site in the SiC where it will form more stable SiO_2 or other complex oxides upon cooling, while the C reaction product remains at the corrosion site (Minato et al. 1991). Consistent with this mechanism, the residual low-Z material in the localized corrosion region of the Compact 3-3-2 particles was primarily carbon with limited observation of silicon and oxygen, less than ~3% total concentration based on standardless analysis, along with low concentrations of molybdenum (Figure 8-9). The chlorine peak shown in Figure 8-9 was typical of features containing some residual epoxy that can be introduced in open volumes across the polished section. The increased ratio of carbon to silicon in the corroded region provides additional validation to the conclusion that CO corrosion was the predominant degradation mechanism.

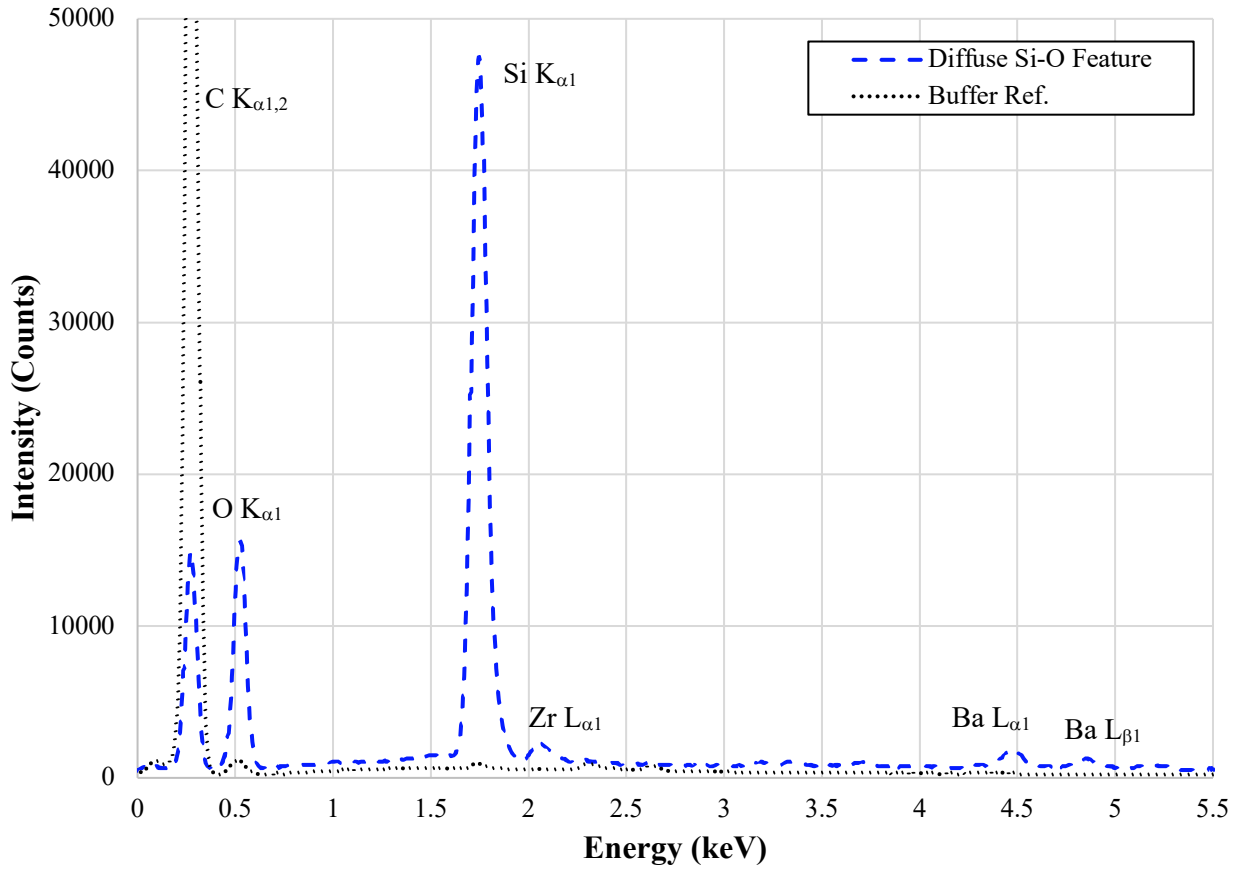

Figure 8-8. Representative EDS spectra of diffuse banded Si-O buffer feature in Particle 332-SP02.

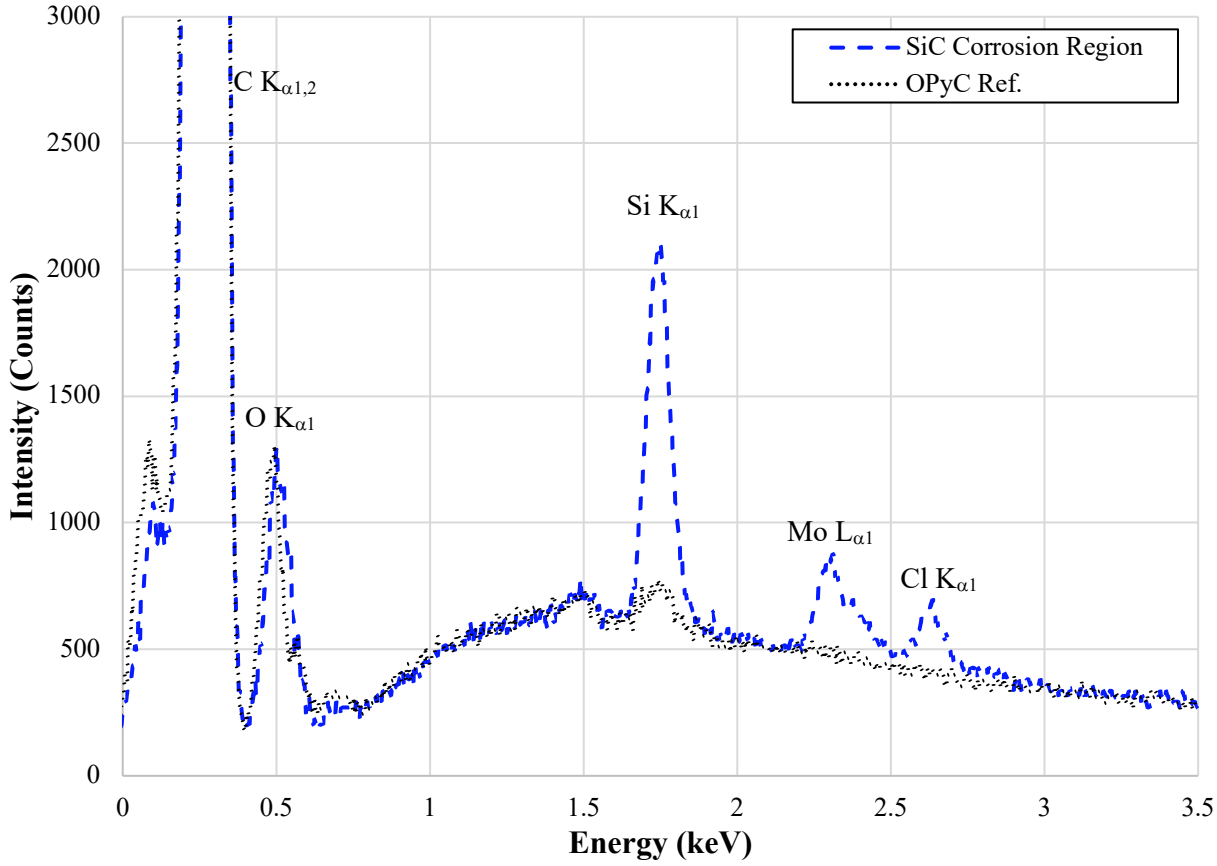

Figure 8-9. Representative EDS spectra of residual material in a corroded SiC region of Particle 332-SP02.

Analysis of the SiC in Particles 332-SP02, 332-SP03, and 332-SP04 at locations away from the localized corroded regions showed no clear indication of general CO corrosion in areas where the SiC inner surface was protected by a fully attached IPyC layer (Figure 8-10). In contrast, locations where the IPyC layer was detached and the SiC was exposed showed suggestions of general CO corrosion (Figure 8-11). The CO corrosion in these areas was faint and appeared as somewhat linear, fine-scale, intergranular features confined to the first 10 µm of the SiC layer. The features differed from typical PyC inclusions observed in the RS particle analysis, which were typically more spherical in nature.

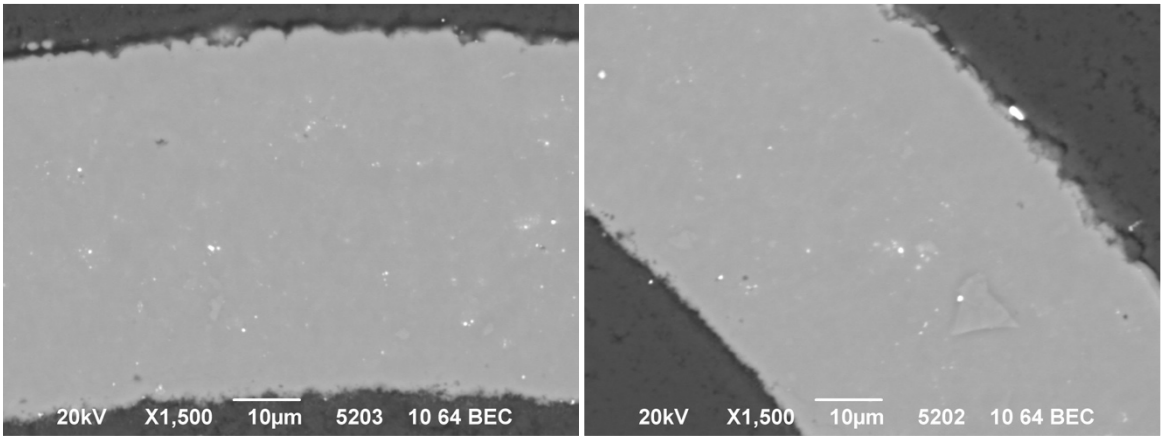

Figure 8-10. BEC images of connected IPyC/SiC interface in Particle 332-SP02.

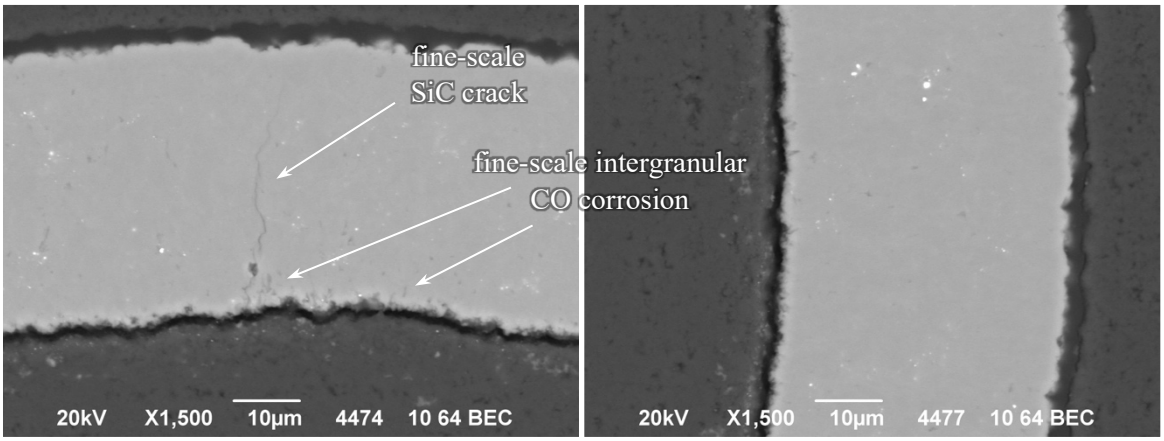

Figure 8-11. BEC images of detached IPyC/SiC interface in Particle 332-SP03.

Although lacking a large localized region of corroded SiC, Particle 332-SP01 still showed clear features associated with CO corrosion Figure 8-12. Obvious intergranular corrosion was present at the internal SiC surface and was predominately co-located with IPyC cracks and a gap in the IPyC/SiC interface region. Large-scale Si-O precipitates were observed in open gaps created by buffer fracture and buffer/IPyC detachment. The large-scale Si-O precipitates had a heterogenous microstructure, with large sections of seemingly single-phase material vs. regions with a layered structure. Compositional analysis of these two structures indicated the single-phase material was SiO_2 and the layered structure contained more carbon and concentrations of zirconium and uranium (Figure 8-13).

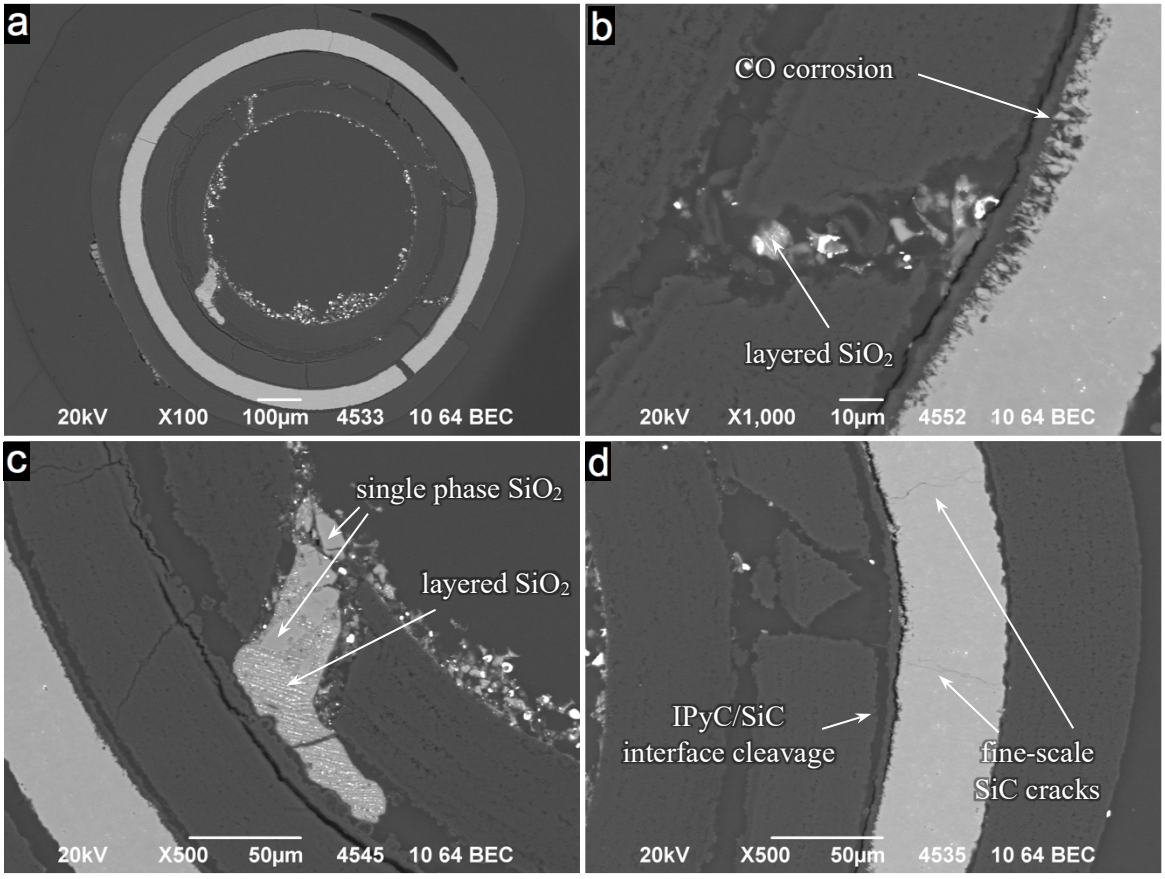

Figure 8-12. BEC images of regions of interest in Particle 332-SP01.

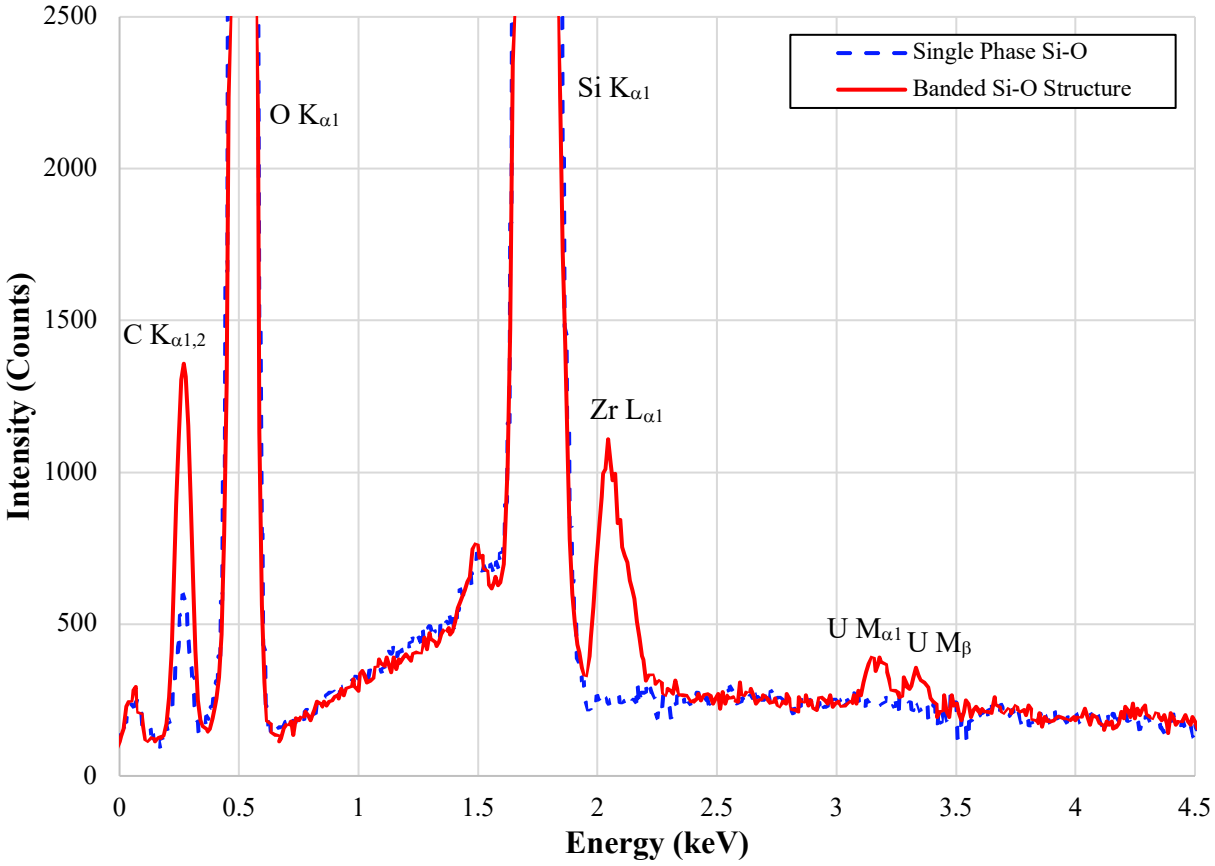

Figure 8-13. Representative EDS spectra of large-scale Si-O precipitate with layer structure in Particle 332-SP01 (Figure 8-12c).

The IPyC/SiC interface region in Particle 332-SP01 showed an obvious cleavage ~5–10 µm from the SiC boundary around nearly the entire revealed circumference of the particle (Figure 8-12 and Figure 8-14). It is possible that this cleavage was related to the banded porosity frequently observed in the IPyC/SiC interface regions of the AGR-2 UO_2 RS particles. This cleavage in the IPyC near the SiC boundary evidently elevated the level of general corrosion in the particle. Fine-scale and large-scale SiC cracks were observed in multiple locations, consistent with the XCT findings and possibly related to the elevated levels of corrosion in this particle.

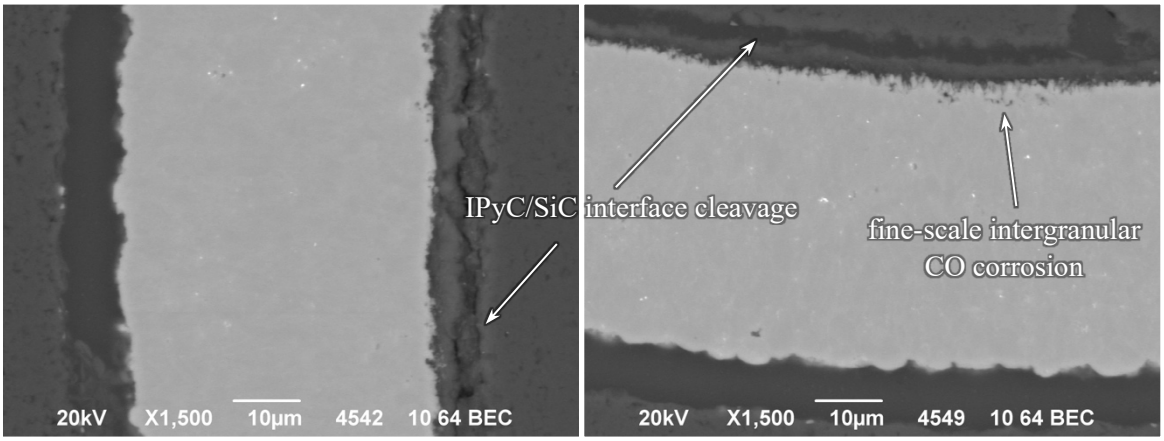

Figure 8-14. BEC images of IPyC/SiC layers in Particle 332-SP01.

Regardless of whether the IPyC/SiC interface was attached or detached, no obvious high-Z interface features were observed in the four Compact 3-3-2 special particles examined with the SEM, and there was a limited presence of high-Z boundary features. This was significantly different from what was observed in the Compact 3-3-2 RS particles (Figure 7-23–Figure 7-25). The apparent reduction of high-Z material in the IPyC/SiC interface region of these special particles was presumably related with the SiC failure and/or subsequent leaching during DLBL. Some of the high-Z material in the IPyC/SiC interface region may have diffused out after SiC failure, while the particles were still at 1,600°C. It is also plausible that this high-Z material was removed with most of the kernel material during leaching. Fine-scale, high-Z SiC features were still present across the entire SiC layer thickness, and these features were very similar to those found in the RS particles, both in population and composition (predominately Pd-only). There were no indications of additional concentrations of high-Z SiC features surrounding the corroded SiC regions. This was in dramatic contrast to what was observed in AGR-1 and AGR-2 UCO TRISO particles with failed SiC (Hunn et al. 2014a; Hunn et al. 2018a). Figure 8-15 shows how palladium and uranium typically piled up in the degraded SiC region of UCO TRISO particles. The absence of these high-Z SiC features in UO_2 TRISO particles with failed SiC provided further evidence that the SiC failed via a different mechanism.

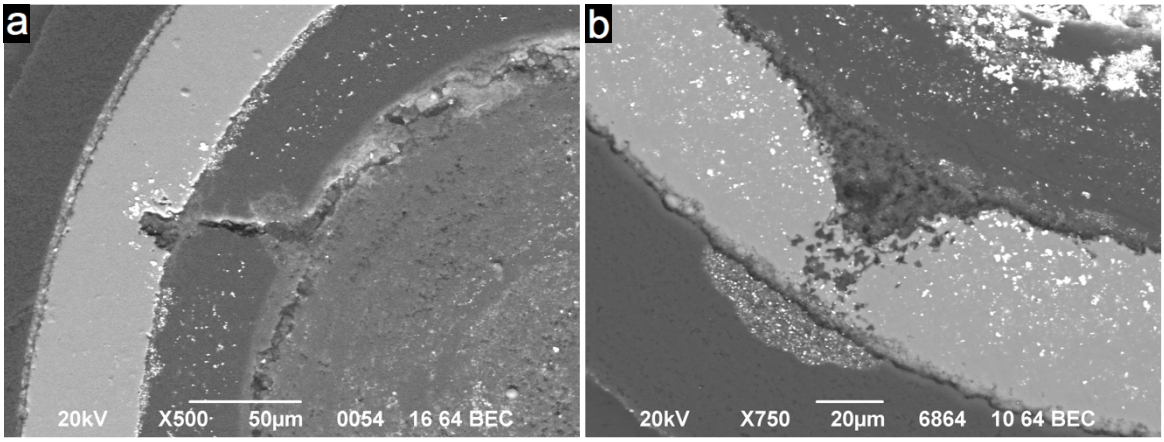

Figure 8-15. BEC images of SiC degradation in UCO TRISO particles from (a) AGR-1 Compact 3-3-1 after 1,700°C safety testing and (b) AGR-2 Compact 5-4-1 after 1,800°C safety testing.

8.3 1,600°C SAFETY-TESTED COMPACT 3-4-2 SPECIAL PARTICLES

Table 8-1 lists the four special particles from Compact 3-4-2 subjected to SEM analysis. Schedule and budget did not support analysis of every special particle from Compact 3-4-2. Particle 342-SP01 was chosen for further analysis to represent the four particles from Compact 3-4-2 with failed SiC and leached kernels. The behavior of these four particles was expected to duplicate the four leached special particles from Compact 3-3-2. Particle 342-SP01 had low ^{144}Ce and ^{154}Eu activities (Table 8-1), like all special particles discussed up to this point whose kernels were leached during DLBL. As discussed in Section 8.1 with regard to Particle 312-SP02, minor retention of ^{134}Cs and ^{137}Cs in Particle 342-SP01 suggested some of the cesium was sequestered in the pyrocarbon layers, and relatively high retained ^{106}Ru and ^{125}Sb inventories indicated they were present in compounds with lower acid solubility.

The XCT imaging of Particle 342-SP01 showed all the typical features associated with localized corrosion (Figure 5-34); namely, IPyC fracture related to incomplete buffer/IPyC detachment and degradation of the SiC layer where it was exposed by the IPyC crack. There were two separate localized regions in Particle 342-SP01 where the SiC was extensively degraded. However, neither of these regions appeared to penetrate the layer, whereas the corrosion sites in Particles 332-SP02, 332-SP03, and 332-SP04 went all the way through the SiC layers. The XCT imaging of Particle 342-SP01 revealed an extended crack in the SiC that was associated with one of the localized corroded SiC regions. Figure 8-16 shows several BEC images of regions of interest in Particle 342-SP01. The targeted cross sectioning for

SEM analysis successfully revealed all the key features related to the SiC failure. As expected, there was a broad arc of corrosion in the SiC that extended about halfway through the layer, and a crack provided a pathway through the outer half of the SiC layer. Figure 8-16d shows that there was evidence that CO corrosion had occurred along the SiC fracture surface, which indicated that the crack formed during the safety test. The crack through the SiC shown in Figure 8-16e was part of the same crack shown in Figure 8-16d. This crack extended around half the circumference of the particle, as revealed by the XCT imaging (Figure 5-35). There was a crack in the OPyC visible in the particle cross section that was not directly associated with the SiC crack Figure 8-16f. This crack presumably formed during the pre-IMGA DLBL process, given the lack of ^{85}Kr release during safety testing (Table 3-2) and the onset of uranium leaching after deconsolidation of the compact (Table 4-1).

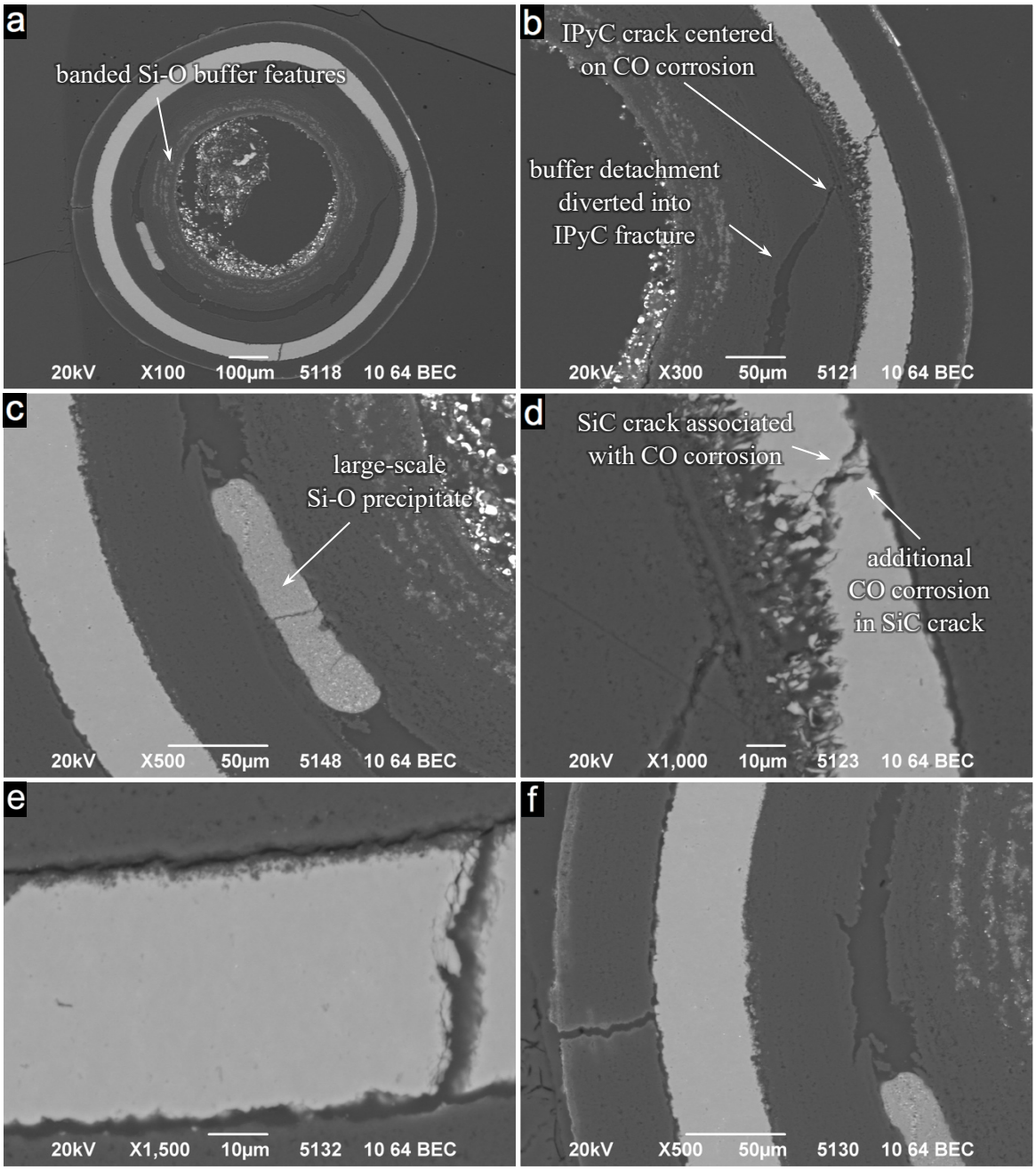

Figure 8-16. BEC images of regions of interest in Particle 342-SP01.

As with the Compact 3-3-2 special particles discussed in Section 8.2, reaction products from the CO corrosion in Particle 342-SP01 were observed away from the corroded SiC region in the form of a large-scale Si-O precipitate in the buffer/IPyC gap and banded Si-O buffer features. The composition of the large-scale Si-O precipitate was similar to that shown in Figure 8-13 for the layered Si-O precipitate structure, in which low intensities of zirconium were present in addition to the SiO_2. The compositions of the diffuse buffer features were similar to those shown in Figure 8-8, with the exception that the signal from molybdenum was of similar intensity to the zirconium and barium, while uranium and cesium were at trace levels relative to the reference buffer like they were in the Particle 332-SP02 analysis.

Figure 8-17 shows example regions of the Particle 342-SP01 IPyC/SiC interface away from the localized corrosion sites, with both connected and detached regions represented. Similar to Particles 332-SP02, 332-SP03, and 332-SP04, there were clear indications of general CO corrosion where there was a gap at the IPyC/SiC interface. There were indications of possible corrosion in regions with no IPyC/SiC gap in the form of what appeared to be fine-scale, intergranular lines of corrosion extending inward from the SiC boundary. These features were similar to the features observed in some locations where the IPyC/SiC interface was detached in Particles 332-SP01 and 332-SP03 (Figure 8-11).

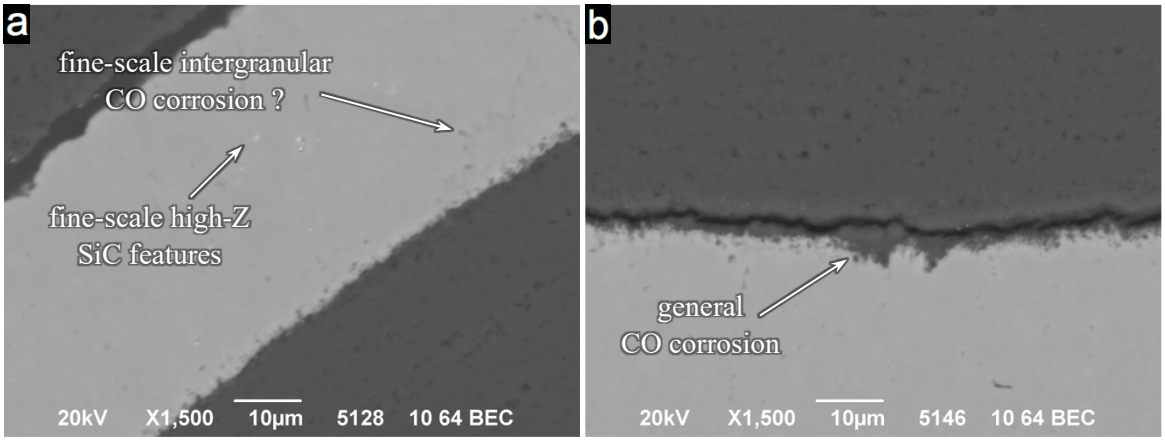

Figure 8-17. BEC images of IPyC/SiC interface region of Particle 342-SP01 showing representative areas with either (a) a connected interface or (b) a detached interface.

Similar to the Compact 3-3-2 particles with failed SiC, Particle 342-SP01 had faint high-Z SiC features, but no high-Z boundary or high-Z interface features were observed. As discussed in Section 8.2, the lack of high-Z boundary and high-Z interface features suggested that high-Z material either diffused out after SiC failure, while the particles were still at 1,600°C, or was removed by the nitric acid during DLBL.

Figure 8-18 shows several regions of interest in Particle 342-SP06. The partial kernel leaching indicated by the XCT imaging (Figure 5-39) was clearly revealed in Figure 8-18a. There were significant gaps at the IPyC/SiC and SiC/OPyC interfaces and a large through-layer SiC crack (Figure 8-18d). Much of the regions in and around the through-layer SiC crack were filled with epoxy, which showed a typical cracked and mottled texture after carbon coating. There were Si-O precipitates in the interface gaps scattered throughout the particle, some appeared as isolated round volumes not spanning the width of the gap (Figure 8-18c), while others spanned the gap and were elongated along its length (Figure 8-18b). The formation of round SiO_2 precipitates was not unexpected where their formation was not constrained by the available open volume. High-Z material was distributed throughout the buffer (Figure 8-18b and Figure 8-18c). The intensity was greater than any high-Z material observed in the buffer layer of the RS particles (Section 7) or in the buffer layer of Compact 3-3-2 particles with localized corroded SiC (Section 8.2). Compositional analysis of this high-Z material showed it to be predominantly uranium, with limited contributions from other radionuclide elements. An EDS map is presented in Figure 8-19. Less obvious diffuse, banded IPyC features (Figure 8-18b) were also predominantly uranium. The Si-O precipitates were illuminated in the EDS maps of silicon and oxygen.

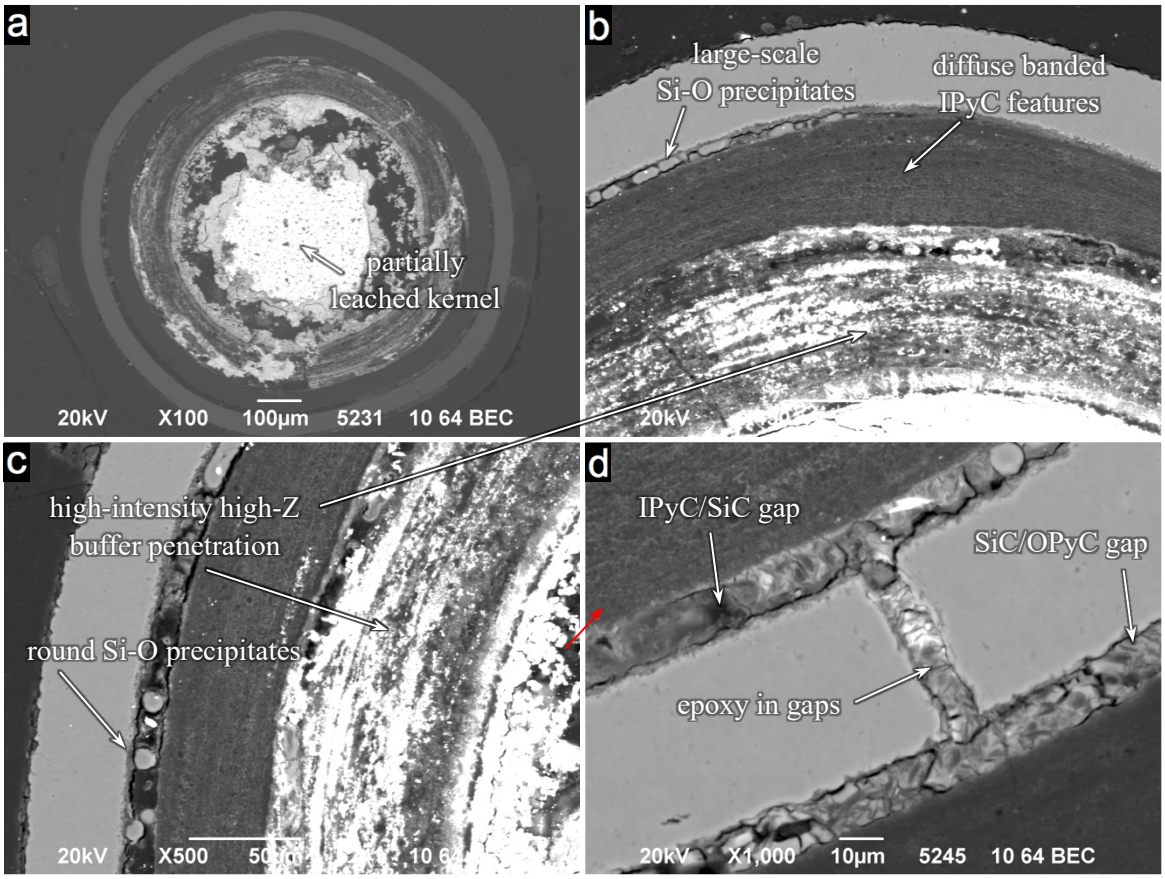

Figure 8-18. BEC images of regions of interest in Particle 342-SP06.

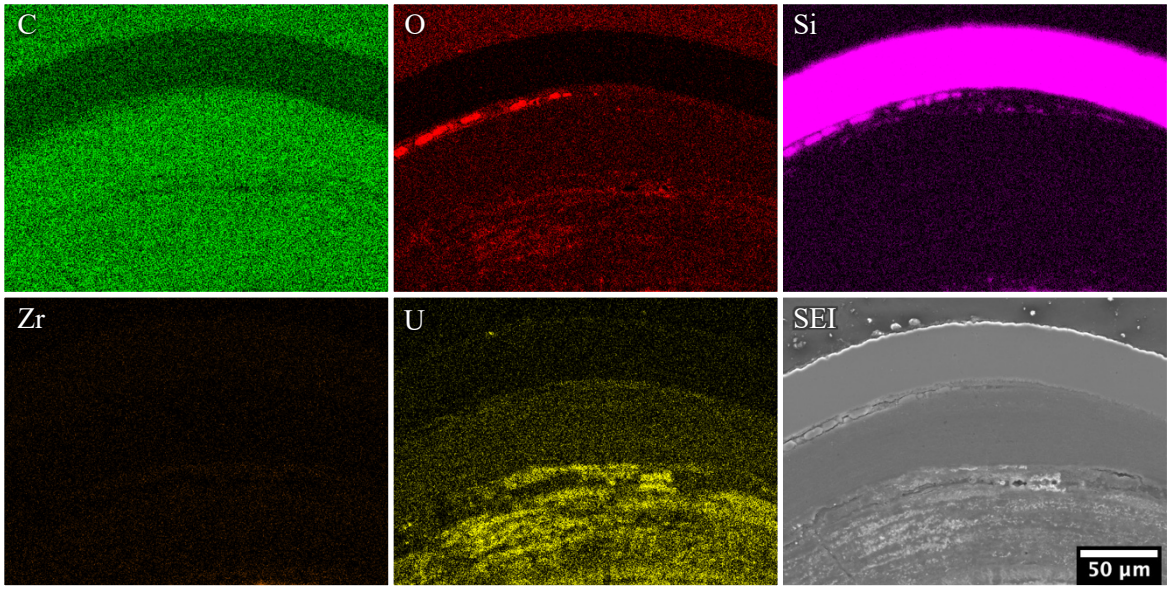

Figure 8-19. EDS maps showing uranium dispersion in buffer region and large-scale Si-O precipitates in IPyC/SiC gap (intensity is relative to counts above background).

General corrosion around the inside surface of the SiC layer was observed, which was not unsurprising as a gap was present around most of the circumference of the IPyC/SiC interface region. The extent of the general corrosion observed in the polished cross-section of Particle 342-SP06 was limited compared to the Compact 3-3-2 particles with localized CO corrosion (Section 8.2). The corrosion was typified by

linear features at the inner SiC surface, many of which were fine-scale (Figure 8-20). Similar fine-scale, intergranular corrosion was seen in Particle 332-SP03 (Figure 8-11), Particle 332-SP01 (Figure 8-14) and Particle 342-SP01 (Figure 8-17), though the general corrosion was limited in Particle 342-SP06 relative to these other particles. The presence of SiC corrosion was unambiguously confirmed by the large-scale Si-O precipitates in the IPyC/SiC gap (Figure 8-19). A few high-Z boundary and high-Z interface features were observed in the Particle 342-SP06 cross section, but no obvious high-Z SiC features were revealed.

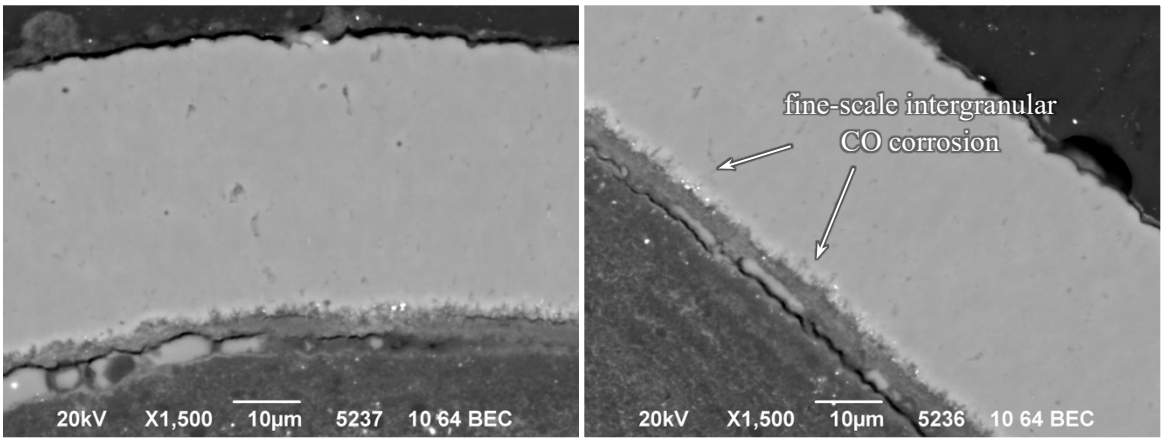

Figure 8-20. BEC images of IPyC/SiC layers in Particle 342-SP06.

Images of Particle 342-SP07 are shown in Figure 8-21 and Figure 8-22. A dense buffer region was observed adjacent to the kernel, which was not significantly different from the more intensive examples of this feature observed in the RS particles for Compact 3-4-2 (Figure 7-35 and Figure 7-38). However, an above-average amount of high-Z material was distributed throughout the buffer that was not observed in the RS particles and was similar to, but less intense than, what was observed in Particle 342-SP06 (Figure 8-18). This high-Z material was distributed in banded features that were likely related to the porosity. High-Z material was also piled up in the buffer/IPyC gap and decorating the tears in the IPyC. Compositional analysis (Figure 8-23) showed this material to be uranium-rich with a balance of carbon and oxygen, similar to what was observed for Particle 342-SP06 (Figure 8-19). As discussed in Section 5.5, Particle 342-SP07 had a gap at the IPyC/SiC interface that extended around most, if not all of the particle. The IPyC/SiC gap was populated by numerous Si-O precipitates that EDS analysis confirmed to be SiO_2 (Figure 8-23).

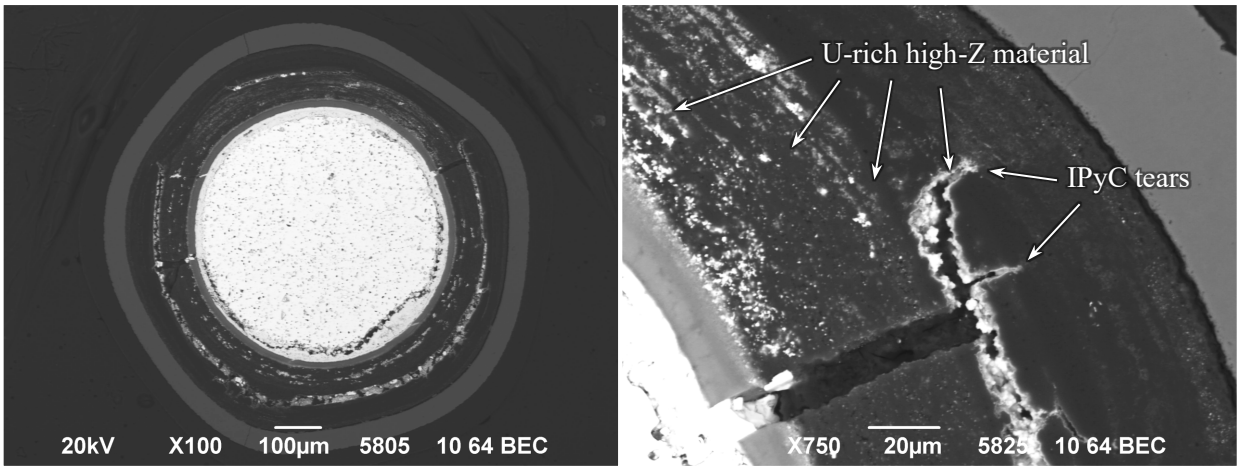

Figure 8-21. BEC images of regions of interest in Particle 342-SP07.

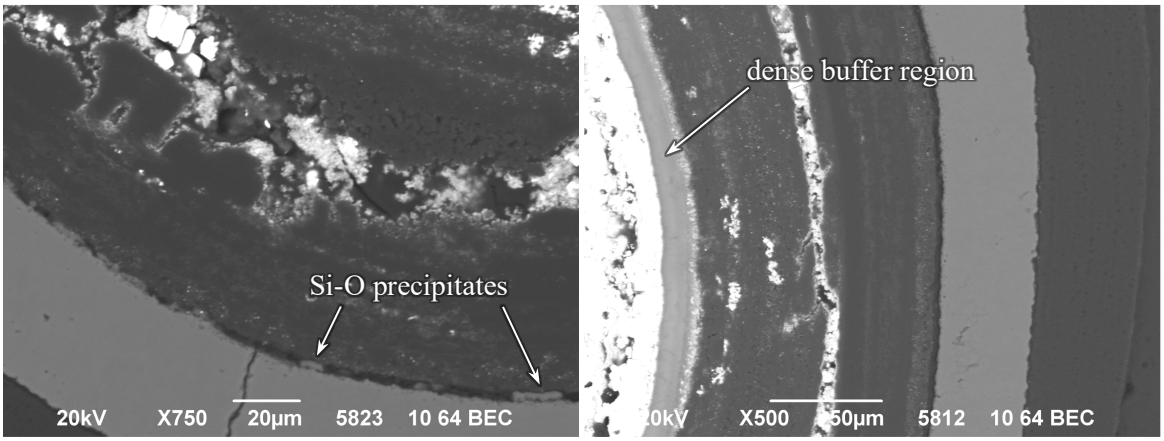

Figure 8-22. BEC images of regions of interest in Particle 342-SP07.

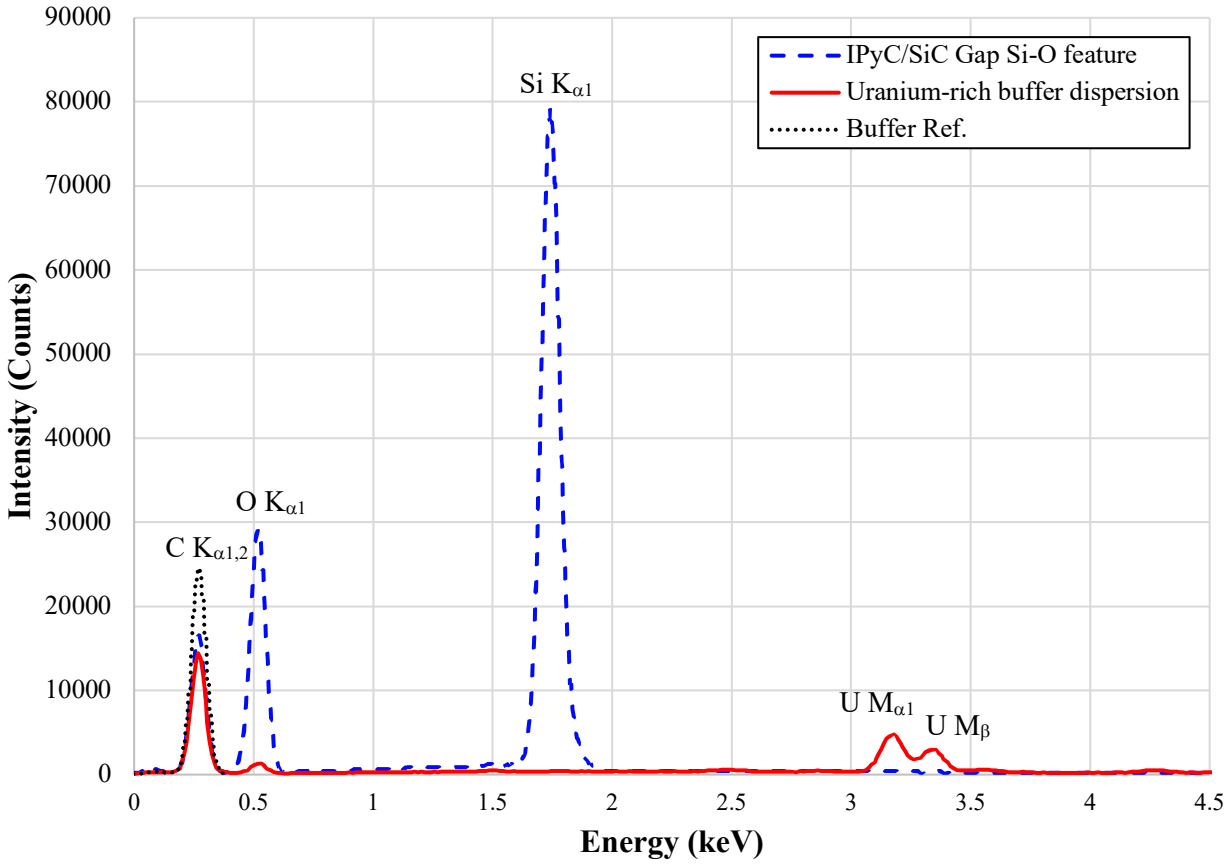

Figure 8-23 Representative EDS spectra of large-scale Si-O precipitates in the IPyC/SiC gap and uranium-rich buffer features.

Figure 8-24 shows BEC images of the Particle 342-SP07 SiC and IPyC/SiC interface region acquired with higher magnification. The CO corrosion of the inner SiC surface was not as obvious as Particle 342-SP06 (Figure 8-20) and difficult to differentiate from PyC inclusions observed in RS particles. However, the Si-O precipitates in the IPyC/SiC gap confirmed that CO corrosion had occurred. Fine-scale SiC cracks or intergranular lines of corrosion were present in the particle, and appeared to extend across the thickness of the SiC layer, which possibly explained the cesium loss and uranium dispersion in this particle. No high-Z SiC features were noted; however, both high-Z boundary and high-Z interface features were readily observed along with diffuse banded high-Z IPyC features. The compositions of these features were identical to those in the Compact 3-4-2 RS particles (i.e., Pd-Rh and Pd-Rh-Ru).

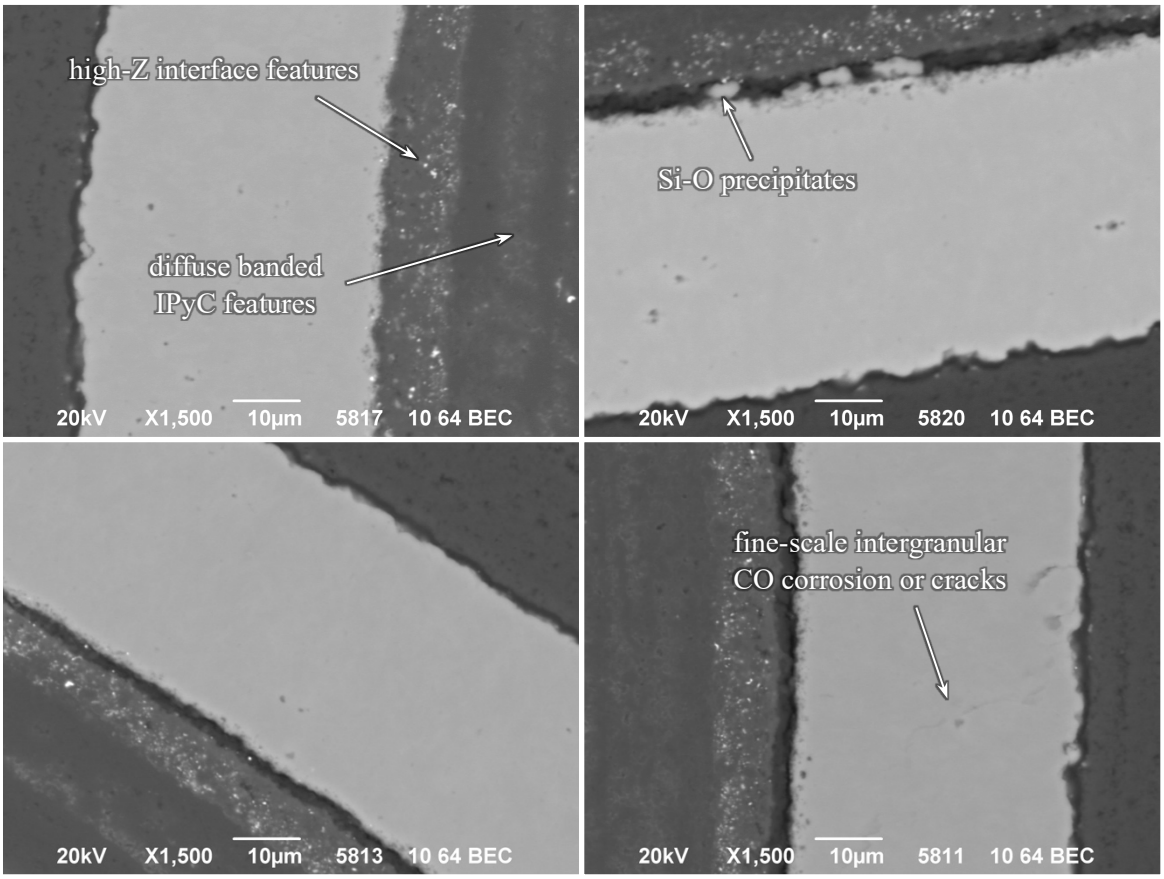

Figure 8-24. BEC images of IPyC and SiC layers from Particle 342-SP07.

As discussed in Section 5.5, the analysis of Particle 342-SP09 revealed it was slightly under-sized, which could account for its 10–18% below average M/A values for ^{106}Ru, ^{125}Sb, ^{144}Ce, and ^{154}Eu (Table 8-1). There was no obvious defective or degraded region visible in the SiC layer to explain the apparent preferential loss of cesium (Figure 5-41). However, there was a through-layer fracture in the IPyC and a gap in the IPyC/SiC interface region surrounding this fracture, which can be precursors to SiC failure. Figure 8-25 shows the IPyC fracture, although it does not cross the entire layer in this plane of observation. The gap at the IPyC/SiC interface had a slight arch centered on the IPyC fracture that suggested advanced corrosion was beginning to thin the SiC.

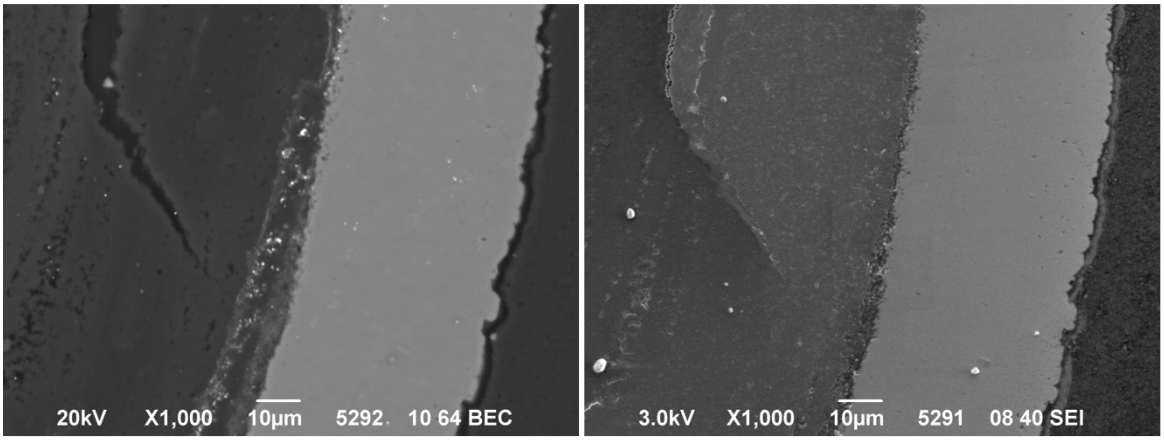

Figure 8-25. BEC/SEI image pair showing IPyC crack and possibly corroded SiC in Particle 342-SP09.

Particle 342-SP09 displayed all features typical of a Compact 3-4-2 RS particle, namely, high-Z SiC, high-Z boundary, high-Z interface, and high-Z IPyC features. Examples of these features are shown in Figure 8-26. The compositions of all identified feature types were identical to the Compact 3-4-2 RS particles, with predominantly Pd-only high-Z SiC features and Pd-Rh or Pd-Rh-Ru high-Z boundary and high-Z interface features.

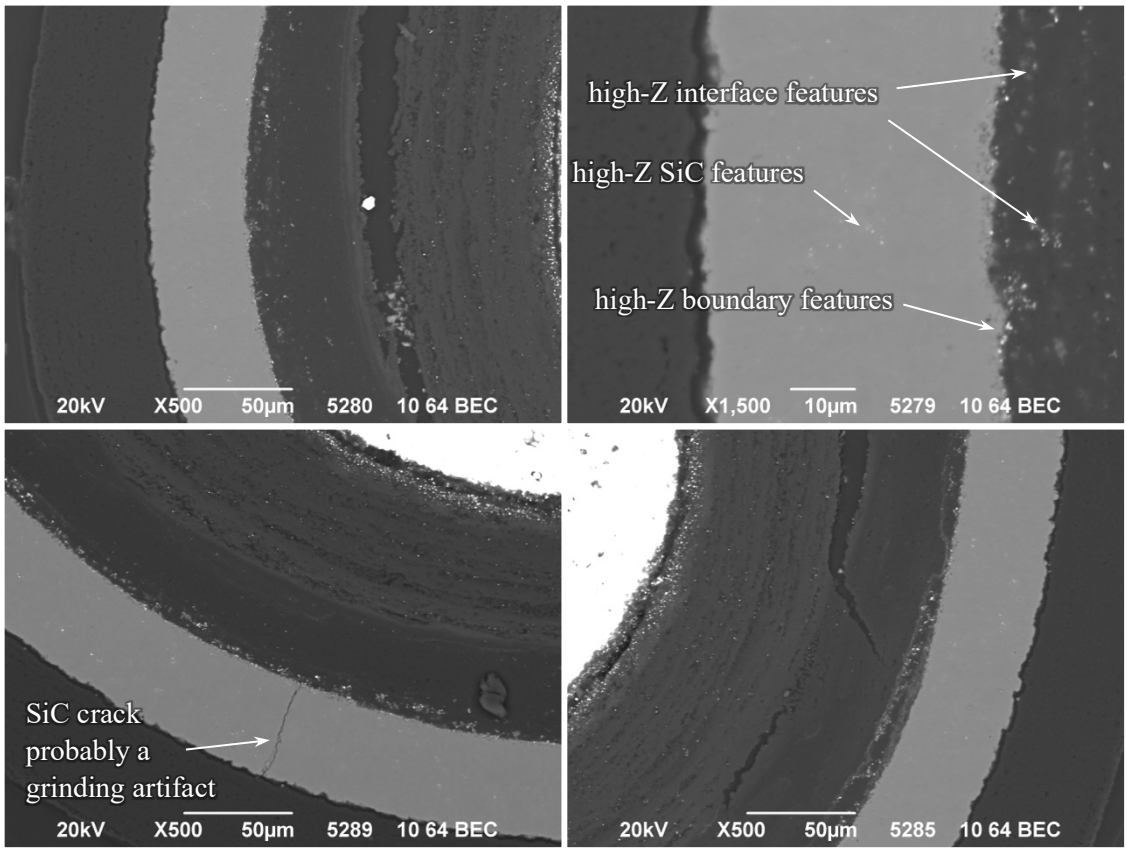

Figure 8-26. BEC images of regions of interest in Particle 342-SP09.

Cracks across the SiC layer were observed in two regions (Figure 8-27). The larger crack in the SiC was not visible in the XCT imaging and was probably a grinding artifact. The fine-scale crack would not have been visible with XCT. However, there was also no indication that these features were present during irradiation or safety testing as there were not clear indications of high-Z material within the cracks or depletion at the IPyC/SiC interface of mobile high-Z material near the crack.

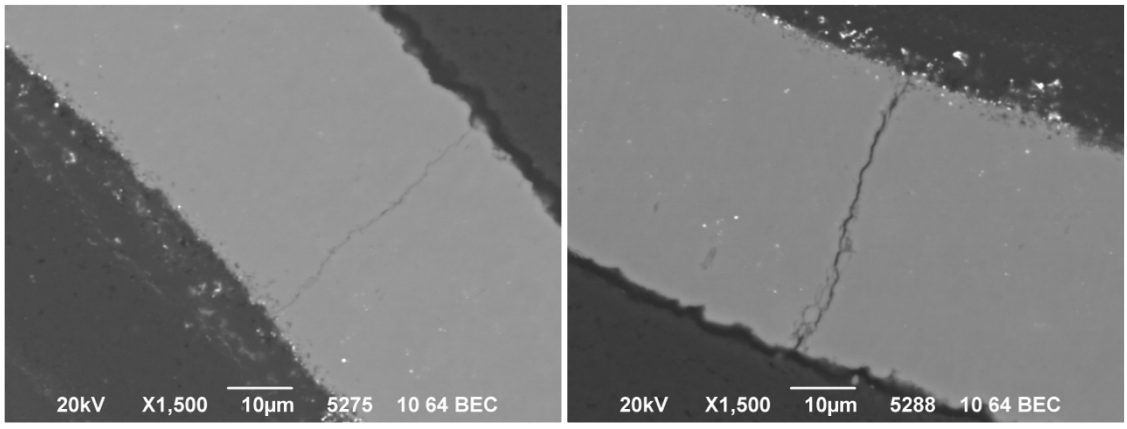

Figure 8-27. BEC images of IPyC/SiC layers from Particle 342-SP09.

As discussed in Section 5.5, Particles 342-SP10 and 342-SP14 had low europium activities, in addition to indications of significantly below-average retained inventories of cesium, silver, and cerium. Both particles had significant dispersion of uranium in the buffer (especially in Particle 342-SP10) and uranium deposits in gaps between the IPyC and SiC layers (Figure 8-28 and Figure 8-29). The familiar IPyC fracture at the boundary of buffer detachment was observed in Particle 342-SP10, and the IPyC crack was filled with uranium-rich material (Figure 8-28c). IPyC fracture was not clearly observed in Particle 342-SP14, although unusually low resolution in the XCT image data limited the reliability of the inspection. There were no obvious localized sites of through-layer CO corrosion of the SiC, but the presence of significant corrosion was indicated by numerous Si-O precipitates throughout both particles. Round SiO_2 precipitates, like those observed in Particle 342-SP06 (Figure 8-18), were observed in a wide IPyC/SiC gap in Particle 342-SP10 (Figure 8-28d). Large-scale Si-O precipitates resided in the buffer/IPyC gap of Particle 342-SP14 (Figure 8-29). While no obvious pathway through the SiC layer could be found, it was clear that the abnormal structures in these particles were not coincidental or unrelated to their abnormal fission product retention.

Banded high-Z features in the buffer and IPyC, and most high-Z interface features were predominantly uranium, with a balance of carbon and oxygen, and minor components of zirconium and molybdenum in some features. Some high-Z interface features contained the Pd-Rh-Ru compositions typically seen in Compact 3-4-2 RS particles, as well as many special particles. A few Pd-only high-Z SiC features were observed in Particle 342-SP10. There appeared to be some infiltration of uranium in the SiC layer immediately adjacent to where the uranium-rich deposits were in contact with the SiC boundary. Although smearing of the heavy deposits at the boundary may have occurred during polishing, the linear appearance of this infiltration evident in Figure 8-29e suggests it was related to intergranular corrosion.

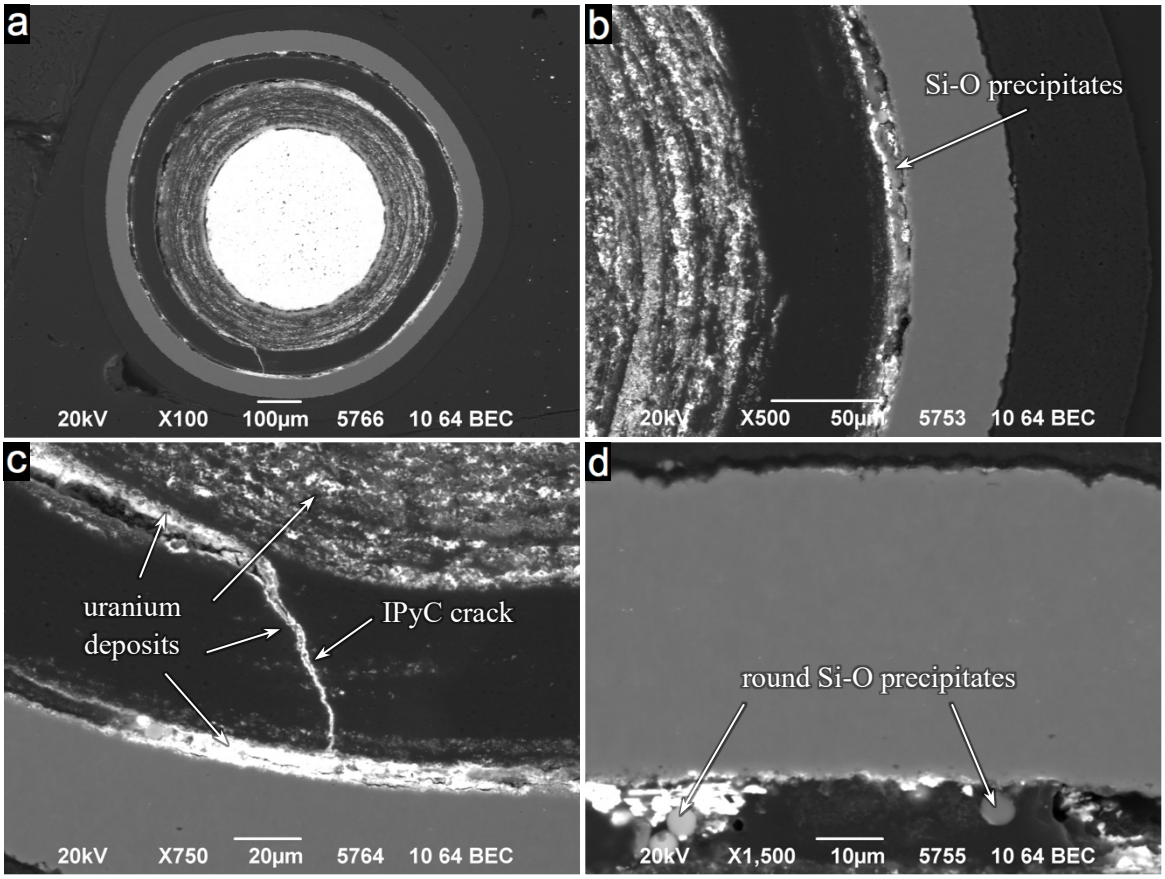

Figure 8-28. BEC images of regions of interest in Particle 342-SP10.

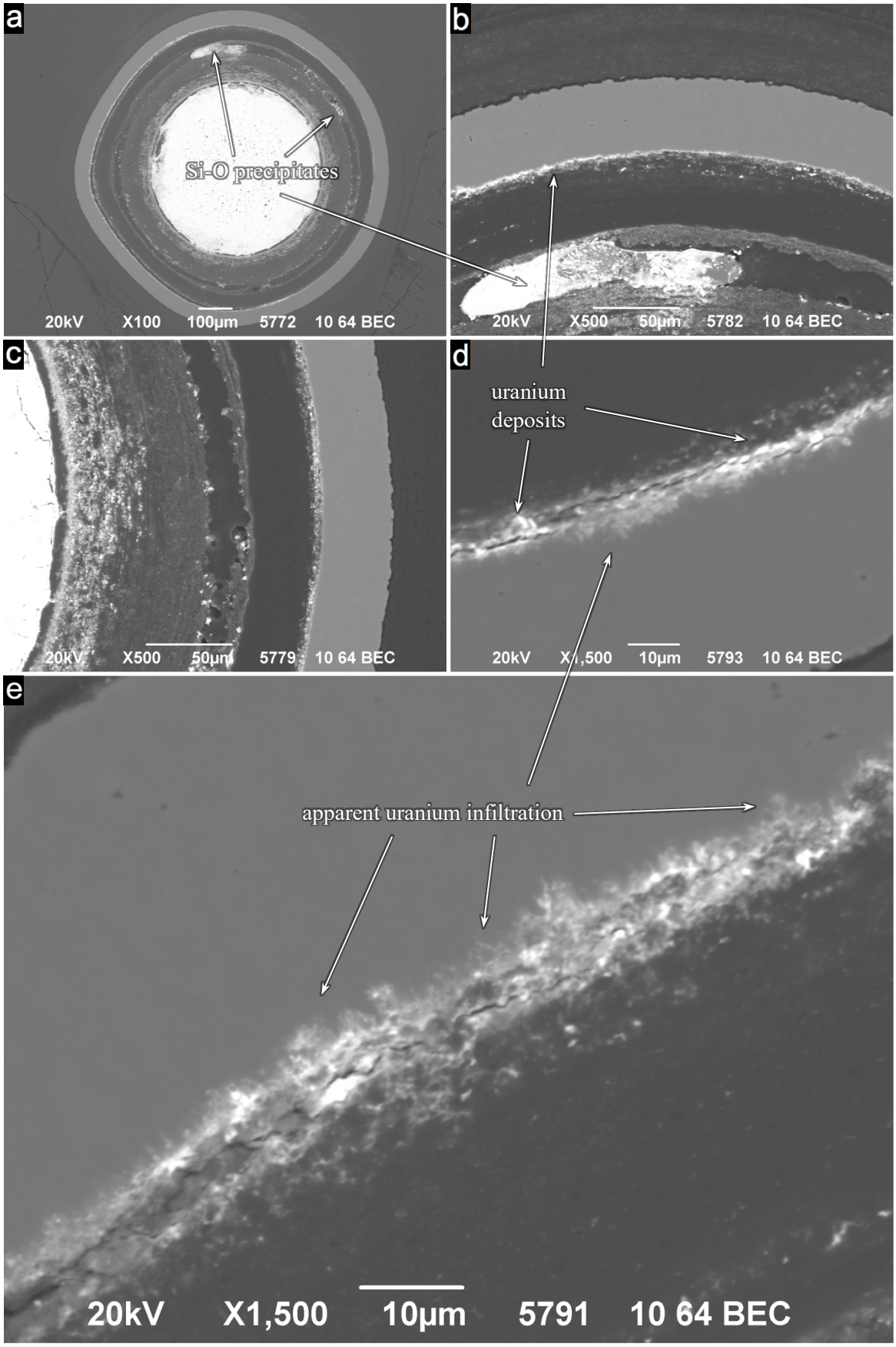

Figure 8-29. BEC images of regions of interest in Particle 342-SP14.

8.4 1,700°C SAFETY-TESTED COMPACT 3-4-1 SPECIAL PARTICLES

Three special particles from Compact 3-4-1 (Table 8-1) were subjected to comprehensive SEM analysis to support the understanding of the observed particle failures discussed in Section 5.6. Images of Particle 341-SP01 are shown in Figure 8-30. The XCT imaging revealed that Particle 341-SP01 had an unusual buffer morphology, in which it remained attached to the IPyC. Typical features associated with CO corrosion were immediately identified in the SEM. These features included intragranular corrosion and large Si-O precipitates in the gap between the buffer/IPyC fragments, which had fractured as a unit as discussed in Section 5.6. The SiO_2 composition of these precipitates was confirmed by EDS, and their sizes were larger than other CO corroded particles, which suggested more extensive corrosion of the SiC layer. General corrosion was observed around the exposed inner surface of the SiC, as well as more pronounced locally corroded regions. Fine-scale high-Z SiC features were observed throughout the SiC layer.

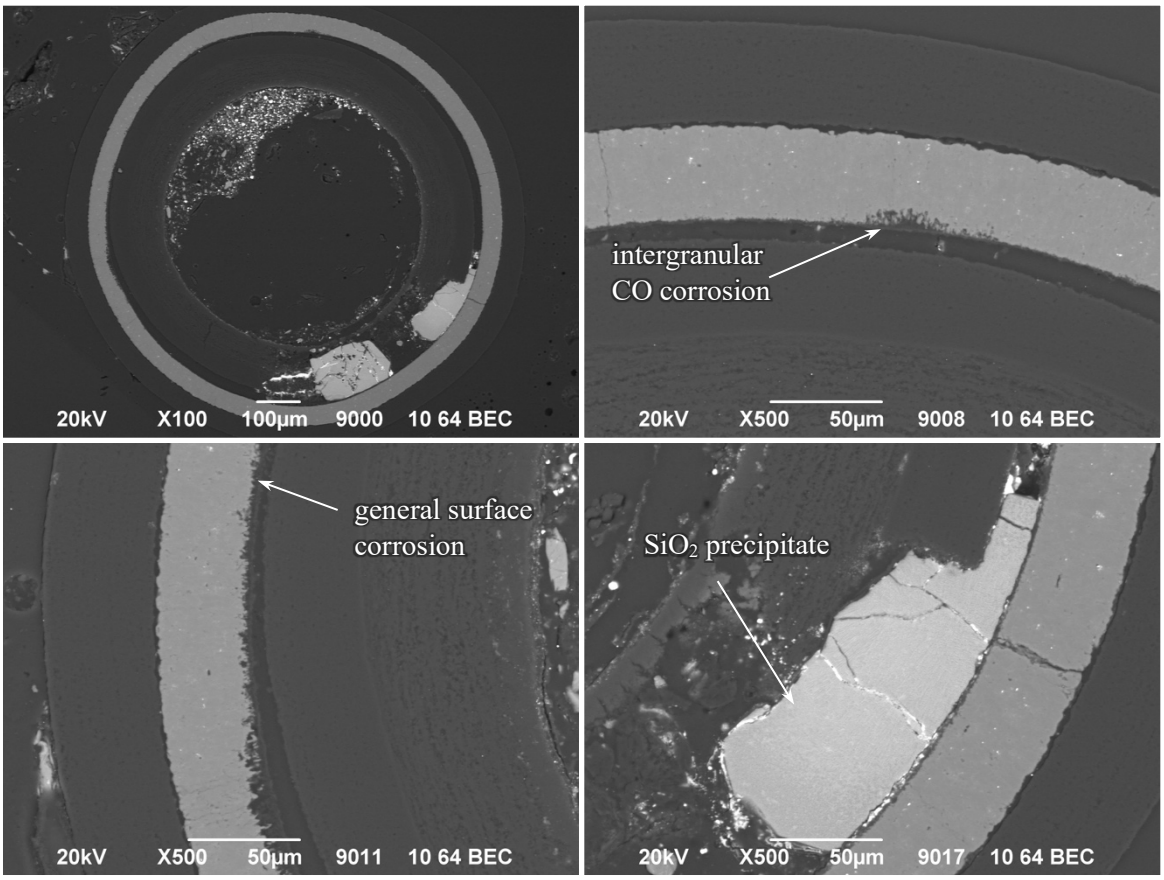

Figure 8-30. BEC images of regions of interest in Particle 341-SP01 showing evidence of SiC corrosion.

Figure 8-31 shows BEC/SEI image pairs of the corroded SiC in Particle 341-SP01. More low-Z inclusions were observed in the internal regions of the SiC layer than in sister Compact 3-4-2 particles. These low-Z inclusions were analyzed by EDS, which suggested they were carbon rich, although like the low-Z inclusions observed in all other particles, EDS analysis was uncertain for low-Z elements such as carbon and oxygen. The predominance of these low-Z inclusions in Particle 341-SP01 was consistent with the overall more advanced state of corrosion in this particle. Figure 8-31 also shows fine-scale, intergranular lines of corrosion extended across the thickness of the SiC, starting from the heavily corroded area. These features were similar to those observed on a smaller scale in 1,600°C special particles. The preferential location adjacent to the localized corrosion suggested they were related to the intragranular corrosion mechanism.

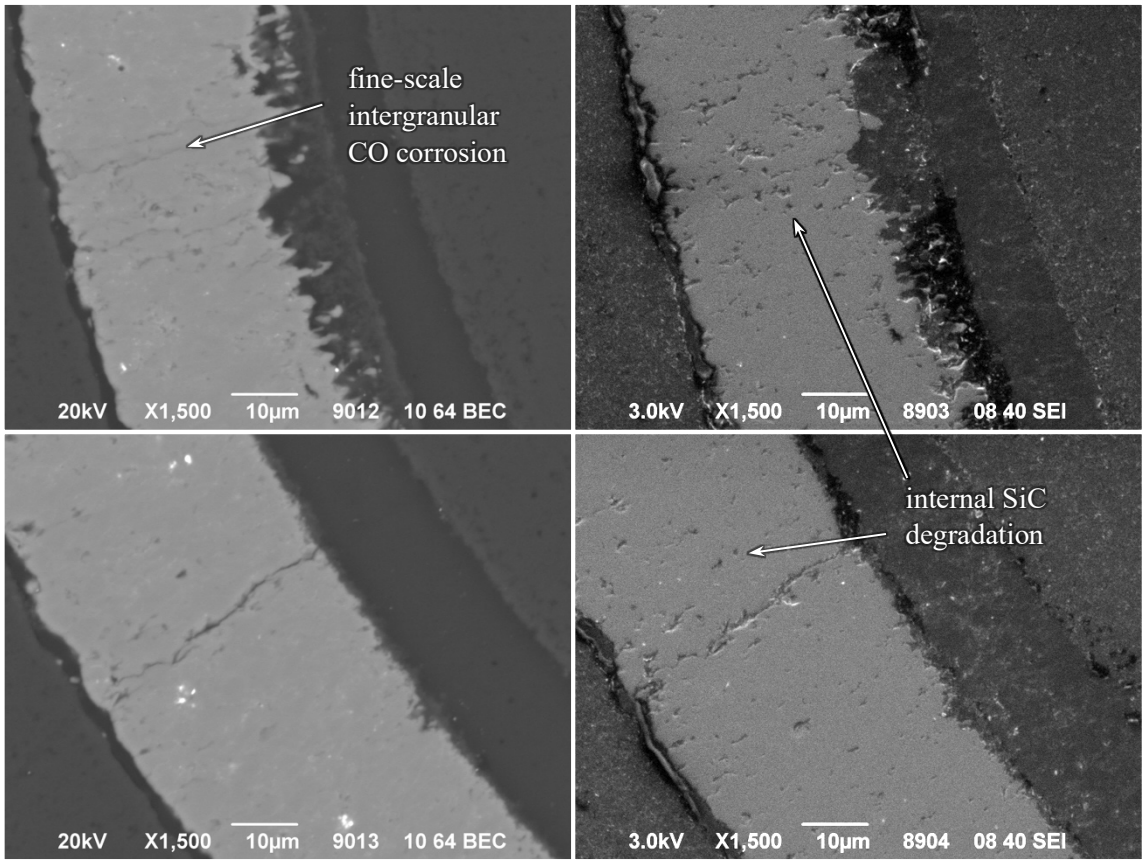

Figure 8-31. BEC/SEI image pairs of relevant IPyC/SiC layer features in Particle 341-SP01 highlighting SiC corrosion and degradation.

The high-Z SiC features in Particle 341-SP01, such as those visible in Figure 8-32, were more intense and more frequent than those observed in Particle 341-RS21, which was the Compact 3-4-1 RS particle observed to have the greatest degree of high-Z SiC features (Figure 7-44). Compositional analysis of the high-Z SiC features in Particle 341-SP01 showed the features were exclusively uranium-rich with trace cerium and neodymium. Representative spectra for a uranium-rich high-Z SiC feature and a SiC reference area are shown in Figure 8-33. The uranium-rich features were unique to this particle, as all other RS particles from Compact 3-4-1 showed palladium-rich features in the SiC layer. The presence of near exclusive uranium-rich features in the SiC layer, with significant internal SiC degradation was observed previously for UCO TRISO particles exposed to 1,800°C for 650 h (Gerczak et al. 2020a).

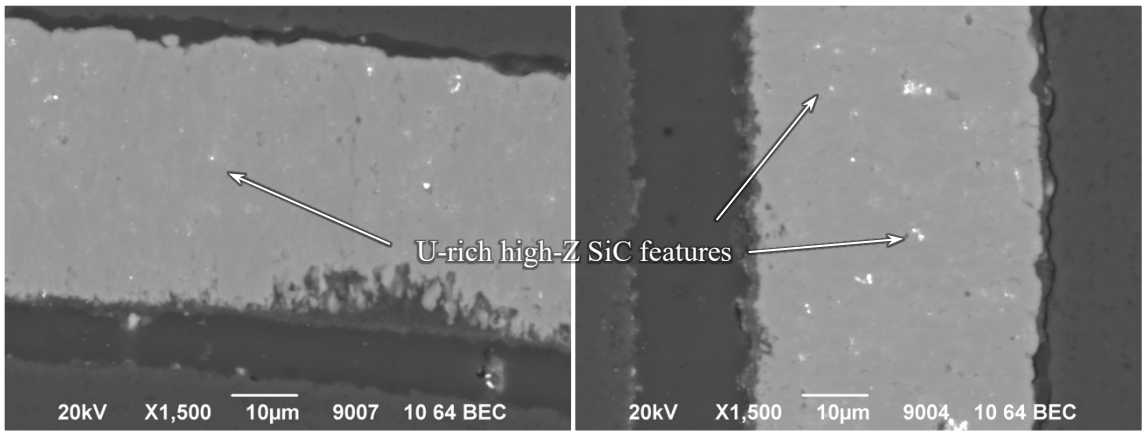

Figure 8-32. BEC/SEI image pair showing high-Z SiC features in Particle 341-SP01.

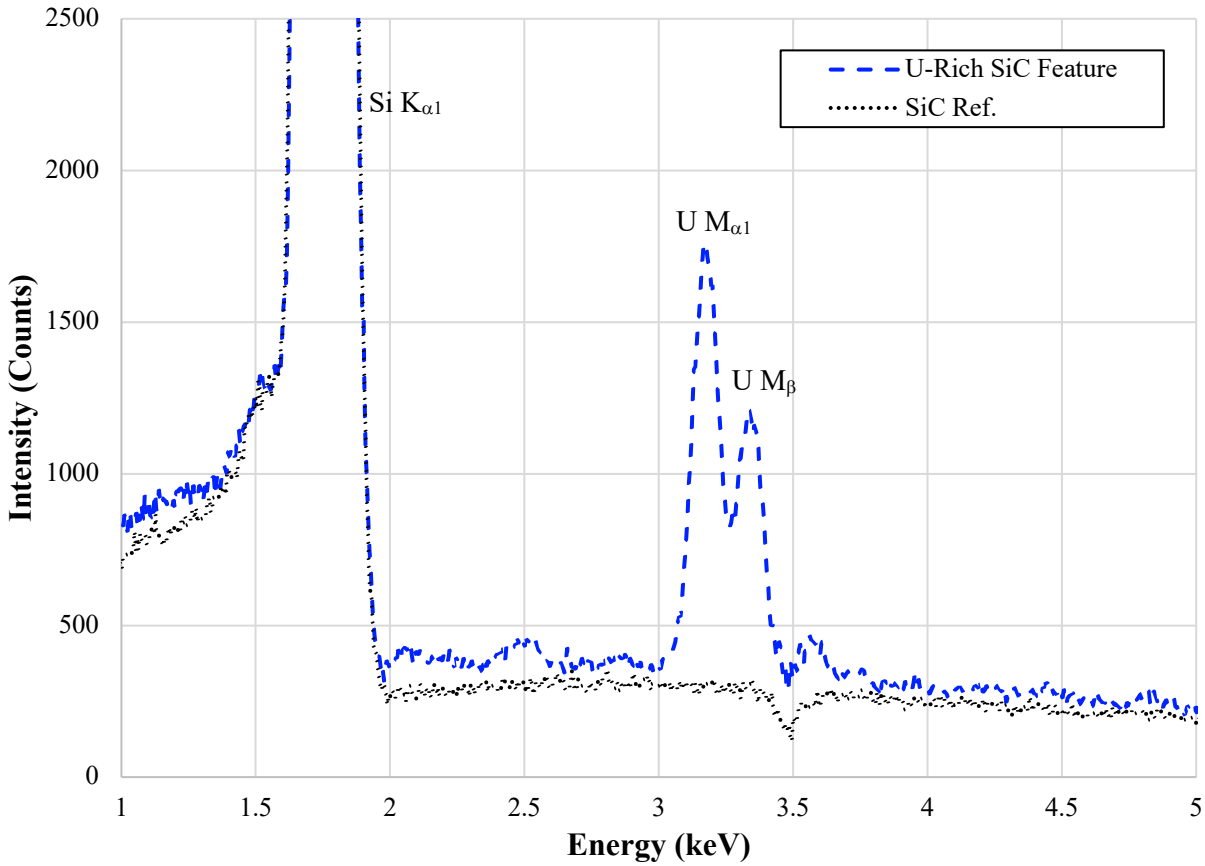

Figure 8-33. Representative EDS spectra of uranium-rich high-Z SiC features in Particle 341-SP01.

Images of Particle 341-SP03 are shown Figure 8-34 and Figure 8-35. Typical features associated with localized CO corrosion were identified, namely, an IPyC/SiC crack exposing the SiC and subsequent intragranular corrosion. Unlike Particle 341-SP01, no large-scale SiO_2 precipitates were identified. However, as seen in the XCT images (Figure 5-48 and Figure 5-49), significant high-Z features were observed dispersed in the buffer and IPyC layers, as well as heavy accumulations in the gaps. The kernel had been partially eroded, as suggested by the XCT. The intensity of the high-Z features in the buffer and IPyC layers varied, with some regions showing more diffuse features and some regions having relatively more intense features. Unlike all other particles with locally corroded SiC, high-Z material was also observed in the SiC cracks and the locally corroded region of Particle 341-SP03.

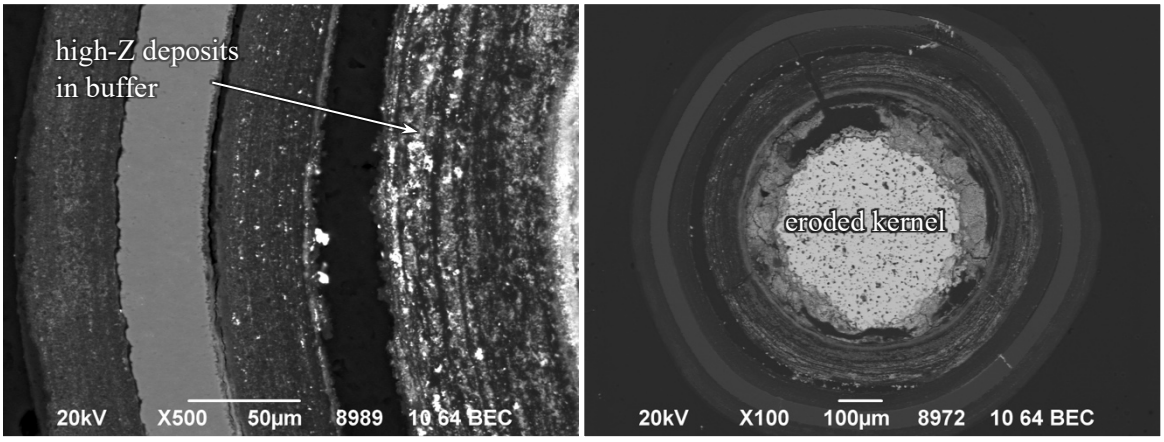

Figure 8-34. BEC images of regions of interest in Particle 341-SP03 highlighting the eroded kernel and high-Z features in the buffer and IPyC.

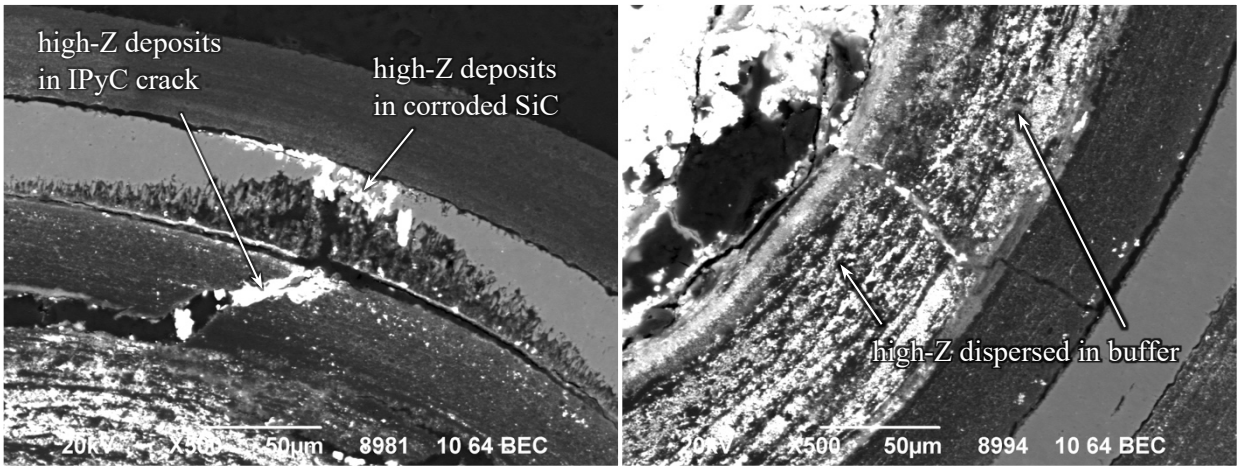

Figure 8-35. BEC images of regions of interest in Particle 341-SP03 highlighting localized CO corrosion and high-Z features in the buffer, IPyC, and SiC.

An EDS map of the locally corroded SiC region is shown in Figure 8-36. The map shows the high-Z material in the corroded region was primarily uranium. Similar uranium-rich compositions were observed in the SiC layer crack. The EDS map also shows uranium-rich deposits in the IPyC crack. These deposits had slightly different compositions from those in the SiC, in which low intensities of molybdenum were also present. The EDS map shows the high-Z material dispersed in the buffer was predominantly uranium, with some U-Si compositions in buffer regions closer to the kernel.

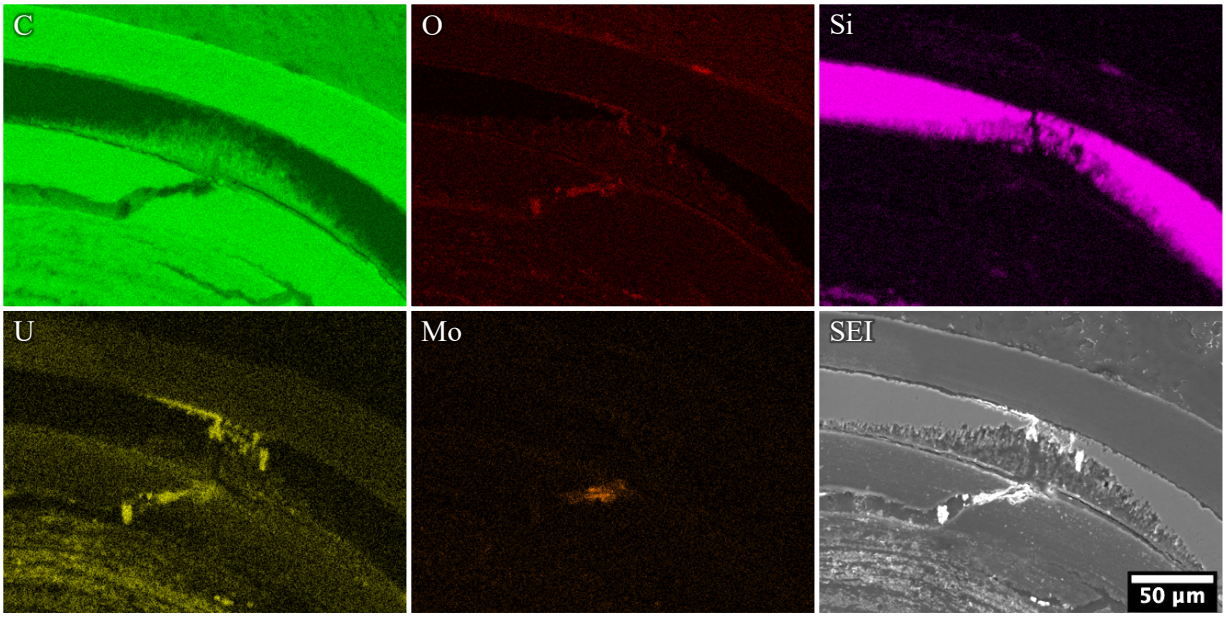

Figure 8-36. EDS maps of localized corroded SiC region with uranium-rich features in all layers.

Figure 8-37 shows BEC/SEI image pairs of select areas of Particle 341-SP03. Like Particle 341-SP01, more low-Z inclusions were observed in the internal regions of the SiC layer than in sister Compact 3-4-2 particles, and these low-Z inclusions were carbon rich. Particle 341-SP03 had fewer high-Z SiC features than Particle 341-SP01, but they had uranium-rich compositions similar to the spectra shown in Figure 8-33.

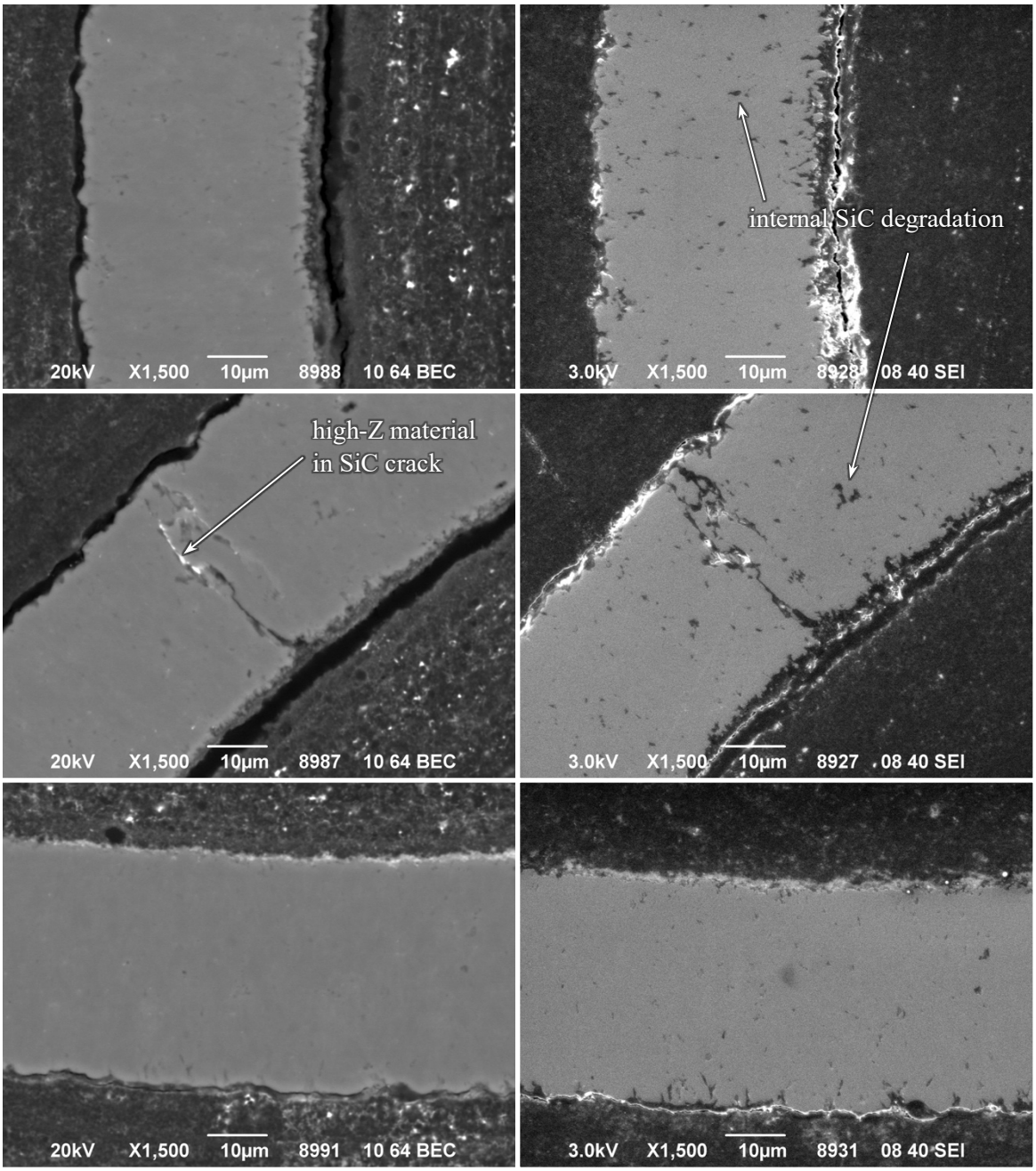

Figure 8-37. BEC and SEI image pairs of select region of SiC layer in Particle 341-SP03.

The high-Z features throughout the buffer, IPyC, and IPyC/SiC interface region of Particle 341-SP03 differed from those typically observed in Compact 3-4-1 RS particles. There were noticeably fewer high-Z interface and high-Z boundary features, and more high-Z IPyC features. High-intensity and low-intensity high-Z buffer features were explored, and were similar to Particles 342-SP01 and 342-SP06, respectively. Example spectra are shown in Figure 8-38, and the locations of the analyzed features are shown in Figure 8-39. All features were uranium-rich and had a balance of carbon from the matrix and oxygen. The high-intensity buffer features were predominantly uranium with trace cesium. The low-intensity buffer features were predominantly uranium and silicon with trace zirconium and cesium. The faint, fine-scale high-Z IPyC features were predominantly uranium-only, while the high-Z interface features were uranium and silicon. The uranium and silicon compositions in Particle 341-SP03 were notably different from the diffuse banded Si-O buffer features in 1,600°C safety-tested particles, which had silicon and oxygen compositions, with no obvious uranium contributions (Figure 8-8); this difference

was likely related to the higher safety test temperature. The compositions of these features showed less silicon intensity in the interior of the IPyC and buffer compared with the inner buffer near the kernel and outer IPyC near the SiC layer. The apparently higher silicon intensity in features closer to the kernel, identified by point ID and observed in the EDS mapping, indicated silicon had moved toward the kernel.

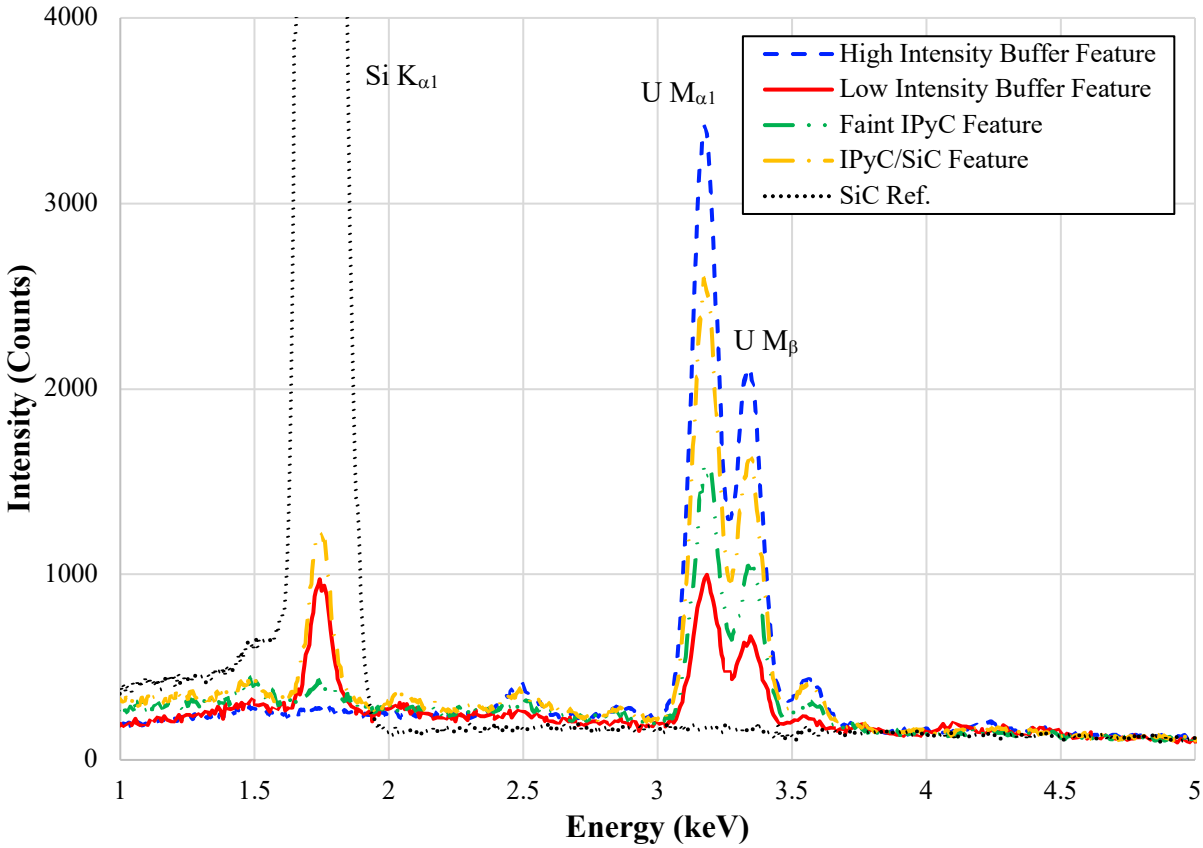

Figure 8-38. Example EDS spectra of U-rich features in the Buffer and IPyC regions of Particle 341-SP03.

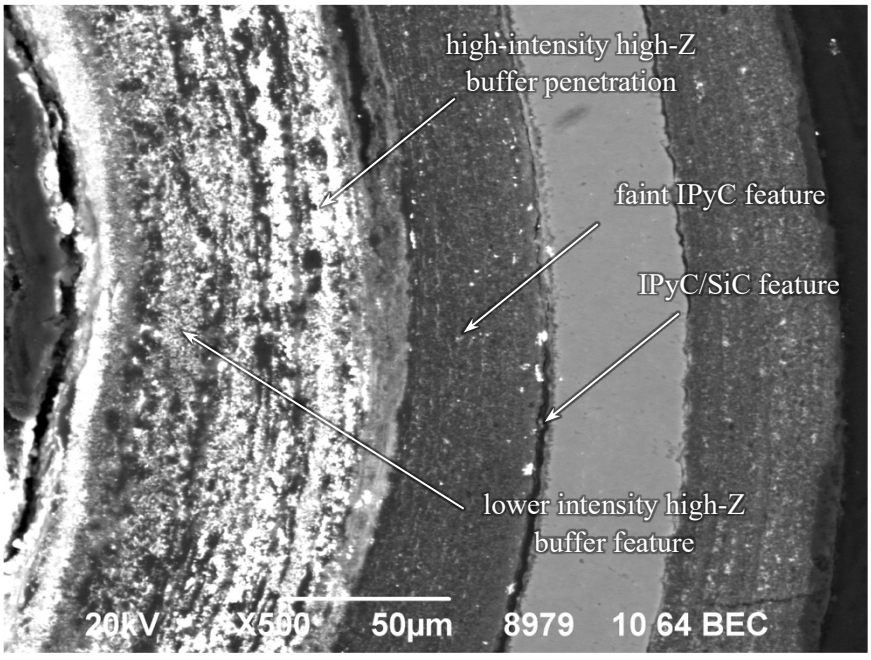

Figure 8-39. BEC image showing location of analyzed features in Figure 8-38.

The lack of SiO_2 deposits and limited silicon presence in the layers prompted exploration of the kernel to account for the silicon missing from the significantly corroded SiC layer. An EDS map of the kernel center is shown in Figure 8-40. The analysis showed the kernel contained silicon-rich precipitates. The compositions of the precipitates were mostly Mo-Tc-Ru-Si with trace rhodium. The kernel matrix was mostly uranium and oxygen with zirconium, neodymium, and cesium apparently in solution. The high frequency of silicon-rich precipitates confirmed silicon transport and accommodation in the kernel. Similar behavior was reported by Minato et al. for particles with corroded SiC in UO_2 TRISO fuel (Minato et al. 1991). Accommodation of silicon in the kernel was also observed in UCO TRISO particles with significantly degraded SiC after safety testing at 1,800°C (Gerczak et al, 2020a). The significant presence of the silicon-rich precipitates in the kernel and uranium-silicon buffer features may be why no large SiO_2 features were observed in Particle 341-SP03.

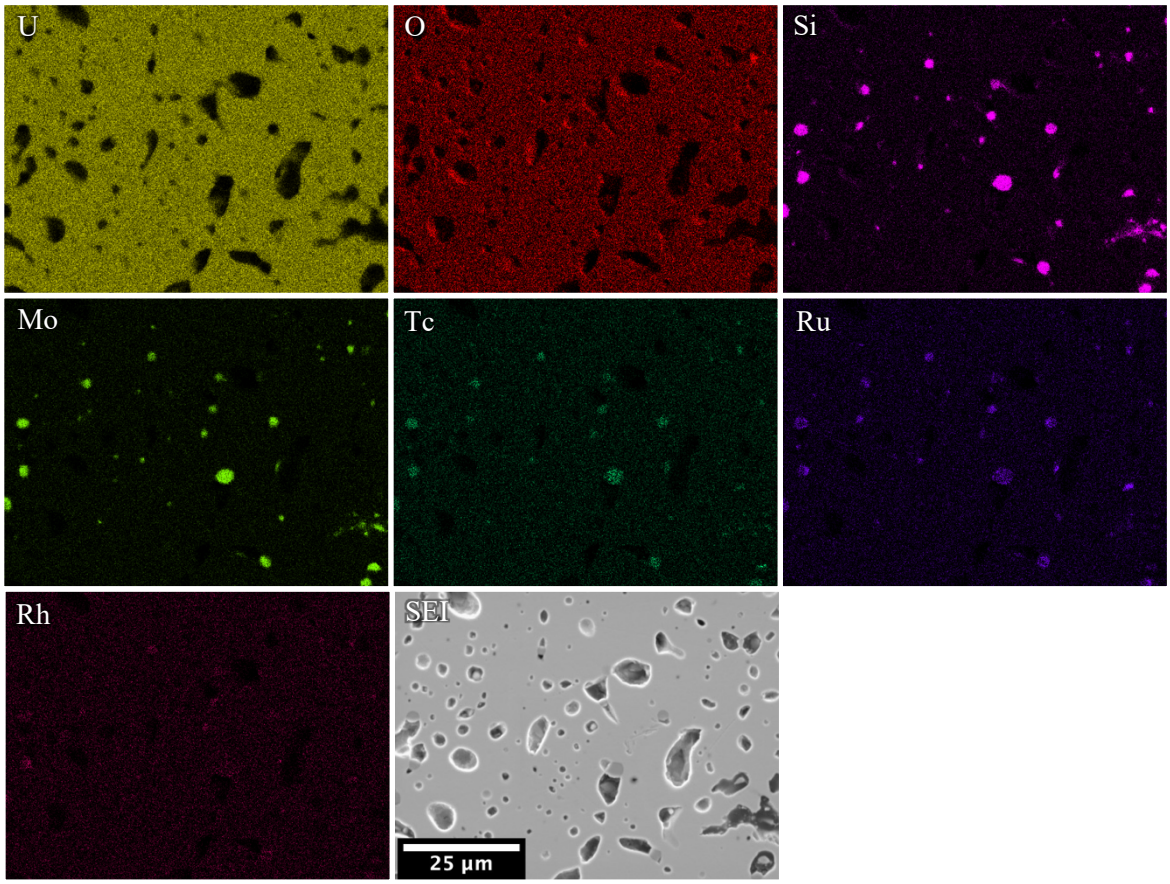

Figure 8-40. EDS maps of central kernel region showing Mo-Tc-Ru-Si precipitates in Particle 341-SP03.

As discussed in Section 5.6, Particle 341-SP15 was chosen for microstructural analysis from a large number of particles that exhibited marginal cesium release. The XCT imaging revealed this particle had an unusual microstructure, where all layers were essentially intact and there were no significant separations at the interfaces. Nevertheless, no specific observation could be made to explain why this particle apparently released cesium. Figure 8-41 shows some BEC images, and images of the IPyC/SiC layer taken at higher magnification are in Figure 8-42. High-Z interface features, high-Z boundary features, and limited high-Z SiC features in the first 5 µm of the SiC layer were observed. The appearances of these features were like those typically associated with RS particles and were comparable to Particle 341-RS36 (Section 7.5). The Pd-Rh-Ru and Pd-Rh compositions of the high-Z interface features were also similar to RS particles, with no predominance for either composition type. This was different from the three analyzed Compact 3-4-1 RS particles, in which high-Z interface features were exclusively Pd-Rh-Ru. All analyzed high-Z boundary features in Particle 341-SP15 were Pd-Rh with no Pd-Rh-Ru compositions. The diffuse, banded high-Z interface features had Ba-Sr-Cs-U compositions that

possibly included oxygen, similar to Compact 3-4-1 RS particles (e.g., Figure 7-46). The crack in the SiC layer can be presumed to have been introduced during grinding, because it was not observed in the XCT imaging and there were no associated features indicating it was present during safety testing.

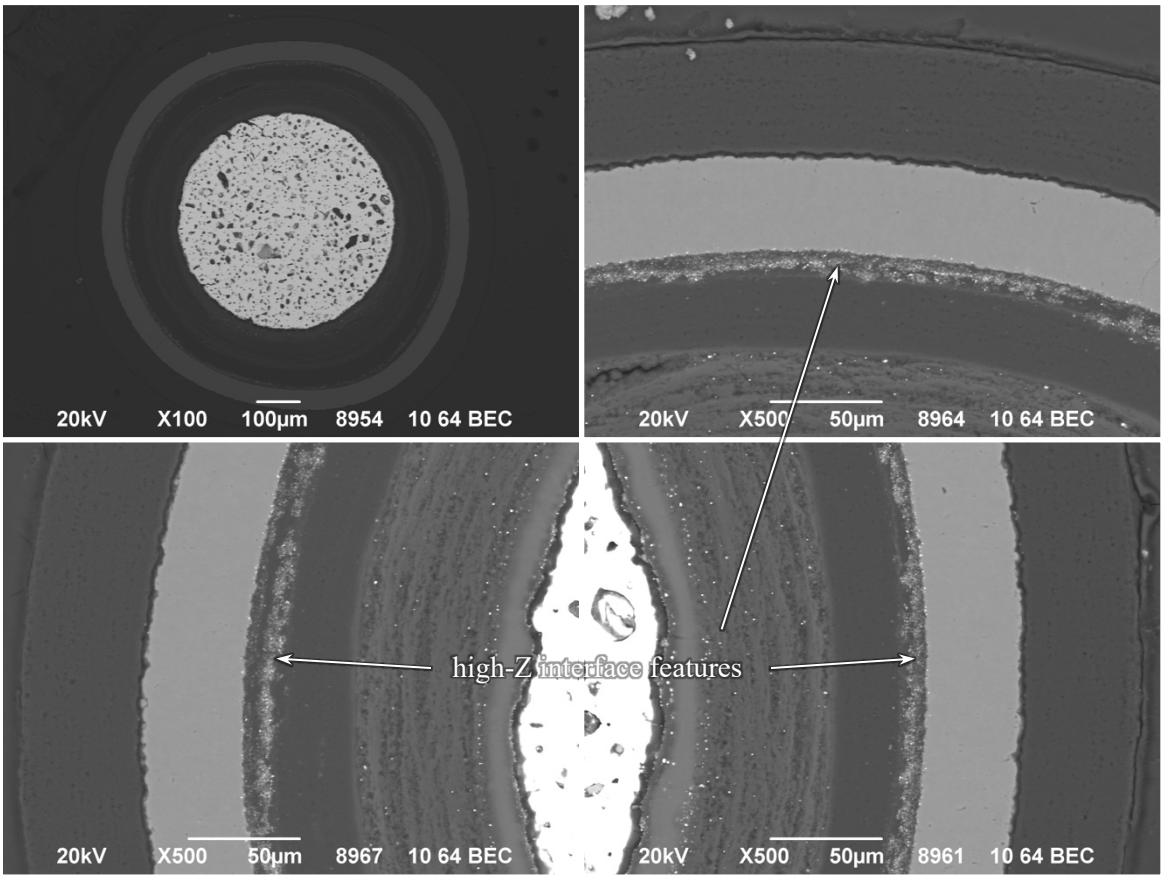

Figure 8-41. BEC images of Particle 341-SP15.

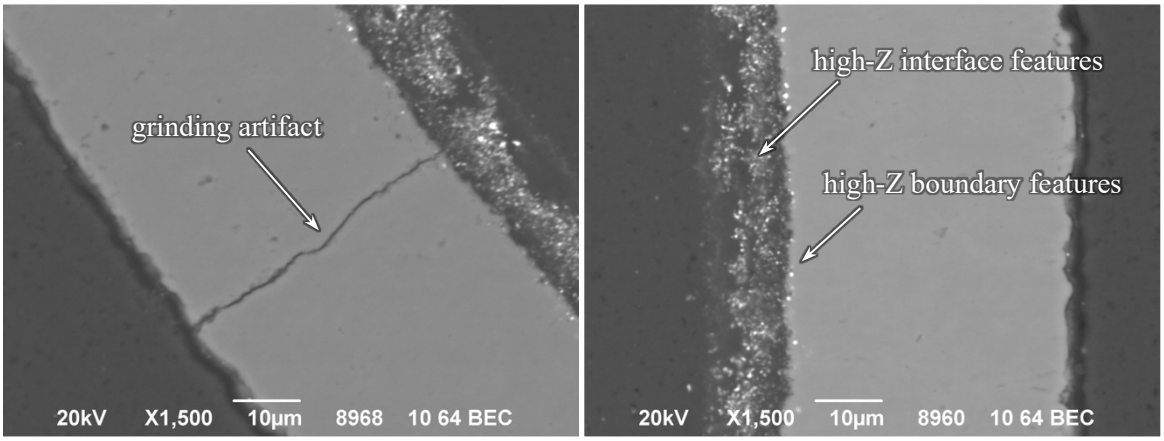

Figure 8-42. BEC images of IPyC/SiC region in Particle 341-SP15.

8.5 DISCUSSION OF SEM ANALYSIS OF SPECIAL PARTICLES

While particles that exhibited cesium release during safety testing did not always have obvious through-layer pathways in the SiC, those that did clearly exhibited intergranular CO corrosion of the SiC layer, often accompanied by SiC fracture. The SiC layer was susceptible to CO corrosion by two primary sequences, both involving restructuring of the internal TRISO layers. The first sequence involved

densification of the buffer and an associated incomplete tearing of the buffer adjacent to the IPyC internal surface. The incomplete tearing led to crack propagation through the IPyC that terminated at the SiC internal surface. This local SiC exposure provided a direct pathway for concentrated CO attack of the SiC and resulted in corrosion that progressed through the layer. The corrosion was often concentrated to a small surface area of the SiC layer and radiated out from the location of the IPyC fracture, which suggested that the detachment of the IPyC from the SiC in particles with localized corrosion proceeded as a consequence of the corrosion. This resulted in aggressive local intergranular CO corrosion leading to a through layer failure either by the corrosion penetrating the thickness of the SiC layer or formation of a SiC crack due to the local thinning and structural weakening of the SiC. The second observed sequence was associated with the formation of an IPyC/SiC gap and subsequent general CO corrosion of the internal SiC layer surface, followed by SiC fracture. In these cases, the separation of the IPyC from the SiC may have occurred first, or soon followed the initiation of corrosion. Extensive separation at the IPyC/SiC interface resulted in corrosion over a larger area, but the corrosion was less concentrated compared to cases where exposure was limited to a smaller area and corrosion was localized.

As-irradiated Particle 312-SP02 had an IPyC/SiC gap that had formed during irradiation, however clear evidence for corrosion was not observed in the SEM. It is possible that this absence of obvious corrosion was due to the gap forming near the end of the irradiation. However, in combination with the absence of obvious SiC failure in the as-irradiated AGR-2 UO_2 particles, it is more likely that the absence of observable corrosion in Particle 312-SP02 was due to corrosion being significantly less active at the irradiation temperatures, compared with the higher safety testing temperatures.

The reason for the formation of an IPyC/SiC gap was not always explicitly obvious, and observations indicated there may have been several factors that contributed to this structural change. Densification of the buffer occurred in all particles, but various microstructures were observed as a result of shrinkage of the buffer. In most of the irradiated particles that were analyzed, it was observed that the buffer had torn away from the IPyC sometime during irradiation, which would have relieved the stress the shrinking buffer put on the IPyC. When or if the buffer tore away was likely an important factor impacting formation of an IPyC/SiC gap. In particles with significant areas where the buffer was not torn away, the IPyC/SiC interface was under greater tensile stress. This may have led to separation of the IPyC from the SiC in some particles. As mentioned above, corrosion may have played a role in weakening the IPyC/SiC interface, making it more susceptible to separation under the right conditions, or it may have caused the gap directly. It is also possible that the banded porosity frequently observed at the IPyC/SiC interface region may have resulted in a higher susceptibility to IPyC/SiC gap formation in some of the AGR-2 UO_2 particles. Some of the cross sectioned particles, such as in Particle 332-SP01 (Figure 8-14), showed residual IPyC material on the SiC inner surface that suggested separation occurred along a band of weaker IPyC several microns away from the SiC boundary. It was observed that regions where the buffer/IPyC interface was connected throughout the radiation and safety testing tended to correlate to wider gaps between the IPyC and SiC. Particles 332-SP01 and 342-SP07 had detached buffer/IPyC interfaces and gaps at the IPyC/SiC interface that were generally less than ~5 μm. Particles 342-SP06 and 341-SP01 had gaps greater than ~10 μm adjacent to connected buffer/IPyC interfaces. Particle 312-SP02 (Figure 8-1e) had an IPyC/SiC gap on either side of a buffer/IPyC fracture, in which the IPyC/SiC gap was wider on the side where the buffer and IPyC were still connected. Some analyzed particles had regions where there were gaps at both the IPyC/SiC and buffer/IPyC interfaces. It is possible that the IPyC/SiC gap in these region formed first, because the inward movement of the IPyC may not have been sufficient to relieve the continuously increasing stress on the buffer/IPyC interface as the buffer continued to densify.

9. CONCLUSION

Safety testing and destructive PIE have been completed on six of the AGR-2 Capsule 3 UO_2 compacts. Compacts 3-1-2 and 3-3-1 were examined in the as-irradiated state. The compacts were deconsolidated to break up the matrix and the particles and matrix debris were leached in hot nitric acid to detect exposed actinides and fission products. Particles were separated for IMGA survey, while the matrix debris was burned and leached again to measure any remaining actinides and fission products not removed by the previous leaches. Any particles with abnormal inventories of the gamma-emitting isotopes measured with the IMGA were culled out for further analysis, which included longer, 6 h gamma counting and various combinations of XCT, optical microscopy, and SEM/EDS. Additional particles were randomly-selected and subjected to the same examinations. Safety testing was performed on Compacts 3-1-1, 3-3-2, 3-4-2, and 3-4-1. The primary focus of the safety testing was release of cesium, which would indicate failure of the normally high retention of this isotope exhibited by good SiC. Low krypton release indicated that no particles experienced complete TRISO failure. After completion of a safety test, each safety-tested compact was subjected to the same series of examinations performed on the as-irradiated compacts.

Compact 3-1-1 was safety tested by heating in helium to 1,500°C and holding at that temperature for ~400 h, in which the planned 300 h test was extended by 100 h because of an uptick in the previously negligible cesium release rate after 256 h at 1,500°C. The amount of cesium that was released during the Compact 3-1-1 safety test and the time dependence of the cesium release rate were consistent with the presence of one particle with failed SiC. Compacts 3-3-2 and 3-4-2 were safety tested at 1,600°C for ~300 h. The fraction of particles with failed SiC was dramatically higher at 1,600°C than 1,500°C. The SiC failure fractions in these two UO_2 compacts were also noticeably higher than AGR-1 and AGR-2 UCO compacts tested under similar conditions (Demkowicz et al. 2016, Hunn et al. 2018a). In fact, UO_2 compact failure fractions were closer to the UCO compact failure fractions observed in AGR-1 fuel at 1800°C. Compact 3-4-1 was originally planned for safety testing at 1,800°C, but concern about the higher UO_2 compact failure fractions at 1,600°C resulted in a decision to reduce the test temperature to 1,700°C. Cesium release began soon after reaching 1,700°C, and a dramatically escalating rate of release, which reached one particle equivalent of ^{134}Cs per hour after ~100 h, indicated wholesale SiC failure that required premature termination of the test. Release of other fission products typically monitored during safety testing (^{90}Sr, ^{110m}Ag, and ^{154}Eu) was dominated by SiC failure at 1,600 and 1,700°C. At 1,500°C, ^{110m}Ag release was consistent with release of silver previously released through good SiC during irradiation, in which the silver had been temporarily sequestered in the matrix and/or OPyC until heating above the irradiation temperature during safety testing.

It was notable that no ^{85}Kr release from TRISO failure was observed in conjunction with the numerous SiC failures in the AGR-2 UO_2 compacts safety tested at 1,600 and 1,700°C. A similar situation was observed in AGR-1 PIE, even during 1,800°C safety testing in which as many as 11 particles in AGR-1 UCO Compact 3-2-3 exhibited cesium release from SiC failure (Hunn et al. 2014b). In AGR-1 PIE, krypton retention in particles with failed SiC was credited to intact OPyC layers. That appeared to be the case for the UO_2 fuel as well. In many of the failed SiC particles that later experienced kernel leaching during DLBL, the leaching appeared to be related with post-test fracture of the OPyC, and the OPyC cracks often appeared remote and not related to the cracks in the underlying SiC.

The DLBL analysis of the as-irradiated compacts indicated there were no particles with defective or radiation-failed SiC or TRISO. A particle in Compact 3-1-2 was leached partway through the DLBL process, which indicated damage to the TRISO coating due to the analysis. Non-destructive 3D imaging of this particle with XCT suggested the SiC and OPyC layers had been broken because they were weakened by fracture in the buffer and IPyC layers during irradiation. Separation of the IPyC from the SiC during irradiation had introduced cracks in the SiC that did not penetrate the layer; however, these cracks likely made the SiC more susceptible to handling damage during PIE. No particles were damaged during the DLBL of Compact 3-3-1, so this compact provided a good baseline for exposed actinides and fission products in the as-irradiated fuel (Appendix A).

The DLBL of safety tested compacts provided information that aided with the analysis of particle failure during safety testing. Analysis of the acid used to deconsolidate Compacts 3-1-1, 3-3-2, and 3-4-2 confirmed that there were no particles with failed TRISO. All safety tested compacts exhibited kernel leaching at some stage of the pre-IMGA DLBL due to the weakened state of particles with failed SiC. The DLBL uranium analysis was used to support interpretation of the IMGA and XCT data. The DLBL analysis performed after safety testing of Compacts 3-1-1 clearly indicated that one compromised particle was broken at the end of the second preburn leach and that the kernel material was dissolved. Based on the amount of cesium released during safety testing and the absence of any abnormally low cesium particles in the 1,509 particles counted with the IMGA, it was presumed that there was only one particle with failed SiC and that this particle was the particle that was leached during DLBL.

Survey of the retention of ^{137}Cs, ^{144}Ce, and ^{106}Ru with the IMGA was used as the primary tool for finding and attempting to count particles with failed SiC, in addition to other abnormalities. Unusual particles identified in as-irradiated Compact 3-3-1 included a particle with a ZrO_2 kernel that was unintentionally included in the irradiation test. Another such particle was identified in Compact 3-4-2, but IMGA and subsequent microstructural analysis were able to isolate this particle from inclusion in the identified number of failed particles. A dimpled particle was found in Compact 3-3-1, and its presence was not unexpected based on inspection of the as-fabricated AGR-2 UO_2 TRISO particles. Survival of this particle throughout the irradiation test provided insight into the resilience of the TRISO coating design. A particle in the AGR-1 UCO test fuel with similar high curvature from a soot inclusion only failed after being heated to 1,600°C during safety testing. In addition to the particle in Compact 3-1-2 that was leached partway through the DLBL, IMGA survey and XCT imaging revealed three particles with UCO kernels that were probably mixed in during particle handling in the IMGA hot cell, unless they were also somehow unintentionally included in the as-fabricated AGR-2 UO_2 TRISO particle batch prior to irradiation. In any case, the presence of these particles did not impact the interpretation of the irradiation and safety test results, as they were readily identified by the PIE methodology and it was determined that they did not have failed SiC or release significant fission product inventory.

The IMGA survey of particles from the safety-tested compacts identified and culled out many of the particles with failed SiC, including those missing most of their kernel material due to acid infiltration during DLBL. In those particles, although most of the kernel was removed, the particle layers remained in one piece because cracks in the coatings did not circumnavigate the entire particle sphere. Particles with leached kernels tended to be those with the most advanced SiC failure. Failure was localized, and in almost every instance SiC degradation could be directly associated with an IPyC crack that had exposed the inner surface of the SiC. These IPyC cracks did not appear to be caused by inherent insufficiencies in the IPyC layer, but were rather related to cracks propagating from or initiated by the detachment of the buffer near the buffer/IPyC interface. These connected events were previously identified as the primary failure mechanism in AGR-1 UCO TRISO fuel (Hunn et al. 2014), with one exception. Degradation of the exposed SiC layer in UCO fuel was dominated by palladium silicide formation. Degradation of the exposed SiC layer in UO_2 fuel was dominated by CO corrosion. The absence of CO corrosion in the UCO fuel was due to the addition of uranium carbide to the kernel, which reduced CO formation because the oxidation potential of uranium carbide is lower than carbon (Homan et al. 1977).

CO corrosion was clearly identified during SEM/EDS analysis of failed particles by the presence of intergranular corrosion and the formation of SiO_2 precipitates, which tended to agglomerate in the void space within the particles (e.g., the buffer/IPyC gap). In addition to localized CO corrosion through the entire thickness of the SiC layer, general CO corrosion was often observed in safety-tested particles that had a separation between the IPyC and SiC layers. In some cases, the detachment of the IPyC layer could be related to the layer mechanically pulling away from the SiC as a result of IPyC fracture adjacent to attached buffer, in which the continued shrinkage in the buffer pulled the IPyC inward. However, it could also be argued that the SiC corrosion may have occurred before or in conjunction with the IPyC separation. The connection between the IPyC and SiC layers is usually strong due to mechanical stitching of the two layers, in which fingers of SiC penetrate into open porosity at the IPyC surface during the SiC

deposition. Chemical corrosion at this interface could have either caused an eventual separation as the reaction progressed or weakened the interface bond to the point where it became susceptible to mechanical separation.

The connection between CO corrosion and particles with failed SiC was obvious for those particles with advanced locally corroded SiC, in which the corroded region fully penetrated the layer, or thinned it to a state where it eventually cracked. General corrosion was not as obviously related to SiC failure, but likely compromised the SiC and apparently led to fracture in some particles. However, not every special particle with preferential loss of cesium during safety testing had obvious through-layer cracks or enough corrosion of the SiC to allow observation of the cesium release pathway, especially those particles from Compacts 3-4-2 and 3-4-1 with lower cesium release. Nevertheless, particles with preferential loss of cesium commonly were found to have abnormal microstructures and indicators of corrosion, which suggested that there was a correlation between the cesium release and observed abnormal microstructures that was not coincidental.

While IPyC fracture was found in most particles with failed SiC, IPyC fracture was not a commonly observed microstructure in the randomly-selected as-irradiated particles from Compacts 3-1-2, 3-3-1, and 3-2-3 that were observed in cross section. Out of 209 particles, only 3 were noted as having visible IPyC tears. Thus, not only were IPyC tears prevalent in particles with failed SiC, but it can also be inferred that particles with IPyC tears had a high probability for SiC failure.

The SEM and EDS analysis of the AGR-2 UO_2 TRISO particles before and after safety testing showed that there were variations in the actinide and fission product distributions that could be connected to the temperatures of irradiation and subsequent safety testing. However, the varied mobility and apparent interactions between these metallic species and the various layers did not appear to impact the AGR-2 UO_2 fuel performance, which could be considered relatively good during irradiation, but compromised by CO corrosion at accident temperatures above 1,500°C.

10. REFERENCES

Amian, Winfried, and Detlev Stöver. 1983. "Diffusion of Silver and Cesium in Silicon-Carbide Coatings of Fuel Particles for High-Temperature Gas-Cooled Reactors," *Nucl. Tech*. 61: 475–486.

Baldwin, Charles A., John D. Hunn, Robert N. Morris, Fred C. Montgomery, Chinthaka M. Silva, and Paul A. Demkowicz. 2012. "First Elevated Temperature Performance Testing of Coated Particle Fuel Compacts from the AGR-1 Irradiation Experiment." *Proc. 6th International Topical Meeting on High Temperature Reactor Technology (HTR-2012)*. Tokyo, October 28–November 1, 2012. Also published in *Nucl. Eng. Des.* 271: 131–141.

Barnes, Charles M. and Douglas W. Marshall. 2009. *FY 2009 Particle Fabrication and Coater Test Report.* INL/EXT-09-16545, Revision 0. Idaho Falls: Idaho National Laboratory.

Collin, Blaise P. 2014. *AGR-2 Irradiation Test Final As-Run Report.* INL/EXT-14-32277, Revision 4. Idaho Falls: Idaho National Laboratory.

Croff, Allen G. 1983. "ORIGEN2: A Versatile Computer Code for Calculating the Nuclide Compositions and Characteristics of Nuclear Materials." *Nucl. Tech.* 62: 335–352.

Demkowicz, Paul A., Edward L. Reber, Dawn M. Scates, Les Scott, and Blaise P. Collin. 2015a. "First High Temperature Safety Tests of AGR-1 TRISO Fuel with the Fuel Accident Condition Simulator (FACS) Furnace." *J. Nucl. Mater.* 464: 320–330.

Demkowicz, Paul A., John D. Hunn, Robert N. Morris, Isabella J. van Rooyen, Tyler J. Gerczak, Jason M. Harp, and Scott A. Ploger. 2015b. *AGR-1 Post Irradiation Examination Final Report.* INL/EXT-15-36407, Revision 0. Idaho Falls: Idaho National Laboratory.

Demkowicz, Paul A., John D. Hunn, David A. Petti, and Robert N. Morris. 2016. "Key results from irradiation and post-irradiation examination of AGR-1 UCO TRISO fuel." *Proc. 8th International Topical Meeting on High Temperature Reactor Technology (HTR-2016)*. Las Vegas, November 6–10, 2016. Also published in *Nucl. Eng. Des*. 329: 102–109.

Gerczak, Tyler J., John D. Hunn, Robert N. Morris, Fred C. Montgomery, Darren J. Skitt, Charles A. Baldwin, John A. Dyer, and Brian D. Eckhart. 2018. "Analysis of Fission Product Distribution and Composition in the TRISO Layers of AGR-2 Fuel." *Proc. 9th International Topical Meeting on High Temperature Reactor Technology (HTR-2018)*. Warsaw, October 8–10, 2018.

Gerczak, Tyler J., Rachel L. Seibert, John D. Hunn, Charles A. Baldwin, Fred C. Montgomery, and Robert N. Morris. 2020a. "Redistribution of Radionuclides in Irradiated AGR-1 UCO TRISO Fuel After 1800 °C Safety Testing." *J. Nucl. Mater.* 542: 152453.

Gerczak, Tyler J., Rachel L. Seibert, and John D. Hunn. 2020b. "Role of Microstructure on CO Corrosion of SiC Layer in UO_2-TRISO fuel." *J. Nucl. Mater.* 537: 152185.

Harp, Jason M., Paul A. Demkowicz, and John D. Stempien. 2016. "Fission Product Inventory and Burnup Evaluation of the AGR-2 Irradiation by Gamma Spectrometry." *Proc. 8th International Topical Meeting on High Temperature Reactor Technology (HTR-2016)*. Las Vegas, November 6–10, 2016. Also published in *Nucl. Eng. Des.* 329: 134–141.

Hawkes, Grant L. 2014. *AGR-2 Daily As-Run Thermal Analyses.* INL/ECAR-2476, Revision 1. Idaho Falls: Idaho National Laboratory.

Homan, Franklin J., Terrence B. Lindemer, Ernest L. Long, Jr., Terry N. Tiegs, and Ronald L. Beatty. 1977. "Stoichiometric Effects on Performance of High-Temperature Gas-Cooled Reactor Fuels from the U-C-O System." *Nucl. Tech.* 35: 428–441.

Hunn, John D., Fred C. Montgomery, and Peter J. Pappano. 2010. *Data Compilation for AGR-2 UO_2 Compact Lot LEU11-OP2-Z.* ORNL/TM-2010/055, Revision 1. Oak Ridge: Oak Ridge National Laboratory.

Hunn, John D., Traig W. Savage, and Chinthaka M. Silva. 2010. *AGR-2 Fuel Compact Pre-Irradiation Characterization Summary Report.* ORNL/TM-2010/226, Revision 0. Oak Ridge: Oak Ridge National Laboratory.

Hunn, John D., Robert N. Morris, Charles A. Baldwin, Fred C. Montgomery, Chinthaka M. Silva, and Tyler J. Gerczak. 2012. *AGR-1 Irradiated Compact 6-1-1 PIE Report: Evaluation of As-Irradiated Fuel Performance Using Leach Burn Leach, IMGA, Materialography, and X-ray Tomography*. ORNL/TM-2012/233, Revision 0. Oak Ridge: Oak Ridge National Laboratory.

Hunn, John D., Robert N. Morris, Charles A. Baldwin, Fred C. Montgomery, Chinthaka M. Silva, and Tyler J. Gerczak. 2013. *AGR-1 Irradiated Compact 4-4-2 PIE Report: Evaluation of As-Irradiated Fuel Performance with Leach Burn Leach, IMGA, Materialography, and X-ray Tomography*. ORNL/TM-2013/236, Revision 0. Oak Ridge: Oak Ridge National Laboratory.

Hunn, John D., Charles A. Baldwin, Tyler J. Gerczak, Fred C. Montgomery, Robert N. Morris, Chinthaka M. Silva, Paul A. Demkowicz, Jason M. Harp, Scott A. Ploger, Isabella J. van Rooyen, and Karen E. Wright. 2014a. "Detection and Analysis of Particles with Failed SiC in AGR-1 Fuel Compacts." *Proc. 7th International Topical Meeting on High Temperature Reactor Technology (HTR-2014)*. Weihai, October 27–31, 2014. Also published in *Nucl. Eng. Des.* 360: 36–46.

Hunn, John D., Robert N. Morris, Charles A. Baldwin, Fred C. Montgomery, and Tyler J. Gerczak. 2014b. *PIE on Safety-Tested AGR-1 Compacts 5-3-3, 5-1-3, and 3-2-3*. ORNL/TM-2014/484, Revision 0. Oak Ridge: Oak Ridge National Laboratory.

Hunn, John D., Robert N. Morris, Charles A. Baldwin, and Fred C. Montgomery. 2015a. *Safety-Testing of AGR-2 UO_2 Compacts 3-3-2 and 3-4-2*. ORNL/TM-2015/388, Revision 0. Oak Ridge: Oak Ridge National Laboratory.

Hunn, John D., Robert N. Morris, Charles A. Baldwin, Fred C. Montgomery, and Tyler J. Gerczak. 2015b. *PIE on Safety-Tested AGR-1 Compact 5-1-1*. ORNL/TM-2015/317, Revision 0. Oak Ridge: Oak Ridge National Laboratory.

Hunn, John D., Charles A. Baldwin, Fred C. Montgomery, Tyler J. Gerczak, Robert N. Morris, Grant W. Helmreich, Paul A. Demkowicz, Jason M. Harp, and John D. Stempien. 2016. "Initial Examination of Fuel Compacts and TRISO Particles from the US AGR-2 Irradiation Test." *Proc. 8th International Topical Meeting on High Temperature Reactor Technology (HTR-2016)*. Las Vegas, November 6–10, 2016. Also published in *Nucl. Eng. Des.* 329: 89–101.

Hunn, John D., Robert N. Morris, Fred C. Montgomery, Tyler J. Gerczak, Darren J. Skitt, Charles A. Baldwin, John A. Dyer, Grant W. Helmreich, Brian D. Eckhart, Zachary M. Burns, Paul A. Demkowicz, and John D. Stempien. 2018a. "Post-Irradiation Examination and Safety Testing of US AGR-2 Irradiation Test Compacts." *Proc. 9th International Topical Meeting on High Temperature Reactor Technology (HTR-2018)*. Warsaw, October 8–10, 2018.

Hunn, John D., Robert N. Morris, Fred C. Montgomery, Tyler J. Gerczak, Darren J. Skitt, Grant W. Helmreich, Brian D. Eckhart, and Zachary M. Burns. 2018b. *Safety Testing and Post-Safety-Test Examination of AGR-2 UCO Compact 2-3-2 and AGR-2 UO_2 Compact 3-4-1*. ORNL/TM-2018/956, Revision 0. Oak Ridge: Oak Ridge National Laboratory.

Hunn, John D., Tyler J. Gerczak, Fred C. Montgomery, Darren J. Skitt, Charles A. Baldwin, Grant W. Helmreich, Brian D. Eckhart, and John A. Dyer. 2018c. *AGR-2 As-Irradiated UCO Compact 5-4-2 PIE Report*. ORNL/TM-2018/863, Revision 0. Oak Ridge: Oak Ridge National Laboratory.

Hunn, John D., Tyler J. Gerczak, Robert N. Morris, Fred C. Montgomery, Darren J. Skitt, Brian D. Eckhart, Zachary M. Burns. 2019. *Safety-Testing and Destructive Examination of AGR-2 UCO Compact 6-4-3*. ORNL/TM-2019/1200, Revision 0. Oak Ridge: Oak Ridge National Laboratory.

Hunn, John D., Robert N. Morris, Fred C. Montgomery, Darren J. Skitt, and Zachary M. Burns. 2020. *Safety-Testing and Destructive Examination of AGR-2 UO_2 Compact 3-1-1*. ORNL/TM-2020/1451, Revision 0. Oak Ridge: Oak Ridge National Laboratory.

Hunn, John D., and Fred C. Montgomery. 2020. *Data Acquisition Method: Leach-Burn-Leach Analysis of Irradiated Fuel Compacts Using a Soxhlet Extractor in the 3525 Hot Cell*. AGR-CHAR-DAM-37, Revision 4. Oak Ridge: Oak Ridge National Laboratory.

Lowden, Richard A. 2006. *Fabrication of Baseline and Variant Particle Fuel for AGR-1*. ORNL/CF-2006/02, Revision 0. Oak Ridge: Oak Ridge National Laboratory.

Ludwig, Scott B., and Allen G. Croff. 2002. *ORIGEN2.2—Isotope Generation and Depletion Code Matrix Exponential Method*. Oak Ridge: Oak Ridge National Laboratory.

Minato, Kazuo, Toru Ogawa, Satoru Kashimura, Kousaku Fukuda, Ishio Takahashi, Michio Shimizu, and Yoshinobu Tayama. 1991. "Carbon Monoxide-Silicon Carbide Interaction in HTGR Fuel Particles." *J. Mater. Sci.* 26: 2379–2388.

Morris, Robert N., Paul A. Demkowicz, John D. Hunn, Charles A. Baldwin, and Edward L. Reber. 2014. "Performance of AGR-1 High Temperature Reactor Fuel During Post-Irradiation Heating Tests." *Proc. 7th International Topical Meeting on High Temperature Reactor Technology (HTR-2014)*. Weihai, October 27–31, 2014. Also published in *Nucl. Eng. Des.* 306: 24–35.

Morris, Robert N., John D. Hunn, Charles A. Baldwin, Fred C. Montgomery, Tyler J. Gerczak, and Paul A. Demkowicz. 2016. "Initial Results from Safety Testing of US AGR-2 Irradiation Test Fuel." *Proc. 8th International Topical Meeting on High Temperature Reactor Technology (HTR-2016)*. Las Vegas, November 6–10, 2016. Also published in *Nucl. Eng. Design* 329: 124–133.

Nabielek, Heinz, P. E. Brown, and Peter B. Offerman. 1977. "Silver Release from Coated Particle Fuel." *Nucl. Tech.* 35: 483-493.

Petrie, Christian M., Joseph R. Burns, Alicia M. Raftery, Andrew T. Nelson, and Kurt A. Terrani. 2019. "Separate Effects Irradiation Testing of Miniature Fuel Specimens." *J. Nucl. Mater.* 526: 151783.

Petti, David A., John T. Maki, Jacopo Buongiorno, Richard R. Hobbins, and Gregory K. Miller. 2002. *Key Differences in the Fabrication, Irradiation and Safety Testing of U.S. and German TRISO-coated Particle Fuel and Their Implications on Fuel Performance*. INEEL/EXT-02-00300, Revision 0. Idaho Falls: Idaho National Laboratory.

Phillips, Jeffrey A., Charles M. Barnes, and John D. Hunn. 2010. "Fabrication and Comparison of Fuels for Advanced Gas Reactor Irradiation Tests." *Proc. 5th International Topical Meeting on High Temperature Reactor Technology (HTR-2010)*. Prague, October 18–20, 2010.

Ploger, Scott A., Paul A. Demkowicz, John D. Hunn, and Jay S Kehn. 2012. "Microscopic Analysis of Irradiated AGR-1 Coated Particle Fuel Compacts." *Proc. 6th International Topical Meeting on High Temperature Reactor Technology (HTR-2012)*. Tokyo, October 28–November 1, 2012. Also published in *Nucl. Eng. Des.* 271: 221–230.

Ploger, Scott A., Paul A. Demkowicz, and Jason M. Harp. 2015. *AGR-2 Irradiated Test Train Preliminary Inspection and Disassembly First Look.* INL/EXT-15-34997, Revision 0. Idaho Falls: Idaho National Laboratory.

Rice, Francine J., John D. Stempien, and Paul A. Demkowicz. 2016. *Ceramography of Irradiated TRISO Fuel from the AGR-2 Experiment.* INL/EXT-16-39462, Revision 0. Idaho Falls: Idaho National Laboratory.

Stempien, John D., Mitchell A. Plummer, and Jason L. Schulthess. 2019. *Measurement of Kernel Swelling and Buffer Densification in Irradiated UCO and UO_2 TRISO Fuel Particles from AGR-2.* INL/EXT-19-54502, Revision 0. Idaho Falls: Idaho National Laboratory.

Stempien, John D., and Paul A. Demkowicz. 2020. *AGR-2 Irradiation Experiment Fission Product Mass Balance.* INL/EXT-19-53559, Revision 1. Idaho Falls: Idaho National Laboratory.

Sterbentz, James W. 2014. *JMOCUP As-Run Daily Depletion Calculation for the AGR-2 Experiment in the ATR B-12 Position.* ECAR-2066, Revision 2. Idaho Falls: Idaho National Laboratory.

van Rooyen, Isabella J., Dawn E. Janney, Brandon D. Miller, Paul A. Demkowicz, Jessica L. Riesterer. 2012. "Electron Microscopic Evaluation and Fission Product Identification of Irradiated TRISO Coated Particles from the AGR-1 Experiment: A Preliminary Review." *Proc. 6th International Topical Meeting on High Temperature Reactor Technology (HTR-2012)*. Tokyo, October 28–November 1, 2012. Also published in *Nucl. Eng. Des.* 271: 114–122.

van Rooyen, Isabella J., Thomas M. Lillo, Yaqiao Q. Wu. 2014. "Identification of Silver and Palladium in Irradiated TRISO Coated Particles of the AGR-1 Experiment." *J. Nucl. Mater.* 446: 178–186.

X-5 Monte Carlo Team. 2003. *MCNP—A General Monte Carlo N-Particle Transport Code.* Version 5, Volume I (LA-UR-03-1987) and Volume II (LA-CP-03-0245). Los Alamos: Los Alamos National Laboratory.

APPENDIX A. DLBL DATA

The tables in this appendix document the DLBL data for select actinides and fission products (both radioisotopes and stable isotopes). Data is provided for each primary leach solution. Values are reported as compact fraction and particle equivalents, in which the particle equivalents are calculated from the compact fraction by multiplying by the average number of particles per compact (1543 particles per average AGR-2 UO_2 compact). Compact fraction was calculated as described in Section 2.1 using the calculated inventories tabulated in Appendix E.

Appendix Table A-1. Exposed U and Pu detected by DLBL of AGR-2 Compact 3-1-2

DLBL Step	^{235}U	^{236}U	^{238}U	^{239}Pu	^{240}Pu
Deconsolidation acid					
Preburn leach 1	1.44E-5 (0.022)	8.97E-6 (0.014)	2.82E-5 (0.043)	1.20E-5 (0.018)	1.44E-5 (0.022)
Preburn leach 2	7.54E-5 (0.116)	7.13E-5 (0.110)	7.34E-5 (0.113)	6.72E-5 (0.104)	7.17E-5 (0.111)
Postburn matrix leach 1	6.65E-4 (1.027)	6.25E-4 (0.964)	6.55E-4 (1.011)	5.21E-4 (0.803)	5.92E-4 (0.913)
Postburn matrix leach 2	3.52E-6 (0.0054)	3.25E-6 (0.0050)	3.77E-6 (0.0058)	4.42E-6 (0.0068)	5.26E-6 (0.0081)
Postburn particle leach 1	2.77E-3 (4.269)	2.75E-3 (4.241)	2.89E-3 (4.466)	2.38E-3 (3.674)	2.50E-3 (3.864)
Postburn particle leach 2	8.94E-6 (0.014)	8.38E-6 (0.013)	1.06E-5 (0.016)	7.97E-6 (0.012)	8.63E-6 (0.013)
Total	3.53E-3 (5.453)	3.47E-3 (5.348)	3.67E-3 (5.656)	2.99E-3 (4.619)	3.20E-3 (4.931)

Note: Values are reported as compact inventory fractions and particle equivalents (in parentheses).

Appendix Table A-2. Exposed U and Pu detected by DLBL of AGR-2 Compact 3-3-1

DLBL Step	^{235}U	^{236}U	^{238}U	^{239}Pu	^{240}Pu
Deconsolidation acid	8.64E-6 (0.013)	2.94E-6 (0.0045)	8.18E-6 (0.013)	5.57E-6 (0.0086)	7.16E-6 (0.011)
Preburn leach 1	5.95E-6 (0.0092)	1.76E-6 (0.0027)	4.68E-6 (0.0072)	3.57E-6 (0.0055)	4.04E-6 (0.0062)
Preburn leach 2	2.13E-6 (0.0033)	9.19E-7 (0.0014)	2.93E-6 (0.0045)	1.56E-6 (0.0024)	1.82E-6 (0.0028)
Postburn matrix leach 1	2.18E-5 (0.034)	1.71E-5 (0.026)	5.52E-5 (0.085)	2.59E-5 (0.040)	3.35E-5 (0.052)
Postburn matrix leach 2	1.69E-6 (0.0026)	7.17E-7 (0.0011)	2.40E-6 (0.0037)	1.27E-6 (0.0020)	1.57E-6 (0.0024)
Postburn particle leach 1	9.66E-6 (0.015)	2.90E-6 (0.0045)	6.37E-6 (0.0098)	4.32E-6 (0.0067)	5.33E-6 (0.0082)
Postburn particle leach 2	3.83E-6 (0.0059)	6.09E-7 (0.0009)	1.87E-6 (0.0029)	1.30E-6 (0.0020)	1.57E-6 (0.0024)
Total	5.37E-5 (0.083)	2.69E-5 (0.042)	8.17E-5 (0.126)	4.35E-5 (0.067)	5.50E-5 (0.085)

Note: Values are reported as compact inventory fractions and particle equivalents (in parentheses).
[a] A scaling factor was applied to account for ~169 particles not included in the postburn analysis.

Appendix Table A-3. Exposed U and Pu detected by DLBL of AGR-2 Compact 3-1-1

DLBL Step	^{235}U	^{236}U	^{238}U	^{239}Pu	^{240}Pu
Deconsolidation acid	3.35E-6 (0.0052)	1.46E-6 (0.0023)	3.75E-6 (0.0058)	2.87E-6 (0.0044)	3.52E-6 (0.0054)
Preburn leach 1	9.12E-7 (0.0014)	5.52E-7 (0.0009)	1.17E-6 (0.0018)	9.40E-7 (0.0015)	9.57E-7 (0.0015)
Preburn leach 2	5.51E-6 (0.0085)	5.04E-6 (0.0078)	6.72E-6 (0.010)	3.67E-6 (0.0057)	3.95E-6 (0.0061)
Postburn matrix leach 1	9.12E-4 (1.407)	7.69E-4 (1.186)	6.85E-4 (1.058)	5.87E-4 (0.906)	6.49E-4 (1.001)
Postburn matrix leach 2	7.96E-6 (0.012)	6.65E-6 (0.010)	6.68E-6 (0.010)	6.30E-6 (0.0097)	6.80E-6 (0.010)
Postburn particle leach 1	2.59E-5 (0.040)	9.27E-6 (0.014)	1.49E-5 (0.023)	9.33E-6 (0.014)	1.12E-5 (0.017)
Postburn particle leach 2	3.43E-6 (0.0053)	1.52E-6 (0.0023)	4.62E-6 (0.0071)	1.65E-6 (0.0026)	2.18E-6 (0.0034)
Total	9.59E-4 (1.479)	7.93E-4 (1.224)	7.23E-4 (1.116)	6.12E-4 (0.944)	6.77E-4 (1.045)

Note: Values are reported as compact inventory fractions and particle equivalents (in parentheses).
[a] A scaling factor was applied to account for ~207 particles not included in the postburn analysis.

Appendix Table A-4. Exposed U and Pu detected by DLBL of AGR-2 Compact 3-3-2

DLBL Step	^{235}U	^{236}U	^{238}U	^{239}Pu	^{240}Pu
Deconsolidation acid	2.83E-6 (0.0044)	9.07E-7 (0.0014)	2.24E-6 (0.0035)	1.77E-6 (0.0027)	2.02E-6 (0.0031)
Preburn leach 1	1.44E-3 (2.223)	1.49E-3 (2.301)	1.38E-3 (2.137)	1.54E-3 (2.373)	1.62E-3 (2.492)
Preburn leach 2	7.05E-4 (1.088)	6.79E-4 (1.048)	5.99E-4 (0.924)	6.33E-4 (0.977)	6.74E-4 (1.040)
Preburn water rinse	2.14E-4 (0.330)	2.16E-4 (0.334)	2.01E-4 (0.310)	1.68E-5 (0.026)	1.69E-5 (0.026)
Postburn matrix leach 1	4.21E-4 (0.649)	3.98E-4 (0.615)	4.15E-4 (0.640)	3.40E-4 (0.525)	3.61E-4 (0.557)
Postburn matrix leach 2	1.45E-5 (0.022)	9.74E-6 (0.015)	1.15E-5 (0.018)	8.73E-6 (0.013)	9.85E-6 (0.015)
Postburn particle leach 1	1.14E-5 (0.018)	4.81E-6 (0.0074)	6.74E-6 (0.010)	5.09E-6 (0.0079)	5.72E-6 (0.0088)
Postburn particle leach 2	1.72E-6 (0.0027)	5.81E-7 (0.0009)	1.89E-6 (0.0029)	1.22E-6 (0.0019)	1.62E-6 (0.0025)
Total	2.81E-3 (4.337)	2.80E-3 (4.322)	2.62E-3 (4.046)	2.54E-3 (3.927)	2.69E-3 (4.145)

Note: Values are reported as compact inventory fractions and particle equivalents (in parentheses).
[a] A scaling factor was applied to account for ~189 particles not included in the postburn analysis.

Appendix Table A-5. Exposed U and Pu detected by DLBL of AGR-2 Compact 3-4-2

DLBL Step	^{235}U	^{236}U	^{238}U	^{239}Pu	^{240}Pu
Deconsolidation acid	2.94E-6 (0.0045)	1.13E-6 (0.0017)	1.93E-6 (0.0030)	1.38E-6 (0.0021)	1.65E-6 (0.0026)
Preburn leach 1	4.52E-4 (0.697)	5.18E-4 (0.800)	4.49E-4 (0.692)	5.04E-4 (0.778)	5.42E-4 (0.837)
Preburn leach 2	8.41E-4 (1.297)	9.10E-4 (1.404)	8.43E-4 (1.301)	7.61E-4 (1.174)	8.19E-4 (1.264)
Preburn water rinse	4.12E-4 (0.636)	4.34E-4 (0.669)	4.13E-4 (0.637)	4.64E-5 (0.072)	4.71E-5 (0.073)
Postburn matrix leach 1	1.16E-3 (1.797)	1.30E-3 (2.010)	1.41E-3 (2.170)	9.33E-4 (1.440)	9.76E-4 (1.507)
Postburn matrix leach 2	9.16E-5 (0.141)	1.01E-4 (0.156)	1.01E-4 (0.156)	8.06E-5 (0.124)	8.46E-5 (0.131)
Postburn particle leach 1	4.06E-3 (6.263)	4.76E-3 (7.340)	4.74E-3 (7.314)	4.17E-3 (6.439)	4.33E-3 (6.678)
Postburn particle leach 2	4.79E-6 (0.0074)	3.60E-6 (0.0056)	4.56E-6 (0.0070)	4.95E-6 (0.0076)	5.13E-6 (0.0079)
Total	7.03E-3 (10.843)	8.03E-3 (12.387)	7.96E-3 (12.281)	6.50E-3 (10.037)	6.80E-3 (10.499)

Note: Values are reported as compact inventory fractions and particle equivalents (in parentheses).

Appendix Table A-6. Exposed U and Pu detected by DLBL of AGR-2 Compact 3-4-1

DLBL Step	^{235}U	^{236}U	^{238}U	^{239}Pu	^{240}Pu
Postburn matrix leach 1 [a]	2.71E-3 (4.178)	2.93E-3 (4.524)	2.96E-3 (4.562)	2.00E-3 (3.080)	2.16E-3 (3.326)
Postburn matrix leach 2	1.20E-6 (0.0019)	8.03E-7 (0.0012)	1.78E-6 (0.0027)	1.62E-6 (0.0025)	1.93E-6 (0.0030)
Postburn particle leach 1	1.30E-3 (2.009)	1.45E-3 (2.233)	1.47E-3 (2.263)	1.25E-3 (1.932)	1.39E-3 (2.145)
Postburn particle leach 2	4.28E-6 (0.0066)	2.88E-6 (0.0044)	4.96E-6 (0.0077)	6.79E-6 (0.010)	7.58E-6 (0.012)
Total	4.01E-3 (6.195)	4.38E-3 (6.762)	4.43E-3 (6.835)	3.26E-3 (5.025)	3.56E-3 (5.486)

Note: Values are reported as compact inventory fractions and particle equivalents (in parentheses).
[a] Reported values for the first postburn matrix leach include analyzed values for acid solution removed after deconsolidation, sieving, and digestion and solutions removed after each of two preburn matrix leaches.

Appendix Table A-7. Exposed inventory of typically tracked beta/gamma-emitting fission products detected by DLBL of AGR-2 Compact 3-1-2

DLBL Step	^{90}Sr	^{106}Ru	^{110m}Ag	^{125}Sb	^{134}Cs	^{137}Cs	^{144}Ce	^{154}Eu	^{155}Eu
Deconsolidation acid									
Preburn leach 1	8.41E-6 (0.013)	6.73E-6 (0.010)	<2.7E-3 <(4.097)	<9.0E-6 <(0.014)	1.29E-6 (0.0020)	1.72E-5 (0.027)	<4.4E-6 <(0.0068)	4.37E-5 (0.067)	5.33E-5 (0.082)
Preburn leach 2	6.89E-6 (0.011)	<1.5E-5 <(0.024)	<1.9E-3 <(2.903)	<2.5E-5 <(0.039)	9.82E-5 (0.152)	1.24E-4 (0.192)	8.64E-5 (0.133)	7.64E-5 (0.118)	9.07E-5 (0.140)
Postburn matrix leach 1	1.57E-4 (0.242)	6.18E-5 (0.095)	<2.6E-3 <(3.953)	<2.7E-5 <(0.042)	1.45E-4 (0.223)	1.98E-4 (0.306)	5.15E-4 (0.794)	4.35E-4 (0.671)	5.13E-4 (0.792)
Postburn matrix leach 2	8.98E-7 (0.0014)	1.51E-6 (0.0023)	<3.6E-4 <(0.554)	7.10E-6 (0.011)	5.56E-6 (0.0086)	8.85E-6 (0.014)	4.17E-6 (0.0064)	3.60E-6 (0.0056)	4.69E-6 (0.0072)
Postburn particle leach 1	3.05E-3 (4.711)	<4.9E-5 <(0.075)	<6.7E-3 <(10.277)	6.86E-4 (1.058)	1.12E-3 (1.728)	1.52E-3 (2.349)	2.86E-3 (4.419)	1.91E-3 (2.951)	2.43E-3 (3.751)
Postburn particle leach 2	7.35E-6 (0.011)	8.85E-6 (0.014)	<9.3E-4 <(1.428)	4.37E-5 (0.067)	3.02E-5 (0.047)	3.73E-5 (0.058)	7.37E-6 (0.011)	5.39E-6 (0.0083)	5.65E-6 (0.0087)
Total	3.23E-3 (4.989)	7.89E-5 (0.122)	- -	7.37E-4 (1.136)	1.40E-3 (2.160)	1.91E-3 (2.945)	3.48E-3 (5.364)	2.48E-3 (3.821)	3.10E-3 (4.781)

Note: Chemical separation and beta analysis were used to measure ^{90}Sr; other isotopes were measured by gamma spectrometry.
Note: Values are reported as compact inventory fractions and particle equivalents (in parentheses).
Note: A less-than value indicates that the concentration in the leachate was below the minimum detectable limit; these values are not included in the totals.

Appendix Table A-8. Exposed inventory of typically tracked beta/gamma-emitting fission products detected by DLBL of AGR-2 Compact 3-3-1

DLBL Step	^{90}Sr	^{106}Ru	^{110m}Ag	^{125}Sb	^{134}Cs	^{137}Cs	^{144}Ce	^{154}Eu	^{155}Eu
Deconsolidation acid	5.40E-6 (0.0083)	1.70E-6 (0.0026)	1.18E-3 (1.822)	<5.2E-6 <(0.0081)	<1.6E-7 <(0.0002)	3.98E-6 (0.0061)	4.83E-7 (0.0007)	5.64E-5 (0.087)	4.64E-5 (0.072)
Preburn leach 1	2.18E-6 (0.0034)	<6.9E-7 <(0.0011)	6.00E-4 (0.926)	<3.0E-6 <(0.0046)	1.41E-7 (0.0002)	2.05E-6 (0.0032)	5.32E-7 (0.0008)	4.25E-5 (0.066)	1.93E-5 (0.030)
Preburn leach 2	1.20E-6 (0.0019)	2.67E-7 (0.0004)	<3.1E-5 <(0.048)	<2.3E-6 <(0.0036)	7.63E-8 (0.0001)	1.80E-6 (0.0028)	9.22E-8 (0.0001)	7.39E-6 (0.011)	6.85E-6 (0.011)
Postburn matrix leach 1	5.11E-5 (0.079)	1.14E-6 (0.0018)	<5.4E-5 <(0.083)	<3.5E-6 <(0.0054)	2.88E-7 (0.0004)	1.44E-5 (0.022)	1.32E-6 (0.0020)	7.94E-5 (0.123)	8.69E-5 (0.134)
Postburn matrix leach 2	8.08E-7 (0.0012)	<1.1E-7 <(0.0002)	<7.5E-6 <(0.012)	<7.0E-7 <(0.0011)	3.82E-8 (0.0001)	1.33E-6 (0.0020)	4.60E-8 (0.0001)	1.63E-6 (0.0025)	1.20E-6 (0.0018)
Postburn particle leach 1 [a]	4.90E-6 (0.0076)	<1.4E-6 <(0.0021)	<1.1E-4 <(0.168)	<6.5E-6 <(0.010)	1.05E-5 (0.016)	1.57E-5 (0.024)	1.12E-6 (0.0017)	2.39E-5 (0.037)	2.73E-5 (0.042)
Postburn particle leach 2 [a]	8.24E-7 (0.0013)	<3.4E-7 <(0.0005)	<2.0E-5 <(0.030)	<1.7E-6 <(0.0027)	5.07E-7 (0.0008)	1.69E-6 (0.0026)	<1.1E-7 <(0.0002)	<1.8E-6 <(0.0028)	<1.3E-6 <(0.0020)
Total	6.65E-5 (0.103)	3.11E-6 (0.0048)	1.78E-3 (2.749)	- -	1.15E-5 (0.018)	4.09E-5 (0.063)	3.59E-6 (0.0055)	2.11E-4 (0.326)	1.88E-4 (0.290)

Note: Chemical separation and beta analysis were used to measure ^{90}Sr; other isotopes were measured by gamma spectrometry.
Note: Values are reported as compact inventory fractions and particle equivalents (in parentheses).
Note: A less-than value indicates that the concentration in the leachate was below the minimum detectable limit; these values are not included in the totals.
[a] A scaling factor was applied to account for ~169 particles not included in the postburn analysis

Appendix Table A-9. Exposed inventory of typically tracked beta/gamma-emitting fission products detected by DLBL of AGR-2 Compact 3-1-1

DLBL Step	^{90}Sr	^{106}Ru	^{110m}Ag	^{125}Sb	^{134}Cs	^{137}Cs	^{144}Ce	^{154}Eu	^{155}Eu
Deconsolidation acid	4.73E-5 (0.073)	<1.6E-6 <(0.0024)	<2.3E-4 <(0.351)	<2.9E-6 <(0.0045)	2.25E-6 (0.0035)	4.43E-6 (0.0068)	<1.1E-6 <(0.0017)	2.22E-5 (0.034)	2.67E-5 (0.041)
Preburn leach 1	1.95E-4 (0.301)	<3.0E-6 <(0.0046)	<3.9E-4 <(0.609)	<6.0E-6 <(0.0092)	5.51E-6 (0.0085)	1.39E-5 (0.021)	<2.2E-6 <(0.0034)	6.23E-5 (0.096)	7.53E-5 (0.116)
Preburn leach 2	1.27E-5 (0.020)	<6.2E-6 <(0.0096)	<5.1E-4 <(0.792)	<1.4E-5 <(0.022)	7.78E-6 (0.012)	3.20E-5 (0.049)	<4.0E-6 <(0.0062)	1.39E-5 (0.022)	1.97E-5 (0.030)
Postburn matrix leach 1	4.49E-4 (0.693)	3.04E-5 (0.047)	<1.1E-3 <(1.623)	4.42E-5 (0.068)	1.05E-4 (0.162)	1.60E-4 (0.247)	7.41E-4 (1.144)	4.65E-4 (0.718)	5.80E-4 (0.896)
Postburn matrix leach 2	4.71E-6 (0.0073)	3.55E-6 (0.0055)	<2.7E-4 <(0.416)	1.31E-5 (0.020)	4.36E-6 (0.0067)	7.48E-6 (0.012)	6.59E-6 (0.010)	8.46E-6 (0.013)	7.40E-6 (0.011)
Postburn particle leach 1 [a]	4.95E-5 (0.076)	<5.6E-6 <(0.0087)	<8.5E-4 <(1.316)	<8.5E-6 <(0.013)	1.90E-5 (0.029)	2.89E-5 (0.045)	9.91E-6 (0.015)	4.06E-5 (0.063)	5.37E-5 (0.083)
Postburn particle leach 2 [a]	1.97E-6 (0.0030)	4.14E-6 (0.0064)	<6.5E-4 <(1.007)	<5.8E-6 <(0.009)	3.48E-6 (0.0054)	5.73E-6 (0.0088)	1.33E-5 (0.020)	<2.4E-6 <(0.0037)	<2.5E-6 <(0.0038)
Total	7.60E-4 (1.173)	3.81E-5 (0.059)	- -	5.73E-5 (0.088)	1.48E-4 (0.228)	2.53E-4 (0.390)	7.71E-4 (1.190)	6.13E-4 (0.946)	7.63E-4 (1.178)

Note: Chemical separation and beta analysis were used to measure ^{90}Sr; other isotopes were measured by gamma spectrometry.
Note: Values are reported as compact inventory fractions and particle equivalents (in parentheses).
Note: A less-than value indicates that the concentration in the leachate was below the minimum detectable limit; these values are not included in the totals.
[a] A scaling factor was applied to account for ~207 particles not included in the postburn analysis.

Appendix Table A-10. Exposed inventory of typically tracked beta/gamma-emitting fission products detected by DLBL of AGR-2 Compact 3-3-2

DLBL Step	^{90}Sr	^{106}Ru	^{110m}Ag	^{125}Sb	^{134}Cs	^{137}Cs	^{144}Ce	^{154}Eu	^{155}Eu
Deconsolidation acid	1.24E-3 (1.909)	<8.1E-7 <(0.0012)	<3.3E-5 <(0.052)	<6.6E-6 <(0.010)	2.21E-5 (0.034)	2.67E-5 (0.041)	4.57E-7 (0.0007)	1.76E-4 (0.271)	2.22E-3 (3.422)
Preburn leach 1	2.91E-3 (4.494)	2.07E-4 (0.319)	1.89E-4 (0.291)	<4.3E-5 <(0.066)	4.42E-4 (0.682)	5.30E-4 (0.818)	1.54E-3 (2.374)	6.73E-4 (1.039)	5.53E-4 (0.853)
Preburn leach 2	1.14E-4 (0.176)	2.59E-4 (0.399)	1.56E-4 (0.241)	<2.6E-5 <(0.041)	2.26E-4 (0.349)	2.78E-4 (0.428)	7.31E-4 (1.128)	2.30E-4 (0.354)	1.38E-4 (0.213)
Preburn water rinse	2.25E-4 (0.347)	2.71E-5 (0.042)	<3.5E-5 <(0.054)	2.31E-5 (0.036)	2.43E-5 (0.038)	3.52E-5 (0.054)	5.01E-5 (0.077)	2.51E-5 (0.039)	2.29E-5 (0.035)
Postburn matrix leach 1	2.46E-3 (3.796)	5.79E-5 (0.089)	<7.5E-5 <(0.115)	<1.3E-5 <(0.021)	2.75E-4 (0.425)	3.52E-4 (0.544)	3.08E-4 (0.476)	9.64E-4 (1.487)	9.69E-4 (1.496)
Postburn matrix leach 2	1.97E-5 (0.030)	4.66E-5 (0.072)	1.56E-5 (0.024)	5.06E-5 (0.078)	3.04E-5 (0.047)	4.15E-5 (0.064)	1.72E-5 (0.027)	5.57E-5 (0.086)	5.89E-5 (0.091)
Postburn particle leach 1 [a]	8.55E-3 (13.187)	<9.4E-7 <(0.0014)	<3.8E-5 <(0.059)	<6.9E-6 <(0.011)	4.34E-5 (0.067)	5.32E-5 (0.082)	6.28E-6 (0.0097)	1.95E-4 (0.302)	2.31E-4 (0.356)
Postburn particle leach 2 [a]	4.05E-5 (0.062)	<2.9E-7 <(0.0005)	<1.2E-5 <(0.019)	<2.4E-6 <(0.0037)	2.31E-6 (0.0036)	3.71E-6 (0.0057)	<8.6E-8 <(0.0001)	2.51E-6 (0.0039)	2.26E-6 (0.0035)
Total	1.56E-2 (24.001)	5.97E-4 (0.921)	3.60E-4 (0.556)	7.37E-5 (0.114)	1.07E-3 (1.645)	1.32E-3 (2.037)	2.65E-3 (4.092)	2.32E-3 (3.581)	4.19E-3 (6.471)

Note: Chemical separation and beta analysis were used to measure ^{90}Sr; other isotopes were measured by gamma spectrometry.
Note: Values are reported as compact inventory fractions and particle equivalents (in parentheses).
Note: A less-than value indicates that the concentration in the leachate was below the minimum detectable limit; these values are not included in the totals.
[a] A scaling factor was applied to account for ~189 particles not included in the postburn analysis.

Appendix Table A-11. Exposed inventory of typically tracked beta/gamma-emitting fission products detected by DLBL of AGR-2 Compact 3-4-2

DLBL Step	^{90}Sr	^{106}Ru	^{110m}Ag	^{125}Sb	^{134}Cs	^{137}Cs	^{144}Ce	^{154}Eu	^{155}Eu
Deconsolidation acid	9.69E-4 (1.496)	<1.3E-6 <(0.0021)	<4.8E-5 <(0.075)	<1.0E-5 <(0.016)	8.98E-5 (0.139)	1.06E-4 (0.163)	<4.1E-7 <(0.0006)	7.01E-5 (0.108)	8.12E-5 (0.125)
Preburn leach 1	4.84E-3 (7.472)	6.16E-5 (0.095)	<4.1E-4 <(0.631)	<1.7E-4 <(0.259)	1.31E-3 (2.024)	1.31E-3 (2.021)	6.03E-4 (0.930)	4.57E-4 (0.706)	3.90E-4 (0.602)
Preburn leach 2	3.18E-4 (0.491)	2.06E-4 (0.318)	2.41E-4 (0.372)	<1.8E-5 <(0.028)	2.95E-4 (0.456)	3.53E-4 (0.545)	9.70E-4 (1.496)	2.41E-4 (0.372)	1.14E-4 (0.176)
Preburn water rinse	2.76E-4 (0.427)	1.20E-4 (0.186)	9.44E-5 (0.146)	<1.5E-5 <(0.023)	7.01E-5 (0.108)	8.32E-5 (0.128)	3.85E-4 (0.594)	1.23E-4 (0.189)	7.63E-5 (0.118)
Postburn matrix leach 1	6.71E-3 (10.355)	1.09E-4 (0.168)	4.02E-4 (0.620)	<9.9E-5 <(0.153)	9.10E-4 (1.405)	9.63E-4 (1.485)	1.26E-3 (1.951)	2.05E-3 (3.168)	2.10E-3 (3.246)
Postburn matrix leach 2	4.51E-4 (0.696)	1.29E-4 (0.198)	6.33E-5 (0.098)	1.68E-5 (0.026)	6.49E-5 (0.100)	8.09E-5 (0.125)	1.46E-4 (0.226)	2.25E-4 (0.346)	2.28E-4 (0.352)
Postburn particle leach 1	5.45E-4 (0.842)	3.22E-4 (0.497)	3.82E-3 (5.888)	5.52E-4 (0.851)	2.67E-3 (4.124)	2.75E-3 (4.238)	4.55E-3 (7.016)	4.11E-3 (6.341)	3.75E-3 (5.787)
Postburn particle leach 2	1.20E-5 (0.019)	2.53E-5 (0.039)	<3.6E-5 <(0.056)	2.37E-5 (0.037)	3.60E-5 (0.056)	4.33E-5 (0.067)	3.37E-6 (0.0052)	5.06E-6 (0.0078)	3.20E-6 (0.0049)
Total	1.41E-2 (21.797)	9.73E-4 (1.502)	4.62E-3 (7.122)	5.92E-4 (0.914)	5.45E-3 (8.411)	5.69E-3 (8.772)	7.92E-3 (12.219)	7.28E-3 (11.238)	6.75E-3 (10.410)

Note: Chemical separation and beta analysis were used to measure ^{90}Sr; other isotopes were measured by gamma spectrometry.
Note: Values are reported as compact inventory fractions and particle equivalents (in parentheses).
Note: A less-than value indicates that the concentration in the leachate was below the minimum detectable limit; these values are not included in the totals.

Appendix Table A-12. Exposed inventory of typically tracked beta/gamma-emitting fission products detected by DLBL of AGR-2 Compact 3-4-1

DLBL Step	^{90}Sr	^{106}Ru	^{110m}Ag	^{125}Sb	^{134}Cs	^{137}Cs	^{144}Ce	^{154}Eu	^{155}Eu
Postburn matrix leach 1 [a]	3.82E-2 (58.984)	3.50E-4 (0.539)	<3.5E-3 <(5.411)	<4.4E-4 <(0.681)	7.94E-3 (12.254)	7.97E-3 (12.302)	3.23E-3 (4.987)	4.72E-3 (7.279)	4.22E-3 (6.515)
Postburn matrix leach 2	1.86E-4 (0.288)	7.53E-7 (0.0012)	<3.9E-5 <(0.061)	6.98E-6 (0.011)	2.10E-6 (0.0032)	3.42E-6 (0.0053)	1.05E-6 (0.0016)	2.70E-5 (0.042)	3.04E-5 (0.047)
Postburn particle leach 1	7.80E-3 (12.031)	<2.2E-5 <(0.034)	<1.8E-3 <(2.720)	5.14E-5 (0.079)	1.12E-3 (1.731)	1.36E-3 (2.093)	1.27E-3 (1.964)	1.53E-3 (2.353)	1.73E-3 (2.675)
Postburn particle leach 2	3.10E-5 (0.048)	<5.7E-6 <(0.0088)	<3.7E-4 <(0.565)	<2.0E-5 <(0.031)	5.23E-5 (0.081)	6.35E-5 (0.098)	2.69E-6 (0.0041)	<6.1E-6 <(0.0094)	<1.1E-5 <(0.017)
Total	4.62E-2 (71.351)	3.50E-4 (0.541)	- -	5.84E-5 (0.090)	9.12E-3 (14.068)	9.40E-3 (14.498)	4.51E-3 (6.957)	6.27E-3 (9.674)	5.99E-3 (9.237)

Note: Chemical separation and beta analysis were used to measure ^{90}Sr; other isotopes were measured by gamma spectrometry.
Note: Values are reported as compact inventory fractions and particle equivalents (in parentheses).
Note: A less-than value indicates that the concentration in the leachate was below the minimum detectable limit; these values are not included in the totals.
[a] Reported values for the first postburn matrix leach include analyzed values for acid solution removed after deconsolidation, sieving, and digestion and solutions removed after each of two preburn matrix leaches.

Appendix Table A-13. Exposed inventory of stable isotopes of interest detected by DLBL of AGR-2 Compact 3-1-2

DLBL Step	^{105}Pd	^{109}Ag	^{133}Cs	^{139}La	^{140}Ce	^{141}Pr	^{146}Nd	^{152}Sm	^{153}Eu	^{156}Gd
Deconsolidation acid										
Preburn leach 1	2.29E-4 (0.354)	1.76E-3 (2.719)	2.74E-5 (0.042)	3.67E-4 (0.566)	2.99E-4 (0.461)	4.92E-5 (0.076)	3.73E-5 (0.058)	6.20E-5 (0.096)	1.60E-4 (0.246)	3.62E-4 (0.558)
Preburn leach 2	<3.4E-5 <(0.052)	1.36E-4 (0.210)	1.24E-4 (0.192)	1.02E-4 (0.158)	1.02E-4 (0.158)	9.04E-5 (0.139)	7.59E-5 (0.117)	9.09E-5 (0.140)	1.10E-4 (0.170)	1.60E-4 (0.247)
Postburn matrix leach 1	2.55E-4 (0.394)	1.34E-4 (0.207)	2.00E-4 (0.309)	6.55E-4 (1.010)	6.86E-4 (1.059)	5.67E-4 (0.874)	4.92E-4 (0.759)	5.49E-4 (0.848)	6.42E-4 (0.990)	1.01E-3 (1.565)
Postburn matrix leach 2	<1.7E-5 <(0.026)	3.42E-5 (0.053)	7.52E-6 (0.012)	5.24E-6 (0.0081)	1.34E-5 (0.021)	3.52E-6 (0.0054)	3.10E-6 (0.0048)	<7.0E-6 <(0.011)	<9.2E-6 <(0.014)	<1.2E-5 <(0.019)
Postburn particle leach 1	9.53E-4 (1.470)	2.36E-3 (3.638)	1.44E-3 (2.229)	2.75E-3 (4.236)	2.67E-3 (4.113)	2.58E-3 (3.983)	2.22E-3 (3.418)	2.55E-3 (3.936)	2.38E-3 (3.679)	1.19E-3 (1.842)
Postburn particle leach 2	2.36E-4 (0.364)	5.09E-5 (0.079)	3.73E-5 (0.058)	9.32E-6 (0.014)	1.21E-5 (0.019)	7.45E-6 (0.012)	6.49E-6 (0.010)	<1.0E-5 <(0.015)	<1.3E-5 <(0.020)	<1.7E-5 <(0.027)
Total	1.67E-3 (2.582)	4.47E-3 (6.904)	1.84E-3 (2.841)	3.88E-3 (5.992)	3.78E-3 (5.830)	3.30E-3 (5.090)	2.83E-3 (4.367)	3.25E-3 (5.020)	3.30E-3 (5.086)	2.73E-3 (4.212)

Note: Chemical separation and beta analysis were used to measure ^{90}Sr; other isotopes were measured by gamma spectrometry.
Note: Values are reported as compact inventory fractions and particle equivalents (in parentheses).
Note: A less-than value indicates that the concentration in the leachate was below the minimum detectable limit; these values are not included in the totals.

Appendix Table A-14. Exposed inventory of stable isotopes of interest detected by DLBL of AGR-2 Compact 3-3-1

DLBL Step	^{105}Pd	^{109}Ag	^{133}Cs	^{139}La	^{140}Ce	^{141}Pr	^{146}Nd	^{152}Sm	^{153}Eu	^{156}Gd
Deconsolidation acid	2.66E-3 (4.108)	1.17E-3 (1.808)	<9.2E-7 <(0.0014)	4.18E-4 (0.645)	5.03E-4 (0.776)	6.96E-5 (0.107)	4.90E-5 (0.076)	2.09E-5 (0.032)	8.95E-5 (0.138)	3.11E-4 (0.479)
Preburn leach 1	2.11E-2 (32.524)	5.80E-4 (0.895)	8.10E-6 (0.013)	2.68E-4 (0.414)	3.54E-4 (0.547)	4.24E-5 (0.065)	3.03E-5 (0.047)	<9.2E-6 <(0.014)	7.54E-5 (0.116)	2.20E-4 (0.339)
Preburn leach 2	1.02E-3 (1.566)	<3.5E-5 <(0.054)	7.55E-6 (0.012)	<1.8E-6 <(0.0028)	2.17E-5 (0.033)	6.59E-6 (0.010)	3.29E-6 (0.0051)	<1.6E-5 <(0.025)	<2.2E-5 <(0.034)	<3.0E-5 <(0.046)
Postburn matrix leach 1	2.27E-2 (35.002)	<1.1E-4 <(0.173)	1.69E-5 (0.026)	1.98E-4 (0.306)	2.47E-4 (0.382)	5.13E-5 (0.079)	3.10E-5 (0.048)	<5.3E-5 <(0.081)	1.48E-4 (0.229)	2.97E-4 (0.458)
Postburn matrix leach 2	5.68E-5 (0.088)	<1.0E-5 <(0.015)	1.67E-6 (0.0026)	3.49E-6 (0.0054)	8.52E-6 (0.013)	1.50E-6 (0.0023)	<7.9E-7 <(0.0012)	<4.7E-6 <(0.0072)	<6.3E-6 <(0.0097)	<8.5E-6 <(0.013)
Postburn particle leach 1 [a]	2.25E-3 (3.479)	1.32E-4 (0.203)	2.62E-5 (0.040)	2.58E-4 (0.398)	2.68E-4 (0.413)	4.69E-5 (0.072)	3.66E-5 (0.056)	2.40E-5 (0.037)	6.75E-5 (0.104)	3.33E-4 (0.514)
Postburn particle leach 2 [a]	1.64E-4 (0.253)	<2.8E-5 <(0.043)	2.62E-6 (0.004)	6.84E-6 (0.011)	7.84E-6 (0.012)	2.16E-6 (0.0033)	<2.2E-6 <(0.0034)	<1.3E-5 <(0.020)	<1.7E-5 <(0.027)	<2.4E-5 <(0.036)
Total	4.99E-2 (77.020)	1.88E-3 (2.907)	6.31E-5 (0.097)	1.15E-3 (1.779)	1.41E-3 (2.177)	2.21E-4 (0.340)	1.50E-4 (0.232)	4.49E-5 (0.069)	3.81E-4 (0.588)	1.16E-3 (1.790)

Note: Chemical separation and beta analysis were used to measure ^{90}Sr; other isotopes were measured by gamma spectrometry.
Note: Values are reported as compact inventory fractions and particle equivalents (in parentheses).
Note: A less-than value indicates that the concentration in the leachate was below the minimum detectable limit; these values are not included in the totals.
[a] A scaling factor was applied to account for ~169 particles not included in the postburn analysis

Appendix Table A-15. Exposed inventory of stable isotopes of interest detected by DLBL of AGR-2 Compact 3-1-1

DLBL Step	^{105}Pd	^{109}Ag	^{133}Cs	^{139}La	^{140}Ce	^{141}Pr	^{146}Nd	^{152}Sm	^{153}Eu	^{156}Gd
Deconsolidation acid	<1.9E-5 <(0.029)	1.30E-4 (0.200)	4.86E-6 (0.0075)	2.24E-5 (0.034)	1.55E-5 (0.024)	3.38E-6 (0.0052)	2.63E-6 (0.0041)	1.05E-5 (0.016)	4.19E-5 (0.065)	3.47E-5 (0.054)
Preburn leach 1	<2.1E-5 <(0.032)	1.61E-4 (0.249)	1.68E-5 (0.026)	8.21E-5 (0.127)	7.42E-5 (0.115)	7.93E-6 (0.012)	5.26E-6 (0.0081)	3.57E-5 (0.055)	1.26E-4 (0.194)	1.12E-4 (0.172)
Preburn leach 2	<2.8E-5 <(0.044)	1.08E-4 (0.167)	3.34E-5 (0.052)	1.76E-5 (0.027)	2.08E-5 (0.032)	5.36E-6 (0.0083)	4.43E-6 (0.0068)	<1.2E-5 <(0.018)	2.42E-5 (0.037)	3.09E-5 (0.048)
Postburn matrix leach 1	1.51E-4 (0.233)	1.87E-4 (0.289)	1.38E-4 (0.212)	9.06E-4 (1.397)	8.62E-4 (1.331)	6.45E-4 (0.996)	5.52E-4 (0.851)	6.42E-4 (0.991)	5.92E-4 (0.914)	1.04E-3 (1.608)
Postburn matrix leach 2	<2.1E-5 <(0.033)	<1.9E-5 <(0.029)	4.89E-6 (0.0075)	1.10E-5 (0.017)	1.90E-5 (0.029)	6.24E-6 (0.0096)	5.39E-6 (0.0083)	<9.0E-6 <(0.014)	<1.2E-5 <(0.018)	<1.6E-5 <(0.024)
Postburn particle leach 1 [a]	3.06E-5 (0.047)	7.34E-5 (0.113)	2.99E-5 (0.046)	1.34E-4 (0.207)	9.88E-5 (0.152)	2.35E-5 (0.036)	1.88E-5 (0.029)	2.16E-5 (0.033)	8.99E-5 (0.139)	2.87E-4 (0.443)
Postburn particle leach 2 [a]	<3.5E-5 <(0.054)	9.59E-5 (0.148)	6.90E-6 (0.011)	5.22E-6 (0.0081)	6.83E-6 (0.011)	2.66E-6 (0.0041)	2.56E-6 (0.0039)	<1.5E-5 <(0.023)	<1.9E-5 <(0.030)	<2.6E-5 <(0.040)
Total	1.81E-4 (0.280)	7.56E-4 (1.167)	2.34E-4 (0.361)	1.18E-3 (1.818)	1.10E-3 (1.694)	6.94E-4 (1.071)	5.91E-4 (0.911)	7.10E-4 (1.096)	8.74E-4 (1.349)	1.51E-3 (2.324)

Note: Chemical separation and beta analysis were used to measure ^{90}Sr; other isotopes were measured by gamma spectrometry.
Note: Values are reported as compact inventory fractions and particle equivalents (in parentheses).
Note: A less-than value indicates that the concentration in the leachate was below the minimum detectable limit; these values are not included in the totals.
[a] A scaling factor was applied to account for ~207 particles not included in the postburn analysis.

Appendix Table A-16. Exposed inventory of stable isotopes of interest detected by DLBL of AGR-2 Compact 3-3-2

DLBL Step	^{105}Pd	^{109}Ag	^{133}Cs	^{139}La	^{140}Ce	^{141}Pr	^{146}Nd	^{152}Sm	^{153}Eu	^{156}Gd
Deconsolidation acid	<1.6E-5 <(0.025)	8.61E-5 (0.133)	2.65E-5 (0.041)	5.42E-5 (0.084)	4.04E-5 (0.062)	6.94E-6 (0.011)	4.97E-6 (0.0077)	3.01E-5 (0.047)	2.52E-4 (0.389)	9.67E-5 (0.149)
Preburn leach 1	2.01E-4 (0.310)	5.41E-4 (0.835)	5.28E-4 (0.815)	1.76E-3 (2.718)	1.68E-3 (2.594)	1.62E-3 (2.493)	1.40E-3 (2.159)	1.57E-3 (2.422)	8.77E-4 (1.354)	2.58E-3 (3.987)
Preburn leach 2	1.29E-4 (0.199)	3.11E-4 (0.479)	2.38E-4 (0.368)	5.86E-4 (0.904)	6.03E-4 (0.930)	6.19E-4 (0.955)	5.44E-4 (0.839)	6.08E-4 (0.938)	2.40E-4 (0.370)	9.46E-4 (1.460)
Preburn water rinse	<2.7E-5 <(0.042)	6.16E-5 (0.095)	3.52E-5 (0.054)	4.89E-5 (0.075)	4.89E-5 (0.075)	4.69E-5 (0.072)	4.09E-5 (0.063)	4.47E-5 (0.069)	2.24E-5 (0.035)	7.24E-5 (0.112)
Postburn matrix leach 1	6.93E-4 (1.069)	3.77E-4 (0.582)	3.53E-4 (0.545)	5.19E-4 (0.801)	4.66E-4 (0.719)	3.60E-4 (0.555)	3.12E-4 (0.482)	4.04E-4 (0.624)	1.31E-3 (2.015)	7.80E-4 (1.204)
Postburn matrix leach 2	<1.7E-5 <(0.027)	2.56E-5 (0.040)	1.91E-5 (0.030)	1.09E-5 (0.017)	1.39E-5 (0.021)	8.64E-6 (0.013)	7.68E-6 (0.012)	8.54E-6 (0.013)	2.47E-5 (0.038)	2.18E-5 (0.034)
Postburn particle leach 1 [a]	<8.1E-5 <(0.125)	<7.1E-5 <(0.109)	1.69E-4 (0.261)	3.57E-4 (0.550)	2.70E-4 (0.417)	6.06E-5 (0.093)	4.63E-5 (0.071)	9.04E-5 (0.139)	8.10E-4 (1.250)	5.30E-4 (0.818)
Postburn particle leach 2 [a]	<3.2E-5 <(0.049)	<2.8E-5 <(0.043)	3.75E-6 (0.0058)	3.18E-6 (0.0049)	4.19E-6 (0.0065)	<1.6E-6 <(0.0024)	<2.2E-6 <(0.0034)	<1.3E-5 <(0.020)	<1.8E-5 <(0.027)	<2.4E-5 <(0.036)
Total	1.02E-3 (1.578)	1.40E-3 (2.164)	1.37E-3 (2.119)	3.34E-3 (5.154)	3.13E-3 (4.826)	2.72E-3 (4.193)	2.36E-3 (3.634)	2.76E-3 (4.251)	3.53E-3 (5.450)	5.03E-3 (7.764)

Note: Chemical separation and beta analysis were used to measure ^{90}Sr; other isotopes were measured by gamma spectrometry.
Note: Values are reported as compact inventory fractions and particle equivalents (in parentheses).
Note: A less-than value indicates that the concentration in the leachate was below the minimum detectable limit; these values are not included in the totals.
[a] A scaling factor was applied to account for ~189 particles not included in the postburn analysis.

Appendix Table A-17. Exposed inventory of stable isotopes of interest detected by DLBL of AGR-2 Compact 3-4-2

DLBL Step	^{105}Pd	^{109}Ag	^{133}Cs	^{139}La	^{140}Ce	^{141}Pr	^{146}Nd	^{152}Sm	^{153}Eu	^{156}Gd
Deconsolidation acid	<3.5E-5 <(0.054)	3.69E-5 (0.057)	1.00E-4 (0.155)	3.18E-5 (0.049)	2.68E-5 (0.041)	4.89E-6 (0.0076)	3.95E-6 (0.0061)	1.93E-5 (0.030)	1.07E-4 (0.165)	3.81E-5 (0.059)
Preburn leach 1	1.66E-4 (0.257)	2.38E-4 (0.367)	1.28E-3 (1.976)	7.61E-4 (1.174)	7.42E-4 (1.145)	5.86E-4 (0.905)	5.05E-4 (0.779)	6.09E-4 (0.940)	5.69E-4 (0.879)	8.93E-4 (1.378)
Preburn leach 2	2.82E-4 (0.435)	4.20E-4 (0.648)	3.68E-4 (0.567)	1.16E-3 (1.783)	1.07E-3 (1.652)	1.00E-3 (1.551)	8.44E-4 (1.303)	8.96E-4 (1.382)	2.93E-4 (0.451)	1.27E-3 (1.953)
Preburn water rinse	<8.4E-5 <(0.129)	8.75E-5 (0.135)	7.37E-5 (0.114)	3.57E-4 (0.550)	3.46E-4 (0.534)	3.27E-4 (0.505)	2.87E-4 (0.442)	2.98E-4 (0.460)	1.33E-4 (0.206)	4.39E-4 (0.678)
Postburn matrix leach 1	9.37E-4 (1.446)	2.20E-3 (3.402)	8.39E-4 (1.295)	1.37E-3 (2.115)	1.33E-3 (2.058)	1.19E-3 (1.837)	1.05E-3 (1.614)	1.25E-3 (1.922)	2.17E-3 (3.343)	1.81E-3 (2.796)
Postburn matrix leach 2	4.33E-5 (0.067)	1.93E-4 (0.297)	6.89E-5 (0.106)	1.20E-4 (0.186)	1.18E-4 (0.182)	1.03E-4 (0.159)	9.03E-5 (0.139)	1.04E-4 (0.160)	1.83E-4 (0.283)	1.56E-4 (0.240)
Postburn particle leach 1	1.21E-3 (1.862)	3.94E-3 (6.076)	2.96E-3 (4.563)	5.42E-3 (8.361)	5.35E-3 (8.262)	5.33E-3 (8.231)	4.64E-3 (7.156)	5.33E-3 (8.229)	5.33E-3 (8.231)	7.84E-3 (12.095)
Postburn particle leach 2	3.24E-4 (0.499)	5.28E-5 (0.082)	4.34E-5 (0.067)	5.79E-6 (0.0089)	7.40E-6 (0.011)	4.01E-6 (0.0062)	3.89E-6 (0.0060)	<1.1E-5 <(0.016)	<1.4E-5 <(0.021)	<1.8E-5 <(0.028)
Total	2.96E-3 (4.566)	7.17E-3 (11.063)	5.73E-3 (8.843)	9.22E-3 (14.228)	9.00E-3 (13.887)	8.56E-3 (13.201)	7.42E-3 (11.446)	8.51E-3 (13.124)	8.79E-3 (13.558)	1.24E-2 (19.199)

Note: Chemical separation and beta analysis were used to measure ^{90}Sr; other isotopes were measured by gamma spectrometry.
Note: Values are reported as compact inventory fractions and particle equivalents (in parentheses).
Note: A less-than value indicates that the concentration in the leachate was below the minimum detectable limit; these values are not included in the totals.

Appendix Table A-18. Exposed inventory of stable isotopes of interest detected by DLBL of AGR-2 Compact 3-4-1

DLBL Step	^{105}Pd	^{109}Ag	^{133}Cs	^{139}La	^{140}Ce	^{141}Pr	^{146}Nd	^{152}Sm	^{153}Eu	^{156}Gd
Postburn matrix leach 1	1.01E-3 (1.556)	9.18E-4 (1.417)	8.55E-3 (13.187)	3.92E-3 (6.041)	3.82E-3 (5.887)	3.61E-3 (5.575)	3.11E-3 (4.801)	3.43E-3 (5.286)	5.59E-3 (8.628)	6.11E-3 (9.421)
Postburn matrix leach 2	<1.3E-5 <(0.020)	2.87E-5 (0.044)	3.07E-6 (0.0047)	3.34E-6 (0.0052)	6.51E-6 (0.010)	1.62E-6 (0.0025)	1.58E-6 (0.0024)	<5.3E-6 <(0.0082)	2.71E-5 (0.042)	<9.2E-6 <(0.014)
Postburn particle leach 1	7.91E-5 (0.122)	8.60E-4 (1.327)	1.47E-3 (2.264)	1.53E-3 (2.355)	1.52E-3 (2.345)	1.44E-3 (2.225)	1.25E-3 (1.936)	1.49E-3 (2.296)	2.13E-3 (3.289)	1.98E-3 (3.048)
Postburn particle leach 2	3.52E-5 (0.054)	3.53E-5 (0.054)	6.06E-5 (0.094)	7.94E-6 (0.012)	1.41E-5 (0.022)	4.77E-6 (0.0074)	4.33E-6 (0.0067)	<9.1E-6 <(0.014)	1.31E-5 (0.020)	<1.6E-5 <(0.024)
Total	1.12E-3 (1.732)	1.84E-3 (2.842)	1.01E-2 (15.549)	5.45E-3 (8.414)	5.36E-3 (8.264)	5.06E-3 (7.809)	4.37E-3 (6.746)	4.91E-3 (7.582)	7.76E-3 (11.979)	8.08E-3 (12.469)

Note: Chemical separation and beta analysis were used to measure ^{90}Sr; other isotopes were measured by gamma spectrometry.
Note: Values are reported as compact inventory fractions and particle equivalents (in parentheses).
Note: A less-than value indicates that the concentration in the leachate was below the minimum detectable limit; these values are not included in the totals.
[a] Reported values for the first postburn matrix leach include analyzed values for acid solution removed after deconsolidation, sieving, and digestion and solutions removed after each of two preburn matrix leaches.

Appendix Table A-19. ^{238}U detected in DLBL solutions

DLBL Step	3-1-2	3-3-1	3-1-1	3-3-2	3-4-2	3-4-1
Deconsolidation acid [a]		8.18E-6 (0.013)	3.75E-6 (0.0058)	2.24E-6 (0.0035)	1.93E-6 (0.0030)	
Preburn leach 1	2.82E-5 (0.043)	4.68E-6 (0.0072)	1.17E-6 (0.0018)	1.38E-3 (2.137)	4.49E-4 (0.692)	
Preburn leach 2 [b]	7.34E-5 (0.113)	2.93E-6 (0.0045)	6.72E-6 (0.010)	8.00E-4 (1.235)	1.26E-3 (1.938)	
Postburn matrix leach 1 [c]	6.55E-4 (1.011)	5.52E-5 (0.085)	6.85E-4 (1.058)	4.15E-4 (0.640)	1.41E-3 (2.170)	2.96E-3 (4.562)
Postburn matrix leach 2	3.77E-6 (0.0058)	2.40E-6 (0.0037)	6.68E-6 (0.010)	1.15E-5 (0.018)	1.01E-4 (0.156)	1.78E-6 (0.0027)
Postburn particle leach 1	2.89E-3 (4.466)	6.37E-6 (0.0098)	1.49E-5 (0.023)	6.74E-6 (0.010)	4.74E-3 (7.314)	1.47E-3 (2.263)
Postburn particle leach 2	1.06E-5 (0.016)	1.87E-6 (0.0029)	4.62E-6 (0.0071)	1.89E-6 (0.0029)	4.56E-6 (0.0070)	4.96E-6 (0.0077)
Subtotal of ^{238}U removed before IMGA survey	7.61E-4 (1.174)	7.34E-5 (0.113)	7.04E-4 (1.086)	2.61E-3 (4.032)	3.21E-3 (4.960)	2.96E-3 (4.565)
Total	3.67E-3 (5.656)	8.17E-5 (0.126)	7.23E-4 (1.116)	2.62E-3 (4.046)	7.96E-3 (12.281)	4.43E-3 (6.835)

Note: Values are reported as compact inventory fractions and particle equivalents (in parentheses).
[a] The deconsolidation acid from Compact 3-1-2 was combined with the first preburn leach acid.
[b] The second preburn leach values for Compacts 3-3-2 and 3-4-2 include analyses of a subsequent water rinse.
[c] The first postburn matrix leach values for Compact 3-4-1 include analyses of prior leach solutions.

Appendix Table A-20. ^{144}Ce detected in DLBL solutions

DLBL Step	3-1-2	3-3-1	3-1-1	3-3-2	3-4-2	3-4-1
Deconsolidation acid [a]		4.83E-7 (0.0007)	<1.1E-6 <(0.0017)	4.57E-7 (0.0007)	<4.1E-7 <(0.0006)	
Preburn leach 1	<4.4E-6 <(0.0068)	5.32E-7 (0.0008)	<2.2E-6 <(0.0034)	1.54E-3 (2.374)	6.03E-4 (0.930)	
Preburn leach 2	8.64E-5 (0.133)	9.22E-8 (0.0001)	<4.0E-6 <(0.0062)	7.81E-4 (1.205)	1.35E-3 (2.090)	
Postburn matrix leach 1	5.15E-4 (0.794)	1.32E-6 (0.0020)	7.41E-4 (1.144)	3.08E-4 (0.476)	1.26E-3 (1.951)	3.23E-3 (4.987)
Postburn matrix leach 2	4.17E-6 (0.0064)	4.60E-8 (0.0001)	6.59E-6 (0.010)	1.72E-5 (0.027)	1.46E-4 (0.226)	1.05E-6 (0.0016)
Postburn particle leach 1	2.86E-3 (4.419)	1.12E-6 (0.0017)	9.91E-6 (0.015)	6.28E-6 (0.0097)	4.55E-3 (7.016)	1.27E-3 (1.964)
Postburn particle leach 2	7.37E-6 (0.011)	<1.1E-7 <(0.0002)	1.33E-5 (0.020)	<8.6E-8 <(0.0001)	3.37E-6 (0.0052)	2.69E-6 (0.0041)
Subtotal of ^{238}U removed before IMGA survey	6.05E-4 (0.934)	2.47E-6 (0.0038)	7.48E-4 (1.154)	2.65E-3 (4.082)	3.37E-3 (5.198)	3.23E-3 (4.988)
Total	3.48E-3 (5.364)	3.59E-6 (0.0055)	7.71E-4 (1.190)	2.65E-3 (4.092)	7.92E-3 (12.219)	4.51E-3 (6.957)

Note: Values are reported as compact inventory fractions and particle equivalents (in parentheses).
[a] The deconsolidation acid from Compact 3-1-2 was combined with the first preburn leach acid.
[b] The second preburn leach values for Compacts 3-3-2 and 3-4-2 include analyses of a subsequent water rinse.
[c] The first postburn matrix leach values for Compact 3-4-1 include analyses of prior leach solutions.

APPENDIX B. IMGA DATA

The tables in this appendix document the IMGA data for key gamma-emitting fission products. Values are reported as measured activities in units of Bq that have been decay-corrected to one day after EOL and as various unitless ratios, as described in Section 2.2. The M/A values (e.g., Equation 2.1) are indicative of particle-to-particle variation in isotopic content. For particles with negligible radioisotope release, this particle-to-particle variation may be related to variation in fissionable material and/or burnup. Fissionable material in an as-fabricated particle may vary due to variation in kernel size (e.g., spherical kernels with different diameters or fragmented kernels), variation in kernel uranium fraction, and/or variation in uranium enrichment. Variation in local neutron fluence will cause a variation in burnup between spatially-separated particles even if the physical properties of the particles are identical. The M/AA values were adjusted using a normally well retained isotope, usually ^{137}Cs, to attempt to separate the variation in M/A as a function of fission product retention from the variation as a function of fissionable material and/or burnup. This makes the M/AA values (e.g., Equation 2.5) indicative of the fission product retention in a particle relative to the average of all measured RS particles. Particles with M/AA near unity for a given isotope exhibited close to average retention of that isotope. However, if a given isotope was released from a large fraction of particles, then an M/AA value of unity does not indicate good retention of that isotope. Such was often the case for ^{110m}Ag in particles from the AGR-1 and AGR-2 experiments (Demkowicz et al. 2016, Hunn et al. 2018a). The M/C values (e.g., Equation 2.4) provide an indication of the particle inventory relative to the average calculated inventory (Appendix E). For well retained isotopes, the mean M/C values are typically 1.00±0.10, in which the variation is mostly due to error in the calculated average inventories stemming from uncertainty in the values used for the calculation. For the AGR-1 and AGR-2 irradiations, the mean M/C values for ^{125}Sb and ^{154}Eu have been consistently offset from unity by more than 10% due to larger errors in the calculated values. For AGR-2 UO_2 compacts, the mean ^{125}Sb M/C values were 0.71–0.76 and the mean ^{154}Eu M/C values were 0.87–0.90, with no indications of significant general release of either isotope.

Appendix Table B-1. Radioisotopic inventories of particles from AGR-2 Compact 3-1-2

Particle	Value	^{106}Ru	^{110m}Ag	^{125}Sb	^{134}Cs	^{137}Cs	^{144}Ce	^{154}Eu
312-SP01	Bq	1.18E+7	<6.7E+4	2.35E+5	3.93E+6	4.83E+6	5.21E+7	1.32E+5
312-SP01	M/A	0.37	<0.46	0.53	0.39	0.60	0.82	0.41
312-SP01	M/AA	0.61	<0.76	0.88	0.66	1.00	1.36	0.68
312-SP01	M/C	0.69	<0.78	0.64	0.68	1.06	1.41	0.61
312-SP02	Bq	2.40E+7	<4.6E+4	3.75E+5	1.88E+6	1.32E+6	9.97E+4	6.84E+2
312-SP02	M/A	0.75	<0.32	0.84	0.19	0.16	0.00	0.00
312-SP02	M/AA	4.57	<1.95	5.13	1.15	1.00	0.01	0.01
312-SP02	M/C	5.12	<2.00	3.76	1.20	1.06	0.01	0.01
312-SP03	Bq	3.19E+7	<9.5E+4	4.43E+5	8.00E+6	6.61E+6	6.39E+7	3.17E+5
312-SP03	M/A	1.00	<0.66	0.99	0.80	0.82	1.00	0.99
312-SP03	M/AA	1.21	<0.80	1.21	0.98	1.00	1.22	1.20
312-SP03	M/C	1.36	<0.82	0.89	1.01	1.06	1.26	1.08
312-SP04	Bq	2.82E+7	1.86E+5	3.99E+5	8.55E+6	6.98E+6	5.80E+7	2.75E+5
312-SP04	M/A	0.88	1.28	0.90	0.86	0.87	0.91	0.86
312-SP04	M/AA	1.02	1.47	1.03	0.99	1.00	1.05	0.98
312-SP04	M/C	1.14	1.51	0.76	1.03	1.06	1.08	0.88
312-SP05	Bq	1.19E+7	<6.6E+4	2.44E+5	3.80E+6	4.89E+6	5.48E+7	1.27E+5
312-SP05	M/A	0.37	<0.45	0.55	0.38	0.61	0.86	0.39
312-SP05	M/AA	0.61	<0.74	0.90	0.63	1.00	1.41	0.65
312-SP05	M/C	0.69	<0.76	0.66	0.65	1.06	1.46	0.58
312-SP06	Bq	2.08E+7	<8.9E+4	3.30E+5	8.48E+6	6.76E+6	6.11E+7	2.53E+5
312-SP06	M/A	0.65	<0.61	0.74	0.85	0.84	0.96	0.79
312-SP06	M/AA	0.77	<0.73	0.88	1.01	1.00	1.14	0.94
312-SP06	M/C	0.87	<0.75	0.65	1.05	1.06	1.18	0.84
312-RS01	Bq	3.18E+7	<9.5E+4	4.53E+5	9.41E+6	7.97E+6	6.59E+7	3.11E+5
312-RS01	M/A	1.00	<0.66	1.02	0.94	0.99	1.04	0.97
312-RS01	M/AA	1.00	<0.66	1.03	0.95	1.00	1.04	0.98
312-RS01	M/C	1.13	<0.68	0.75	0.99	1.06	1.08	0.88
312-RS02	Bq	3.28E+7	2.31E+5	4.65E+5	9.89E+6	8.29E+6	6.85E+7	3.15E+5
312-RS02	M/A	1.03	1.59	1.04	0.99	1.03	1.08	0.98
312-RS02	M/AA	0.99	1.54	1.01	0.96	1.00	1.04	0.95
312-RS02	M/C	1.12	1.58	0.74	1.00	1.06	1.08	0.85
312-RS03	Bq	2.98E+7	1.40E+5	4.08E+5	8.89E+6	7.65E+6	6.35E+7	2.91E+5
312-RS03	M/A	0.93	0.96	0.92	0.89	0.95	1.00	0.91
312-RS03	M/AA	0.98	1.01	0.96	0.94	1.00	1.05	0.95
312-RS03	M/C	1.10	1.04	0.71	0.97	1.06	1.08	0.85
312-RS04	Bq	3.34E+7	<9.8E+4	4.39E+5	1.05E+7	8.34E+6	6.45E+7	3.32E+5
312-RS04	M/A	1.04	<0.67	0.99	1.06	1.04	1.01	1.03
312-RS04	M/AA	1.01	<0.65	0.95	1.02	1.00	0.98	1.00
312-RS04	M/C	1.13	<0.66	0.70	1.06	1.06	1.01	0.89
312-RS05	Bq	3.31E+7	1.56E+5	4.51E+5	1.06E+7	8.15E+6	6.29E+7	3.31E+5
312-RS05	M/A	1.04	1.07	1.01	1.06	1.02	0.99	1.03
312-RS05	M/AA	1.02	1.06	1.00	1.04	1.00	0.97	1.01
312-RS05	M/C	1.14	1.08	0.73	1.09	1.06	1.01	0.91
312-RS06	Bq	2.99E+7	<9.3E+4	4.15E+5	9.89E+6	7.65E+6	5.96E+7	3.11E+5
312-RS06	M/A	0.94	<0.64	0.93	0.99	0.95	0.94	0.97
312-RS06	M/AA	0.98	<0.67	0.98	1.04	1.00	0.98	1.02
312-RS06	M/C	1.10	<0.69	0.72	1.08	1.06	1.02	0.91

Note: All M/AA and M/C values were adjusted with the normalized ^{137}Cs activity.
Note: ^{110m}Ag M/A and M/AA values were normalized with the maximum mean value (i.e., MDL used for undetectable values).

Appendix Table B-1 continued. Radioisotopic inventories of particles from AGR-2 Compact 3-1-2

Particle	Value	^{106}Ru	^{110m}Ag	^{125}Sb	^{134}Cs	^{137}Cs	^{144}Ce	^{154}Eu
312-RS07	Bq	3.14E+7	<9.3E+4	4.49E+5	9.41E+6	7.89E+6	6.71E+7	3.02E+5
312-RS07	M/A	0.98	<0.64	1.01	0.94	0.98	1.05	0.94
312-RS07	M/AA	1.00	<0.65	1.03	0.96	1.00	1.07	0.96
312-RS07	M/C	1.12	<0.67	0.75	1.00	1.06	1.11	0.86
312-RS08	Bq	3.45E+7	1.23E+5	4.89E+5	1.16E+7	8.73E+6	6.48E+7	3.67E+5
312-RS08	M/A	1.08	0.84	1.10	1.17	1.09	1.02	1.14
312-RS08	M/AA	0.99	0.78	1.01	1.07	1.00	0.94	1.05
312-RS08	M/C	1.11	0.80	0.74	1.12	1.06	0.97	0.94
312-RS09	Bq	3.60E+7	<1.0E+5	4.81E+5	1.18E+7	8.90E+6	6.48E+7	3.81E+5
312-RS09	M/A	1.13	<0.71	1.08	1.19	1.11	1.02	1.19
312-RS09	M/AA	1.01	<0.64	0.98	1.07	1.00	0.92	1.07
312-RS09	M/C	1.14	<0.66	0.72	1.11	1.06	0.95	0.96
312-RS10	Bq	3.11E+7	1.36E+5	4.21E+5	9.62E+6	7.55E+6	5.82E+7	3.10E+5
312-RS10	M/A	0.97	0.93	0.95	0.97	0.94	0.91	0.96
312-RS10	M/AA	1.04	0.99	1.01	1.03	1.00	0.97	1.03
312-RS10	M/C	1.16	1.02	0.74	1.07	1.06	1.01	0.92
312-RS11	Bq	3.12E+7	2.25E+5	4.36E+5	8.94E+6	7.77E+6	6.51E+7	2.96E+5
312-RS11	M/A	0.98	1.55	0.98	0.90	0.97	1.02	0.92
312-RS11	M/AA	1.01	1.60	1.01	0.93	1.00	1.06	0.95
312-RS11	M/C	1.13	1.64	0.74	0.96	1.06	1.09	0.85
312-RS12	Bq	3.23E+7	1.32E+5	4.54E+5	9.58E+6	8.29E+6	6.82E+7	3.15E+5
312-RS12	M/A	1.01	0.91	1.02	0.96	1.03	1.07	0.98
312-RS12	M/AA	0.98	0.88	0.99	0.93	1.00	1.04	0.95
312-RS12	M/C	1.10	0.90	0.73	0.97	1.06	1.07	0.85
312-RS13	Bq	3.49E+7	1.54E+5	4.82E+5	1.05E+7	8.64E+6	6.94E+7	3.45E+5
312-RS13	M/A	1.09	1.06	1.08	1.05	1.08	1.09	1.08
312-RS13	M/AA	1.02	0.99	1.01	0.98	1.00	1.01	1.00
312-RS13	M/C	1.14	1.01	0.74	1.02	1.06	1.05	0.90
312-RS14	Bq	2.91E+7	1.48E+5	4.23E+5	9.01E+6	7.53E+6	6.14E+7	2.93E+5
312-RS14	M/A	0.91	1.02	0.95	0.90	0.94	0.97	0.91
312-RS14	M/AA	0.97	1.08	1.01	0.96	1.00	1.03	0.97
312-RS14	M/C	1.09	1.11	0.74	1.00	1.06	1.06	0.87
312-RS15	Bq	3.55E+7	1.12E+5	4.84E+5	1.06E+7	8.73E+6	7.04E+7	3.48E+5
312-RS15	M/A	1.11	0.77	1.09	1.06	1.09	1.11	1.08
312-RS15	M/AA	1.02	0.71	1.00	0.98	1.00	1.02	1.00
312-RS15	M/C	1.15	0.73	0.73	1.02	1.06	1.05	0.90
312-RS16	Bq	3.16E+7	1.61E+5	4.41E+5	9.26E+6	7.76E+6	6.40E+7	3.07E+5
312-RS16	M/A	0.99	1.11	0.99	0.93	0.97	1.01	0.96
312-RS16	M/AA	1.02	1.15	1.03	0.96	1.00	1.04	0.99
312-RS16	M/C	1.15	1.17	0.75	1.00	1.06	1.08	0.89
312-RS17	Bq	3.08E+7	1.13E+5	4.39E+5	9.87E+6	7.95E+6	6.06E+7	3.24E+5
312-RS17	M/A	0.96	0.77	0.99	0.99	0.99	0.95	1.01
312-RS17	M/AA	0.97	0.78	1.00	1.00	1.00	0.96	1.02
312-RS17	M/C	1.09	0.80	0.73	1.04	1.06	0.99	0.91
312-RS18	Bq	2.70E+7	<8.8E+4	3.87E+5	8.27E+6	6.92E+6	5.84E+7	2.66E+5
312-RS18	M/A	0.85	<0.60	0.87	0.83	0.86	0.92	0.83
312-RS18	M/AA	0.98	<0.70	1.01	0.96	1.00	1.06	0.96
312-RS18	M/C	1.10	<0.72	0.74	1.00	1.06	1.10	0.86

Note: All M/AA and M/C values were adjusted with the normalized ^{137}Cs activity.
Note: ^{110m}Ag M/A and M/AA values were normalized with the maximum mean value (i.e., MDL used for undetectable values).

Appendix Table B-1 continued. Radioisotopic inventories of particles from AGR-2 Compact 3-1-2

Particle	Value	^{106}Ru	^{110m}Ag	^{125}Sb	^{134}Cs	^{137}Cs	^{144}Ce	^{154}Eu
312-RS19	Bq	3.03E+7	1.54E+5	4.17E+5	9.76E+6	7.37E+6	5.60E+7	3.13E+5
312-RS19	M/A	0.95	1.06	0.94	0.98	0.92	0.88	0.97
312-RS19	M/AA	1.03	1.15	1.02	1.07	1.00	0.96	1.06
312-RS19	M/C	1.16	1.18	0.75	1.11	1.06	0.99	0.95
312-RS20	Bq	3.15E+7	1.80E+5	4.43E+5	9.76E+6	7.92E+6	6.35E+7	3.17E+5
312-RS20	M/A	0.99	1.24	1.00	0.98	0.99	1.00	0.99
312-RS20	M/AA	1.00	1.26	1.01	0.99	1.00	1.01	1.00
312-RS20	M/C	1.12	1.29	0.74	1.03	1.06	1.05	0.90
312-RS21	Bq	3.73E+7	<1.1E+5	5.09E+5	1.18E+7	9.19E+6	7.01E+7	3.88E+5
312-RS21	M/A	1.17	<0.73	1.14	1.18	1.14	1.10	1.21
312-RS21	M/AA	1.02	<0.64	1.00	1.03	1.00	0.96	1.06
312-RS21	M/C	1.14	<0.65	0.73	1.07	1.06	0.99	0.95
312-RS22	Bq	3.56E+7	2.35E+5	4.90E+5	1.15E+7	8.85E+6	6.62E+7	3.70E+5
312-RS22	M/A	1.11	1.62	1.10	1.15	1.10	1.04	1.15
312-RS22	M/AA	1.01	1.47	1.00	1.05	1.00	0.94	1.05
312-RS22	M/C	1.13	1.51	0.73	1.09	1.06	0.98	0.94
312-RS23	Bq	3.07E+7	1.98E+5	4.34E+5	9.35E+6	7.54E+6	6.08E+7	3.05E+5
312-RS23	M/A	0.96	1.36	0.98	0.94	0.94	0.96	0.95
312-RS23	M/AA	1.02	1.45	1.04	1.00	1.00	1.02	1.01
312-RS23	M/C	1.15	1.49	0.76	1.04	1.06	1.05	0.91
312-RS24	Bq	3.39E+7	1.24E+5	4.73E+5	1.04E+7	8.33E+6	6.63E+7	3.37E+5
312-RS24	M/A	1.06	0.85	1.06	1.05	1.04	1.04	1.05
312-RS24	M/AA	1.02	0.82	1.03	1.01	1.00	1.00	1.01
312-RS24	M/C	1.15	0.84	0.75	1.05	1.06	1.04	0.91
312-RS25	Bq	3.30E+7	1.71E+5	4.54E+5	1.03E+7	7.92E+6	6.18E+7	3.32E+5
312-RS25	M/A	1.03	1.17	1.02	1.04	0.99	0.97	1.03
312-RS25	M/AA	1.05	1.19	1.04	1.05	1.00	0.99	1.05
312-RS25	M/C	1.17	1.22	0.76	1.10	1.06	1.02	0.94
312-RS26	Bq	2.92E+7	1.73E+5	4.07E+5	9.06E+6	7.32E+6	5.86E+7	2.83E+5
312-RS26	M/A	0.91	1.19	0.91	0.91	0.91	0.92	0.88
312-RS26	M/AA	1.00	1.31	1.00	1.00	1.00	1.01	0.97
312-RS26	M/C	1.12	1.34	0.74	1.04	1.06	1.04	0.87
312-RS27	Bq	3.27E+7	2.51E+5	4.66E+5	9.55E+6	8.24E+6	7.05E+7	3.07E+5
312-RS27	M/A	1.02	1.73	1.05	0.96	1.03	1.11	0.96
312-RS27	M/AA	1.00	1.69	1.02	0.93	1.00	1.08	0.93
312-RS27	M/C	1.12	1.73	0.75	0.97	1.06	1.12	0.84
312-RS28	Bq	3.31E+7	2.21E+5	4.71E+5	1.06E+7	8.68E+6	6.62E+7	3.46E+5
312-RS28	M/A	1.04	1.52	1.06	1.06	1.08	1.04	1.08
312-RS28	M/AA	0.96	1.41	0.98	0.98	1.00	0.96	1.00
312-RS28	M/C	1.08	1.45	0.72	1.02	1.06	0.99	0.89
312-RS29	Bq	2.83E+7	<9.1E+4	4.15E+5	8.48E+6	7.15E+6	5.82E+7	2.80E+5
312-RS29	M/A	0.89	<0.62	0.93	0.85	0.89	0.91	0.87
312-RS29	M/AA	1.00	<0.70	1.05	0.96	1.00	1.03	0.98
312-RS29	M/C	1.12	<0.72	0.77	1.00	1.06	1.06	0.88
312-RS30	Bq	2.56E+7	1.53E+5	3.63E+5	8.04E+6	6.59E+6	5.53E+7	2.58E+5
312-RS30	M/A	0.80	1.06	0.82	0.81	0.82	0.87	0.80
312-RS30	M/AA	0.98	1.29	0.99	0.98	1.00	1.06	0.98
312-RS30	M/C	1.10	1.32	0.73	1.02	1.06	1.09	0.88

Note: All M/AA and M/C values were adjusted with the normalized ^{137}Cs activity.
Note: ^{110m}Ag M/A and M/AA values were normalized with the maximum mean value (i.e., MDL used for undetectable values).

Appendix Table B-1 continued. Radioisotopic inventories of particles from AGR-2 Compact 3-1-2

Particle	Value	^{106}Ru	^{110m}Ag	^{125}Sb	^{134}Cs	^{137}Cs	^{144}Ce	^{154}Eu
312-RS31	Bq	3.40E+7	2.14E+5	4.71E+5	1.07E+7	8.42E+6	6.49E+7	3.49E+5
312-RS31	M/A	1.06	1.48	1.06	1.08	1.05	1.02	1.09
312-RS31	M/AA	1.02	1.41	1.01	1.03	1.00	0.97	1.04
312-RS31	M/C	1.14	1.44	0.74	1.07	1.06	1.01	0.93
312-RS32	Bq	3.12E+7	<9.9E+4	4.40E+5	9.92E+6	8.04E+6	6.19E+7	3.16E+5
312-RS32	M/A	0.98	<0.68	0.99	1.00	1.00	0.97	0.98
312-RS32	M/AA	0.98	<0.68	0.99	0.99	1.00	0.97	0.98
312-RS32	M/C	1.09	<0.69	0.72	1.03	1.06	1.00	0.88
312-RS33	Bq	3.28E+7	1.64E+5	4.53E+5	1.09E+7	8.51E+6	6.59E+7	3.38E+5
312-RS33	M/A	1.03	1.13	1.02	1.09	1.06	1.03	1.05
312-RS33	M/AA	0.97	1.06	0.96	1.03	1.00	0.98	0.99
312-RS33	M/C	1.09	1.09	0.71	1.07	1.06	1.01	0.89
312-RS34	Bq	2.94E+7	1.65E+5	4.21E+5	9.52E+6	7.70E+6	6.15E+7	3.01E+5
312-RS34	M/A	0.92	1.13	0.95	0.96	0.96	0.97	0.94
312-RS34	M/AA	0.96	1.18	0.99	1.00	1.00	1.01	0.98
312-RS34	M/C	1.08	1.21	0.73	1.04	1.06	1.04	0.88
312-RS35	Bq	2.87E+7	<9.2E+4	4.04E+5	9.07E+6	7.39E+6	6.13E+7	2.86E+5
312-RS35	M/A	0.90	<0.63	0.91	0.91	0.92	0.96	0.89
312-RS35	M/AA	0.98	<0.69	0.99	0.99	1.00	1.05	0.97
312-RS35	M/C	1.10	<0.71	0.72	1.03	1.06	1.08	0.87
312-RS36	Bq	3.35E+7	1.95E+5	4.45E+5	1.05E+7	8.19E+6	6.53E+7	3.30E+5
312-RS36	M/A	1.05	1.34	1.00	1.05	1.02	1.03	1.03
312-RS36	M/AA	1.03	1.31	0.98	1.03	1.00	1.01	1.01
312-RS36	M/C	1.15	1.35	0.72	1.08	1.06	1.04	0.90
312-RS37	Bq	2.99E+7	1.31E+5	4.24E+5	9.90E+6	7.85E+6	6.13E+7	3.16E+5
312-RS37	M/A	0.93	0.90	0.95	0.99	0.98	0.96	0.98
312-RS37	M/AA	0.96	0.93	0.97	1.02	1.00	0.99	1.01
312-RS37	M/C	1.07	0.95	0.72	1.06	1.06	1.02	0.90
312-RS38	Bq	3.01E+7	<9.6E+4	4.27E+5	9.66E+6	7.84E+6	6.02E+7	3.08E+5
312-RS38	M/A	0.94	<0.66	0.96	0.97	0.98	0.95	0.96
312-RS38	M/AA	0.97	<0.68	0.98	0.99	1.00	0.97	0.98
312-RS38	M/C	1.08	<0.69	0.72	1.03	1.06	1.00	0.88
312-RS39	Bq	3.31E+7	1.58E+5	4.64E+5	1.00E+7	8.44E+6	6.84E+7	3.32E+5
312-RS39	M/A	1.04	1.09	1.04	1.00	1.05	1.07	1.03
312-RS39	M/AA	0.98	1.03	0.99	0.96	1.00	1.02	0.98
312-RS39	M/C	1.10	1.06	0.73	0.99	1.06	1.06	0.88
312-RS40	Bq	2.93E+7	1.08E+5	3.99E+5	9.47E+6	7.37E+6	5.51E+7	3.02E+5
312-RS40	M/A	0.92	0.74	0.90	0.95	0.92	0.87	0.94
312-RS40	M/AA	1.00	0.81	0.98	1.04	1.00	0.94	1.02
312-RS40	M/C	1.12	0.83	0.72	1.08	1.06	0.97	0.92
312-RS41	Bq	3.14E+7	<9.8E+4	4.39E+5	9.75E+6	7.81E+6	6.13E+7	3.21E+5
312-RS41	M/A	0.98	<0.67	0.99	0.98	0.97	0.96	1.00
312-RS41	M/AA	1.01	<0.69	1.02	1.01	1.00	0.99	1.03
312-RS41	M/C	1.13	<0.71	0.74	1.05	1.06	1.02	0.92
312-RS42	Bq	3.52E+7	1.31E+5	4.74E+5	1.07E+7	8.51E+6	6.63E+7	3.43E+5
312-RS42	M/A	1.10	0.90	1.07	1.08	1.06	1.04	1.07
312-RS42	M/AA	1.04	0.85	1.01	1.01	1.00	0.98	1.01
312-RS42	M/C	1.16	0.87	0.74	1.06	1.06	1.02	0.91

Note: All M/AA and M/C values were adjusted with the normalized ^{137}Cs activity.
Note: ^{110m}Ag M/A and M/AA values were normalized with the maximum mean value (i.e., MDL used for undetectable values).

Appendix Table B-1 continued. Radioisotopic inventories of particles from AGR-2 Compact 3-1-2

Particle	Value	^{106}Ru	^{110m}Ag	^{125}Sb	^{134}Cs	^{137}Cs	^{144}Ce	^{154}Eu
312-RS43	Bq	3.43E+7	1.79E+5	4.60E+5	1.07E+7	8.46E+6	6.62E+7	3.46E+5
312-RS43	M/A	1.07	1.23	1.03	1.07	1.05	1.04	1.08
312-RS43	M/AA	1.02	1.17	0.98	1.02	1.00	0.99	1.02
312-RS43	M/C	1.14	1.20	0.72	1.06	1.06	1.02	0.92
312-RS44	Bq	3.36E+7	1.47E+5	4.65E+5	1.01E+7	8.34E+6	6.76E+7	3.27E+5
312-RS44	M/A	1.05	1.01	1.04	1.01	1.04	1.06	1.02
312-RS44	M/AA	1.01	0.97	1.01	0.97	1.00	1.02	0.98
312-RS44	M/C	1.13	1.00	0.74	1.01	1.06	1.06	0.88
312-RS45	Bq	3.41E+7	<1.1E+5	4.72E+5	1.12E+7	8.69E+6	6.51E+7	3.54E+5
312-RS45	M/A	1.07	<0.73	1.06	1.13	1.08	1.02	1.10
312-RS45	M/AA	0.99	<0.68	0.98	1.04	1.00	0.95	1.02
312-RS45	M/C	1.11	<0.69	0.72	1.08	1.06	0.98	0.92
Maximum	Bq	3.73E+7	2.51E+5	5.09E+5	1.18E+7	9.19E+6	7.05E+7	3.88E+5
Maximum	M/A	1.17	1.73	1.14	1.19	1.14	1.11	1.21
Maximum	M/AA	1.05	1.69	1.05	1.07	1.00	1.08	1.07
Maximum	M/C	1.17	1.73	0.77	1.12	1.06	1.12	0.96
Minimum	Bq	2.56E+7	<8.8E+4	3.63E+5	8.04E+6	6.59E+6	5.51E+7	2.58E+5
Minimum	M/A	0.80	<0.60	0.82	0.81	0.82	0.87	0.80
Minimum	M/AA	0.96	<0.64	0.95	0.93	1.00	0.92	0.93
Minimum	M/C	1.07	<0.65	0.70	0.96	1.06	0.95	0.84
Mean [a]	Bq	3.20E+7	1.2–1.5E+5	4.45E+5	9.97E+6	8.03E+6	6.36E+7	3.21E+5
Mean	M/A	1.00	<1.00	1.00	1.00	1.00	1.00	1.00
Mean	M/AA	1.00	<1.00	1.00	1.00	1.00	1.00	1.00
Mean	M/C	1.12	<1.03	0.73	1.04	1.06	1.03	0.90
SD	Bq	7.8%	>31.2%	6.8%	8.9%	7.0%	6.3%	8.8%
SD	M/A	7.8%	>31.2%	6.8%	8.9%	7.0%	6.3%	8.8%
SD	M/AA	2.3%	>30.5%	2.1%	3.9%	0.0%	4.0%	3.3%
SD	M/C	2.3%	>30.5%	2.1%	3.9%	0.0%	4.0%	3.3%

Note: All M/AA and M/C values were adjusted with the normalized ^{137}Cs activity.
Note: ^{110m}Ag M/A and M/AA values were normalized with the maximum mean value (i.e., MDL used for undetectable values).
Note: Special particles were not included in summary values.
[a] The range in mean activity for ^{110m}Ag was determined by assuming zero or MDL for undetectable values.

Appendix Table B-2. Radioisotopic inventories of particles from AGR-2 Compact 3-3-1

Particle	Value	^{106}Ru	^{110m}Ag	^{125}Sb	^{134}Cs	^{137}Cs	^{144}Ce	^{154}Eu
331-SP01	Bq	8.90E+4	<3.7E+3	0.00E+0	4.49E+4	1.06E+5	2.14E+5	2.48E+3
331-SP01	M/A	0.00	<0.03	0.00	0.00	0.01	0.00	0.01
331-SP01	M/AA	0.22	<2.18	0.00	0.36	1.00	0.25	0.62
331-SP01	M/C	0.24	<1.98	0.00	0.36	1.05	0.25	0.54
331-SP04	Bq	2.66E+7	1.46E+5	3.92E+5	8.46E+6	6.84E+6	5.64E+7	2.66E+5
331-SP04	M/A	0.89	1.17	0.89	0.91	0.88	0.89	0.90
331-SP04	M/AA	1.01	1.34	1.01	1.04	1.00	1.01	1.03
331-SP04	M/C	1.10	1.21	0.75	1.06	1.05	1.04	0.89
331-RS01	Bq	3.45E+7	1.63E+5	5.04E+5	1.02E+7	8.52E+6	6.97E+7	3.11E+5
331-RS01	M/A	1.15	1.31	1.14	1.10	1.09	1.10	1.05
331-RS01	M/AA	1.05	1.20	1.05	1.01	1.00	1.01	0.97
331-RS01	M/C	1.15	1.09	0.78	1.02	1.05	1.03	0.84
331-RS02	Bq	3.00E+7	1.11E+5	4.52E+5	8.80E+6	8.00E+6	6.81E+7	2.93E+5
331-RS02	M/A	1.00	0.90	1.02	0.95	1.02	1.07	0.99
331-RS02	M/AA	0.97	0.87	1.00	0.93	1.00	1.05	0.97
331-RS02	M/C	1.06	0.79	0.74	0.94	1.05	1.08	0.84
331-RS03	Bq	2.67E+7	1.18E+5	4.03E+5	8.70E+6	7.32E+6	5.83E+7	2.81E+5
331-RS03	M/A	0.89	0.95	0.91	0.94	0.94	0.92	0.95
331-RS03	M/AA	0.95	1.02	0.97	1.00	1.00	0.98	1.01
331-RS03	M/C	1.04	0.92	0.73	1.02	1.05	1.01	0.88
331-RS04	Bq	2.88E+7	7.65E+4	4.42E+5	8.97E+6	7.78E+6	6.31E+7	2.93E+5
331-RS04	M/A	0.96	0.62	1.00	0.97	1.00	0.99	0.99
331-RS04	M/AA	0.96	0.62	1.00	0.97	1.00	1.00	1.00
331-RS04	M/C	1.05	0.56	0.75	0.99	1.05	1.02	0.86
331-RS05	Bq	2.72E+7	1.32E+5	4.03E+5	8.18E+6	7.06E+6	5.94E+7	2.64E+5
331-RS05	M/A	0.90	1.06	0.91	0.88	0.90	0.94	0.89
331-RS05	M/AA	1.00	1.17	1.01	0.98	1.00	1.04	0.99
331-RS05	M/C	1.09	1.06	0.75	0.99	1.05	1.06	0.86
331-RS06	Bq	3.06E+7	1.27E+5	4.52E+5	1.01E+7	8.19E+6	6.28E+7	3.19E+5
331-RS06	M/A	1.02	1.03	1.02	1.09	1.05	0.99	1.08
331-RS06	M/AA	0.97	0.98	0.98	1.04	1.00	0.94	1.03
331-RS06	M/C	1.06	0.89	0.73	1.05	1.05	0.97	0.90
331-RS07	Bq	3.10E+7	1.18E+5	4.73E+5	8.77E+6	8.01E+6	6.88E+7	2.88E+5
331-RS07	M/A	1.03	0.95	1.07	0.95	1.03	1.09	0.97
331-RS07	M/AA	1.01	0.93	1.04	0.92	1.00	1.06	0.95
331-RS07	M/C	1.10	0.84	0.78	0.94	1.05	1.09	0.82
331-RS08	Bq	3.44E+7	1.54E+5	5.03E+5	1.12E+7	8.93E+6	6.61E+7	3.49E+5
331-RS08	M/A	1.15	1.25	1.14	1.21	1.14	1.04	1.18
331-RS08	M/AA	1.00	1.09	1.00	1.06	1.00	0.91	1.03
331-RS08	M/C	1.09	0.99	0.74	1.07	1.05	0.94	0.90
331-RS09	Bq	2.83E+7	1.09E+5	4.25E+5	9.05E+6	7.61E+6	6.12E+7	2.91E+5
331-RS09	M/A	0.94	0.88	0.96	0.98	0.97	0.97	0.99
331-RS09	M/AA	0.97	0.90	0.99	1.00	1.00	0.99	1.01
331-RS09	M/C	1.05	0.81	0.74	1.02	1.05	1.02	0.88
331-RS10	Bq	2.89E+7	1.02E+5	4.32E+5	9.42E+6	7.81E+6	6.13E+7	2.98E+5
331-RS10	M/A	0.96	0.82	0.98	1.02	1.00	0.97	1.01
331-RS10	M/AA	0.96	0.82	0.98	1.02	1.00	0.97	1.01
331-RS10	M/C	1.05	0.74	0.73	1.03	1.05	0.99	0.88

Note: All M/AA and M/C values were adjusted with the normalized ^{137}Cs activity.

Appendix Table B-2 continued. Radioisotopic inventories of particles from AGR-2 Compact 3-3-1

Particle	Value	^{106}Ru	^{110m}Ag	^{125}Sb	^{134}Cs	^{137}Cs	^{144}Ce	^{154}Eu
331-RS11	Bq	3.11E+7	1.46E+5	4.45E+5	8.89E+6	7.68E+6	6.49E+7	2.84E+5
331-RS11	M/A	1.03	1.18	1.01	0.96	0.98	1.02	0.96
331-RS11	M/AA	1.05	1.20	1.02	0.98	1.00	1.04	0.98
331-RS11	M/C	1.14	1.09	0.76	0.99	1.05	1.07	0.85
331-RS12	Bq	2.81E+7	1.12E+5	4.15E+5	8.84E+6	7.43E+6	6.02E+7	2.79E+5
331-RS12	M/A	0.93	0.90	0.94	0.96	0.95	0.95	0.94
331-RS12	M/AA	0.98	0.95	0.99	1.00	1.00	1.00	0.99
331-RS12	M/C	1.07	0.86	0.74	1.02	1.05	1.02	0.86
331-RS13	Bq	2.99E+7	1.04E+5	4.49E+5	9.34E+6	8.18E+6	6.79E+7	3.02E+5
331-RS13	M/A	0.99	0.84	1.02	1.01	1.05	1.07	1.02
331-RS13	M/AA	0.95	0.80	0.97	0.96	1.00	1.02	0.98
331-RS13	M/C	1.04	0.72	0.72	0.98	1.05	1.05	0.85
331-RS14	Bq	2.79E+7	9.17E+4	4.24E+5	7.78E+6	7.20E+6	6.54E+7	2.58E+5
331-RS14	M/A	0.93	0.74	0.96	0.84	0.92	1.03	0.88
331-RS14	M/AA	1.01	0.80	1.04	0.91	1.00	1.12	0.95
331-RS14	M/C	1.10	0.73	0.78	0.92	1.05	1.15	0.82
331-RS15	Bq	2.91E+7	8.43E+4	4.16E+5	9.52E+6	7.83E+6	6.12E+7	2.98E+5
331-RS15	M/A	0.97	0.68	0.94	1.03	1.00	0.97	1.01
331-RS15	M/AA	0.97	0.68	0.94	1.03	1.00	0.96	1.01
331-RS15	M/C	1.05	0.61	0.70	1.04	1.05	0.99	0.87
331-RS16	Bq	2.98E+7	9.79E+4	4.40E+5	9.06E+6	7.92E+6	6.22E+7	3.07E+5
331-RS16	M/A	0.99	0.79	1.00	0.98	1.01	0.98	1.04
331-RS16	M/AA	0.98	0.78	0.98	0.97	1.00	0.97	1.03
331-RS16	M/C	1.07	0.71	0.73	0.98	1.05	0.99	0.89
331-RS17	Bq	3.24E+7	1.95E+5	4.51E+5	1.01E+7	7.97E+6	6.17E+7	3.22E+5
331-RS17	M/A	1.08	1.57	1.02	1.09	1.02	0.97	1.09
331-RS17	M/AA	1.06	1.54	1.00	1.07	1.00	0.95	1.07
331-RS17	M/C	1.15	1.39	0.74	1.08	1.05	0.98	0.93
331-RS18	Bq	2.81E+7	1.25E+5	4.15E+5	8.47E+6	7.44E+6	6.36E+7	2.69E+5
331-RS18	M/A	0.93	1.00	0.94	0.92	0.95	1.00	0.91
331-RS18	M/AA	0.98	1.05	0.99	0.96	1.00	1.05	0.96
331-RS18	M/C	1.07	0.96	0.73	0.97	1.05	1.08	0.83
331-RS19	Bq	2.84E+7	7.34E+4	4.15E+5	8.66E+6	7.53E+6	5.95E+7	2.91E+5
331-RS19	M/A	0.94	0.59	0.94	0.94	0.96	0.94	0.99
331-RS19	M/AA	0.98	0.61	0.98	0.97	1.00	0.97	1.02
331-RS19	M/C	1.07	0.56	0.73	0.98	1.05	1.00	0.89
331-RS20	Bq	3.25E+7	1.71E+5	4.56E+5	1.01E+7	8.02E+6	6.24E+7	3.13E+5
331-RS20	M/A	1.08	1.38	1.03	1.09	1.03	0.98	1.06
331-RS20	M/AA	1.05	1.35	1.00	1.06	1.00	0.96	1.03
331-RS20	M/C	1.15	1.22	0.75	1.08	1.05	0.98	0.90
331-RS21	Bq	3.27E+7	1.38E+5	4.75E+5	1.06E+7	8.69E+6	6.76E+7	3.30E+5
331-RS21	M/A	1.09	1.12	1.08	1.15	1.11	1.07	1.12
331-RS21	M/AA	0.98	1.00	0.97	1.03	1.00	0.96	1.01
331-RS21	M/C	1.07	0.91	0.72	1.05	1.05	0.98	0.87
331-RS22	Bq	3.13E+7	1.55E+5	4.34E+5	9.68E+6	7.64E+6	5.97E+7	2.98E+5
331-RS22	M/A	1.04	1.25	0.98	1.05	0.98	0.94	1.01
331-RS22	M/AA	1.07	1.28	1.01	1.07	1.00	0.96	1.03
331-RS22	M/C	1.16	1.16	0.75	1.08	1.05	0.99	0.90

Note: All M/AA and M/C values were adjusted with the normalized ^{137}Cs activity.

Appendix Table B-2 continued. Radioisotopic inventories of particles from AGR-2 Compact 3-3-1

Particle	Value	^{106}Ru	^{110m}Ag	^{125}Sb	^{134}Cs	^{137}Cs	^{144}Ce	^{154}Eu
331-RS23	Bq	3.61E+7	1.90E+5	5.12E+5	1.12E+7	8.78E+6	6.85E+7	3.43E+5
331-RS23	M/A	1.20	1.53	1.16	1.21	1.12	1.08	1.16
331-RS23	M/AA	1.07	1.36	1.03	1.07	1.00	0.96	1.03
331-RS23	M/C	1.17	1.23	0.77	1.09	1.05	0.99	0.90
331-RS24	Bq	3.12E+7	1.24E+5	4.64E+5	9.87E+6	8.19E+6	6.63E+7	3.06E+5
331-RS24	M/A	1.04	1.00	1.05	1.07	1.05	1.05	1.04
331-RS24	M/AA	0.99	0.95	1.00	1.02	1.00	1.00	0.99
331-RS24	M/C	1.08	0.86	0.75	1.03	1.05	1.02	0.86
331-RS25	Bq	2.81E+7	1.19E+5	4.18E+5	7.45E+6	7.21E+6	6.39E+7	2.59E+5
331-RS25	M/A	0.94	0.96	0.95	0.81	0.92	1.01	0.88
331-RS25	M/AA	1.01	1.04	1.03	0.87	1.00	1.09	0.95
331-RS25	M/C	1.10	0.94	0.76	0.88	1.05	1.12	0.82
331-RS26	Bq	2.42E+7	1.07E+5	3.60E+5	7.30E+6	6.50E+6	5.53E+7	2.39E+5
331-RS26	M/A	0.81	0.86	0.81	0.79	0.83	0.87	0.81
331-RS26	M/AA	0.97	1.03	0.98	0.95	1.00	1.05	0.97
331-RS26	M/C	1.06	0.94	0.73	0.96	1.05	1.08	0.84
331-RS27	Bq	2.89E+7	9.59E+4	4.39E+5	9.11E+6	7.73E+6	6.23E+7	2.95E+5
331-RS27	M/A	0.96	0.77	0.99	0.98	0.99	0.98	1.00
331-RS27	M/AA	0.97	0.78	1.00	0.99	1.00	0.99	1.01
331-RS27	M/C	1.06	0.71	0.75	1.01	1.05	1.02	0.88
331-RS28	Bq	3.01E+7	1.13E+5	4.49E+5	9.03E+6	8.01E+6	6.77E+7	3.06E+5
331-RS28	M/A	1.00	0.91	1.02	0.98	1.03	1.07	1.04
331-RS28	M/AA	0.98	0.89	0.99	0.95	1.00	1.04	1.01
331-RS28	M/C	1.06	0.80	0.74	0.96	1.05	1.07	0.88
331-RS29	Bq	3.05E+7	1.20E+5	4.53E+5	9.70E+6	8.15E+6	6.55E+7	2.90E+5
331-RS29	M/A	1.01	0.97	1.03	1.05	1.04	1.03	0.98
331-RS29	M/AA	0.97	0.93	0.98	1.00	1.00	0.99	0.94
331-RS29	M/C	1.06	0.84	0.73	1.02	1.05	1.01	0.82
331-RS30	Bq	2.56E+7	9.68E+4	3.80E+5	8.33E+6	6.86E+6	5.53E+7	2.58E+5
331-RS30	M/A	0.85	0.78	0.86	0.90	0.88	0.87	0.87
331-RS30	M/AA	0.97	0.89	0.98	1.02	1.00	0.99	0.99
331-RS30	M/C	1.06	0.80	0.73	1.04	1.05	1.02	0.86
331-RS31	Bq	3.21E+7	1.48E+5	4.60E+5	9.98E+6	7.94E+6	6.15E+7	3.14E+5
331-RS31	M/A	1.07	1.20	1.04	1.08	1.02	0.97	1.06
331-RS31	M/AA	1.05	1.18	1.02	1.06	1.00	0.95	1.05
331-RS31	M/C	1.15	1.06	0.76	1.07	1.05	0.98	0.91
331-RS32	Bq	2.94E+7	1.31E+5	4.45E+5	8.34E+6	7.45E+6	6.51E+7	2.74E+5
331-RS32	M/A	0.98	1.06	1.01	0.90	0.95	1.03	0.93
331-RS32	M/AA	1.02	1.11	1.06	0.94	1.00	1.08	0.97
331-RS32	M/C	1.12	1.01	0.79	0.96	1.05	1.10	0.84
331-RS33	Bq	3.39E+7	1.80E+5	4.83E+5	1.02E+7	8.31E+6	6.88E+7	3.12E+5
331-RS33	M/A	1.13	1.45	1.09	1.10	1.06	1.09	1.06
331-RS33	M/AA	1.06	1.37	1.03	1.04	1.00	1.02	0.99
331-RS33	M/C	1.15	1.24	0.76	1.05	1.05	1.05	0.86
331-RS34	Bq	3.05E+7	1.34E+5	4.41E+5	9.36E+6	7.55E+6	6.03E+7	2.90E+5
331-RS34	M/A	1.02	1.08	1.00	1.01	0.97	0.95	0.98
331-RS34	M/AA	1.05	1.12	1.03	1.05	1.00	0.98	1.02
331-RS34	M/C	1.15	1.01	0.77	1.06	1.05	1.01	0.88

Note: All M/AA and M/C values were adjusted with the normalized ^{137}Cs activity.

Appendix Table B-2 continued. Radioisotopic inventories of particles from AGR-2 Compact 3-3-1

Particle	Value	^{106}Ru	^{110m}Ag	^{125}Sb	^{134}Cs	^{137}Cs	^{144}Ce	^{154}Eu
331-RS35	Bq	2.91E+7	9.76E+4	4.31E+5	9.30E+6	7.96E+6	6.48E+7	2.96E+5
331-RS35	M/A	0.97	0.79	0.98	1.00	1.02	1.02	1.00
331-RS35	M/AA	0.95	0.77	0.96	0.99	1.00	1.00	0.98
331-RS35	M/C	1.04	0.70	0.71	1.00	1.05	1.03	0.85
331-RS36	Bq	3.07E+7	1.04E+5	4.40E+5	9.49E+6	7.73E+6	6.14E+7	3.04E+5
331-RS36	M/A	1.02	0.83	1.00	1.03	0.99	0.97	1.03
331-RS36	M/AA	1.03	0.84	1.01	1.04	1.00	0.98	1.04
331-RS36	M/C	1.12	0.76	0.75	1.05	1.05	1.00	0.90
Maximum	Bq	3.61E+7	1.95E+5	5.12E+5	1.12E+7	8.93E+6	6.97E+7	3.49E+5
Maximum	M/A	1.20	1.57	1.16	1.21	1.14	1.10	1.18
Maximum	M/AA	1.07	1.54	1.06	1.07	1.00	1.12	1.07
Maximum	M/C	1.17	1.39	0.79	1.09	1.05	1.15	0.93
Minimum	Bq	2.42E+7	7.34E+4	3.60E+5	7.30E+6	6.50E+6	5.53E+7	2.39E+5
Minimum	M/A	0.81	0.59	0.81	0.79	0.83	0.87	0.81
Minimum	M/AA	0.95	0.61	0.94	0.87	1.00	0.91	0.94
Minimum	M/C	1.04	0.56	0.70	0.88	1.05	0.94	0.82
Mean	Bq	3.01E+7	1.24E+5	4.42E+5	9.25E+6	7.81E+6	6.34E+7	2.95E+5
Mean	M/A	1.00	1.00	1.00	1.00	1.00	1.00	1.00
Mean	M/AA	1.00	1.00	1.00	1.00	1.00	1.00	1.00
Mean	M/C	1.09	0.90	0.74	1.01	1.05	1.03	0.87
SD	Bq	8.4%	24.5%	7.2%	9.9%	6.6%	5.9%	8.0%
SD	M/A	8.4%	24.5%	7.2%	9.9%	6.6%	5.9%	8.0%
SD	M/AA	3.8%	22.0%	2.7%	4.9%	0.0%	4.5%	3.1%
SD	M/C	3.8%	22.0%	2.7%	4.9%	0.0%	4.5%	3.1%

Note: All M/AA and M/C values were adjusted with the normalized ^{137}Cs activity.
Note: Special particles were not included in summary values.

Appendix Table B-3. Radioisotopic inventories of particles from AGR-2 Compact 3-1-1

Particle	Value	^{106}Ru	^{110m}Ag	^{125}Sb	^{134}Cs	^{137}Cs	^{144}Ce	^{154}Eu
311-RS01	Bq	3.83E+7	1.33E+5	4.98E+5	1.19E+7	9.40E+6	7.38E+7	3.76E+5
311-RS01	M/A	1.25	1.03	1.17	1.31	1.21	1.16	1.23
311-RS01	M/AA	1.03	0.85	0.97	1.08	1.00	0.96	1.02
311-RS01	M/C	1.13	0.79	0.69	1.03	1.03	1.00	0.88
311-RS02	Bq	2.62E+7	1.21E+5	3.74E+5	7.90E+6	6.71E+6	5.87E+7	2.63E+5
311-RS02	M/A	0.86	0.94	0.88	0.87	0.87	0.92	0.86
311-RS02	M/AA	0.99	1.08	1.02	1.01	1.00	1.07	0.99
311-RS02	M/C	1.08	1.01	0.72	0.96	1.03	1.11	0.86
311-RS03	Bq	2.70E+7	<8.2E+4	3.77E+5	8.71E+6	7.15E+6	6.02E+7	2.79E+5
311-RS03	M/A	0.88	<0.63	0.89	0.96	0.92	0.95	0.91
311-RS03	M/AA	0.95	<0.68	0.96	1.04	1.00	1.03	0.99
311-RS03	M/C	1.05	<0.64	0.68	1.00	1.03	1.07	0.86
311-RS04	Bq	3.01E+7	1.55E+5	4.24E+5	9.79E+6	7.99E+6	6.45E+7	3.14E+5
311-RS04	M/A	0.98	1.20	1.00	1.08	1.03	1.01	1.03
311-RS04	M/AA	0.95	1.16	0.97	1.05	1.00	0.98	1.00
311-RS04	M/C	1.04	1.09	0.69	1.00	1.03	1.03	0.86
311-RS05	Bq	3.31E+7	<9.0E+4	4.55E+5	1.03E+7	8.53E+6	6.79E+7	3.32E+5
311-RS05	M/A	1.08	<0.70	1.07	1.13	1.10	1.07	1.09
311-RS05	M/AA	0.98	<0.63	0.97	1.03	1.00	0.97	0.99
311-RS05	M/C	1.07	<0.59	0.69	0.99	1.03	1.01	0.85
311-RS06	Bq	2.89E+7	<8.1E+4	4.14E+5	8.32E+6	7.41E+6	6.63E+7	2.76E+5
311-RS06	M/A	0.94	<0.62	0.98	0.92	0.96	1.04	0.90
311-RS06	M/AA	0.99	<0.65	1.02	0.96	1.00	1.09	0.94
311-RS06	M/C	1.08	<0.61	0.72	0.92	1.03	1.14	0.82
311-RS07	Bq	3.17E+7	<8.4E+4	4.37E+5	9.48E+6	7.86E+6	6.73E+7	3.03E+5
311-RS07	M/A	1.03	<0.65	1.03	1.04	1.01	1.06	0.99
311-RS07	M/AA	1.02	<0.64	1.01	1.03	1.00	1.04	0.98
311-RS07	M/C	1.12	<0.60	0.72	0.99	1.03	1.09	0.85
311-RS08	Bq	3.17E+7	1.31E+5	4.18E+5	9.99E+6	7.59E+6	5.84E+7	3.14E+5
311-RS08	M/A	1.03	1.01	0.98	1.10	0.98	0.92	1.03
311-RS08	M/AA	1.05	1.03	1.00	1.12	1.00	0.94	1.05
311-RS08	M/C	1.16	0.96	0.71	1.08	1.03	0.98	0.91
311-RS09	Bq	3.24E+7	1.28E+5	4.43E+5	1.00E+7	8.12E+6	6.46E+7	3.15E+5
311-RS09	M/A	1.06	0.99	1.04	1.10	1.05	1.02	1.03
311-RS09	M/AA	1.01	0.94	0.99	1.05	1.00	0.97	0.98
311-RS09	M/C	1.10	0.88	0.71	1.01	1.03	1.01	0.85
311-RS10	Bq	3.44E+7	1.86E+5	4.65E+5	1.06E+7	8.33E+6	6.62E+7	3.31E+5
311-RS10	M/A	1.12	1.44	1.09	1.16	1.07	1.04	1.08
311-RS10	M/AA	1.04	1.34	1.02	1.08	1.00	0.97	1.01
311-RS10	M/C	1.14	1.25	0.72	1.04	1.03	1.01	0.87
311-RS11	Bq	3.01E+7	1.72E+5	4.09E+5	9.12E+6	7.28E+6	5.95E+7	2.88E+5
311-RS11	M/A	0.98	1.33	0.96	1.00	0.94	0.94	0.94
311-RS11	M/AA	1.04	1.42	1.03	1.07	1.00	1.00	1.00
311-RS11	M/C	1.14	1.32	0.73	1.03	1.03	1.04	0.87
311-RS12	Bq	3.02E+7	1.43E+5	4.32E+5	9.32E+6	7.97E+6	6.81E+7	3.00E+5
311-RS12	M/A	0.98	1.11	1.02	1.03	1.03	1.07	0.98
311-RS12	M/AA	0.96	1.07	0.99	1.00	1.00	1.04	0.95
311-RS12	M/C	1.05	1.00	0.70	0.96	1.03	1.08	0.83

Note: All M/AA and M/C values were adjusted with the normalized ^{137}Cs activity.
Note: ^{110m}Ag M/A and M/AA values were normalized with the maximum mean value (i.e., MDL used for undetectable values).

Appendix Table B-3 continued. Radioisotopic inventories of particles from AGR-2 Compact 3-1-1

Particle	Value	^{106}Ru	^{110m}Ag	^{125}Sb	^{134}Cs	^{137}Cs	^{144}Ce	^{154}Eu
311-RS13	Bq	3.14E+7	1.15E+5	4.25E+5	1.04E+7	7.82E+6	6.01E+7	3.29E+5
311-RS13	M/A	1.03	0.89	1.00	1.14	1.01	0.95	1.08
311-RS13	M/AA	1.02	0.88	0.99	1.13	1.00	0.94	1.07
311-RS13	M/C	1.11	0.82	0.70	1.09	1.03	0.98	0.92
311-RS14	Bq	2.87E+7	1.63E+5	4.13E+5	8.33E+6	7.43E+6	6.67E+7	2.74E+5
311-RS14	M/A	0.94	1.26	0.97	0.92	0.96	1.05	0.90
311-RS14	M/AA	0.98	1.32	1.01	0.96	1.00	1.09	0.93
311-RS14	M/C	1.07	1.23	0.72	0.92	1.03	1.14	0.81
311-RS15	Bq	3.50E+7	1.38E+5	4.70E+5	1.14E+7	8.66E+6	6.63E+7	3.61E+5
311-RS15	M/A	1.14	1.07	1.11	1.26	1.12	1.04	1.18
311-RS15	M/AA	1.02	0.96	0.99	1.13	1.00	0.93	1.06
311-RS15	M/C	1.12	0.89	0.70	1.08	1.03	0.97	0.91
311-RS16	Bq	3.24E+7	1.93E+5	4.52E+5	1.05E+7	8.26E+6	6.54E+7	3.31E+5
311-RS16	M/A	1.06	1.49	1.06	1.15	1.07	1.03	1.08
311-RS16	M/AA	0.99	1.40	1.00	1.08	1.00	0.97	1.02
311-RS16	M/C	1.09	1.31	0.71	1.04	1.03	1.01	0.88
311-RS17	Bq	3.22E+7	1.54E+5	4.57E+5	9.39E+6	8.28E+6	7.07E+7	3.12E+5
311-RS17	M/A	1.05	1.19	1.08	1.03	1.07	1.11	1.02
311-RS17	M/AA	0.98	1.12	1.01	0.97	1.00	1.04	0.96
311-RS17	M/C	1.08	1.04	0.71	0.93	1.03	1.08	0.83
311-RS18	Bq	2.73E+7	1.86E+5	3.83E+5	8.05E+6	7.07E+6	6.20E+7	2.63E+5
311-RS18	M/A	0.89	1.44	0.90	0.89	0.91	0.98	0.86
311-RS18	M/AA	0.98	1.58	0.99	0.97	1.00	1.07	0.94
311-RS18	M/C	1.07	1.47	0.70	0.93	1.03	1.11	0.82
311-RS19	Bq	3.43E+7	<1.0E+5	4.66E+5	1.06E+7	8.57E+6	6.82E+7	3.35E+5
311-RS19	M/A	1.12	<0.78	1.10	1.17	1.11	1.07	1.10
311-RS19	M/AA	1.01	<0.70	0.99	1.06	1.00	0.97	0.99
311-RS19	M/C	1.11	<0.65	0.70	1.02	1.03	1.01	0.86
311-RS20	Bq	2.93E+7	<9.3E+4	4.17E+5	9.19E+6	7.79E+6	6.50E+7	2.93E+5
311-RS20	M/A	0.96	<0.72	0.98	1.01	1.01	1.02	0.96
311-RS20	M/AA	0.95	<0.71	0.98	1.01	1.00	1.02	0.96
311-RS20	M/C	1.04	<0.67	0.69	0.97	1.03	1.06	0.83
311-RS21	Bq	2.82E+7	9.81E+4	3.91E+5	8.72E+6	7.29E+6	6.39E+7	2.77E+5
311-RS21	M/A	0.92	0.76	0.92	0.96	0.94	1.01	0.91
311-RS21	M/AA	0.98	0.81	0.98	1.02	1.00	1.07	0.96
311-RS21	M/C	1.07	0.75	0.69	0.98	1.03	1.11	0.84
311-RS22	Bq	2.36E+7	1.49E+5	3.34E+5	7.60E+6	6.05E+6	5.06E+7	2.43E+5
311-RS22	M/A	0.77	1.16	0.79	0.84	0.78	0.80	0.80
311-RS22	M/AA	0.99	1.48	1.01	1.07	1.00	1.02	1.02
311-RS22	M/C	1.08	1.38	0.71	1.03	1.03	1.06	0.88
311-RS23	Bq	2.90E+7	<8.2E+4	4.01E+5	8.48E+6	7.33E+6	6.29E+7	2.76E+5
311-RS23	M/A	0.94	<0.64	0.95	0.93	0.95	0.99	0.90
311-RS23	M/AA	1.00	<0.67	1.00	0.99	1.00	1.04	0.96
311-RS23	M/C	1.09	<0.63	0.71	0.95	1.03	1.09	0.83
311-RS24	Bq	2.78E+7	<8.3E+4	3.95E+5	8.65E+6	7.32E+6	6.40E+7	2.81E+5
311-RS24	M/A	0.91	<0.64	0.93	0.95	0.94	1.01	0.92
311-RS24	M/AA	0.96	<0.68	0.98	1.01	1.00	1.07	0.98
311-RS24	M/C	1.05	<0.64	0.70	0.97	1.03	1.11	0.84

Note: All M/AA and M/C values were adjusted with the normalized ^{137}Cs activity.
Note: ^{110m}Ag M/A and M/AA values were normalized with the maximum mean value (i.e., MDL used for undetectable values).

Appendix Table B-3 continued. Radioisotopic inventories of particles from AGR-2 Compact 3-1-1

Particle	Value	^{106}Ru	^{110m}Ag	^{125}Sb	^{134}Cs	^{137}Cs	^{144}Ce	^{154}Eu
311-RS25	Bq	2.91E+7	<8.5E+4	4.23E+5	8.67E+6	7.44E+6	6.54E+7	2.82E+5
311-RS25	M/A	0.95	<0.66	1.00	0.96	0.96	1.03	0.92
311-RS25	M/AA	0.99	<0.69	1.04	1.00	1.00	1.07	0.96
311-RS25	M/C	1.08	<0.64	0.74	0.95	1.03	1.12	0.83
311-RS26	Bq	2.74E+7	<7.4E+4	3.71E+5	8.76E+6	6.89E+6	5.63E+7	2.77E+5
311-RS26	M/A	0.89	<0.57	0.87	0.97	0.89	0.89	0.91
311-RS26	M/AA	1.00	<0.64	0.98	1.09	1.00	1.00	1.02
311-RS26	M/C	1.10	<0.60	0.70	1.04	1.03	1.04	0.88
311-RS27	Bq	3.51E+7	1.28E+5	4.75E+5	1.11E+7	8.59E+6	6.56E+7	3.61E+5
311-RS27	M/A	1.14	0.99	1.12	1.22	1.11	1.03	1.18
311-RS27	M/AA	1.03	0.90	1.01	1.10	1.00	0.93	1.07
311-RS27	M/C	1.13	0.84	0.72	1.06	1.03	0.97	0.92
311-RS28	Bq	2.86E+7	1.03E+5	3.96E+5	9.14E+6	7.13E+6	5.74E+7	2.86E+5
311-RS28	M/A	0.93	0.80	0.93	1.01	0.92	0.90	0.93
311-RS28	M/AA	1.02	0.87	1.01	1.09	1.00	0.98	1.02
311-RS28	M/C	1.11	0.81	0.72	1.05	1.03	1.02	0.88
311-RS29	Bq	2.70E+7	<8.4E+4	3.81E+5	8.76E+6	7.16E+6	5.88E+7	2.75E+5
311-RS29	M/A	0.88	<0.65	0.90	0.96	0.92	0.93	0.90
311-RS29	M/AA	0.95	<0.70	0.97	1.04	1.00	1.00	0.98
311-RS29	M/C	1.05	<0.66	0.69	1.00	1.03	1.04	0.84
311-RS30	Bq	2.59E+7	1.30E+5	3.60E+5	7.59E+6	6.69E+6	6.05E+7	2.49E+5
311-RS30	M/A	0.84	1.01	0.85	0.84	0.86	0.95	0.81
311-RS30	M/AA	0.98	1.17	0.98	0.97	1.00	1.10	0.94
311-RS30	M/C	1.07	1.09	0.70	0.93	1.03	1.15	0.82
311-RS31	Bq	3.20E+7	1.48E+5	4.23E+5	9.85E+6	7.85E+6	6.58E+7	3.07E+5
311-RS31	M/A	1.05	1.14	1.00	1.09	1.01	1.04	1.01
311-RS31	M/AA	1.03	1.13	0.98	1.07	1.00	1.02	0.99
311-RS31	M/C	1.13	1.05	0.70	1.03	1.03	1.06	0.86
311-RS32	Bq	3.26E+7	1.37E+5	4.36E+5	9.96E+6	7.84E+6	6.39E+7	3.15E+5
311-RS32	M/A	1.06	1.06	1.03	1.10	1.01	1.00	1.03
311-RS32	M/AA	1.05	1.05	1.02	1.08	1.00	0.99	1.02
311-RS32	M/C	1.15	0.98	0.72	1.04	1.03	1.04	0.88
311-RS33	Bq	2.57E+7	1.51E+5	3.59E+5	7.98E+6	6.31E+6	5.20E+7	2.66E+5
311-RS33	M/A	0.84	1.17	0.85	0.88	0.81	0.82	0.87
311-RS33	M/AA	1.03	1.43	1.04	1.08	1.00	1.00	1.07
311-RS33	M/C	1.13	1.34	0.74	1.03	1.03	1.05	0.92
311-RS34	Bq	3.91E+7	1.76E+5	5.24E+5	1.20E+7	9.30E+6	7.23E+7	3.79E+5
311-RS34	M/A	1.27	1.37	1.23	1.33	1.20	1.14	1.24
311-RS34	M/AA	1.06	1.14	1.03	1.11	1.00	0.95	1.03
311-RS34	M/C	1.16	1.06	0.73	1.06	1.03	0.99	0.90
311-RS35	Bq	3.66E+7	1.91E+5	5.07E+5	1.16E+7	8.63E+6	6.63E+7	3.76E+5
311-RS35	M/A	1.20	1.48	1.19	1.28	1.11	1.04	1.23
311-RS35	M/AA	1.07	1.33	1.07	1.15	1.00	0.94	1.11
311-RS35	M/C	1.18	1.24	0.76	1.10	1.03	0.98	0.96
311-RS36	Bq	3.02E+7	1.85E+5	4.10E+5	9.43E+6	7.37E+6	5.88E+7	3.00E+5
311-RS36	M/A	0.99	1.43	0.97	1.04	0.95	0.92	0.98
311-RS36	M/AA	1.04	1.51	1.02	1.09	1.00	0.97	1.03
311-RS36	M/C	1.14	1.41	0.72	1.05	1.03	1.01	0.90

Note: All M/AA and M/C values were adjusted with the normalized ^{137}Cs activity.
Note: ^{110m}Ag M/A and M/AA values were normalized with the maximum mean value (i.e., MDL used for undetectable values).

Appendix Table B-3 continued. Radioisotopic inventories of particles from AGR-2 Compact 3-1-1

Particle	Value	^{106}Ru	^{110m}Ag	^{125}Sb	^{134}Cs	^{137}Cs	^{144}Ce	^{154}Eu
311-RS37	Bq	3.22E+7	1.01E+5	4.53E+5	9.54E+6	8.38E+6	7.36E+7	3.11E+5
311-RS37	M/A	1.05	0.78	1.07	1.05	1.08	1.16	1.02
311-RS37	M/AA	0.97	0.72	0.99	0.97	1.00	1.07	0.94
311-RS37	M/C	1.06	0.68	0.70	0.93	1.03	1.12	0.82
311-RS38	Bq	3.13E+7	1.26E+5	4.38E+5	9.94E+6	7.96E+6	6.22E+7	3.28E+5
311-RS38	M/A	1.02	0.98	1.03	1.09	1.03	0.98	1.08
311-RS38	M/AA	0.99	0.95	1.00	1.07	1.00	0.95	1.05
311-RS38	M/C	1.09	0.89	0.71	1.02	1.03	0.99	0.91
311-RS39	Bq	3.28E+7	1.47E+5	4.56E+5	1.08E+7	8.37E+6	6.44E+7	3.40E+5
311-RS39	M/A	1.07	1.14	1.07	1.19	1.08	1.01	1.11
311-RS39	M/AA	0.99	1.05	0.99	1.10	1.00	0.94	1.03
311-RS39	M/C	1.08	0.98	0.70	1.05	1.03	0.98	0.89
311-RS40	Bq	2.70E+7	<8.3E+4	3.83E+5	8.58E+6	7.05E+6	5.93E+7	2.77E+5
311-RS40	M/A	0.88	<0.64	0.90	0.95	0.91	0.93	0.91
311-RS40	M/AA	0.97	<0.70	0.99	1.04	1.00	1.03	1.00
311-RS40	M/C	1.06	<0.66	0.70	1.00	1.03	1.07	0.86
311-RS41	Bq	2.99E+7	1.63E+5	4.27E+5	9.21E+6	7.83E+6	6.66E+7	3.00E+5
311-RS41	M/A	0.97	1.26	1.01	1.01	1.01	1.05	0.98
311-RS41	M/AA	0.96	1.25	1.00	1.00	1.00	1.04	0.97
311-RS41	M/C	1.06	1.16	0.71	0.96	1.03	1.08	0.84
311-RS42	Bq	2.85E+7	<8.6E+4	3.94E+5	9.27E+6	7.36E+6	5.87E+7	2.95E+5
311-RS42	M/A	0.93	<0.67	0.93	1.02	0.95	0.92	0.96
311-RS42	M/AA	0.98	<0.70	0.98	1.08	1.00	0.97	1.02
311-RS42	M/C	1.07	<0.65	0.69	1.03	1.03	1.01	0.88
311-RS43	Bq	2.88E+7	1.25E+5	4.04E+5	9.30E+6	7.48E+6	6.00E+7	2.93E+5
311-RS43	M/A	0.94	0.97	0.95	1.02	0.97	0.94	0.96
311-RS43	M/AA	0.97	1.00	0.99	1.06	1.00	0.98	0.99
311-RS43	M/C	1.07	0.93	0.70	1.02	1.03	1.02	0.86
311-RS44	Bq	3.45E+7	2.36E+5	4.89E+5	2.14E+5	8.64E+6	6.24E+7	3.54E+5
311-RS44	M/A	1.12	1.83	1.15	0.02	1.12	0.98	1.16
311-RS44	M/AA	1.01	1.64	1.03	0.02	1.00	0.88	1.04
311-RS44	M/C	1.10	1.53	0.73	0.02	1.03	0.92	0.90
311-RS45	Bq	3.20E+7	<9.4E+4	4.51E+5	1.48E+5	8.16E+6	6.92E+7	3.07E+5
311-RS45	M/A	1.04	<0.73	1.06	0.02	1.05	1.09	1.01
311-RS45	M/AA	0.99	<0.69	1.01	0.02	1.00	1.03	0.95
311-RS45	M/C	1.08	<0.64	0.71	0.01	1.03	1.08	0.83

Note: All M/AA and M/C values were adjusted with the normalized ^{137}Cs activity.
Note: ^{110m}Ag M/A and M/AA values were normalized with the maximum mean value (i.e., MDL used for undetectable values).

Appendix Table B-3 continued. Radioisotopic inventories of particles from AGR-2 Compact 3-1-1

Particle	Value	^{106}Ru	^{110m}Ag	^{125}Sb	^{134}Cs	^{137}Cs	^{144}Ce	^{154}Eu
Maximum	Bq	3.91E+7	2.36E+5	5.24E+5	1.20E+7	9.40E+6	7.38E+7	3.79E+5
Maximum	M/A	1.27	1.83	1.23	1.33	1.21	1.16	1.24
Maximum	M/AA	1.07	1.64	1.07	1.15	1.00	1.10	1.11
Maximum	M/C	1.18	1.53	0.76	1.10	1.03	1.15	0.96
Minimum	Bq	2.36E+7	7.40E+4	3.34E+5	1.48E+5	6.05E+6	5.06E+7	2.43E+5
Minimum	M/A	0.77	<0.57	0.79	0.02	0.78	0.80	0.80
Minimum	M/AA	0.95	<0.63	0.96	0.02	1.00	0.88	0.93
Minimum	M/C	1.04	<0.59	0.68	0.01	1.03	0.92	0.81
Mean [a]	Bq	3.07E+7	1.0–1.3E+5	4.25E+5	9.08E+6	7.75E+6	6.36E+7	3.05E+5
Mean	M/A	1.00	<1.00	1.00	1.00	1.00	1.00	1.00
Mean	M/AA	1.00	<1.00	1.00	1.00	1.00	1.00	1.00
Mean	M/C	1.09	<0.94	0.71	0.96	1.03	1.04	0.87
SD	Bq	11.0%	30.4%	9.8%	24.6%	9.4%	7.9%	11.1%
SD	M/A	11.0%	>30.4%	9.8%	24.6%	9.4%	7.9%	11.1%
SD	M/AA	3.2%	>29.7%	2.2%	22.0%	0.0%	5.3%	4.1%
SD	M/C	3.2%	>29.7%	2.2%	22.0%	0.0%	5.3%	4.1%

Note: All M/AA and M/C values were adjusted with the normalized ^{137}Cs activity.
Note: ^{110m}Ag M/A and M/AA values were normalized with the maximum mean value (i.e., MDL used for undetectable values).
Note: Special particles were not included in summary values.
[a] The range in mean activity for ^{110m}Ag was determined by assuming zero or MDL for undetectable values.

Appendix Table B-4. Radioisotopic inventories of particles from AGR-2 Compact 3-3-2

Particle	Value	^{106}Ru	^{110m}Ag	^{125}Sb	^{134}Cs	^{137}Cs	^{144}Ce	^{154}Eu
332-SP01	Bq	2.55E+7	3.16E+3	3.72E+5	7.78E+5	6.78E+5	2.79E+6	6.13E+3
332-SP01	M/A	0.85	0.02	0.82	0.08	0.09	0.04	0.02
332-SP01	M/AA	9.75	0.27	9.37	0.97	1.00	0.50	0.23
332-SP01	M/C	10.36	0.26	7.09	0.96	1.03	0.51	0.20
332-SP02	Bq	1.81E+7	<2.5E+3	4.18E+5	1.32E+6	1.15E+6	1.28E+6	1.36E+4
332-SP02	M/A	0.61	<0.02	0.92	0.14	0.15	0.02	0.05
332-SP02	M/AA	4.07	<0.13	6.17	0.97	1.00	0.14	0.31
332-SP02	M/C	4.32	<0.12	4.67	0.96	1.03	0.14	0.26
332-SP03	Bq	2.20E+7	<2.7E+3	4.75E+5	1.79E+6	1.52E+6	1.18E+6	2.02E+4
332-SP03	M/A	0.74	<0.02	1.05	0.19	0.20	0.02	0.07
332-SP03	M/AA	3.76	<0.11	5.34	0.99	1.00	0.09	0.34
332-SP03	M/C	4.00	<0.10	4.04	0.99	1.03	0.10	0.30
332-SP04	Bq	2.15E+7	<2.7E+3	4.75E+5	1.79E+6	1.57E+6	1.06E+6	1.80E+4
332-SP04	M/A	0.72	<0.02	1.05	0.19	0.20	0.02	0.06
332-SP04	M/AA	3.55	<0.10	5.16	0.96	1.00	0.08	0.30
332-SP04	M/C	3.77	<0.10	3.90	0.95	1.03	0.08	0.26
332-SP05	Bq	3.22E+7	9.83E+4	4.99E+5	5.92E+6	5.26E+6	6.69E+7	3.36E+5
332-SP05	M/A	1.08	0.75	1.10	0.64	0.68	1.05	1.13
332-SP05	M/AA	1.59	1.10	1.62	0.95	1.00	1.55	1.66
332-SP05	M/C	1.69	1.04	1.23	0.94	1.03	1.58	1.44
332-SP06	Bq	3.20E+7	1.54E+5	4.76E+5	7.71E+6	6.71E+6	6.92E+7	2.91E+5
332-SP06	M/A	1.07	1.17	1.05	0.84	0.87	1.09	0.98
332-SP06	M/AA	1.24	1.35	1.21	0.97	1.00	1.26	1.12
332-SP06	M/C	1.31	1.27	0.91	0.96	1.03	1.28	0.97
332-RS01	Bq	3.44E+7	1.67E+5	5.20E+5	1.03E+7	8.59E+6	7.36E+7	3.28E+5
332-RS01	M/A	1.15	1.27	1.15	1.12	1.11	1.16	1.10
332-RS01	M/AA	1.04	1.14	1.03	1.01	1.00	1.04	0.99
332-RS01	M/C	1.10	1.08	0.78	1.00	1.03	1.06	0.86
332-RS02	Bq	2.97E+7	1.20E+5	4.46E+5	8.92E+6	7.50E+6	6.42E+7	2.91E+5
332-RS02	M/A	1.00	0.91	0.98	0.97	0.97	1.01	0.98
332-RS02	M/AA	1.03	0.94	1.01	1.00	1.00	1.04	1.01
332-RS02	M/C	1.09	0.88	0.77	0.99	1.03	1.06	0.87
332-RS03	Bq	3.15E+7	1.31E+5	4.79E+5	9.65E+6	8.10E+6	6.79E+7	3.18E+5
332-RS03	M/A	1.06	0.99	1.06	1.05	1.05	1.07	1.07
332-RS03	M/AA	1.01	0.95	1.01	1.00	1.00	1.02	1.02
332-RS03	M/C	1.07	0.89	0.76	1.00	1.03	1.04	0.88
332-RS04	Bq	2.57E+7	9.90E+4	3.94E+5	8.27E+6	6.96E+6	5.50E+7	2.79E+5
332-RS04	M/A	0.86	0.75	0.87	0.90	0.90	0.87	0.94
332-RS04	M/AA	0.96	0.84	0.96	1.00	1.00	0.96	1.04
332-RS04	M/C	1.02	0.79	0.73	0.99	1.03	0.98	0.90
332-RS05	Bq	2.79E+7	1.28E+5	4.28E+5	8.99E+6	7.45E+6	5.95E+7	2.93E+5
332-RS05	M/A	0.94	0.97	0.94	0.98	0.96	0.94	0.98
332-RS05	M/AA	0.97	1.01	0.98	1.02	1.00	0.97	1.02
332-RS05	M/C	1.03	0.95	0.74	1.01	1.03	0.99	0.88
332-RS06	Bq	2.94E+7	1.26E+5	4.57E+5	9.26E+6	7.85E+6	6.24E+7	3.05E+5
332-RS06	M/A	0.99	0.95	1.01	1.01	1.01	0.98	1.02
332-RS06	M/AA	0.97	0.94	0.99	0.99	1.00	0.97	1.01
332-RS06	M/C	1.03	0.89	0.75	0.99	1.03	0.99	0.87

Note: All M/AA and M/C values were adjusted with the normalized ^{137}Cs activity.

Appendix Table B-4 continued. Radioisotopic inventories of particles from AGR-2 Compact 3-3-2

Particle	Value	^{106}Ru	^{110m}Ag	^{125}Sb	^{134}Cs	^{137}Cs	^{144}Ce	^{154}Eu
332-RS07	Bq	2.53E+7	1.19E+5	3.81E+5	7.80E+6	6.52E+6	5.54E+7	2.50E+5
332-RS07	M/A	0.85	0.90	0.84	0.85	0.84	0.87	0.84
332-RS07	M/AA	1.01	1.07	1.00	1.01	1.00	1.04	0.99
332-RS07	M/C	1.07	1.01	0.75	1.00	1.03	1.06	0.86
332-RS08	Bq	2.87E+7	1.25E+5	4.34E+5	8.04E+6	7.07E+6	6.31E+7	2.63E+5
332-RS08	M/A	0.96	0.95	0.96	0.88	0.91	0.99	0.88
332-RS08	M/AA	1.05	1.04	1.05	0.96	1.00	1.09	0.96
332-RS08	M/C	1.12	0.98	0.79	0.95	1.03	1.11	0.84
332-RS09	Bq	3.11E+7	1.52E+5	4.72E+5	9.71E+6	8.04E+6	6.43E+7	3.12E+5
332-RS09	M/A	1.04	1.15	1.04	1.06	1.04	1.01	1.05
332-RS09	M/AA	1.00	1.11	1.00	1.02	1.00	0.98	1.01
332-RS09	M/C	1.07	1.04	0.76	1.01	1.03	0.99	0.87
332-RS10	Bq	2.85E+7	1.47E+5	4.32E+5	8.95E+6	7.43E+6	6.17E+7	2.84E+5
332-RS10	M/A	0.96	1.11	0.95	0.97	0.96	0.97	0.95
332-RS10	M/AA	1.00	1.16	0.99	1.01	1.00	1.01	0.99
332-RS10	M/C	1.06	1.09	0.75	1.01	1.03	1.03	0.86
332-RS11	Bq	2.88E+7	1.42E+5	4.48E+5	8.92E+6	7.64E+6	6.25E+7	2.90E+5
332-RS11	M/A	0.97	1.08	0.99	0.97	0.99	0.98	0.97
332-RS11	M/AA	0.98	1.09	1.00	0.98	1.00	1.00	0.98
332-RS11	M/C	1.04	1.03	0.76	0.98	1.03	1.02	0.85
332-RS12	Bq	2.88E+7	8.43E+4	4.59E+5	9.24E+6	7.73E+6	5.93E+7	3.04E+5
332-RS12	M/A	0.97	0.64	1.01	1.01	1.00	0.93	1.02
332-RS12	M/AA	0.97	0.64	1.01	1.01	1.00	0.93	1.02
332-RS12	M/C	1.03	0.60	0.77	1.00	1.03	0.95	0.88
332-RS13	Bq	3.40E+7	1.64E+5	4.99E+5	9.90E+6	8.26E+6	7.17E+7	3.17E+5
332-RS13	M/A	1.14	1.24	1.10	1.08	1.07	1.13	1.06
332-RS13	M/AA	1.07	1.17	1.03	1.01	1.00	1.06	1.00
332-RS13	M/C	1.14	1.10	0.78	1.00	1.03	1.08	0.86
332-RS14	Bq	3.17E+7	1.21E+5	4.97E+5	1.01E+7	8.60E+6	6.65E+7	3.34E+5
332-RS14	M/A	1.06	0.92	1.10	1.10	1.11	1.05	1.12
332-RS14	M/AA	0.96	0.83	0.99	0.99	1.00	0.94	1.01
332-RS14	M/C	1.02	0.78	0.75	0.98	1.03	0.96	0.87
332-RS15	Bq	3.16E+7	1.61E+5	4.69E+5	9.97E+6	8.27E+6	6.80E+7	3.16E+5
332-RS15	M/A	1.06	1.22	1.03	1.09	1.07	1.07	1.06
332-RS15	M/AA	0.99	1.14	0.97	1.02	1.00	1.00	0.99
332-RS15	M/C	1.06	1.08	0.73	1.01	1.03	1.02	0.86
332-RS16	Bq	2.95E+7	1.32E+5	4.49E+5	8.67E+6	7.32E+6	6.47E+7	2.73E+5
332-RS16	M/A	0.99	1.01	0.99	0.94	0.95	1.02	0.92
332-RS16	M/AA	1.05	1.06	1.05	1.00	1.00	1.08	0.97
332-RS16	M/C	1.11	1.00	0.79	0.99	1.03	1.10	0.84
332-RS17	Bq	3.18E+7	1.60E+5	4.88E+5	9.73E+6	8.39E+6	6.60E+7	3.26E+5
332-RS17	M/A	1.07	1.22	1.07	1.06	1.09	1.04	1.09
332-RS17	M/AA	0.98	1.12	0.99	0.98	1.00	0.96	1.01
332-RS17	M/C	1.04	1.06	0.75	0.97	1.03	0.98	0.87
332-RS18	Bq	2.70E+7	7.77E+4	4.19E+5	8.46E+6	7.08E+6	5.80E+7	2.72E+5
332-RS18	M/A	0.90	0.59	0.92	0.92	0.91	0.91	0.91
332-RS18	M/AA	0.99	0.65	1.01	1.01	1.00	1.00	1.00
332-RS18	M/C	1.05	0.61	0.76	1.00	1.03	1.02	0.86

Note: All M/AA and M/C values were adjusted with the normalized ^{137}Cs activity.

Appendix Table B-4 continued. Radioisotopic inventories of particles from AGR-2 Compact 3-3-2

Particle	Value	^{106}Ru	^{110m}Ag	^{125}Sb	^{134}Cs	^{137}Cs	^{144}Ce	^{154}Eu
332-RS19	Bq	3.05E+7	1.32E+5	4.68E+5	9.74E+6	8.08E+6	6.51E+7	3.09E+5
332-RS19	M/A	1.02	1.01	1.03	1.06	1.04	1.03	1.04
332-RS19	M/AA	0.98	0.96	0.99	1.01	1.00	0.98	0.99
332-RS19	M/C	1.04	0.91	0.75	1.01	1.03	1.00	0.86
332-RS20	Bq	2.97E+7	1.02E+5	4.57E+5	9.26E+6	7.93E+6	6.20E+7	3.05E+5
332-RS20	M/A	1.00	0.77	1.01	1.01	1.02	0.98	1.02
332-RS20	M/AA	0.97	0.75	0.98	0.98	1.00	0.95	1.00
332-RS20	M/C	1.03	0.71	0.74	0.98	1.03	0.97	0.86
332-RS21	Bq	3.34E+7	1.64E+5	4.95E+5	9.98E+6	8.32E+6	6.99E+7	3.18E+5
332-RS21	M/A	1.12	1.25	1.09	1.09	1.08	1.10	1.07
332-RS21	M/AA	1.04	1.16	1.02	1.01	1.00	1.02	0.99
332-RS21	M/C	1.11	1.09	0.77	1.00	1.03	1.04	0.86
332-RS22	Bq	2.99E+7	1.33E+5	4.63E+5	9.12E+6	7.86E+6	6.29E+7	3.13E+5
332-RS22	M/A	1.00	1.01	1.02	0.99	1.02	0.99	1.05
332-RS22	M/AA	0.99	1.00	1.00	0.98	1.00	0.97	1.03
332-RS22	M/C	1.05	0.94	0.76	0.97	1.03	0.99	0.89
332-RS23	Bq	2.69E+7	1.18E+5	4.08E+5	8.53E+6	7.12E+6	5.78E+7	2.72E+5
332-RS23	M/A	0.90	0.90	0.90	0.93	0.92	0.91	0.91
332-RS23	M/AA	0.98	0.97	0.98	1.01	1.00	0.99	0.99
332-RS23	M/C	1.04	0.92	0.74	1.00	1.03	1.01	0.86
332-RS24	Bq	3.05E+7	1.35E+5	4.80E+5	9.96E+6	8.24E+6	6.44E+7	3.21E+5
332-RS24	M/A	1.02	1.02	1.06	1.08	1.07	1.01	1.08
332-RS24	M/AA	0.96	0.96	0.99	1.02	1.00	0.95	1.01
332-RS24	M/C	1.02	0.90	0.75	1.01	1.03	0.97	0.87
332-RS25	Bq	2.76E+7	1.25E+5	4.30E+5	8.92E+6	7.42E+6	5.71E+7	2.93E+5
332-RS25	M/A	0.93	0.95	0.95	0.97	0.96	0.90	0.98
332-RS25	M/AA	0.97	0.99	0.99	1.01	1.00	0.94	1.03
332-RS25	M/C	1.03	0.93	0.75	1.00	1.03	0.95	0.89
332-RS26	Bq	2.97E+7	1.57E+5	4.40E+5	8.47E+6	7.05E+6	6.16E+7	2.79E+5
332-RS26	M/A	1.00	1.19	0.97	0.92	0.91	0.97	0.93
332-RS26	M/AA	1.09	1.31	1.06	1.01	1.00	1.07	1.03
332-RS26	M/C	1.16	1.23	0.81	1.00	1.03	1.09	0.89
332-RS27	Bq	3.21E+7	1.54E+5	4.95E+5	1.01E+7	8.50E+6	6.96E+7	3.18E+5
332-RS27	M/A	1.08	1.17	1.09	1.09	1.10	1.10	1.07
332-RS27	M/AA	0.98	1.06	0.99	1.00	1.00	1.00	0.97
332-RS27	M/C	1.04	1.00	0.75	0.99	1.03	1.02	0.84
332-RS28	Bq	2.73E+7	1.25E+5	4.14E+5	7.91E+6	6.66E+6	5.91E+7	2.60E+5
332-RS28	M/A	0.92	0.95	0.91	0.86	0.86	0.93	0.87
332-RS28	M/AA	1.07	1.10	1.06	1.00	1.00	1.08	1.01
332-RS28	M/C	1.13	1.04	0.80	0.99	1.03	1.10	0.88
332-RS29	Bq	3.23E+7	1.58E+5	4.66E+5	8.92E+6	7.69E+6	7.03E+7	2.87E+5
332-RS29	M/A	1.08	1.20	1.03	0.97	0.99	1.11	0.96
332-RS29	M/AA	1.09	1.21	1.03	0.98	1.00	1.11	0.97
332-RS29	M/C	1.16	1.14	0.78	0.97	1.03	1.13	0.84
332-RS30	Bq	2.88E+7	1.03E+5	4.50E+5	8.96E+6	7.68E+6	6.21E+7	2.94E+5
332-RS30	M/A	0.96	0.78	0.99	0.97	0.99	0.98	0.99
332-RS30	M/AA	0.97	0.79	1.00	0.98	1.00	0.98	0.99
332-RS30	M/C	1.03	0.74	0.76	0.98	1.03	1.00	0.86

Note: All M/AA and M/C values were adjusted with the normalized ^{137}Cs activity.

Appendix Table B-4 continued. Radioisotopic inventories of particles from AGR-2 Compact 3-3-2

Particle	Value	^{106}Ru	^{110m}Ag	^{125}Sb	^{134}Cs	^{137}Cs	^{144}Ce	^{154}Eu
332-RS31	Bq	3.25E+7	1.69E+5	4.74E+5	9.18E+6	7.72E+6	6.95E+7	2.95E+5
332-RS31	M/A	1.09	1.29	1.05	1.00	1.00	1.09	0.99
332-RS31	M/AA	1.09	1.29	1.05	1.00	1.00	1.10	0.99
332-RS31	M/C	1.16	1.21	0.79	0.99	1.03	1.12	0.86
332-RS32	Bq	2.82E+7	1.34E+5	4.38E+5	9.11E+6	7.65E+6	6.10E+7	3.01E+5
332-RS32	M/A	0.95	1.02	0.96	0.99	0.99	0.96	1.01
332-RS32	M/AA	0.96	1.03	0.98	1.00	1.00	0.97	1.02
332-RS32	M/C	1.02	0.97	0.74	1.00	1.03	0.99	0.88
332-RS33	Bq	2.98E+7	1.30E+5	4.61E+5	9.54E+6	7.81E+6	6.38E+7	3.02E+5
332-RS33	M/A	1.00	0.98	1.02	1.04	1.01	1.00	1.01
332-RS33	M/AA	0.99	0.98	1.01	1.03	1.00	0.99	1.00
332-RS33	M/C	1.05	0.92	0.76	1.02	1.03	1.01	0.87
332-RS34	Bq	3.14E+7	1.07E+5	4.90E+5	9.81E+6	8.43E+6	6.58E+7	3.23E+5
332-RS34	M/A	1.05	0.82	1.08	1.07	1.09	1.04	1.08
332-RS34	M/AA	0.97	0.75	0.99	0.98	1.00	0.95	1.00
332-RS34	M/C	1.03	0.70	0.75	0.97	1.03	0.97	0.86
332-RS35	Bq	3.08E+7	1.11E+5	4.78E+5	9.90E+6	8.38E+6	6.55E+7	3.23E+5
332-RS35	M/A	1.03	0.84	1.05	1.08	1.08	1.03	1.08
332-RS35	M/AA	0.95	0.78	0.97	0.99	1.00	0.95	1.00
332-RS35	M/C	1.01	0.73	0.74	0.99	1.03	0.97	0.86
332-RS36	Bq	2.78E+7	1.01E+5	4.30E+5	8.47E+6	7.05E+6	6.00E+7	2.72E+5
332-RS36	M/A	0.93	0.77	0.95	0.92	0.91	0.95	0.91
332-RS36	M/AA	1.03	0.84	1.04	1.01	1.00	1.04	1.00
332-RS36	M/C	1.09	0.79	0.79	1.00	1.03	1.06	0.87
332-RS37	Bq	2.97E+7	1.47E+5	4.53E+5	9.54E+6	7.92E+6	6.30E+7	2.99E+5
332-RS37	M/A	0.99	1.11	1.00	1.04	1.02	0.99	1.00
332-RS37	M/AA	0.97	1.09	0.97	1.01	1.00	0.97	0.98
332-RS37	M/C	1.03	1.02	0.74	1.01	1.03	0.99	0.85
332-RS38	Bq	3.51E+7	1.68E+5	5.29E+5	1.08E+7	8.91E+6	7.13E+7	3.47E+5
332-RS38	M/A	1.18	1.28	1.17	1.18	1.15	1.12	1.16
332-RS38	M/AA	1.02	1.11	1.01	1.02	1.00	0.97	1.01
332-RS38	M/C	1.09	1.04	0.77	1.01	1.03	0.99	0.88
332-RS39	Bq	2.97E+7	1.09E+5	4.60E+5	9.47E+6	7.97E+6	6.47E+7	3.11E+5
332-RS39	M/A	1.00	0.82	1.01	1.03	1.03	1.02	1.04
332-RS39	M/AA	0.97	0.80	0.98	1.00	1.00	0.99	1.01
332-RS39	M/C	1.03	0.75	0.75	0.99	1.03	1.01	0.88
332-RS40	Bq	3.05E+7	1.48E+5	4.49E+5	8.79E+6	7.38E+6	6.45E+7	2.85E+5
332-RS40	M/A	1.02	1.13	0.99	0.96	0.95	1.02	0.96
332-RS40	M/AA	1.07	1.18	1.04	1.00	1.00	1.06	1.00
332-RS40	M/C	1.14	1.11	0.78	1.00	1.03	1.08	0.87
332-RS41	Bq	3.09E+7	1.25E+5	4.85E+5	9.81E+6	8.32E+6	6.36E+7	3.29E+5
332-RS41	M/A	1.04	0.95	1.07	1.07	1.08	1.00	1.10
332-RS41	M/AA	0.96	0.88	0.99	0.99	1.00	0.93	1.03
332-RS41	M/C	1.02	0.83	0.75	0.99	1.03	0.95	0.89
332-RS42	Bq	3.07E+7	1.44E+5	4.63E+5	9.51E+6	7.85E+6	6.57E+7	3.03E+5
332-RS42	M/A	1.03	1.10	1.02	1.03	1.02	1.04	1.02
332-RS42	M/AA	1.02	1.08	1.00	1.02	1.00	1.02	1.00
332-RS42	M/C	1.08	1.02	0.76	1.01	1.03	1.04	0.87

Note: All M/AA and M/C values were adjusted with the normalized ^{137}Cs activity.

Appendix Table B-4 continued. Radioisotopic inventories of particles from AGR-2 Compact 3-3-2

Particle	Value	^{106}Ru	^{110m}Ag	^{125}Sb	^{134}Cs	^{137}Cs	^{144}Ce	^{154}Eu
332-RS43	Bq	3.08E+7	1.34E+5	4.48E+5	9.41E+6	7.93E+6	6.50E+7	3.08E+5
332-RS43	M/A	1.03	1.02	0.99	1.02	1.03	1.02	1.03
332-RS43	M/AA	1.01	1.00	0.96	1.00	1.00	1.00	1.01
332-RS43	M/C	1.07	0.94	0.73	0.99	1.03	1.02	0.87
332-RS44	Bq	2.79E+7	1.02E+5	4.17E+5	8.79E+6	7.32E+6	5.81E+7	2.85E+5
332-RS44	M/A	0.94	0.78	0.92	0.96	0.95	0.91	0.95
332-RS44	M/AA	0.99	0.82	0.97	1.01	1.00	0.97	1.01
332-RS44	M/C	1.05	0.77	0.73	1.00	1.03	0.98	0.87
332-RS45	Bq	3.19E+7	1.35E+5	4.94E+5	1.02E+7	8.48E+6	6.64E+7	3.26E+5
332-RS45	M/A	1.07	1.03	1.09	1.11	1.10	1.05	1.09
332-RS45	M/AA	0.98	0.94	0.99	1.01	1.00	0.95	1.00
332-RS45	M/C	1.04	0.88	0.75	1.00	1.03	0.97	0.87
332-RS46	Bq	2.57E+7	1.23E+5	3.95E+5	8.10E+6	6.83E+6	5.57E+7	2.63E+5
332-RS46	M/A	0.86	0.93	0.87	0.88	0.88	0.88	0.88
332-RS46	M/AA	0.98	1.06	0.99	1.00	1.00	0.99	1.00
332-RS46	M/C	1.04	0.99	0.75	0.99	1.03	1.01	0.87
332-RS47	Bq	2.70E+7	8.65E+4	3.91E+5	8.41E+6	7.03E+6	5.79E+7	2.70E+5
332-RS47	M/A	0.90	0.66	0.86	0.91	0.91	0.91	0.91
332-RS47	M/AA	1.00	0.72	0.95	1.01	1.00	1.00	1.00
332-RS47	M/C	1.06	0.68	0.72	1.00	1.03	1.02	0.86
332-RS48	Bq	2.98E+7	1.34E+5	4.46E+5	9.23E+6	7.54E+6	6.24E+7	2.92E+5
332-RS48	M/A	1.00	1.02	0.98	1.00	0.97	0.98	0.98
332-RS48	M/AA	1.02	1.05	1.01	1.03	1.00	1.01	1.00
332-RS48	M/C	1.09	0.99	0.76	1.02	1.03	1.03	0.87
332-RS49	Bq	2.83E+7	1.21E+5	4.38E+5	8.79E+6	7.52E+6	5.93E+7	2.96E+5
332-RS49	M/A	0.95	0.92	0.96	0.96	0.97	0.93	0.99
332-RS49	M/AA	0.98	0.95	0.99	0.98	1.00	0.96	1.02
332-RS49	M/C	1.04	0.89	0.75	0.98	1.03	0.98	0.88
332-RS50	Bq	3.12E+7	1.52E+5	4.73E+5	9.65E+6	8.07E+6	6.82E+7	3.06E+5
332-RS50	M/A	1.05	1.16	1.04	1.05	1.04	1.07	1.03
332-RS50	M/AA	1.01	1.11	1.00	1.01	1.00	1.03	0.98
332-RS50	M/C	1.07	1.05	0.76	1.00	1.03	1.05	0.85
332-RS51	Bq	2.84E+7	1.20E+5	4.27E+5	9.17E+6	7.65E+6	5.98E+7	2.97E+5
332-RS51	M/A	0.95	0.91	0.94	1.00	0.99	0.94	0.99
332-RS51	M/AA	0.96	0.92	0.95	1.01	1.00	0.95	1.01
332-RS51	M/C	1.02	0.87	0.72	1.00	1.03	0.97	0.87
332-RS52	Bq	3.12E+7	1.17E+5	4.78E+5	9.79E+6	8.22E+6	6.79E+7	3.11E+5
332-RS52	M/A	1.05	0.89	1.05	1.06	1.06	1.07	1.04
332-RS52	M/AA	0.99	0.84	0.99	1.00	1.00	1.01	0.98
332-RS52	M/C	1.05	0.79	0.75	1.00	1.03	1.03	0.85
332-RS53	Bq	2.77E+7	1.31E+5	4.29E+5	8.91E+6	7.40E+6	6.01E+7	2.84E+5
332-RS53	M/A	0.93	1.00	0.94	0.97	0.96	0.95	0.95
332-RS53	M/AA	0.97	1.04	0.99	1.01	1.00	0.99	0.99
332-RS53	M/C	1.03	0.98	0.75	1.01	1.03	1.01	0.86
332-RS54	Bq	3.06E+7	1.40E+5	4.73E+5	9.55E+6	8.14E+6	6.65E+7	3.08E+5
332-RS54	M/A	1.03	1.06	1.04	1.04	1.05	1.05	1.03
332-RS54	M/AA	0.98	1.01	0.99	0.99	1.00	0.99	0.98
332-RS54	M/C	1.04	0.95	0.75	0.98	1.03	1.01	0.85

Note: All M/AA and M/C values were adjusted with the normalized ^{137}Cs activity.

Appendix Table B-4 continued. Radioisotopic inventories of particles from AGR-2 Compact 3-3-2

Particle	Value	^{106}Ru	^{110m}Ag	^{125}Sb	^{134}Cs	^{137}Cs	^{144}Ce	^{154}Eu
332-RS55	Bq	2.80E+7	1.23E+5	4.25E+5	9.03E+6	7.64E+6	6.01E+7	2.93E+5
332-RS55	M/A	0.94	0.94	0.94	0.98	0.99	0.95	0.98
332-RS55	M/AA	0.95	0.95	0.95	0.99	1.00	0.96	1.00
332-RS55	M/C	1.01	0.89	0.72	0.99	1.03	0.98	0.86
332-RS56	Bq	3.38E+7	1.71E+5	5.07E+5	1.03E+7	8.54E+6	7.18E+7	3.26E+5
332-RS56	M/A	1.13	1.30	1.12	1.12	1.10	1.13	1.09
332-RS56	M/AA	1.03	1.18	1.01	1.01	1.00	1.02	0.99
332-RS56	M/C	1.09	1.11	0.77	1.01	1.03	1.04	0.86
332-RS57	Bq	2.99E+7	1.51E+5	4.53E+5	8.73E+6	7.43E+6	6.44E+7	2.86E+5
332-RS57	M/A	1.00	1.15	1.00	0.95	0.96	1.02	0.96
332-RS57	M/AA	1.05	1.20	1.04	0.99	1.00	1.06	1.00
332-RS57	M/C	1.11	1.13	0.79	0.98	1.03	1.08	0.86
332-RS58	Bq	3.04E+7	1.30E+5	4.64E+5	9.17E+6	7.95E+6	6.41E+7	3.05E+5
332-RS58	M/A	1.02	0.99	1.02	1.00	1.03	1.01	1.02
332-RS58	M/AA	0.99	0.96	0.99	0.97	1.00	0.98	0.99
332-RS58	M/C	1.06	0.90	0.75	0.96	1.03	1.00	0.86
332-RS59	Bq	2.70E+7	1.32E+5	4.17E+5	8.63E+6	7.28E+6	5.64E+7	2.87E+5
332-RS59	M/A	0.91	1.01	0.92	0.94	0.94	0.89	0.96
332-RS59	M/AA	0.96	1.07	0.98	1.00	1.00	0.94	1.02
332-RS59	M/C	1.02	1.01	0.74	0.99	1.03	0.96	0.89
332-RS60	Bq	2.74E+7	1.38E+5	3.97E+5	7.48E+6	6.48E+6	6.06E+7	2.41E+5
332-RS60	M/A	0.92	1.05	0.88	0.81	0.84	0.96	0.81
332-RS60	M/AA	1.10	1.25	1.05	0.97	1.00	1.14	0.96
332-RS60	M/C	1.17	1.18	0.79	0.97	1.03	1.16	0.83
332-RS61	Bq	2.98E+7	1.31E+5	4.55E+5	8.75E+6	7.64E+6	6.36E+7	2.93E+5
332-RS61	M/A	1.00	0.99	1.00	0.95	0.99	1.00	0.98
332-RS61	M/AA	1.01	1.01	1.02	0.96	1.00	1.01	0.99
332-RS61	M/C	1.08	0.95	0.77	0.96	1.03	1.03	0.86
Maximum	Bq	3.51E+7	1.71E+5	5.29E+5	1.08E+7	8.91E+6	7.36E+7	3.47E+5
Maximum	M/A	1.18	1.30	1.17	1.18	1.15	1.16	1.16
Maximum	M/AA	1.10	1.31	1.06	1.03	1.00	1.14	1.04
Maximum	M/C	1.17	1.23	0.81	1.02	1.03	1.16	0.90
Minimum	Bq	2.53E+7	7.77E+4	3.81E+5	7.48E+6	6.48E+6	5.50E+7	2.41E+5
Minimum	M/A	0.85	0.59	0.84	0.81	0.84	0.87	0.81
Minimum	M/AA	0.95	0.64	0.95	0.96	1.00	0.93	0.96
Minimum	M/C	1.01	0.60	0.72	0.95	1.03	0.95	0.83
Mean	Bq	2.98E+7	1.32E+5	4.54E+5	9.19E+6	7.73E+6	6.35E+7	2.98E+5
Mean	M/A	1.00	1.00	1.00	1.00	1.00	1.00	1.00
Mean	M/AA	1.00	1.00	1.00	1.00	1.00	1.00	1.00
Mean	M/C	1.06	0.94	0.76	0.99	1.03	1.02	0.87
SD	Bq	7.3%	16.5%	7.1%	7.4%	7.1%	6.9%	7.3%
SD	M/A	7.3%	16.5%	7.1%	7.4%	7.1%	6.9%	7.3%
SD	M/AA	4.0%	15.2%	2.7%	1.6%	0.0%	4.7%	1.6%
SD	M/C	4.0%	15.2%	2.7%	1.6%	0.0%	4.7%	1.6%

Note: All M/AA and M/C values were adjusted with the normalized ^{137}Cs activity.
Note: Special particles were not included in summary values.

Appendix Table B-5. Radioisotopic inventories of particles from AGR-2 Compact 3-4-2

Particle	Value	^{106}Ru	^{110m}Ag	^{125}Sb	^{134}Cs	^{137}Cs	^{144}Ce	^{154}Eu
342-SP01	Bq	2.39E+7	2.34E+3	4.88E+5	8.63E+5	7.31E+5	1.96E+6	1.64E+3
342-SP01	M/A	0.78	0.01	1.06	0.09	0.09	0.03	0.01
342-SP01	M/AA	8.32	0.16	11.33	0.95	1.00	0.34	0.06
342-SP01	M/C	8.91	0.17	8.55	0.95	1.03	0.34	0.05
342-SP02	Bq	1.81E+7	<2.7E+3	5.08E+5	1.28E+6	9.80E+5	1.34E+5	1.93E+3
342-SP02	M/A	0.59	<0.02	1.10	0.13	0.13	0.00	0.01
342-SP02	M/AA	4.68	<0.14	8.80	1.06	1.00	0.02	0.05
342-SP02	M/C	5.02	<0.15	6.64	1.06	1.03	0.02	0.04
342-SP03	Bq	1.52E+5	<1.6E+3	2.14E+3	3.72E+4	4.66E+4	3.90E+5	0.00E+0
342-SP03	M/A	0.00	<0.01	0.00	0.00	0.01	0.01	0.00
342-SP03	M/AA	0.83	<1.68	0.78	0.65	1.00	1.05	0.00
342-SP03	M/C	0.89	<1.87	0.59	0.64	1.03	1.06	0.00
342-SP04	Bq	1.68E+7	<2.8E+3	4.11E+5	1.35E+6	1.11E+6	1.26E+6	4.31E+3
342-SP04	M/A	0.54	<0.02	0.89	0.14	0.14	0.02	0.01
342-SP04	M/AA	3.85	<0.12	6.32	0.98	1.00	0.14	0.10
342-SP04	M/C	4.13	<0.14	4.77	0.98	1.03	0.14	0.08
342-SP05	Bq	1.99E+7	<2.9E+3	4.76E+5	1.61E+6	1.34E+6	1.59E+6	5.12E+3
342-SP05	M/A	0.65	<0.02	1.03	0.17	0.17	0.03	0.02
342-SP05	M/AA	3.78	<0.10	6.05	0.97	1.00	0.15	0.09
342-SP05	M/C	4.05	<0.12	4.57	0.97	1.03	0.15	0.08
342-SP06	Bq	2.73E+7	6.78E+4	4.71E+5	5.12E+6	4.16E+6	2.31E+7	7.95E+4
342-SP06	M/A	0.89	0.42	1.02	0.53	0.53	0.37	0.25
342-SP06	M/AA	1.66	0.80	1.92	1.00	1.00	0.69	0.47
342-SP06	M/C	1.78	0.88	1.45	0.99	1.03	0.70	0.41
342-SP07	Bq	3.49E+7	1.27E+5	5.23E+5	6.95E+6	5.53E+6	6.64E+7	3.74E+5
342-SP07	M/A	1.13	0.80	1.14	0.72	0.71	1.07	1.18
342-SP07	M/AA	1.60	1.13	1.61	1.02	1.00	1.51	1.68
342-SP07	M/C	1.72	1.25	1.21	1.02	1.03	1.53	1.47
342-SP08	Bq	3.08E+7	1.03E+5	4.67E+5	4.62E+6	3.91E+6	6.24E+7	3.27E+5
342-SP08	M/A	1.00	0.64	1.01	0.48	0.50	1.00	1.04
342-SP08	M/AA	2.00	1.29	2.03	0.96	1.00	2.01	2.07
342-SP08	M/C	2.15	1.43	1.53	0.96	1.03	2.03	1.82
342-SP09	Bq	2.65E+7	1.13E+5	3.98E+5	6.36E+6	5.33E+6	5.61E+7	2.58E+5
342-SP09	M/A	0.86	0.71	0.86	0.66	0.68	0.90	0.82
342-SP09	M/AA	1.26	1.04	1.27	0.97	1.00	1.32	1.20
342-SP09	M/C	1.35	1.15	0.96	0.96	1.03	1.34	1.05
342-SP10	Bq	3.21E+7	1.14E+5	4.86E+5	6.84E+6	5.59E+6	6.00E+7	7.92E+4
342-SP10	M/A	1.04	0.71	1.06	0.71	0.72	0.96	0.25
342-SP10	M/AA	1.46	1.00	1.48	0.99	1.00	1.34	0.35
342-SP10	M/C	1.56	1.11	1.11	0.99	1.03	1.36	0.31
342-SP11	Bq	3.23E+7	2.53E+4	4.70E+5	8.58E+6	6.66E+6	6.35E+7	3.30E+5
342-SP11	M/A	1.05	0.16	1.02	0.89	0.85	1.02	1.05
342-SP11	M/AA	1.23	0.19	1.20	1.04	1.00	1.20	1.23
342-SP11	M/C	1.32	0.21	0.91	1.04	1.03	1.21	1.08
342-SP12	Bq	2.66E+7	1.38E+5	4.09E+5	6.99E+6	5.72E+6	5.76E+7	2.82E+5
342-SP12	M/A	0.87	0.86	0.89	0.72	0.73	0.92	0.89
342-SP12	M/AA	1.18	1.18	1.21	0.99	1.00	1.26	1.22
342-SP12	M/C	1.27	1.30	0.92	0.99	1.03	1.28	1.07

Note: All M/AA and M/C values were adjusted with the normalized ^{137}Cs activity.

Appendix Table B-5 continued. Radioisotopic inventories of particles from AGR-2 Compact 3-4-2

Particle	Value	^{106}Ru	^{110m}Ag	^{125}Sb	^{134}Cs	^{137}Cs	^{144}Ce	^{154}Eu
342-SP13	Bq	3.19E+7	1.63E+5	4.73E+5	8.12E+6	6.36E+6	6.03E+7	3.44E+5
342-SP13	M/A	1.04	1.02	1.03	0.84	0.81	0.97	1.09
342-SP13	M/AA	1.28	1.25	1.26	1.03	1.00	1.19	1.34
342-SP13	M/C	1.37	1.39	0.95	1.03	1.03	1.21	1.17
342-SP14	Bq	2.87E+7	9.08E+4	4.64E+5	5.55E+6	4.46E+6	4.37E+7	4.25E+4
342-SP14	M/A	0.93	0.57	1.01	0.57	0.57	0.70	0.13
342-SP14	M/AA	1.64	1.00	1.77	1.01	1.00	1.23	0.24
342-SP14	M/C	1.76	1.10	1.33	1.01	1.03	1.25	0.21
342-SP15	Bq	3.69E+7	1.92E+5	5.48E+5	9.70E+6	7.64E+6	7.03E+7	3.64E+5
342-SP15	M/A	1.20	1.20	1.19	1.00	0.98	1.13	1.15
342-SP15	M/AA	1.23	1.23	1.22	1.03	1.00	1.16	1.18
342-SP15	M/C	1.32	1.36	0.92	1.03	1.03	1.17	1.03
342-SP16	Bq	3.33E+7	1.64E+5	5.04E+5	8.20E+6	6.48E+6	6.15E+7	3.58E+5
342-SP16	M/A	1.08	1.02	1.09	0.85	0.83	0.99	1.13
342-SP16	M/AA	1.31	1.24	1.32	1.02	1.00	1.19	1.37
342-SP16	M/C	1.40	1.37	1.00	1.02	1.03	1.21	1.20
342-SP17	Bq	3.12E+7	1.64E+5	4.72E+5	8.86E+6	7.09E+6	6.45E+7	3.24E+5
342-SP17	M/A	1.01	1.02	1.02	0.92	0.91	1.03	1.03
342-SP17	M/AA	1.12	1.13	1.13	1.01	1.00	1.14	1.13
342-SP17	M/C	1.20	1.25	0.85	1.01	1.03	1.16	0.99
342-SP18	Bq	3.41E+7	1.56E+5	5.07E+5	9.58E+6	7.66E+6	6.87E+7	3.43E+5
342-SP18	M/A	1.11	0.98	1.10	0.99	0.98	1.10	1.09
342-SP18	M/AA	1.13	1.00	1.12	1.01	1.00	1.12	1.11
342-SP18	M/C	1.21	1.10	0.85	1.01	1.03	1.14	0.97
342-SP19	Bq	3.16E+7	1.65E+5	4.73E+5	8.72E+6	6.85E+6	6.22E+7	3.28E+5
342-SP19	M/A	1.03	1.03	1.03	0.90	0.88	1.00	1.04
342-SP19	M/AA	1.17	1.18	1.17	1.03	1.00	1.14	1.19
342-SP19	M/C	1.26	1.31	0.89	1.03	1.03	1.15	1.04
342-SP20	Bq	3.08E+7	1.63E+5	4.49E+5	8.18E+6	6.45E+6	5.88E+7	3.03E+5
342-SP20	M/A	1.00	1.02	0.97	0.85	0.82	0.94	0.96
342-SP20	M/AA	1.22	1.24	1.18	1.03	1.00	1.14	1.17
342-SP20	M/C	1.30	1.37	0.89	1.03	1.03	1.16	1.02
342-SP21	Bq	3.22E+7	1.76E+5	4.76E+5	8.85E+6	6.80E+6	6.26E+7	3.41E+5
342-SP21	M/A	1.04	1.10	1.03	0.91	0.87	1.00	1.08
342-SP21	M/AA	1.20	1.27	1.19	1.05	1.00	1.16	1.24
342-SP21	M/C	1.29	1.40	0.90	1.05	1.03	1.17	1.09
342-SP22	Bq	3.49E+7	1.84E+5	5.19E+5	9.71E+6	7.47E+6	6.55E+7	3.58E+5
342-SP22	M/A	1.13	1.15	1.13	1.00	0.96	1.05	1.13
342-SP22	M/AA	1.19	1.20	1.18	1.05	1.00	1.10	1.19
342-SP22	M/C	1.27	1.33	0.89	1.05	1.03	1.11	1.04
342-SP23	Bq	3.36E+7	1.85E+5	4.82E+5	8.45E+6	6.71E+6	6.29E+7	3.38E+5
342-SP23	M/A	1.09	1.16	1.05	0.87	0.86	1.01	1.07
342-SP23	M/AA	1.27	1.35	1.22	1.02	1.00	1.18	1.25
342-SP23	M/C	1.36	1.50	0.92	1.02	1.03	1.19	1.09
342-SP24	Bq	2.78E+7	1.25E+5	4.03E+5	7.07E+6	6.04E+6	5.71E+7	2.55E+5
342-SP24	M/A	0.90	0.78	0.87	0.73	0.77	0.92	0.81
342-SP24	M/AA	1.17	1.01	1.13	0.95	1.00	1.19	1.04
342-SP24	M/C	1.25	1.12	0.85	0.95	1.03	1.20	0.92

Note: All M/AA and M/C values were adjusted with the normalized ^{137}Cs activity.

Appendix Table B-5 continued. Radioisotopic inventories of particles from AGR-2 Compact 3-4-2

Particle	Value	^{106}Ru	^{110m}Ag	^{125}Sb	^{134}Cs	^{137}Cs	^{144}Ce	^{154}Eu
342-SP25	Bq	3.26E+7	1.66E+5	5.02E+5	8.57E+6	6.82E+6	6.35E+7	3.50E+5
342-SP25	M/A	1.06	1.04	1.09	0.89	0.87	1.02	1.11
342-SP25	M/AA	1.21	1.19	1.25	1.02	1.00	1.17	1.27
342-SP25	M/C	1.30	1.32	0.94	1.02	1.03	1.18	1.11
342-SP26	Bq	3.40E+7	1.48E+5	4.94E+5	9.12E+6	7.29E+6	6.53E+7	3.33E+5
342-SP26	M/A	1.11	0.92	1.07	0.94	0.93	1.05	1.05
342-SP26	M/AA	1.19	0.99	1.15	1.01	1.00	1.12	1.13
342-SP26	M/C	1.27	1.10	0.87	1.01	1.03	1.14	0.99
342-RS01	Bq	3.04E+7	1.64E+5	4.43E+5	9.02E+6	7.43E+6	6.07E+7	2.96E+5
342-RS01	M/A	0.99	1.03	0.96	0.93	0.95	0.97	0.94
342-RS01	M/AA	1.04	1.08	1.01	0.98	1.00	1.03	0.99
342-RS01	M/C	1.11	1.20	0.76	0.98	1.03	1.04	0.86
342-RS02	Bq	2.66E+7	1.42E+5	3.94E+5	8.26E+6	6.71E+6	5.44E+7	2.68E+5
342-RS02	M/A	0.86	0.89	0.85	0.85	0.86	0.87	0.85
342-RS02	M/AA	1.01	1.04	1.00	1.00	1.00	1.02	0.99
342-RS02	M/C	1.08	1.15	0.75	1.00	1.03	1.03	0.87
342-RS03	Bq	3.43E+7	2.03E+5	5.00E+5	1.11E+7	8.30E+6	5.98E+7	3.63E+5
342-RS03	M/A	1.11	1.27	1.09	1.15	1.06	0.96	1.15
342-RS03	M/AA	1.05	1.20	1.02	1.08	1.00	0.90	1.08
342-RS03	M/C	1.13	1.33	0.77	1.08	1.03	0.92	0.95
342-RS04	Bq	3.19E+7	1.68E+5	4.80E+5	1.02E+7	8.16E+6	6.21E+7	3.36E+5
342-RS04	M/A	1.04	1.05	1.04	1.06	1.04	1.00	1.06
342-RS04	M/AA	0.99	1.01	1.00	1.01	1.00	0.95	1.02
342-RS04	M/C	1.06	1.12	0.75	1.01	1.03	0.97	0.89
342-RS05	Bq	3.02E+7	1.40E+5	4.62E+5	9.65E+6	8.05E+6	6.60E+7	3.12E+5
342-RS05	M/A	0.98	0.87	1.00	1.00	1.03	1.06	0.99
342-RS05	M/AA	0.95	0.85	0.97	0.97	1.00	1.03	0.96
342-RS05	M/C	1.02	0.94	0.74	0.97	1.03	1.04	0.84
342-RS06	Bq	3.08E+7	1.51E+5	4.70E+5	9.98E+6	8.22E+6	6.56E+7	3.27E+5
342-RS06	M/A	1.00	0.94	1.02	1.03	1.05	1.05	1.04
342-RS06	M/AA	0.95	0.90	0.97	0.98	1.00	1.00	0.99
342-RS06	M/C	1.02	1.00	0.73	0.98	1.03	1.01	0.86
342-RS07	Bq	2.99E+7	1.57E+5	4.46E+5	9.83E+6	7.79E+6	6.02E+7	3.02E+5
342-RS07	M/A	0.97	0.98	0.97	1.02	1.00	0.97	0.96
342-RS07	M/AA	0.97	0.99	0.97	1.02	1.00	0.97	0.96
342-RS07	M/C	1.04	1.09	0.73	1.02	1.03	0.98	0.84
342-RS08	Bq	3.43E+7	1.84E+5	5.13E+5	1.11E+7	8.60E+6	6.77E+7	3.66E+5
342-RS08	M/A	1.11	1.15	1.11	1.15	1.10	1.09	1.16
342-RS08	M/AA	1.01	1.05	1.01	1.04	1.00	0.99	1.05
342-RS08	M/C	1.09	1.16	0.77	1.04	1.03	1.00	0.92
342-RS09	Bq	3.39E+7	1.83E+5	4.95E+5	9.74E+6	8.33E+6	7.03E+7	3.26E+5
342-RS09	M/A	1.10	1.15	1.07	1.01	1.06	1.13	1.03
342-RS09	M/AA	1.03	1.08	1.01	0.95	1.00	1.06	0.97
342-RS09	M/C	1.11	1.19	0.76	0.95	1.03	1.07	0.85
342-RS10	Bq	2.82E+7	1.37E+5	4.26E+5	8.55E+6	7.30E+6	5.94E+7	2.85E+5
342-RS10	M/A	0.92	0.85	0.92	0.88	0.93	0.95	0.90
342-RS10	M/AA	0.98	0.92	0.99	0.95	1.00	1.02	0.97
342-RS10	M/C	1.05	1.01	0.75	0.95	1.03	1.04	0.85

Note: All M/AA and M/C values were adjusted with the normalized ^{137}Cs activity.

Appendix Table B-5 continued. Radioisotopic inventories of particles from AGR-2 Compact 3-4-2

Particle	Value	^{106}Ru	^{110m}Ag	^{125}Sb	^{134}Cs	^{137}Cs	^{144}Ce	^{154}Eu
342-RS11	Bq	2.89E+7	1.36E+5	4.25E+5	8.96E+6	7.26E+6	6.04E+7	2.82E+5
342-RS11	M/A	0.94	0.85	0.92	0.93	0.93	0.97	0.89
342-RS11	M/AA	1.01	0.92	0.99	1.00	1.00	1.04	0.96
342-RS11	M/C	1.08	1.02	0.75	1.00	1.03	1.06	0.84
342-RS12	Bq	2.86E+7	1.58E+5	4.39E+5	9.46E+6	7.38E+6	5.67E+7	3.08E+5
342-RS12	M/A	0.93	0.99	0.95	0.98	0.94	0.91	0.98
342-RS12	M/AA	0.99	1.05	1.01	1.04	1.00	0.96	1.03
342-RS12	M/C	1.06	1.16	0.76	1.04	1.03	0.98	0.91
342-RS13	Bq	3.08E+7	1.56E+5	4.53E+5	1.01E+7	8.06E+6	6.15E+7	3.24E+5
342-RS13	M/A	1.00	0.98	0.98	1.04	1.03	0.99	1.03
342-RS13	M/AA	0.97	0.95	0.96	1.01	1.00	0.96	0.99
342-RS13	M/C	1.04	1.05	0.72	1.01	1.03	0.97	0.87
342-RS14	Bq	3.17E+7	1.52E+5	4.76E+5	9.83E+6	8.29E+6	6.85E+7	3.19E+5
342-RS14	M/A	1.03	0.95	1.03	1.02	1.06	1.10	1.01
342-RS14	M/AA	0.97	0.90	0.98	0.96	1.00	1.04	0.95
342-RS14	M/C	1.04	0.99	0.74	0.96	1.03	1.05	0.83
342-RS15	Bq	3.39E+7	1.84E+5	4.83E+5	9.92E+6	7.70E+6	6.38E+7	3.34E+5
342-RS15	M/A	1.10	1.15	1.05	1.03	0.98	1.02	1.06
342-RS15	M/AA	1.12	1.17	1.07	1.04	1.00	1.04	1.08
342-RS15	M/C	1.20	1.30	0.80	1.04	1.03	1.05	0.94
342-RS16	Bq	3.11E+7	1.62E+5	4.58E+5	9.28E+6	7.60E+6	6.31E+7	2.97E+5
342-RS16	M/A	1.01	1.01	1.00	0.96	0.97	1.01	0.94
342-RS16	M/AA	1.04	1.04	1.02	0.99	1.00	1.04	0.97
342-RS16	M/C	1.11	1.15	0.77	0.99	1.03	1.06	0.85
342-RS17	Bq	2.83E+7	1.18E+5	4.33E+5	8.91E+6	7.49E+6	6.10E+7	2.87E+5
342-RS17	M/A	0.92	0.74	0.94	0.92	0.96	0.98	0.91
342-RS17	M/AA	0.96	0.77	0.98	0.96	1.00	1.02	0.95
342-RS17	M/C	1.03	0.86	0.74	0.96	1.03	1.04	0.83
342-RS18	Bq	3.29E+7	1.72E+5	5.11E+5	1.10E+7	8.85E+6	6.58E+7	3.62E+5
342-RS18	M/A	1.07	1.07	1.11	1.13	1.13	1.06	1.15
342-RS18	M/AA	0.94	0.95	0.98	1.00	1.00	0.93	1.01
342-RS18	M/C	1.01	1.05	0.74	1.00	1.03	0.95	0.89
342-RS19	Bq	2.88E+7	1.46E+5	4.33E+5	8.86E+6	7.63E+6	6.29E+7	2.94E+5
342-RS19	M/A	0.94	0.91	0.94	0.92	0.98	1.01	0.93
342-RS19	M/AA	0.96	0.94	0.96	0.94	1.00	1.03	0.96
342-RS19	M/C	1.03	1.04	0.73	0.94	1.03	1.05	0.84
342-RS20	Bq	3.01E+7	1.62E+5	4.53E+5	1.00E+7	8.14E+6	6.37E+7	3.20E+5
342-RS20	M/A	0.98	1.01	0.98	1.03	1.04	1.02	1.01
342-RS20	M/AA	0.94	0.97	0.95	0.99	1.00	0.98	0.98
342-RS20	M/C	1.01	1.08	0.71	0.99	1.03	1.00	0.85
342-RS21	Bq	2.90E+7	1.54E+5	4.27E+5	9.20E+6	7.48E+6	5.98E+7	3.02E+5
342-RS21	M/A	0.94	0.96	0.93	0.95	0.96	0.96	0.96
342-RS21	M/AA	0.98	1.01	0.97	1.00	1.00	1.00	1.00
342-RS21	M/C	1.06	1.11	0.73	1.00	1.03	1.02	0.88
342-RS22	Bq	3.15E+7	1.52E+5	4.62E+5	9.36E+6	7.71E+6	6.48E+7	2.95E+5
342-RS22	M/A	1.02	0.95	1.00	0.97	0.99	1.04	0.93
342-RS22	M/AA	1.04	0.97	1.02	0.98	1.00	1.05	0.95
342-RS22	M/C	1.11	1.07	0.77	0.98	1.03	1.07	0.83

Note: All M/AA and M/C values were adjusted with the normalized ^{137}Cs activity.

Appendix Table B-5 continued. Radioisotopic inventories of particles from AGR-2 Compact 3-4-2

Particle	Value	^{106}Ru	^{110m}Ag	^{125}Sb	^{134}Cs	^{137}Cs	^{144}Ce	^{154}Eu
342-RS23	Bq	3.06E+7	1.51E+5	4.71E+5	1.01E+7	8.28E+6	6.64E+7	3.22E+5
342-RS23	M/A	1.00	0.94	1.02	1.04	1.06	1.07	1.02
342-RS23	M/AA	0.94	0.89	0.97	0.99	1.00	1.01	0.96
342-RS23	M/C	1.01	0.99	0.73	0.99	1.03	1.02	0.84
342-RS24	Bq	3.06E+7	1.64E+5	4.56E+5	9.89E+6	7.89E+6	5.82E+7	3.27E+5
342-RS24	M/A	1.00	1.02	0.99	1.02	1.01	0.93	1.03
342-RS24	M/AA	0.99	1.02	0.98	1.01	1.00	0.93	1.03
342-RS24	M/C	1.06	1.12	0.74	1.01	1.03	0.94	0.90
342-RS25	Bq	3.20E+7	1.58E+5	4.84E+5	9.69E+6	8.12E+6	6.89E+7	3.12E+5
342-RS25	M/A	1.04	0.99	1.05	1.00	1.04	1.11	0.99
342-RS25	M/AA	1.00	0.95	1.01	0.97	1.00	1.06	0.95
342-RS25	M/C	1.07	1.05	0.76	0.97	1.03	1.08	0.83
342-RS26	Bq	2.70E+7	1.50E+5	4.12E+5	8.86E+6	6.97E+6	5.48E+7	2.88E+5
342-RS26	M/A	0.88	0.94	0.90	0.92	0.89	0.88	0.91
342-RS26	M/AA	0.99	1.05	1.00	1.03	1.00	0.99	1.02
342-RS26	M/C	1.06	1.17	0.76	1.03	1.03	1.00	0.90
342-RS27	Bq	2.77E+7	1.43E+5	4.25E+5	9.01E+6	7.40E+6	5.87E+7	2.97E+5
342-RS27	M/A	0.90	0.89	0.92	0.93	0.95	0.94	0.94
342-RS27	M/AA	0.95	0.94	0.98	0.99	1.00	1.00	0.99
342-RS27	M/C	1.02	1.05	0.74	0.99	1.03	1.01	0.87
342-RS28	Bq	3.34E+7	1.77E+5	4.97E+5	1.08E+7	8.67E+6	6.80E+7	3.41E+5
342-RS28	M/A	1.08	1.10	1.08	1.11	1.11	1.09	1.08
342-RS28	M/AA	0.98	1.00	0.97	1.00	1.00	0.98	0.97
342-RS28	M/C	1.05	1.10	0.73	1.00	1.03	1.00	0.85
342-RS29	Bq	2.71E+7	1.18E+5	4.09E+5	8.73E+6	7.15E+6	5.84E+7	2.78E+5
342-RS29	M/A	0.88	0.74	0.89	0.90	0.91	0.94	0.88
342-RS29	M/AA	0.96	0.81	0.97	0.99	1.00	1.02	0.96
342-RS29	M/C	1.03	0.90	0.73	0.99	1.03	1.04	0.84
342-RS30	Bq	2.73E+7	1.45E+5	4.19E+5	8.30E+6	6.79E+6	5.72E+7	2.89E+5
342-RS30	M/A	0.89	0.91	0.91	0.86	0.87	0.92	0.92
342-RS30	M/AA	1.02	1.05	1.05	0.99	1.00	1.06	1.06
342-RS30	M/C	1.10	1.16	0.79	0.99	1.03	1.07	0.92
342-RS31	Bq	3.20E+7	1.72E+5	4.75E+5	9.73E+6	7.97E+6	6.47E+7	3.11E+5
342-RS31	M/A	1.04	1.07	1.03	1.01	1.02	1.04	0.98
342-RS31	M/AA	1.02	1.05	1.01	0.99	1.00	1.02	0.97
342-RS31	M/C	1.09	1.17	0.76	0.99	1.03	1.03	0.85
342-RS32	Bq	3.34E+7	1.84E+5	4.97E+5	1.08E+7	8.25E+6	6.07E+7	3.54E+5
342-RS32	M/A	1.09	1.15	1.08	1.12	1.05	0.97	1.12
342-RS32	M/AA	1.03	1.09	1.02	1.06	1.00	0.92	1.06
342-RS32	M/C	1.10	1.21	0.77	1.06	1.03	0.94	0.93
342-RS33	Bq	4.06E+7	2.24E+5	5.88E+5	1.05E+7	7.94E+6	7.03E+7	4.14E+5
342-RS33	M/A	1.32	1.40	1.28	1.09	1.01	1.13	1.31
342-RS33	M/AA	1.30	1.38	1.26	1.07	1.00	1.11	1.29
342-RS33	M/C	1.39	1.53	0.95	1.07	1.03	1.13	1.13
342-RS34	Bq	3.42E+7	1.86E+5	4.96E+5	1.02E+7	8.24E+6	6.71E+7	3.14E+5
342-RS34	M/A	1.11	1.16	1.08	1.06	1.05	1.08	0.99
342-RS34	M/AA	1.06	1.10	1.02	1.00	1.00	1.02	0.94
342-RS34	M/C	1.13	1.22	0.77	1.00	1.03	1.03	0.83

Note: All M/AA and M/C values were adjusted with the normalized ^{137}Cs activity.

Appendix Table B-5 continued. Radioisotopic inventories of particles from AGR-2 Compact 3-4-2

Particle	Value	^{106}Ru	^{110m}Ag	^{125}Sb	^{134}Cs	^{137}Cs	^{144}Ce	^{154}Eu
342-RS35	Bq	2.81E+7	1.53E+5	4.20E+5	9.39E+6	7.47E+6	5.75E+7	3.01E+5
342-RS35	M/A	0.91	0.96	0.91	0.97	0.96	0.92	0.95
342-RS35	M/AA	0.95	1.00	0.95	1.02	1.00	0.97	1.00
342-RS35	M/C	1.02	1.11	0.72	1.02	1.03	0.98	0.87
342-RS36	Bq	2.74E+7	1.37E+5	4.15E+5	8.67E+6	7.26E+6	5.75E+7	2.83E+5
342-RS36	M/A	0.89	0.85	0.90	0.90	0.93	0.92	0.90
342-RS36	M/AA	0.96	0.92	0.97	0.97	1.00	0.99	0.97
342-RS36	M/C	1.03	1.02	0.73	0.97	1.03	1.01	0.85
342-RS37	Bq	3.06E+7	1.62E+5	4.66E+5	1.02E+7	7.91E+6	5.93E+7	3.34E+5
342-RS37	M/A	1.00	1.01	1.01	1.05	1.01	0.95	1.06
342-RS37	M/AA	0.98	1.00	1.00	1.04	1.00	0.94	1.05
342-RS37	M/C	1.06	1.11	0.76	1.04	1.03	0.95	0.92
342-RS38	Bq	3.18E+7	1.72E+5	4.77E+5	1.00E+7	7.79E+6	5.82E+7	3.46E+5
342-RS38	M/A	1.03	1.07	1.03	1.03	1.00	0.93	1.10
342-RS38	M/AA	1.04	1.08	1.04	1.04	1.00	0.94	1.10
342-RS38	M/C	1.11	1.20	0.78	1.04	1.03	0.95	0.96
342-RS39	Bq	2.71E+7	1.38E+5	4.15E+5	8.49E+6	6.92E+6	5.66E+7	2.85E+5
342-RS39	M/A	0.88	0.86	0.90	0.88	0.89	0.91	0.90
342-RS39	M/AA	1.00	0.97	1.02	0.99	1.00	1.03	1.02
342-RS39	M/C	1.07	1.08	0.77	0.99	1.03	1.04	0.89
342-RS40	Bq	3.10E+7	1.57E+5	4.67E+5	9.64E+6	8.06E+6	6.30E+7	3.17E+5
342-RS40	M/A	1.01	0.98	1.01	1.00	1.03	1.01	1.01
342-RS40	M/AA	0.98	0.95	0.98	0.97	1.00	0.98	0.98
342-RS40	M/C	1.05	1.06	0.74	0.97	1.03	0.99	0.85
342-RS41	Bq	3.28E+7	1.58E+5	4.78E+5	9.57E+6	8.05E+6	6.93E+7	3.04E+5
342-RS41	M/A	1.07	0.99	1.04	0.99	1.03	1.11	0.96
342-RS41	M/AA	1.04	0.96	1.01	0.96	1.00	1.08	0.94
342-RS41	M/C	1.11	1.06	0.76	0.96	1.03	1.09	0.82
342-RS42	Bq	2.98E+7	1.60E+5	4.63E+5	9.89E+6	8.06E+6	6.15E+7	3.12E+5
342-RS42	M/A	0.97	1.00	1.00	1.02	1.03	0.99	0.99
342-RS42	M/AA	0.94	0.97	0.97	0.99	1.00	0.96	0.96
342-RS42	M/C	1.01	1.07	0.74	0.99	1.03	0.97	0.84
342-RS43	Bq	3.22E+7	1.72E+5	4.80E+5	1.03E+7	8.36E+6	6.62E+7	3.24E+5
342-RS43	M/A	1.05	1.08	1.04	1.06	1.07	1.06	1.03
342-RS43	M/AA	0.98	1.01	0.98	0.99	1.00	0.99	0.96
342-RS43	M/C	1.05	1.12	0.74	0.99	1.03	1.01	0.84
342-RS44	Bq	3.19E+7	1.65E+5	4.88E+5	1.08E+7	8.52E+6	6.38E+7	3.46E+5
342-RS44	M/A	1.04	1.03	1.06	1.11	1.09	1.02	1.09
342-RS44	M/AA	0.95	0.95	0.97	1.02	1.00	0.94	1.01
342-RS44	M/C	1.02	1.05	0.73	1.02	1.03	0.95	0.88
342-RS45	Bq	3.02E+7	1.70E+5	4.43E+5	9.38E+6	7.47E+6	6.07E+7	3.02E+5
342-RS45	M/A	0.98	1.07	0.96	0.97	0.95	0.97	0.96
342-RS45	M/AA	1.03	1.12	1.01	1.02	1.00	1.02	1.00
342-RS45	M/C	1.10	1.24	0.76	1.02	1.03	1.03	0.88

Note: All M/AA and M/C values were adjusted with the normalized ^{137}Cs activity.

Appendix Table B-5 continued. Radioisotopic inventories of particles from AGR-2 Compact 3-4-2

Particle	Value	^{106}Ru	^{110m}Ag	^{125}Sb	^{134}Cs	^{137}Cs	^{144}Ce	^{154}Eu
Maximum	Bq	4.06E+7	2.24E+5	5.88E+5	1.11E+7	8.85E+6	7.03E+7	4.14E+5
Maximum	M/A	1.32	1.40	1.28	1.15	1.13	1.13	1.31
Maximum	M/AA	1.30	1.38	1.26	1.08	1.00	1.11	1.29
Maximum	M/C	1.39	1.53	0.95	1.08	1.03	1.13	1.13
Minimum	Bq	2.66E+7	1.18E+5	3.94E+5	8.26E+6	6.71E+6	5.44E+7	2.68E+5
Minimum	M/A	0.86	0.74	0.85	0.85	0.86	0.87	0.85
Minimum	M/AA	0.94	0.77	0.95	0.94	1.00	0.90	0.94
Minimum	M/C	1.01	0.86	0.71	0.94	1.03	0.92	0.82
Mean	Bq	3.08E+7	1.60E+5	4.61E+5	9.67E+6	7.82E+6	6.23E+7	3.16E+5
Mean	M/A	1.00	1.00	1.00	1.00	1.00	1.00	1.00
Mean	M/AA	1.00	1.00	1.00	1.00	1.00	1.00	1.00
Mean	M/C	1.07	1.11	0.76	1.00	1.03	1.01	0.88
SD	Bq	8.7%	12.5%	7.8%	7.7%	6.5%	6.8%	8.9%
SD	M/A	8.7%	12.5%	7.8%	7.7%	6.5%	6.8%	8.9%
SD	M/AA	6.0%	10.3%	4.7%	3.3%	0.0%	4.6%	6.1%
SD	M/C	6.0%	10.3%	4.7%	3.3%	0.0%	4.6%	6.1%

Note: All M/AA and M/C values were adjusted with the normalized ^{137}Cs activity.
Note: Special particles were not included in summary values.

Appendix Table B-6. Radioisotopic inventories of particles from AGR-2 Compact 3-4-1

Particle	Value	^{106}Ru	^{110m}Ag	^{125}Sb	^{134}Cs	^{137}Cs	^{144}Ce	^{154}Eu
341-SP01	Bq	2.85E+7	<9.0E+3	5.01E+5	7.77E+5	6.24E+5	4.73E+6	3.97E+3
341-SP01	M/A	0.90	<0.06	1.10	0.08	0.08	0.08	0.01
341-SP01	M/AA	10.93	<0.73	13.29	1.01	1.00	0.92	0.15
341-SP01	M/C	12.21	<0.77	10.03	0.98	1.00	0.94	0.13
341-SP02	Bq	2.68E+7	<9.4E+3	4.66E+5	1.40E+6	1.13E+6	2.42E+6	3.86E+3
341-SP02	M/A	0.85	<0.06	1.02	0.15	0.15	0.04	0.01
341-SP02	M/AA	5.68	<0.42	6.84	1.00	1.00	0.26	0.08
341-SP02	M/C	6.34	<0.44	5.16	0.98	1.00	0.27	0.07
341-SP03	Bq	3.25E+7	<1.0E+4	4.80E+5	1.58E+6	1.25E+6	2.42E+7	1.47E+4
341-SP03	M/A	1.03	<0.07	1.05	0.17	0.17	0.39	0.05
341-SP03	M/AA	6.22	<0.42	6.36	1.02	1.00	2.34	0.28
341-SP03	M/C	6.95	<0.45	4.80	1.00	1.00	2.40	0.25
341-SP04	Bq	3.69E+7	1.12E+5	5.22E+5	5.17E+6	4.10E+6	7.04E+7	3.44E+5
341-SP04	M/A	1.17	0.75	1.14	0.55	0.54	1.13	1.08
341-SP04	M/AA	2.16	1.38	2.11	1.02	1.00	2.07	1.98
341-SP04	M/C	2.41	1.45	1.59	1.00	1.00	2.13	1.78
341-SP05	Bq	2.96E+7	5.32E+4	4.39E+5	4.58E+6	3.86E+6	6.35E+7	1.64E+5
341-SP05	M/A	0.94	0.36	0.96	0.49	0.51	1.01	0.51
341-SP05	M/AA	1.84	0.70	1.88	0.96	1.00	1.99	1.00
341-SP05	M/C	2.05	0.73	1.42	0.94	1.00	2.04	0.90
341-SP06	Bq	3.10E+7	1.12E+5	4.49E+5	5.12E+6	4.14E+6	5.74E+7	3.04E+5
341-SP06	M/A	0.98	0.75	0.99	0.55	0.55	0.92	0.95
341-SP06	M/AA	1.79	1.37	1.80	1.00	1.00	1.67	1.73
341-SP06	M/C	2.00	1.44	1.36	0.98	1.00	1.72	1.56
341-SP07	Bq	3.01E+7	5.92E+4	4.43E+5	4.01E+6	3.33E+6	6.37E+7	2.94E+5
341-SP07	M/A	0.95	0.40	0.97	0.43	0.44	1.02	0.92
341-SP07	M/AA	2.16	0.90	2.20	0.98	1.00	2.31	2.08
341-SP07	M/C	2.41	0.95	1.66	0.95	1.00	2.37	1.87
341-SP08	Bq	3.44E+7	1.29E+5	4.96E+5	5.29E+6	4.09E+6	6.38E+7	3.47E+5
341-SP08	M/A	1.09	0.87	1.09	0.57	0.54	1.02	1.08
341-SP08	M/AA	2.01	1.60	2.01	1.05	1.00	1.89	2.00
341-SP08	M/C	2.25	1.69	1.52	1.03	1.00	1.94	1.80
341-SP09	Bq	3.76E+7	1.79E+5	5.30E+5	7.20E+6	5.65E+6	6.88E+7	3.79E+5
341-SP09	M/A	1.19	1.20	1.16	0.77	0.75	1.10	1.18
341-SP09	M/AA	1.59	1.61	1.55	1.03	1.00	1.47	1.58
341-SP09	M/C	1.78	1.69	1.17	1.01	1.00	1.51	1.42
341-SP10	Bq	3.08E+7	1.19E+5	4.39E+5	5.69E+6	4.48E+6	5.90E+7	3.15E+5
341-SP10	M/A	0.98	0.80	0.96	0.61	0.59	0.94	0.98
341-SP10	M/AA	1.65	1.34	1.63	1.03	1.00	1.59	1.66
341-SP10	M/C	1.84	1.42	1.23	1.01	1.00	1.63	1.49
341-SP11	Bq	3.47E+7	1.43E+5	5.21E+5	6.58E+6	5.21E+6	6.57E+7	3.73E+5
341-SP11	M/A	1.10	0.96	1.14	0.71	0.69	1.05	1.16
341-SP11	M/AA	1.60	1.39	1.66	1.02	1.00	1.52	1.69
341-SP11	M/C	1.78	1.47	1.25	1.00	1.00	1.56	1.52
341-SP12	Bq	3.56E+7	1.52E+5	5.04E+5	6.88E+6	5.36E+6	6.52E+7	3.72E+5
341-SP12	M/A	1.13	1.02	1.11	0.74	0.71	1.04	1.16
341-SP12	M/AA	1.59	1.44	1.56	1.04	1.00	1.47	1.64
341-SP12	M/C	1.78	1.52	1.18	1.02	1.00	1.51	1.47

Note: All M/AA and M/C values were adjusted with the normalized ^{137}Cs activity.

Appendix Table B-6 continued. Radioisotopic inventories of particles from AGR-2 Compact 3-4-1

Particle	Value	^{106}Ru	^{110m}Ag	^{125}Sb	^{134}Cs	^{137}Cs	^{144}Ce	^{154}Eu
341-SP13	Bq	3.12E+7	1.31E+5	4.48E+5	6.26E+6	4.94E+6	6.26E+7	3.21E+5
341-SP13	M/A	0.99	0.88	0.98	0.67	0.65	1.00	1.00
341-SP13	M/AA	1.51	1.34	1.50	1.03	1.00	1.53	1.53
341-SP13	M/C	1.69	1.41	1.13	1.00	1.00	1.57	1.38
341-SP14	Bq	3.35E+7	1.47E+5	4.81E+5	7.58E+6	5.87E+6	6.47E+7	3.45E+5
341-SP14	M/A	1.06	0.99	1.06	0.81	0.78	1.03	1.08
341-SP14	M/AA	1.37	1.27	1.36	1.05	1.00	1.33	1.39
341-SP14	M/C	1.53	1.34	1.03	1.02	1.00	1.36	1.25
341-SP15	Bq	3.04E+7	1.33E+5	4.49E+5	7.05E+6	5.58E+6	5.94E+7	3.27E+5
341-SP15	M/A	0.96	0.89	0.99	0.76	0.74	0.95	1.02
341-SP15	M/AA	1.30	1.20	1.33	1.02	1.00	1.28	1.38
341-SP15	M/C	1.45	1.27	1.01	1.00	1.00	1.32	1.24
341-RS42	Bq	3.07E+7	1.42E+5	4.45E+5	5.66E+6	4.44E+6	5.94E+7	3.12E+5
341-RS42	M/A	0.97	0.95	0.98	0.61	0.59	0.95	0.98
341-RS42	M/AA	1.65	1.62	1.66	1.03	1.00	1.62	1.66
341-RS42	M/C	1.85	1.70	1.25	1.01	1.00	1.66	1.49
341-RS01	Bq	2.81E+7	1.40E+5	4.21E+5	8.36E+6	6.99E+6	6.00E+7	2.89E+5
341-RS01	M/A	0.89	0.94	0.92	0.90	0.93	0.96	0.90
341-RS01	M/AA	0.96	1.01	1.00	0.97	1.00	1.04	0.98
341-RS01	M/C	1.08	1.07	0.75	0.95	1.00	1.06	0.88
341-RS02	Bq	3.02E+7	1.46E+5	4.36E+5	9.26E+6	7.03E+6	5.34E+7	3.38E+5
341-RS02	M/A	0.96	0.98	0.96	0.99	0.93	0.85	1.05
341-RS02	M/AA	1.03	1.05	1.03	1.07	1.00	0.92	1.13
341-RS02	M/C	1.15	1.11	0.78	1.04	1.00	0.94	1.02
341-RS03	Bq	2.95E+7	1.40E+5	4.26E+5	9.44E+6	7.72E+6	5.72E+7	3.07E+5
341-RS03	M/A	0.94	0.94	0.93	1.01	1.02	0.92	0.96
341-RS03	M/AA	0.92	0.92	0.91	0.99	1.00	0.90	0.94
341-RS03	M/C	1.02	0.97	0.69	0.97	1.00	0.92	0.84
341-RS04	Bq	3.47E+7	1.45E+5	4.79E+5	1.02E+7	8.38E+6	7.13E+7	3.22E+5
341-RS04	M/A	1.10	0.97	1.05	1.09	1.11	1.14	1.01
341-RS04	M/AA	0.99	0.87	0.95	0.98	1.00	1.03	0.91
341-RS04	M/C	1.11	0.92	0.71	0.96	1.00	1.05	0.82
341-RS05	Bq	3.83E+7	2.51E+5	5.33E+5	1.16E+7	8.50E+6	6.39E+7	3.92E+5
341-RS05	M/A	1.21	1.68	1.17	1.24	1.13	1.02	1.22
341-RS05	M/AA	1.08	1.49	1.04	1.10	1.00	0.91	1.09
341-RS05	M/C	1.20	1.57	0.78	1.08	1.00	0.93	0.98
341-RS06	Bq	3.64E+7	1.83E+5	5.02E+5	1.04E+7	8.21E+6	6.81E+7	3.56E+5
341-RS06	M/A	1.15	1.22	1.10	1.12	1.09	1.09	1.11
341-RS06	M/AA	1.06	1.12	1.01	1.03	1.00	1.00	1.02
341-RS06	M/C	1.19	1.18	0.76	1.01	1.00	1.03	0.92
341-RS07	Bq	3.29E+7	1.73E+5	4.73E+5	1.08E+7	8.56E+6	6.65E+7	3.22E+5
341-RS07	M/A	1.04	1.16	1.04	1.15	1.13	1.06	1.00
341-RS07	M/AA	0.92	1.02	0.92	1.02	1.00	0.94	0.89
341-RS07	M/C	1.03	1.08	0.69	1.00	1.00	0.96	0.80
341-RS08	Bq	2.81E+7	1.37E+5	4.17E+5	7.85E+6	6.72E+6	6.01E+7	2.82E+5
341-RS08	M/A	0.89	0.92	0.91	0.84	0.89	0.96	0.88
341-RS08	M/AA	1.00	1.03	1.03	0.95	1.00	1.08	0.99
341-RS08	M/C	1.12	1.09	0.78	0.93	1.00	1.11	0.89

Note: All M/AA and M/C values were adjusted with the normalized ^{137}Cs activity.
Particle 341-RS42 was treated as a special particle because of low cesium inventory, and it was not included in RS statistics.

Appendix Table B-6 continued. Radioisotopic inventories of particles from AGR-2 Compact 3-4-1

Particle	Value	^{106}Ru	^{110m}Ag	^{125}Sb	^{134}Cs	^{137}Cs	^{144}Ce	^{154}Eu
341-RS09	Bq	2.98E+7	1.27E+5	4.33E+5	9.53E+6	7.78E+6	6.34E+7	3.00E+5
341-RS09	M/A	0.94	0.85	0.95	1.02	1.03	1.01	0.94
341-RS09	M/AA	0.92	0.82	0.92	0.99	1.00	0.98	0.91
341-RS09	M/C	1.02	0.87	0.70	0.97	1.00	1.01	0.82
341-RS10	Bq	3.47E+7	1.62E+5	4.98E+5	9.90E+6	8.28E+6	7.50E+7	3.20E+5
341-RS10	M/A	1.10	1.09	1.09	1.06	1.10	1.20	1.00
341-RS10	M/AA	1.00	0.99	1.00	0.97	1.00	1.09	0.91
341-RS10	M/C	1.12	1.04	0.75	0.95	1.00	1.12	0.82
341-RS11	Bq	2.83E+7	1.22E+5	4.12E+5	7.45E+6	6.20E+6	5.62E+7	2.91E+5
341-RS11	M/A	0.90	0.82	0.90	0.80	0.82	0.90	0.91
341-RS11	M/AA	1.09	1.00	1.10	0.97	1.00	1.10	1.11
341-RS11	M/C	1.22	1.05	0.83	0.95	1.00	1.12	1.00
341-RS12	Bq	3.61E+7	1.67E+5	5.22E+5	1.16E+7	8.86E+6	6.20E+7	3.87E+5
341-RS12	M/A	1.14	1.12	1.15	1.25	1.17	0.99	1.21
341-RS12	M/AA	0.98	0.95	0.98	1.06	1.00	0.84	1.03
341-RS12	M/C	1.09	1.00	0.74	1.04	1.00	0.87	0.93
341-RS13	Bq	3.02E+7	1.40E+5	4.34E+5	8.95E+6	7.58E+6	6.68E+7	2.87E+5
341-RS13	M/A	0.96	0.94	0.95	0.96	1.00	1.07	0.90
341-RS13	M/AA	0.95	0.94	0.95	0.96	1.00	1.06	0.89
341-RS13	M/C	1.07	0.99	0.72	0.93	1.00	1.09	0.80
341-RS14	Bq	3.05E+7	1.64E+5	4.36E+5	8.82E+6	6.83E+6	5.78E+7	3.17E+5
341-RS14	M/A	0.97	1.10	0.96	0.95	0.90	0.92	0.99
341-RS14	M/AA	1.07	1.22	1.06	1.05	1.00	1.02	1.10
341-RS14	M/C	1.20	1.28	0.80	1.02	1.00	1.05	0.99
341-RS15	Bq	3.09E+7	1.27E+5	4.57E+5	8.66E+6	7.31E+6	6.51E+7	3.06E+5
341-RS15	M/A	0.98	0.85	1.00	0.93	0.97	1.04	0.96
341-RS15	M/AA	1.01	0.88	1.04	0.96	1.00	1.08	0.99
341-RS15	M/C	1.13	0.93	0.78	0.94	1.00	1.10	0.89
341-RS16	Bq	3.22E+7	1.23E+5	4.76E+5	8.55E+6	7.08E+6	6.53E+7	3.34E+5
341-RS16	M/A	1.02	0.83	1.05	0.92	0.94	1.04	1.04
341-RS16	M/AA	1.09	0.88	1.12	0.98	1.00	1.11	1.11
341-RS16	M/C	1.22	0.93	0.84	0.96	1.00	1.14	1.00
341-RS17	Bq	3.02E+7	1.52E+5	4.53E+5	9.64E+6	7.78E+6	6.02E+7	3.26E+5
341-RS17	M/A	0.96	1.02	0.99	1.03	1.03	0.96	1.02
341-RS17	M/AA	0.93	0.99	0.96	1.00	1.00	0.93	0.99
341-RS17	M/C	1.04	1.04	0.73	0.98	1.00	0.96	0.89
341-RS18	Bq	2.80E+7	1.57E+5	4.22E+5	9.33E+6	7.58E+6	5.65E+7	3.02E+5
341-RS18	M/A	0.89	1.05	0.92	1.00	1.00	0.90	0.94
341-RS18	M/AA	0.88	1.05	0.92	1.00	1.00	0.90	0.94
341-RS18	M/C	0.99	1.10	0.70	0.97	1.00	0.92	0.85
341-RS19	Bq	3.37E+7	1.39E+5	4.88E+5	9.97E+6	8.58E+6	6.85E+7	3.43E+5
341-RS19	M/A	1.07	0.93	1.07	1.07	1.14	1.09	1.07
341-RS19	M/AA	0.94	0.82	0.94	0.94	1.00	0.96	0.94
341-RS19	M/C	1.05	0.87	0.71	0.92	1.00	0.99	0.85
341-RS20	Bq	3.13E+7	1.59E+5	4.51E+5	1.02E+7	8.22E+6	5.92E+7	3.27E+5
341-RS20	M/A	0.99	1.07	0.99	1.09	1.09	0.95	1.02
341-RS20	M/AA	0.91	0.98	0.91	1.00	1.00	0.87	0.94
341-RS20	M/C	1.02	1.03	0.69	0.98	1.00	0.89	0.84

Note: All M/AA and M/C values were adjusted with the normalized ^{137}Cs activity.

Appendix Table B-6 continued. Radioisotopic inventories of particles from AGR-2 Compact 3-4-1

Particle	Value	^{106}Ru	^{110m}Ag	^{125}Sb	^{134}Cs	^{137}Cs	^{144}Ce	^{154}Eu
341-RS21	Bq	2.97E+7	1.05E+5	4.30E+5	8.68E+6	7.60E+6	6.63E+7	2.89E+5
341-RS21	M/A	0.94	0.70	0.94	0.93	1.01	1.06	0.90
341-RS21	M/AA	0.94	0.70	0.94	0.92	1.00	1.05	0.90
341-RS21	M/C	1.05	0.74	0.71	0.90	1.00	1.08	0.81
341-RS22	Bq	3.44E+7	2.03E+5	4.94E+5	1.11E+7	8.91E+6	6.35E+7	3.52E+5
341-RS22	M/A	1.09	1.36	1.08	1.19	1.18	1.01	1.10
341-RS22	M/AA	0.92	1.15	0.92	1.01	1.00	0.86	0.93
341-RS22	M/C	1.03	1.22	0.69	0.98	1.00	0.88	0.84
341-RS23	Bq	3.55E+7	1.72E+5	5.07E+5	1.07E+7	8.66E+6	6.85E+7	3.62E+5
341-RS23	M/A	1.12	1.15	1.11	1.15	1.15	1.10	1.13
341-RS23	M/AA	0.98	1.01	0.97	1.00	1.00	0.96	0.99
341-RS23	M/C	1.09	1.06	0.73	0.98	1.00	0.98	0.89
341-RS24	Bq	3.31E+7	1.73E+5	4.75E+5	9.42E+6	7.64E+6	6.60E+7	3.50E+5
341-RS24	M/A	1.05	1.16	1.04	1.01	1.01	1.06	1.09
341-RS24	M/AA	1.04	1.15	1.03	1.00	1.00	1.04	1.08
341-RS24	M/C	1.16	1.21	0.78	0.98	1.00	1.07	0.97
341-RS25	Bq	2.78E+7	1.23E+5	4.03E+5	7.49E+6	6.18E+6	5.93E+7	2.75E+5
341-RS25	M/A	0.88	0.83	0.88	0.80	0.82	0.95	0.86
341-RS25	M/AA	1.08	1.01	1.08	0.98	1.00	1.16	1.05
341-RS25	M/C	1.20	1.07	0.81	0.96	1.00	1.19	0.94
341-RS26	Bq	3.25E+7	1.38E+5	4.74E+5	8.72E+6	6.63E+6	5.67E+7	3.40E+5
341-RS26	M/A	1.03	0.92	1.04	0.93	0.88	0.91	1.06
341-RS26	M/AA	1.17	1.05	1.19	1.06	1.00	1.03	1.21
341-RS26	M/C	1.31	1.11	0.89	1.04	1.00	1.06	1.09
341-RS27	Bq	2.85E+7	1.40E+5	4.21E+5	8.84E+6	7.45E+6	6.26E+7	2.80E+5
341-RS27	M/A	0.90	0.94	0.92	0.95	0.99	1.00	0.88
341-RS27	M/AA	0.91	0.95	0.94	0.96	1.00	1.01	0.89
341-RS27	M/C	1.02	1.00	0.71	0.94	1.00	1.04	0.80
341-RS28	Bq	3.02E+7	1.31E+5	4.41E+5	9.82E+6	7.82E+6	6.29E+7	3.05E+5
341-RS28	M/A	0.96	0.88	0.97	1.05	1.04	1.00	0.95
341-RS28	M/AA	0.92	0.85	0.93	1.02	1.00	0.97	0.92
341-RS28	M/C	1.03	0.89	0.71	0.99	1.00	1.00	0.83
341-RS29	Bq	2.98E+7	1.35E+5	4.30E+5	8.86E+6	7.27E+6	5.66E+7	3.09E+5
341-RS29	M/A	0.95	0.90	0.94	0.95	0.96	0.90	0.97
341-RS29	M/AA	0.98	0.94	0.98	0.99	1.00	0.94	1.00
341-RS29	M/C	1.10	0.99	0.74	0.96	1.00	0.96	0.90
341-RS30	Bq	3.25E+7	1.39E+5	4.81E+5	8.47E+6	7.22E+6	6.81E+7	3.34E+5
341-RS30	M/A	1.03	0.93	1.05	0.91	0.96	1.09	1.04
341-RS30	M/AA	1.08	0.98	1.10	0.95	1.00	1.14	1.09
341-RS30	M/C	1.20	1.03	0.83	0.93	1.00	1.17	0.98
341-RS31	Bq	3.04E+7	1.36E+5	4.29E+5	8.84E+6	7.47E+6	6.59E+7	2.80E+5
341-RS31	M/A	0.96	0.91	0.94	0.95	0.99	1.05	0.88
341-RS31	M/AA	0.97	0.92	0.95	0.96	1.00	1.07	0.89
341-RS31	M/C	1.09	0.97	0.72	0.94	1.00	1.09	0.80
341-RS32	Bq	3.16E+7	1.32E+5	4.55E+5	8.66E+6	6.69E+6	6.08E+7	3.32E+5
341-RS32	M/A	1.00	0.89	1.00	0.93	0.89	0.97	1.04
341-RS32	M/AA	1.13	1.00	1.13	1.05	1.00	1.10	1.17
341-RS32	M/C	1.26	1.05	0.85	1.02	1.00	1.13	1.05

Note: All M/AA and M/C values were adjusted with the normalized ^{137}Cs activity.

Appendix Table B-6 continued. Radioisotopic inventories of particles from AGR-2 Compact 3-4-1

Particle	Value	^{106}Ru	^{110m}Ag	^{125}Sb	^{134}Cs	^{137}Cs	^{144}Ce	^{154}Eu
341-RS33	Bq	3.13E+7	1.52E+5	4.42E+5	9.03E+6	6.97E+6	6.04E+7	3.15E+5
341-RS33	M/A	0.99	1.02	0.97	0.97	0.92	0.97	0.98
341-RS33	M/AA	1.08	1.11	1.05	1.05	1.00	1.05	1.06
341-RS33	M/C	1.20	1.16	0.79	1.03	1.00	1.07	0.96
341-RS34	Bq	2.74E+7	1.27E+5	4.07E+5	8.65E+6	7.29E+6	5.91E+7	2.81E+5
341-RS34	M/A	0.87	0.85	0.89	0.93	0.96	0.94	0.88
341-RS34	M/AA	0.90	0.88	0.92	0.96	1.00	0.98	0.91
341-RS34	M/C	1.00	0.93	0.70	0.94	1.00	1.01	0.82
341-RS35	Bq	3.62E+7	1.53E+5	5.08E+5	1.00E+7	8.18E+6	6.71E+7	3.61E+5
341-RS35	M/A	1.15	1.02	1.11	1.07	1.08	1.07	1.13
341-RS35	M/AA	1.06	0.95	1.03	0.99	1.00	0.99	1.04
341-RS35	M/C	1.18	1.00	0.78	0.97	1.00	1.02	0.94
341-RS36	Bq	2.91E+7	1.23E+5	4.16E+5	8.78E+6	6.98E+6	5.94E+7	2.92E+5
341-RS36	M/A	0.92	0.82	0.91	0.94	0.92	0.95	0.91
341-RS36	M/AA	1.00	0.89	0.99	1.02	1.00	1.03	0.99
341-RS36	M/C	1.12	0.94	0.75	1.00	1.00	1.05	0.89
341-RS37	Bq	2.98E+7	1.45E+5	4.21E+5	8.27E+6	6.96E+6	6.45E+7	2.80E+5
341-RS37	M/A	0.94	0.97	0.92	0.89	0.92	1.03	0.87
341-RS37	M/AA	1.02	1.05	1.00	0.96	1.00	1.12	0.95
341-RS37	M/C	1.14	1.11	0.76	0.94	1.00	1.15	0.85
341-RS38	Bq	2.60E+7	1.46E+5	3.84E+5	8.57E+6	6.82E+6	5.16E+7	2.68E+5
341-RS38	M/A	0.83	0.98	0.84	0.92	0.90	0.82	0.84
341-RS38	M/AA	0.91	1.09	0.93	1.02	1.00	0.91	0.93
341-RS38	M/C	1.02	1.14	0.70	0.99	1.00	0.94	0.83
341-RS39	Bq	3.08E+7	1.27E+5	4.54E+5	9.18E+6	7.54E+6	6.14E+7	3.26E+5
341-RS39	M/A	0.98	0.85	1.00	0.98	1.00	0.98	1.02
341-RS39	M/AA	0.98	0.85	1.00	0.99	1.00	0.98	1.02
341-RS39	M/C	1.09	0.90	0.75	0.96	1.00	1.01	0.92
341-RS40	Bq	3.02E+7	1.57E+5	4.35E+5	8.71E+6	6.85E+6	5.52E+7	3.11E+5
341-RS40	M/A	0.96	1.05	0.96	0.93	0.91	0.88	0.97
341-RS40	M/AA	1.06	1.16	1.05	1.03	1.00	0.97	1.07
341-RS40	M/C	1.18	1.22	0.80	1.01	1.00	1.00	0.96
341-RS41	Bq	3.32E+7	1.70E+5	4.82E+5	1.02E+7	7.99E+6	6.30E+7	3.43E+5
341-RS41	M/A	1.05	1.14	1.06	1.09	1.06	1.01	1.07
341-RS41	M/AA	1.00	1.08	1.00	1.03	1.00	0.95	1.01
341-RS41	M/C	1.11	1.14	0.75	1.01	1.00	0.98	0.91
341-RS43	Bq	3.76E+7	1.89E+5	5.37E+5	1.02E+7	7.69E+6	6.39E+7	3.93E+5
341-RS43	M/A	1.19	1.27	1.18	1.09	1.02	1.02	1.23
341-RS43	M/AA	1.17	1.25	1.16	1.07	1.00	1.00	1.21
341-RS43	M/C	1.31	1.31	0.87	1.05	1.00	1.03	1.08
341-RS44	Bq	3.36E+7	1.47E+5	4.87E+5	8.54E+6	7.03E+6	6.46E+7	3.39E+5
341-RS44	M/A	1.07	0.99	1.07	0.92	0.93	1.03	1.06
341-RS44	M/AA	1.15	1.06	1.15	0.98	1.00	1.11	1.14
341-RS44	M/C	1.28	1.12	0.87	0.96	1.00	1.14	1.02
341-RS45	Bq	3.25E+7	1.48E+5	4.70E+5	1.02E+7	8.32E+6	6.88E+7	3.23E+5
341-RS45	M/A	1.03	0.99	1.03	1.09	1.10	1.10	1.01
341-RS45	M/AA	0.94	0.90	0.94	0.99	1.00	1.00	0.92
341-RS45	M/C	1.04	0.95	0.71	0.97	1.00	1.02	0.82

Note: All M/AA and M/C values were adjusted with the normalized ^{137}Cs activity.

Appendix Table B-6 continued. Radioisotopic inventories of particles from AGR-2 Compact 3-4-1

Particle	Value	^{106}Ru	^{110m}Ag	^{125}Sb	^{134}Cs	^{137}Cs	^{144}Ce	^{154}Eu
Maximum	Bq	3.83E+7	2.51E+5	5.37E+5	1.16E+7	8.91E+6	7.50E+7	3.93E+5
Maximum	M/A	1.21	1.68	1.18	1.25	1.18	1.20	1.23
Maximum	M/AA	1.17	1.49	1.19	1.10	1.00	1.16	1.21
Maximum	M/C	1.31	1.57	0.89	1.08	1.00	1.19	1.09
Minimum	Bq	2.60E+7	1.05E+5	3.84E+5	7.45E+6	6.18E+6	5.16E+7	2.68E+5
Minimum	M/A	0.83	0.70	0.84	0.80	0.82	0.82	0.84
Minimum	M/AA	0.88	0.70	0.91	0.92	1.00	0.84	0.89
Minimum	M/C	0.99	0.74	0.69	0.90	1.00	0.87	0.80
Mean	Bq	3.15E+7	1.49E+5	4.56E+5	9.33E+6	7.55E+6	6.26E+7	3.20E+5
Mean	M/A	1.00	1.00	1.00	1.00	1.00	1.00	1.00
Mean	M/AA	1.00	1.00	1.00	1.00	1.00	1.00	1.00
Mean	M/C	1.12	1.05	0.76	0.98	1.00	1.03	0.90
SD	Bq	9.2%	17.0%	8.1%	10.6%	9.3%	7.9%	9.9%
SD	M/A	9.2%	17.0%	8.1%	10.6%	9.3%	7.9%	9.9%
SD	M/AA	7.7%	13.5%	7.4%	4.0%	0.0%	7.9%	9.1%
SD	M/C	7.7%	13.5%	7.4%	4.0%	0.0%	7.9%	9.1%

Note: All M/AA and M/C values were adjusted with the normalized ^{137}Cs activity.
Note: Special particles were not included in summary values.

APPENDIX C. OPTICAL MICROGRAPHS

This appendix contains optical micrographs of particles that were ground and polished in mounts designed to hold ~30 AGR-2 UO_2 TRISO particles. The microstructures observed in the imaged cross sections of random samples from as-irradiated Compacts 3-1-2 and 3-3-1 (Appendix Figure C-1 and Appendix Figure C-2, respectively) are discussed in Section 6. After IMGA survey of particles from 1,700°C safety tested Compact 3-4-1, particles from Bin 6 with ^{137}Cs M/AA < 0.60 and ^{144}Ce M/A > 0.40 (Appendix Figure C-3) and particles from Bin 8 with 0.60 < ^{137}Cs M/AA < 0.70 and ^{144}Ce M/A > 0.40 (Appendix Figure C-4) were cross sectioned and imaged to examine overall microstructure in particles with reduced cesium retention, as discussed in Section 5.6.

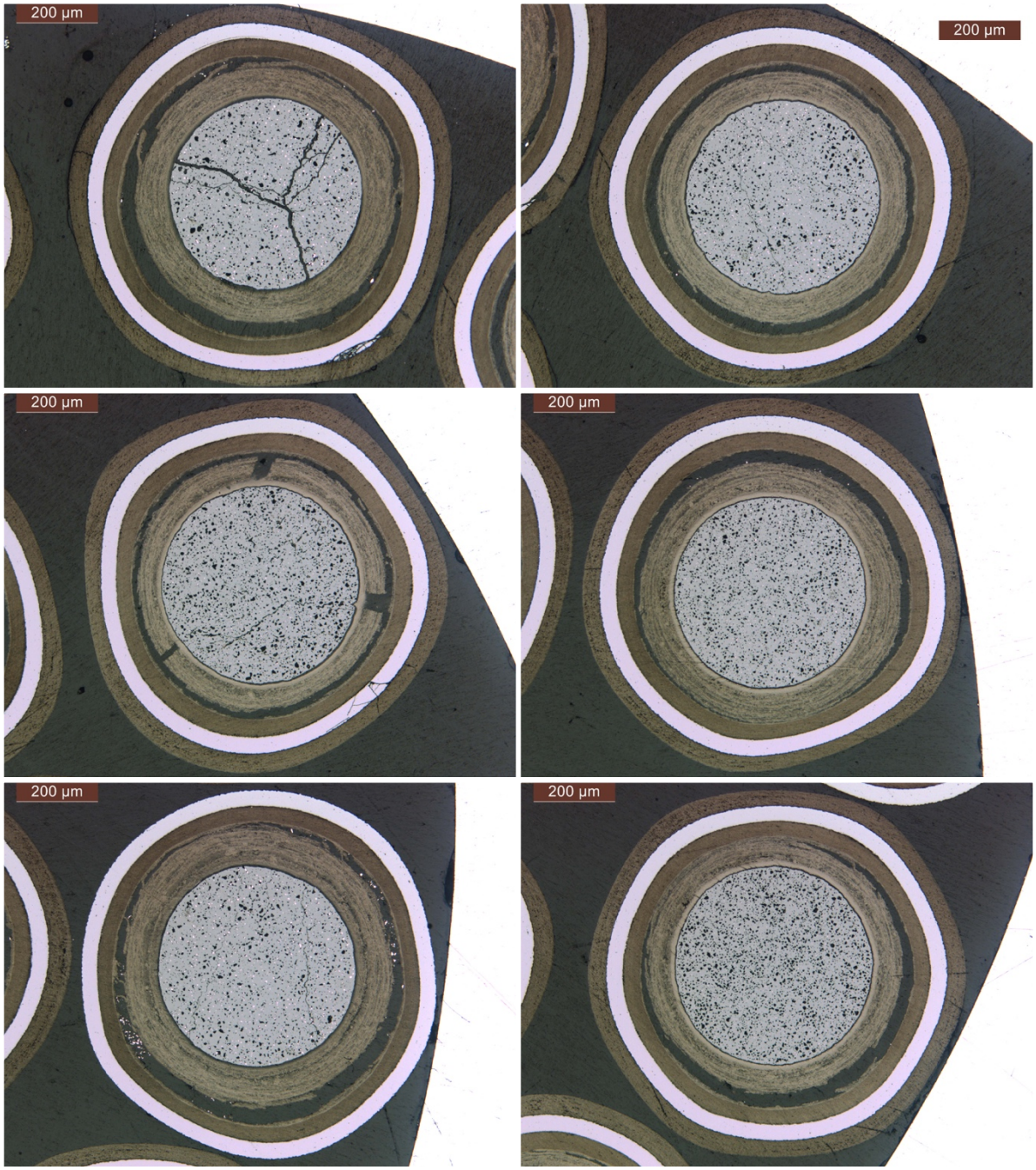

Appendix Figure C-1. Random sections from AGR-2 Compact 3-1-2.

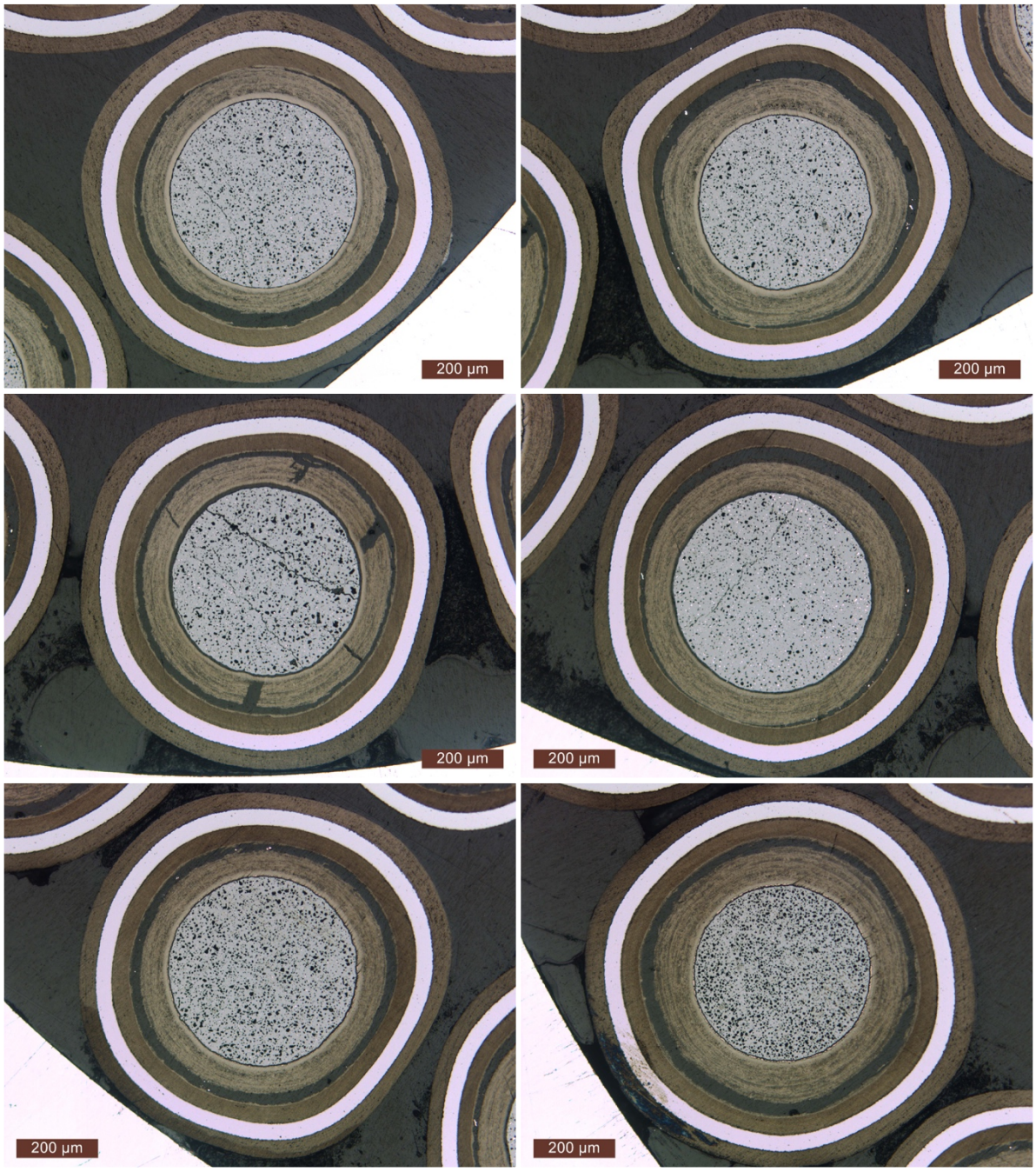

Appendix Figure C-1 continued. Random sections from AGR-2 Compact 3-1-2.

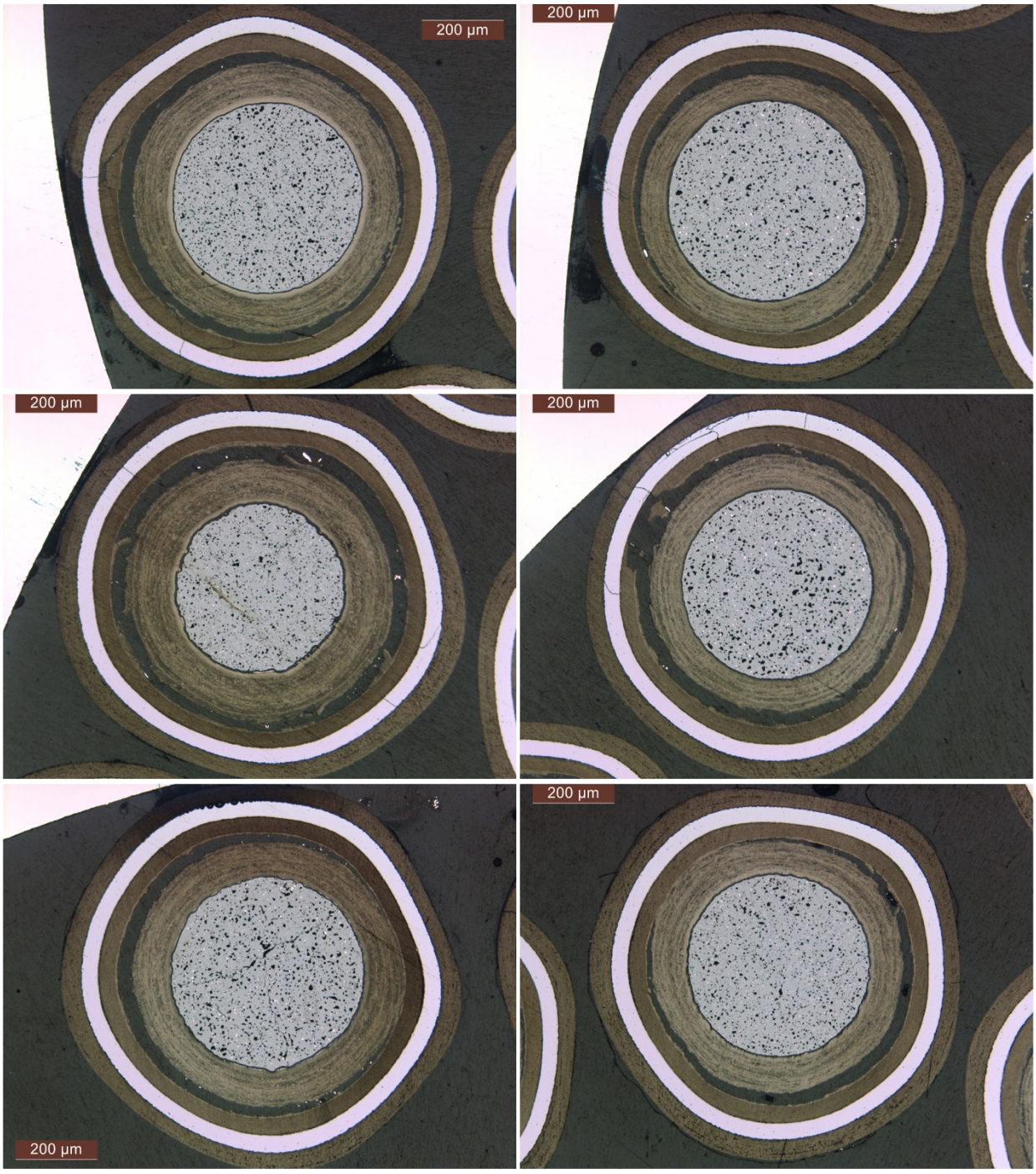

Appendix Figure C-1 continued. Random sections from AGR-2 Compact 3-1-2.

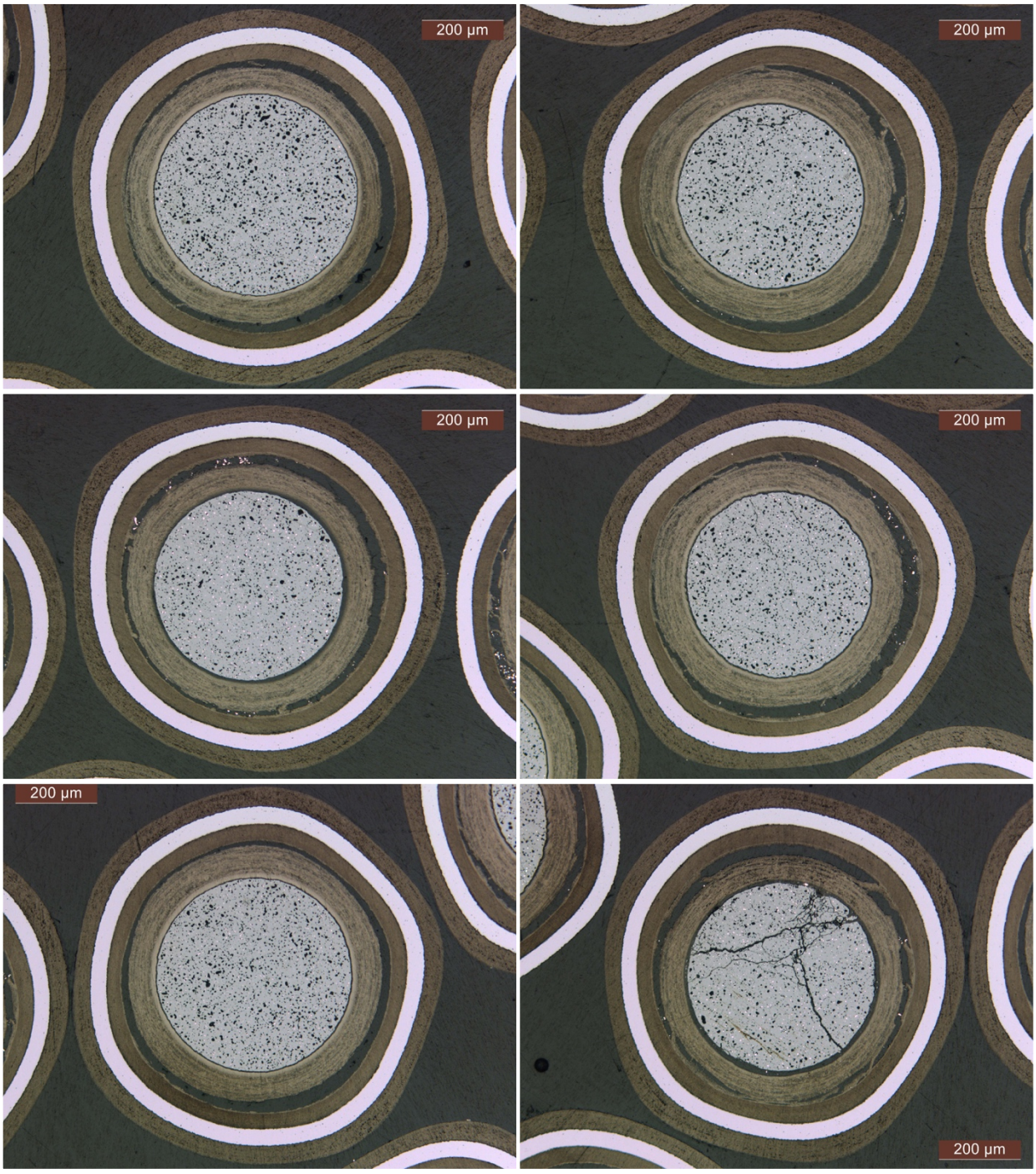

Appendix Figure C-1 continued. Random sections from AGR-2 Compact 3-1-2.

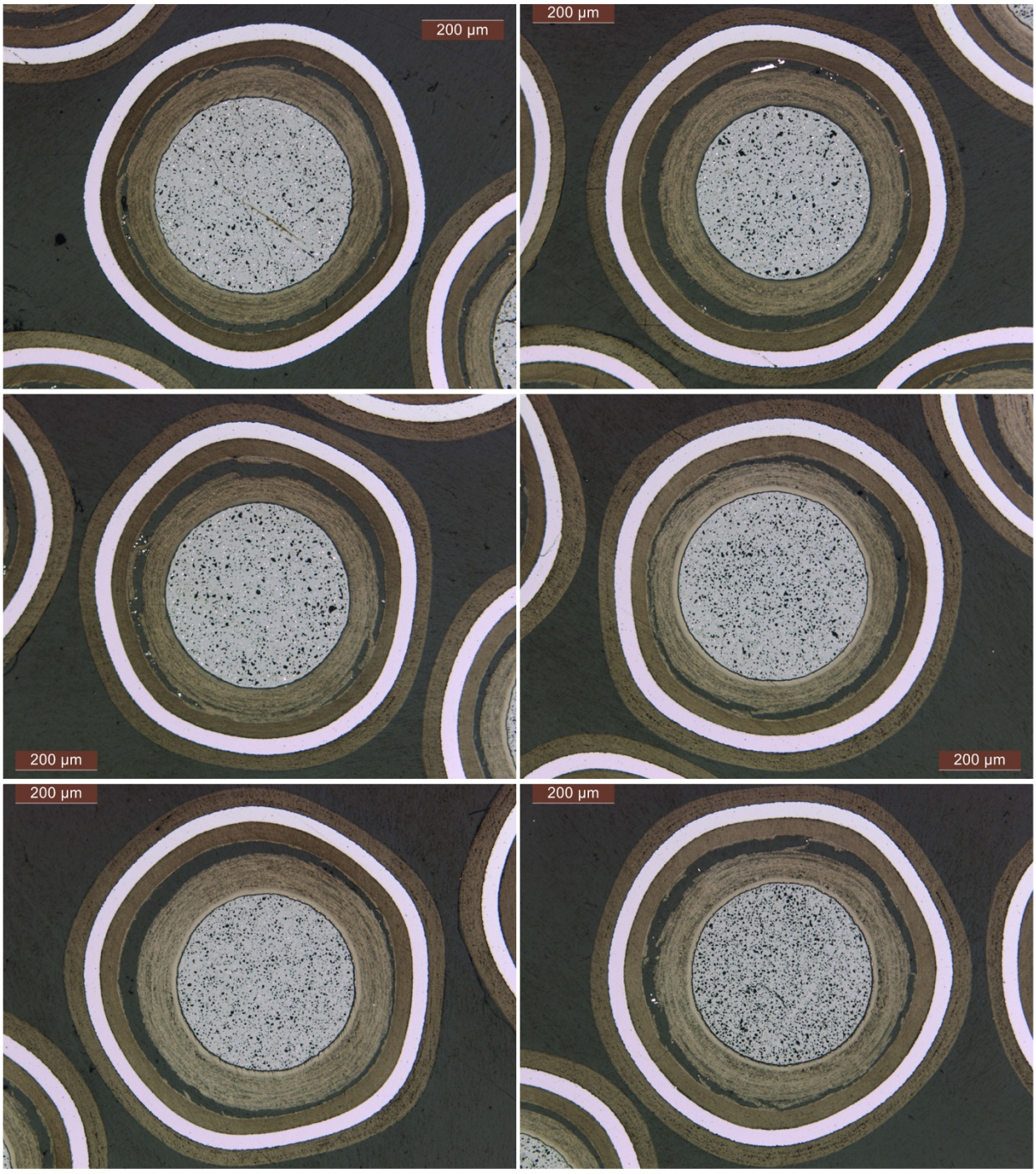

Appendix Figure C-1 continued. Random sections from AGR-2 Compact 3-1-2.

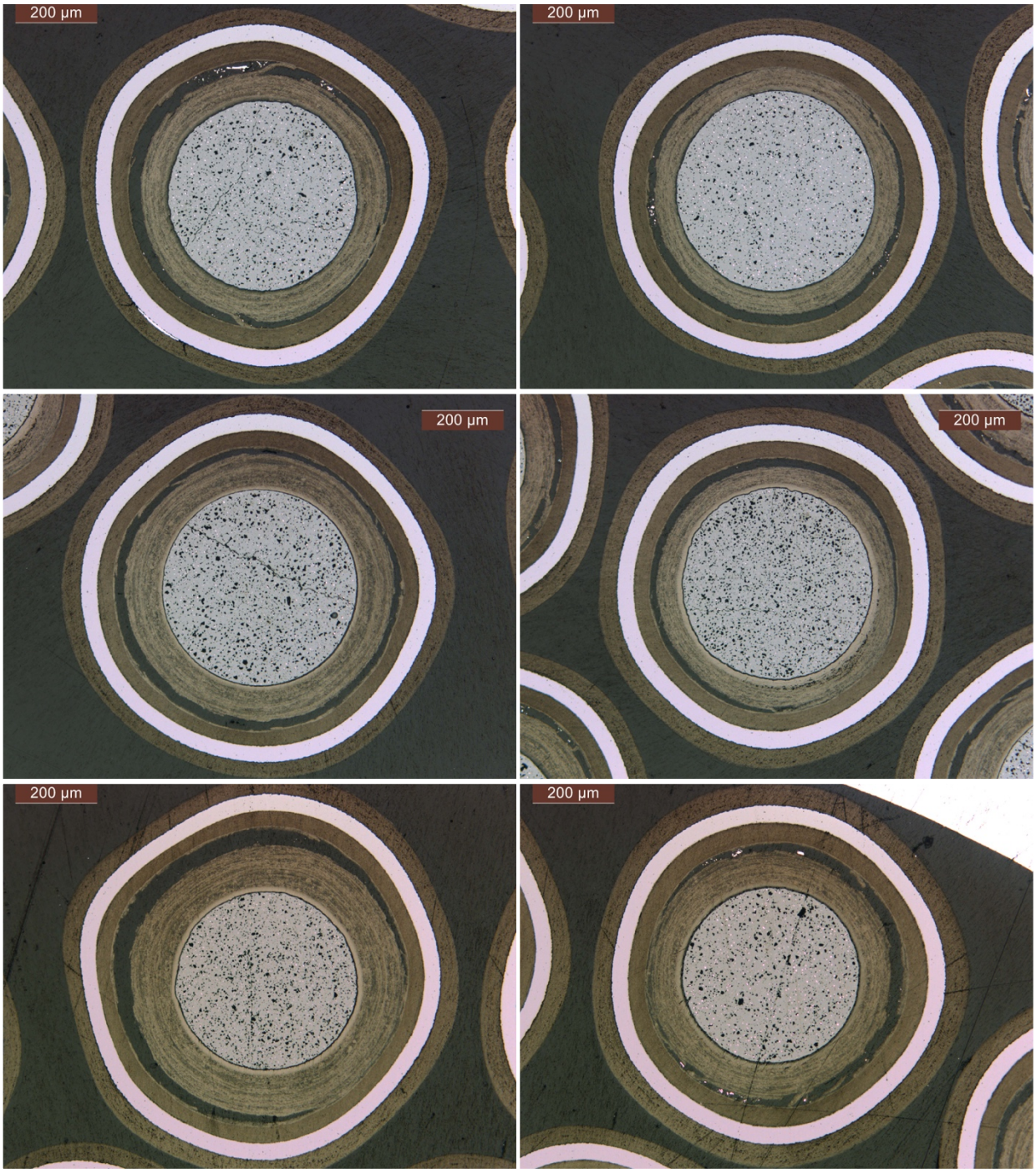

Appendix Figure C-1 continued. Random sections from AGR-2 Compact 3-1-2.

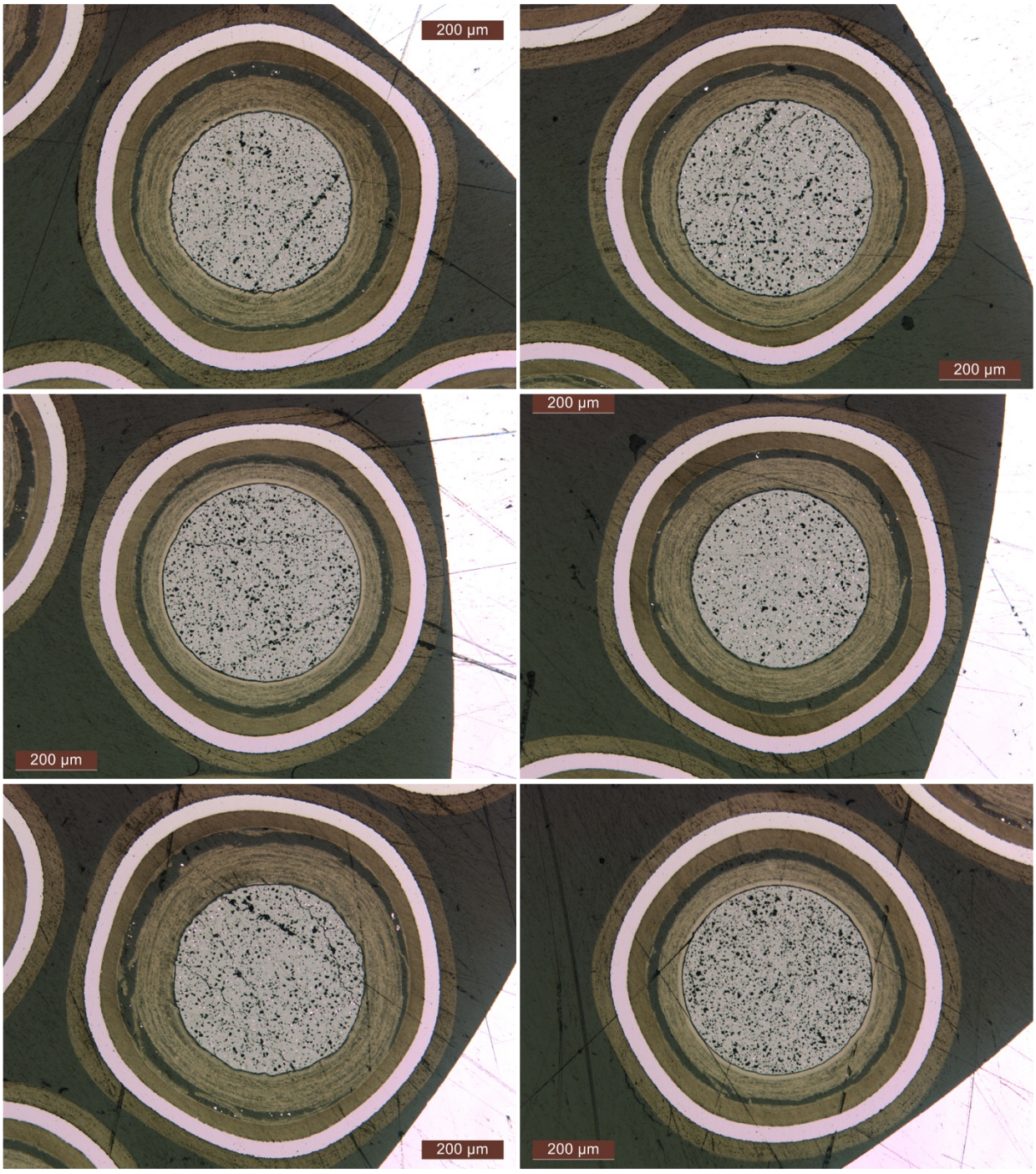

Appendix Figure C-1 continued. Random sections from AGR-2 Compact 3-1-2.

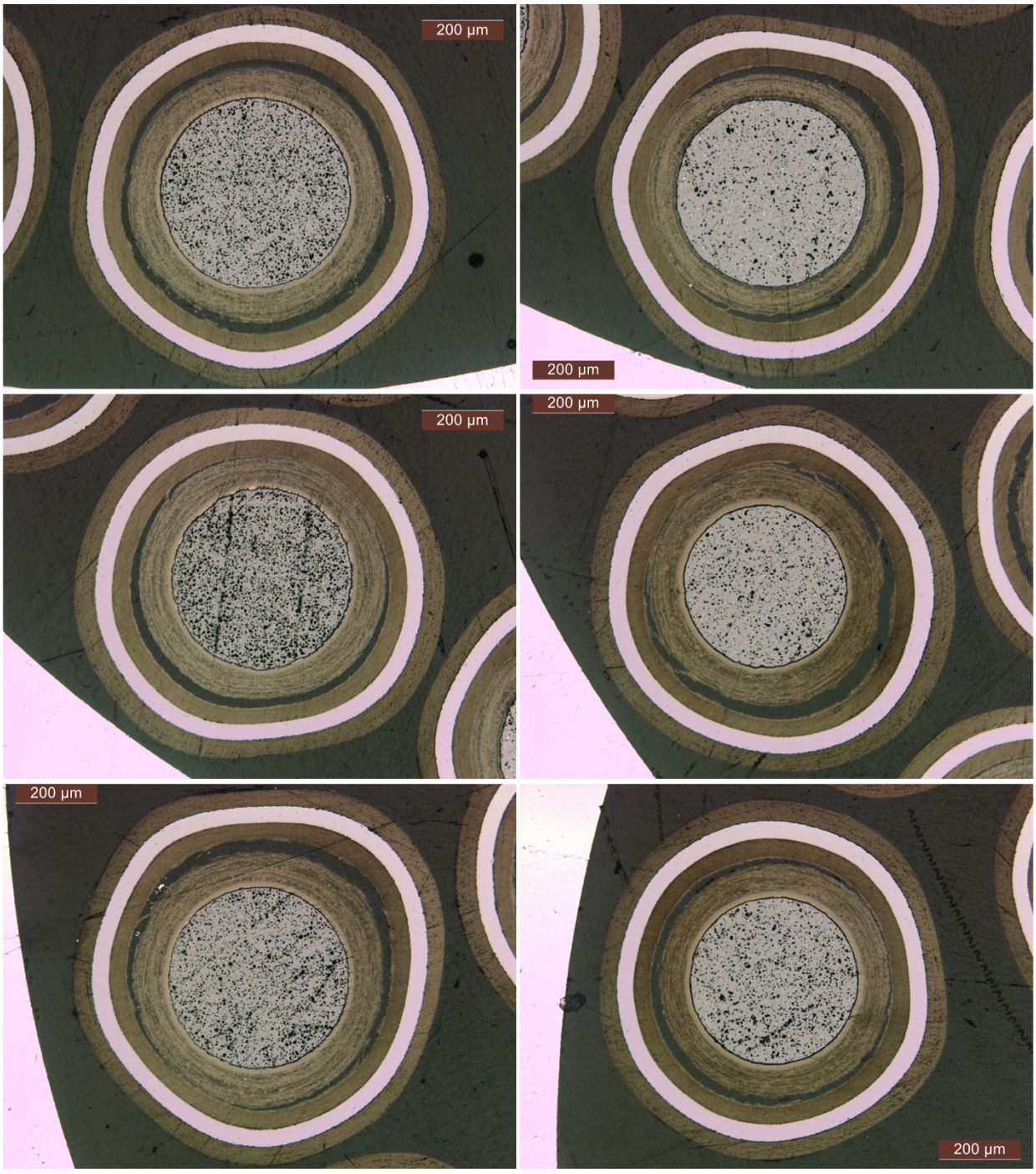

Appendix Figure C-1 continued. Random sections from AGR-2 Compact 3-1-2.

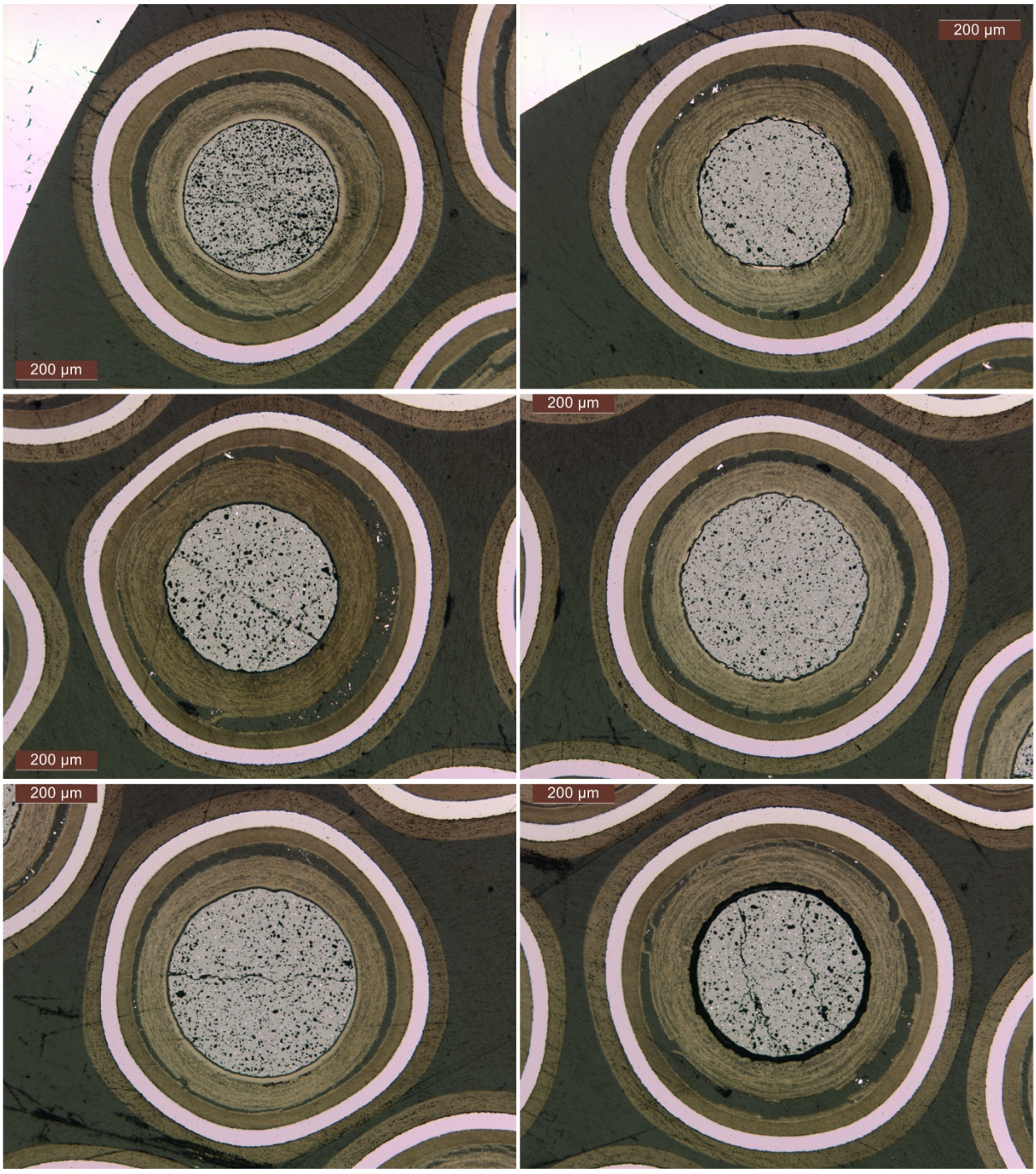

Appendix Figure C-1 continued. Random sections from AGR-2 Compact 3-1-2.

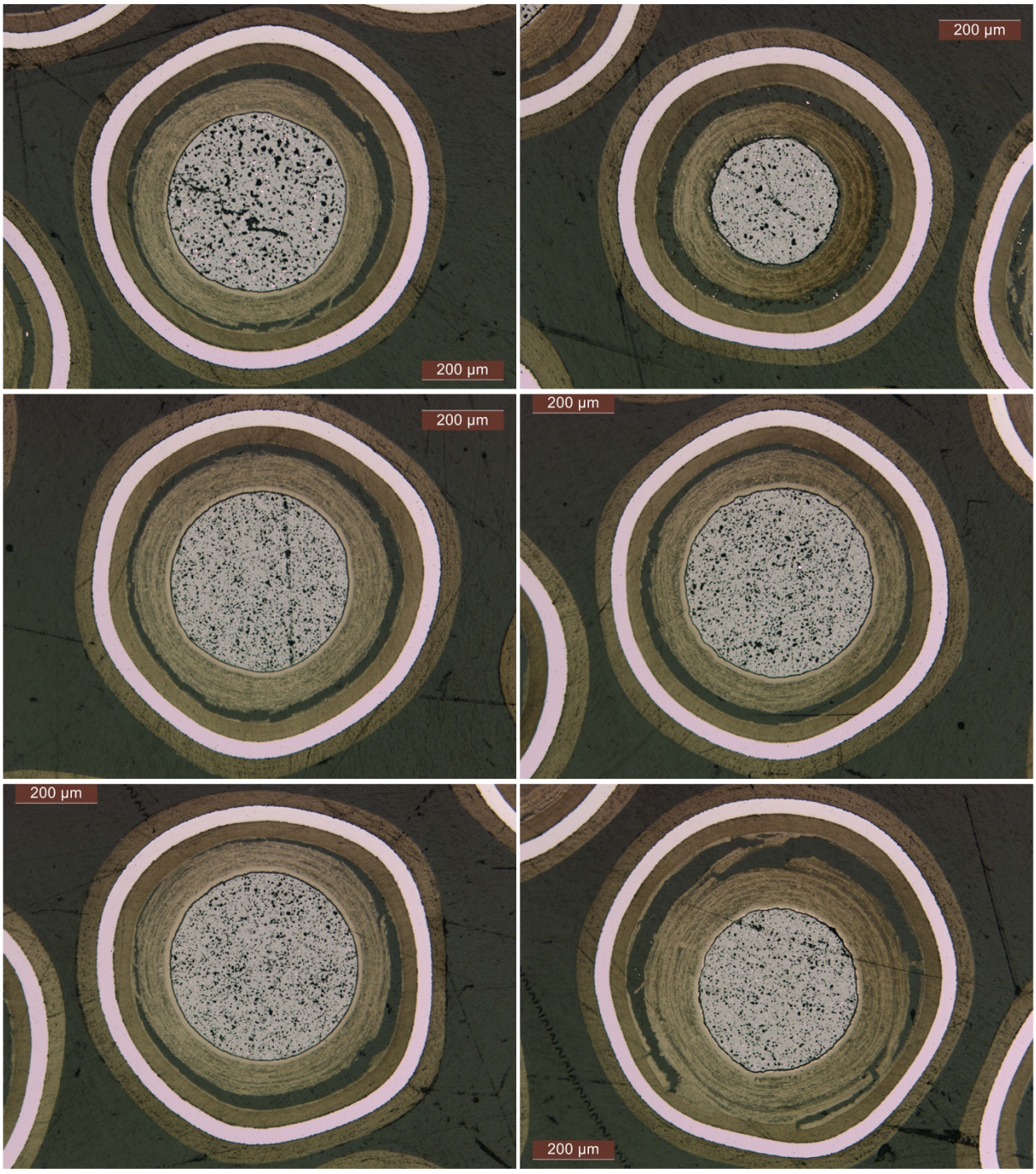

Appendix Figure C-1 continued. Random sections from AGR-2 Compact 3-1-2.

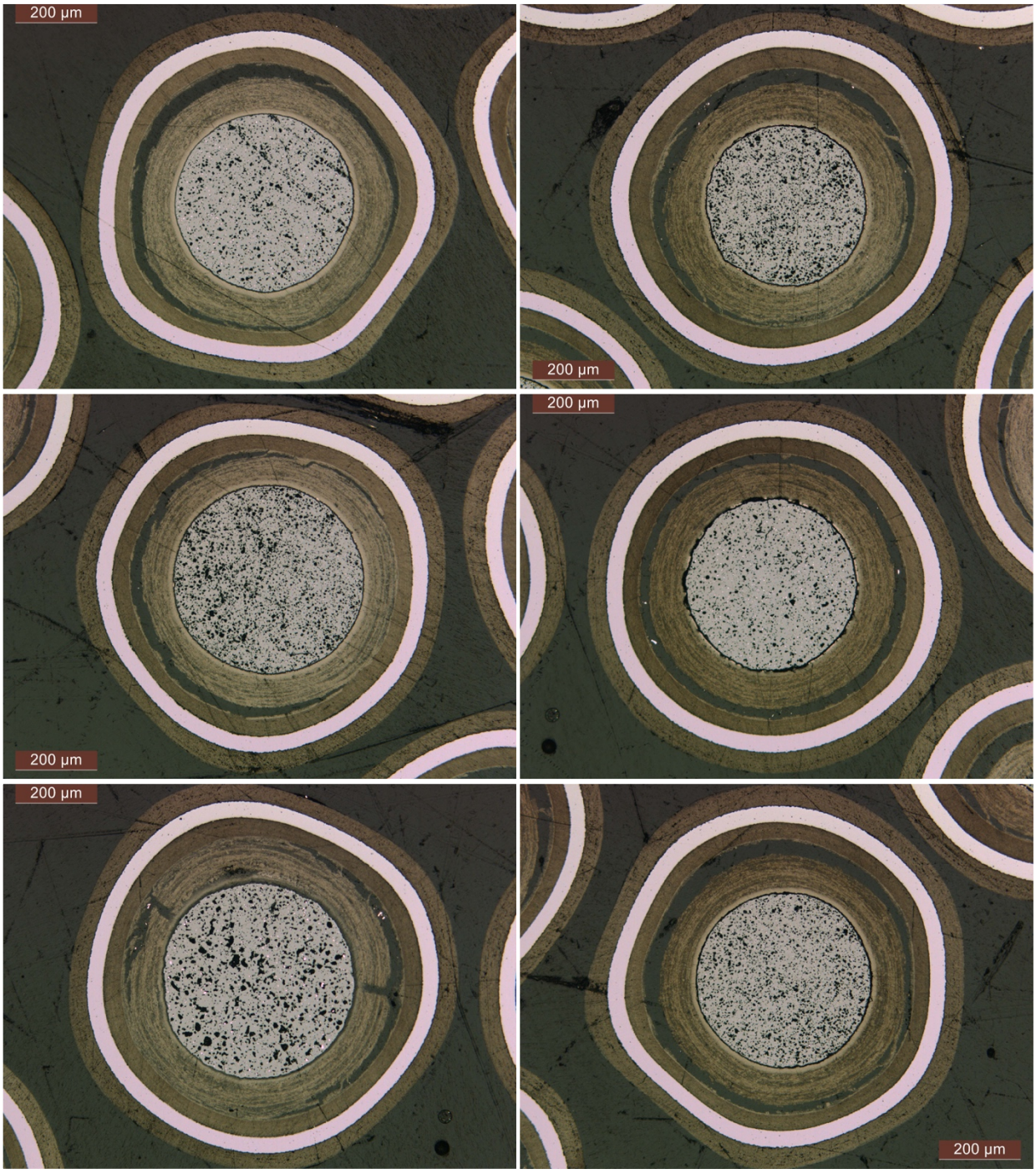

Appendix Figure C-1 continued. Random sections from AGR-2 Compact 3-1-2.

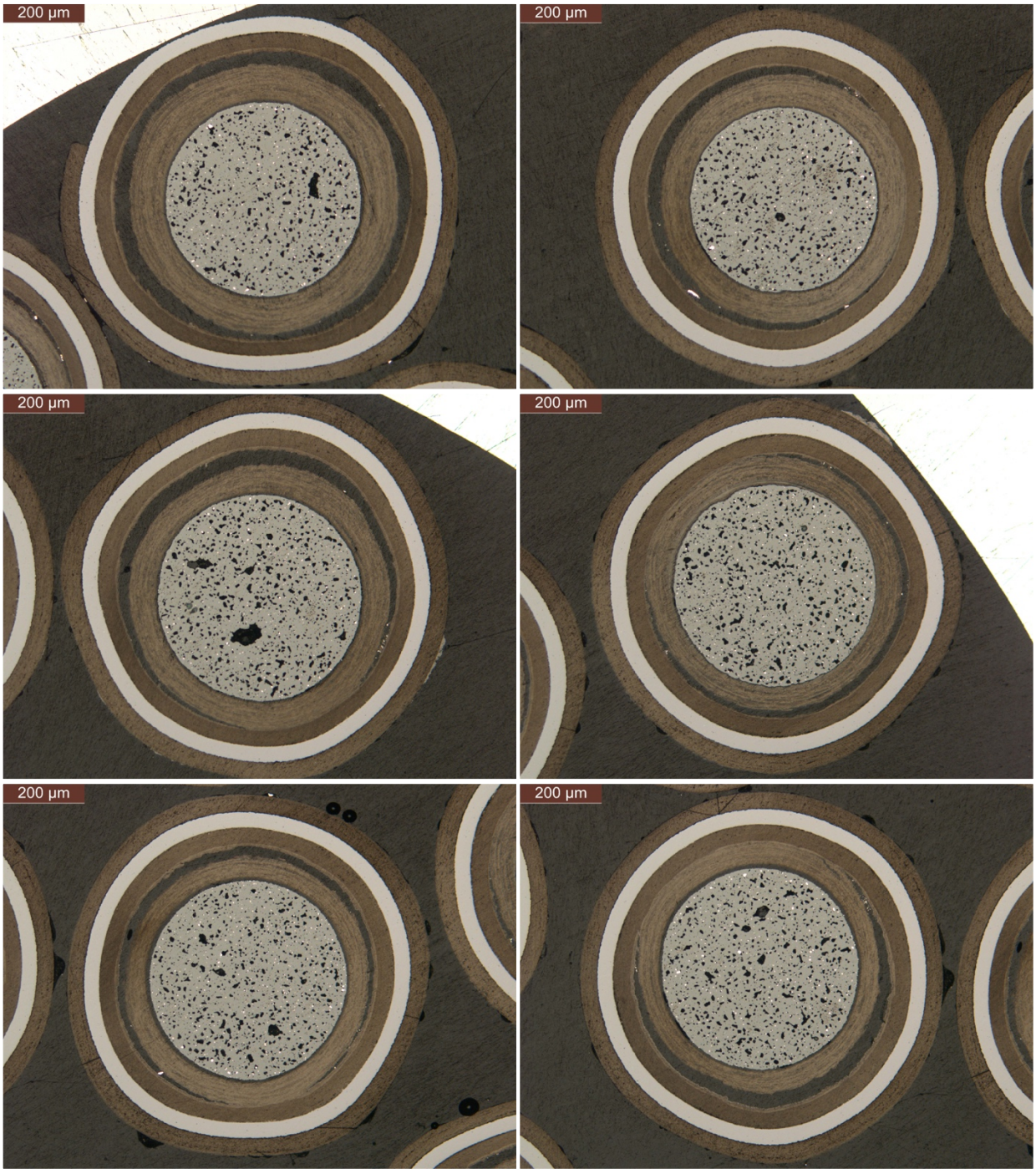

Appendix Figure C-2. Random sections from AGR-2 Compact 3-3-1.

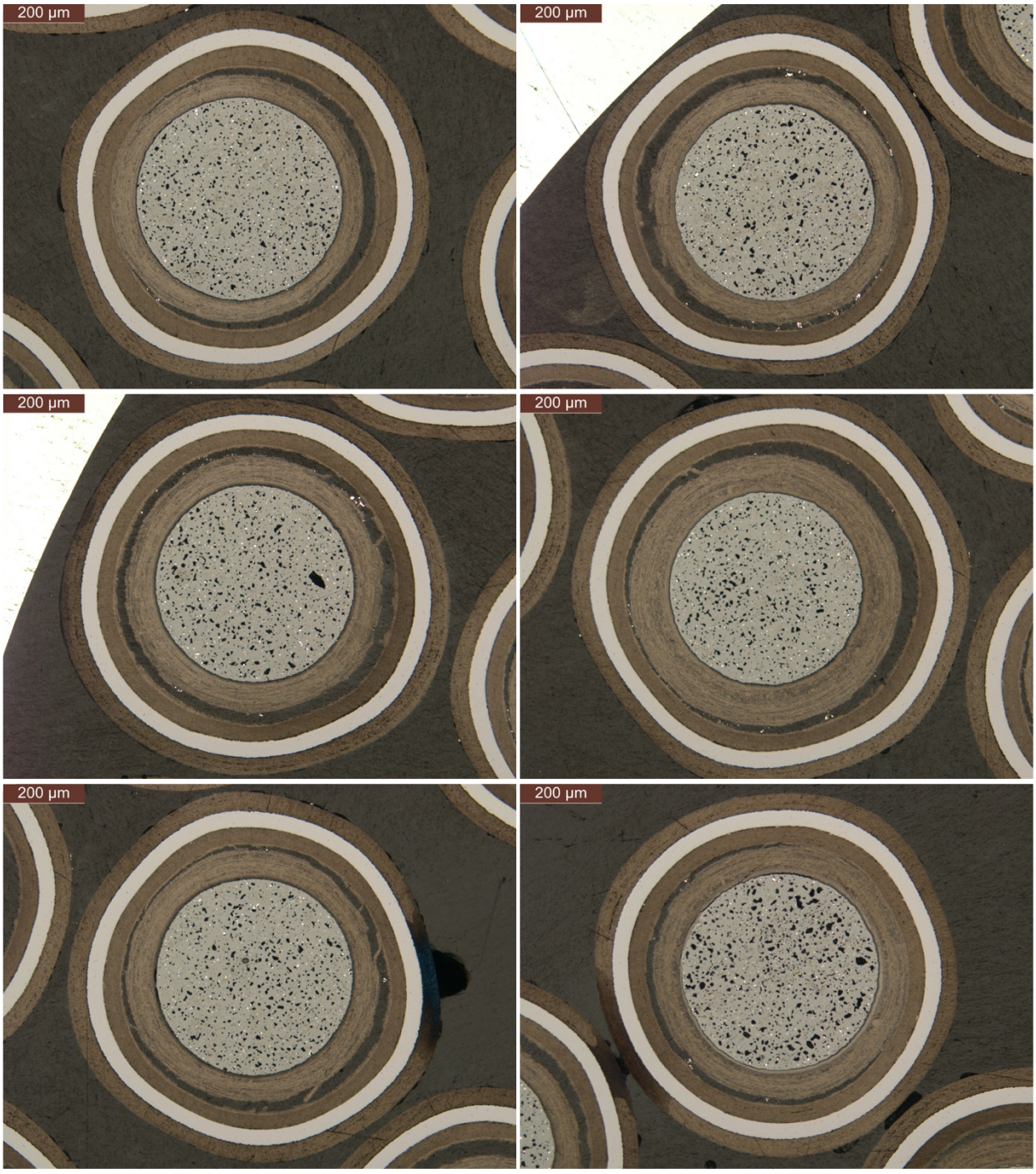

Appendix Figure C-2 continued. Random sections from AGR-2 Compact 3-3-1.

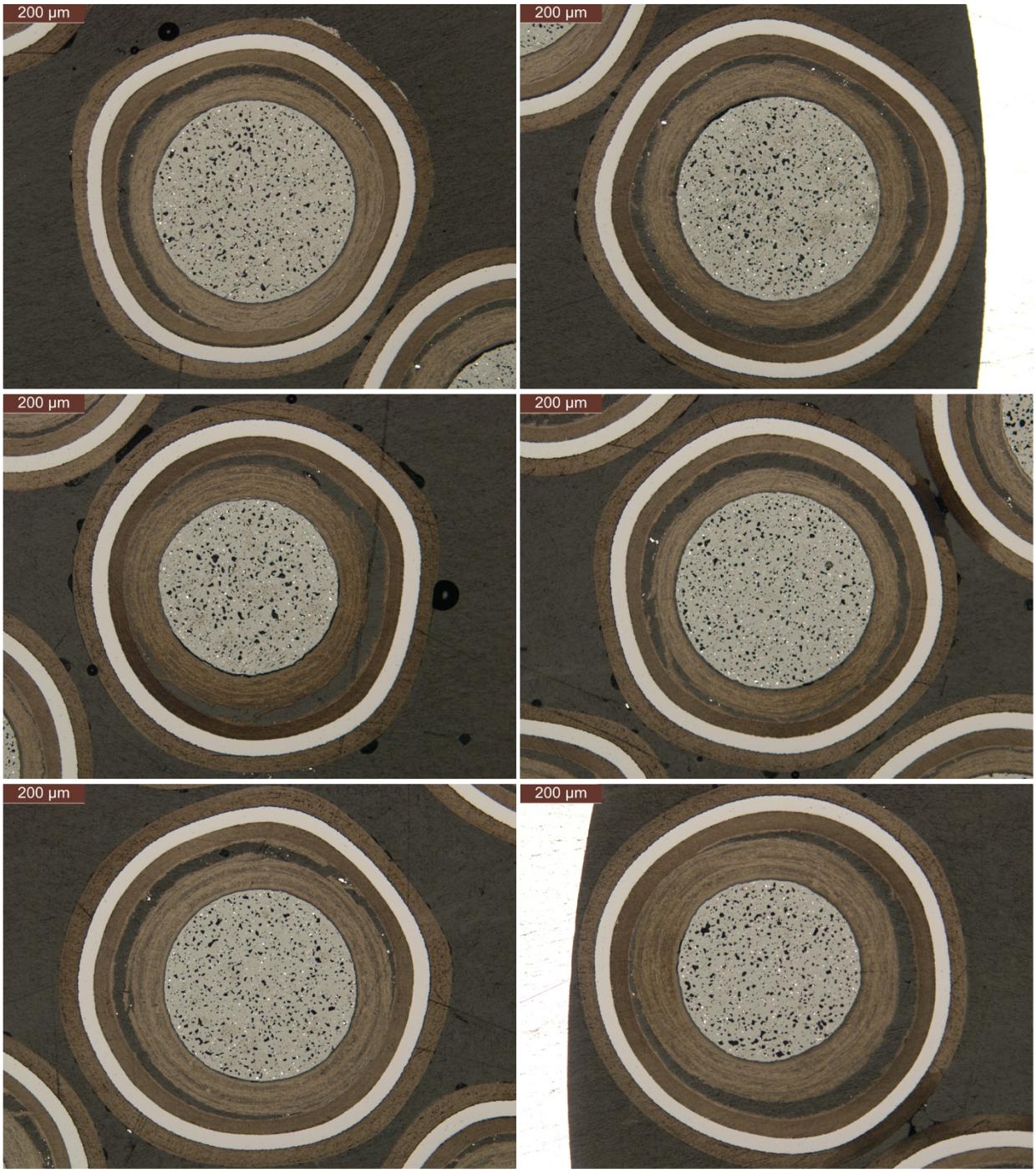

Appendix Figure C-2 continued. Random sections from AGR-2 Compact 3-3-1.

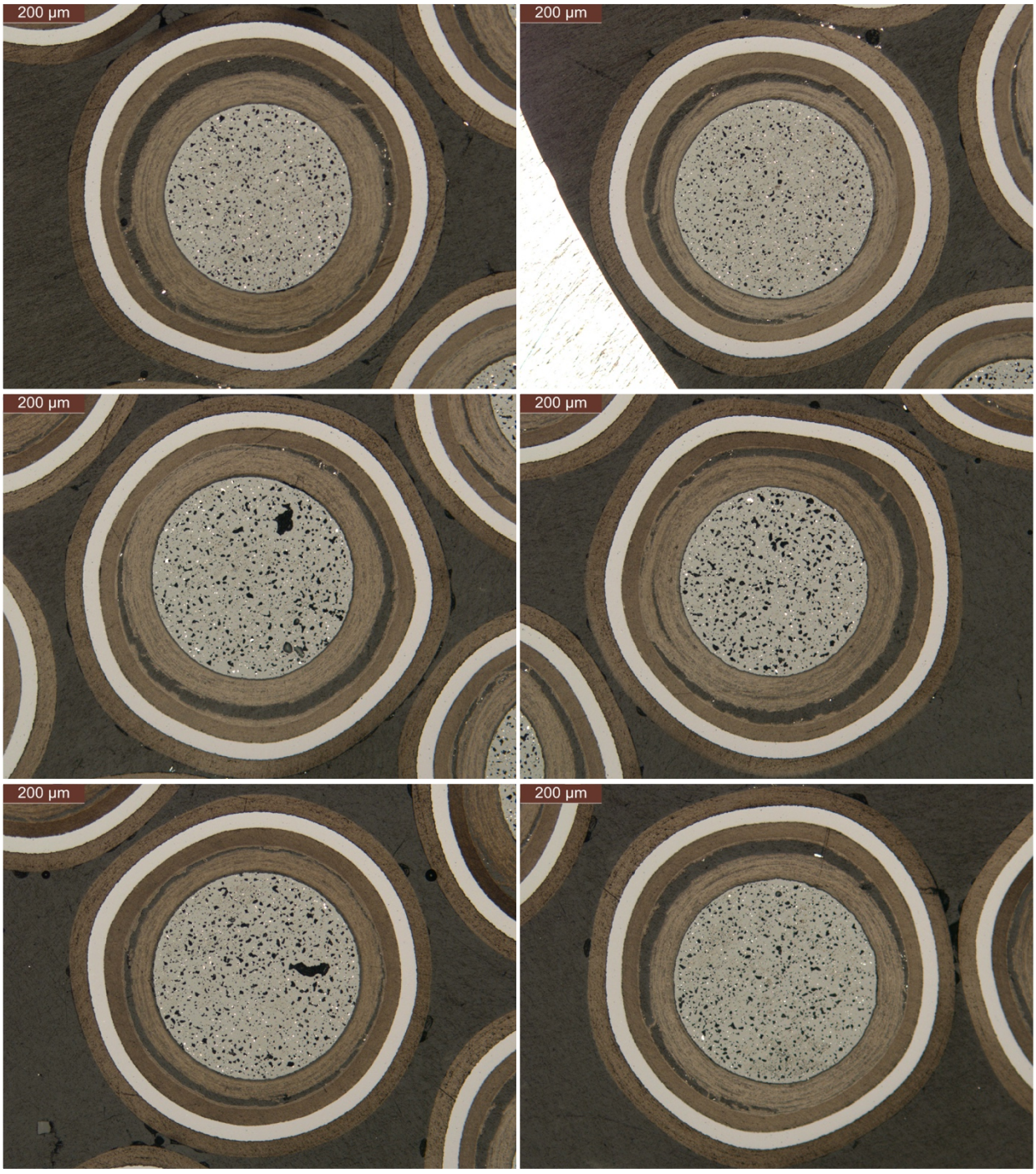

Appendix Figure C-2 continued. Random sections from AGR-2 Compact 3-3-1.

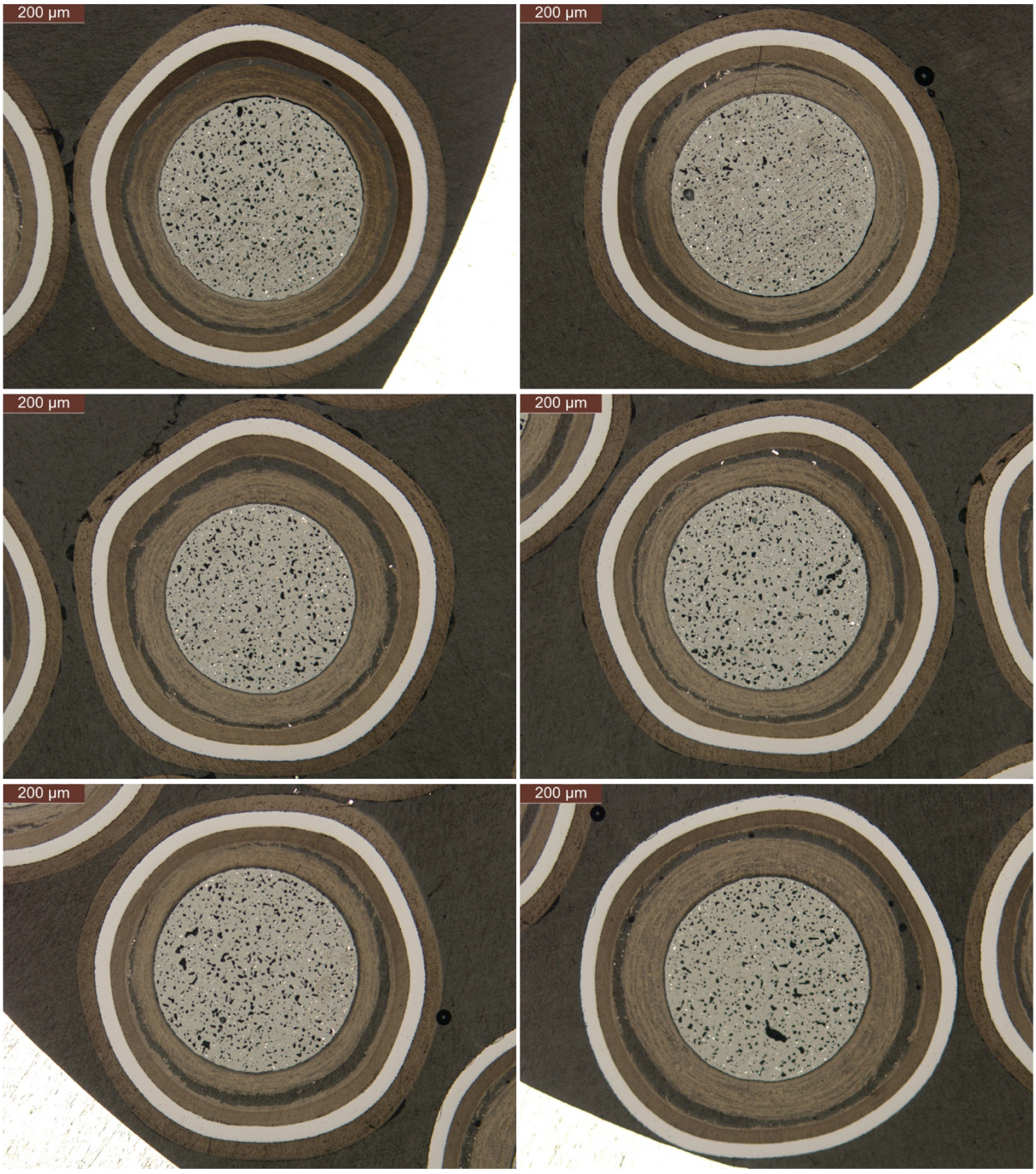

Appendix Figure C-2 continued. Random sections from AGR-2 Compact 3-3-1.

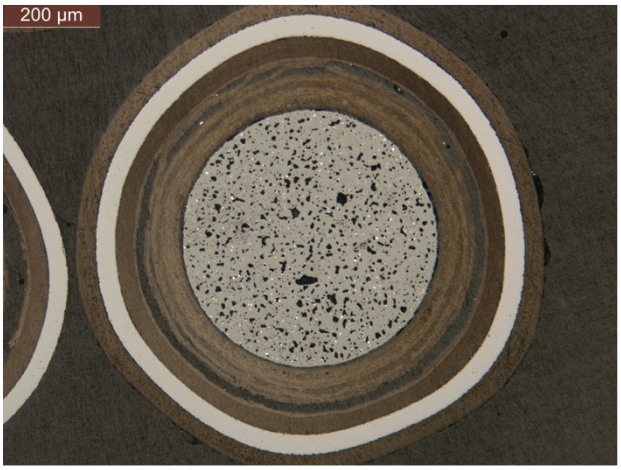

Appendix Figure C-2 continued. Random sections from AGR-2 Compact 3-3-1.

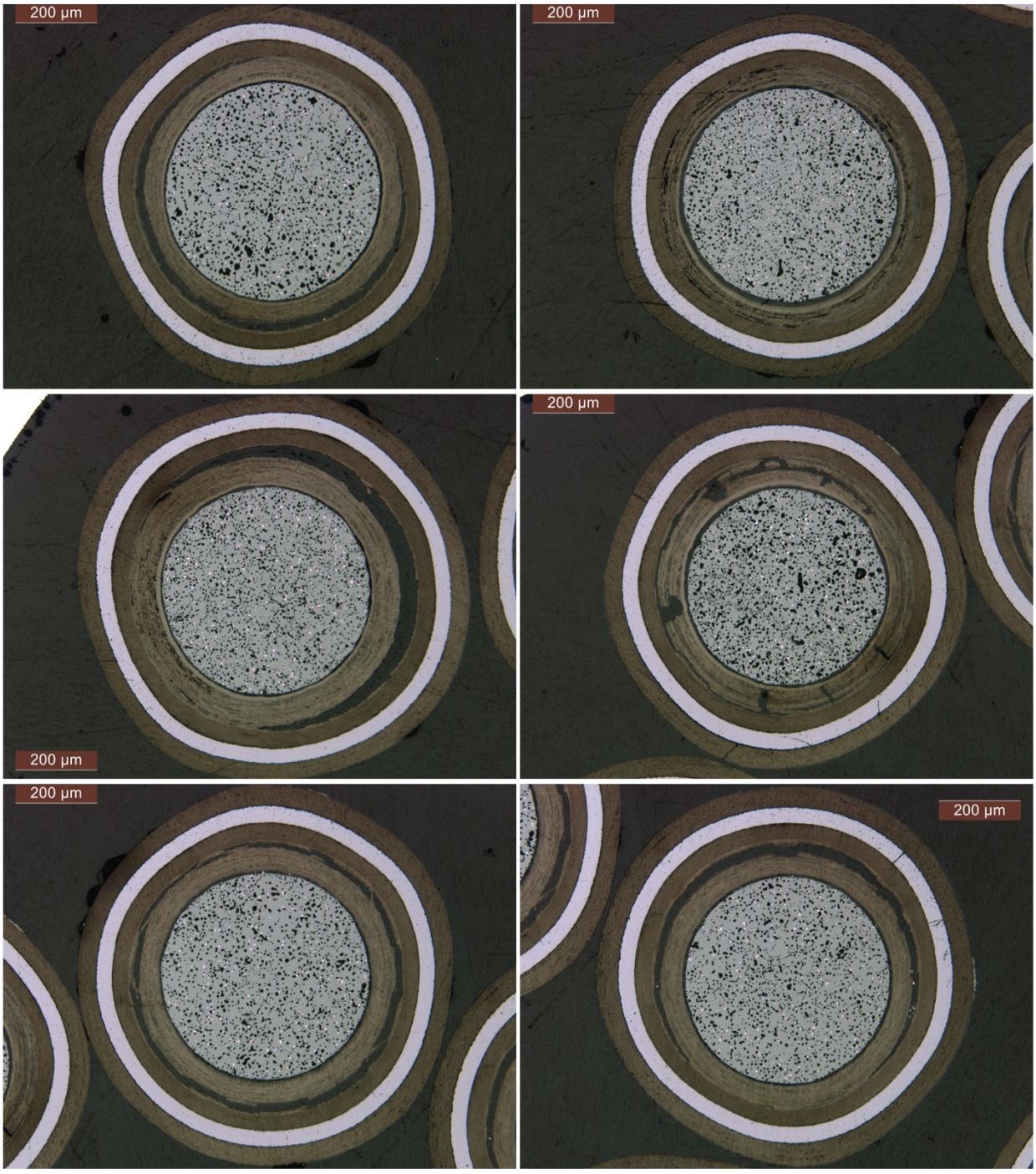

Appendix Figure C-3. AGR-2 Compact 3-4-1 particle from Bin 6.

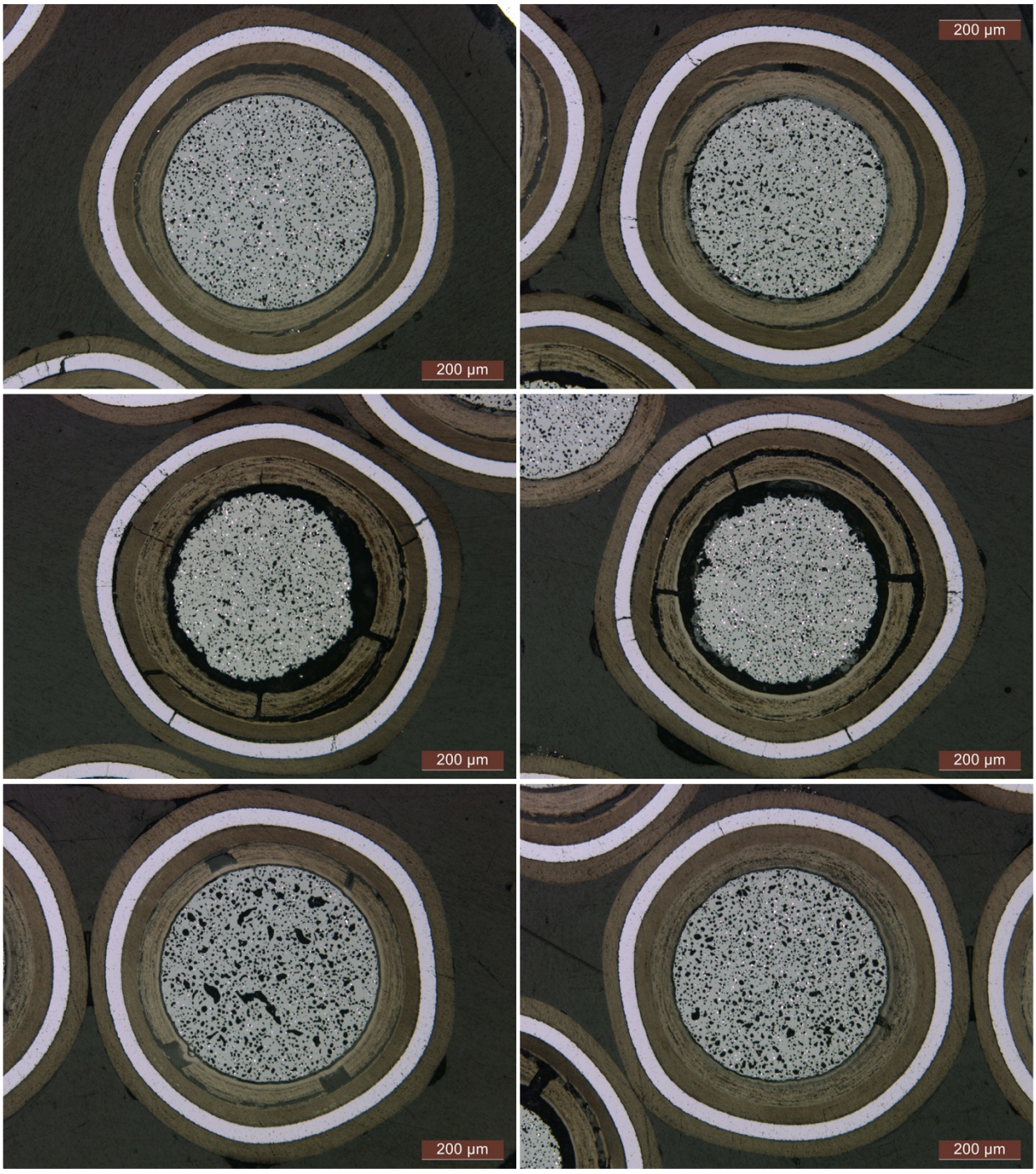

Appendix Figure C-3 continued. AGR-2 Compact 3-4-1 particle from Bin 6.

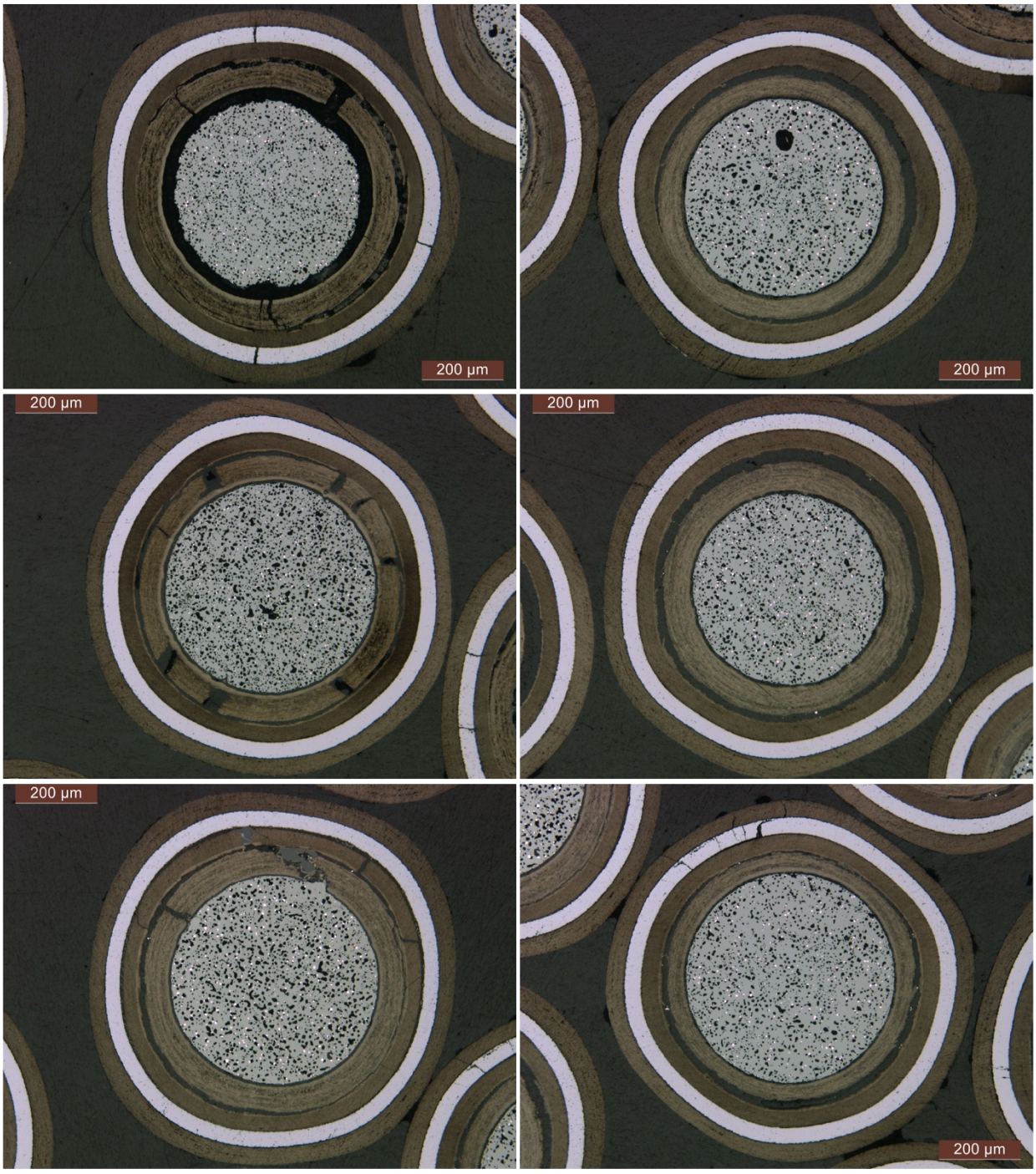

Appendix Figure C-3 continued. AGR-2 Compact 3-4-1 particle from Bin 6.

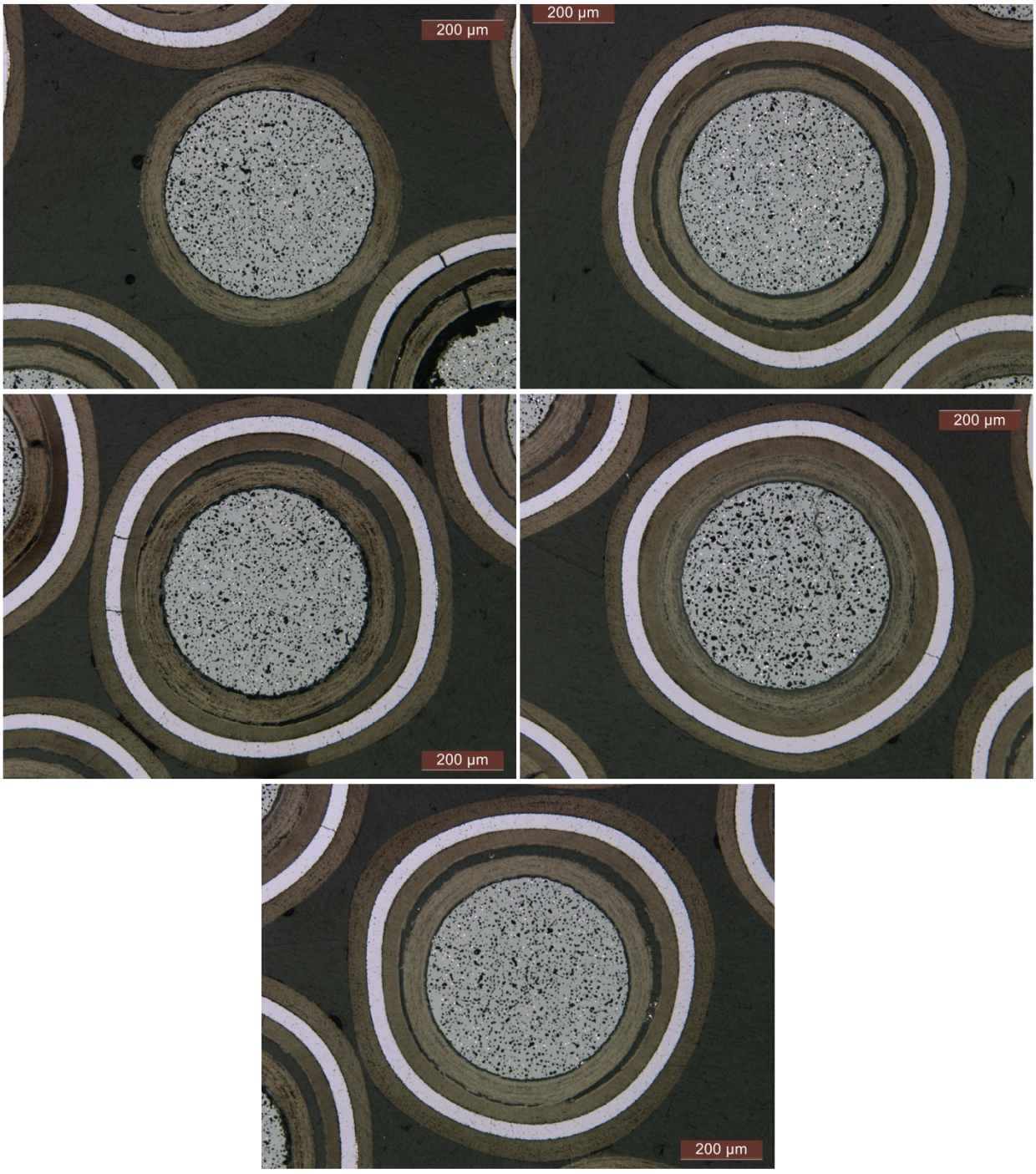

Appendix Figure C-3 continued. AGR-2 Compact 3-4-1 particle from Bin 6.

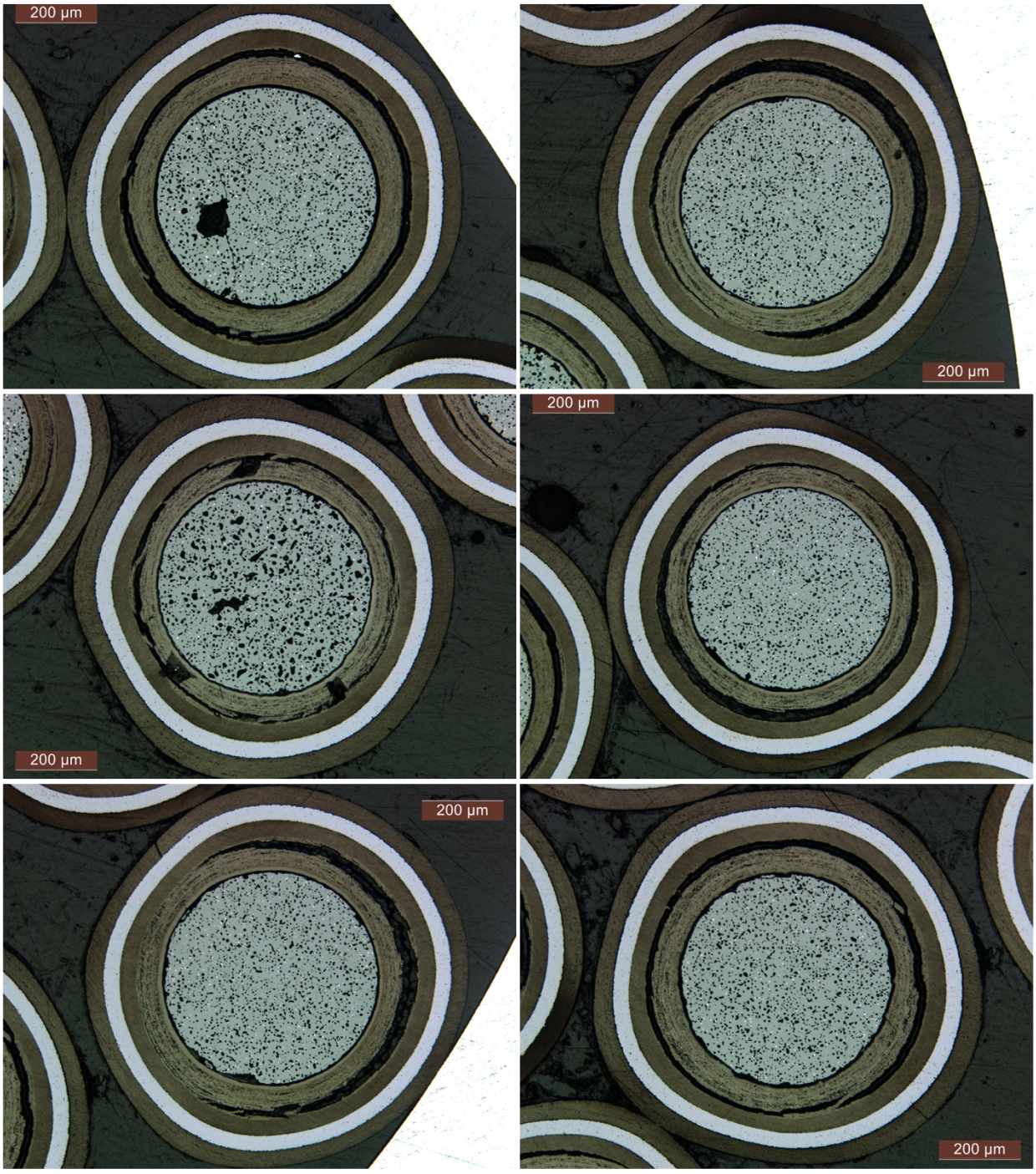

Appendix Figure C-4. AGR-2 Compact 3-4-1 particle from Bin 8.

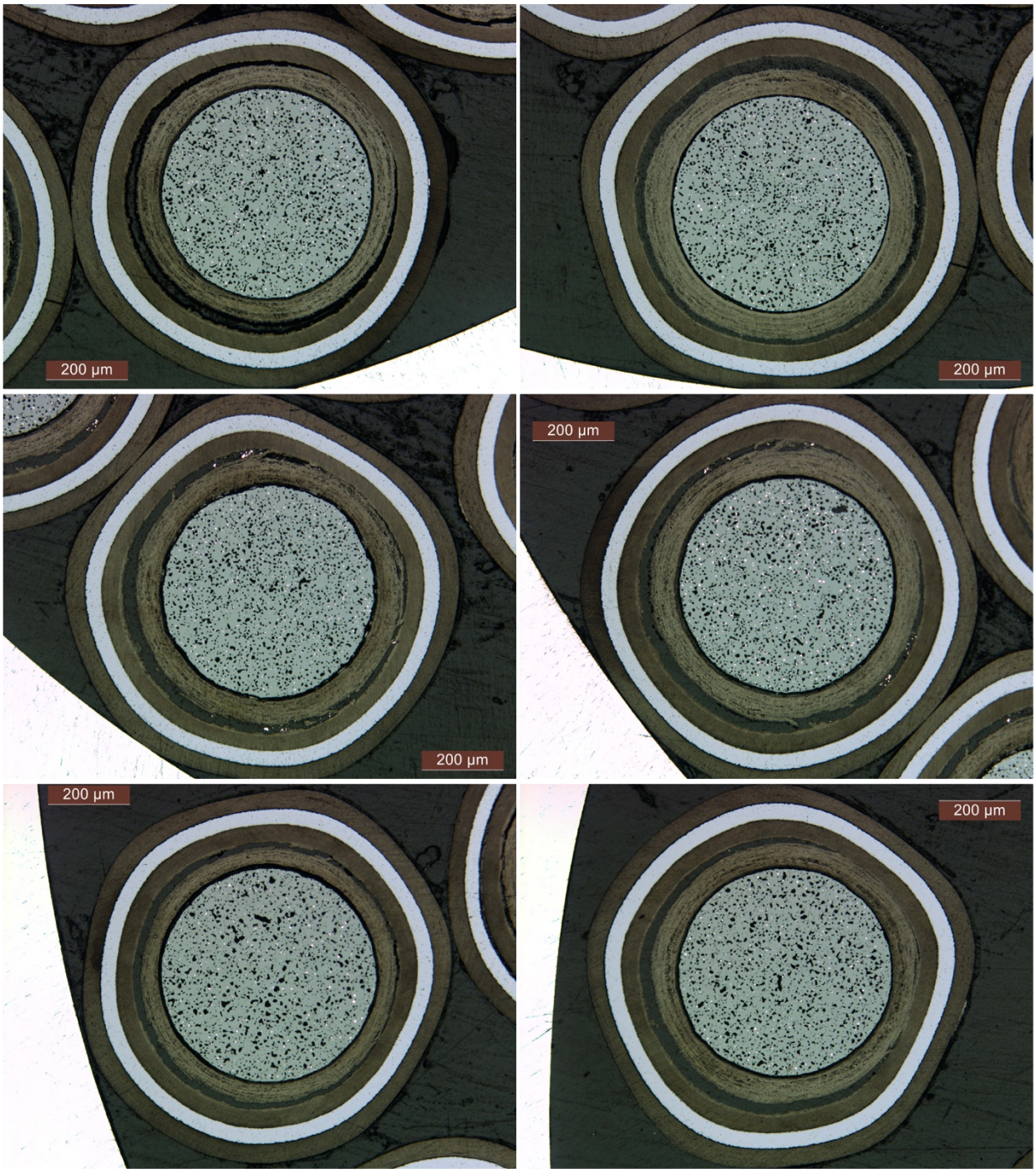

Appendix Figure C-4 continued. AGR-2 Compact 3-4-1 particle from Bin 8.

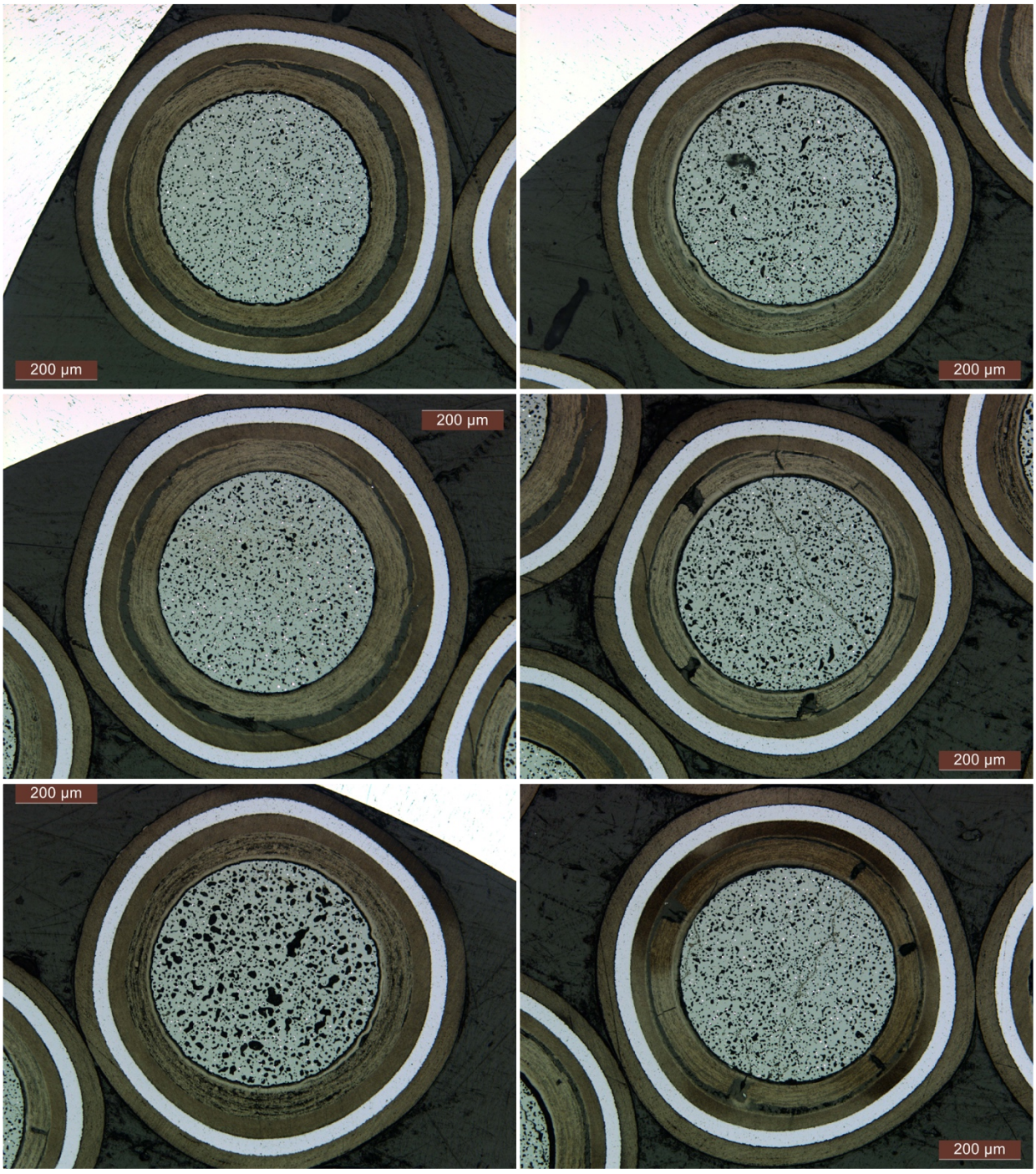

Appendix Figure C-4 continued. AGR-2 Compact 3-4-1 particle from Bin 8.

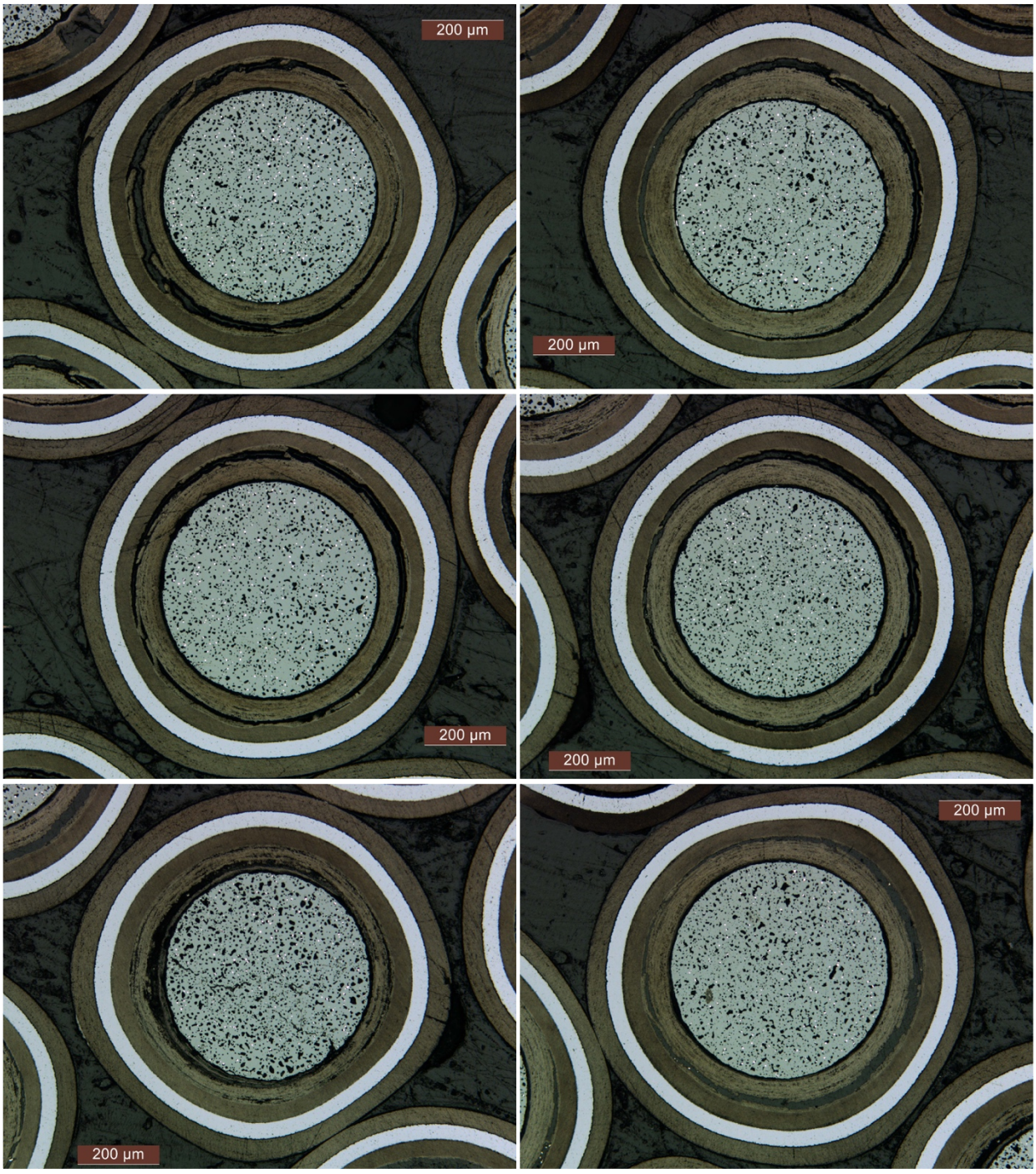

Appendix Figure C-4 continued. AGR-2 Compact 3-4-1 particle from Bin 8.

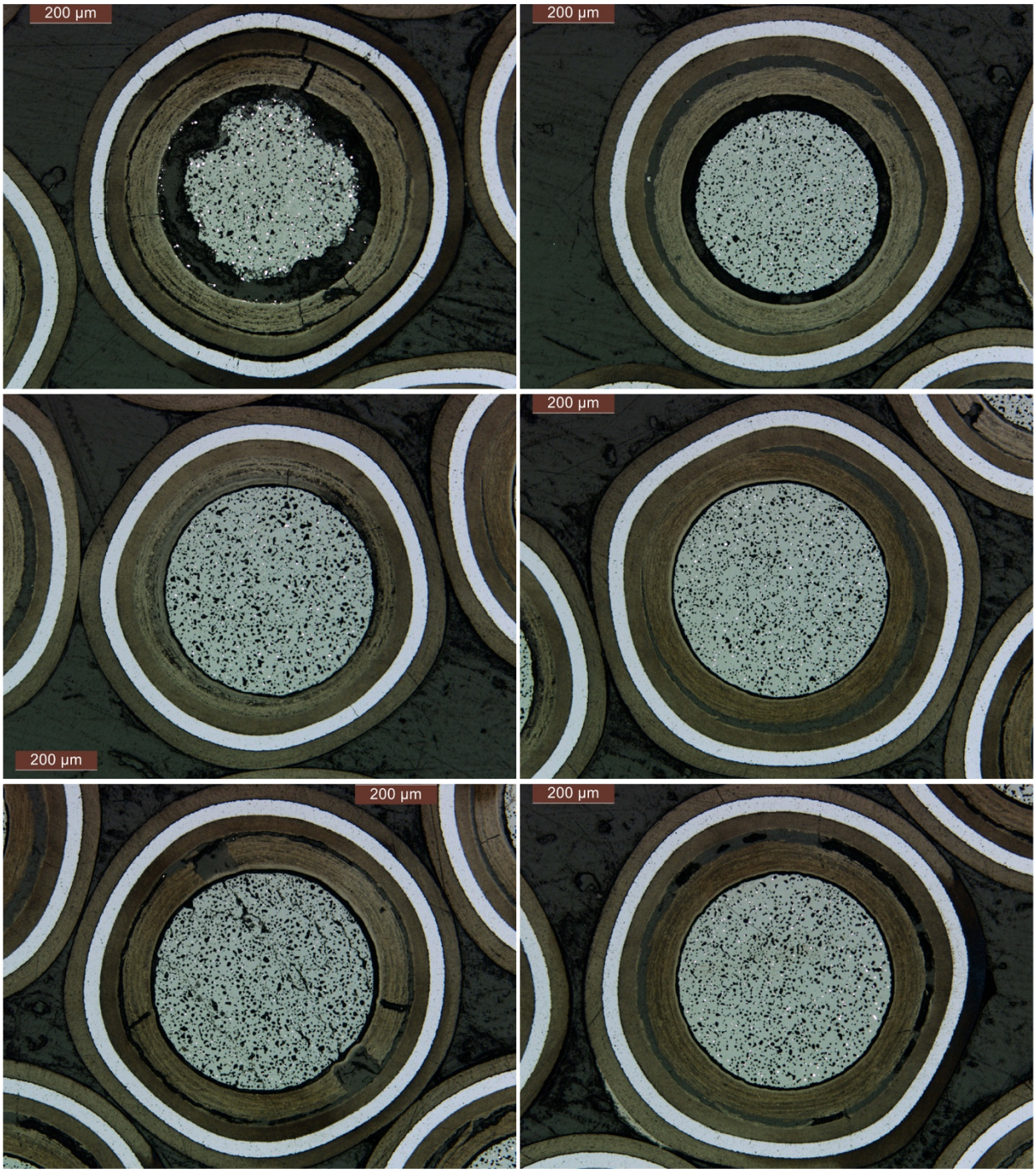

Appendix Figure C-4 continued. AGR-2 Compact 3-4-1 particle from Bin 8.

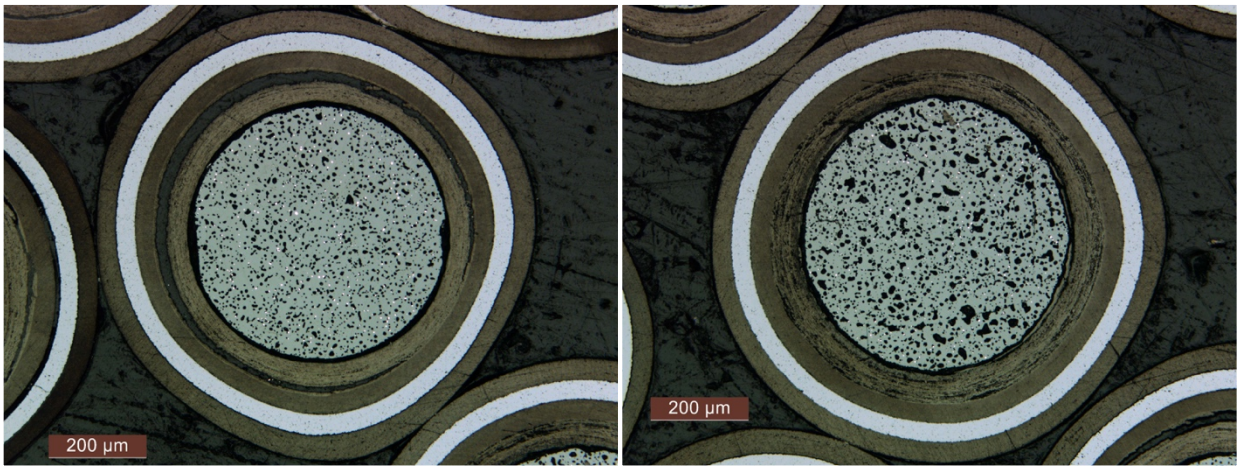

Appendix Figure C-4 continued. AGR-2 Compact 3-4-1 particle from Bin 8.

APPENDIX D. SEM MICROGRAPHS

This appendix contains the SEM and BEC survey images of each analyzed particle, which were generally acquired using two magnifications, 500× to show the TRISO layers and 1,500× to show the SiC and IPyC/SiC interface. Images were typically taken around the circumference of the particles at locations in the four cardinal directions and the four intercardinal directions. Appendix Table D-1 provides a list of the images in this appendix.

Appendix Table D-1. Guide to SEM images

Particle	500× SEI	1,500× SEI	500× BEC	1,500× BEC
312-RS06	Appendix Figure D-1	Appendix Figure D-2	Appendix Figure D-3	Appendix Figure D-4
312-RS32	Appendix Figure D-5		Appendix Figure D-6	
312-RS05	Appendix Figure D-7		Appendix Figure D-8	
312-RS34	Appendix Figure D-9	Appendix Figure D-10	Appendix Figure D-11	Appendix Figure D-12
312-RS02	Appendix Figure D-13		Appendix Figure D-14	
312-RS11	Appendix Figure D-15	Appendix Figure D-16	Appendix Figure D-17	Appendix Figure D-18
312-SP02			Appendix Figure D-19	Appendix Figure D-20
331-RS04	Appendix Figure D-21	Appendix Figure D-22	Appendix Figure D-23	Appendix Figure D-24
331-RS19	Appendix Figure D-25	Appendix Figure D-26	Appendix Figure D-27	Appendix Figure D-28
331-RS03	Appendix Figure D-29	Appendix Figure D-30	Appendix Figure D-31	Appendix Figure D-32
331-RS12	Appendix Figure D-33	Appendix Figure D-34	Appendix Figure D-35	Appendix Figure D-36
311-RS07	Appendix Figure D-37	Appendix Figure D-38	Appendix Figure D-39	Appendix Figure D-40
311-RS29	Appendix Figure D-41	Appendix Figure D-42	Appendix Figure D-43	Appendix Figure D-44
311-RS08	Appendix Figure D-45	Appendix Figure D-46	Appendix Figure D-47	Appendix Figure D-48
311-RS32	Appendix Figure D-49	Appendix Figure D-50	Appendix Figure D-51	Appendix Figure D-52
311-RS18	Appendix Figure D-53	Appendix Figure D-54	Appendix Figure D-55	Appendix Figure D-56
311-RS36	Appendix Figure D-57	Appendix Figure D-58	Appendix Figure D-59	Appendix Figure D-60
332-RS12	Appendix Figure D-61	Appendix Figure D-62	Appendix Figure D-63	Appendix Figure D-64
332-RS18	Appendix Figure D-65	Appendix Figure D-66	Appendix Figure D-67	Appendix Figure D-68
332-RS22	Appendix Figure D-69	Appendix Figure D-70	Appendix Figure D-71	Appendix Figure D-72
332-RS43	Appendix Figure D-73	Appendix Figure D-74	Appendix Figure D-75	Appendix Figure D-76
332-RS26	Appendix Figure D-77	Appendix Figure D-78	Appendix Figure D-79	Appendix Figure D-80
332-RS31	Appendix Figure D-81	Appendix Figure D-82	Appendix Figure D-83	Appendix Figure D-84
332-SP01			Appendix Figure D-85	Appendix Figure D-86
332-SP02			Appendix Figure D-87	Appendix Figure D-88
332-SP03			Appendix Figure D-89	Appendix Figure D-90

Appendix Table D-1 continued. Guide to SEM images

Particle	500× SEI	1,500× SEI	500× BEC	1,500× BEC
342-RS17	Appendix Figure D-91		Appendix Figure D-92	Appendix Figure D-93
342-RS29	Appendix Figure D-94		Appendix Figure D-95	Appendix Figure D-96
342-RS07	Appendix Figure D-97		Appendix Figure D-98	Appendix Figure D-99
342-RS21	Appendix Figure D-100		Appendix Figure D-101	Appendix Figure D-102
342-RS03	Appendix Figure D-103		Appendix Figure D-104	Appendix Figure D-105
342-RS15	Appendix Figure D-106		Appendix Figure D-107	Appendix Figure D-108
342-SP01			Appendix Figure D-109	Appendix Figure D-110
342-SP06			Appendix Figure D-111	Appendix Figure D-112
342-SP07			Appendix Figure D-113	Appendix Figure D-114
342-SP09			Appendix Figure D-115	Appendix Figure D-116
342-SP10			Appendix Figure D-117	Appendix Figure D-118
342-SP14			Appendix Figure D-119	Appendix Figure D-120
342-SP17			Appendix Figure D-121	Appendix Figure D-122
341-RS21	Appendix Figure D-123	Appendix Figure D-124	Appendix Figure D-125	Appendix Figure D-126
341-RS36	Appendix Figure D-127	Appendix Figure D-128	Appendix Figure D-129	Appendix Figure D-130
341-RS01	Appendix Figure D-131	Appendix Figure D-132	Appendix Figure D-133	Appendix Figure D-134
341-SP01			Appendix Figure D-135	Appendix Figure D-136
341-SP03			Appendix Figure D-137	Appendix Figure D-138
341-SP15			Appendix Figure D-139	Appendix Figure D-140

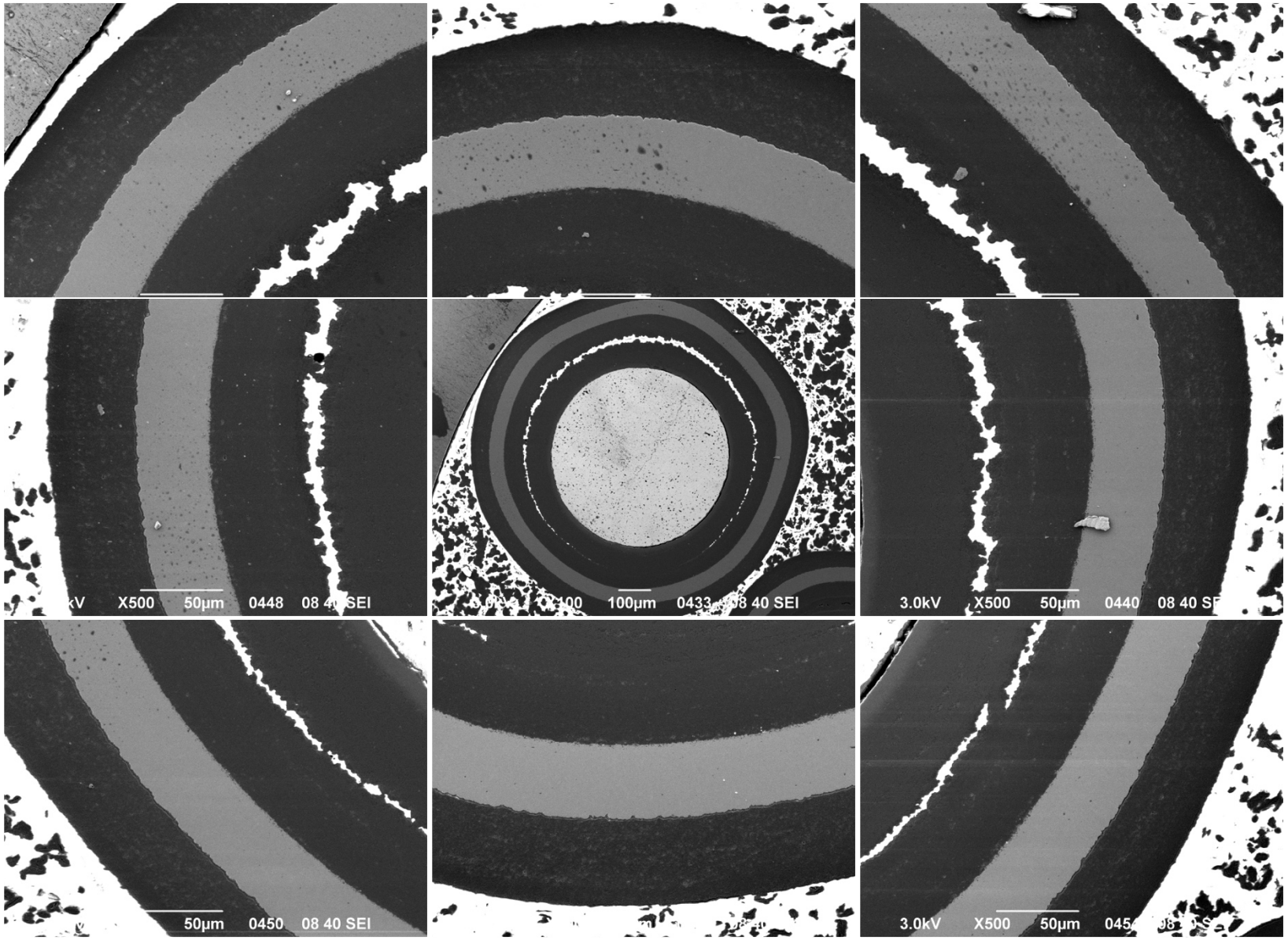

Appendix Figure D-1. 500× SEI micrographs of Particle 312-RS06.

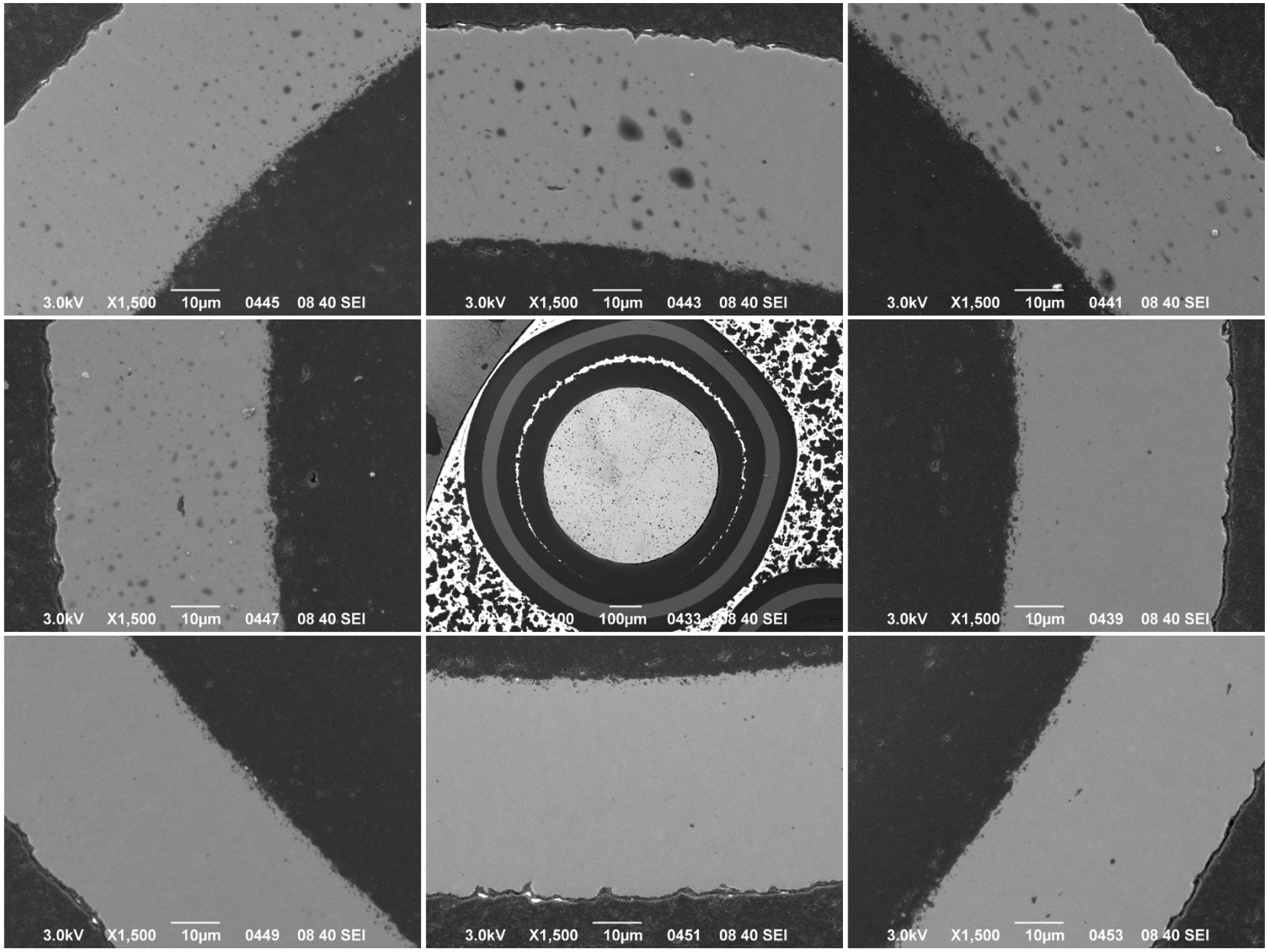

Appendix Figure D-2. 1,500× SEI micrographs of Particle 312-RS06.

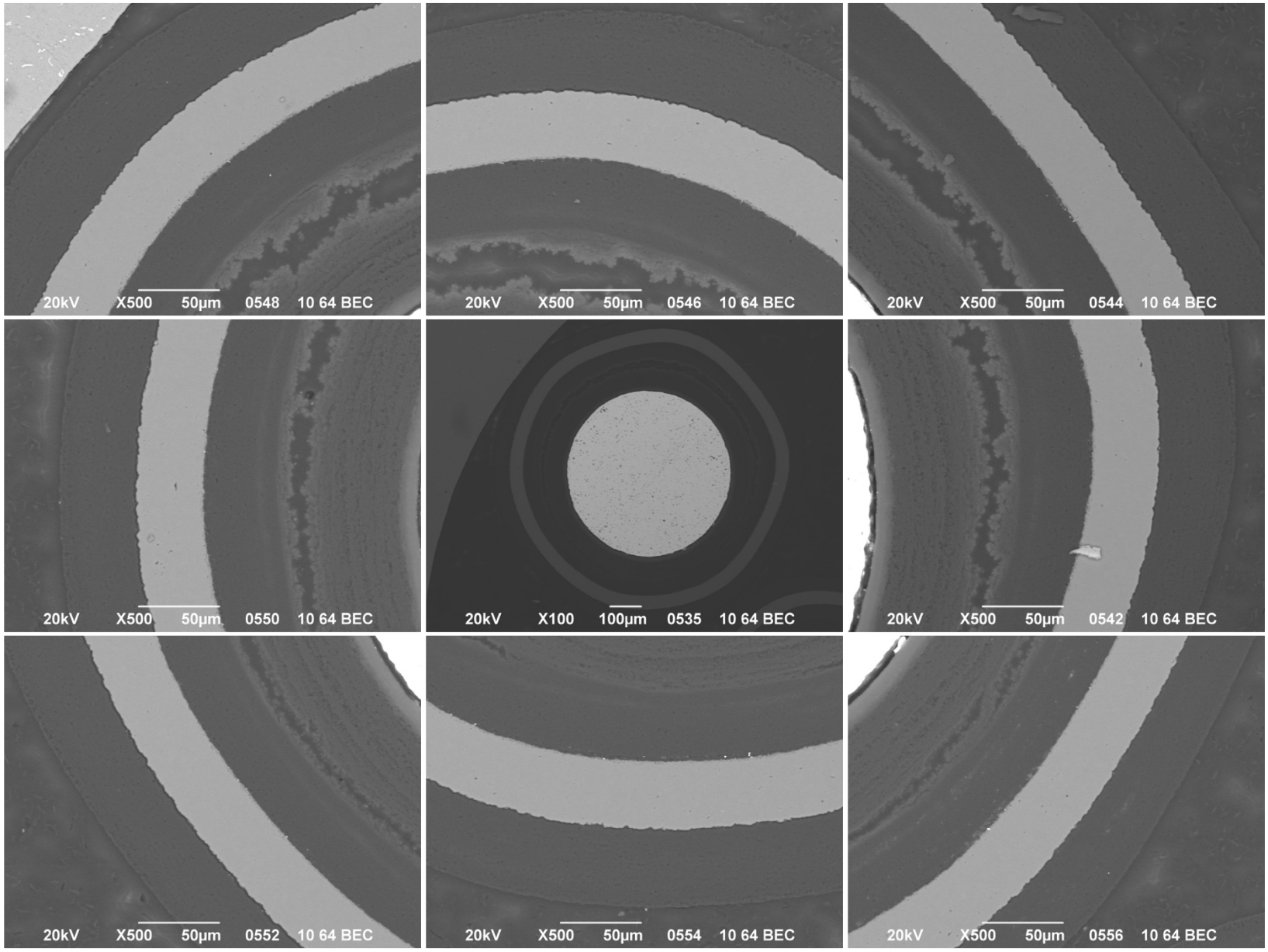

Appendix Figure D-3. 500× BEC micrographs of Particle 312-RS06.

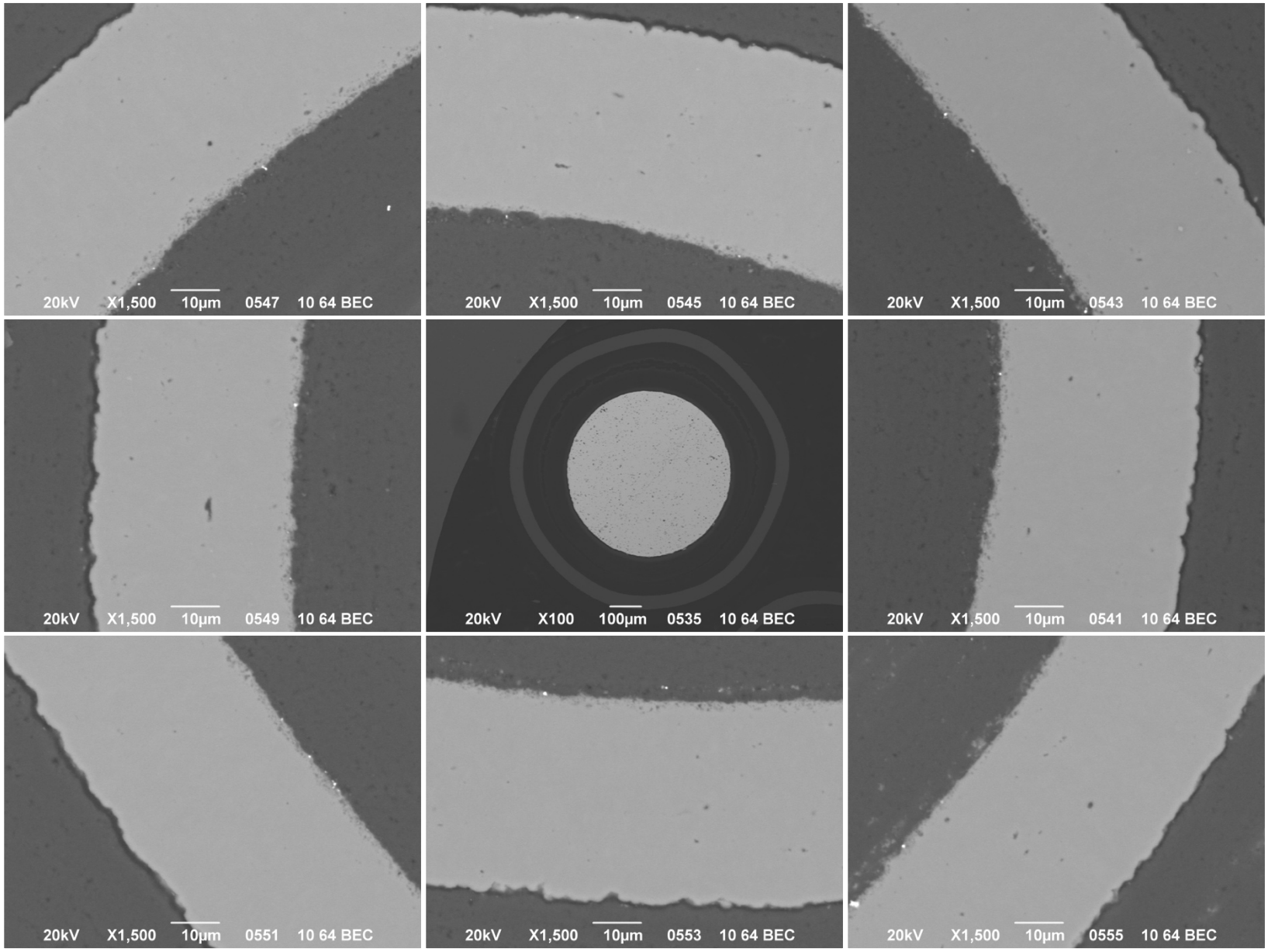

Appendix Figure D-4. 1,500× BEC micrographs of Particle 312-RS06.

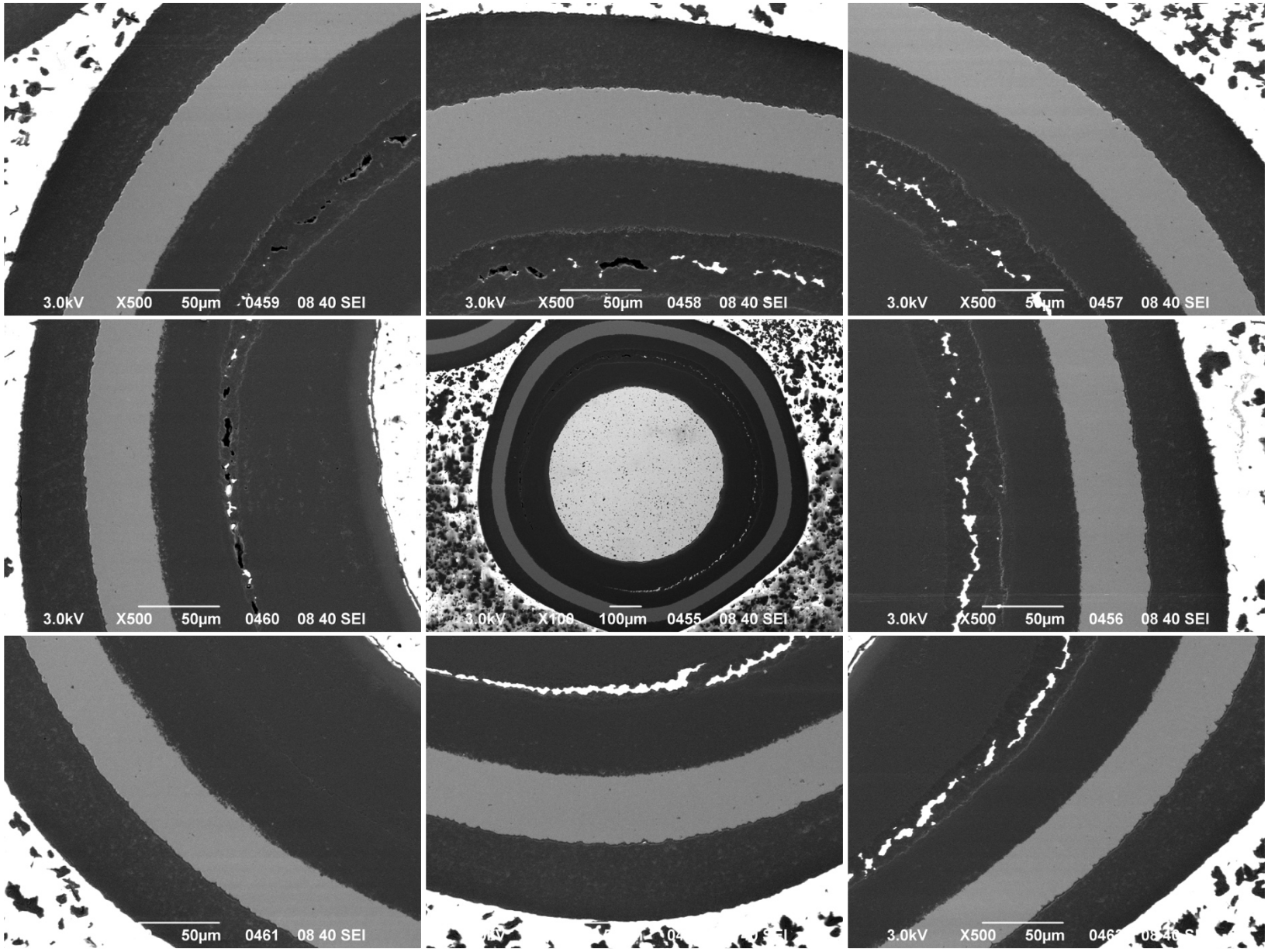

Appendix Figure D-5. 500× SEI micrographs of Particle 312-RS32.

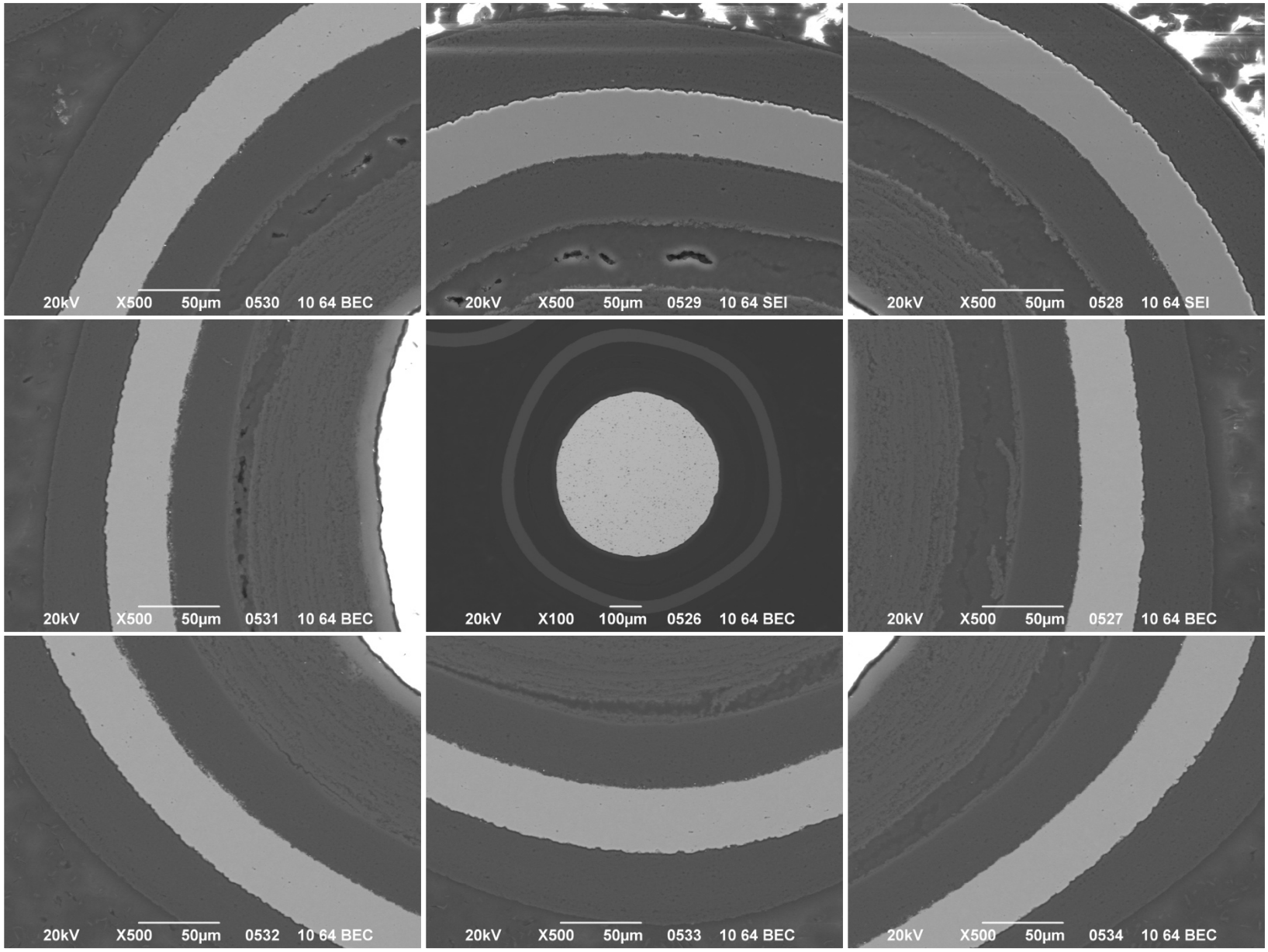

Appendix Figure D-6. 500× BEC micrographs of Particle 312-RS32.

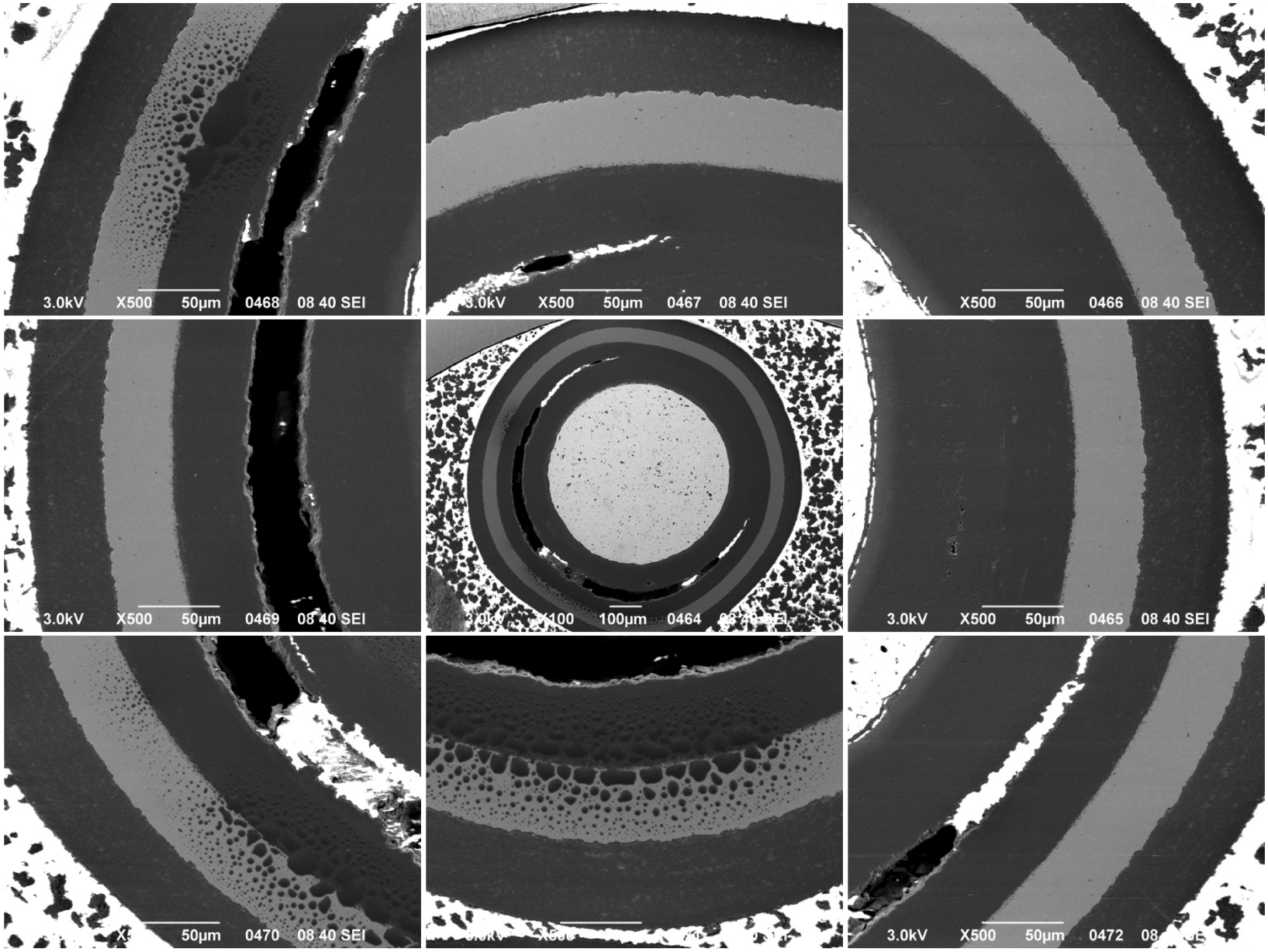

Appendix Figure D-7. 500× SEI micrographs of Particle 312-RS05.

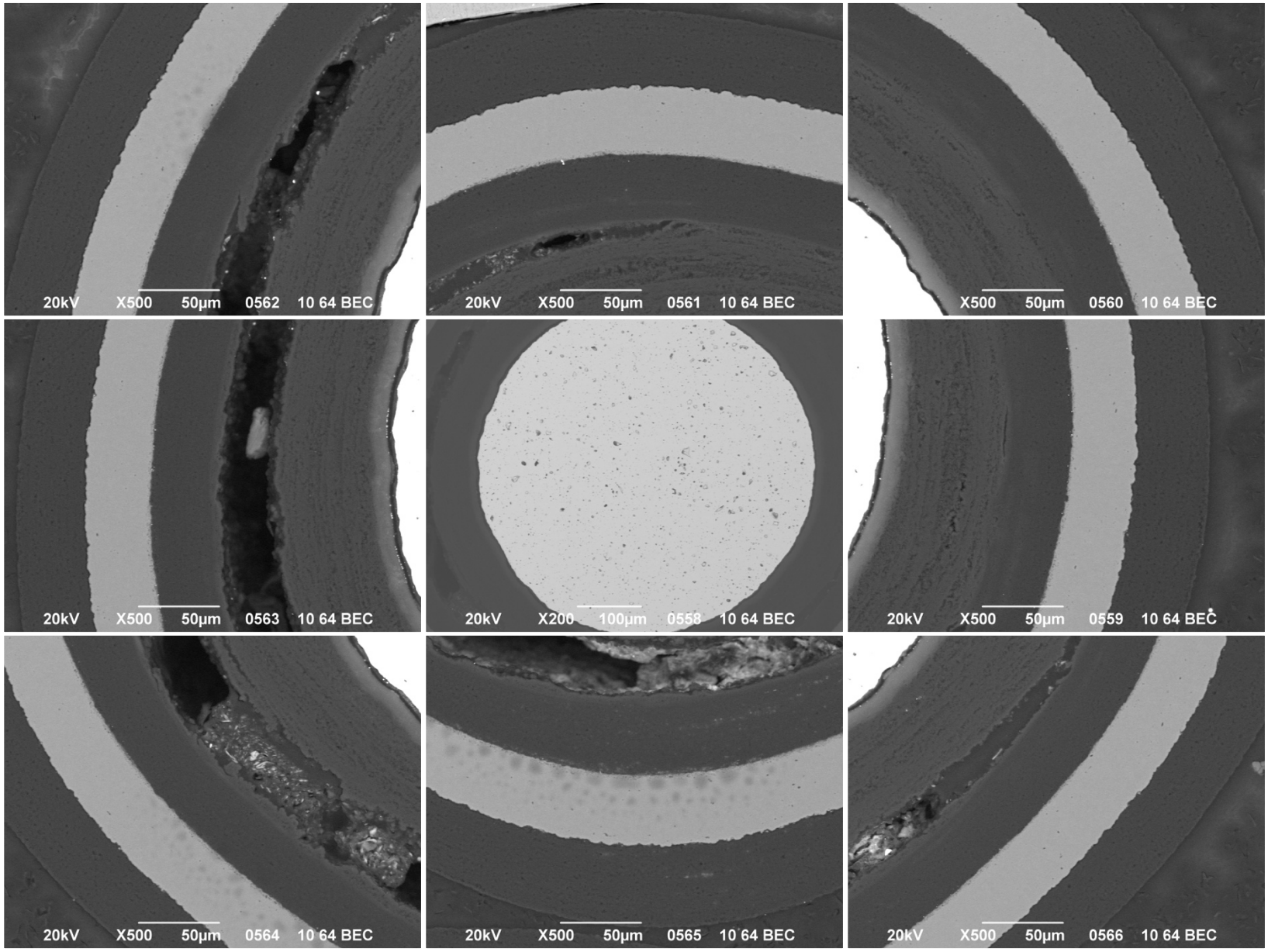

Appendix Figure D-8. 500× BEC micrographs of Particle 312-RS05.

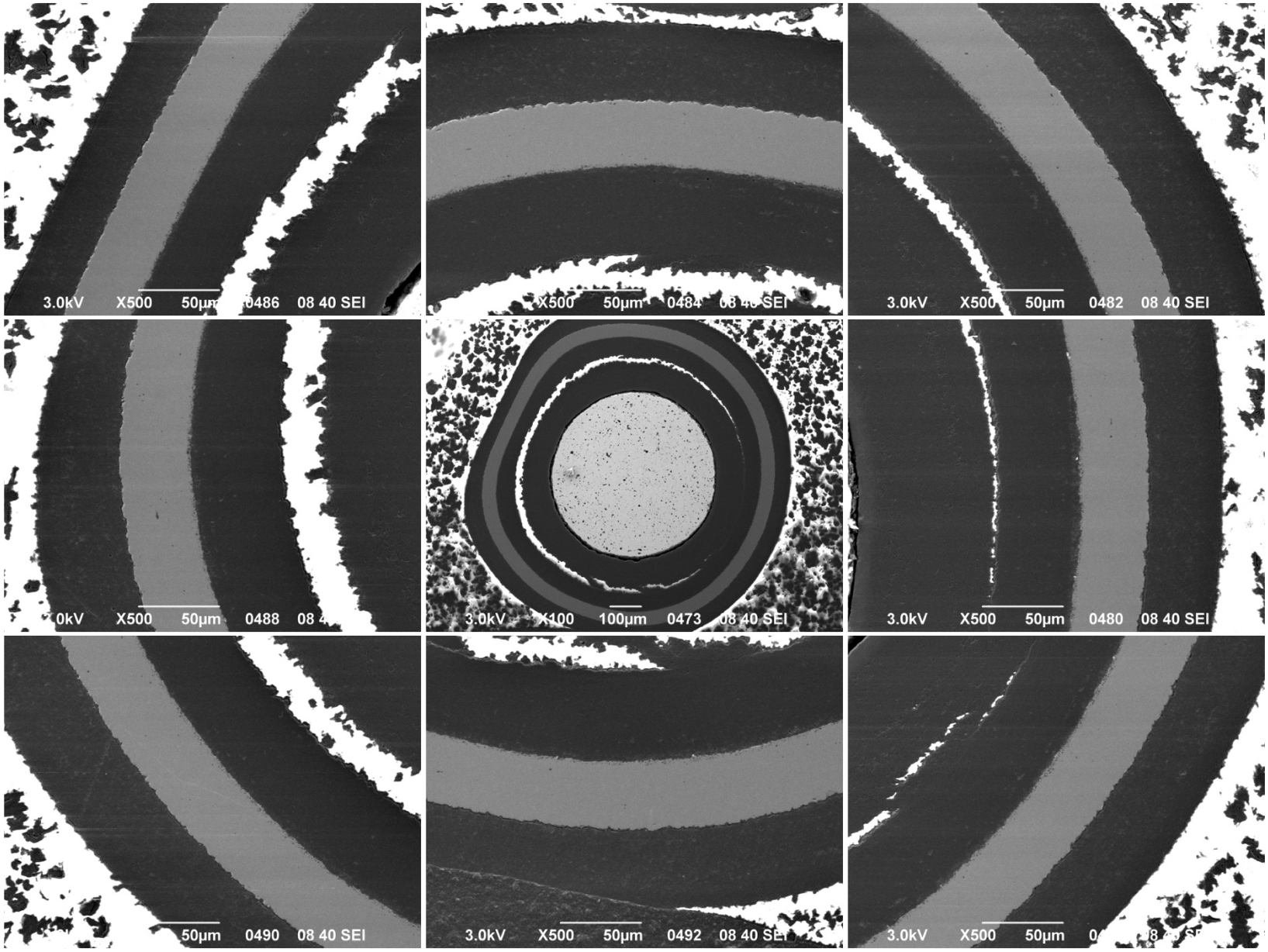

Appendix Figure D-9. 500× SEI micrographs of Particle 312-RS34.

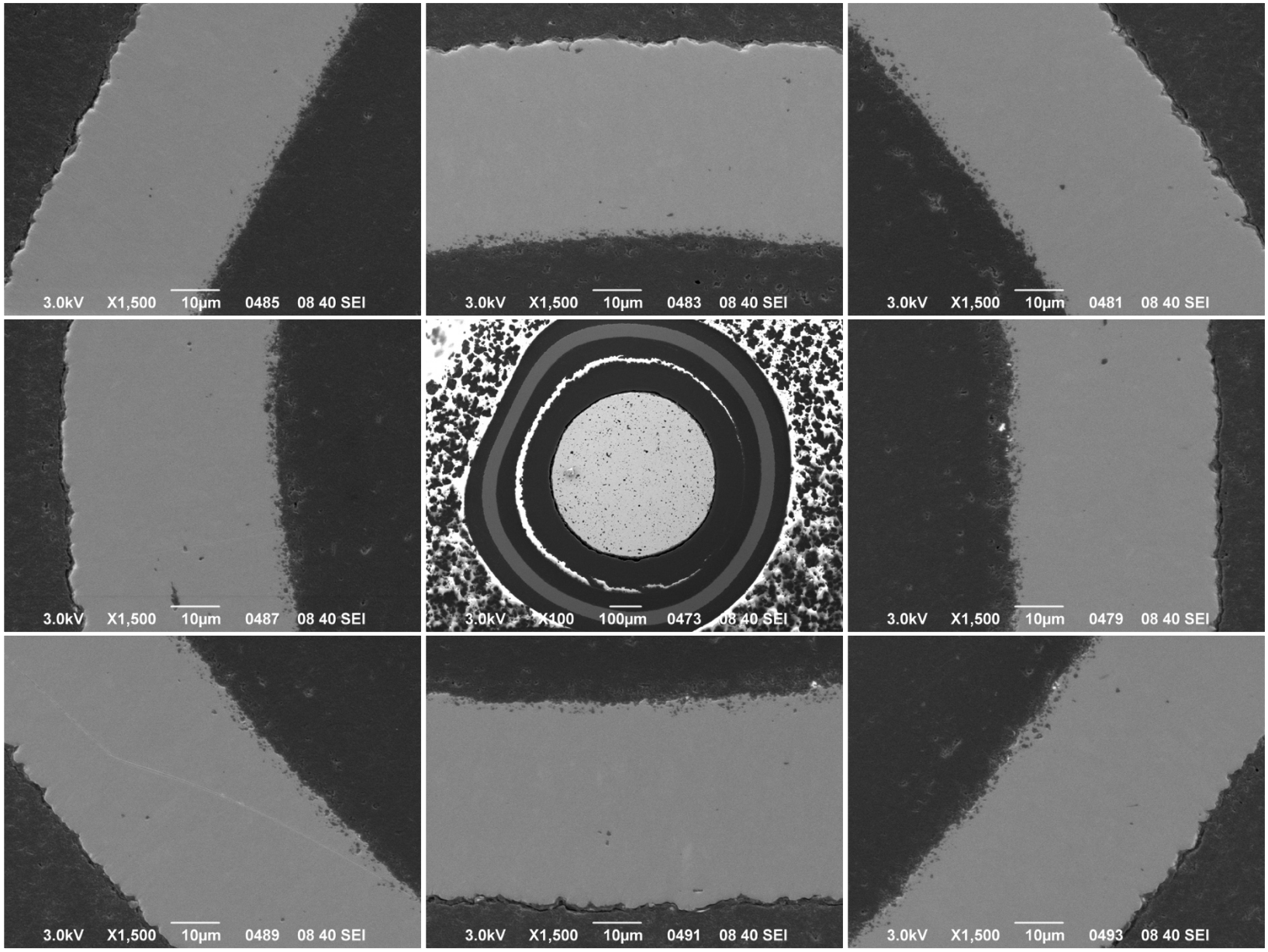

Appendix Figure D-10. 1,500× SEI micrographs of Particle 312-RS34.

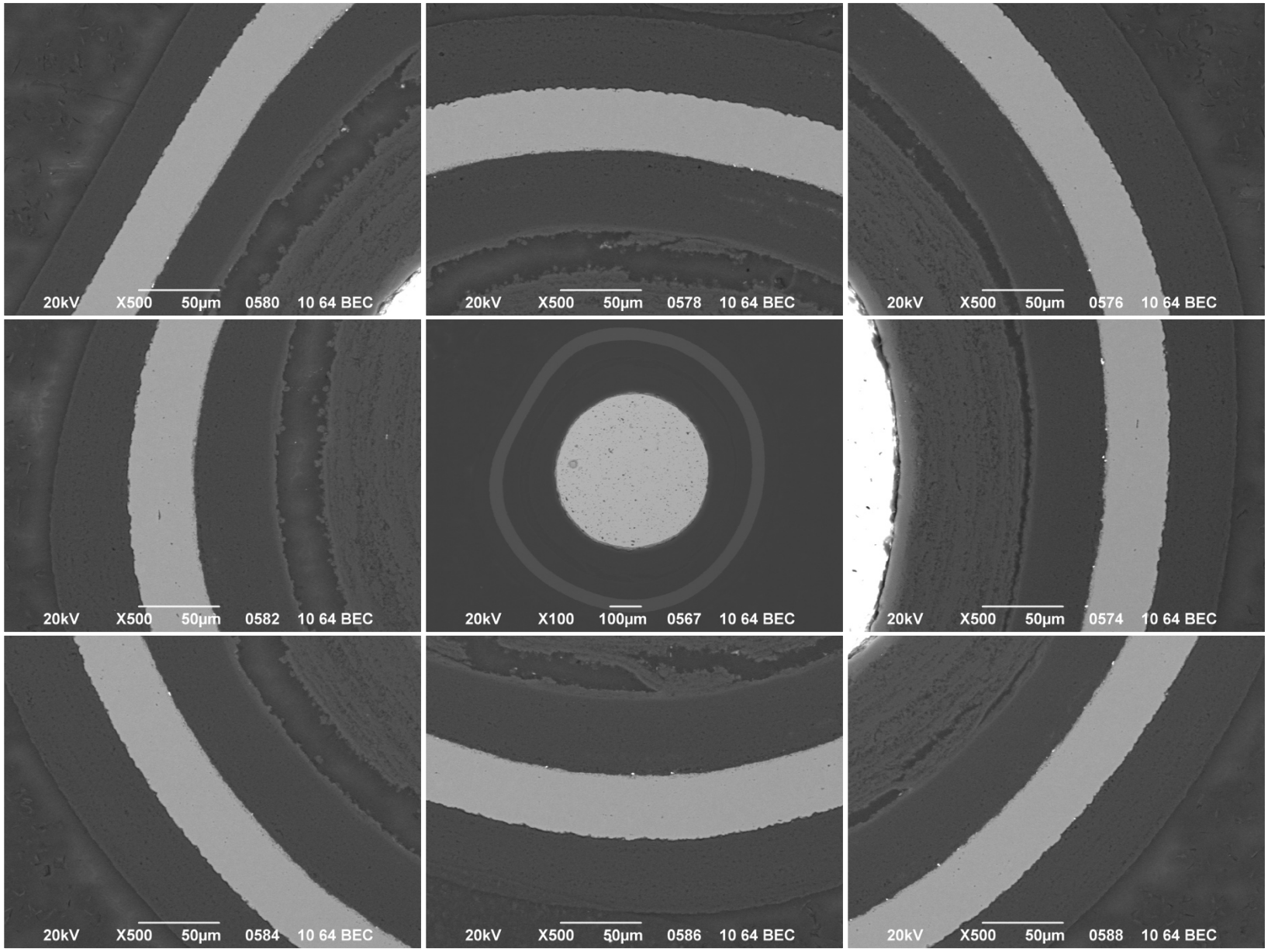

Appendix Figure D-11. 500× BEC micrographs of Particle 312-RS34.

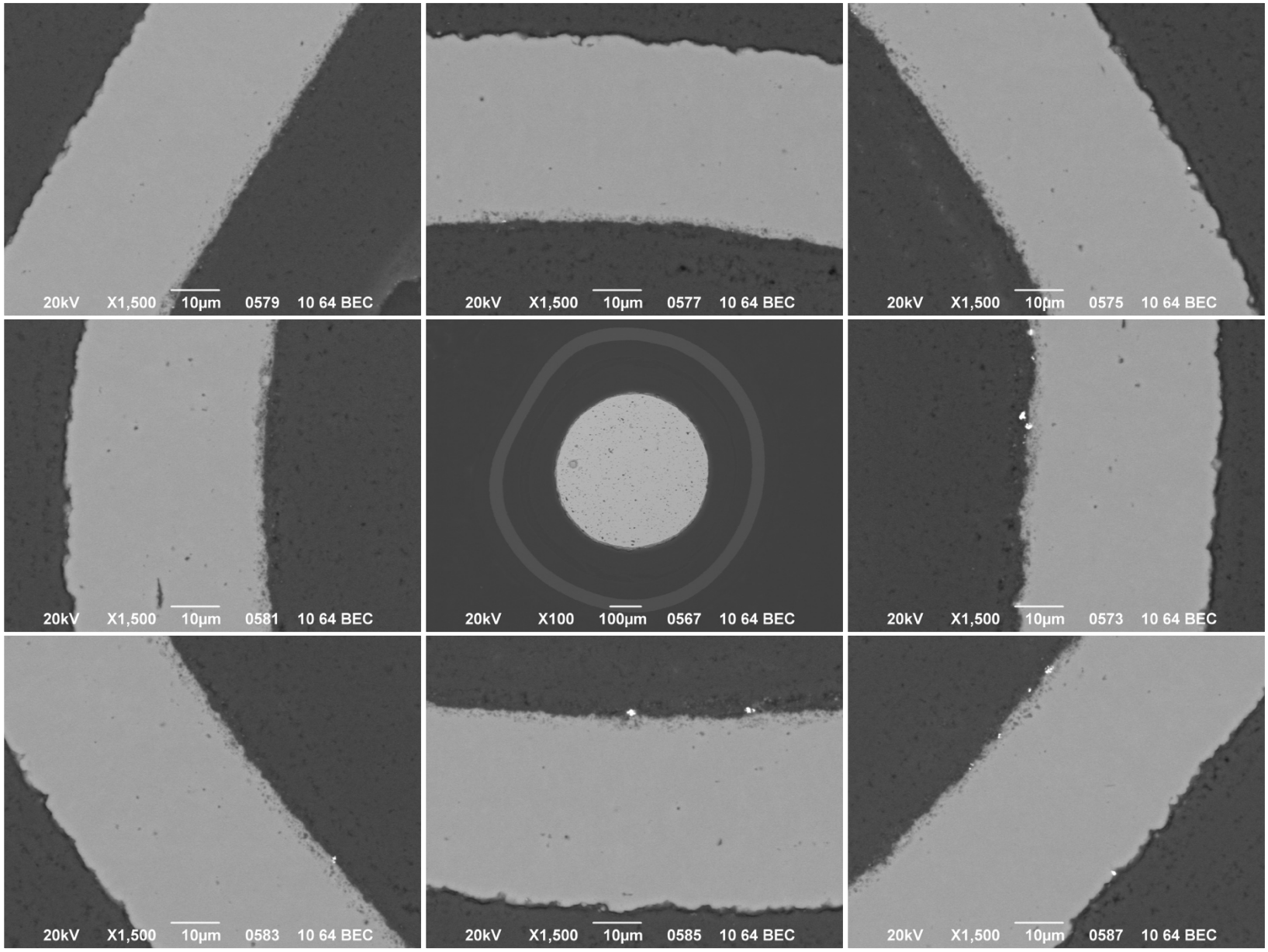

Appendix Figure D-12. 1,500× BEC micrographs of Particle 312-RS34.

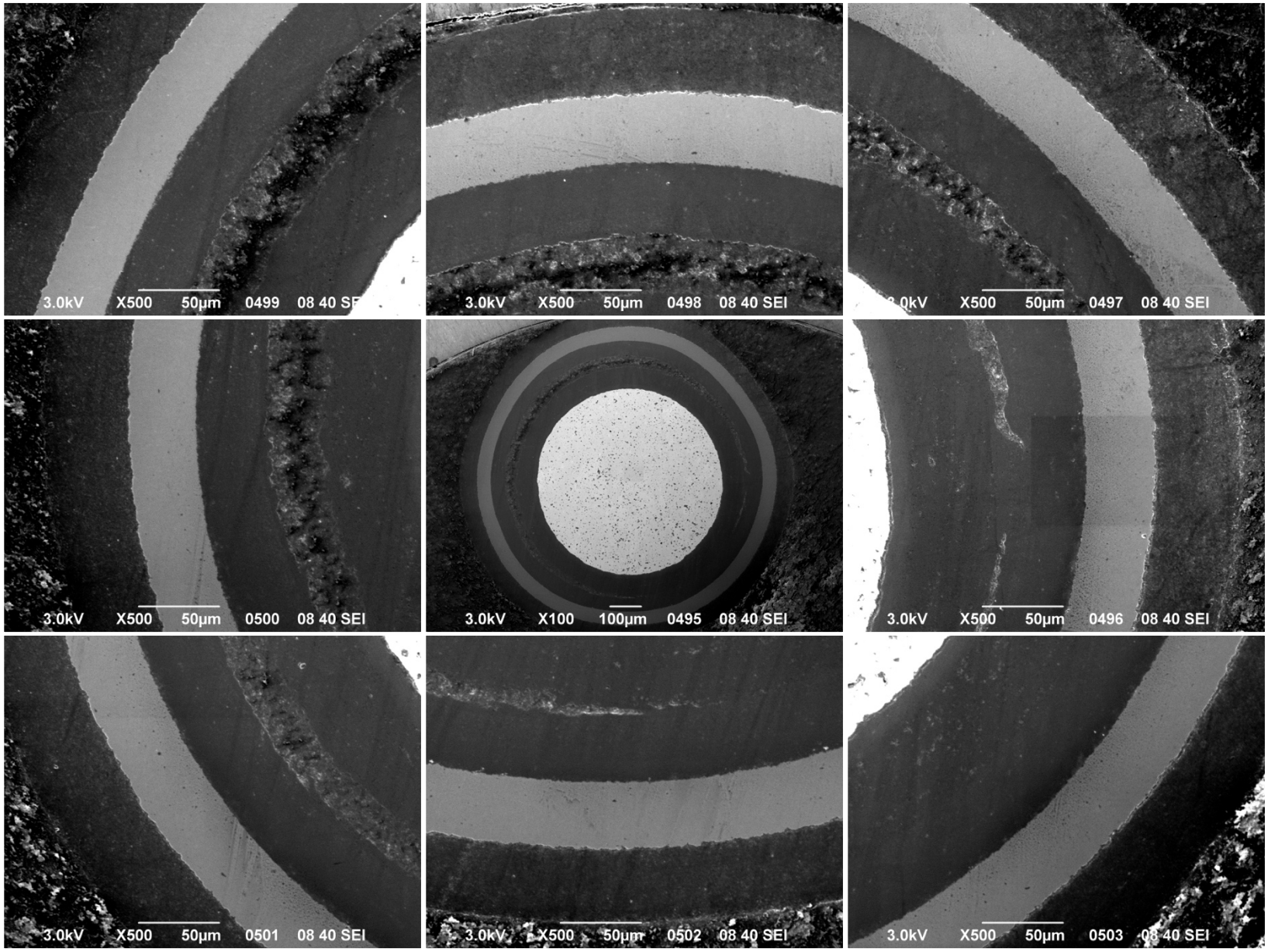

Appendix Figure D-13. 500× SEI micrographs of Particle 312-RS02.

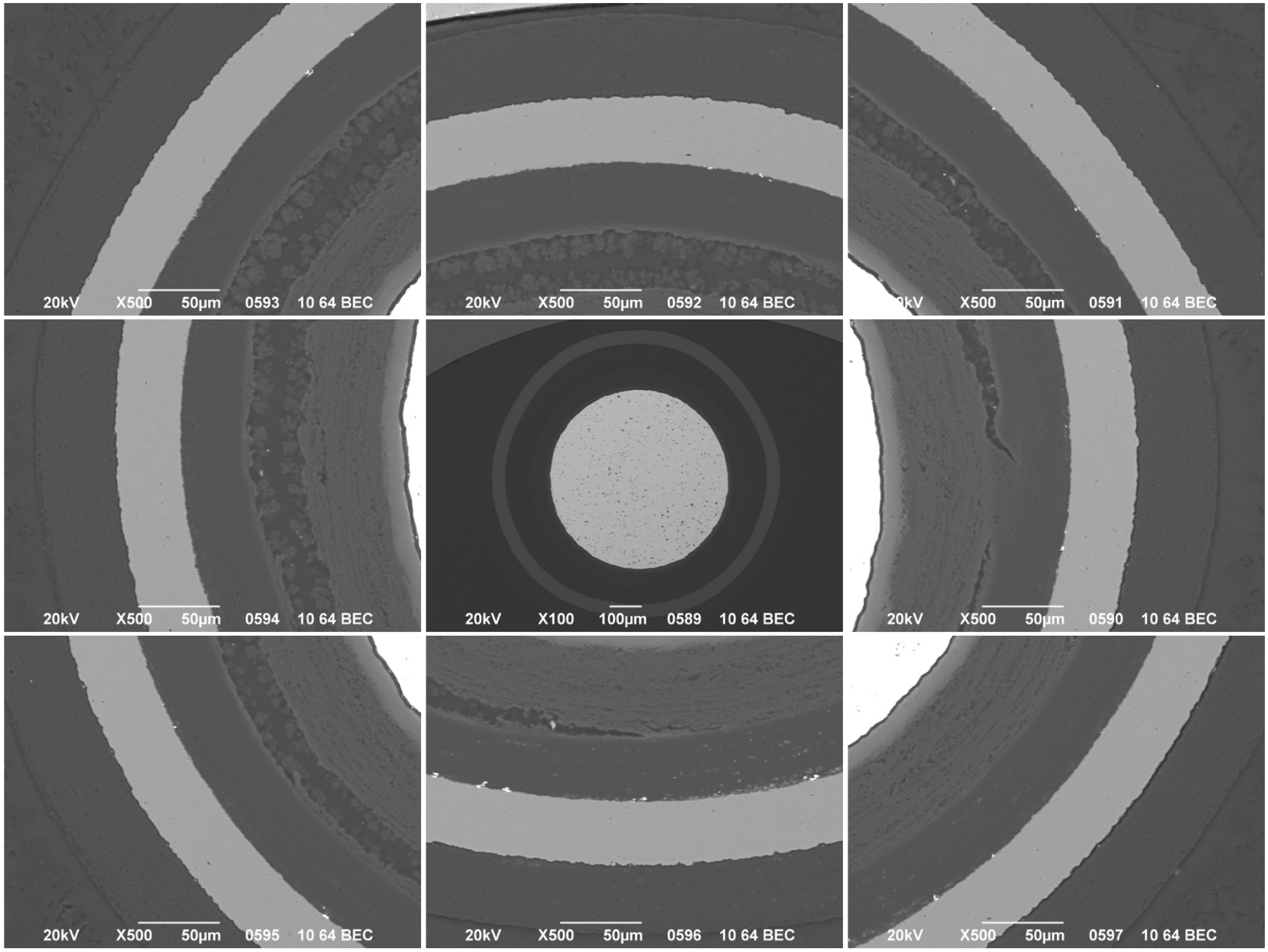

Appendix Figure D-14. 500× BEC micrographs of Particle 312-RS02.

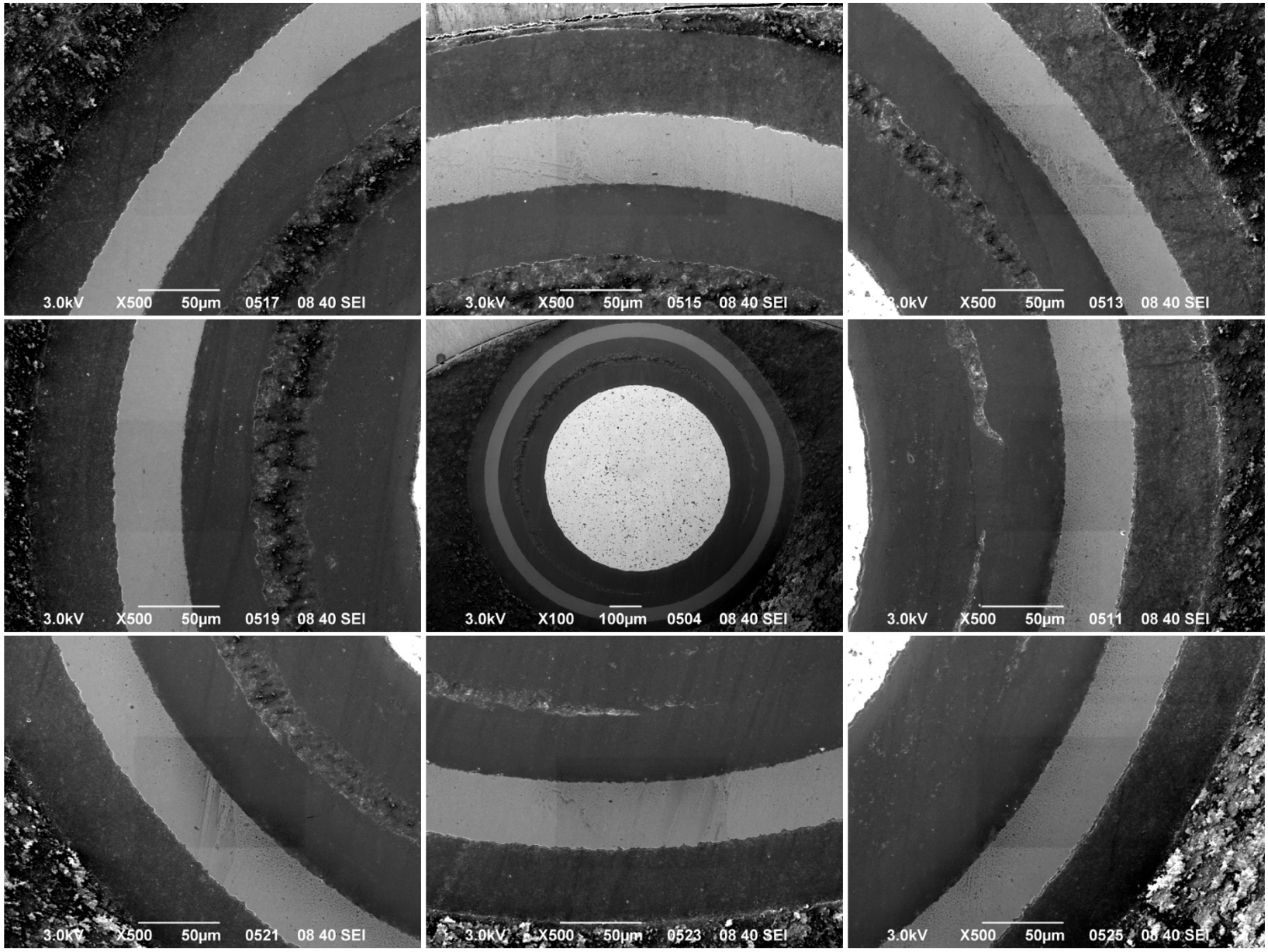

Appendix Figure D-15. 500× SEI micrographs of Particle 312-RS11.

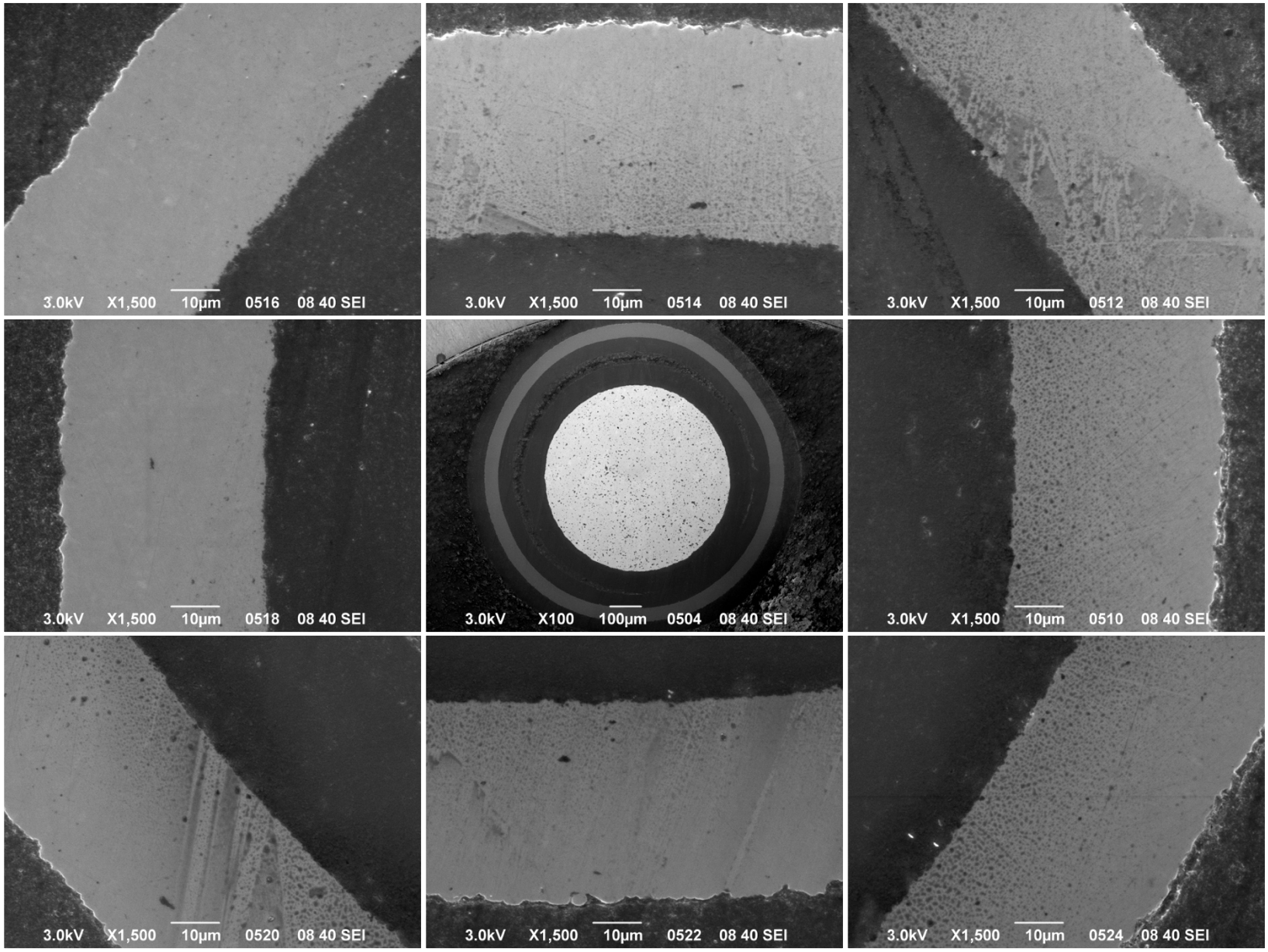

Appendix Figure D-16. 1,500× SEI micrographs of Particle 312-RS11.

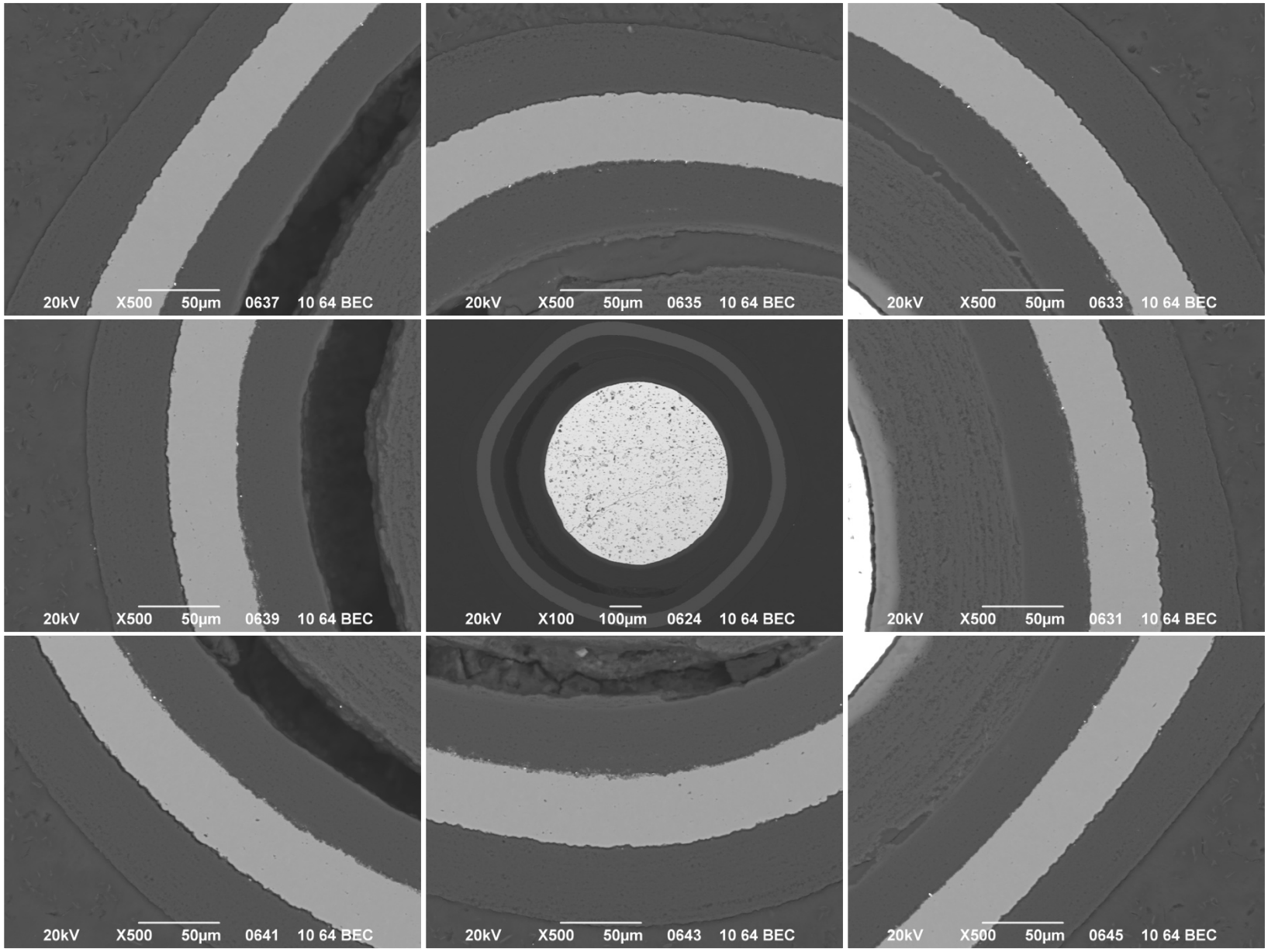

Appendix Figure D-17. 500× BEC micrographs of Particle 312-RS11.

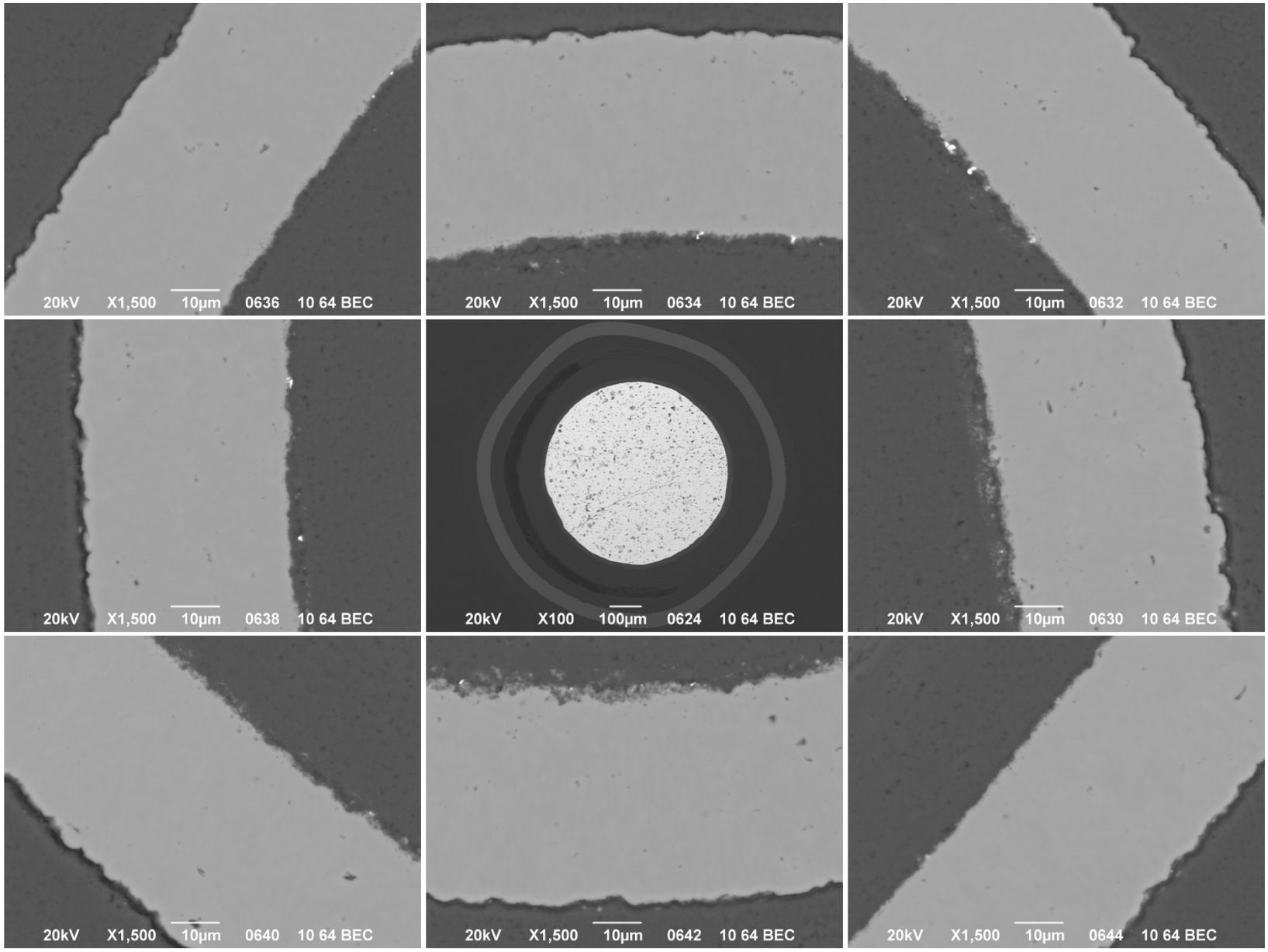

Appendix Figure D-18. 1,500× BEC micrographs of Particle 312-RS11.

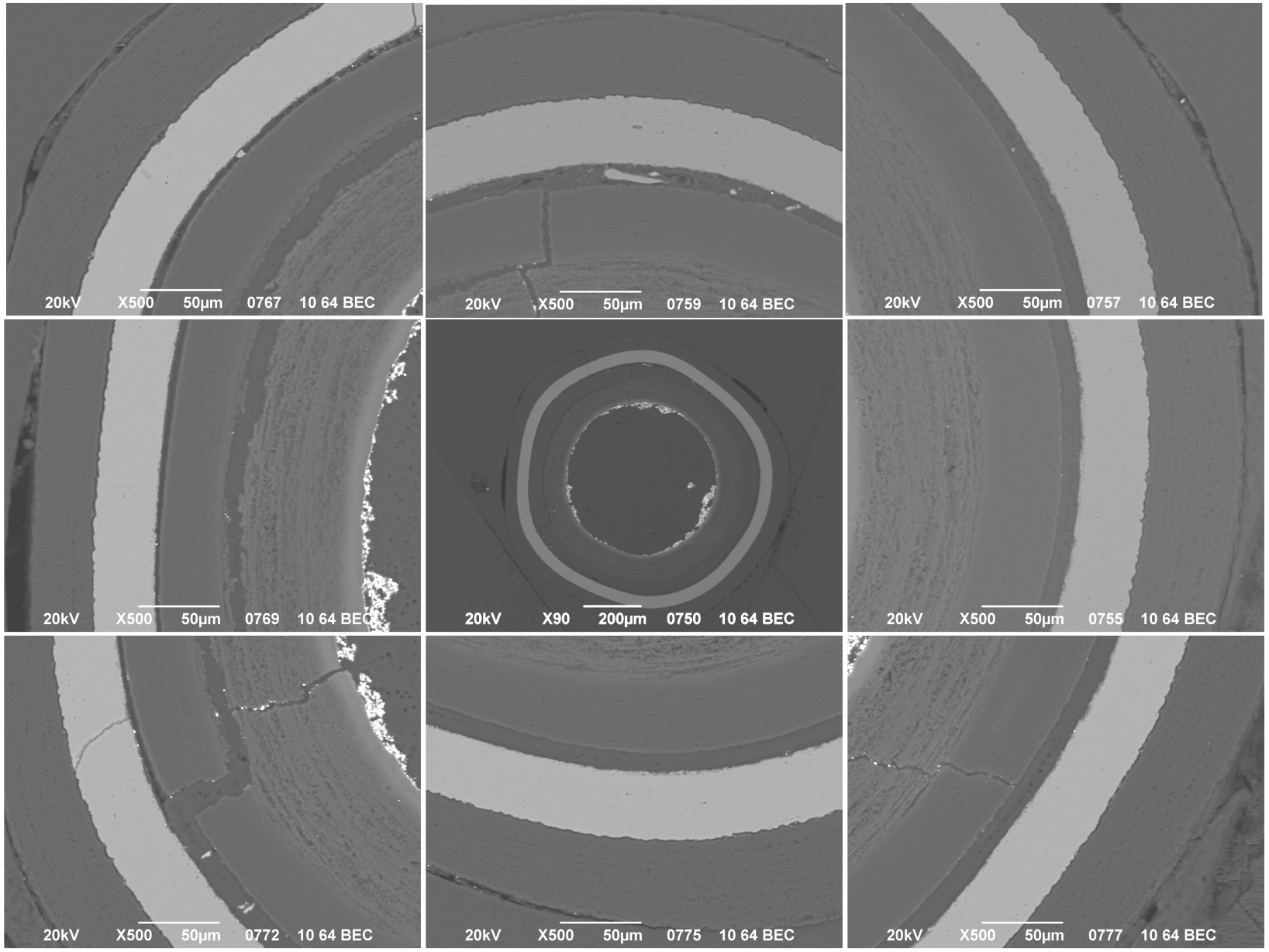

Appendix Figure D-19. 500× BEC micrographs of Particle 312-SP02.

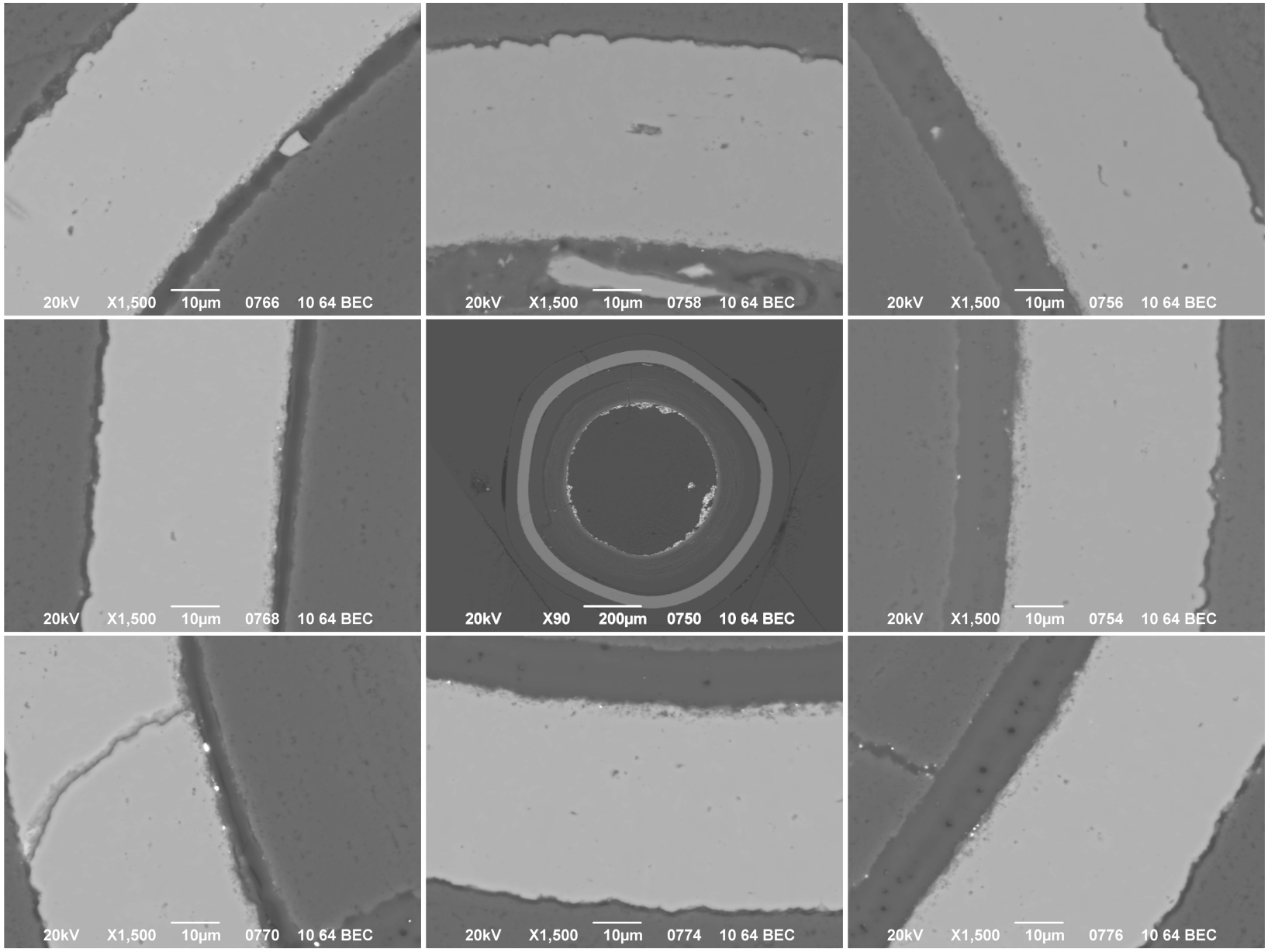

Appendix Figure D-20. 1,500× BEC micrographs of Particle 312-SP02.

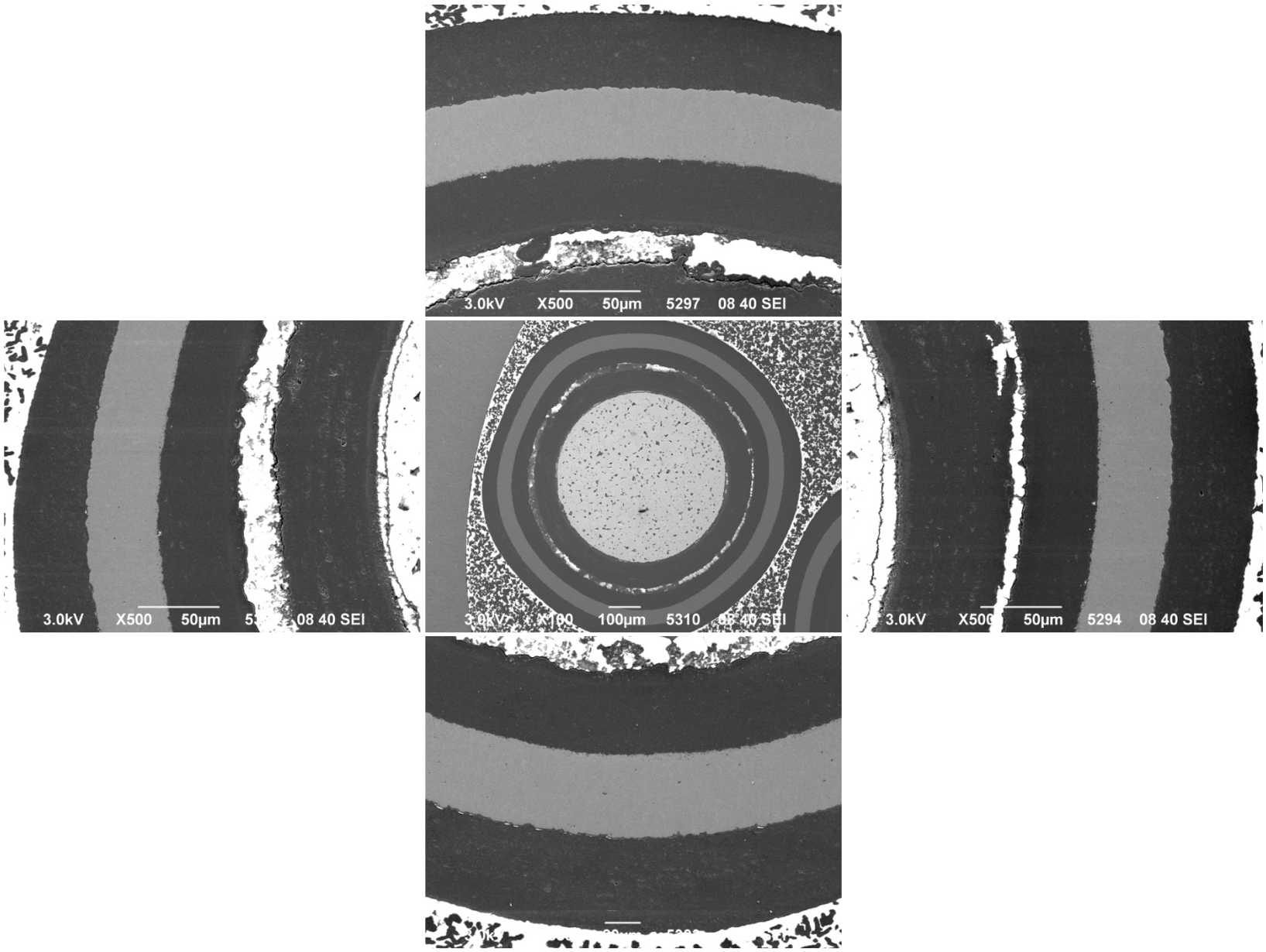

Appendix Figure D-21. 500× SEI micrographs of Particle 331-RS04.

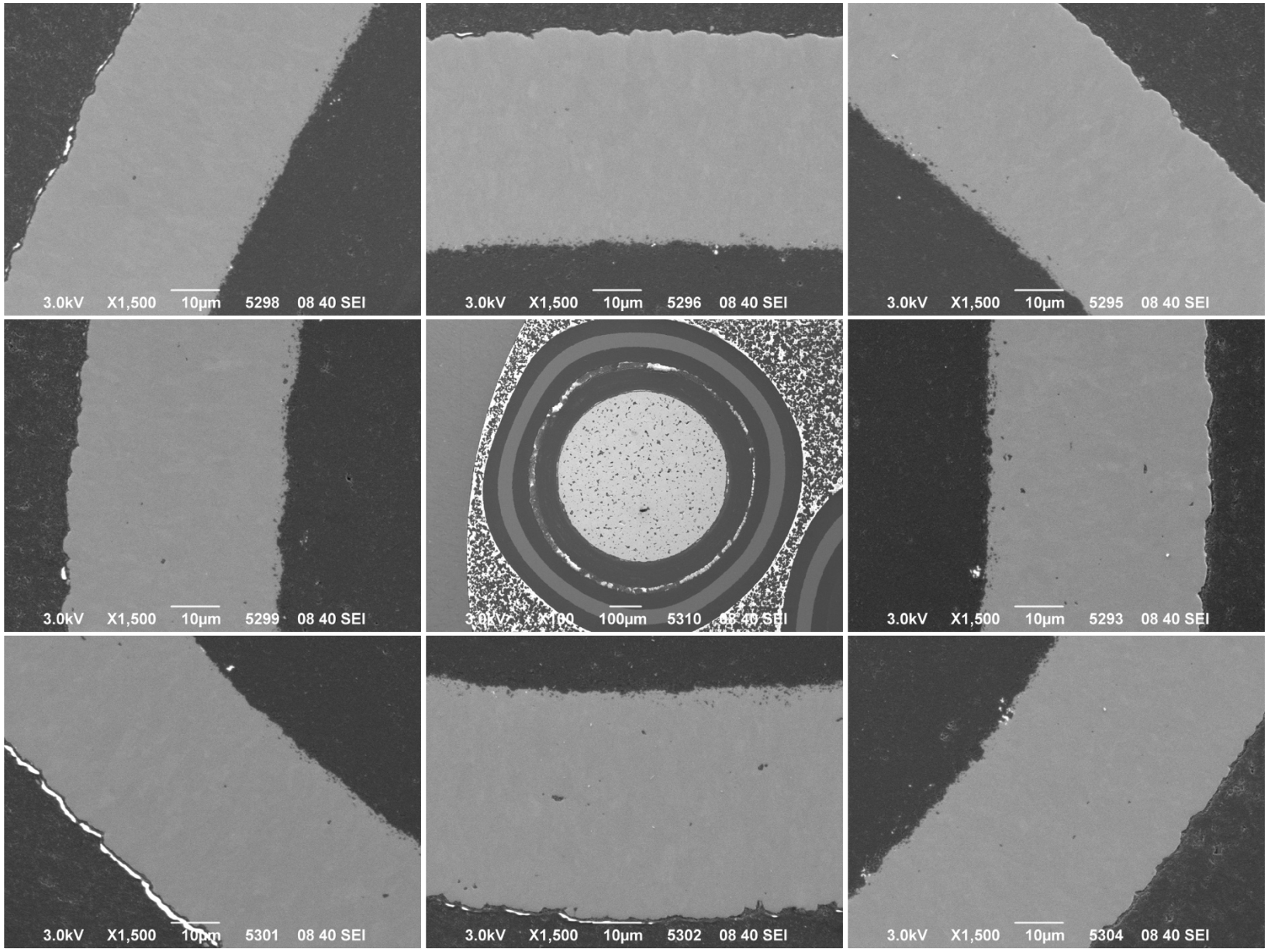

Appendix Figure D-22. 1,500× SEI micrographs of Particle 331-RS04.

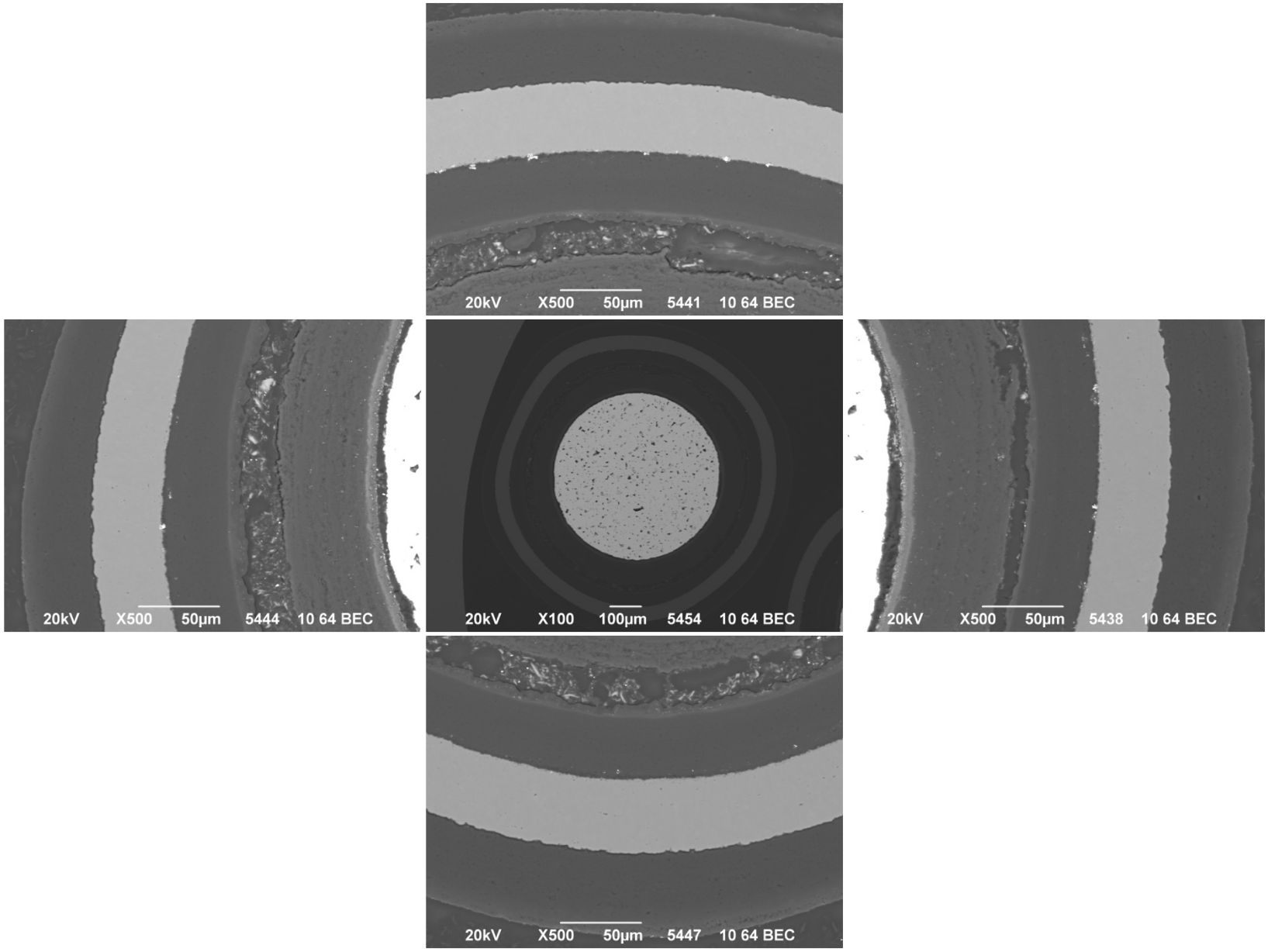

Appendix Figure D-23. 500× BEC micrographs of Particle 331-RS04.

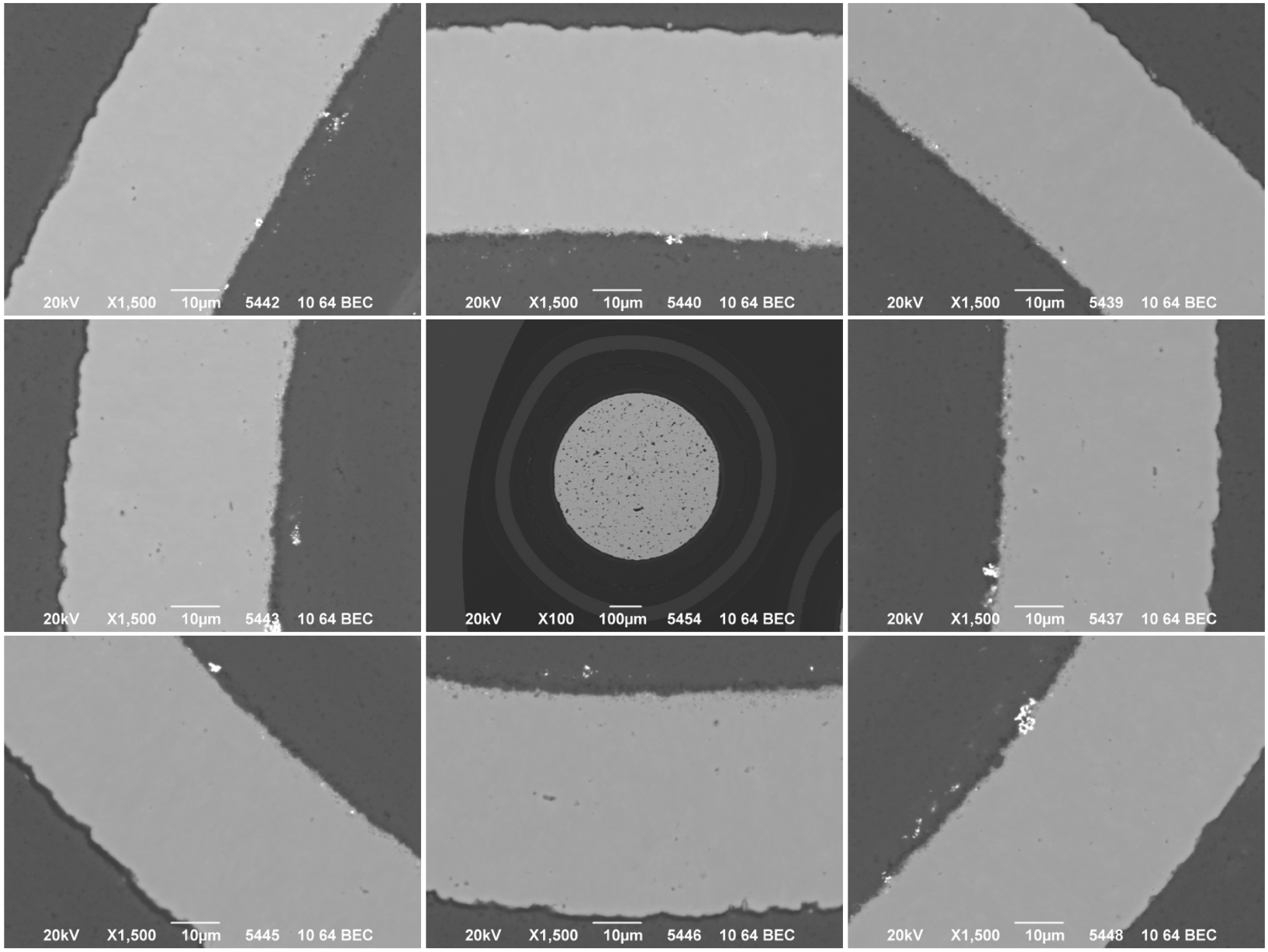

Appendix Figure D-24. 1,500× BEC micrographs of Particle 331-RS04.

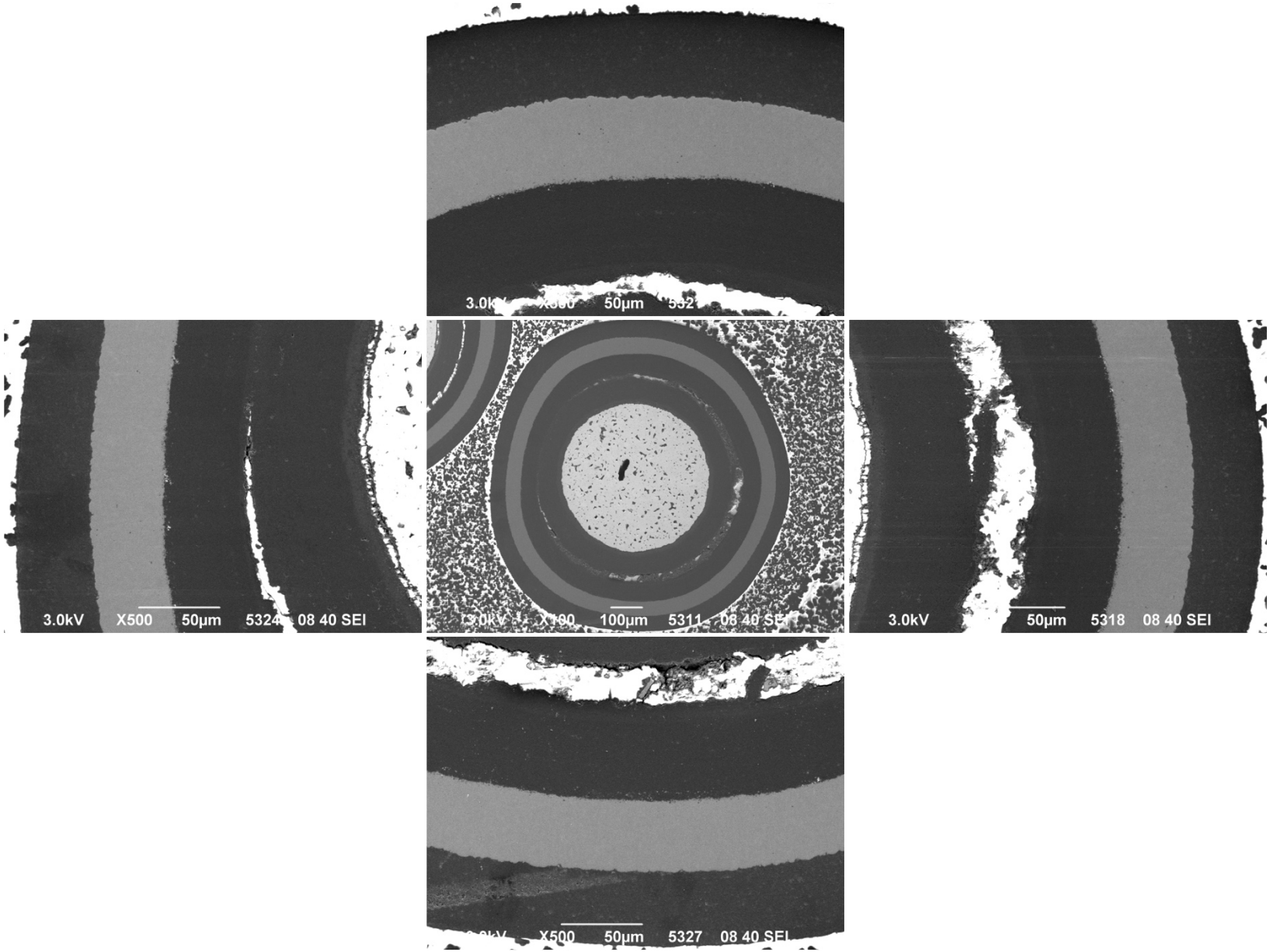

Appendix Figure D-25. 500× SEI micrographs of Particle 331-RS19.

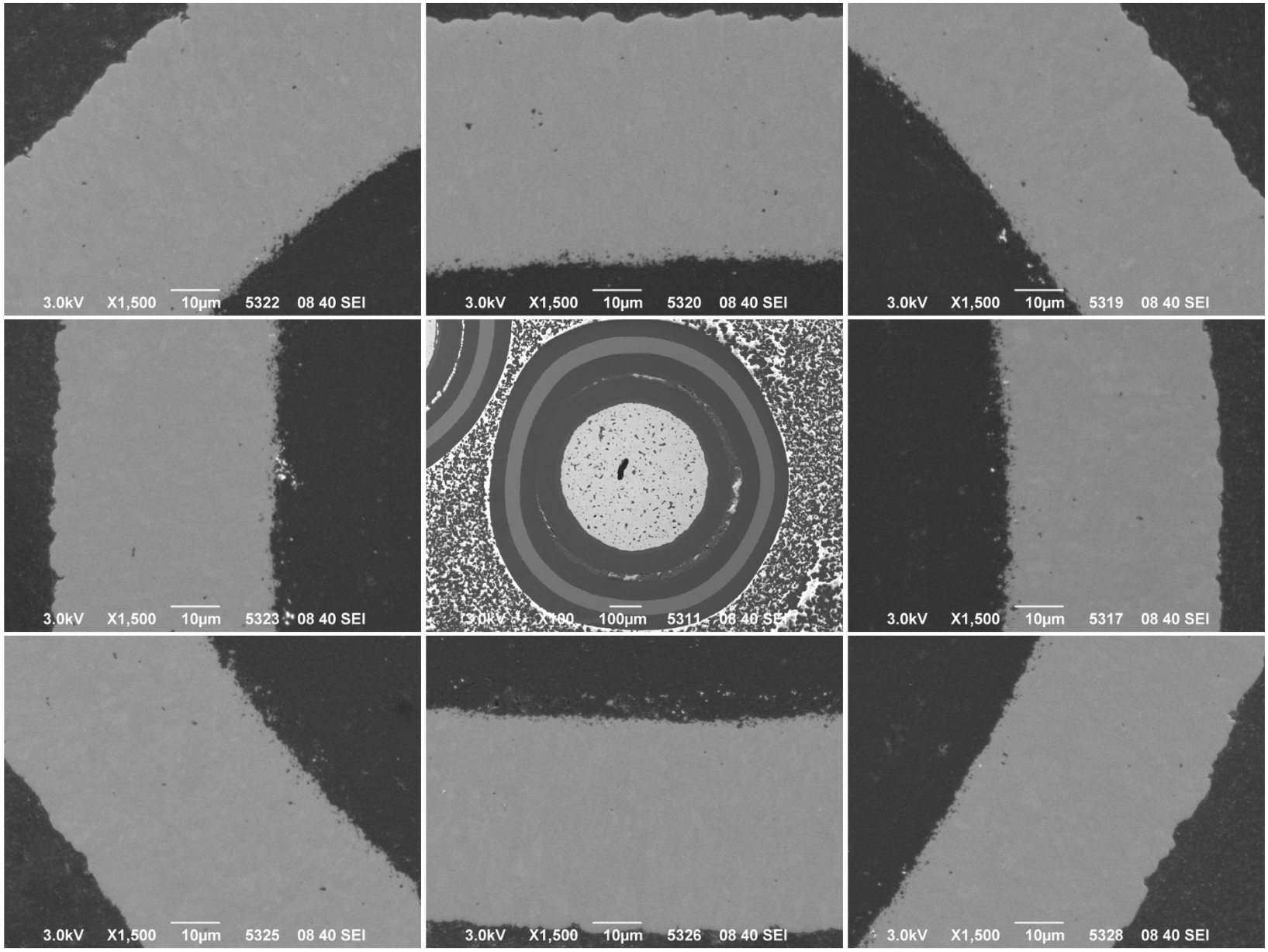

Appendix Figure D-26. 1,500× SEI micrographs of Particle 331-RS19.

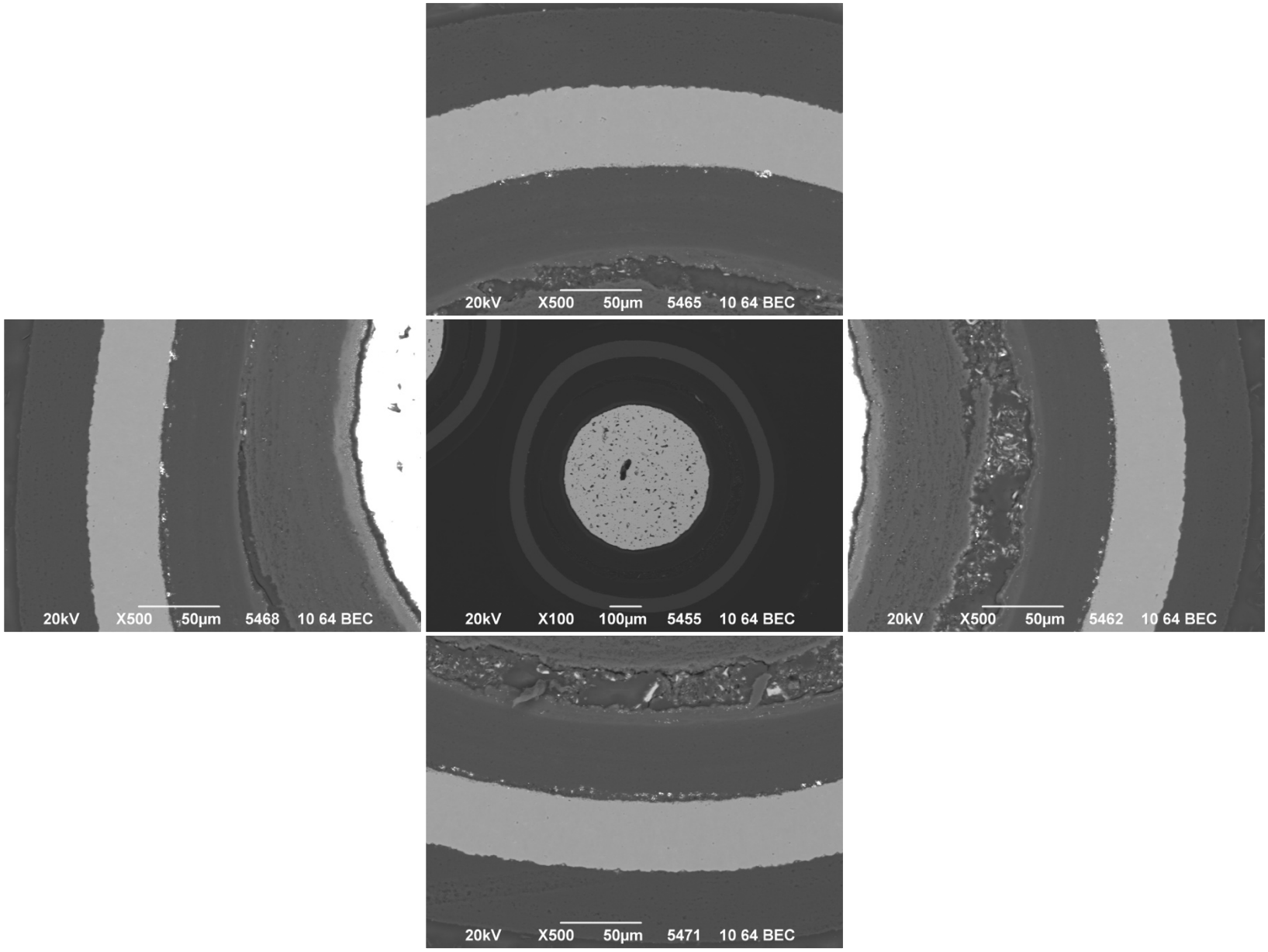

Appendix Figure D-27. 500× BEC micrographs of Particle 331-RS19.

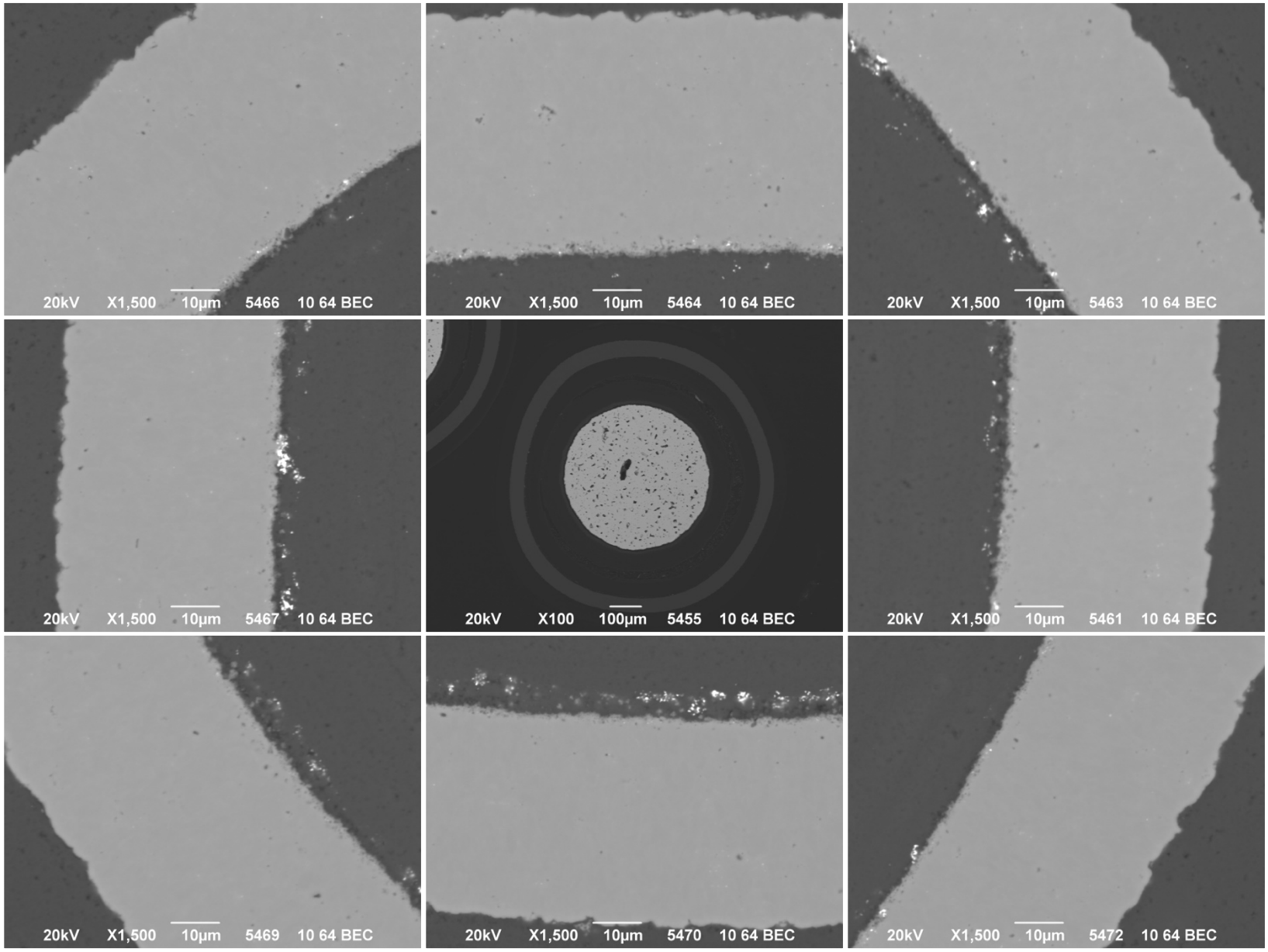

Appendix Figure D-28. 1,500× BEC micrographs of Particle 331-RS19.

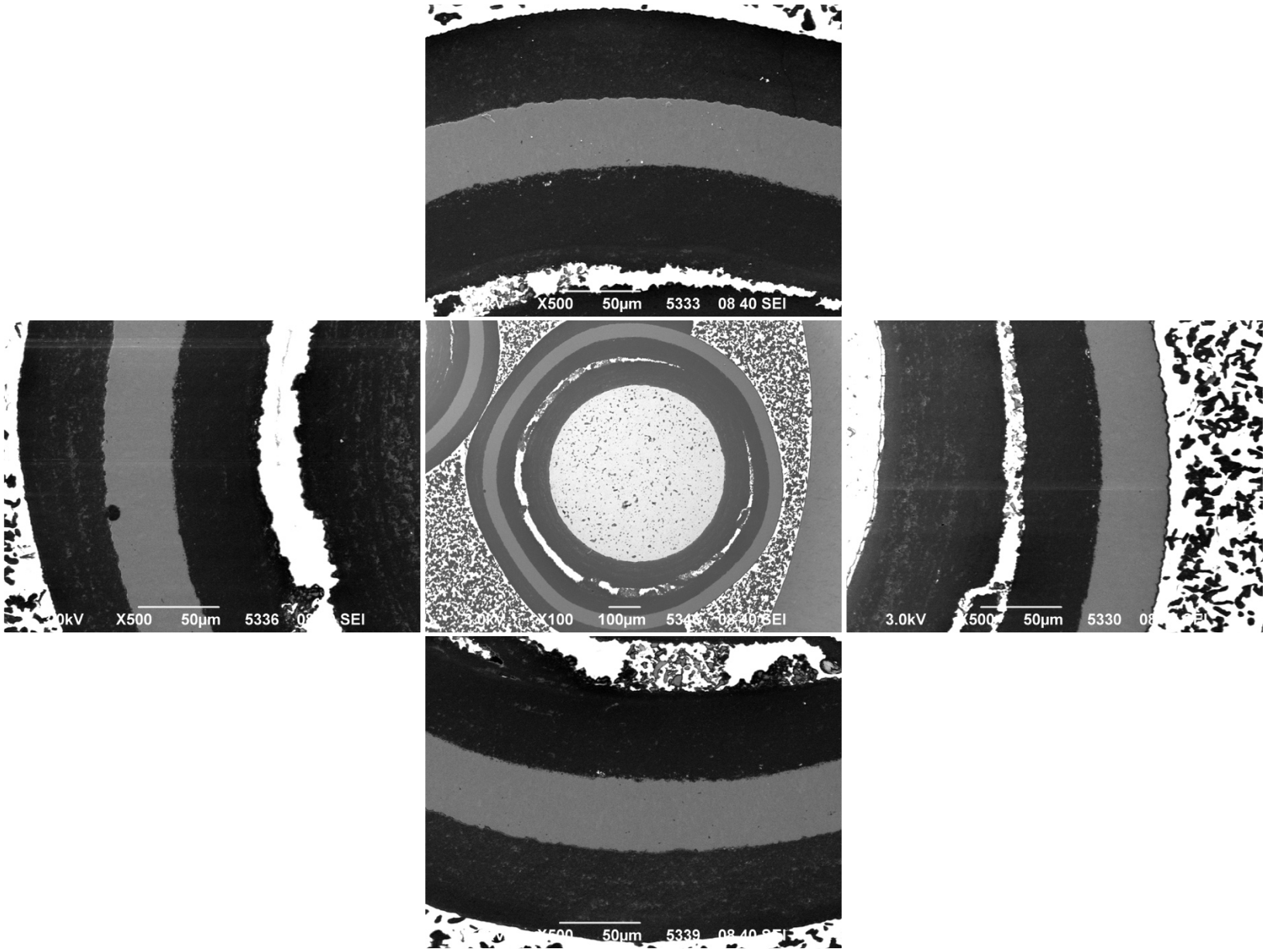

Appendix Figure D-29. 500× SEI micrographs of Particle 331-RS03.

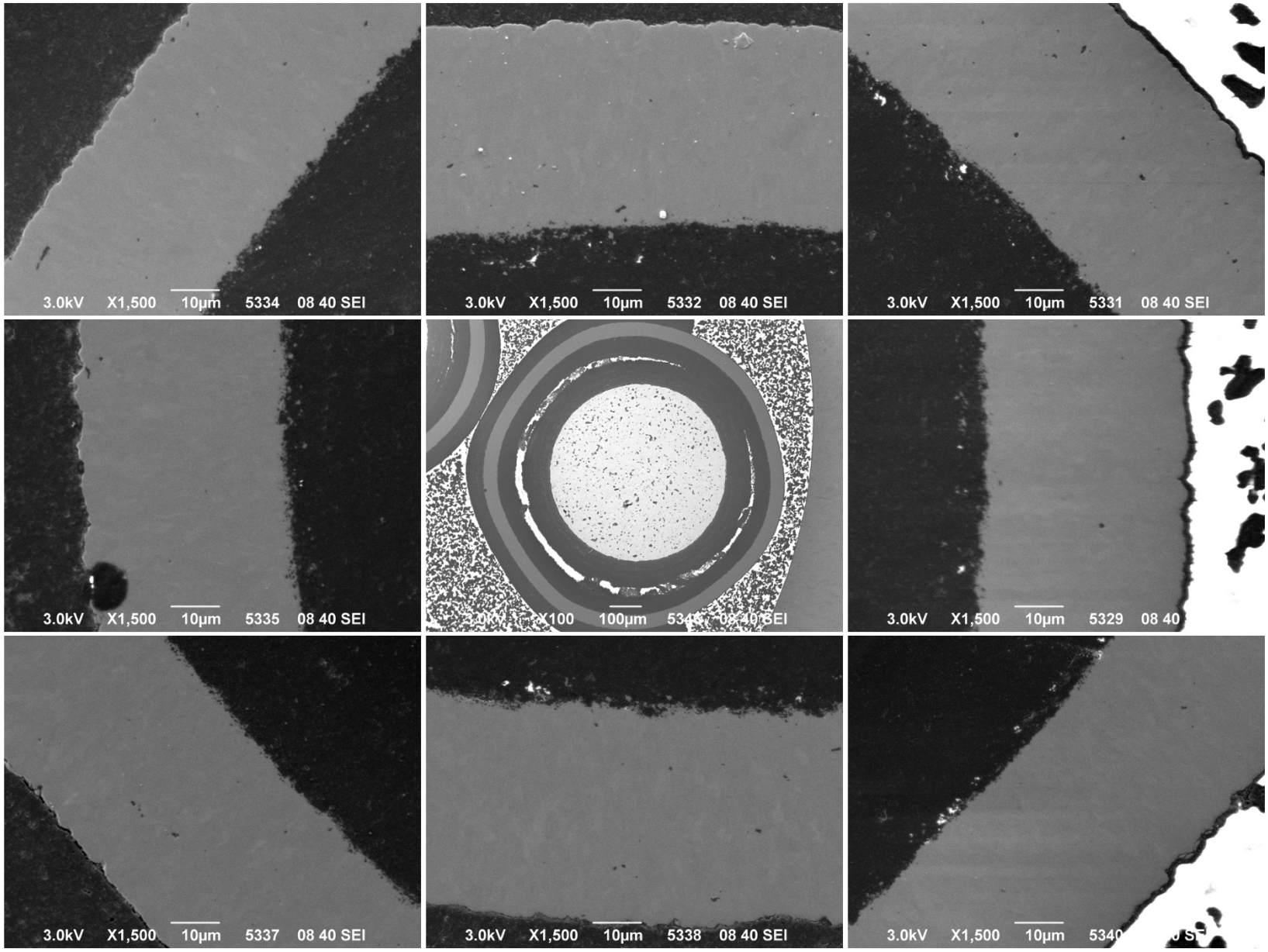

Appendix Figure D-30. 1,500× SEI micrographs of Particle 331-RS03.

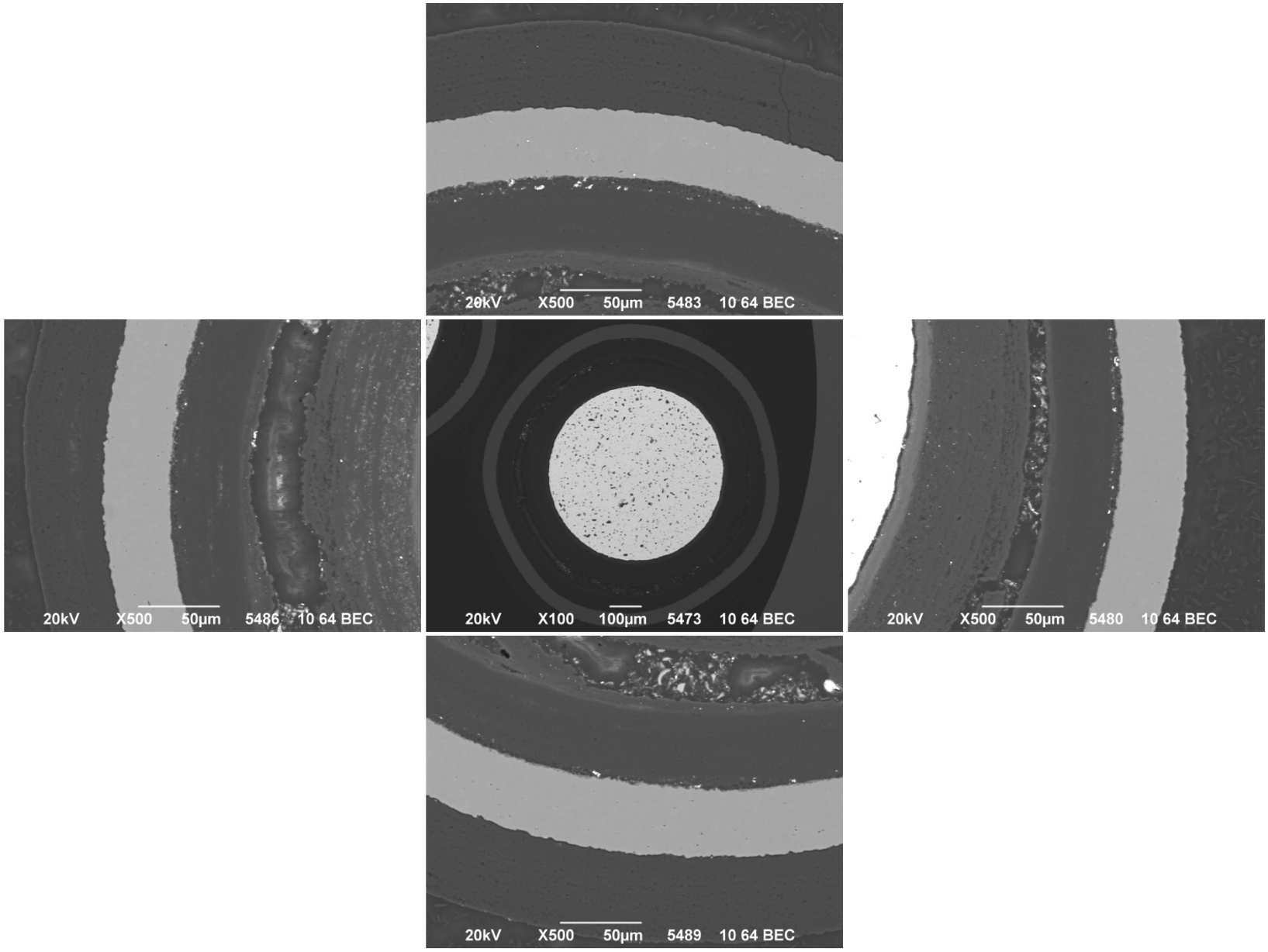

Appendix Figure D-31. 500× BEC micrographs of Particle 331-RS03.

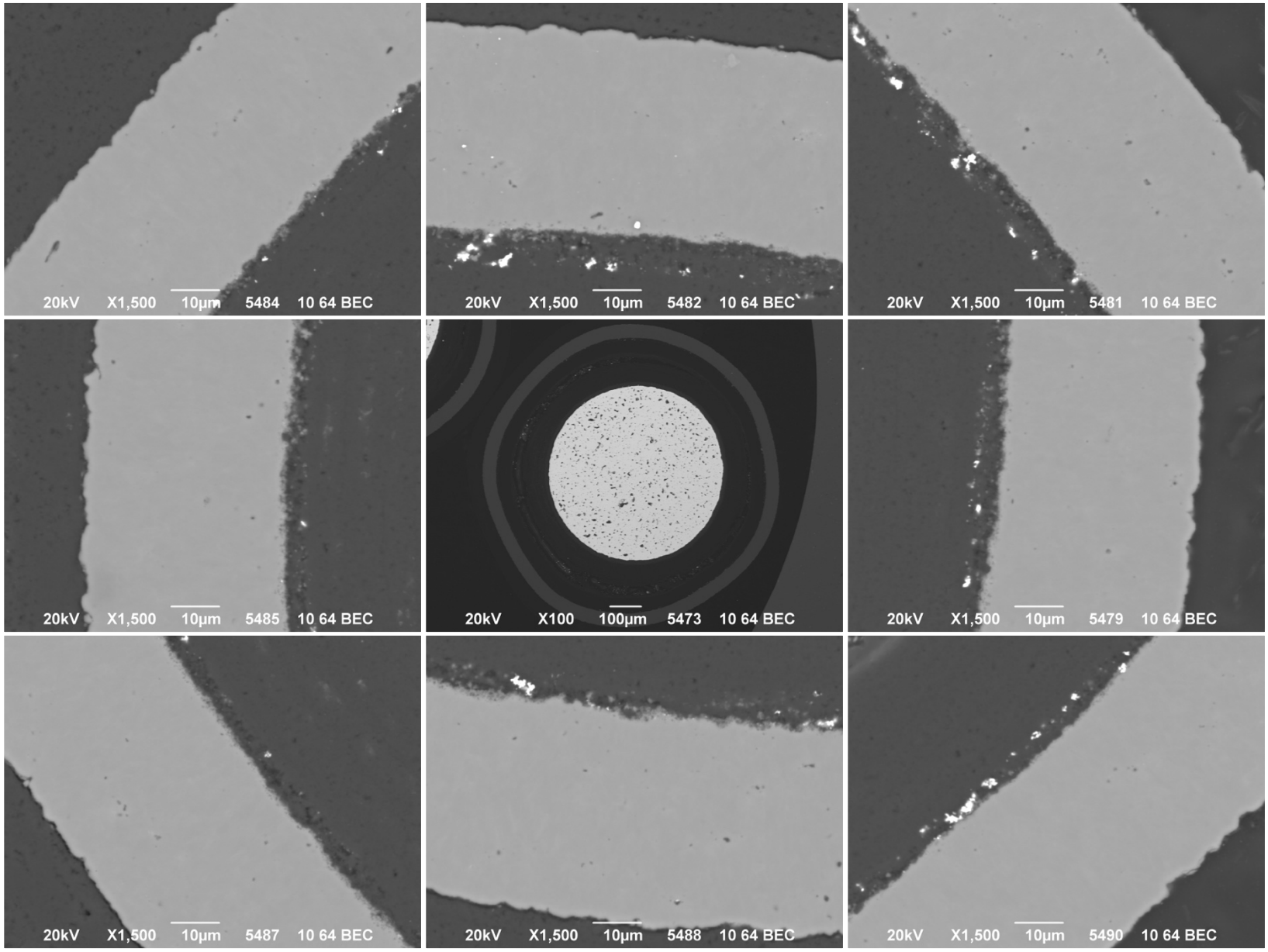

Appendix Figure D-32. 1,500× BEC micrographs of Particle 331-RS03.

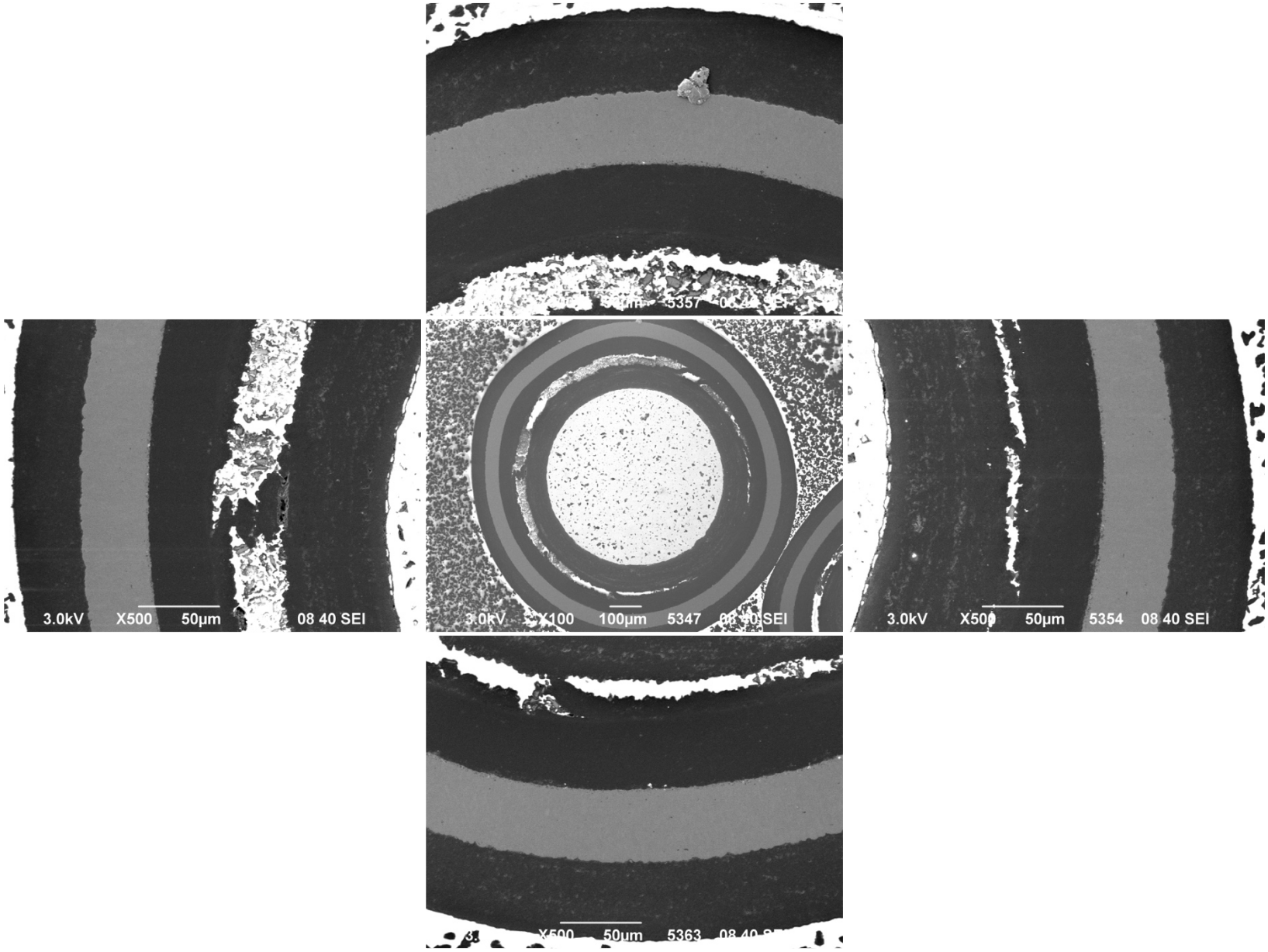

Appendix Figure D-33. 500× SEI micrographs of Particle 331-RS12.

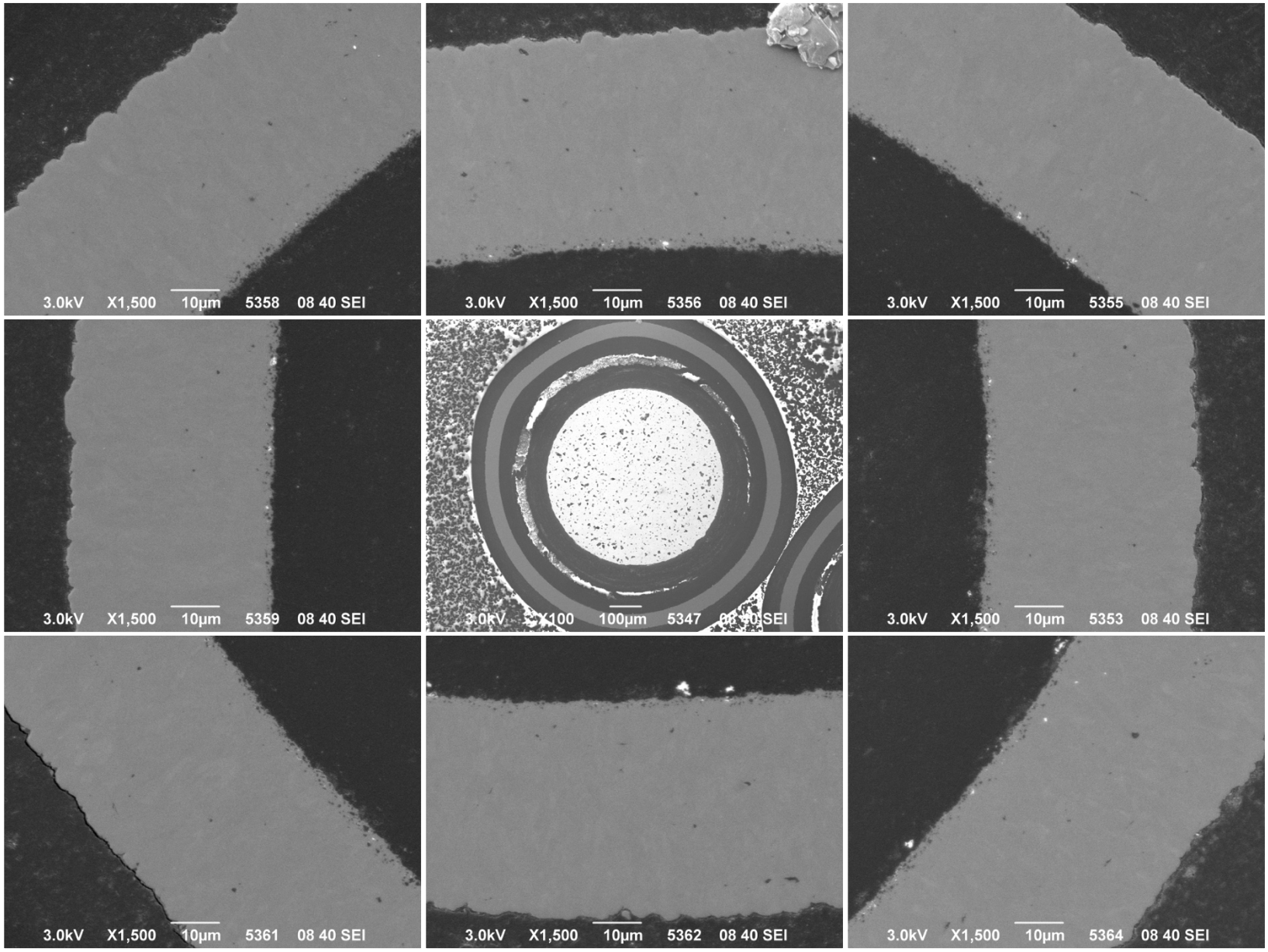

Appendix Figure D-34. 1,500× SEI micrographs of Particle 331-RS12.

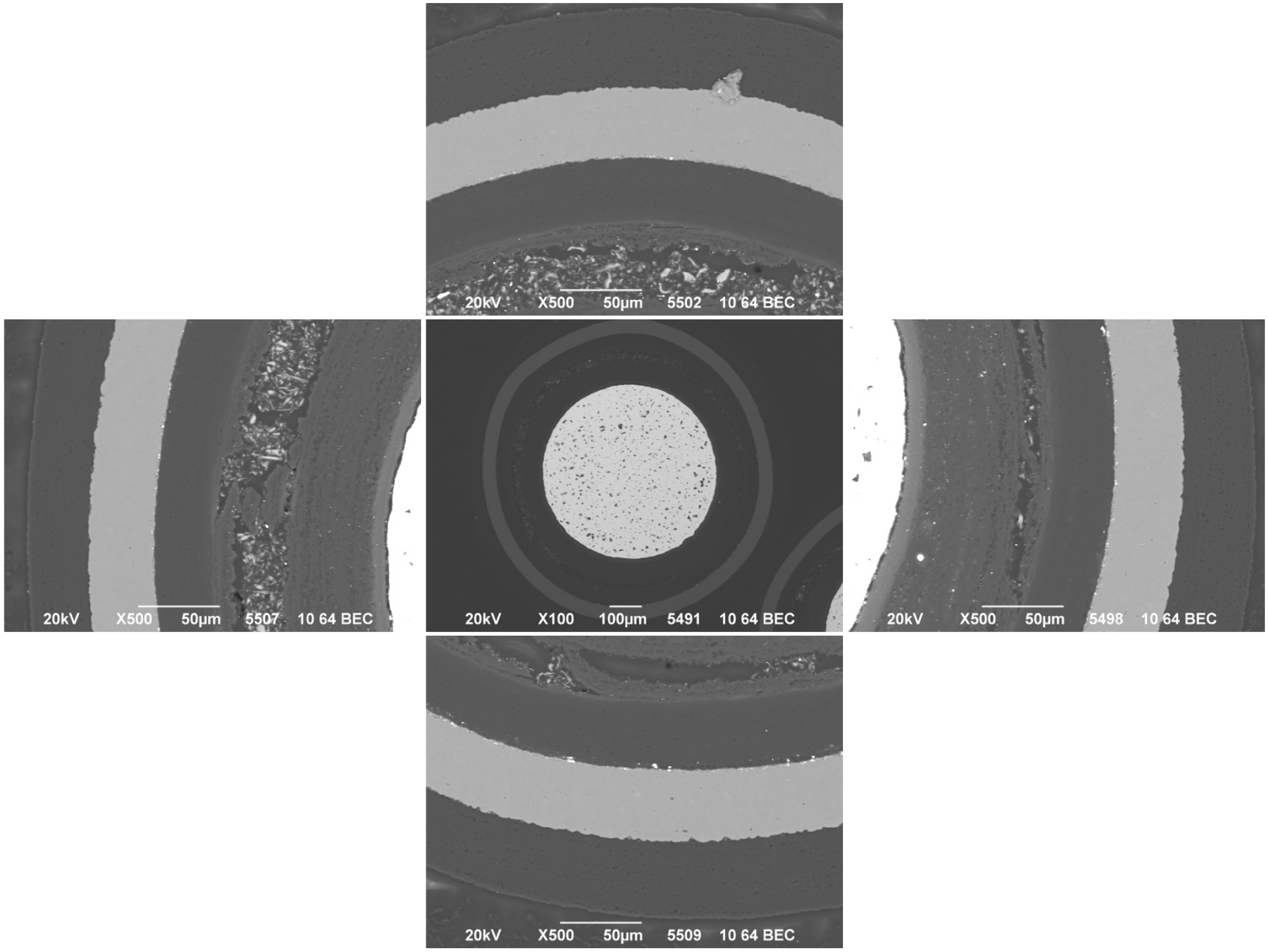

Appendix Figure D-35. 500× BEC micrographs of Particle 331-RS12.

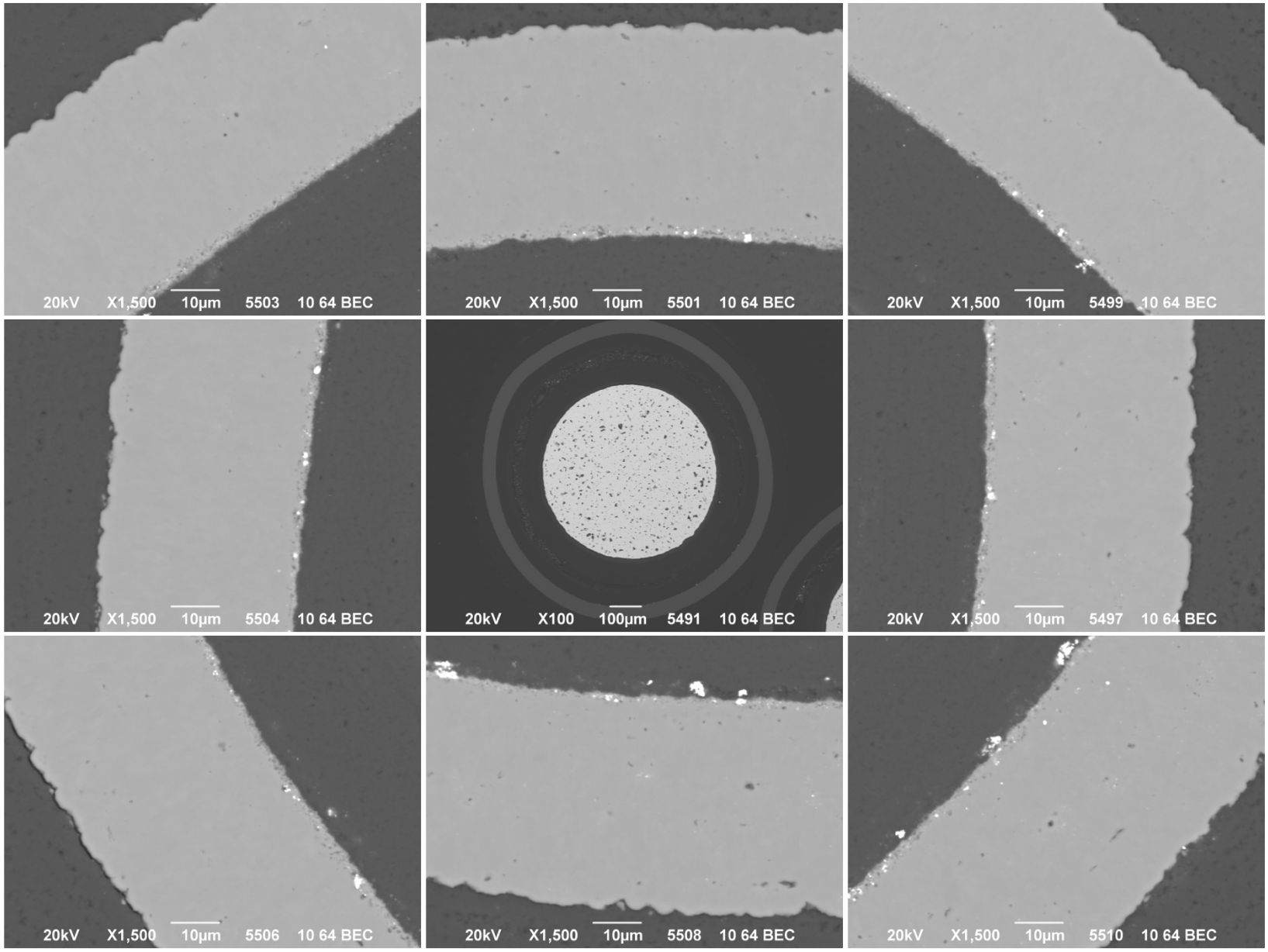

Appendix Figure D-36. 1,500× BEC micrographs of Particle 331-RS12.

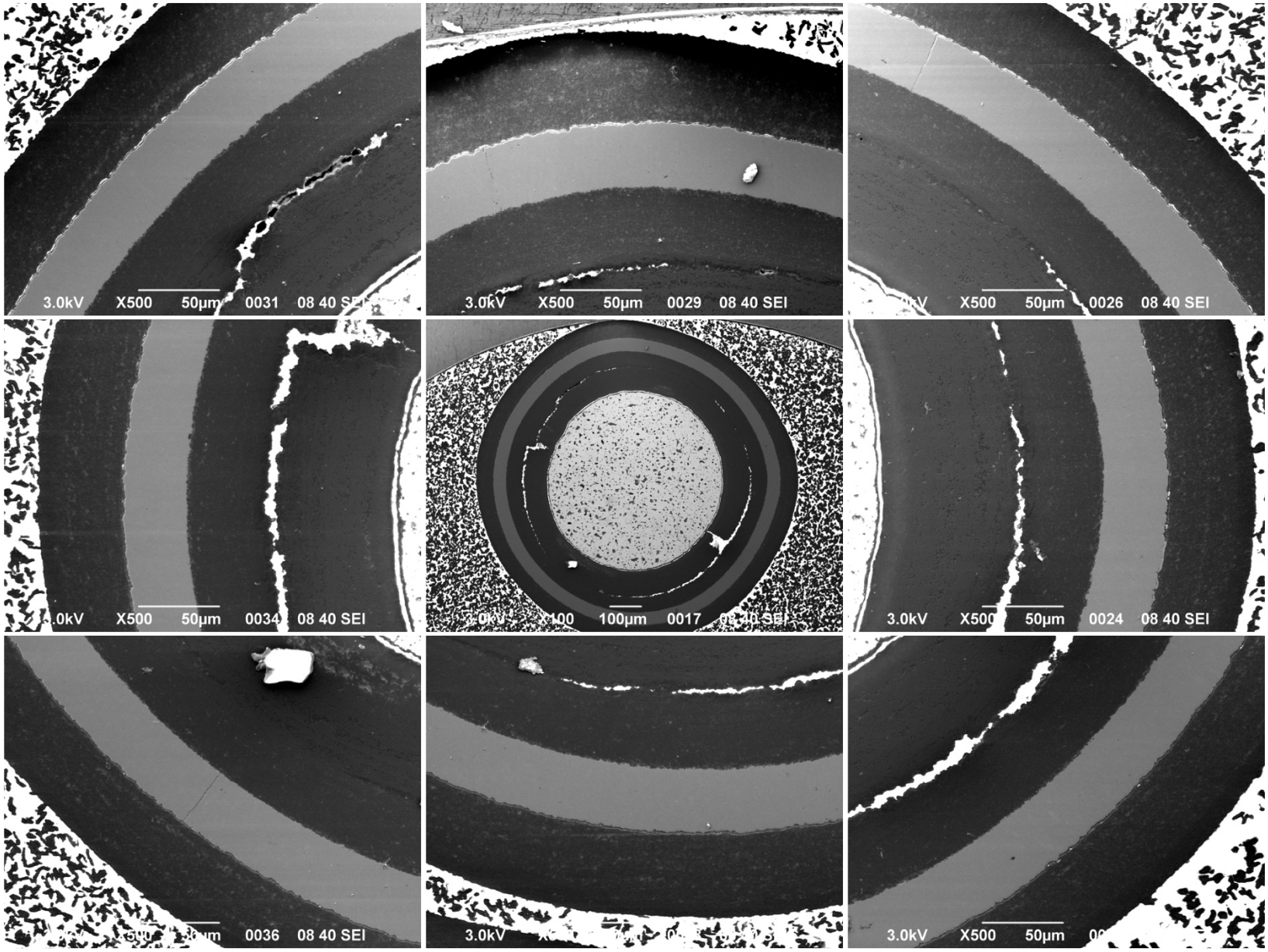

Appendix Figure D-37. 500× SEI micrographs of Particle 311-RS07.

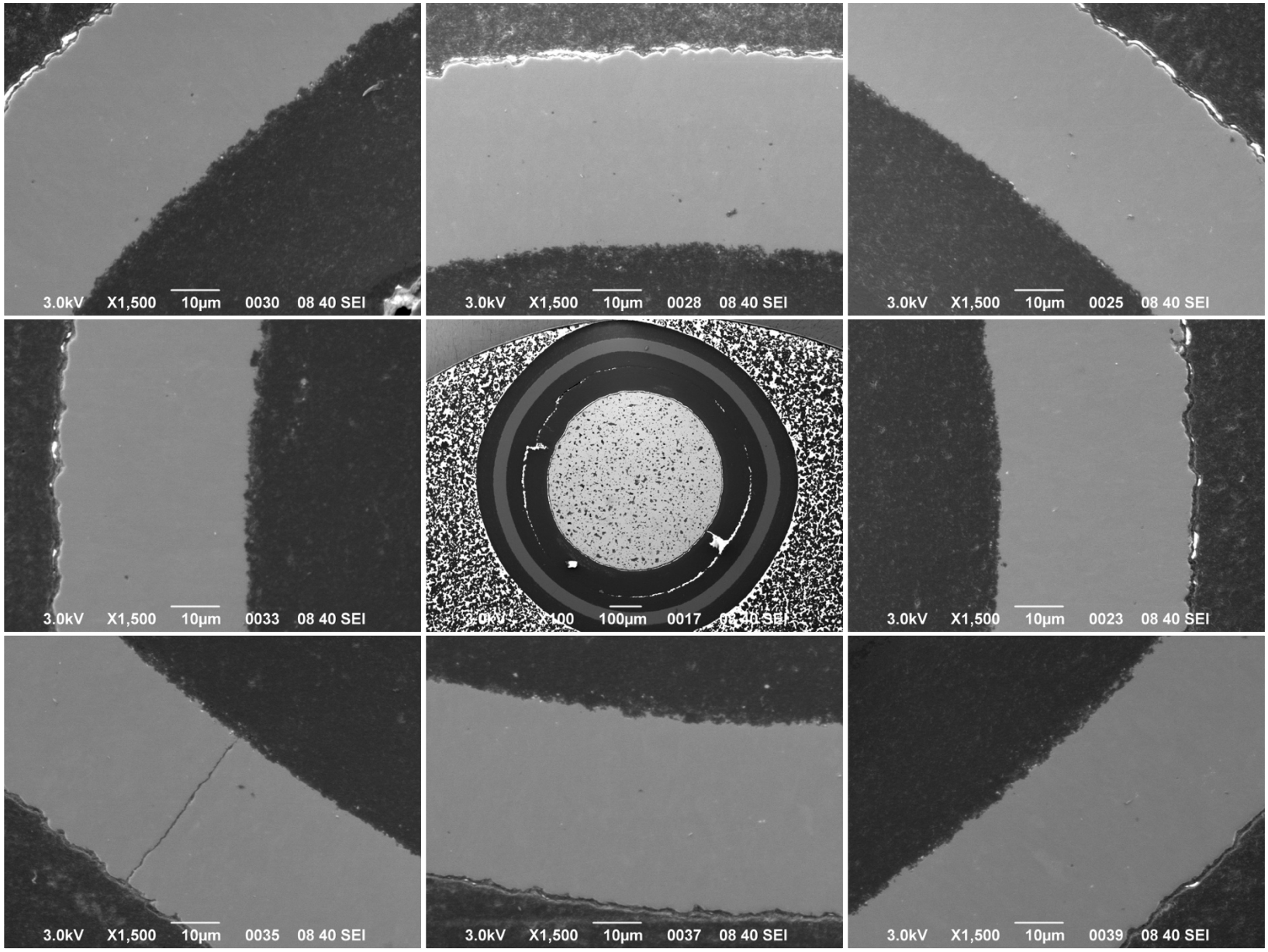

Appendix Figure D-38. 1,500× SEI micrographs of Particle 311-RS07.

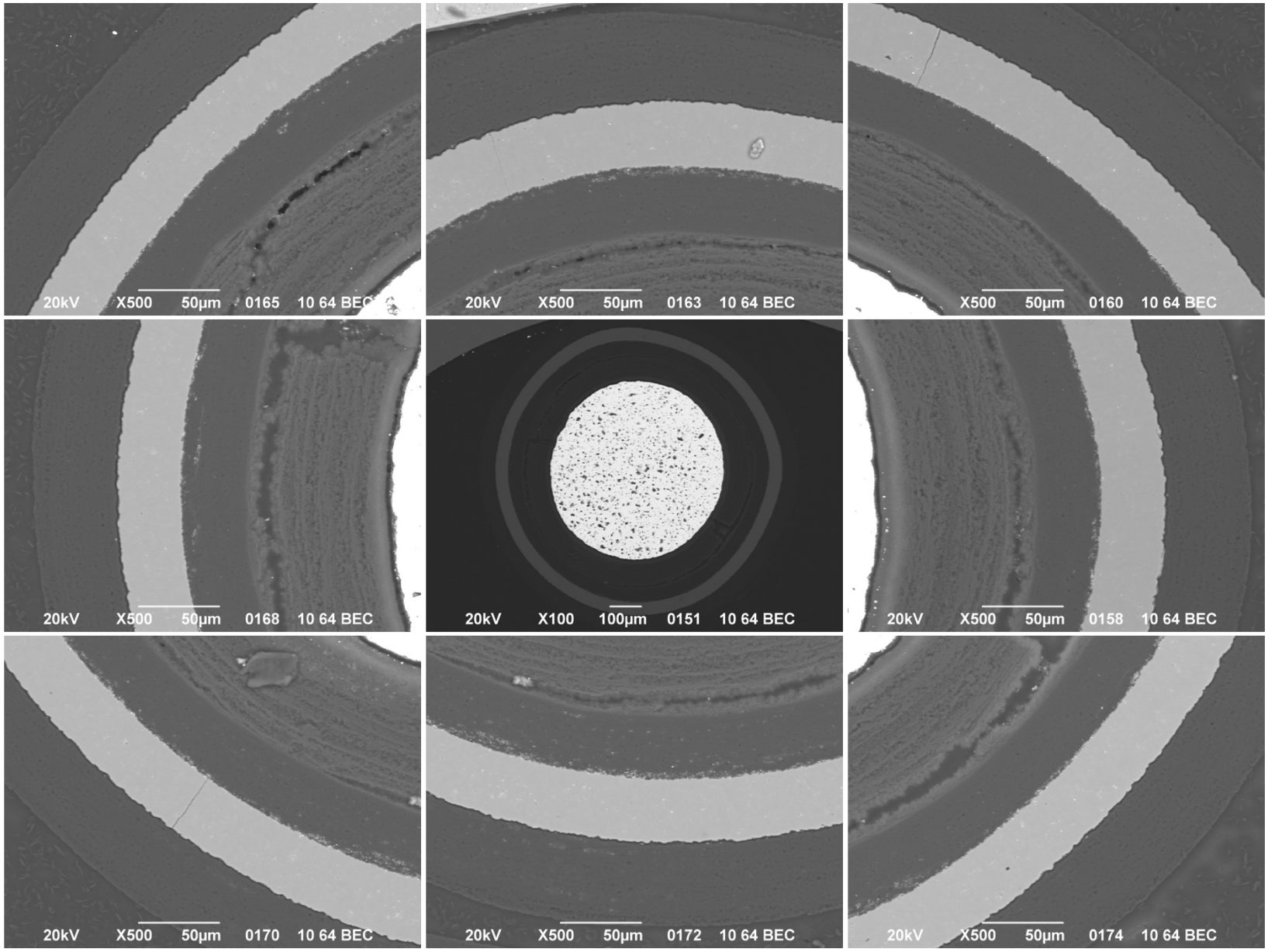

Appendix Figure D-39. 500× BEC micrographs of Particle 311-RS07.

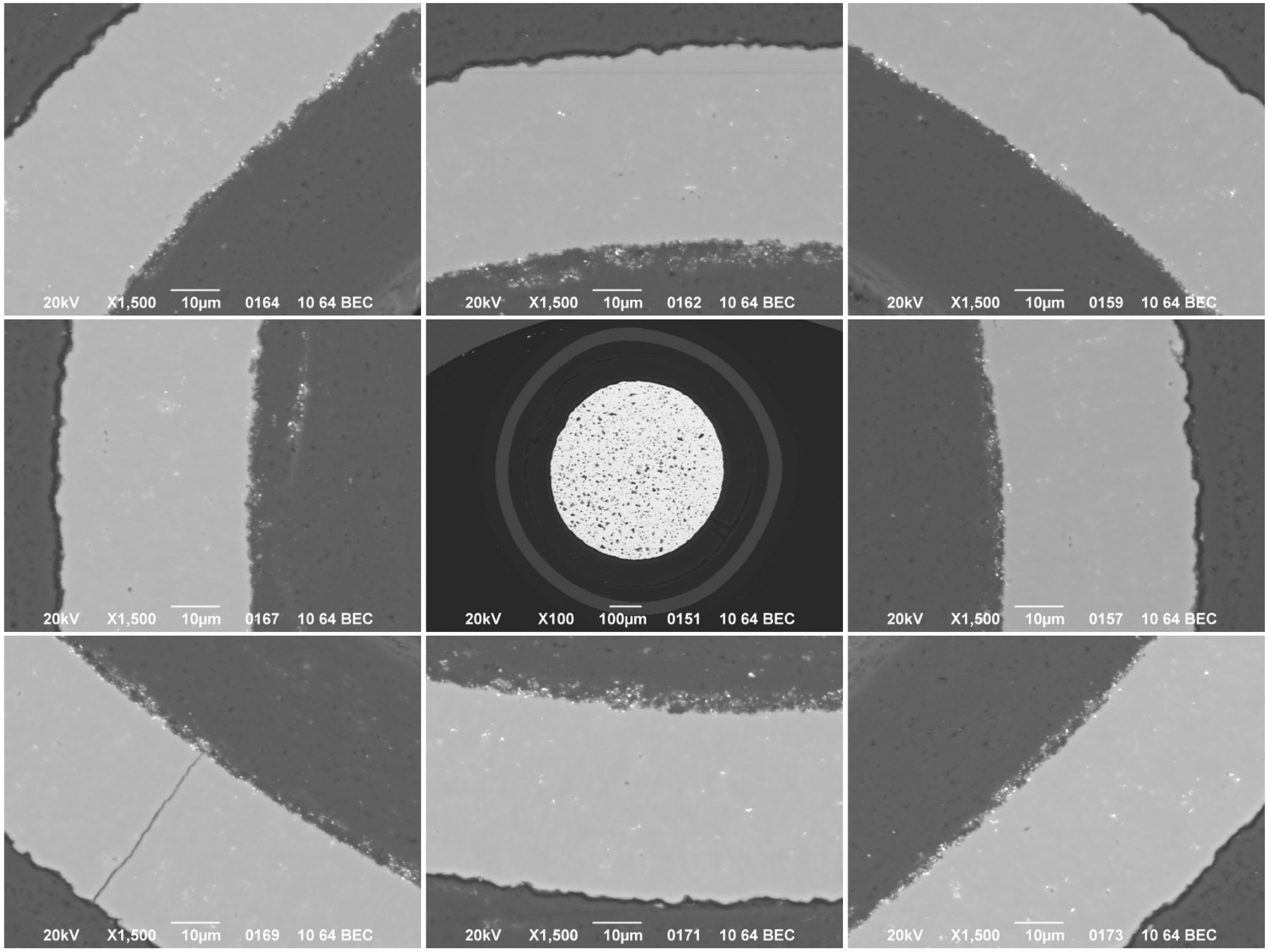

Appendix Figure D-40. 1,500× BEC micrographs of Particle 311-RS07.

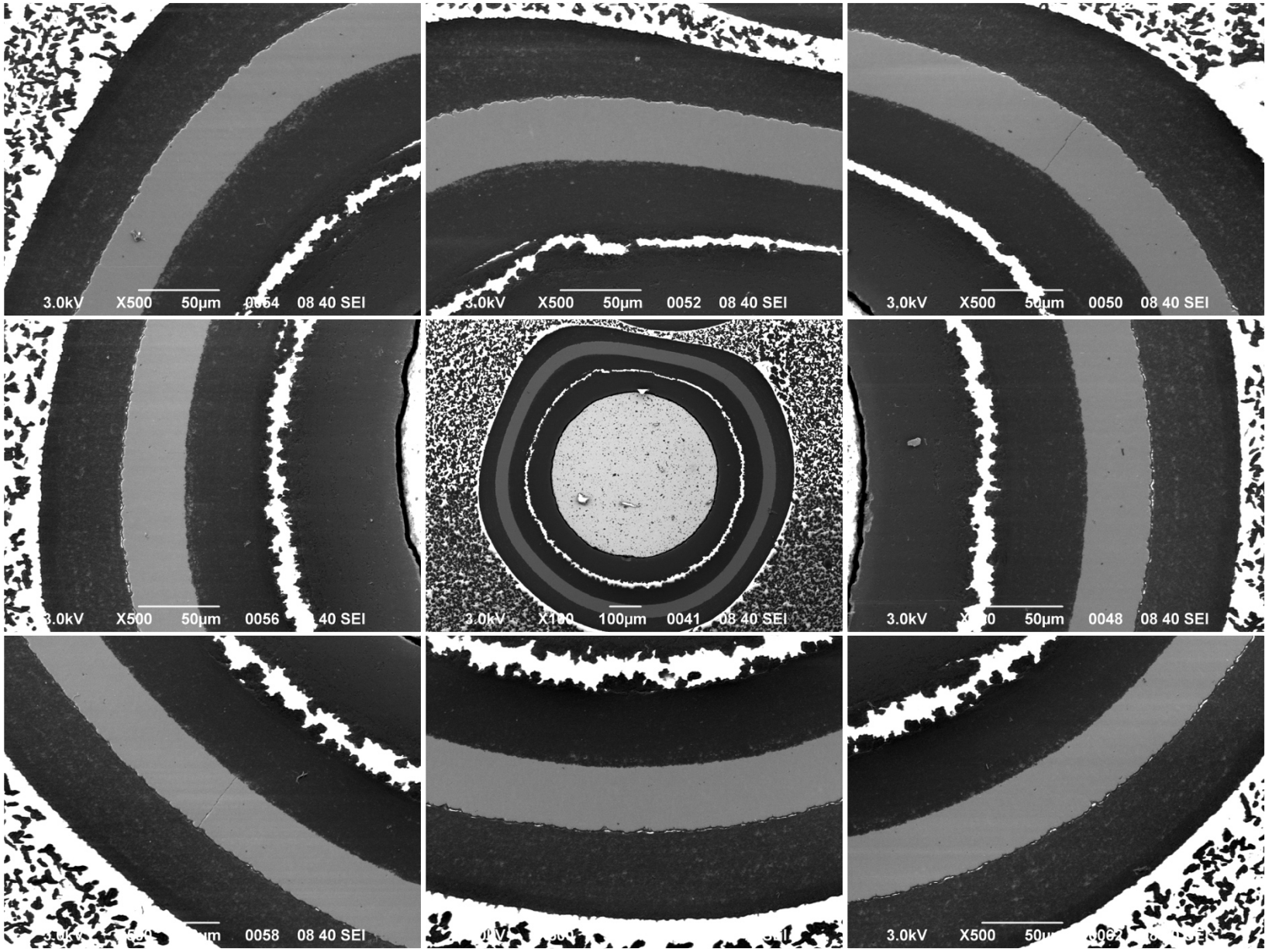

Appendix Figure D-41. 500× SEI micrographs of Particle 311-RS29.

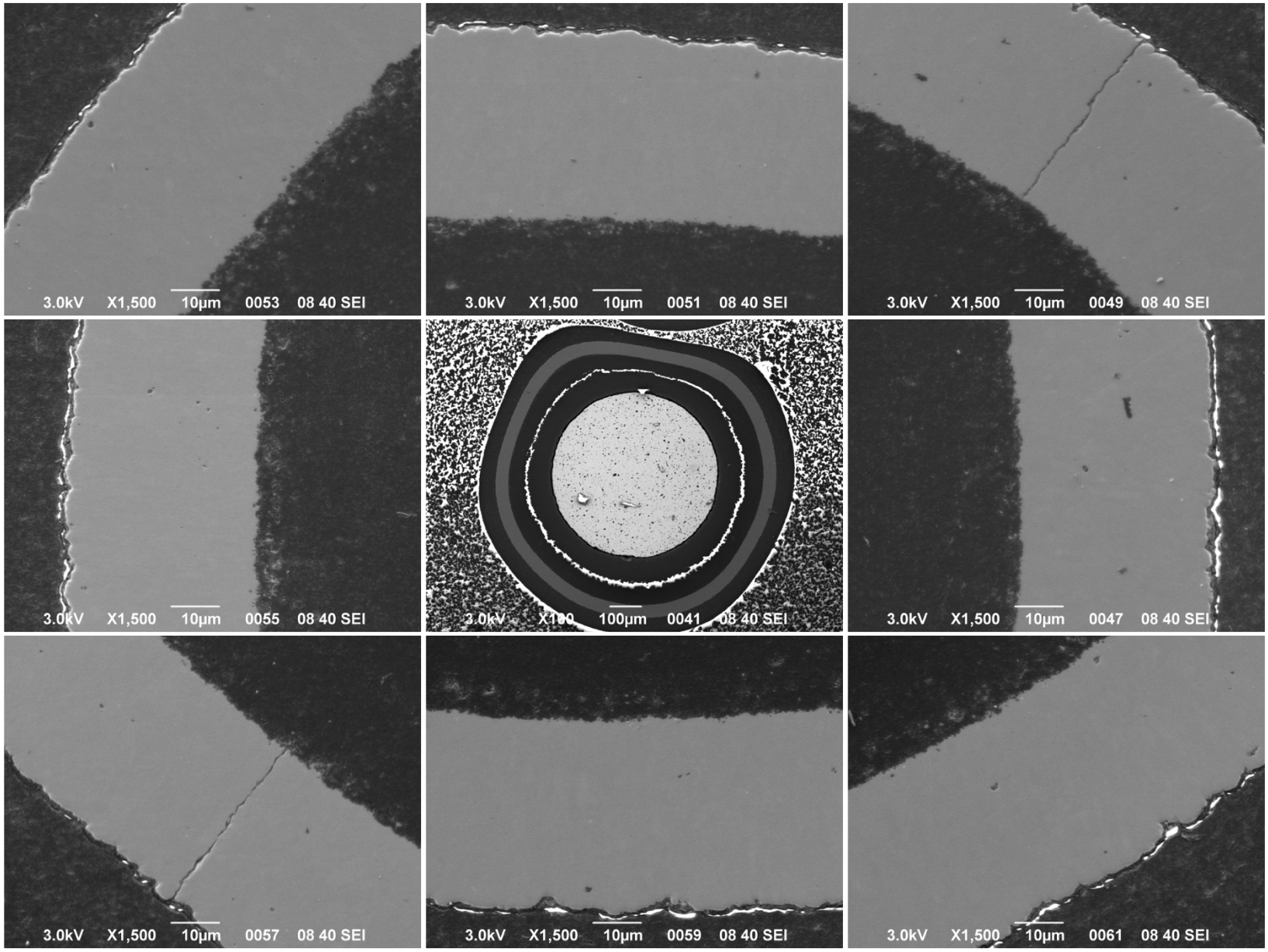

Appendix Figure D-42. 1,500× SEI micrographs of Particle 311-RS29.

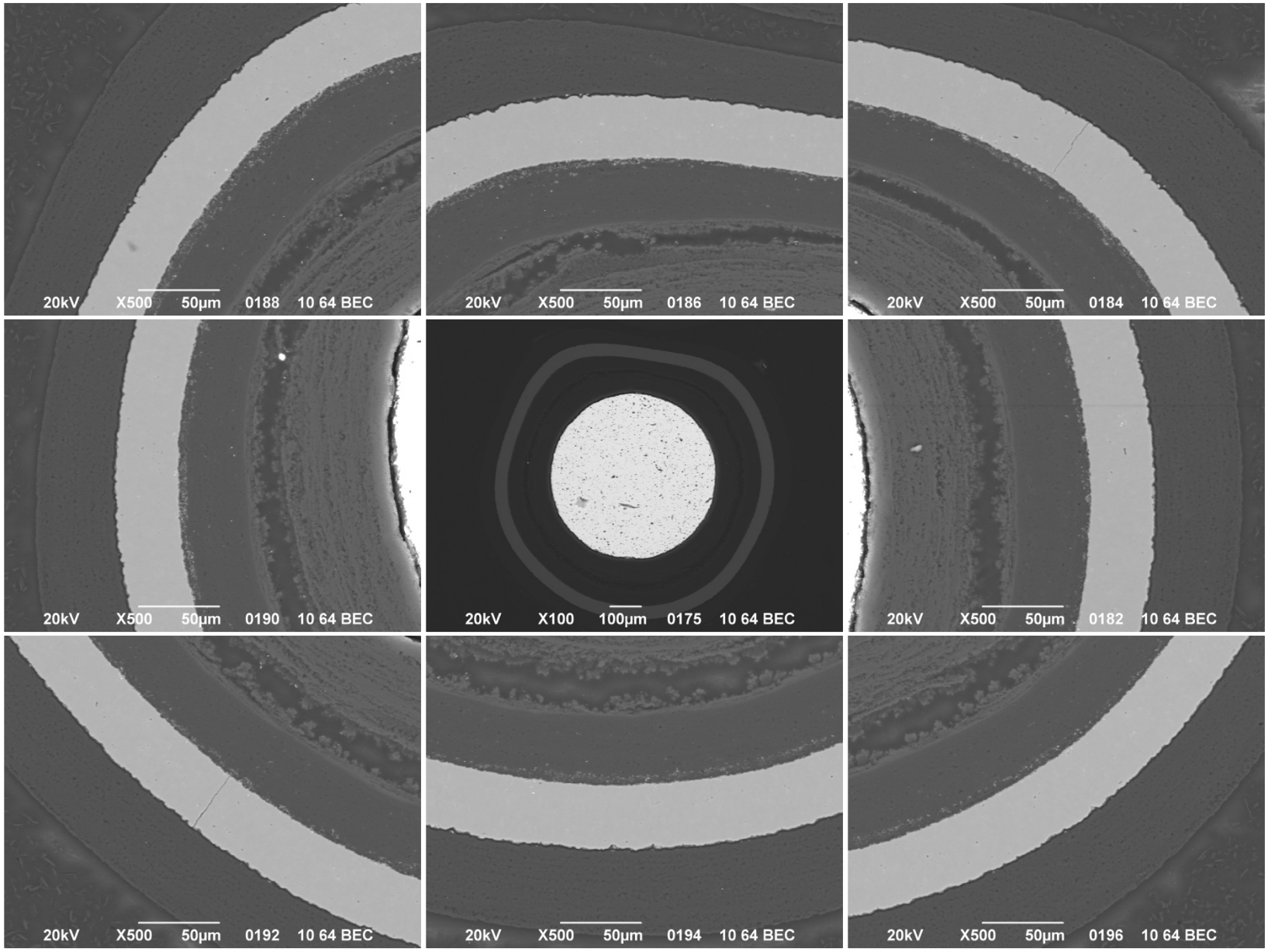

Appendix Figure D-43. 500× BEC micrographs of Particle 311-RS29.

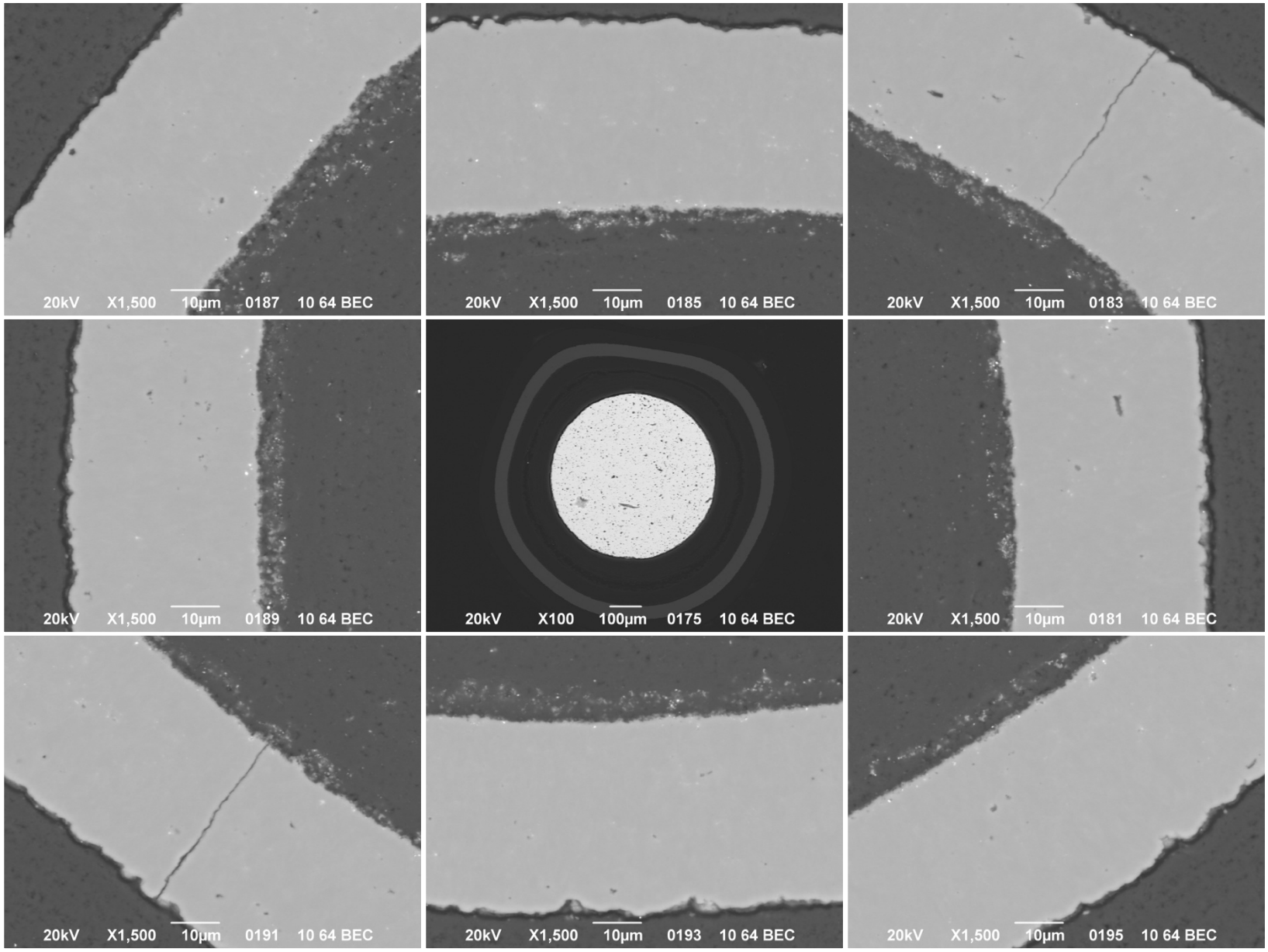

Appendix Figure D-44. 1,500× BEC micrographs of Particle 311-RS29.

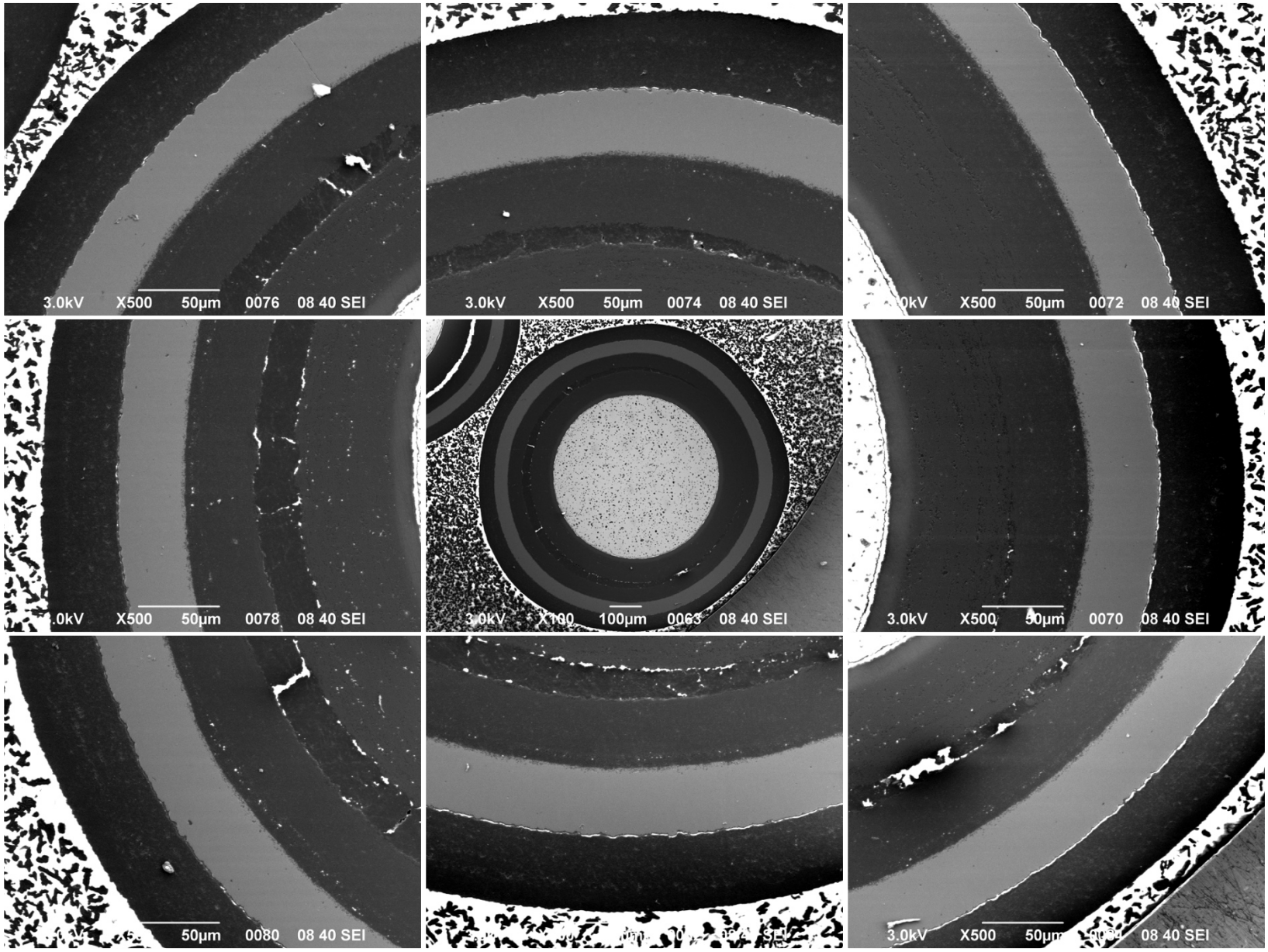

Appendix Figure D-45. 500× SEI micrographs of Particle 311-RS08.

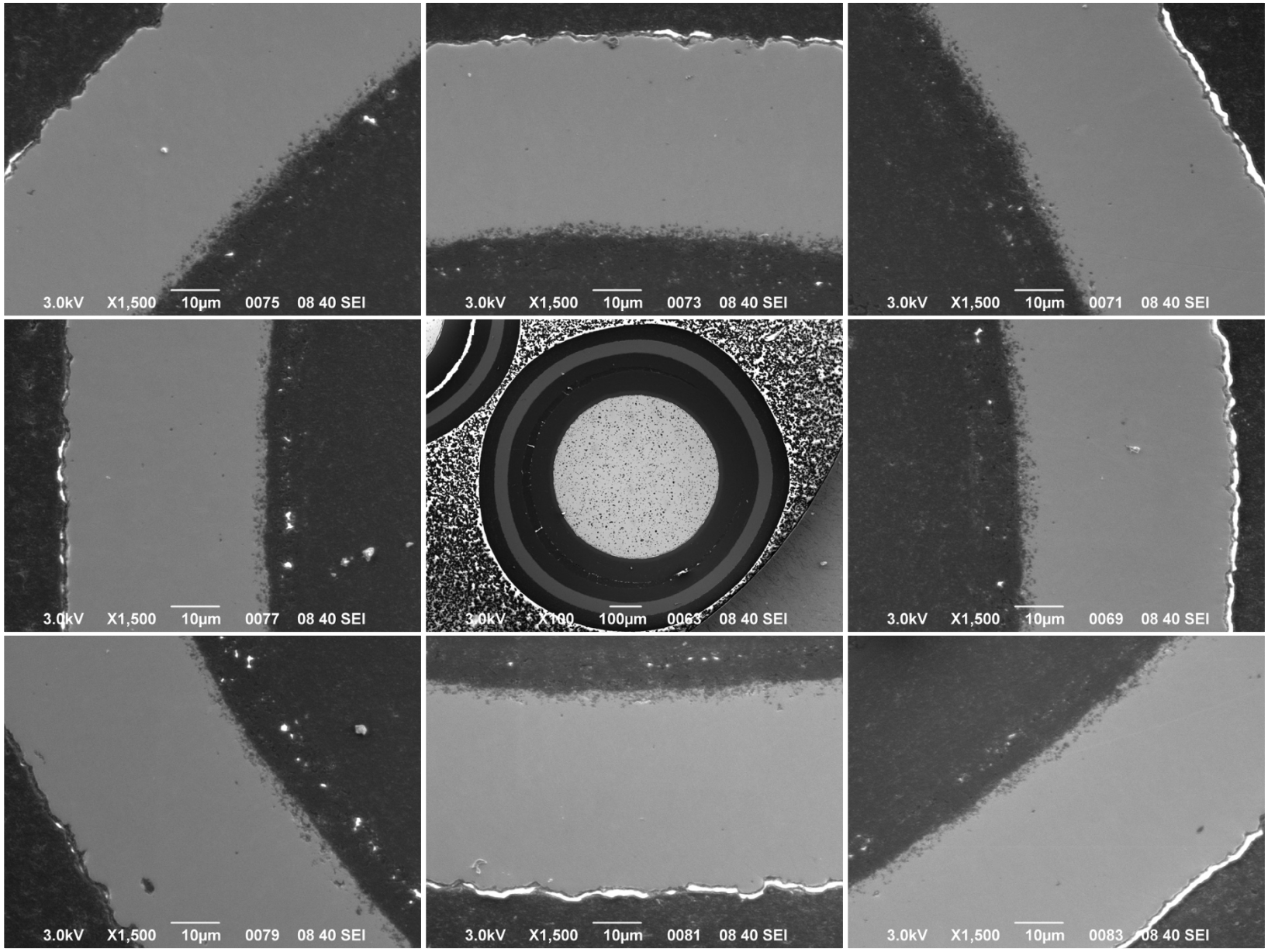

Appendix Figure D-46. 1,500× SEI micrographs of Particle 311-RS08.

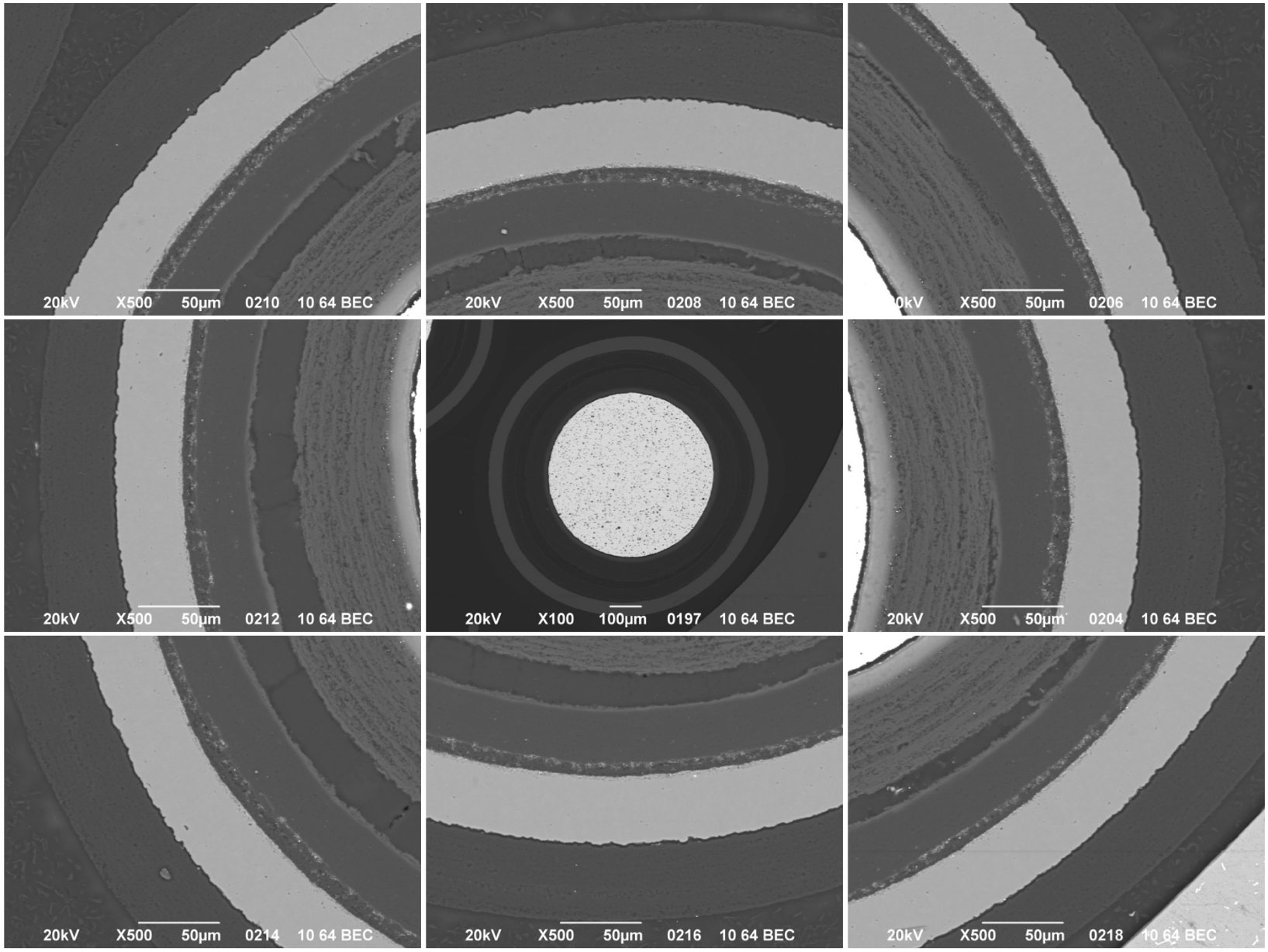

Appendix Figure D-47. 500× BEC micrographs of Particle 311-RS08.

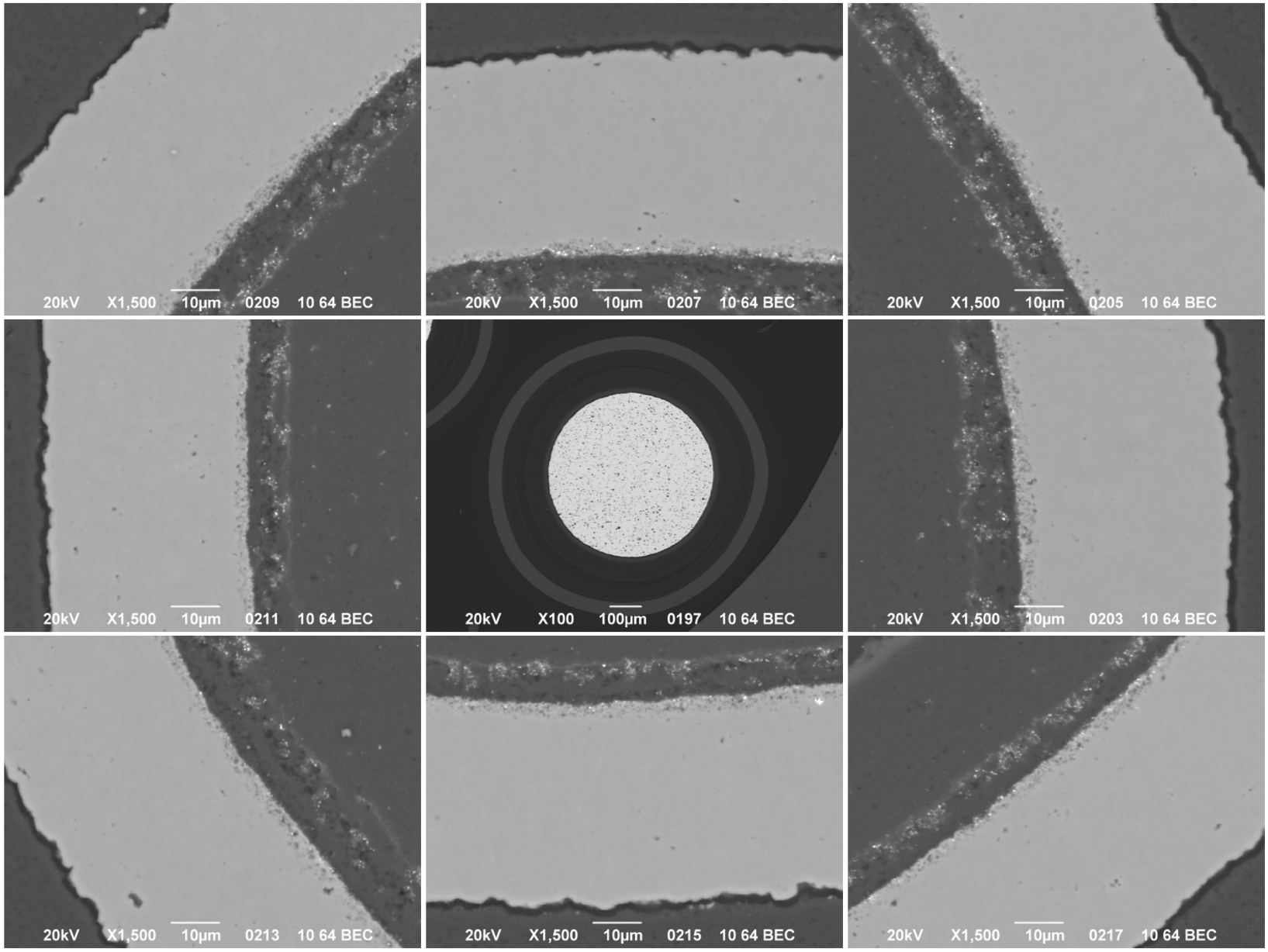

Appendix Figure D-48. 1,500× BEC micrographs of Particle 311-RS08.

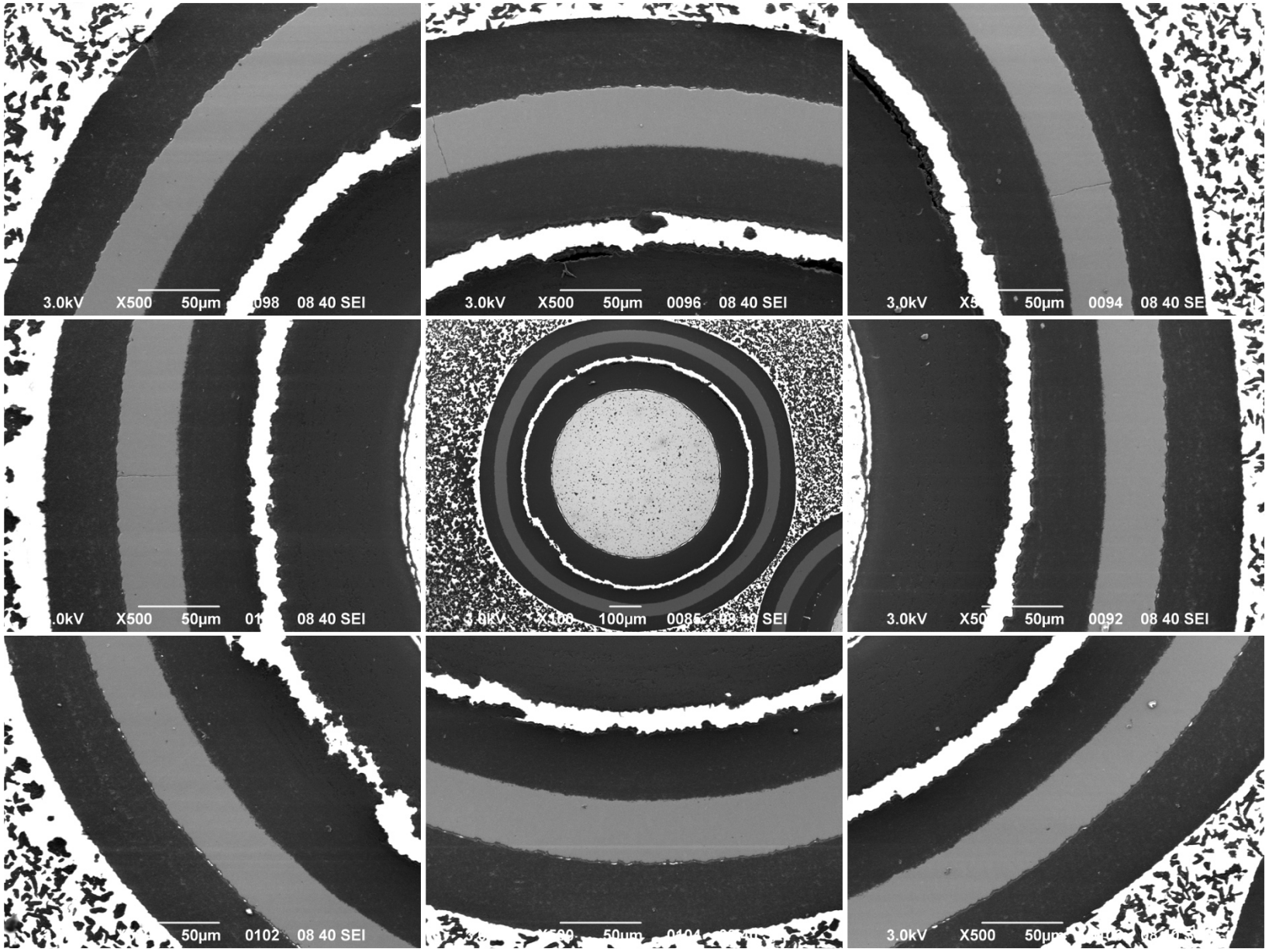

Appendix Figure D-49. 500× SEI micrographs of Particle 311-RS32.

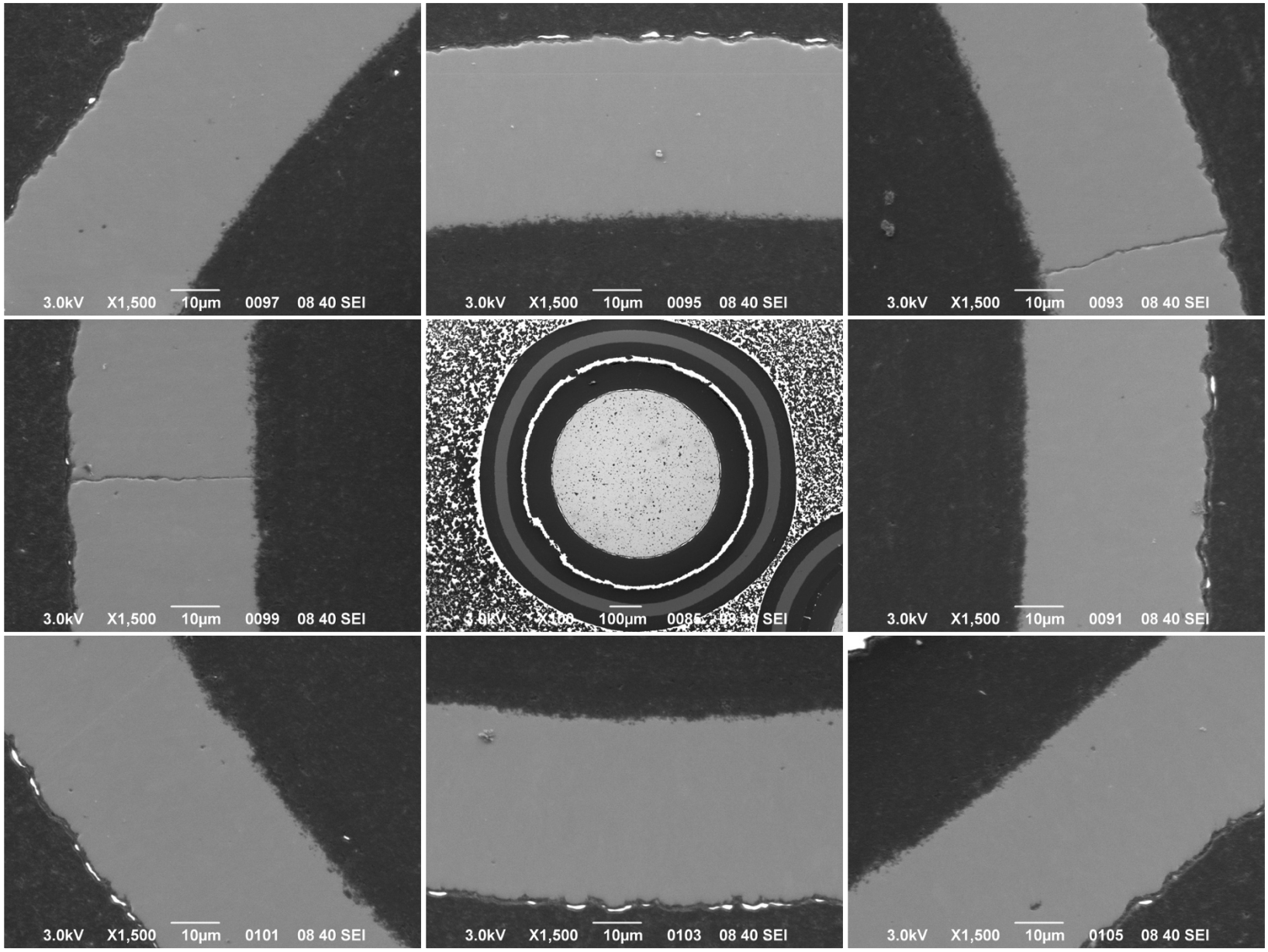

Appendix Figure D-50. 1,500× SEI micrographs of Particle 311-RS32.

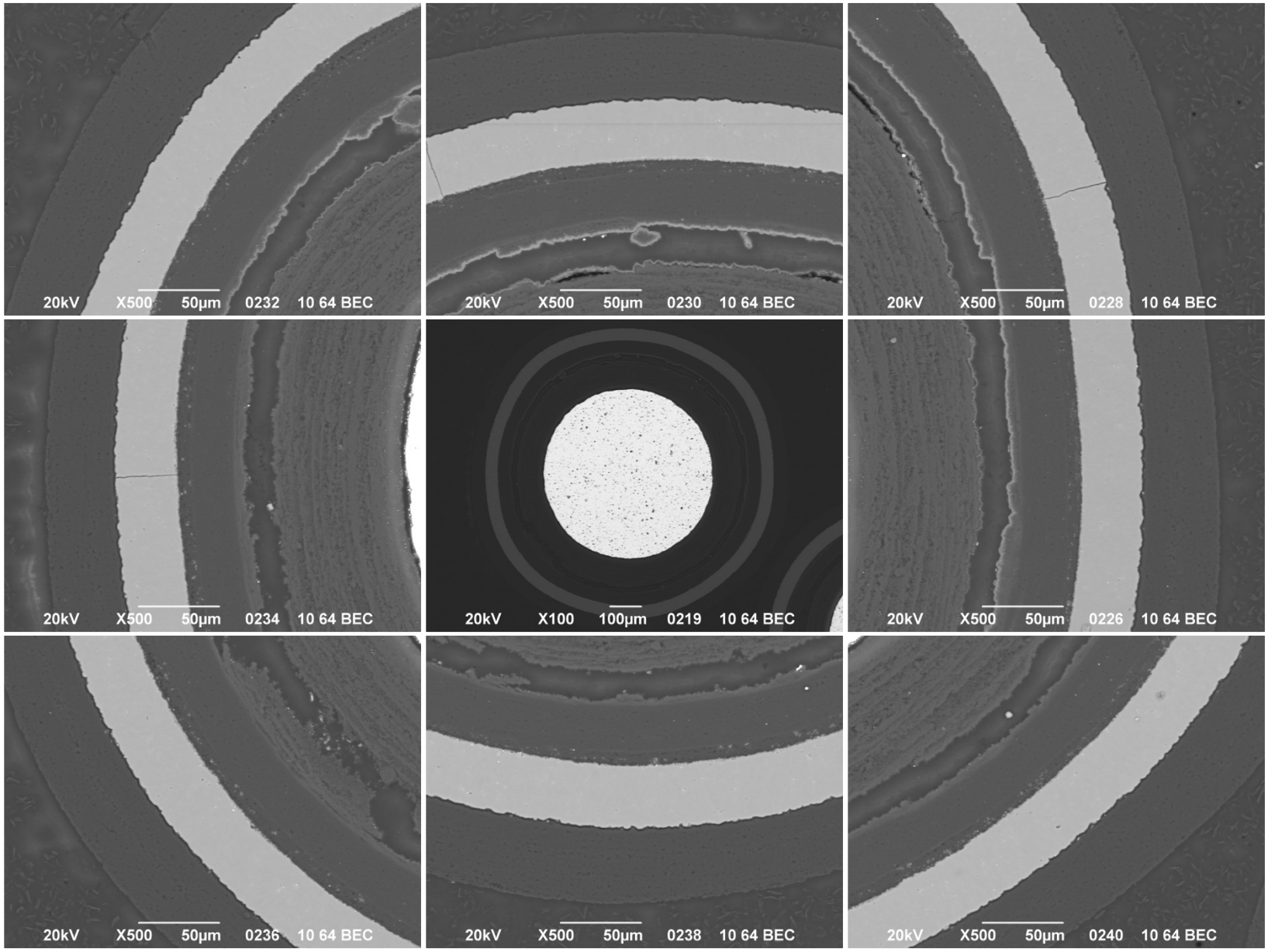

Appendix Figure D-51. 500× BEC micrographs of Particle 311-RS32.

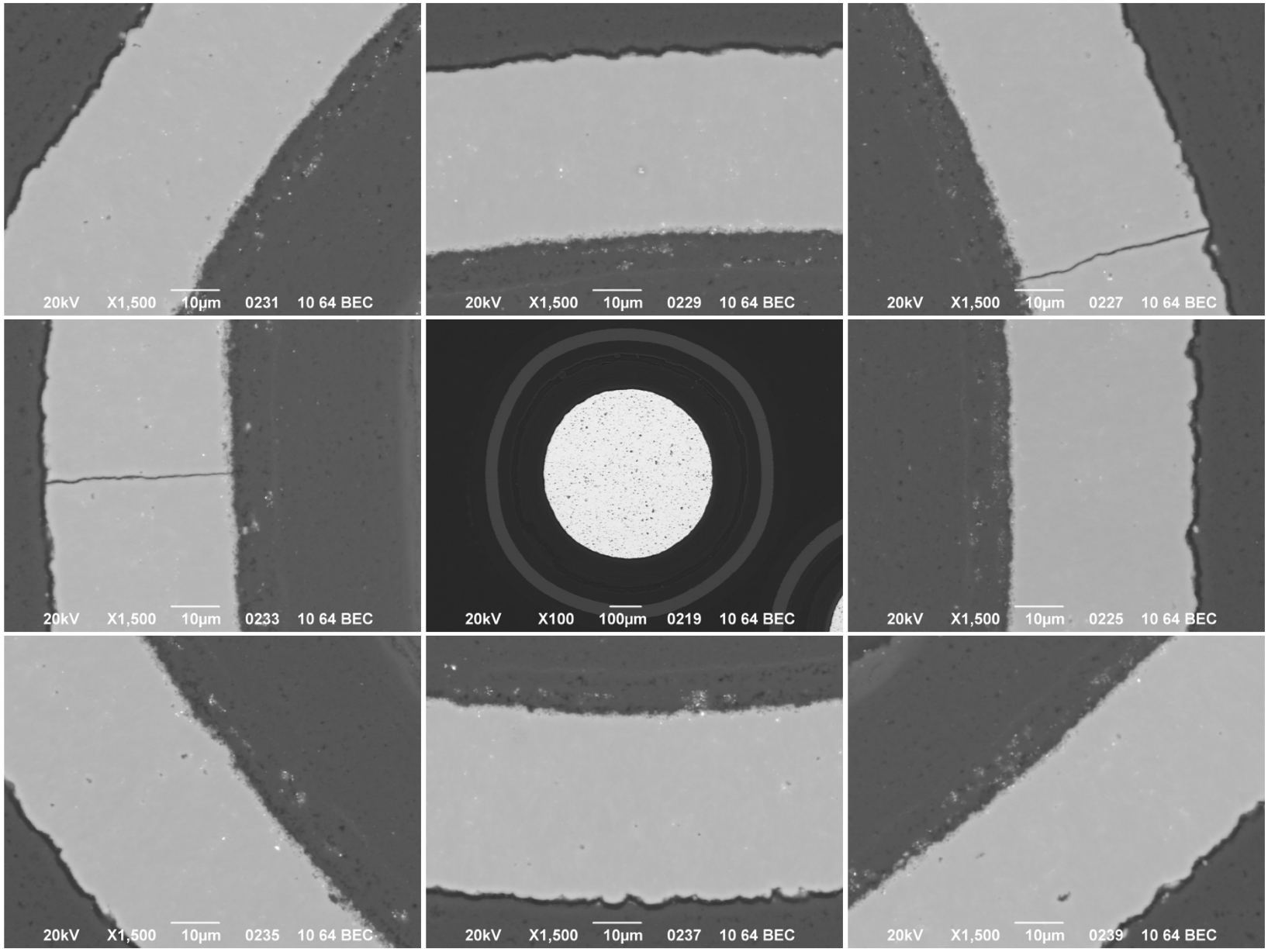

Appendix Figure D-52. 1,500× BEC micrographs of Particle 311-RS32.

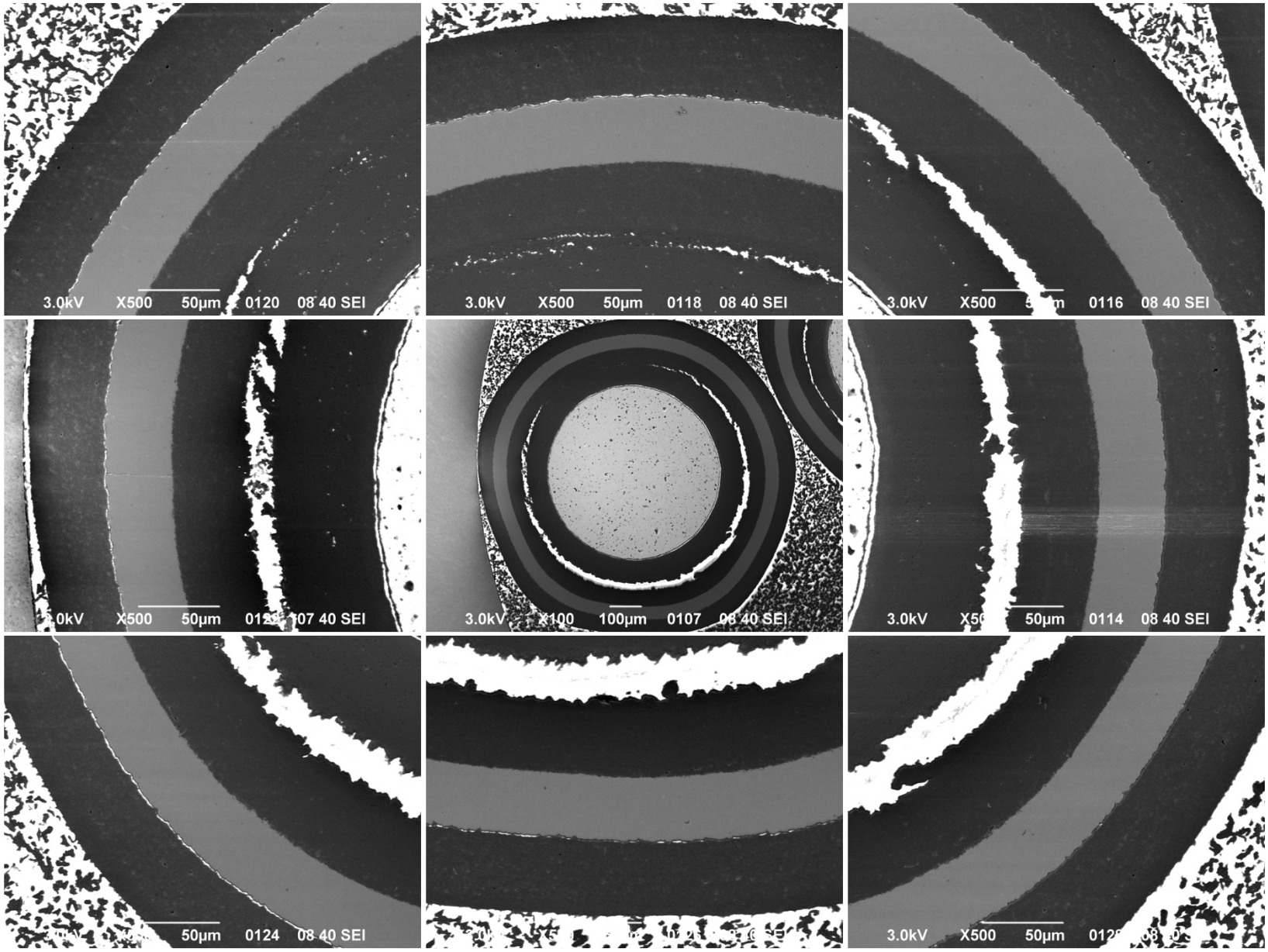

Appendix Figure D-53. 500× SEI micrographs of Particle 311-RS18.

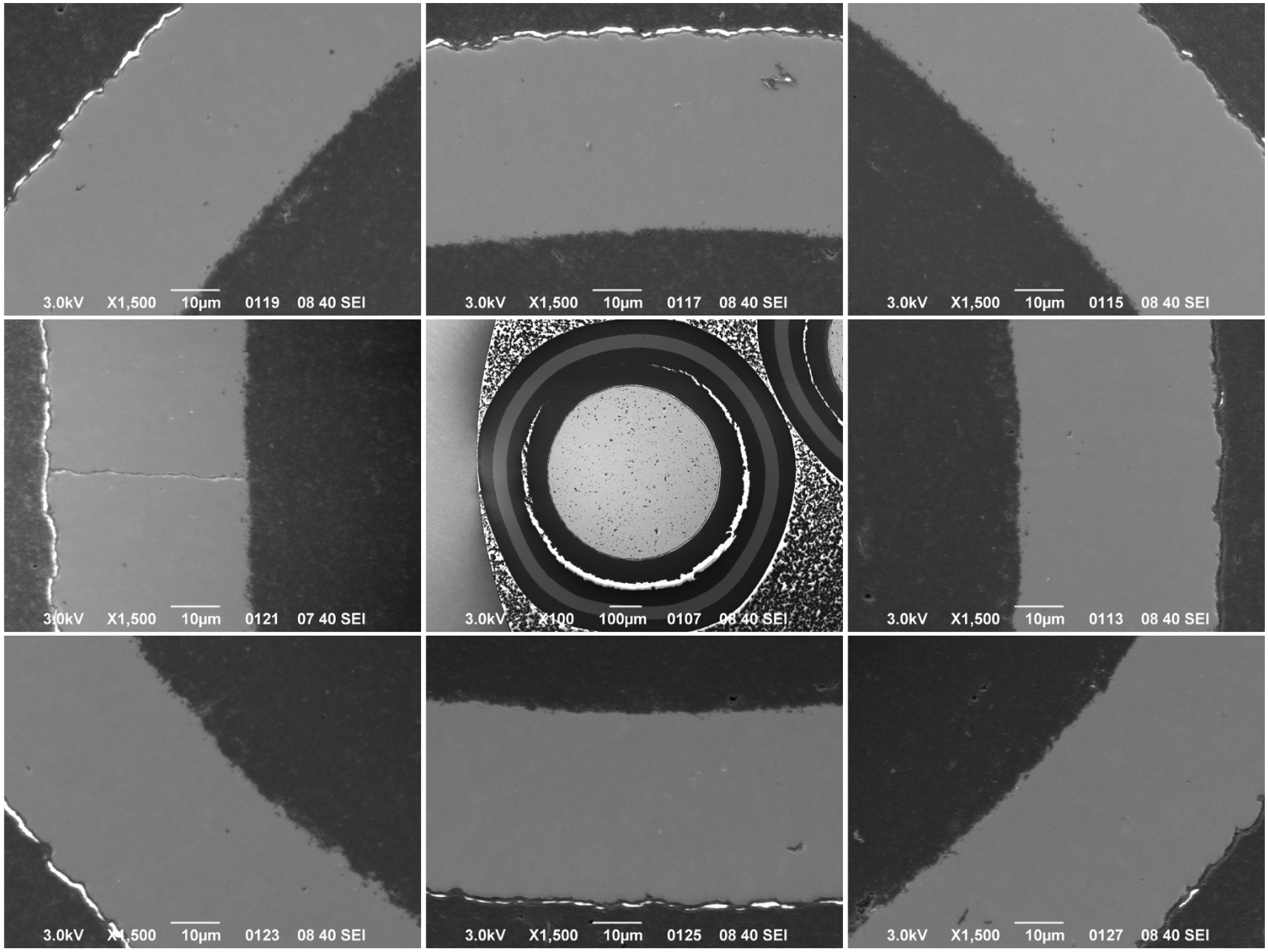

Appendix Figure D-54. 1,500× SEI micrographs of Particle 311-RS18.

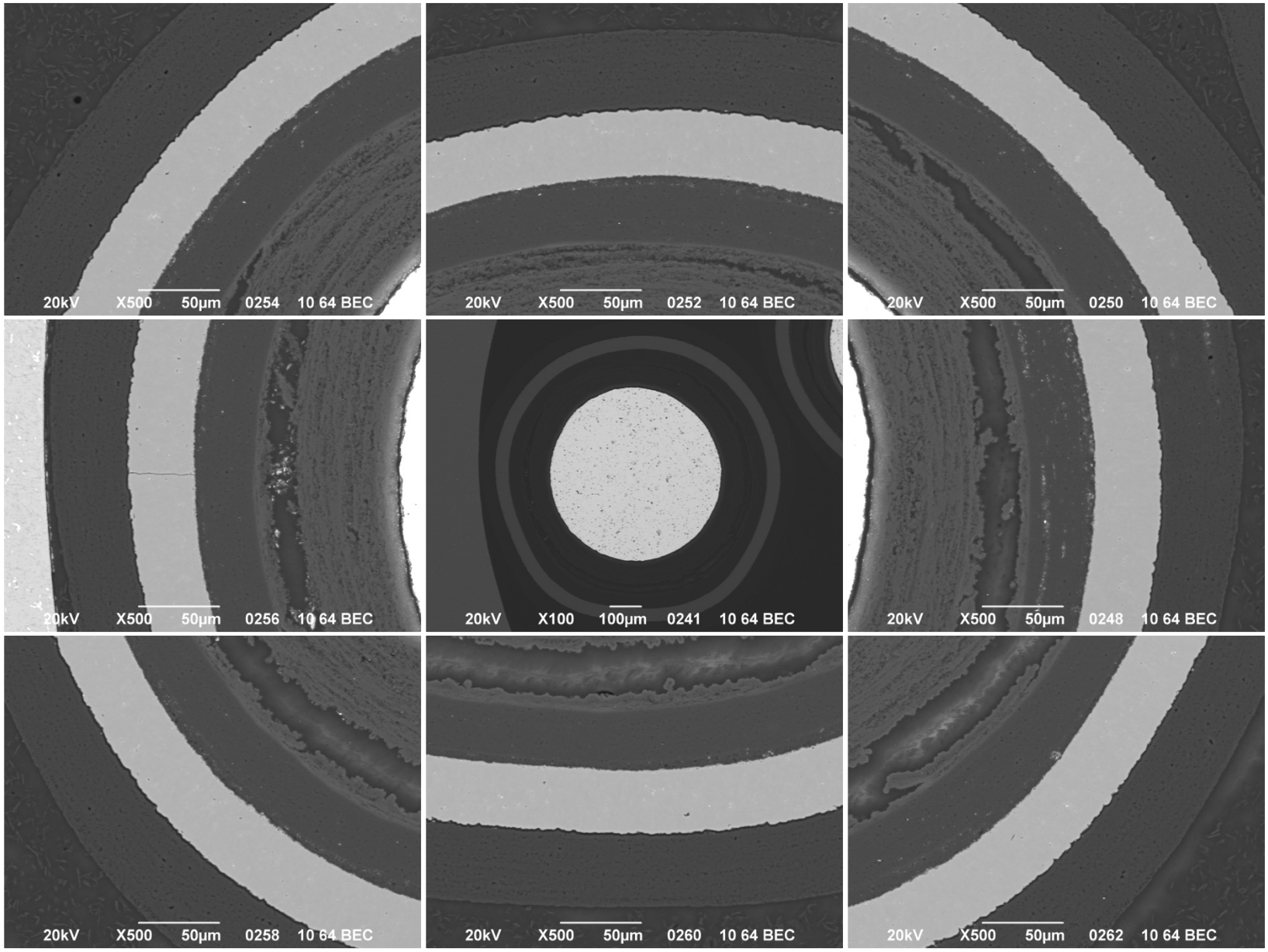

Appendix Figure D-55. 500× BEC micrographs of Particle 311-RS18.

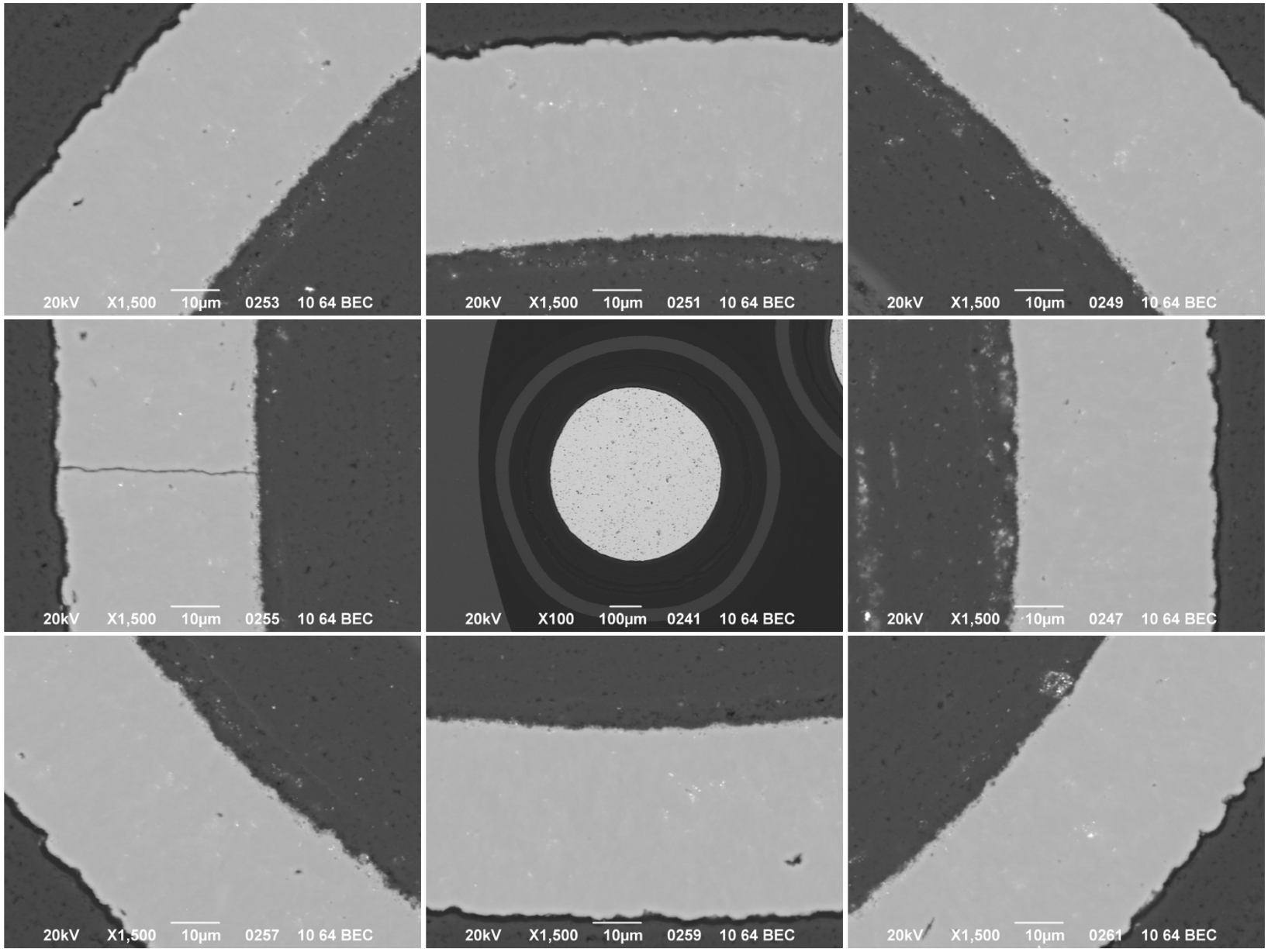

Appendix Figure D-56. 1,500× BEC micrographs of Particle 311-RS18.

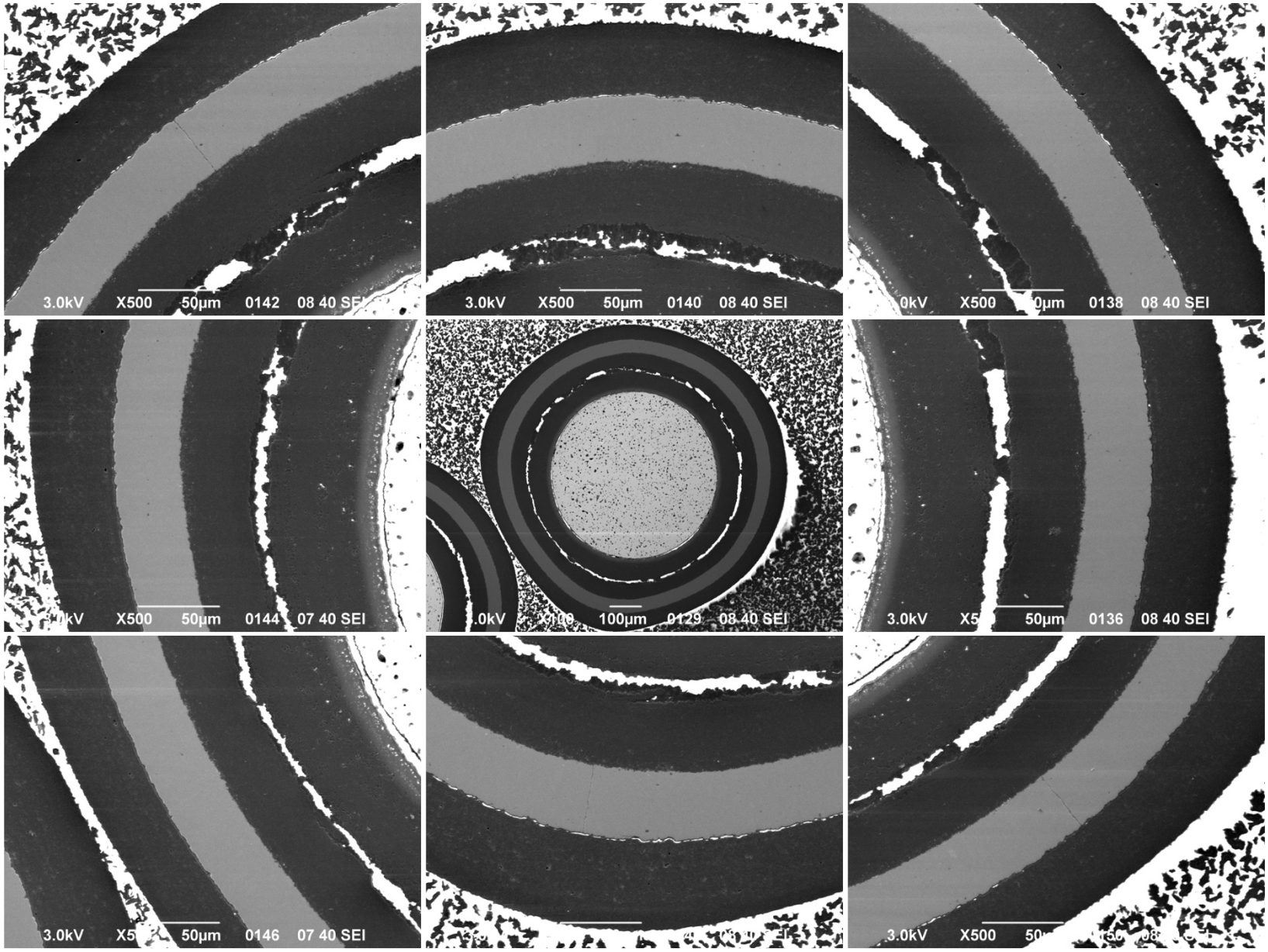

Appendix Figure D-57. 500× SEI micrographs of Particle 311-RS36.

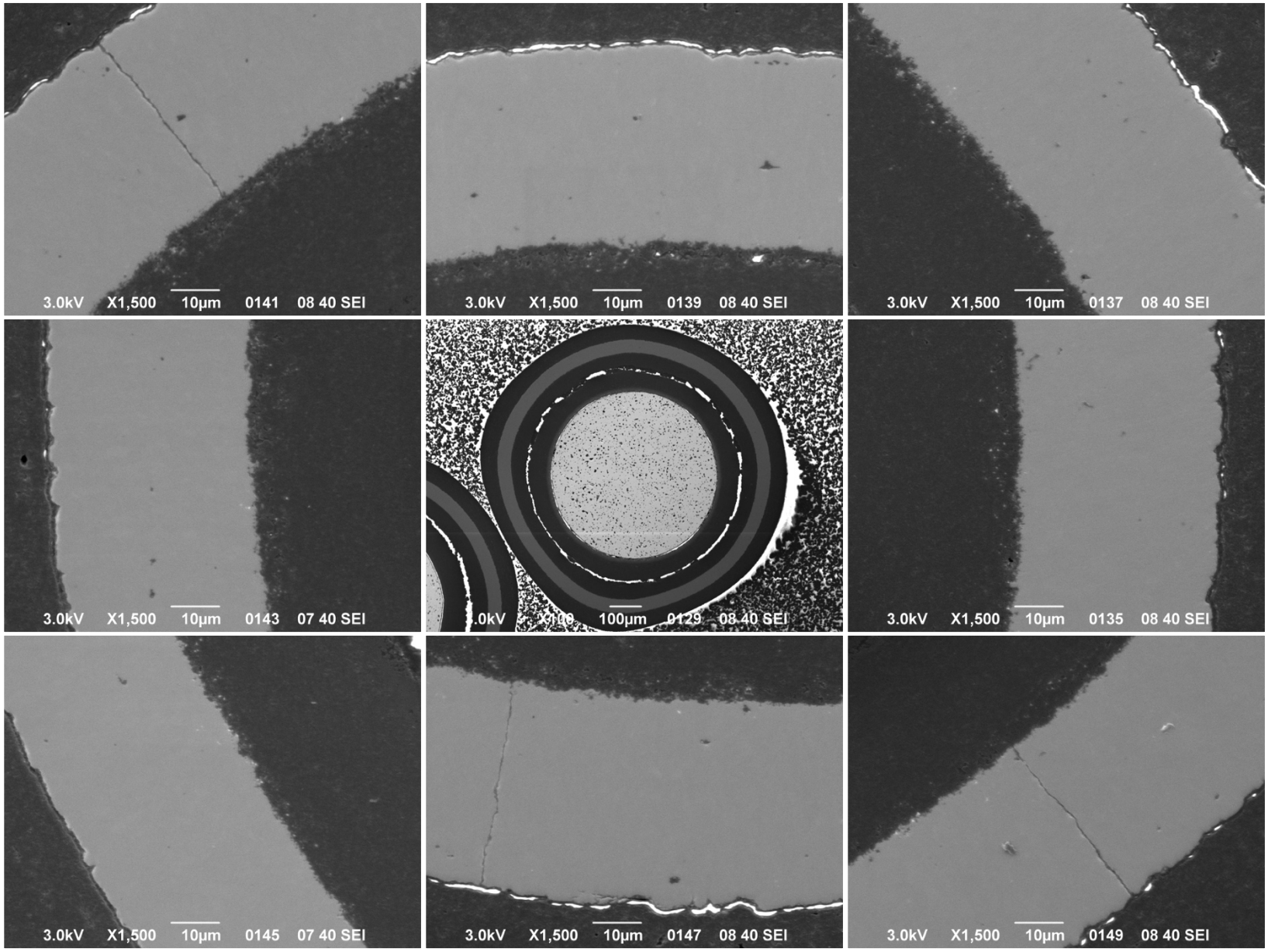

Appendix Figure D-58. 1,500× SEI micrographs of Particle 311-RS36.

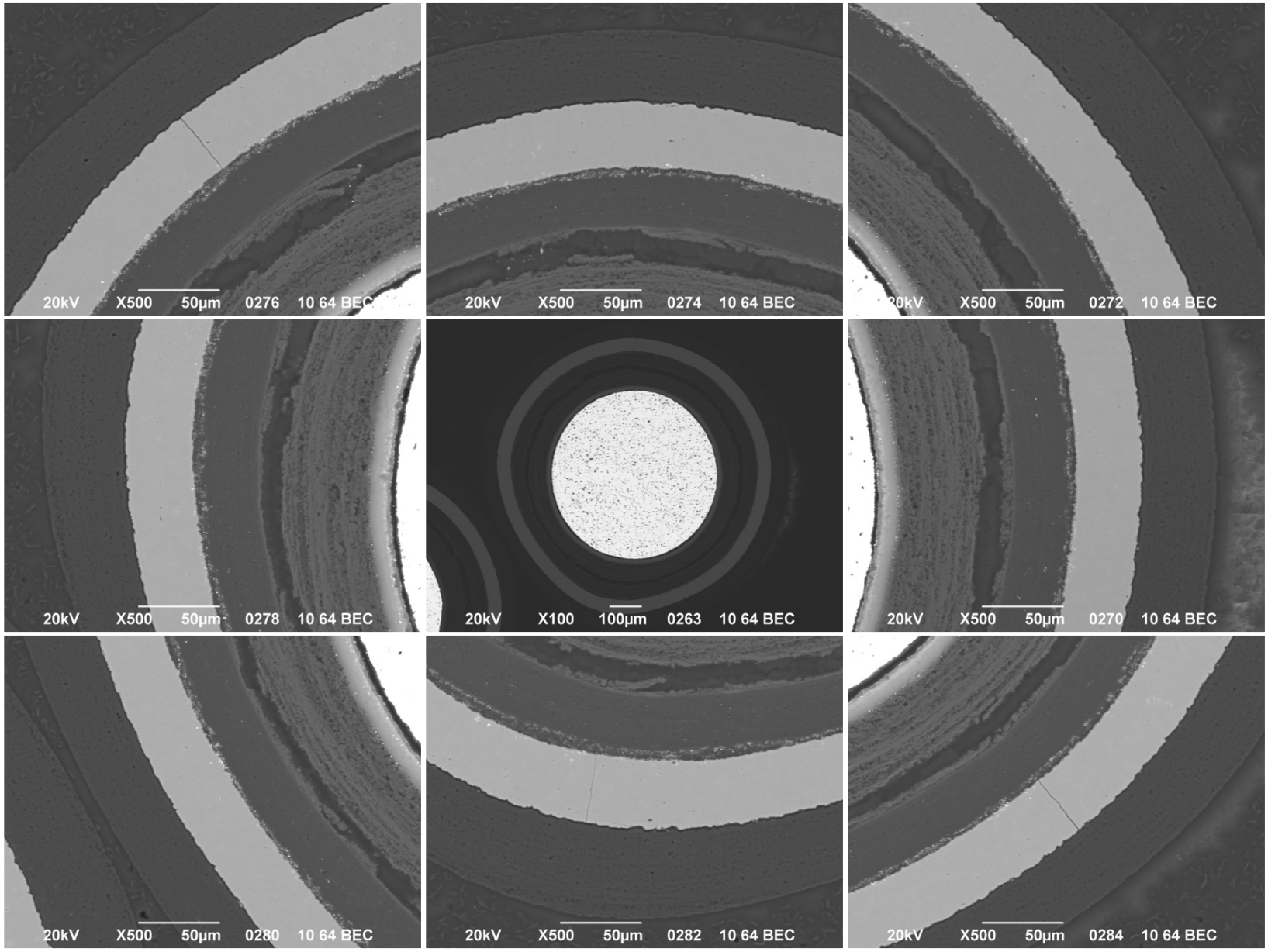

Appendix Figure D-59. 500× BEC micrographs of Particle 311-RS36.

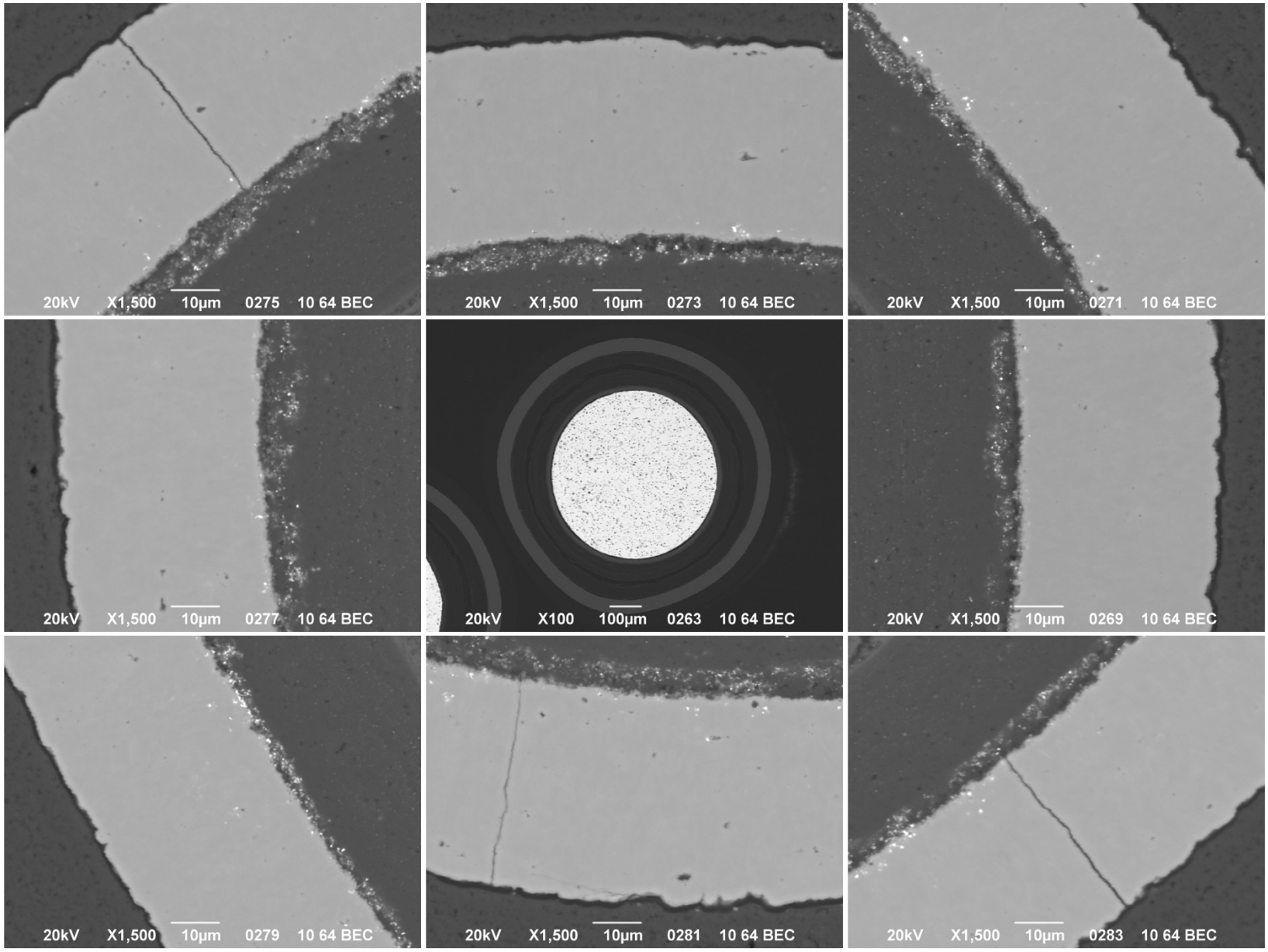

Appendix Figure D-60. 1,500× BEC micrographs of Particle 311-RS36.

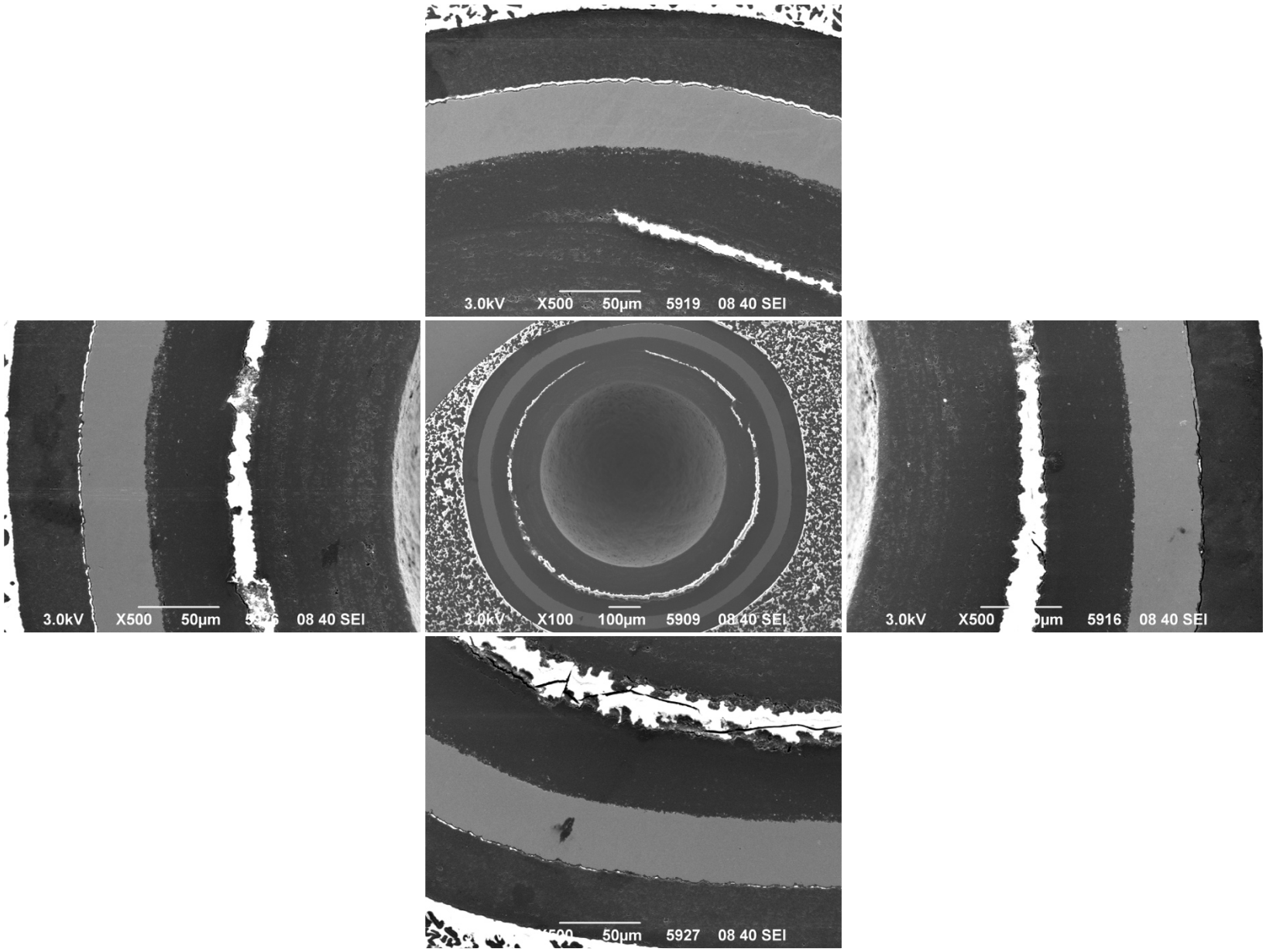

Appendix Figure D-61. 500× SEI micrographs of Particle 332-RS12.

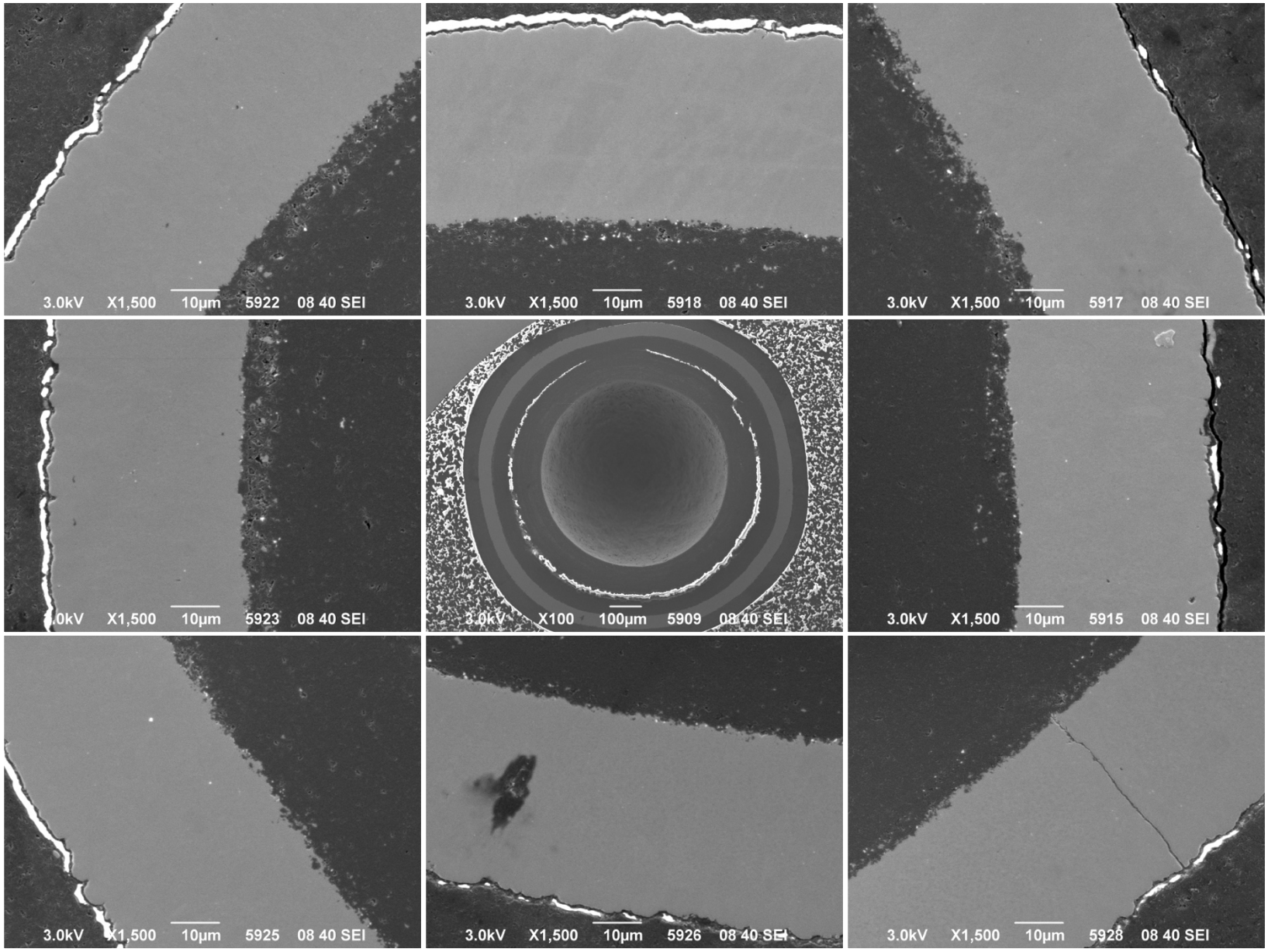

Appendix Figure D-62. 1,500× SEI micrographs of Particle 332-RS12.

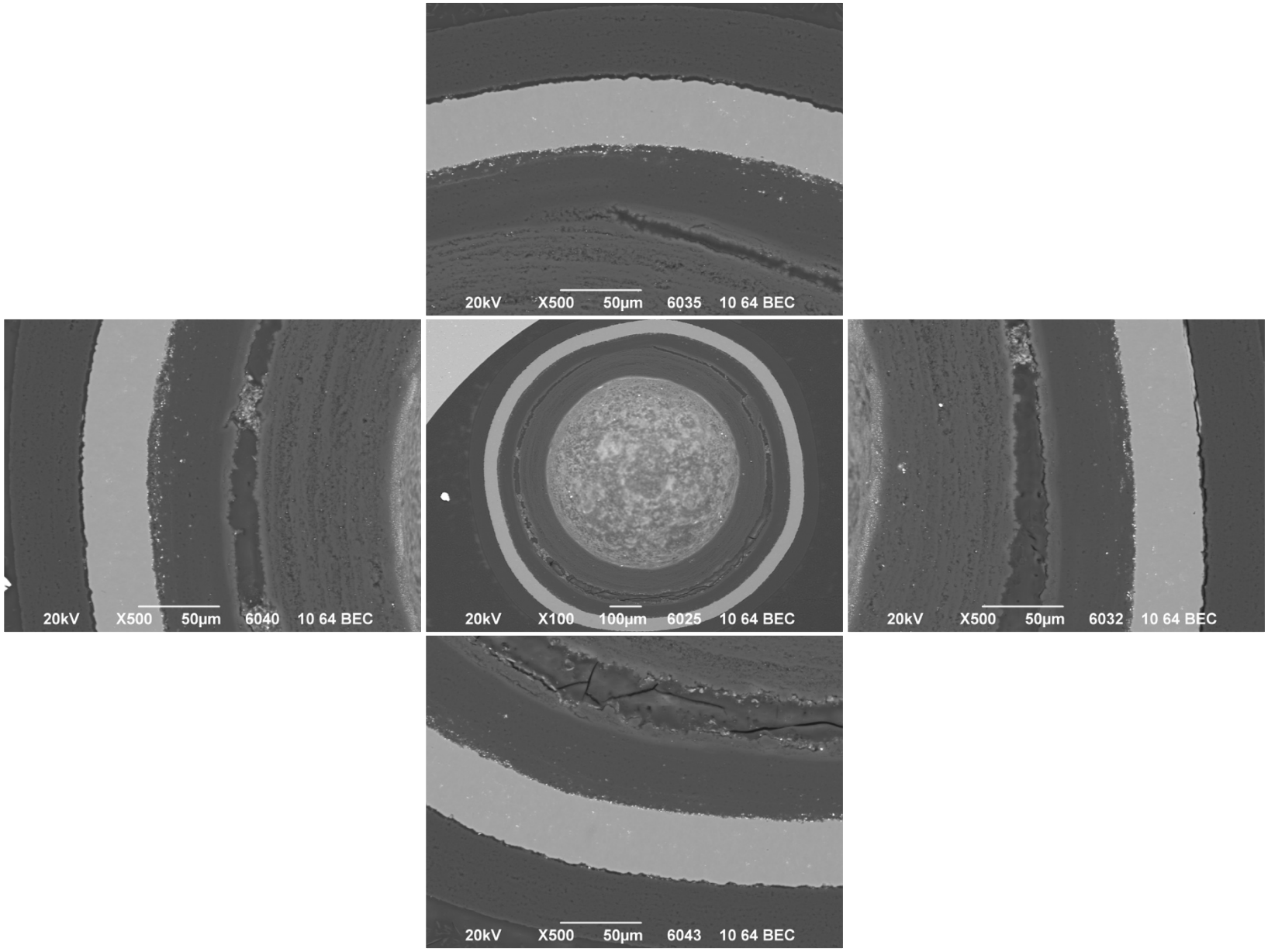

Appendix Figure D-63. 500× BEC micrographs of Particle 332-RS12.

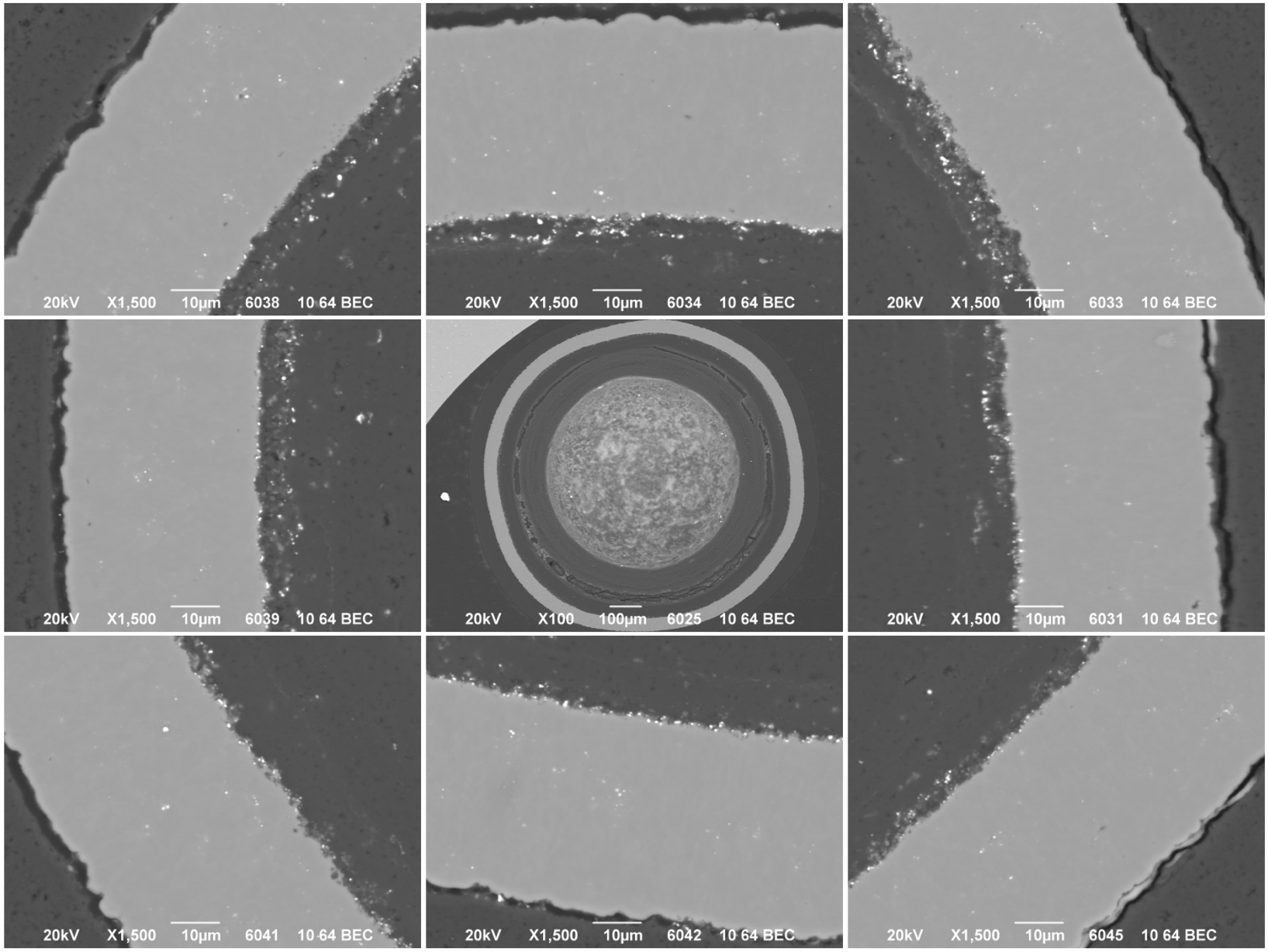

Appendix Figure D-64. 1,500× BEC micrographs of Particle 332-RS12.

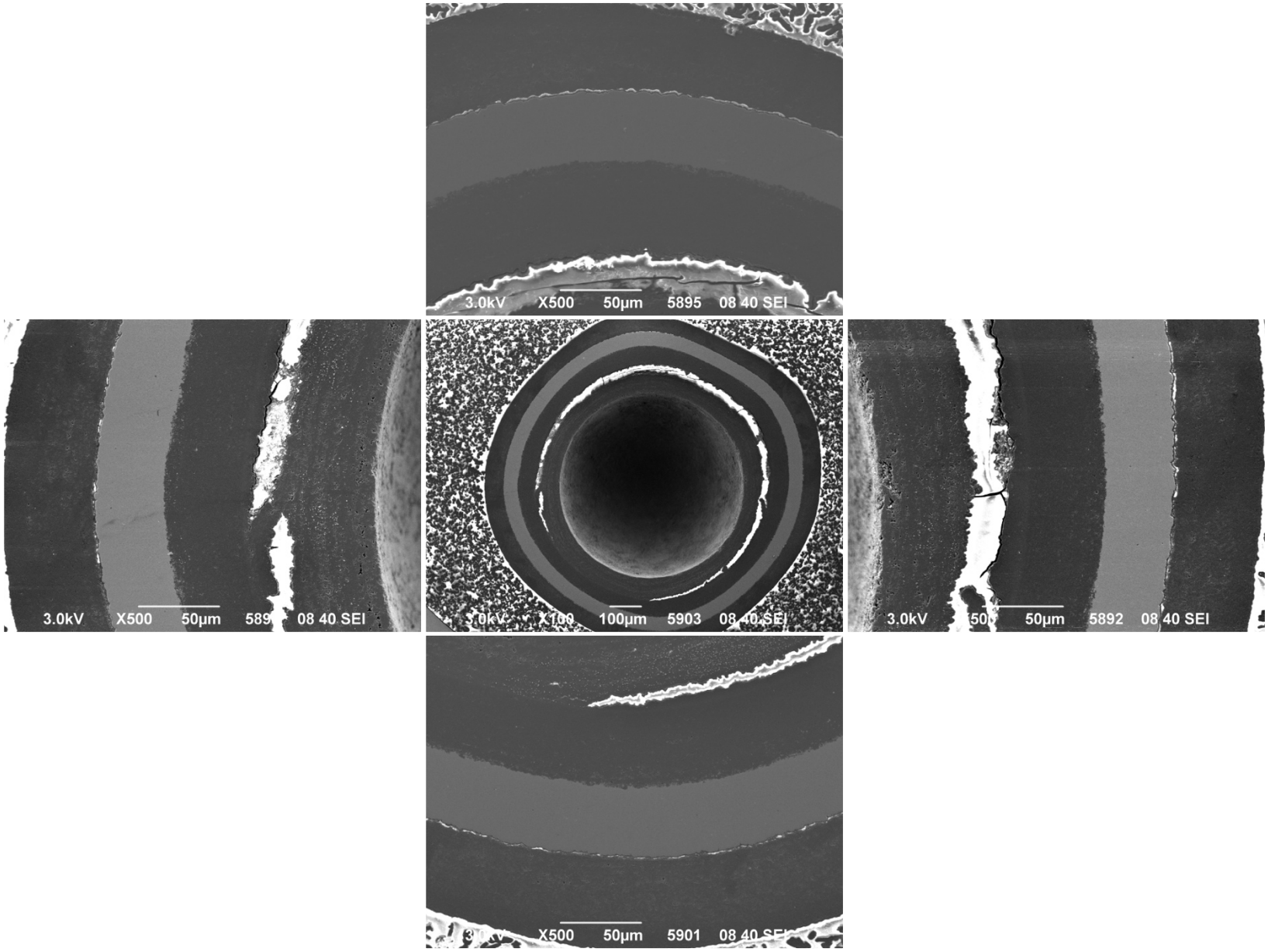

Appendix Figure D-65. 500× SEI micrographs of Particle 332-RS18.

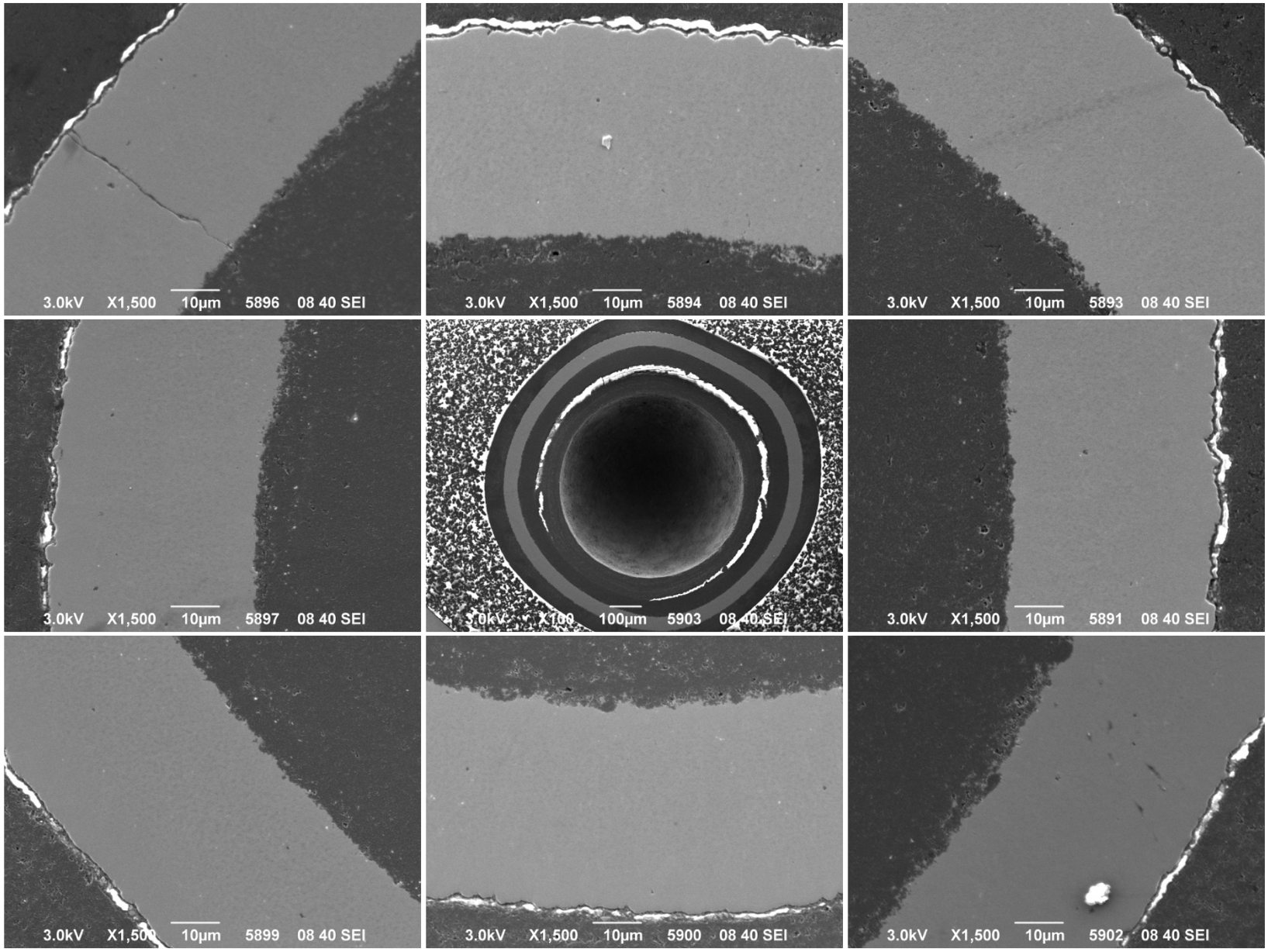

Appendix Figure D-66. 1,500× SEI micrographs of Particle 332-RS18.

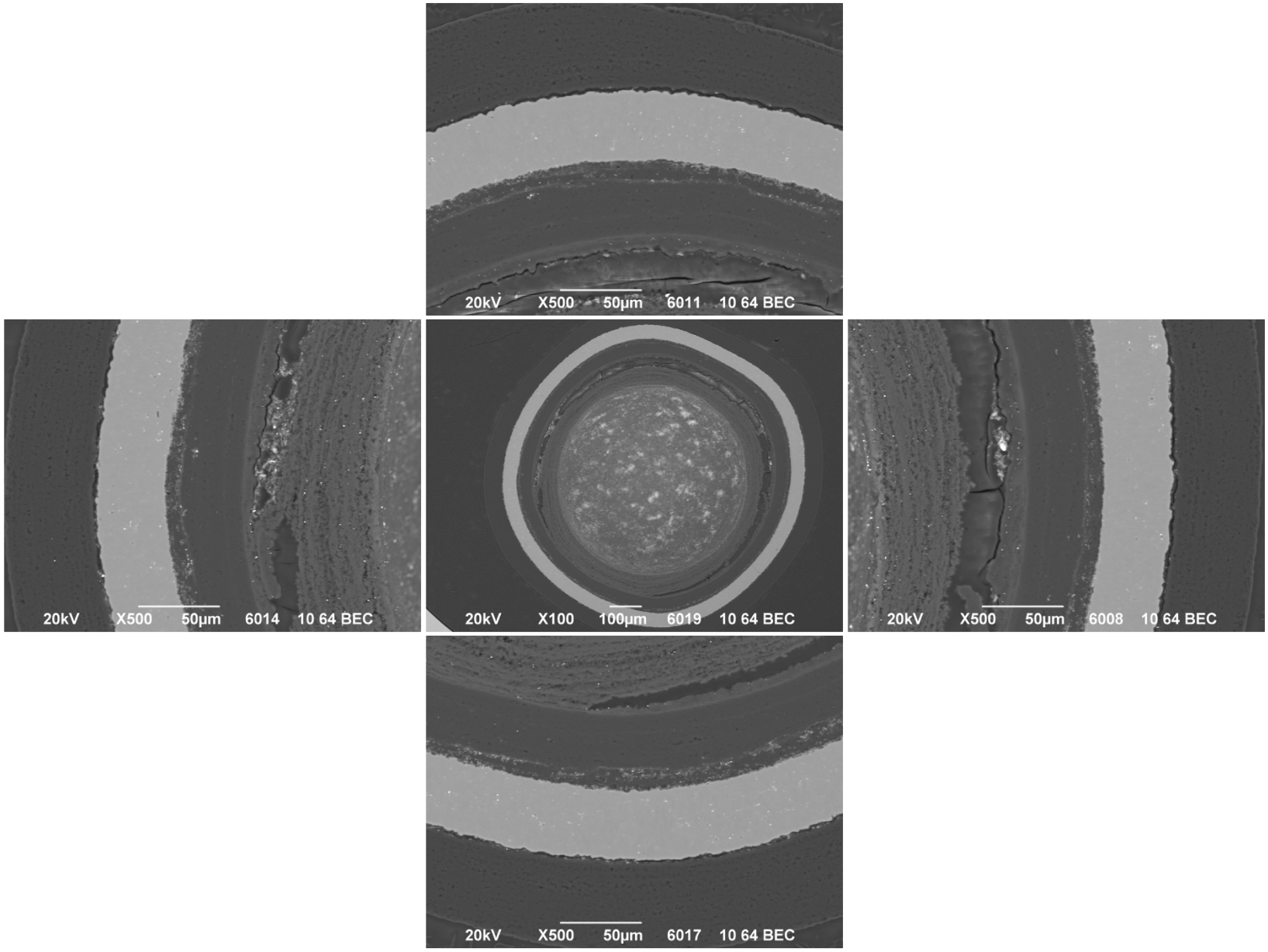

Appendix Figure D-67. 500× BEC micrographs of Particle 332-RS18.

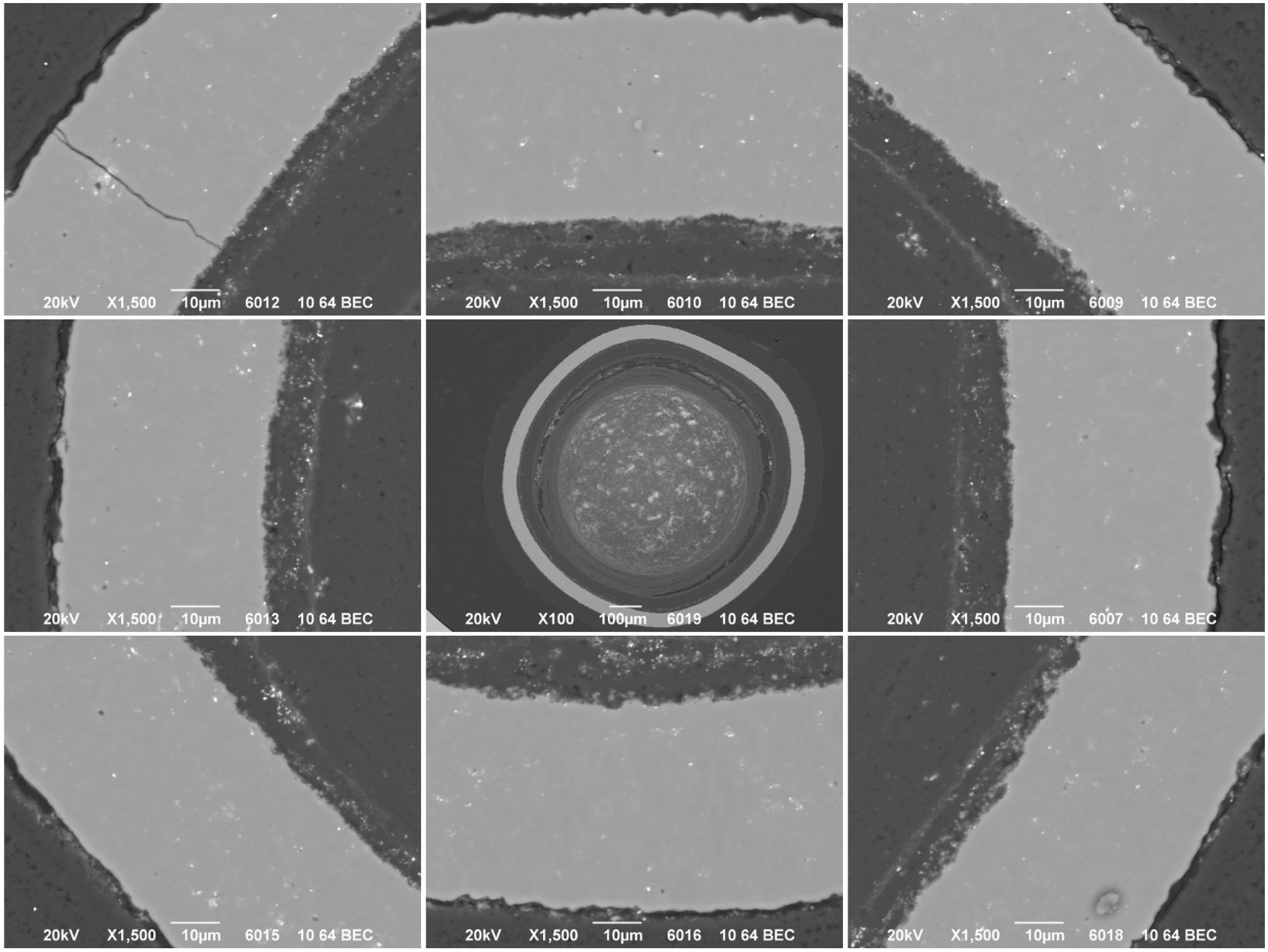

Appendix Figure D-68. 1,500× BEC micrographs of Particle 332-RS18.

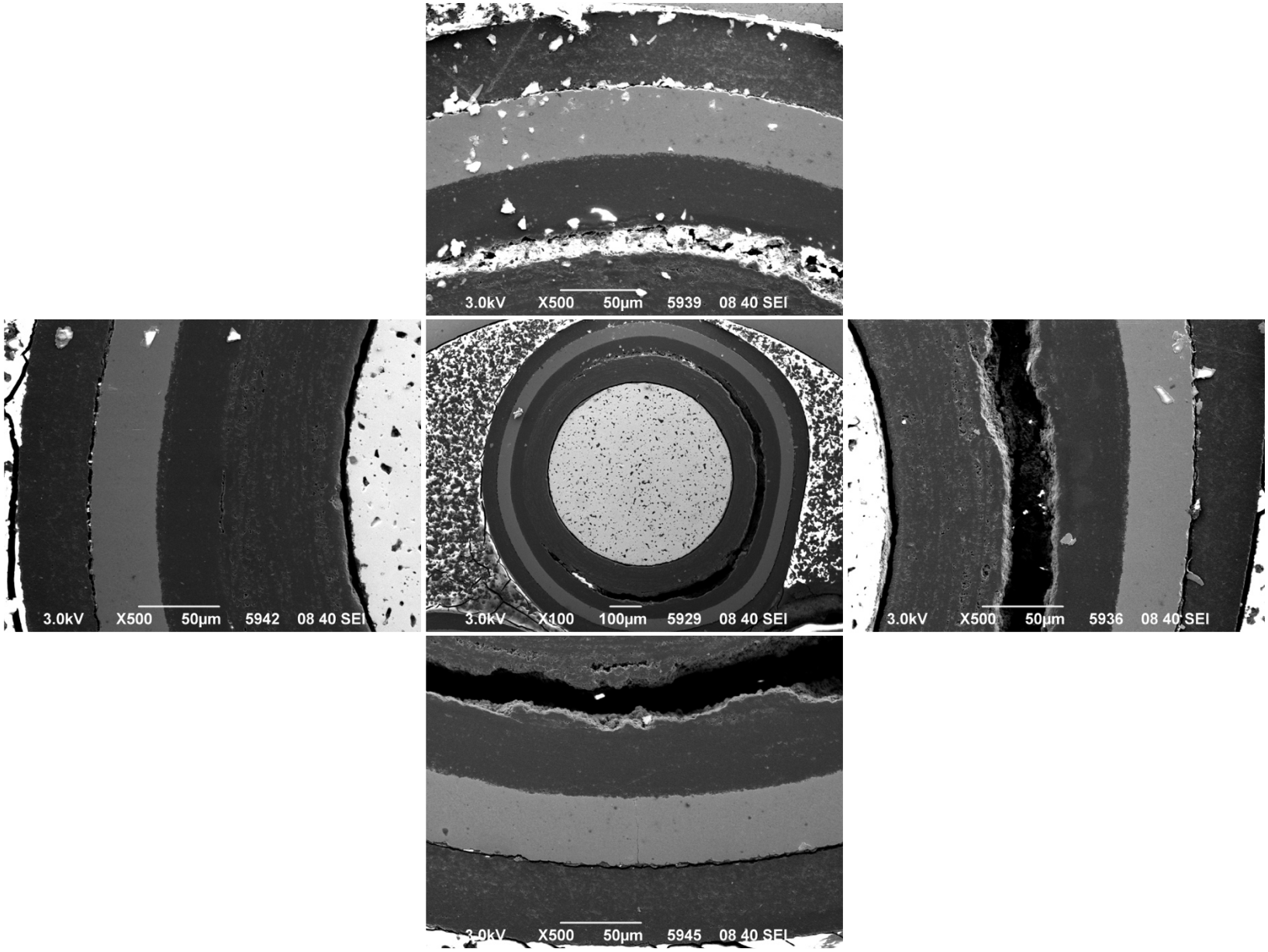

Appendix Figure D-69. 500× SEI micrographs of Particle 332-RS22.

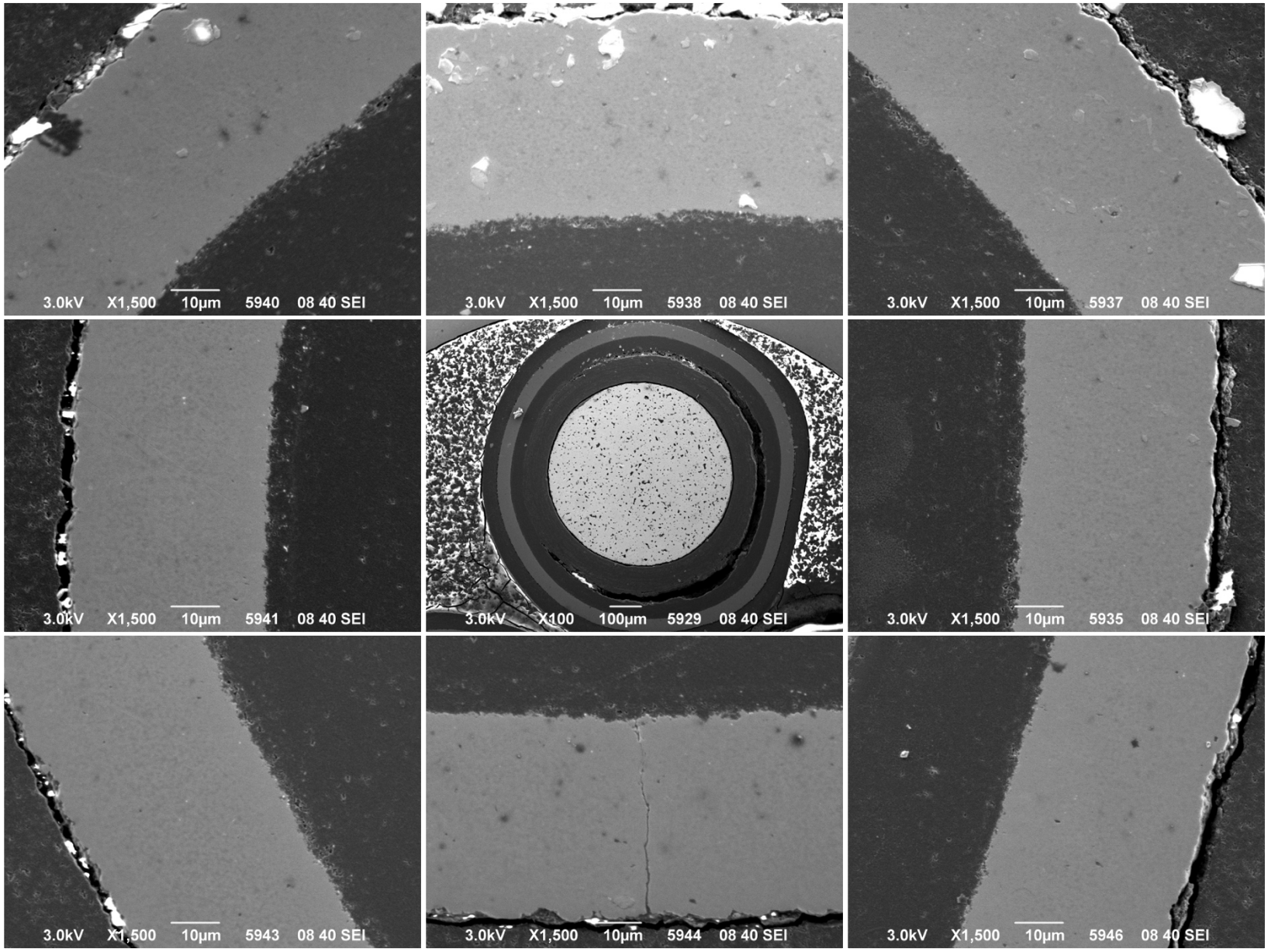

Appendix Figure D-70. 1,500× SEI micrographs of Particle 332-RS22.

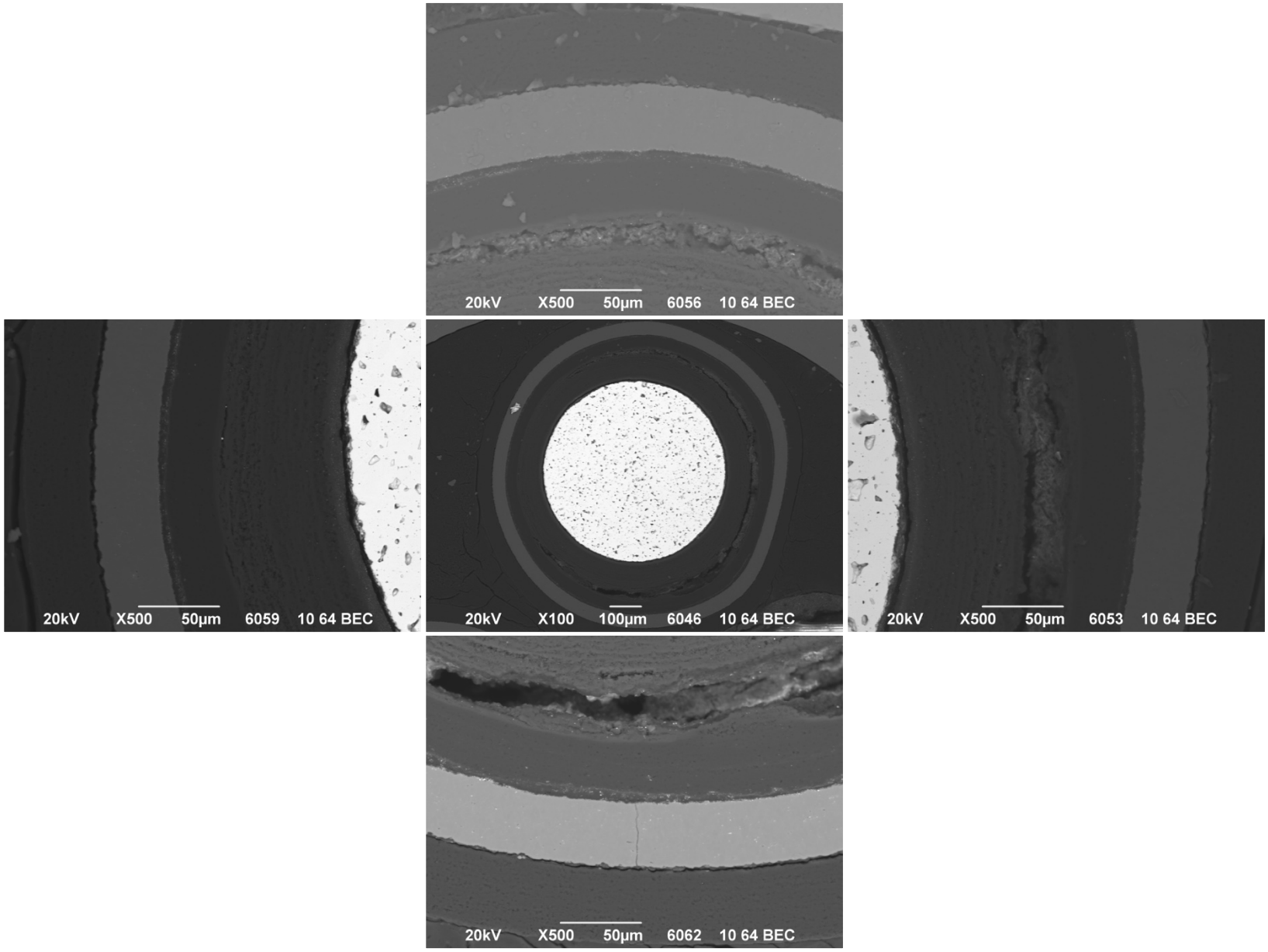

Appendix Figure D-71. 500× BEC micrographs of Particle 332-RS22.

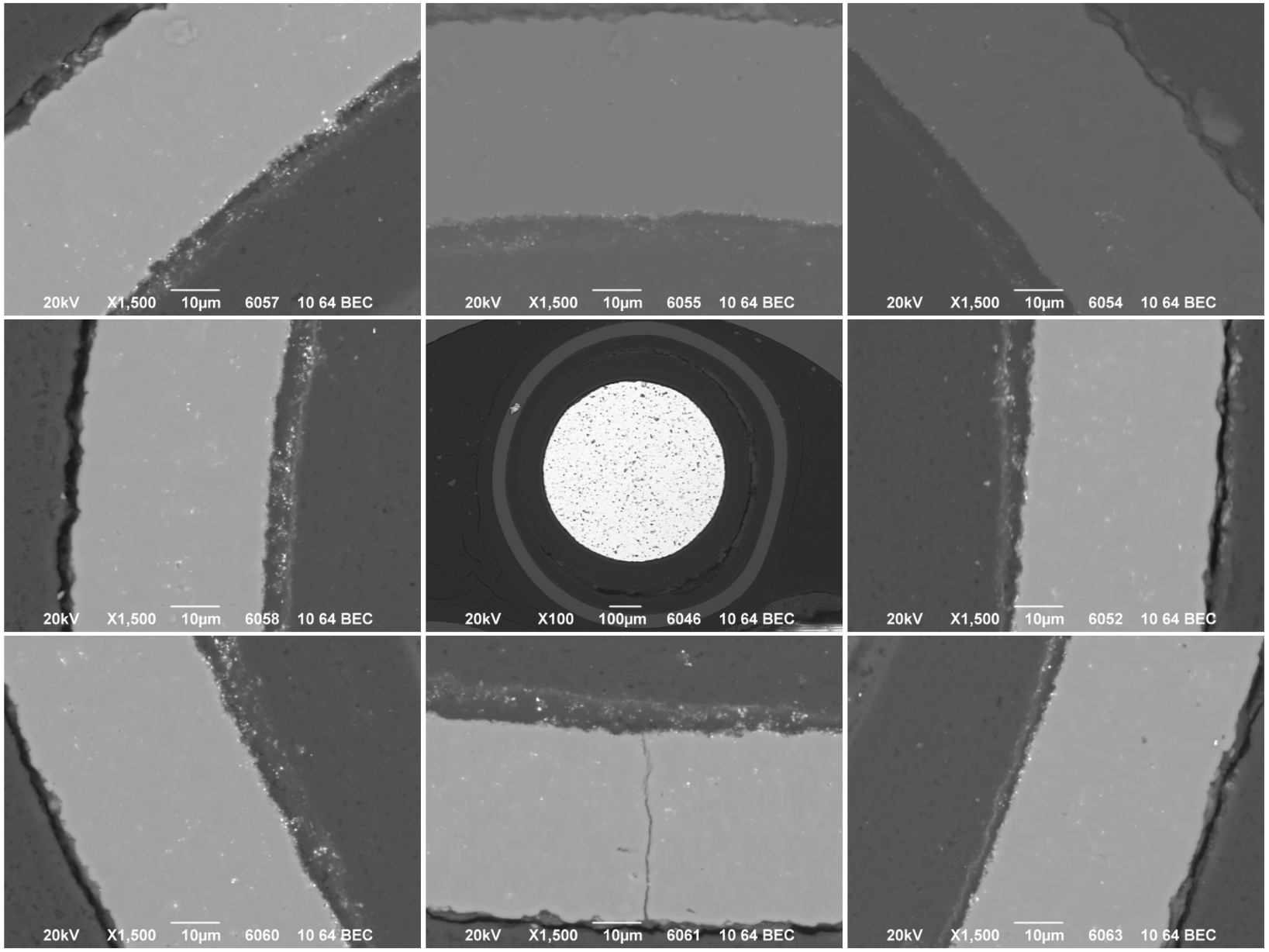

Appendix Figure D-72. 1,500× BEC micrographs of Particle 332-RS22.

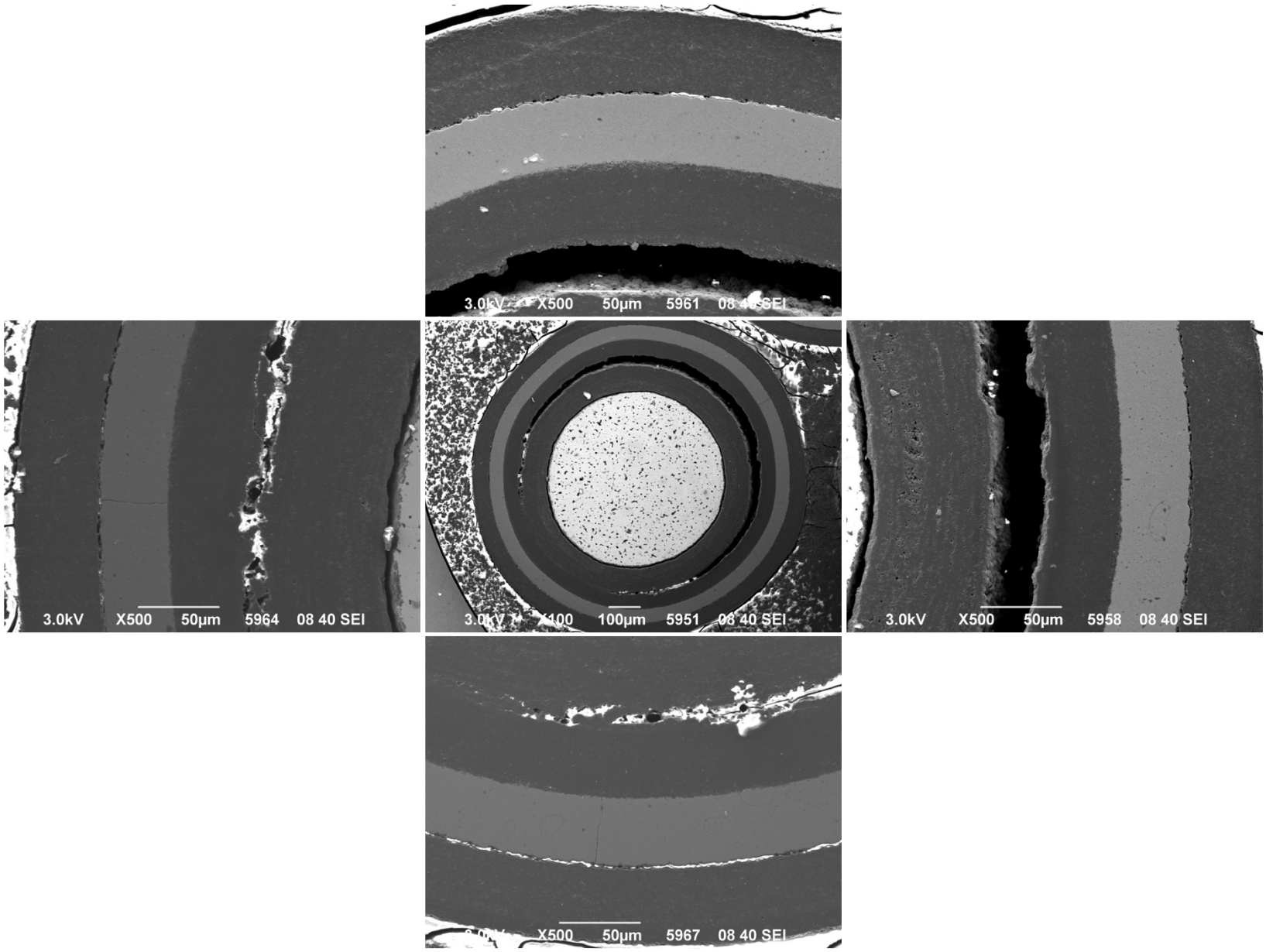

Appendix Figure D-73. 500× SEI micrographs of Particle 332-RS43.

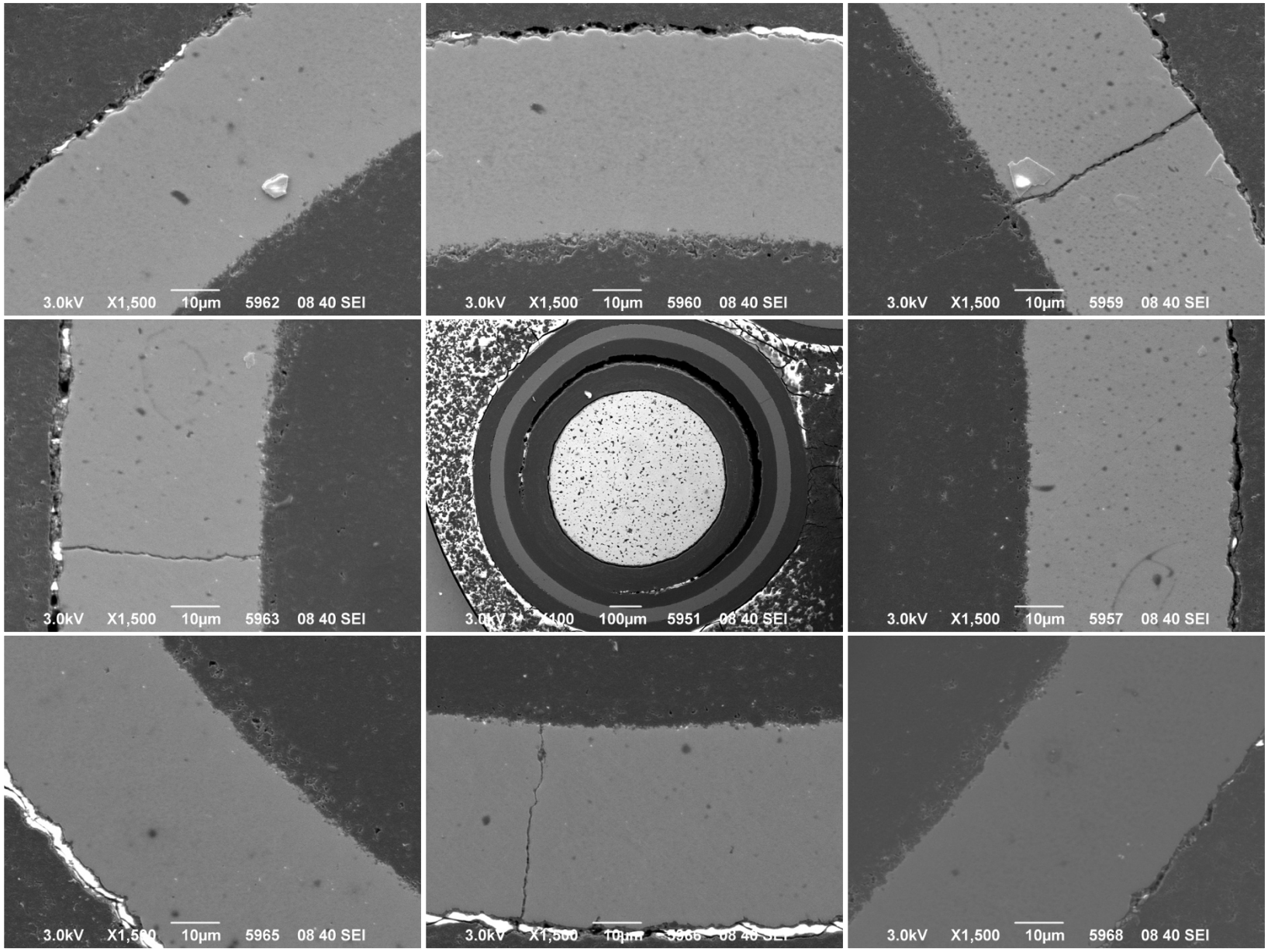

Appendix Figure D-74. 1,500× SEI micrographs of Particle 332-RS43.

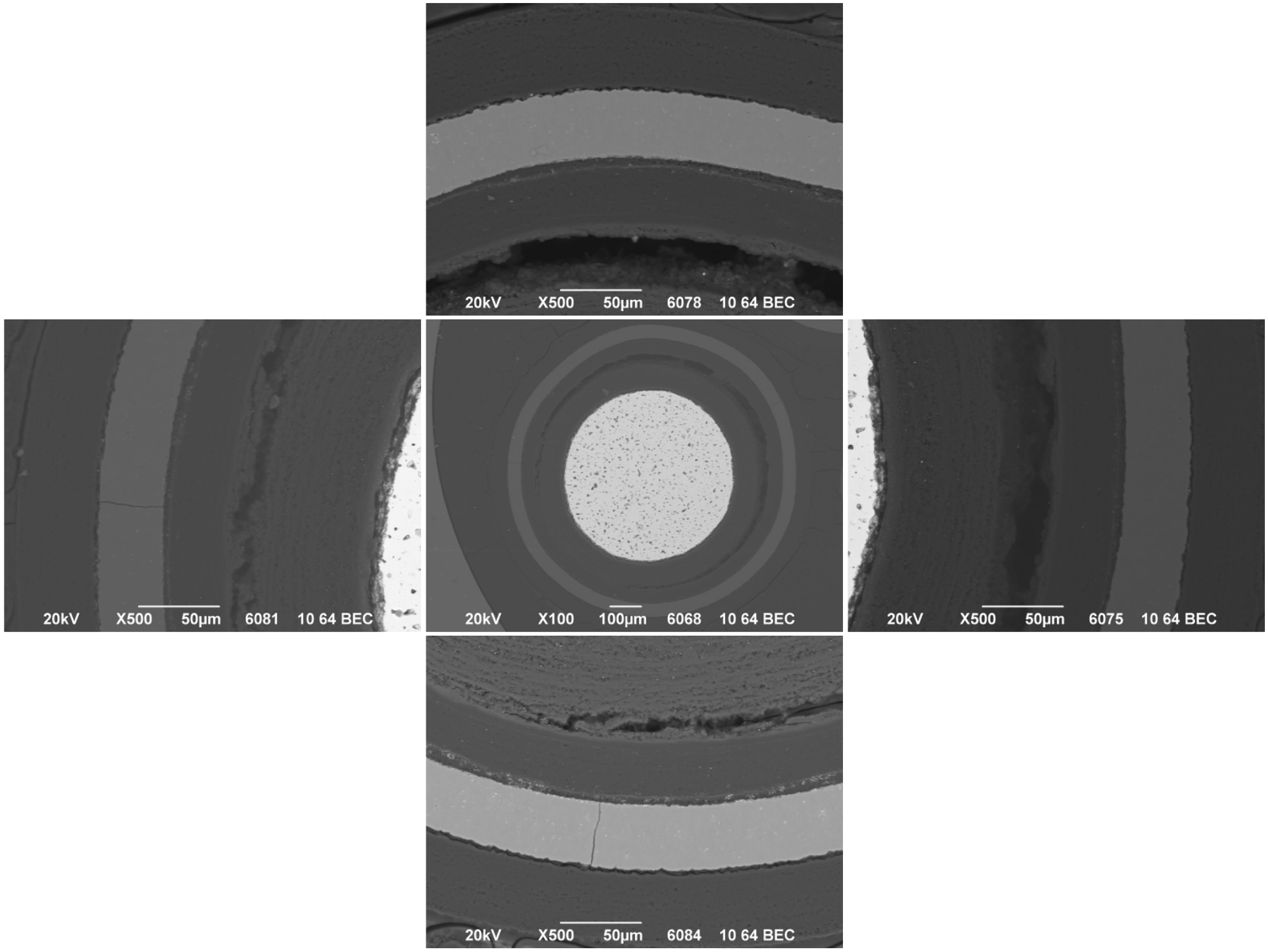

Appendix Figure D-75. 500× BEC micrographs of Particle 332-RS43.

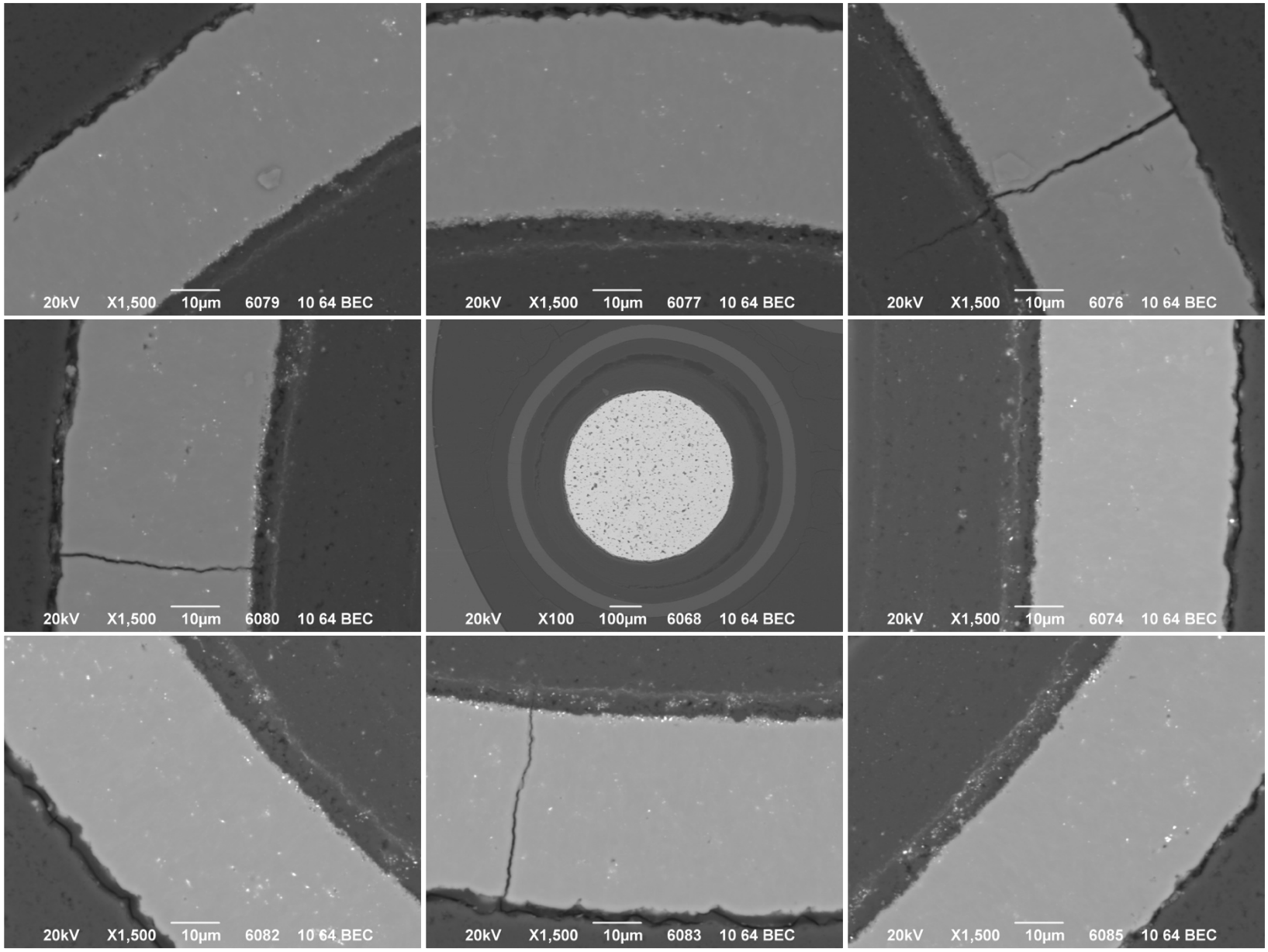

Appendix Figure D-76. 1,500× BEC micrographs of Particle 332-RS43.

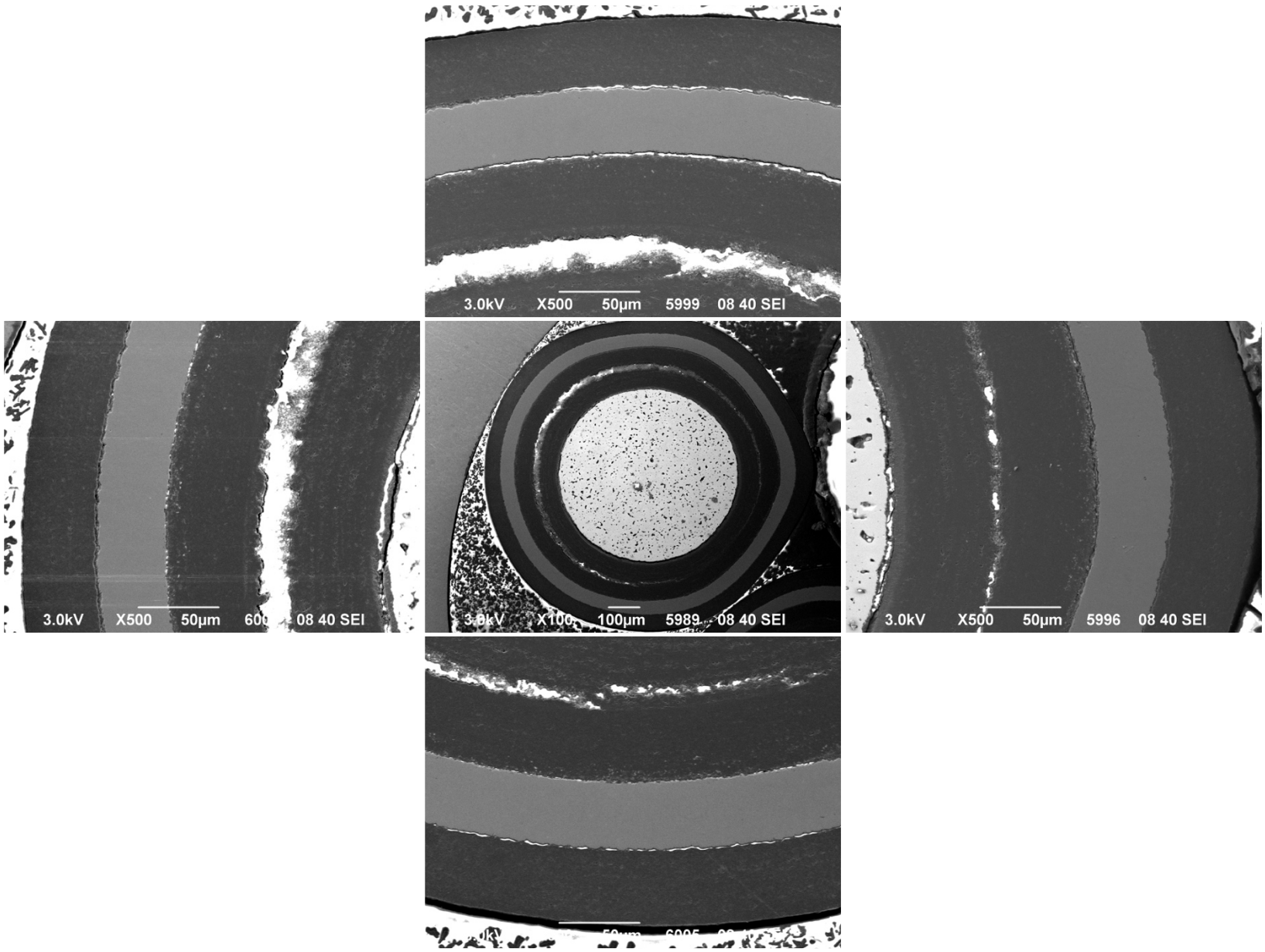

Appendix Figure D-77. 500× SEI micrographs of Particle 332-RS26.

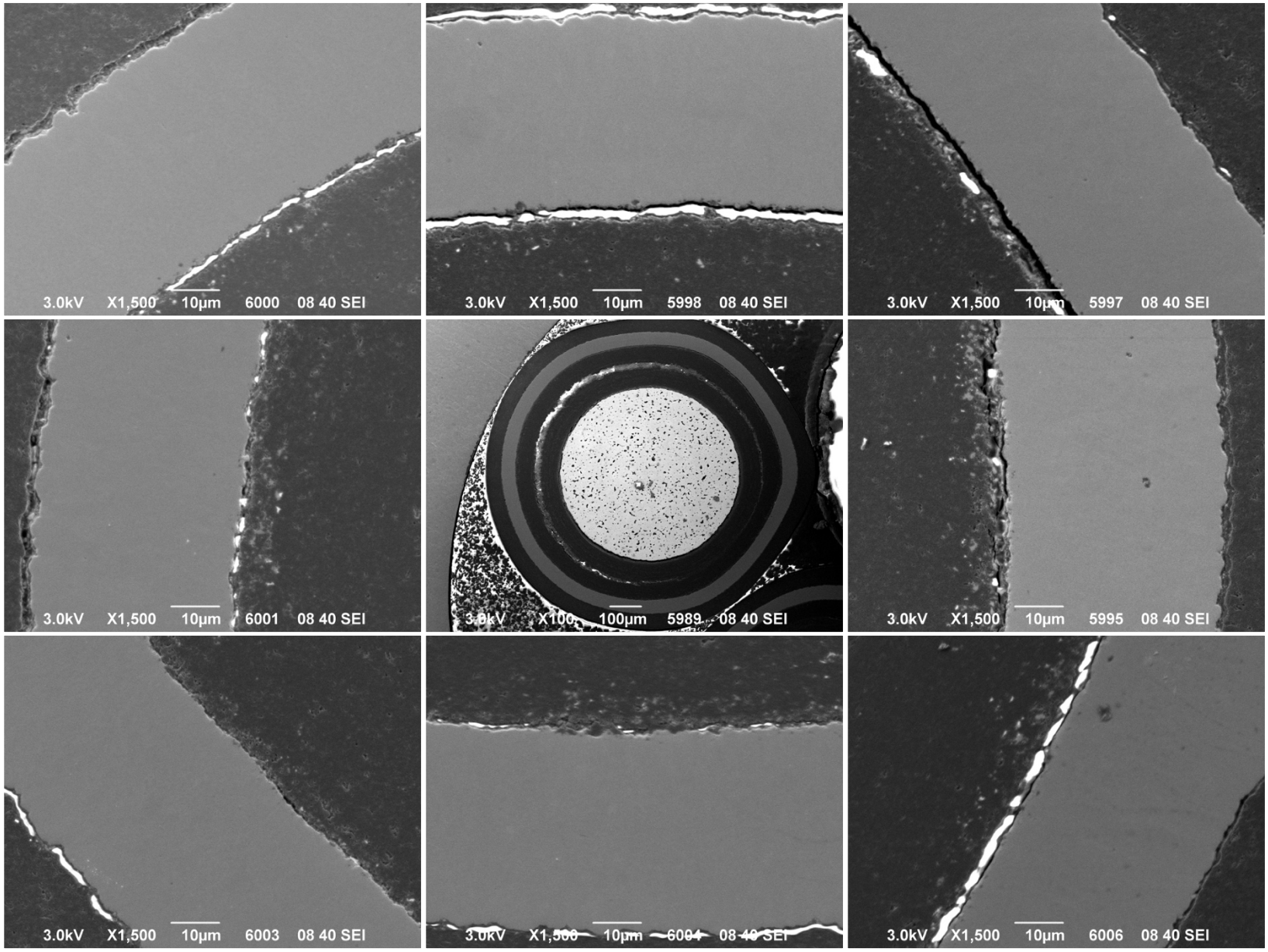

Appendix Figure D-78. 1,500× SEI micrographs of Particle 332-RS26.

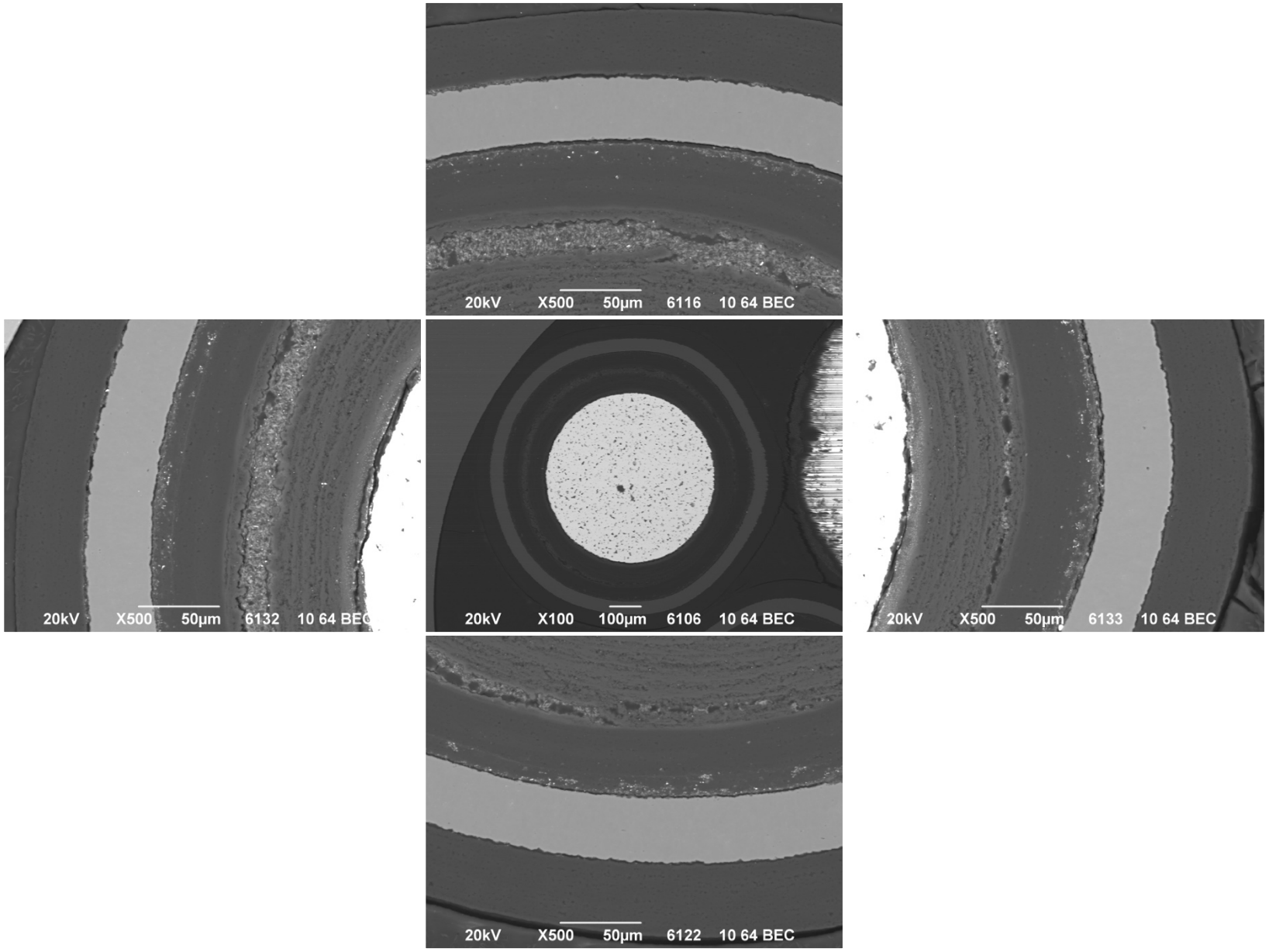

Appendix Figure D-79. 500× BEC micrographs of Particle 332-RS26.

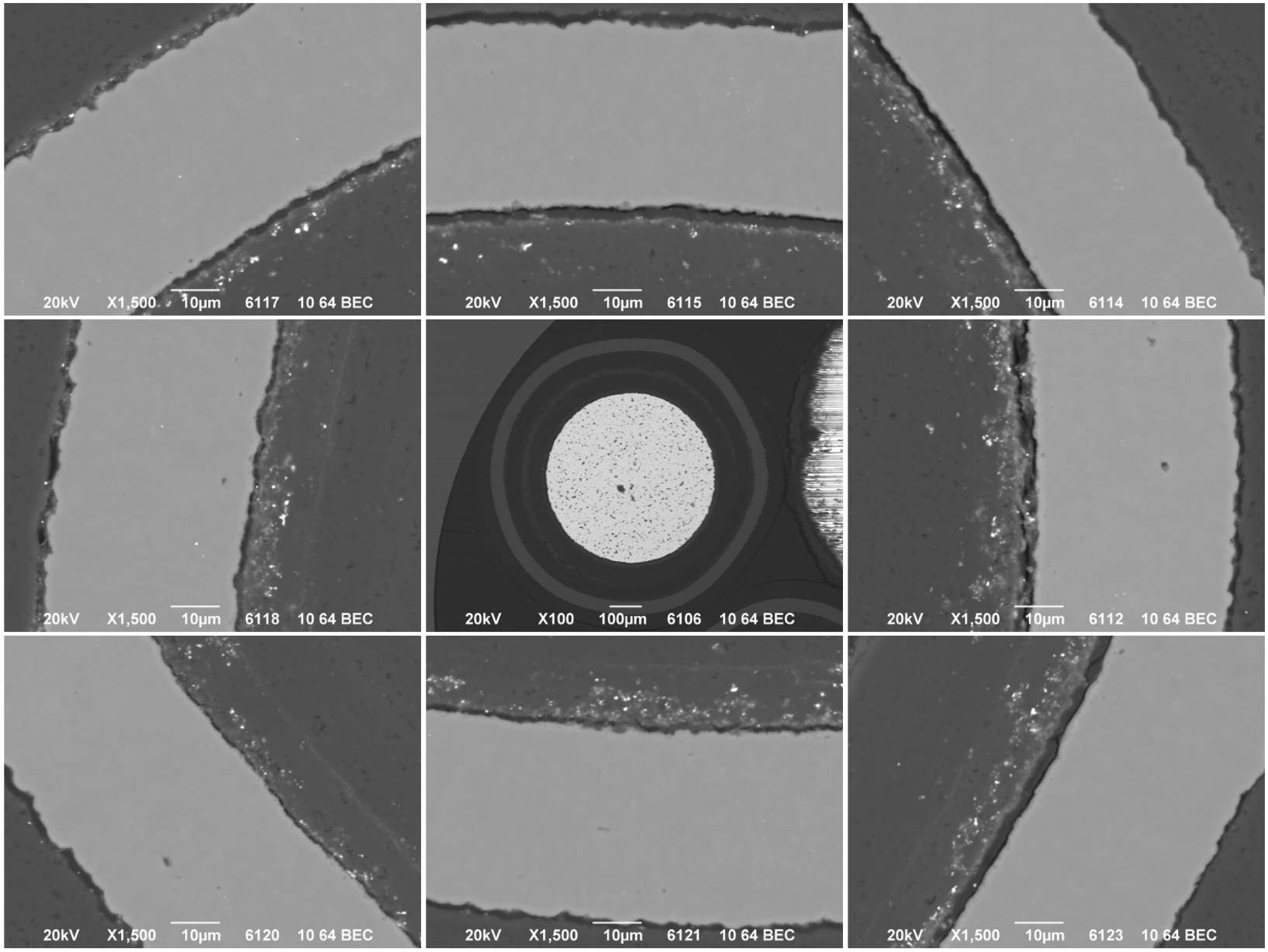

Appendix Figure D-80. 1,500× BEC micrographs of Particle 332-RS26.

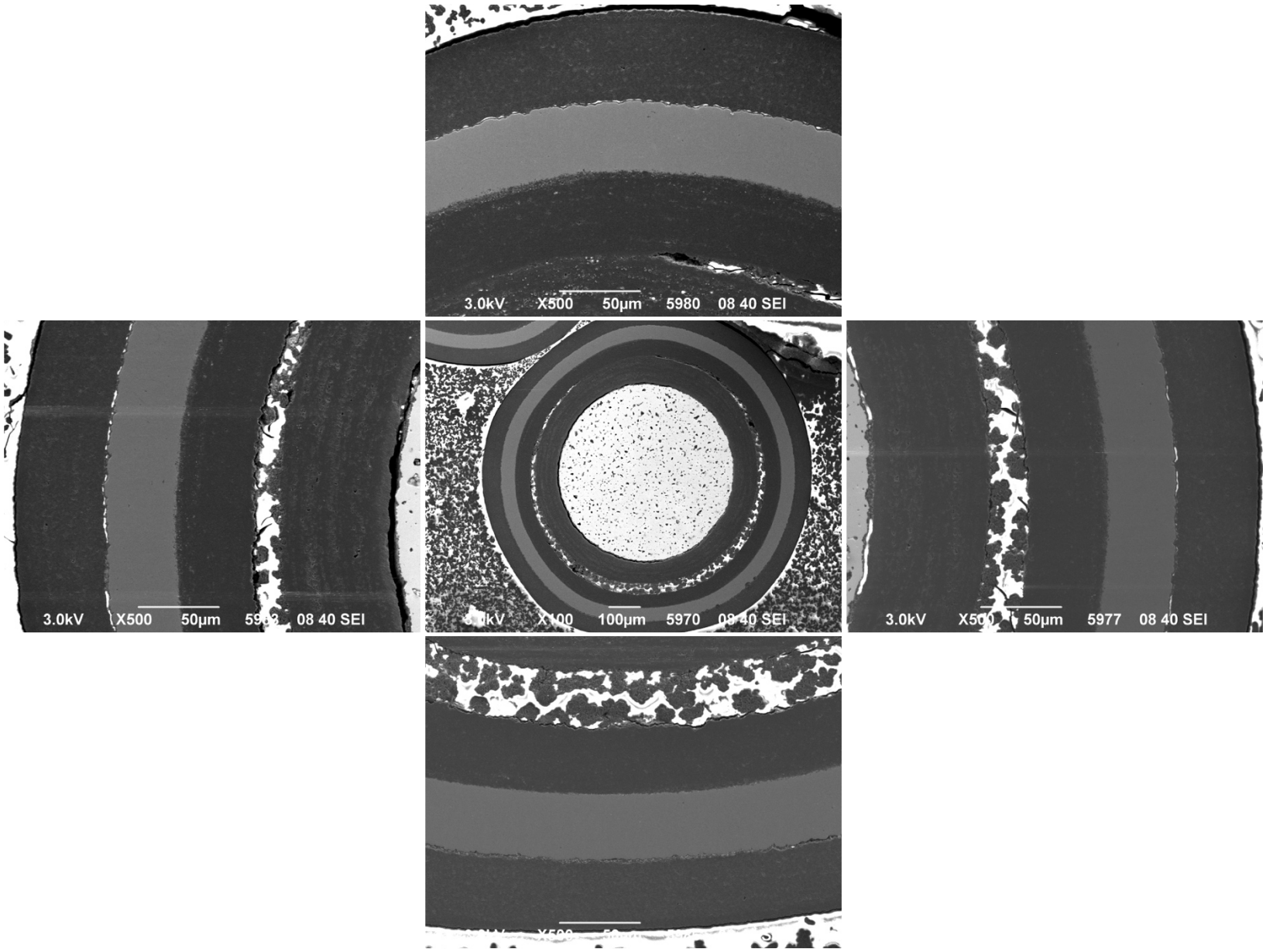

Appendix Figure D-81. 500× SEI micrographs of Particle 332-RS31.

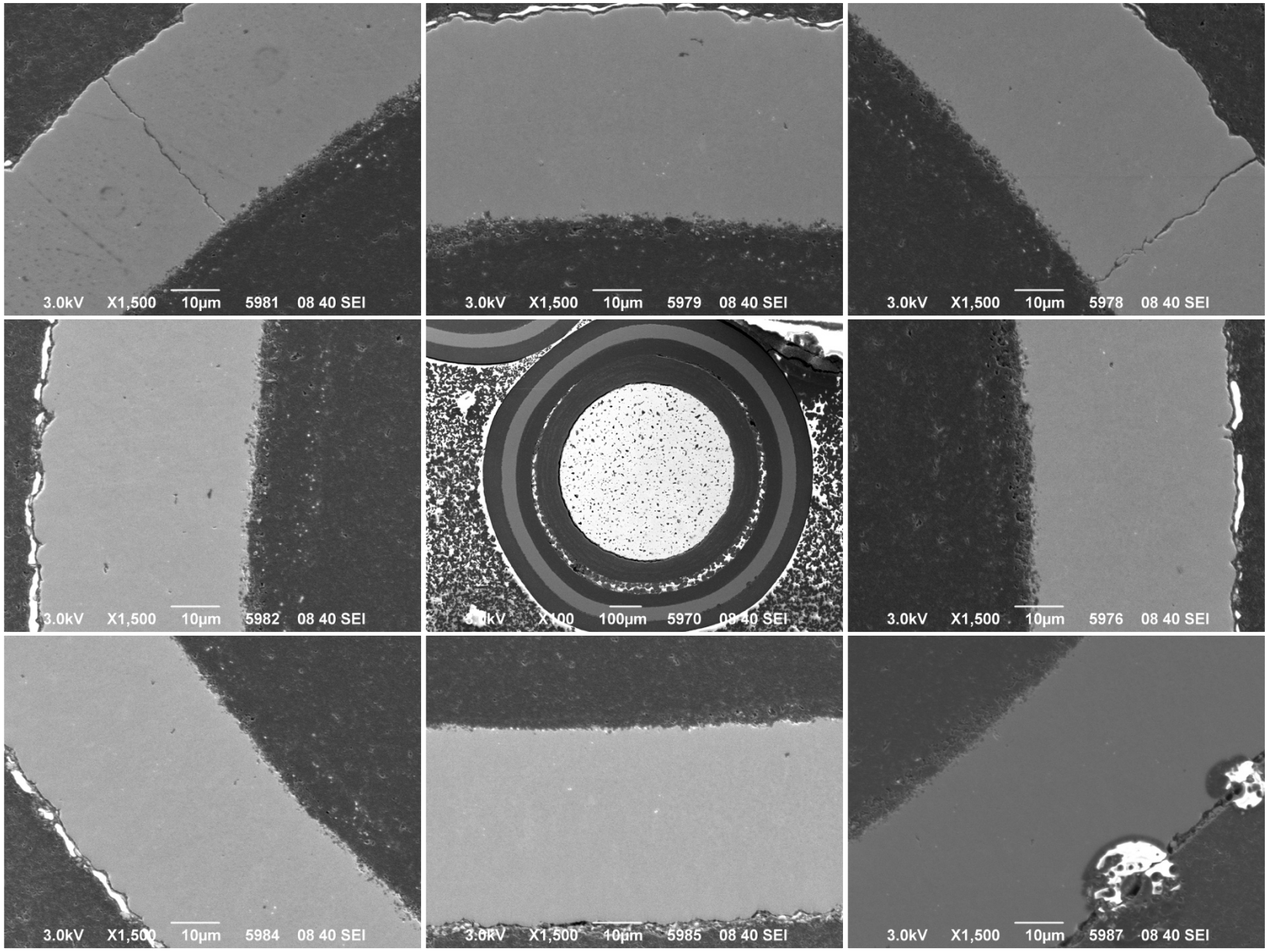

Appendix Figure D-82. 1,500× SEI micrographs of Particle 332-RS31.

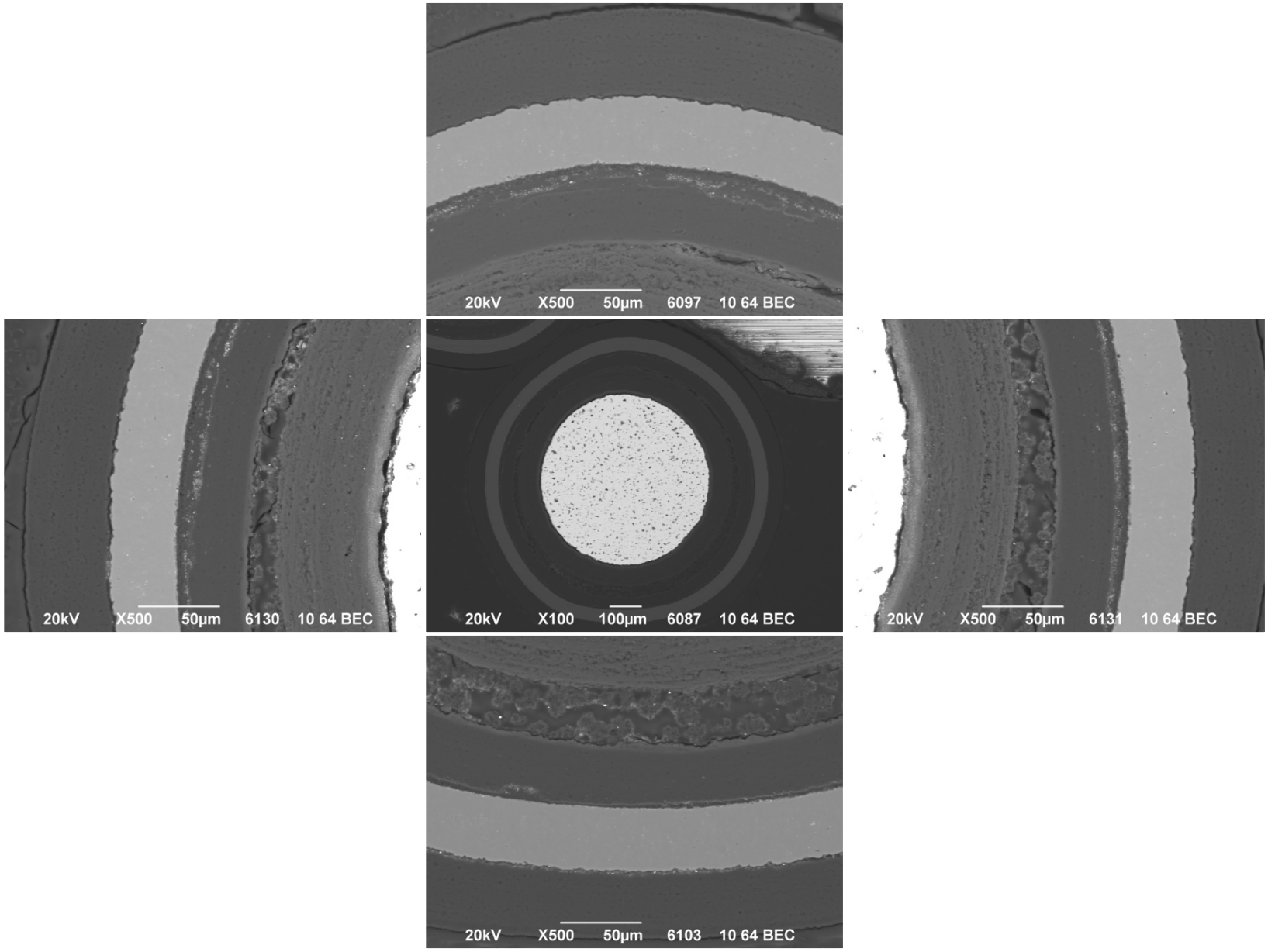

Appendix Figure D-83. 500× BEC micrographs of Particle 332-RS31.

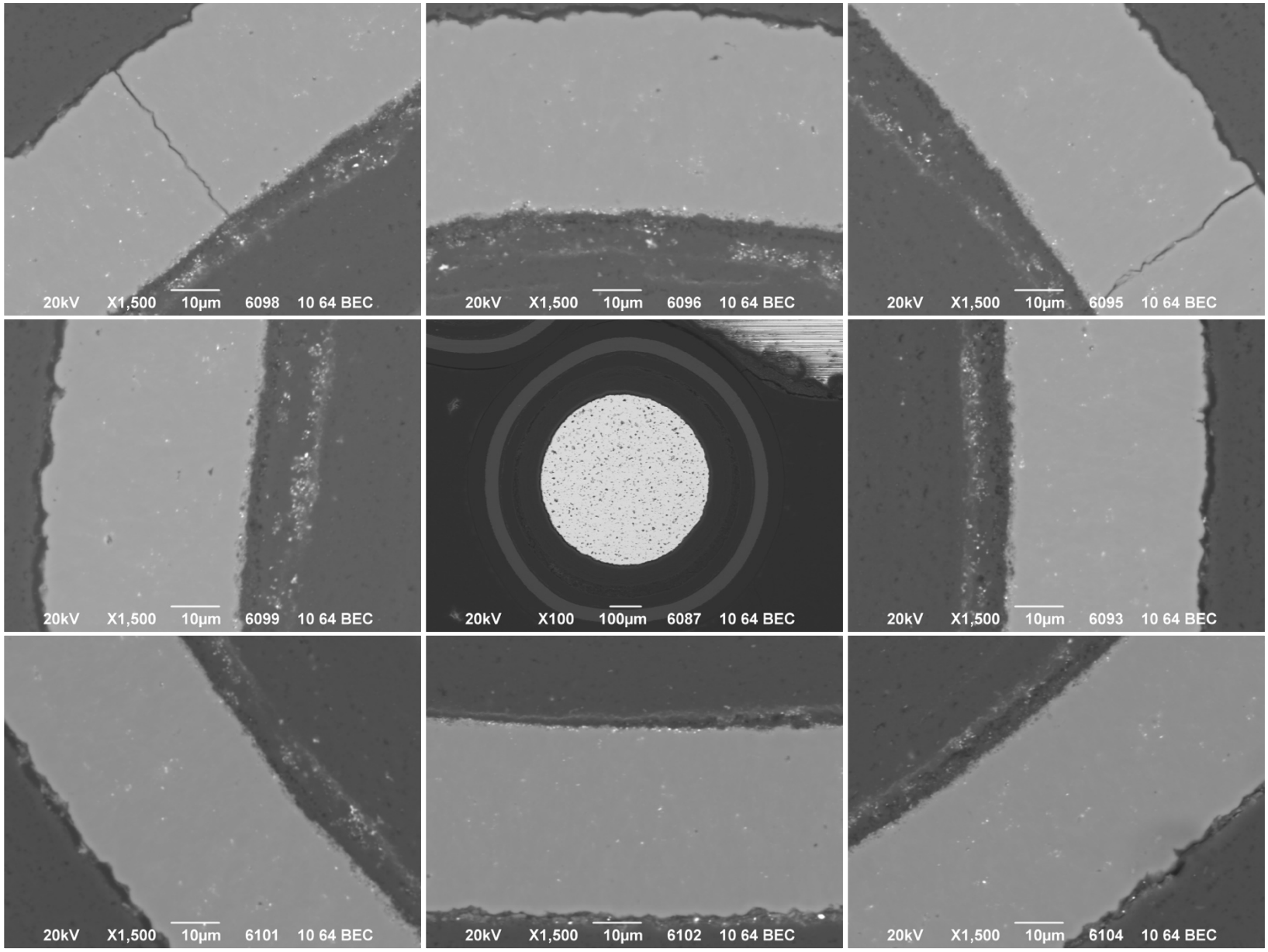

Appendix Figure D-84. 1,500× BEC micrographs of Particle 332-RS31.

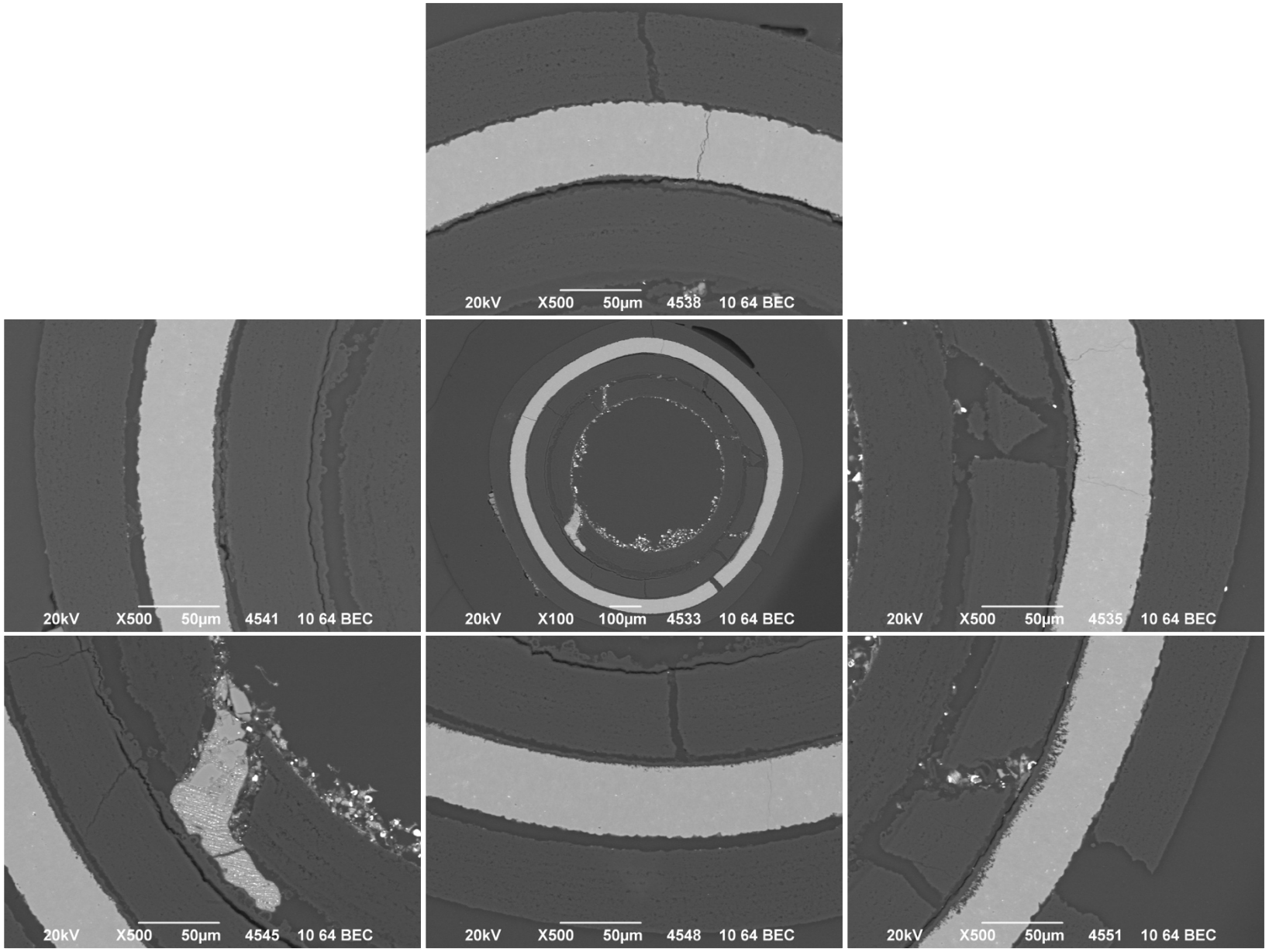

Appendix Figure D-85. 500× BEC micrographs of Particle 332-SP01.

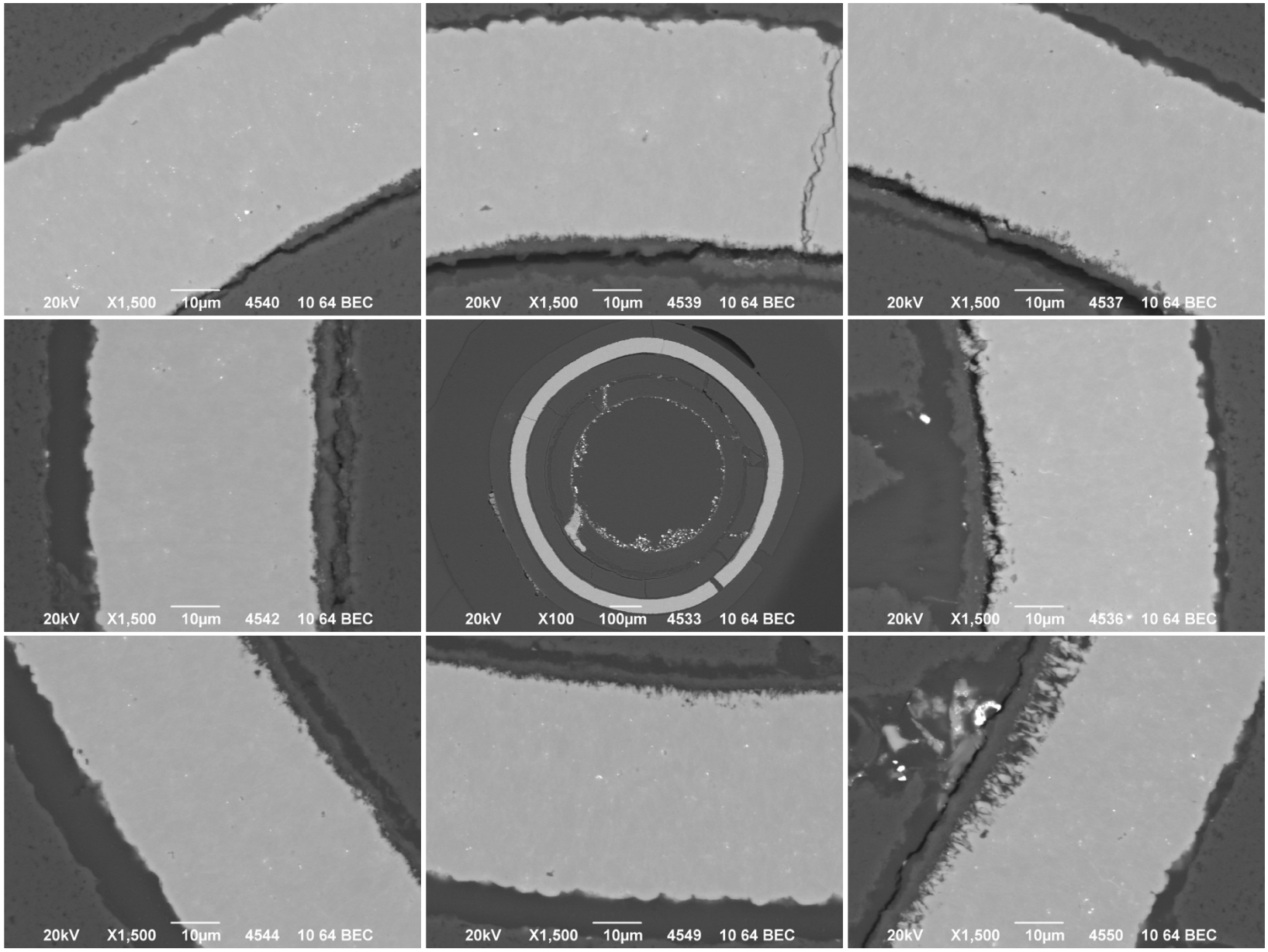

Appendix Figure D-86. 1,500× BEC micrographs of Particle 332-SP01.

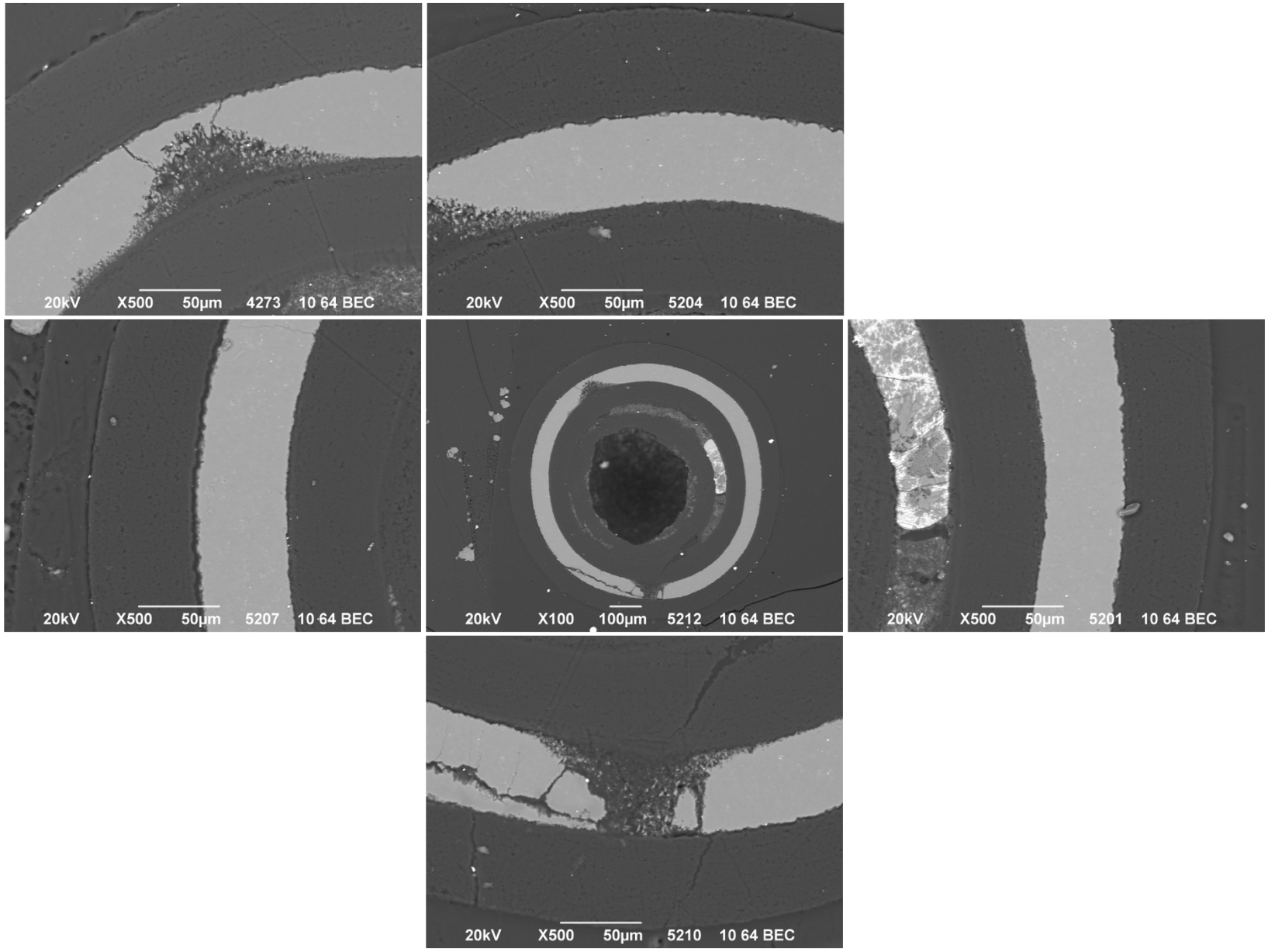

Appendix Figure D-87. 500× BEC micrographs of Particle 332-SP02.

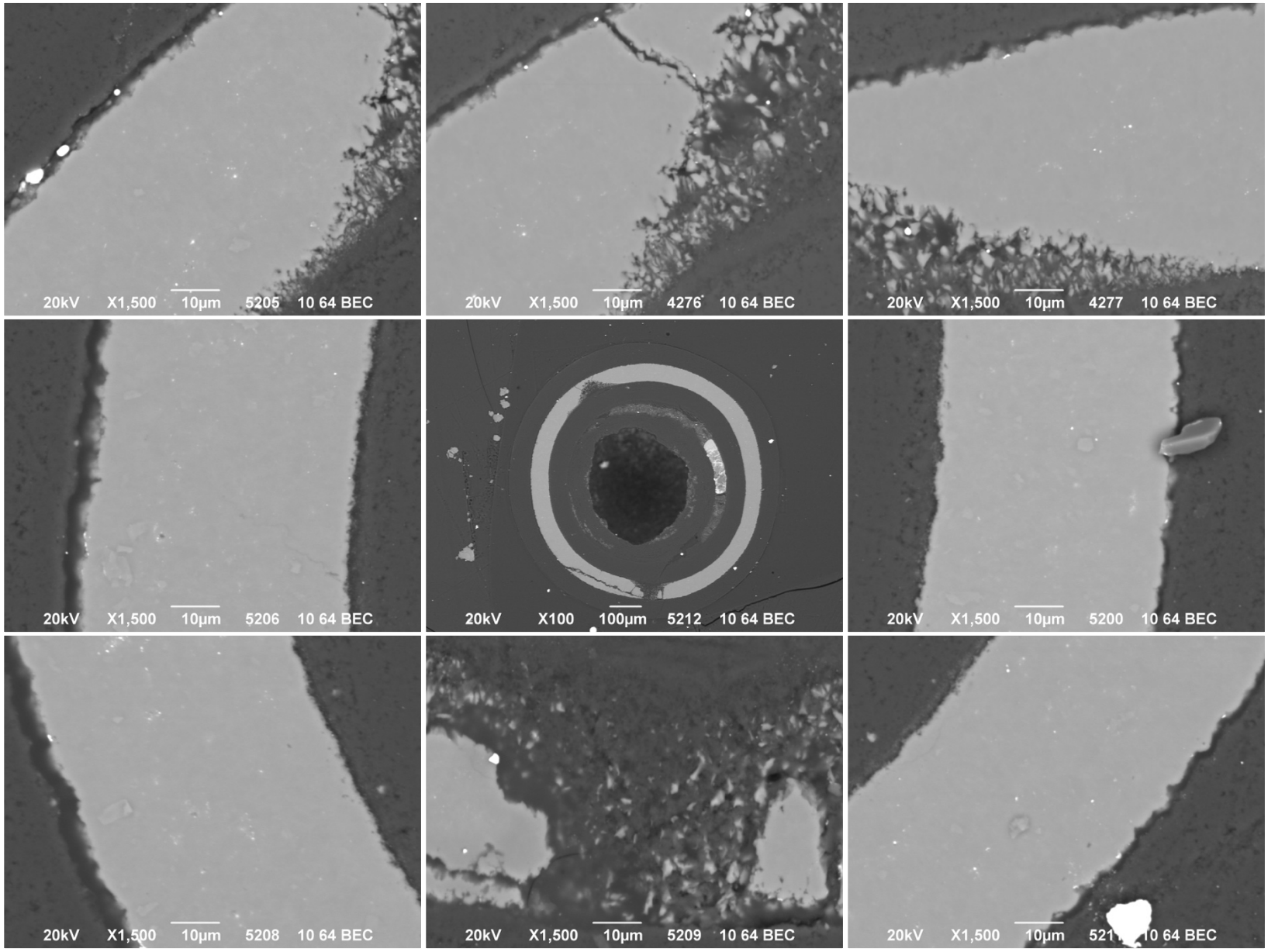

Appendix Figure D-88. 1,500× BEC micrographs of Particle 332-SP02.

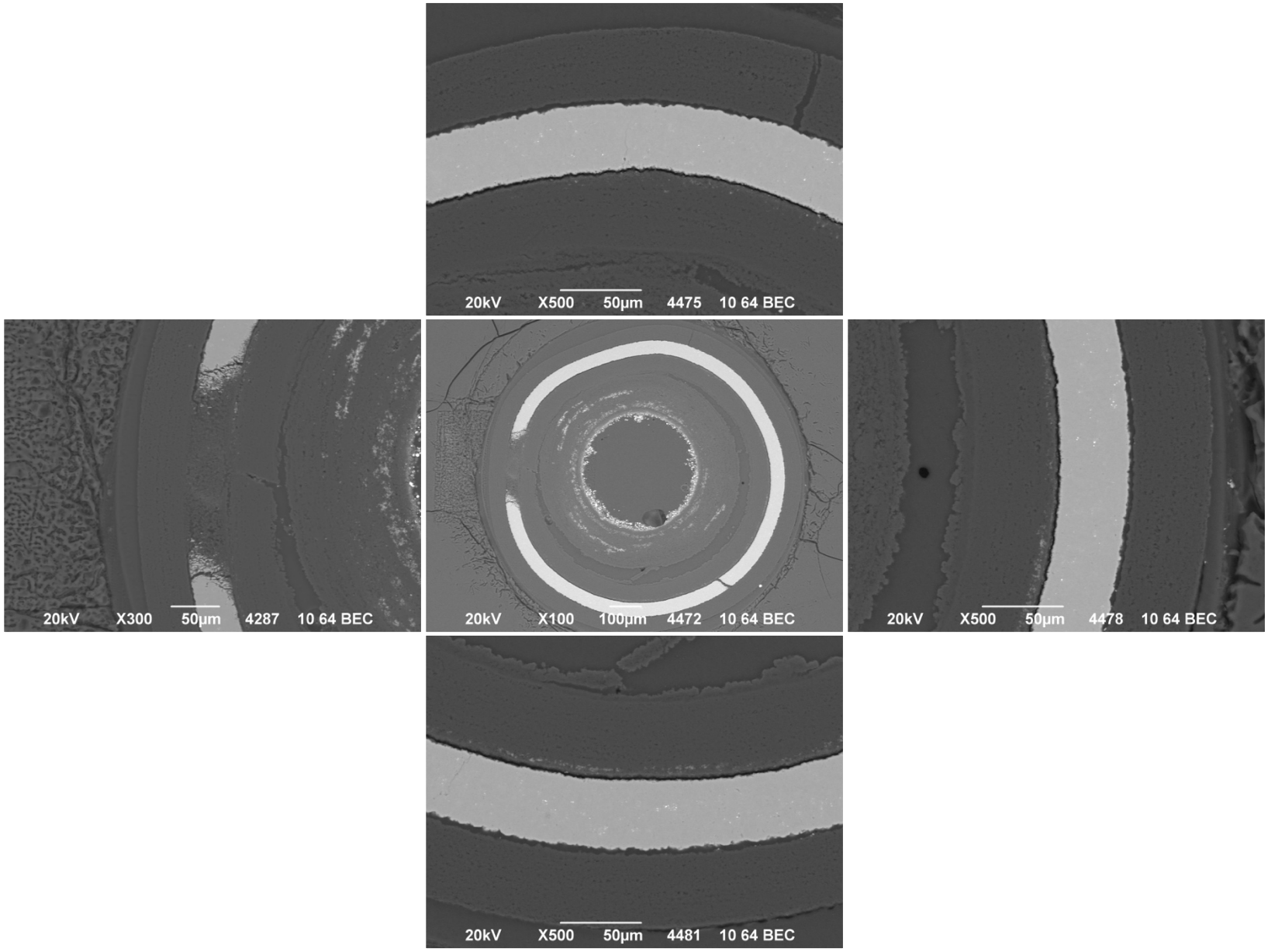

Appendix Figure D-89. 500× BEC micrographs of Particle 332-SP03.

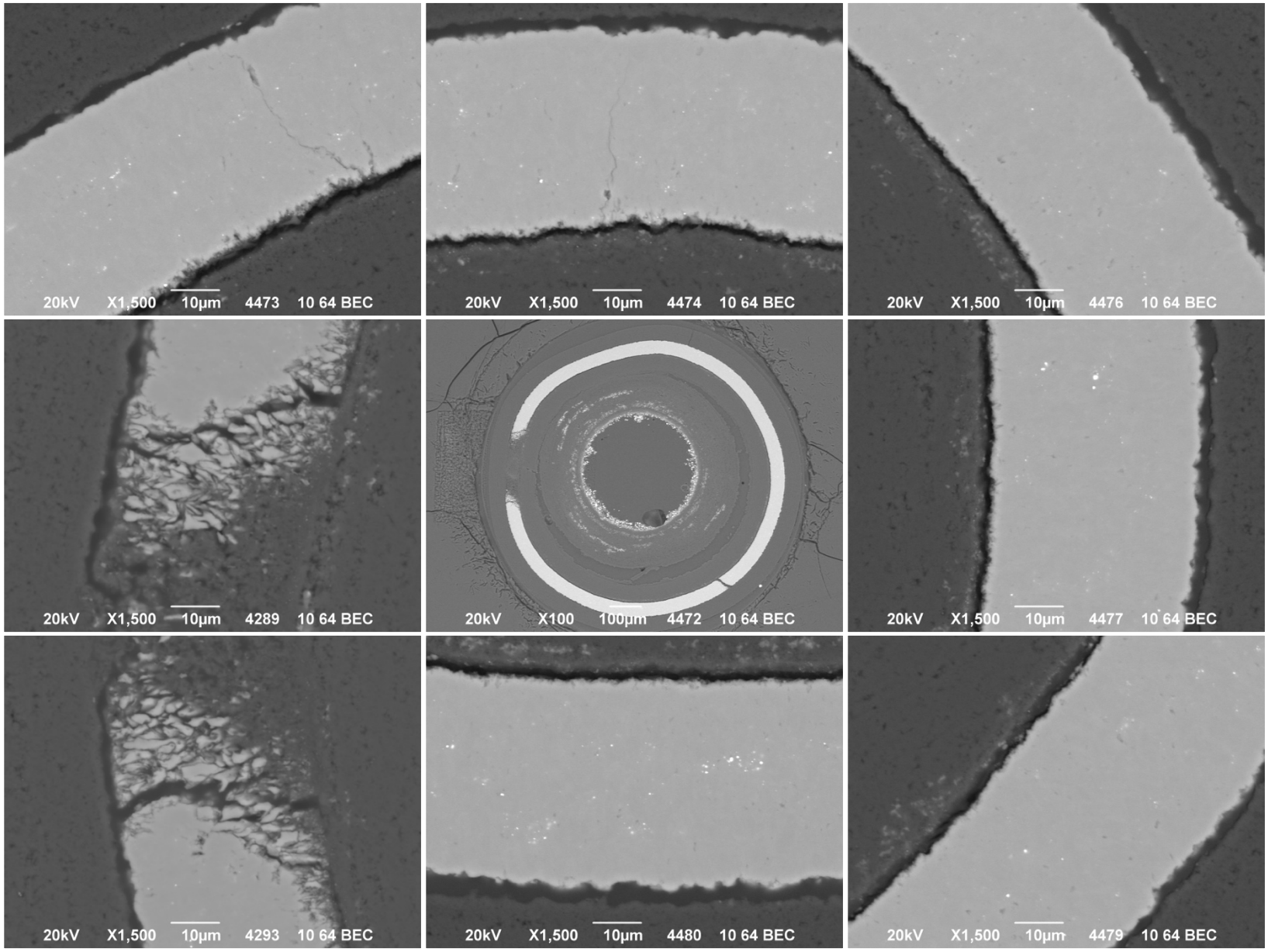

Appendix Figure D-90. 1,500× BEC micrographs of Particle 332-SP03.

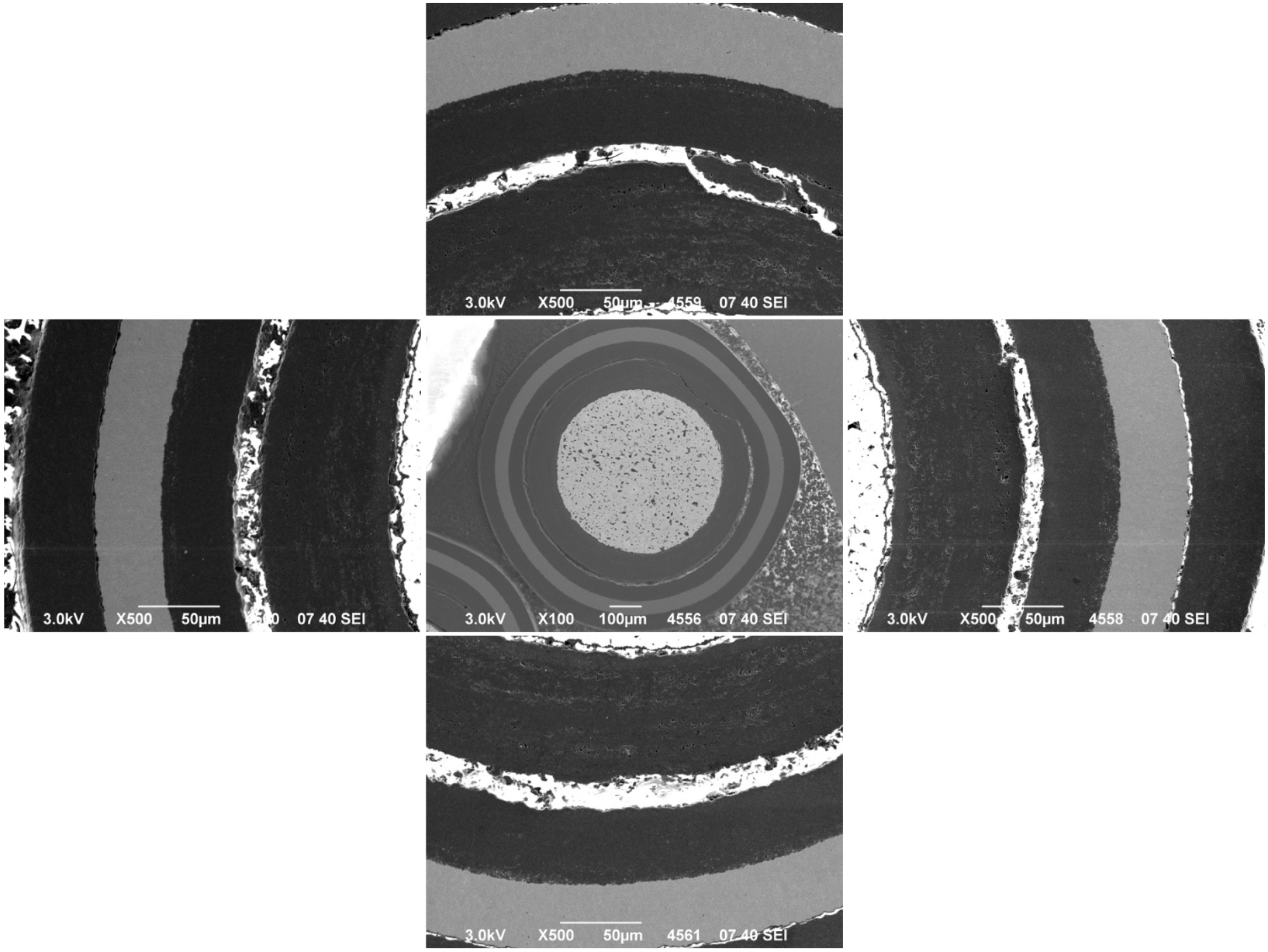

Appendix Figure D-91. 500× SEI micrographs of Particle 342-RS17.

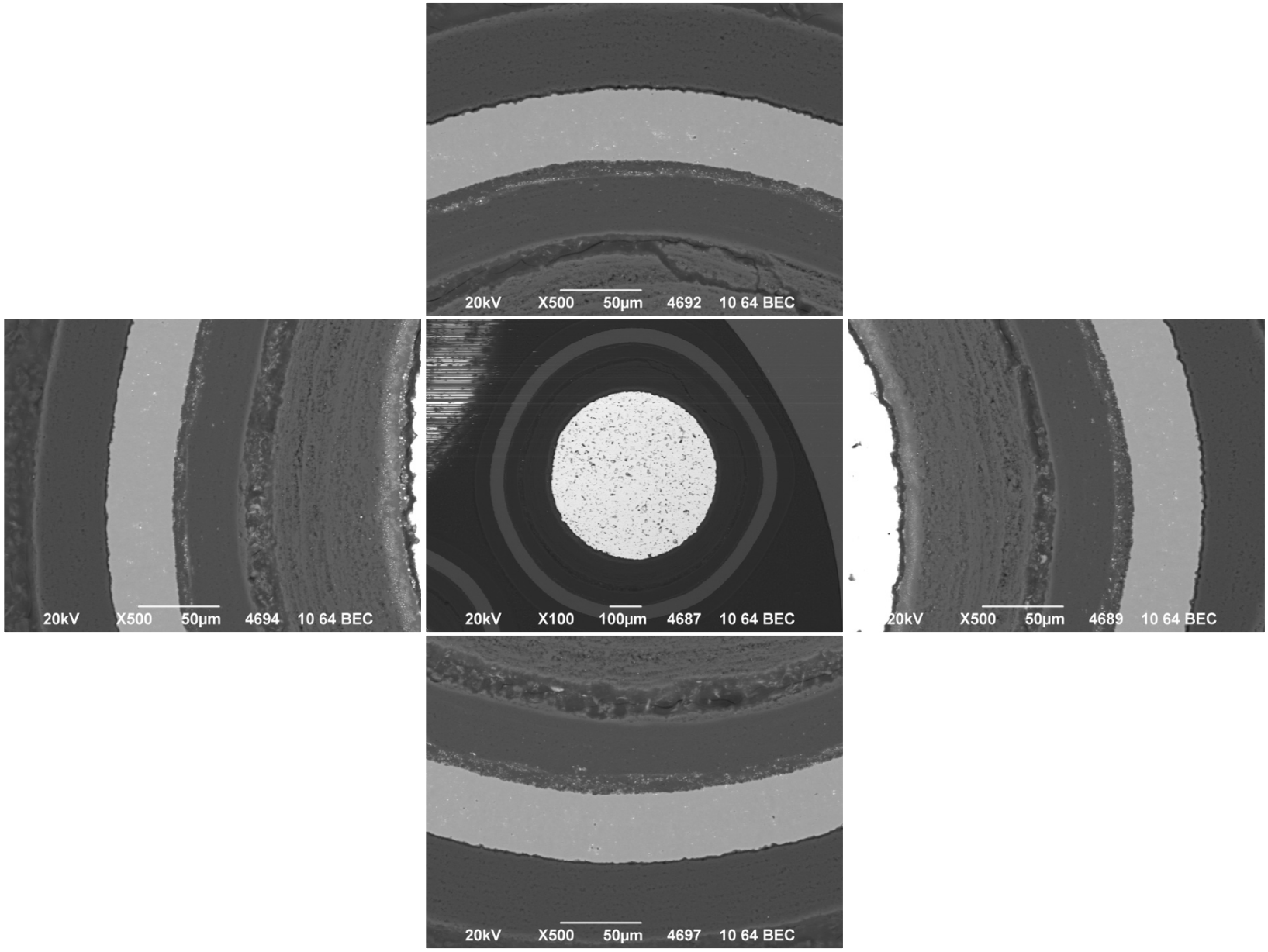

Appendix Figure D-92. 500× BEC micrographs of Particle 342-RS17.

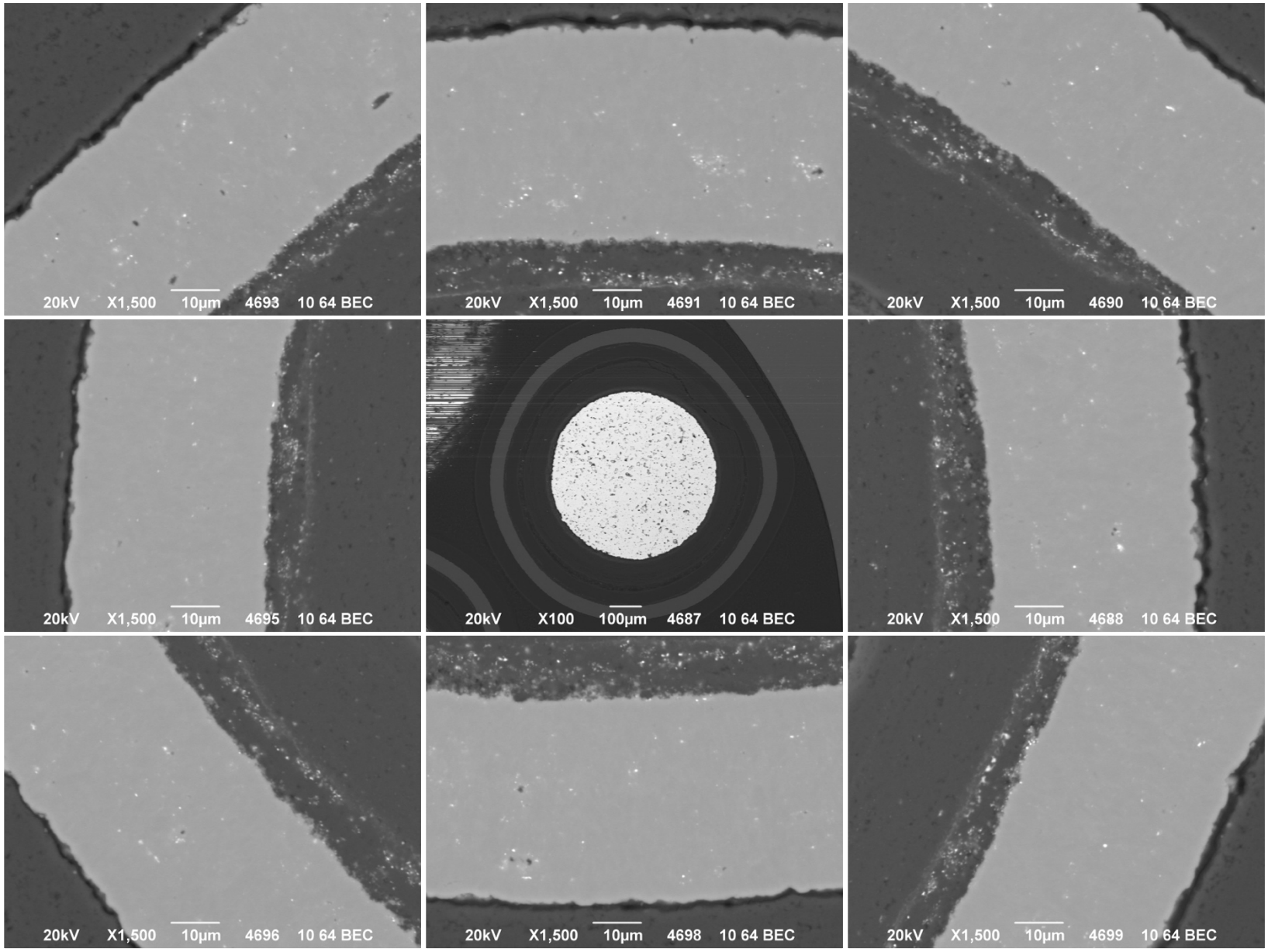

Appendix Figure D-93. 1,500× BEC micrographs of Particle 342-RS17.

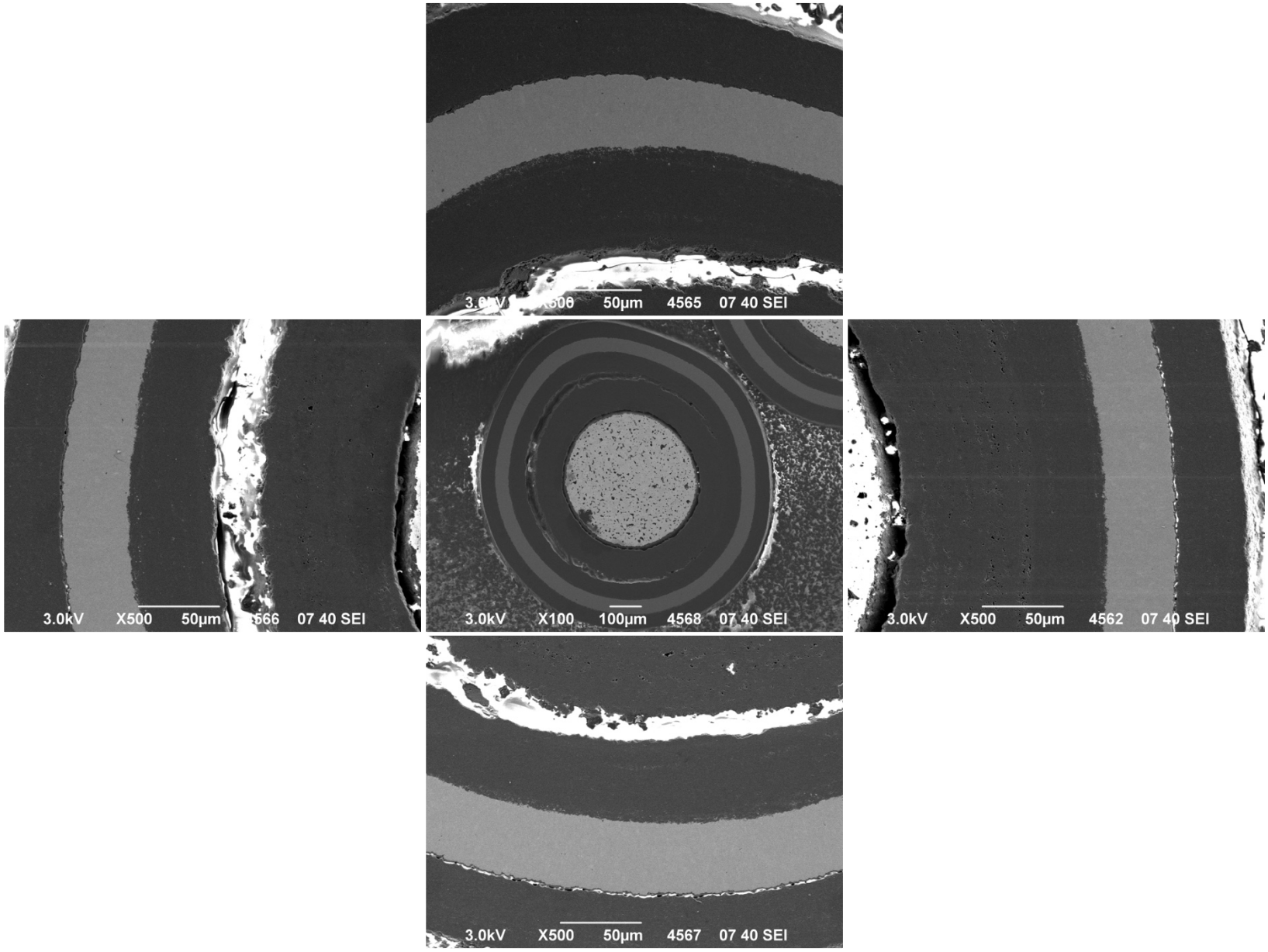

Appendix Figure D-94. 500× SEI micrographs of Particle 342-RS29.

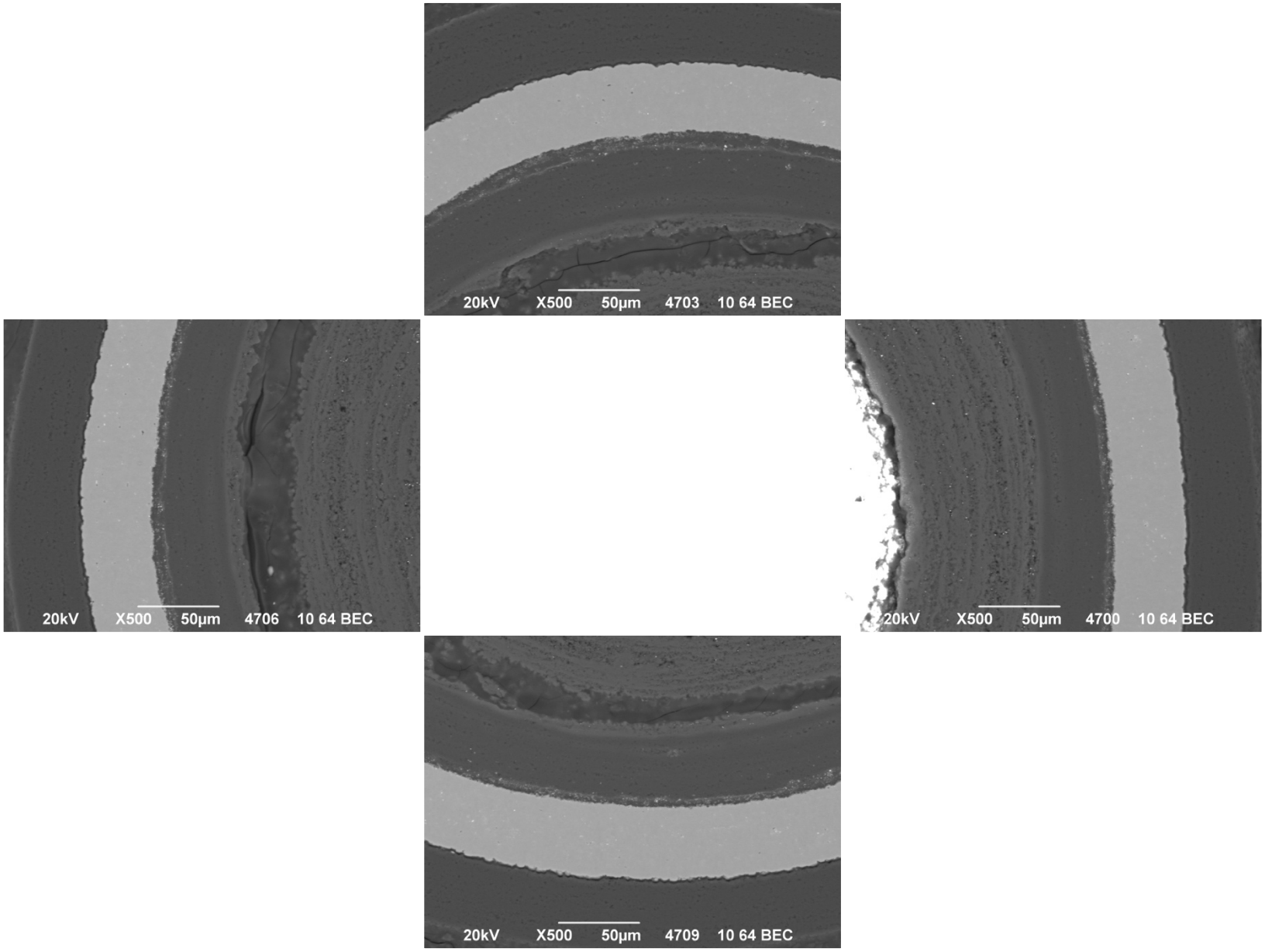

Appendix Figure D-95. 500× BEC micrographs of Particle 342-RS29.

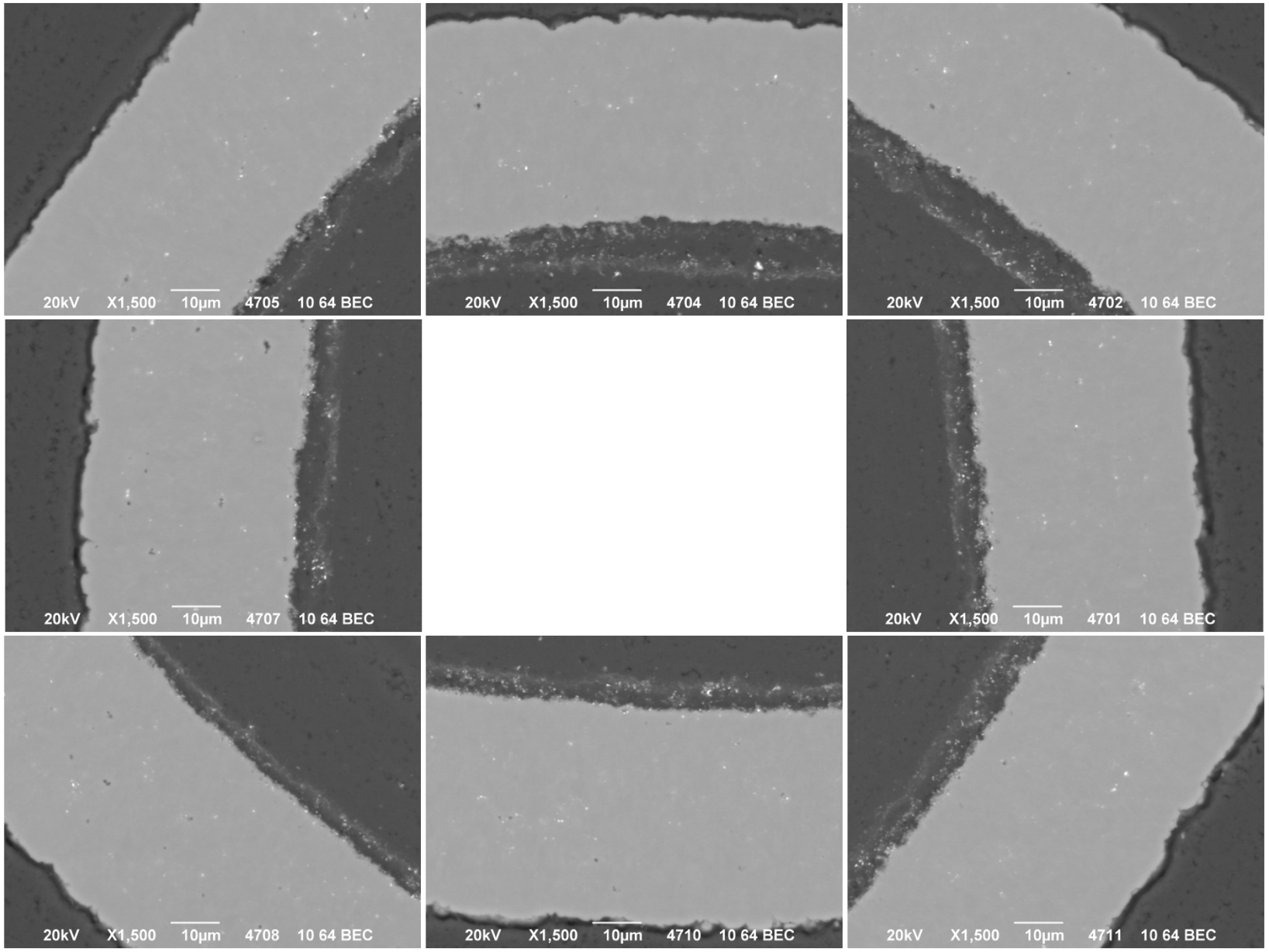

Appendix Figure D-96. 1,500× BEC micrographs of Particle 342-RS29.

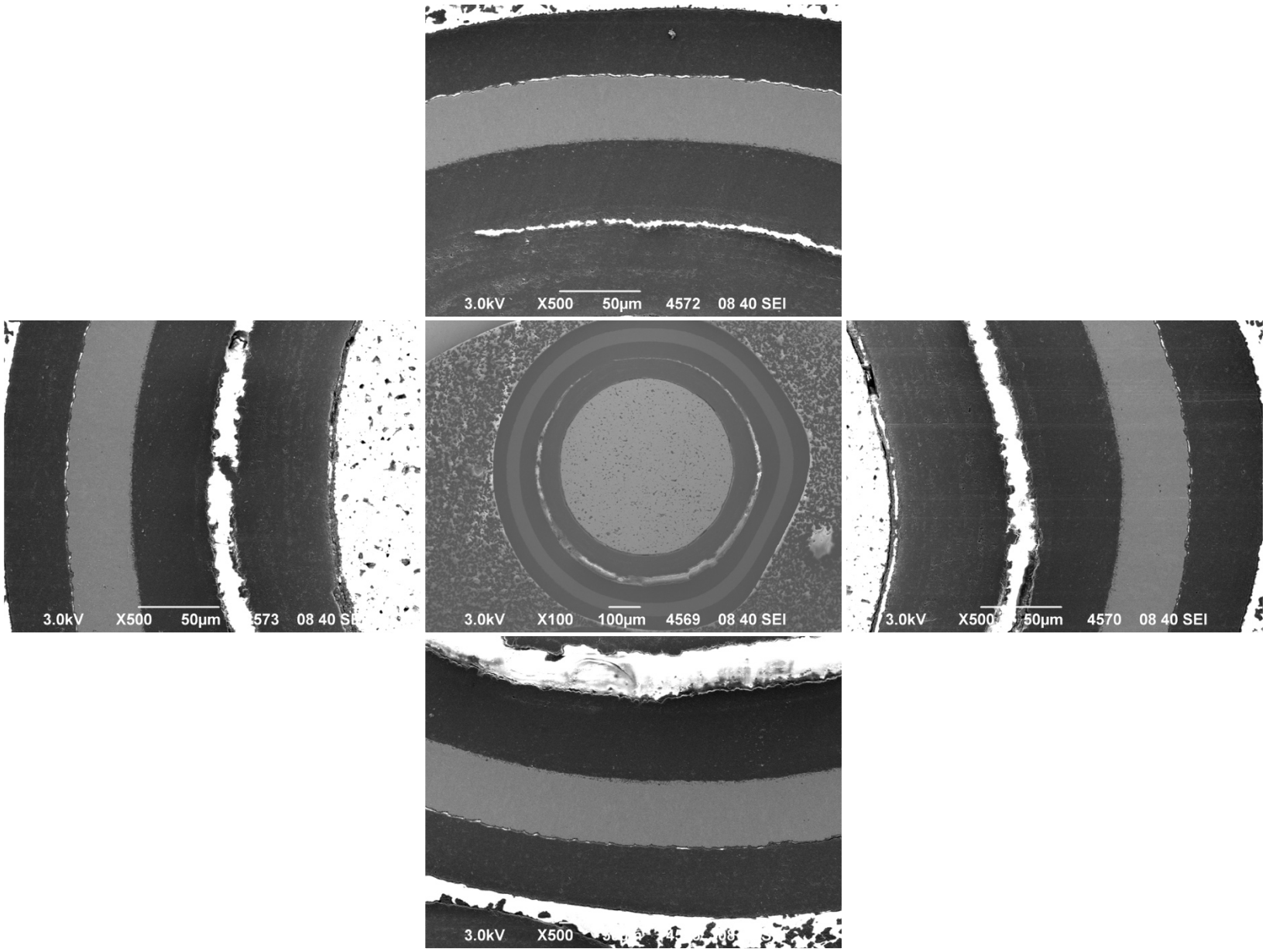

Appendix Figure D-97. 500× SEI micrographs of Particle 342-RS07.

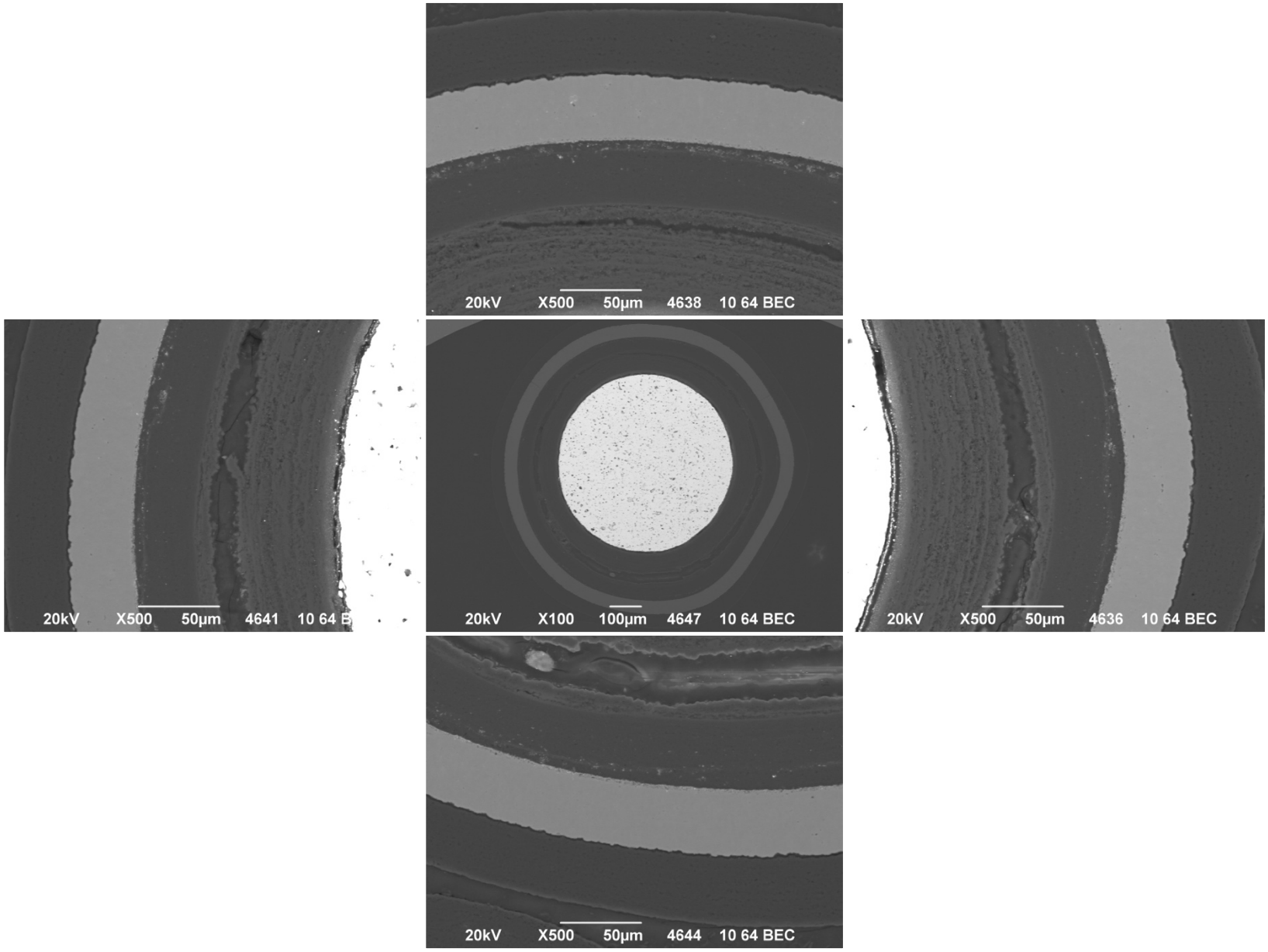

Appendix Figure D-98. 500× BEC micrographs of Particle 342-RS07.

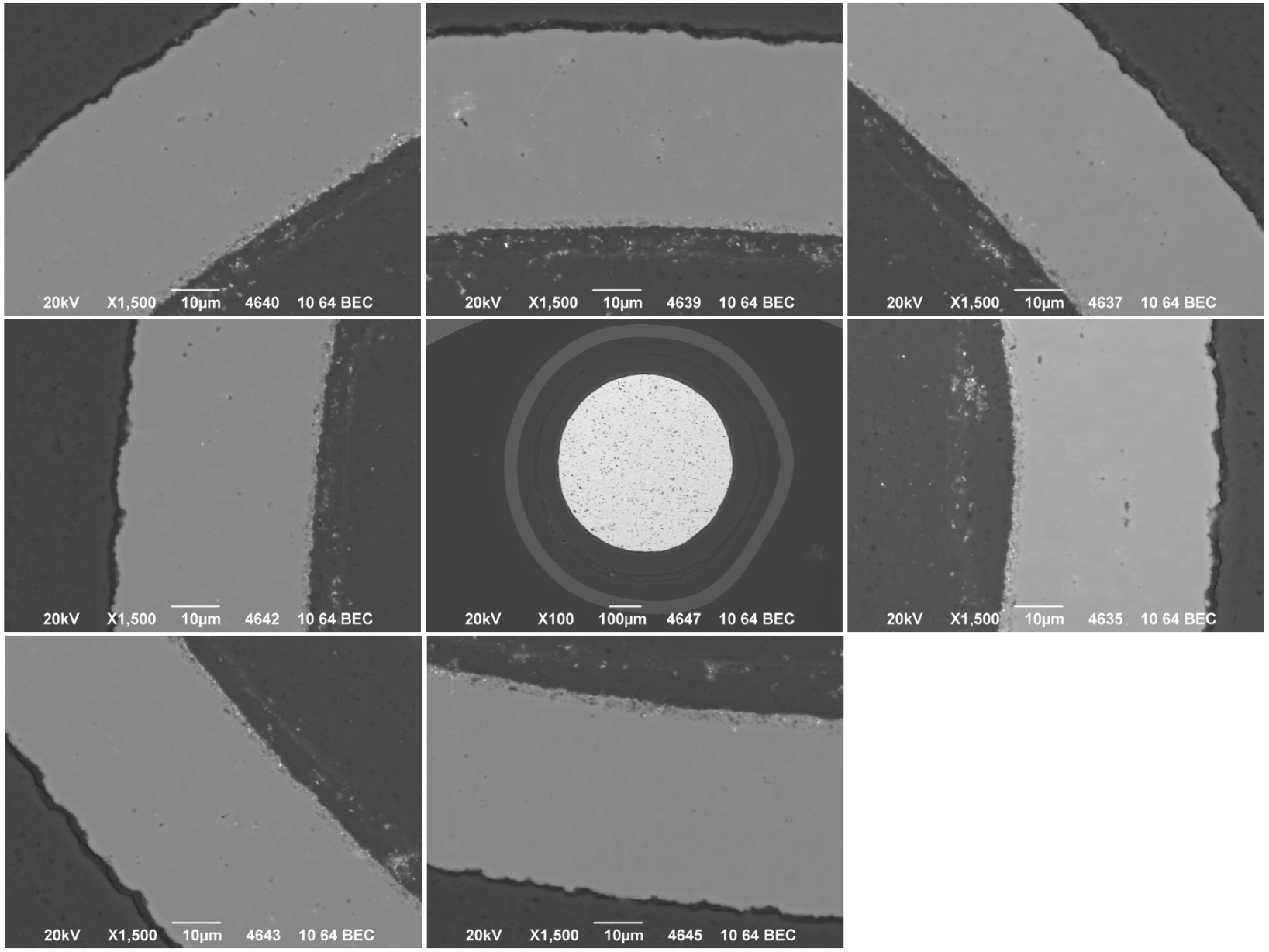

Appendix Figure D-99. 1,500× BEC micrographs of Particle 342-RS07.

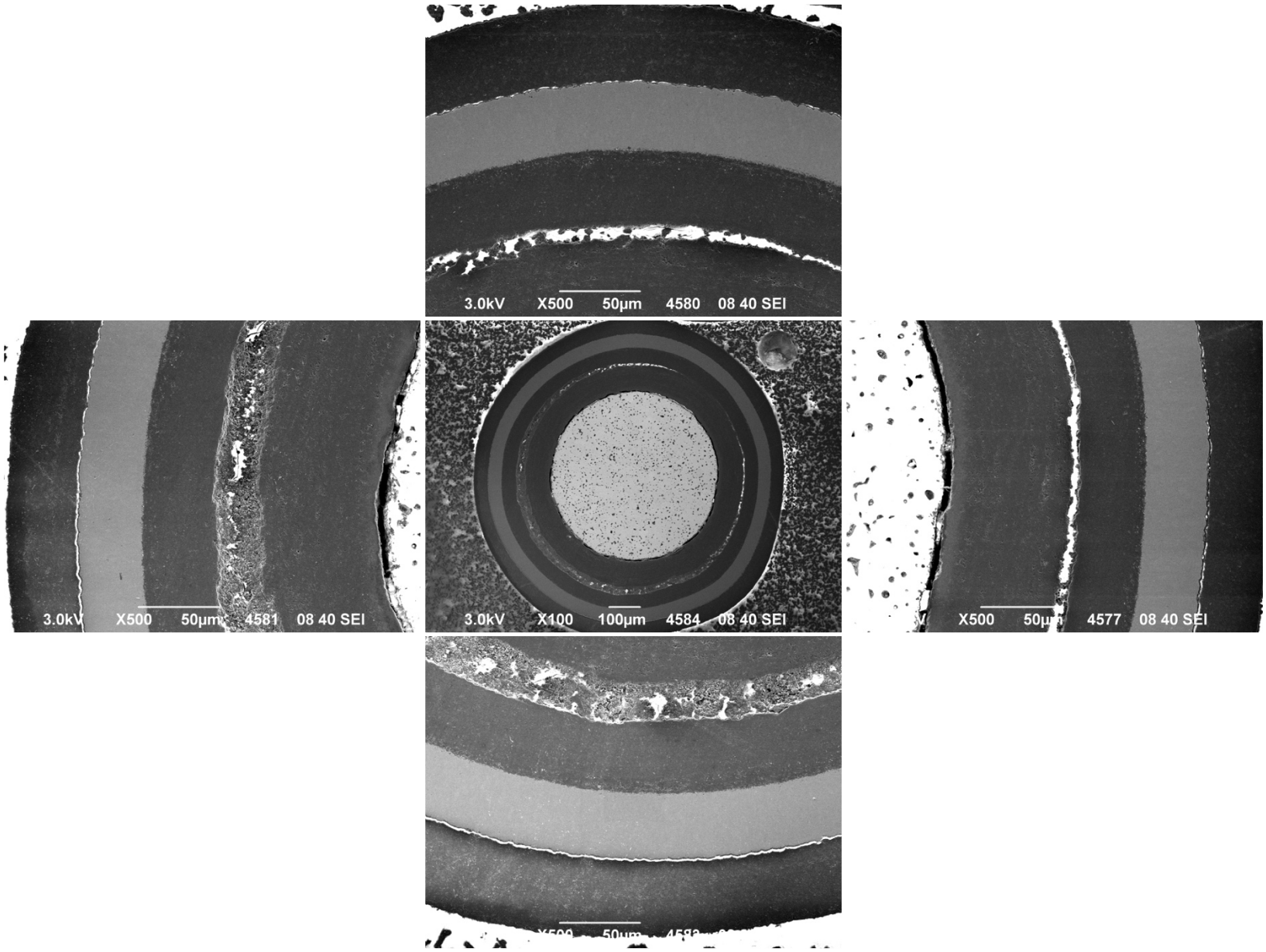

Appendix Figure D-100. 500× SEI micrographs of Particle 342-RS21.

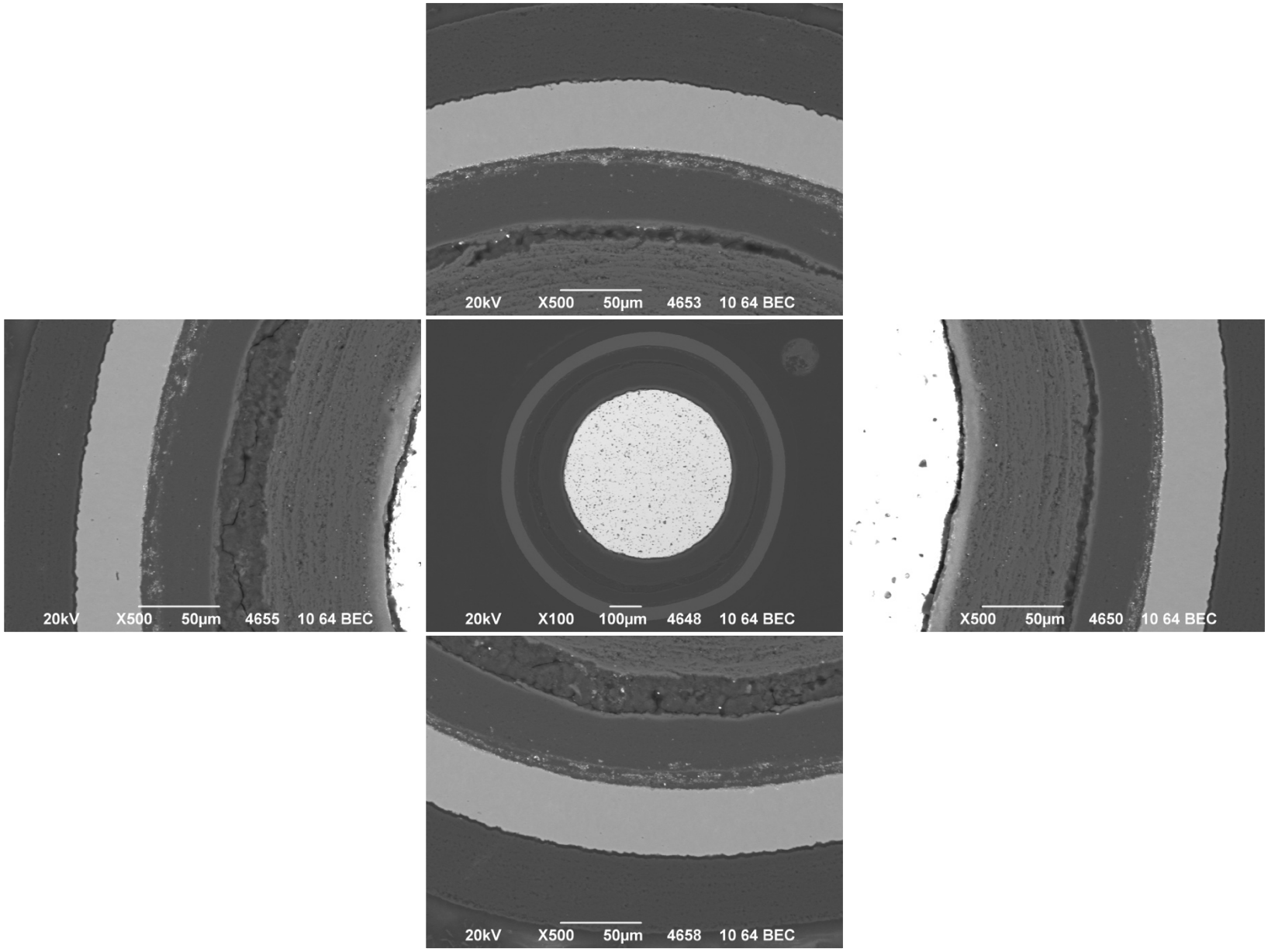

Appendix Figure D-101. 500× BEC micrographs of Particle 342-RS21.

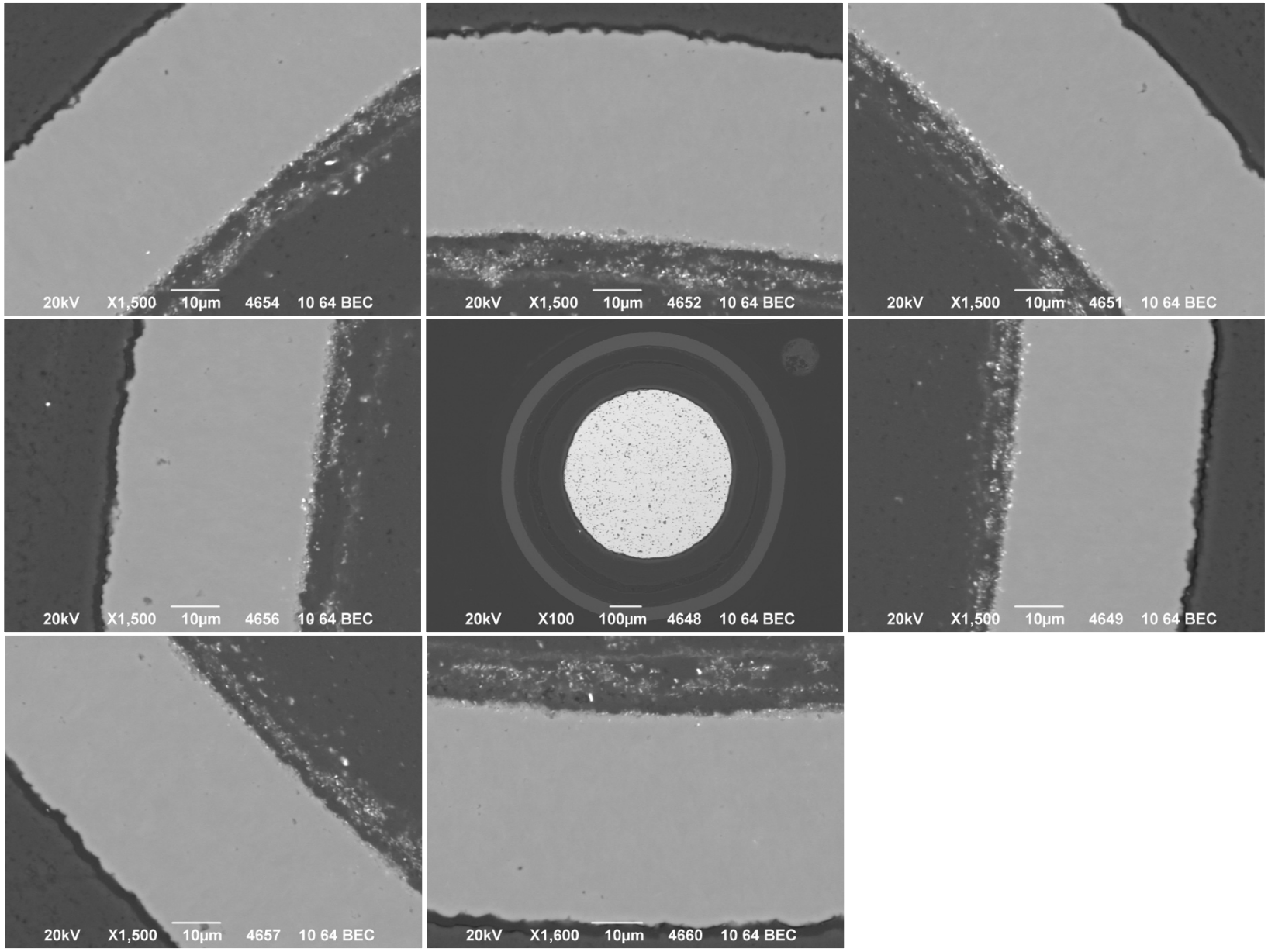

Appendix Figure D-102. 1,500× BEC micrographs of Particle 342-RS21.

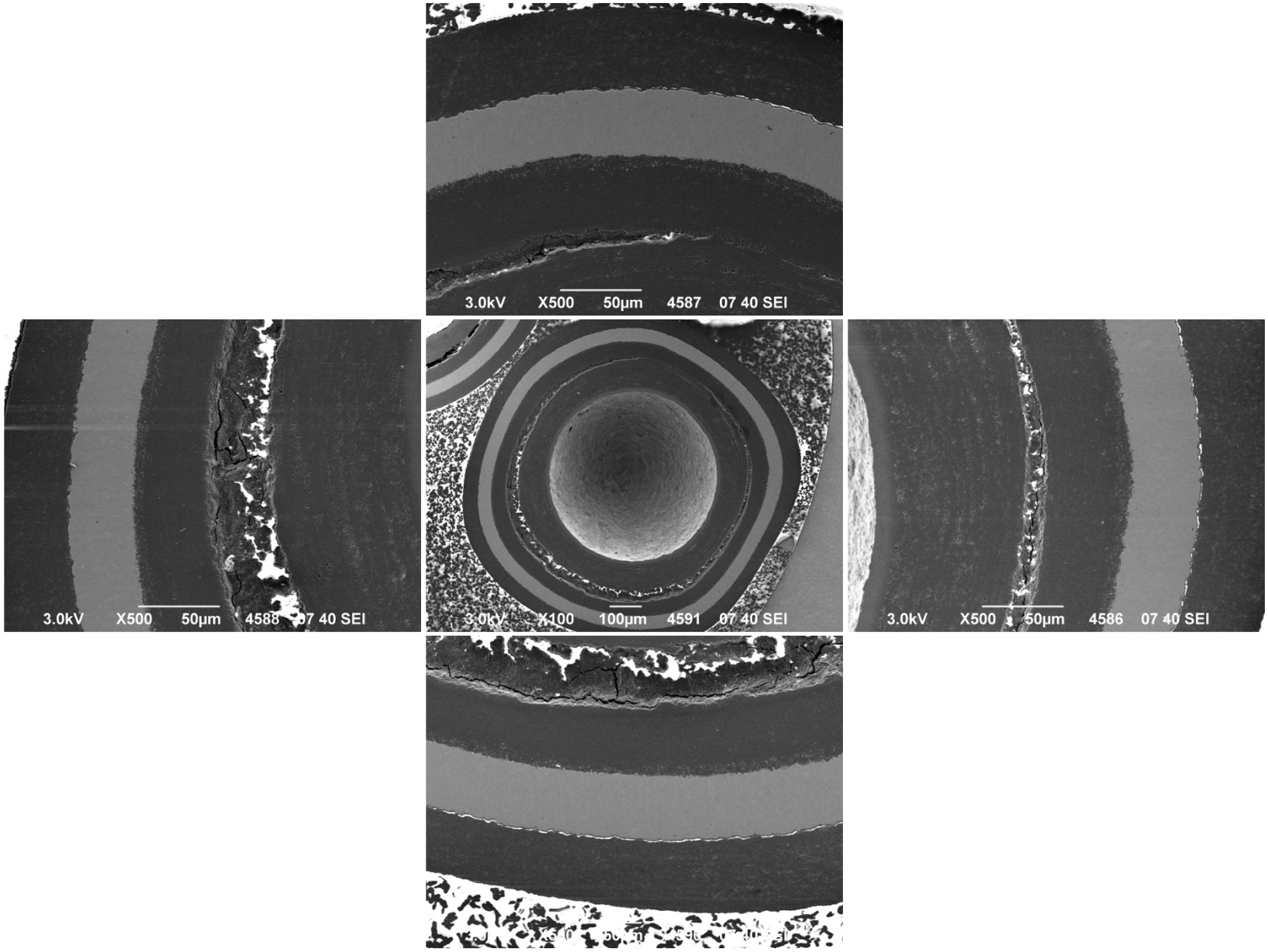

Appendix Figure D-103. 500× SEI micrographs of Particle 342-RS03.

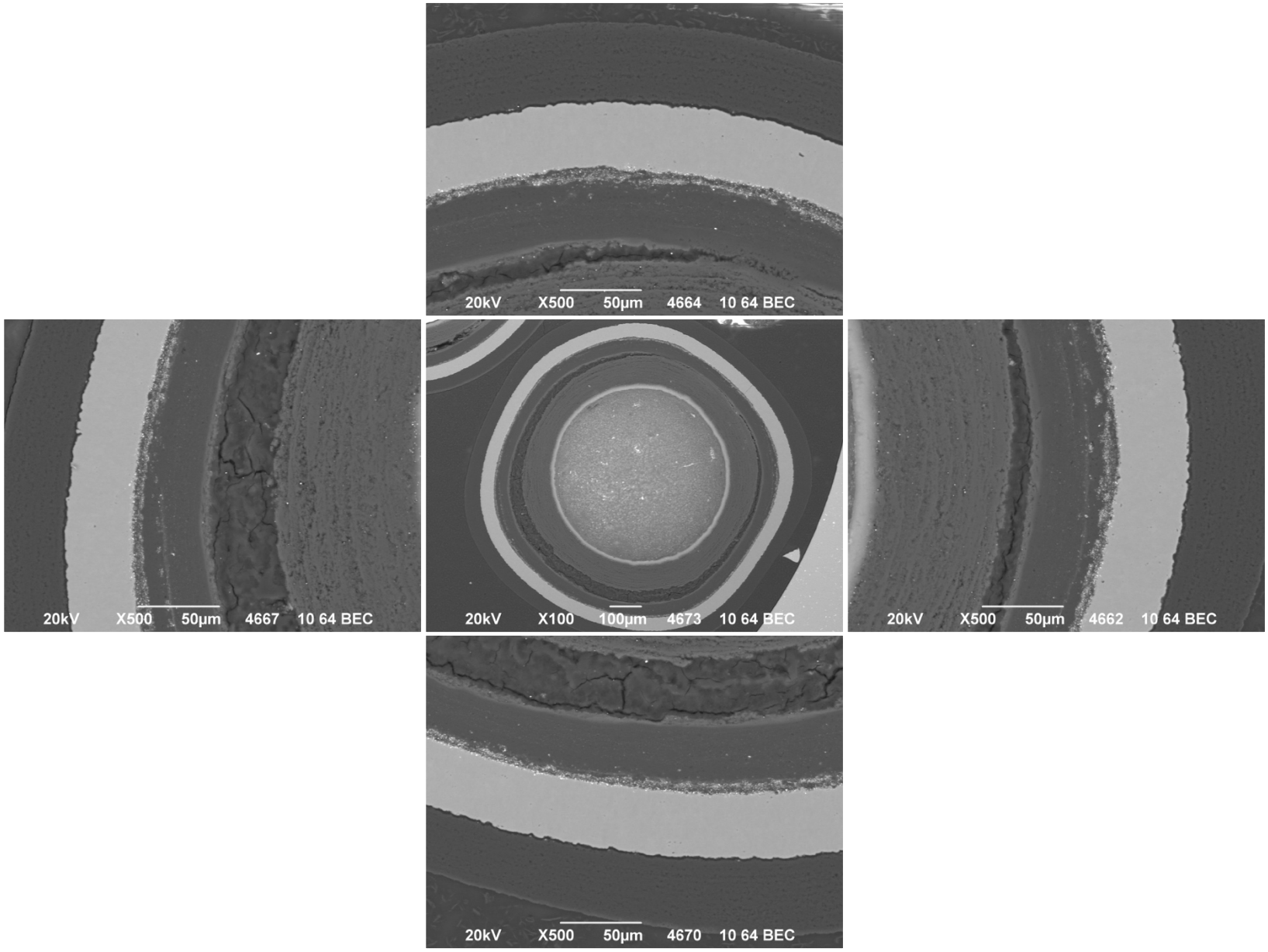

Appendix Figure D-104. 500× BEC micrographs of Particle 342-RS03.

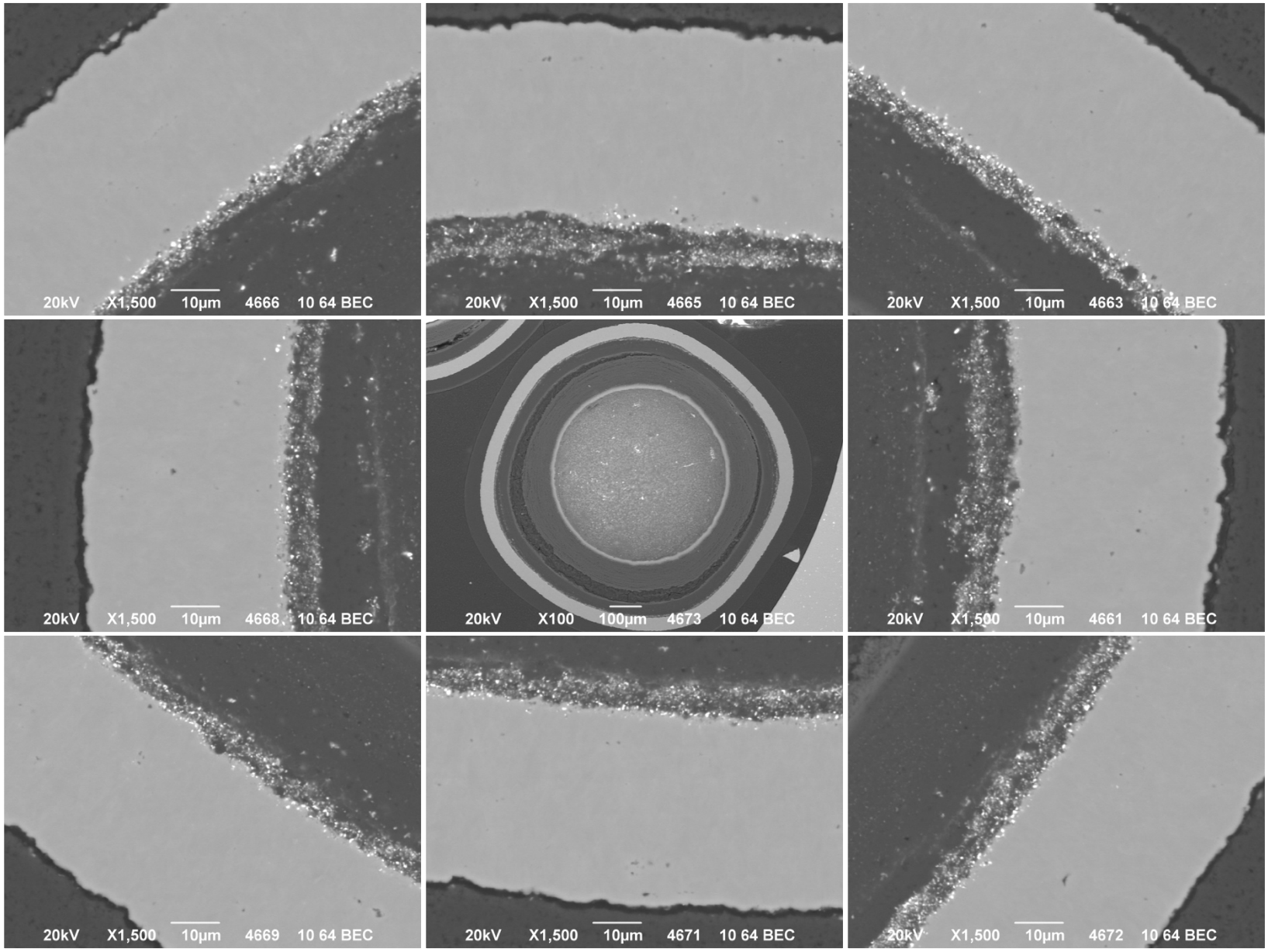

Appendix Figure D-105. 1,500× BEC micrographs of Particle 342-RS03.

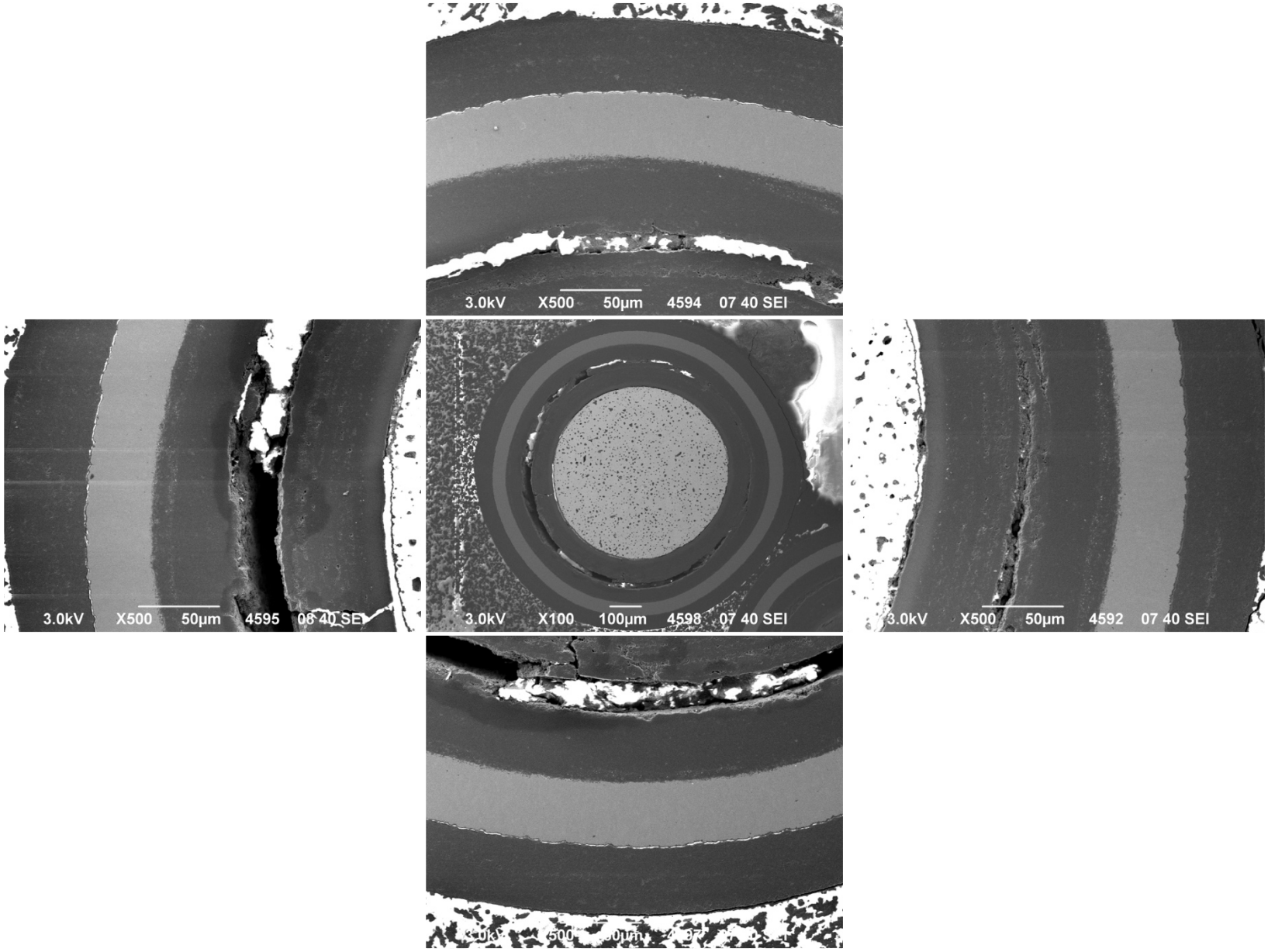

Appendix Figure D-106. 500× SEI micrographs of Particle 342-RS15.

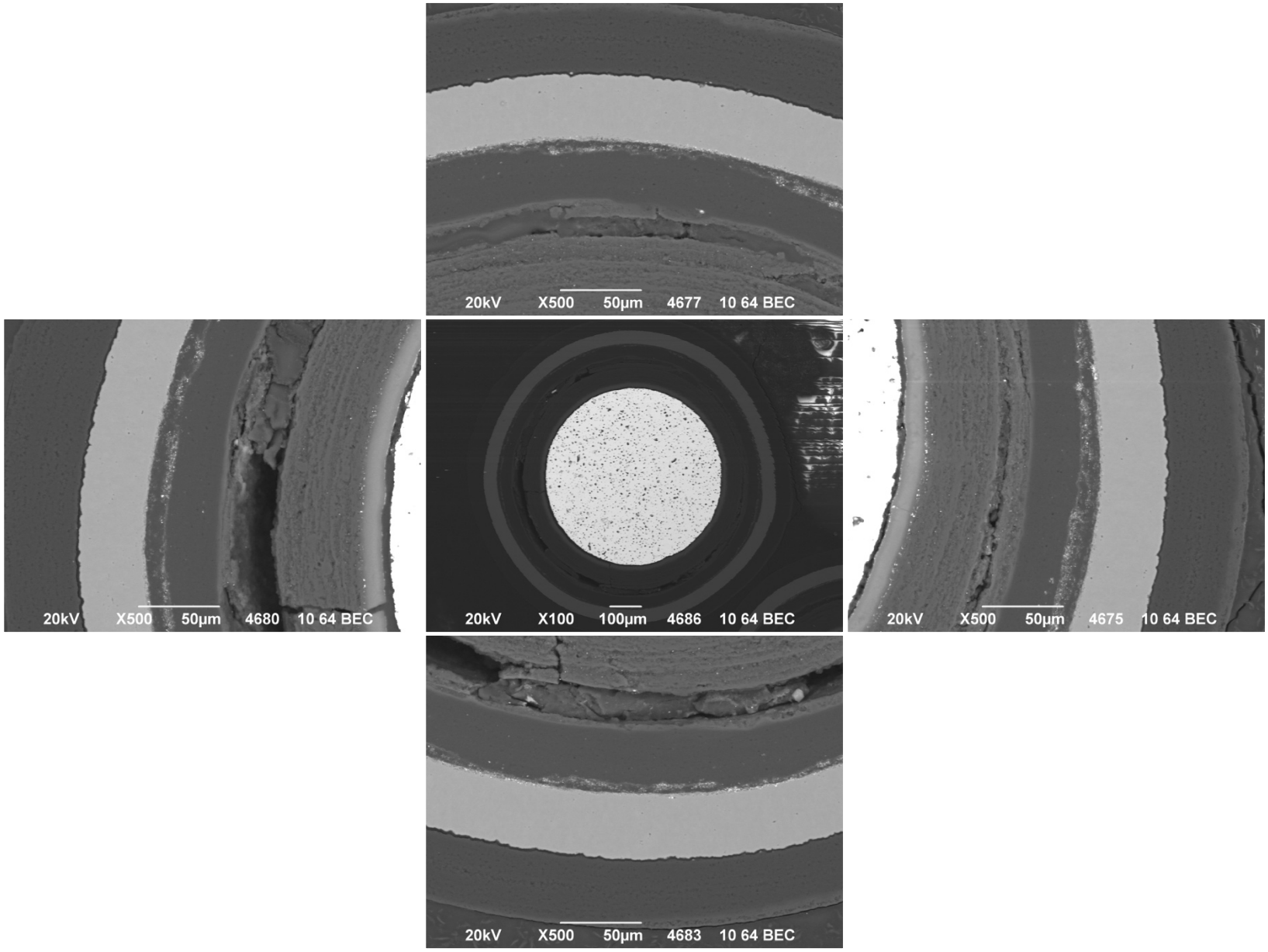

Appendix Figure D-107. 500× BEC micrographs of Particle 342-RS15.

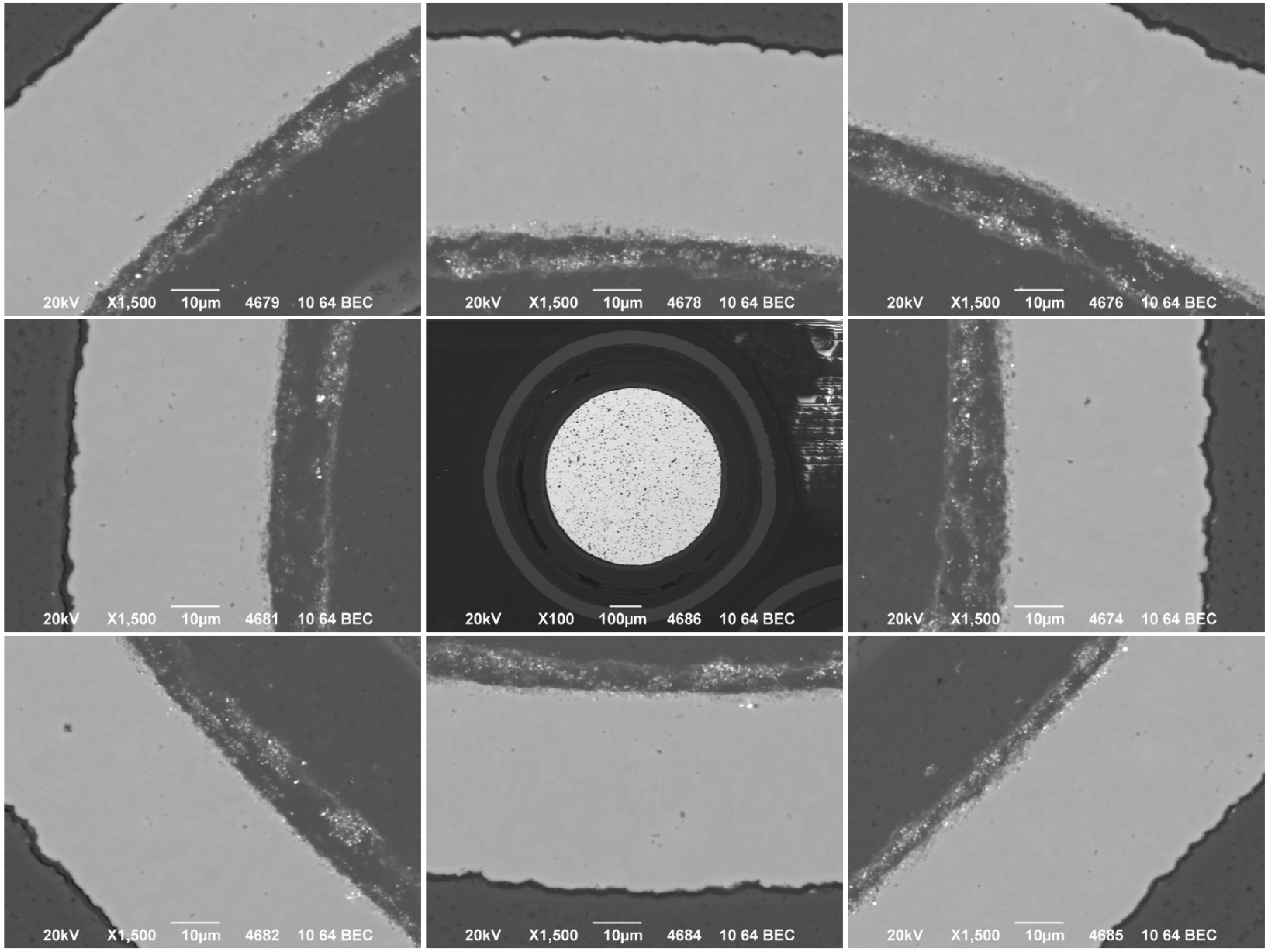

Appendix Figure D-108. 1,500× BEC micrographs of Particle 342-RS15.

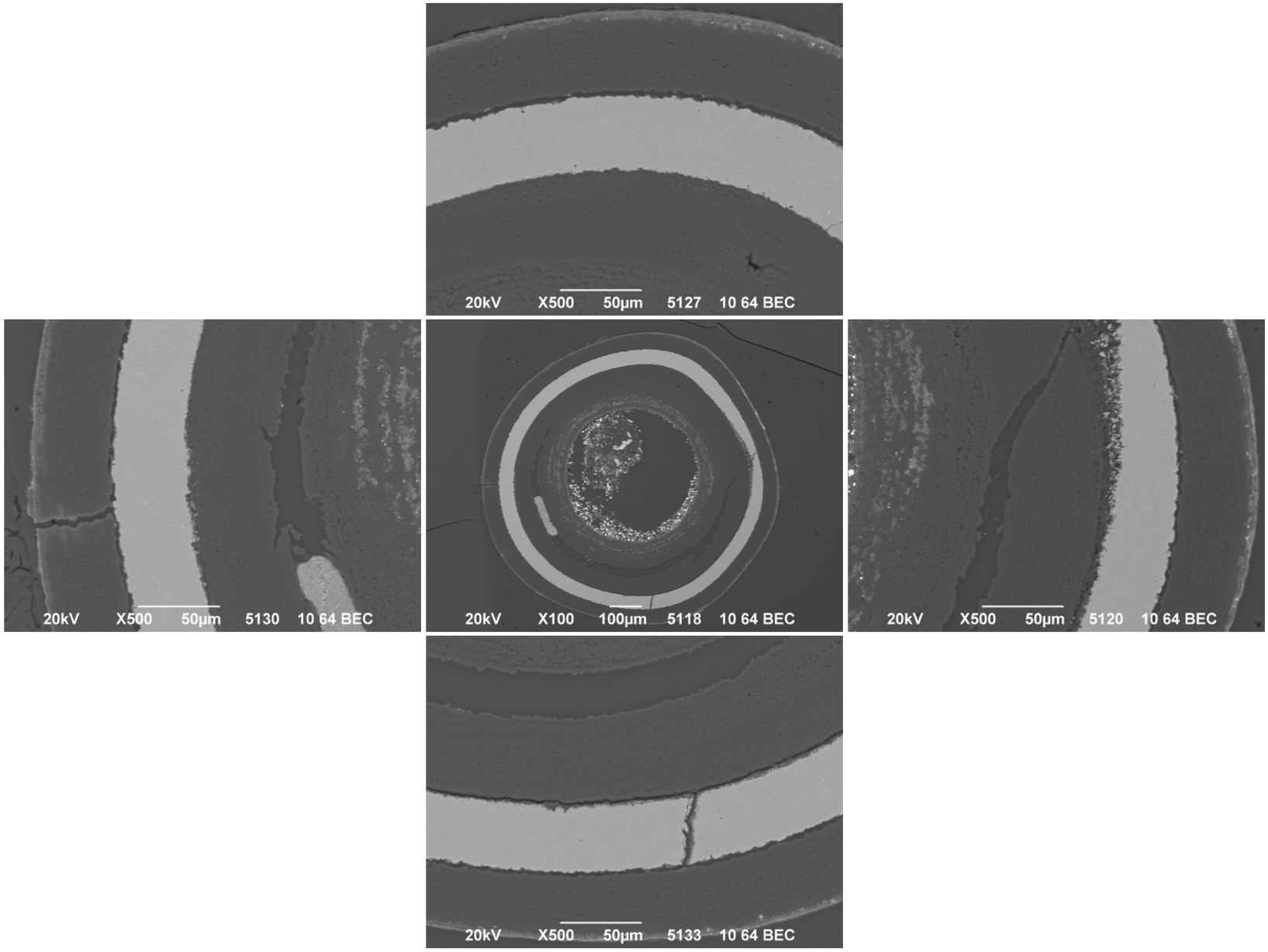

Appendix Figure D-109. 500× BEC micrographs of Particle 342-SP01.

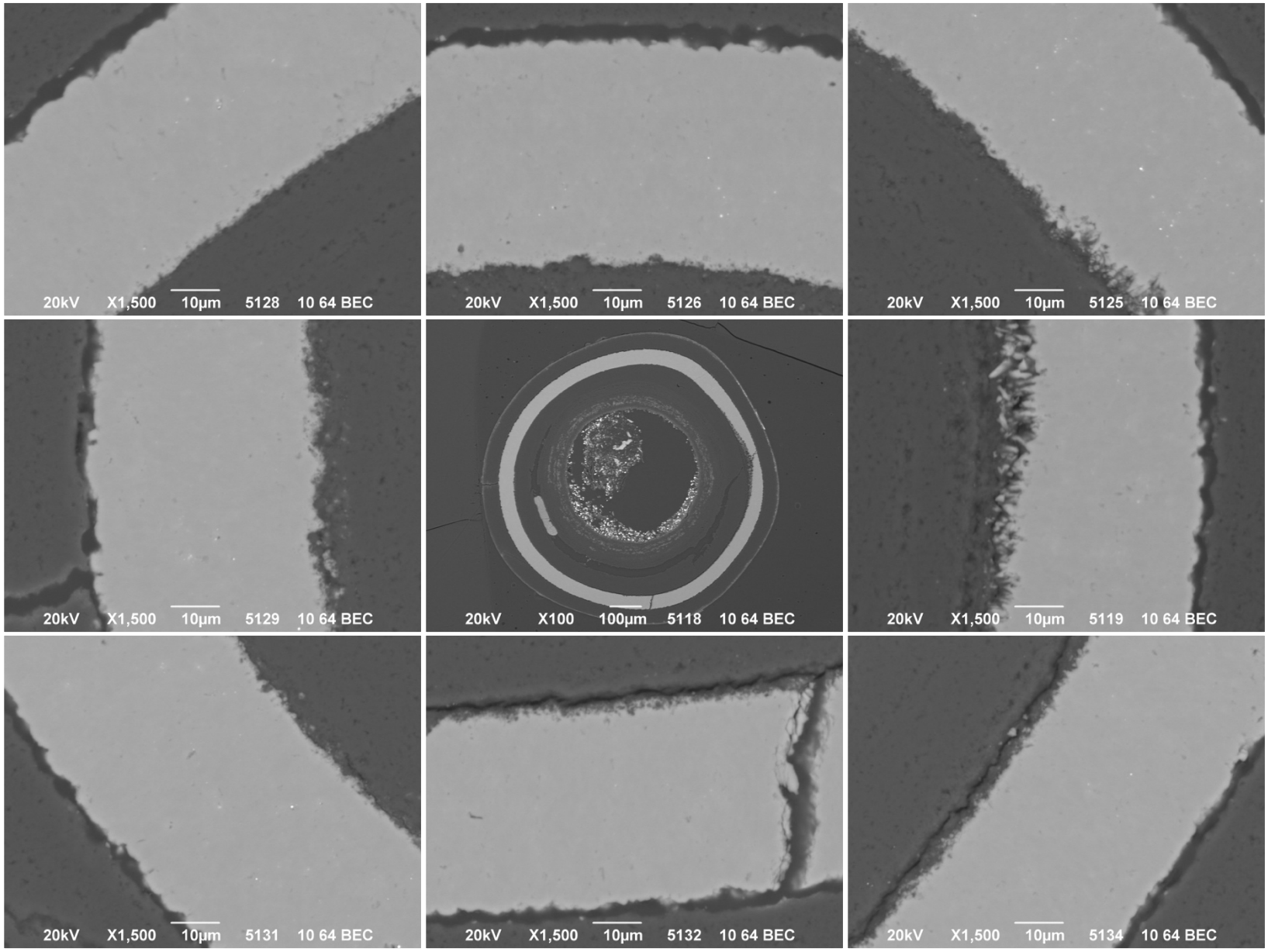

Appendix Figure D-110. 1,500× BEC micrographs of Particle 342-SP01.

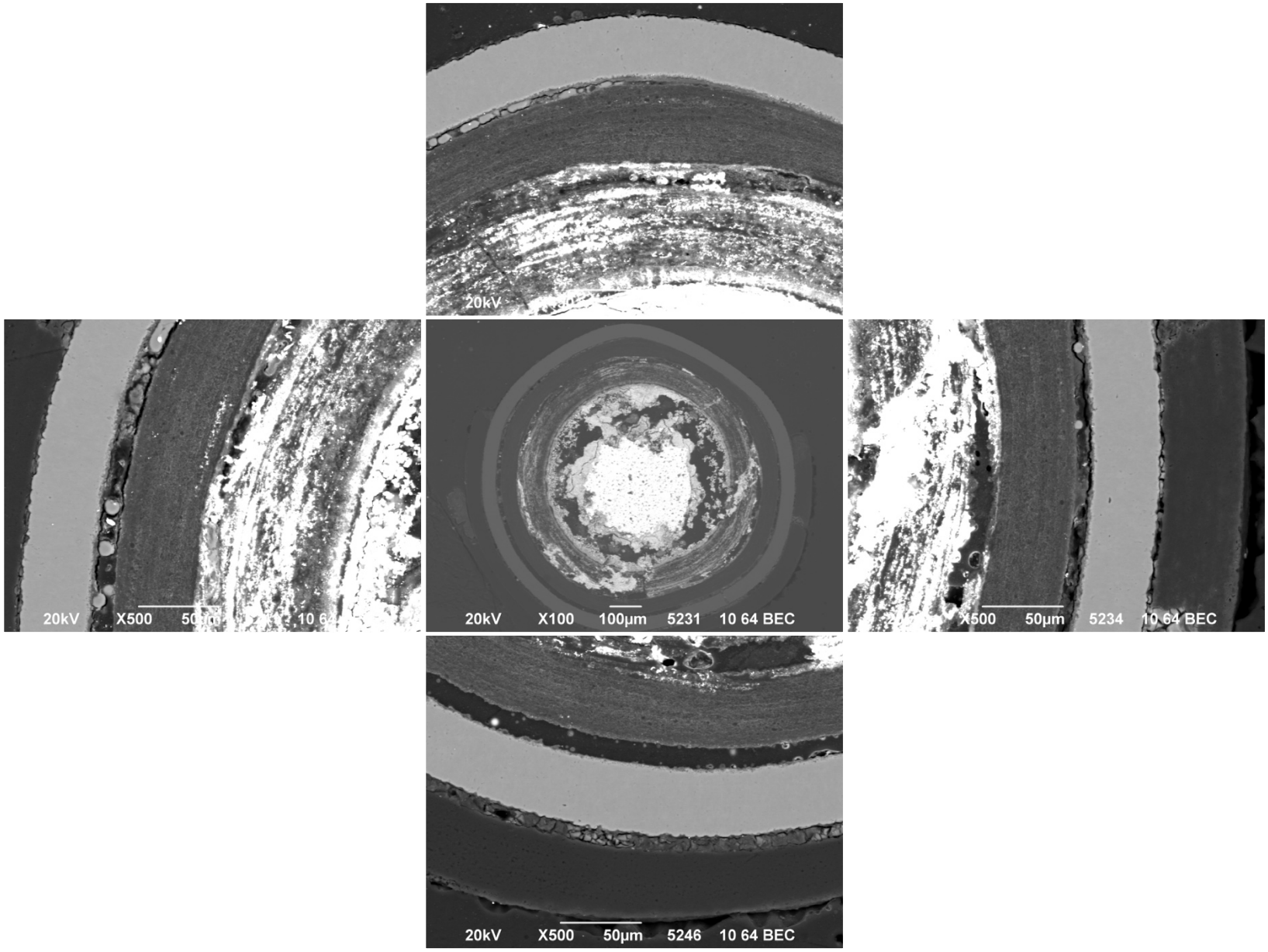

Appendix Figure D-111. 500× BEC micrographs of Particle 342-SP06.

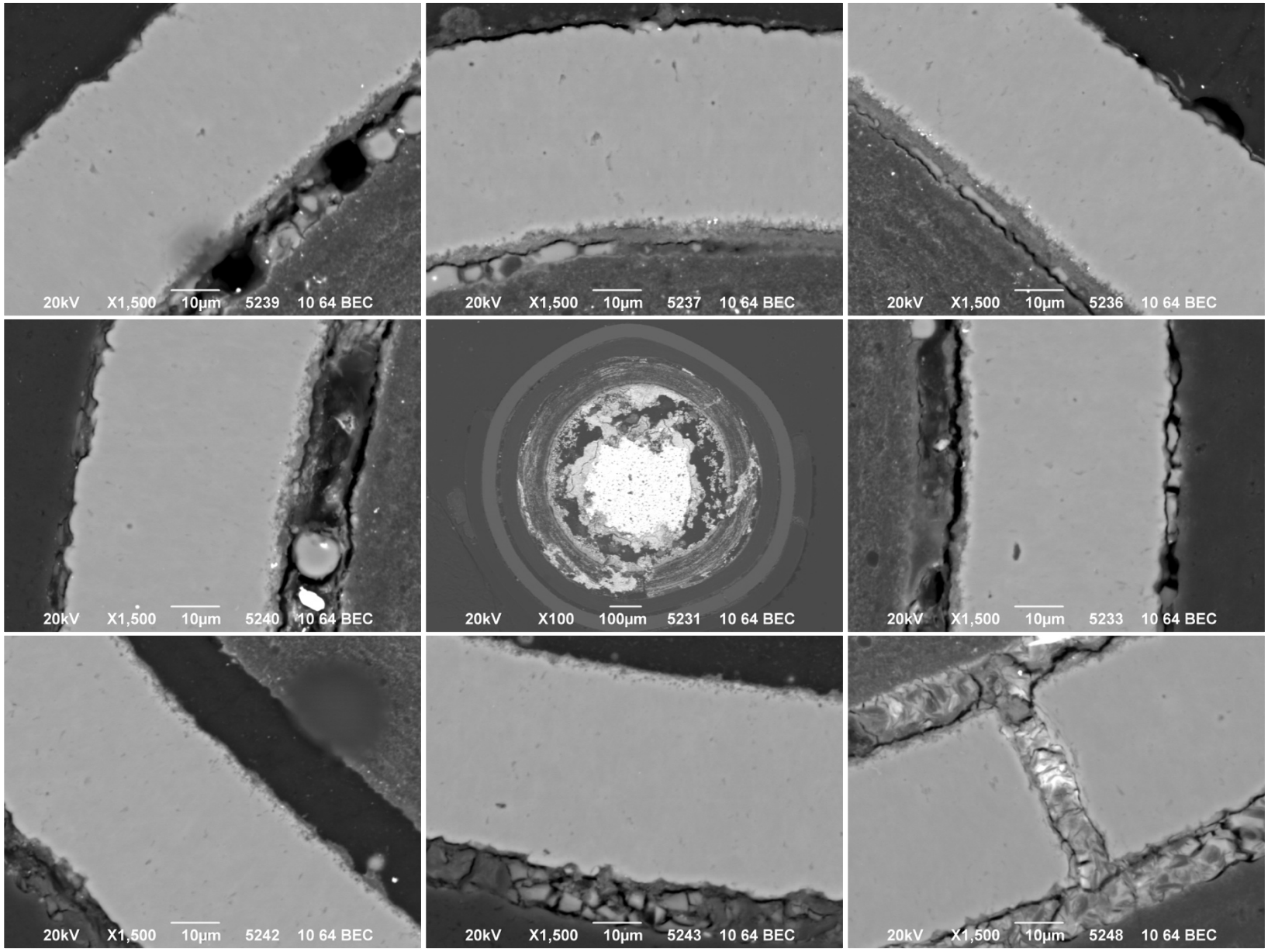

Appendix Figure D-112. 1,500× BEC micrographs of Particle 342-SP06.

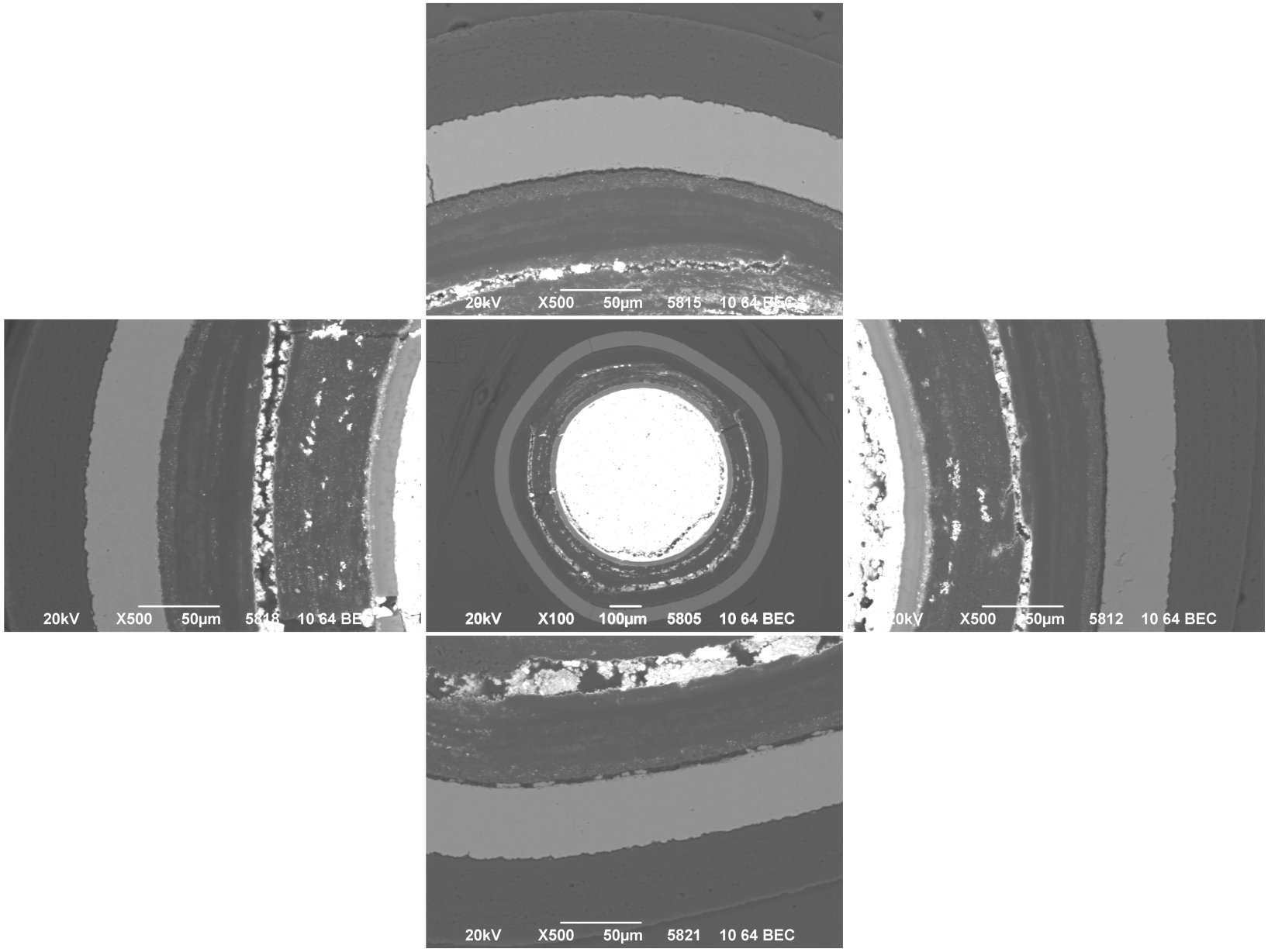

Appendix Figure D-113. 500× BEC micrographs of Particle 342-SP07.

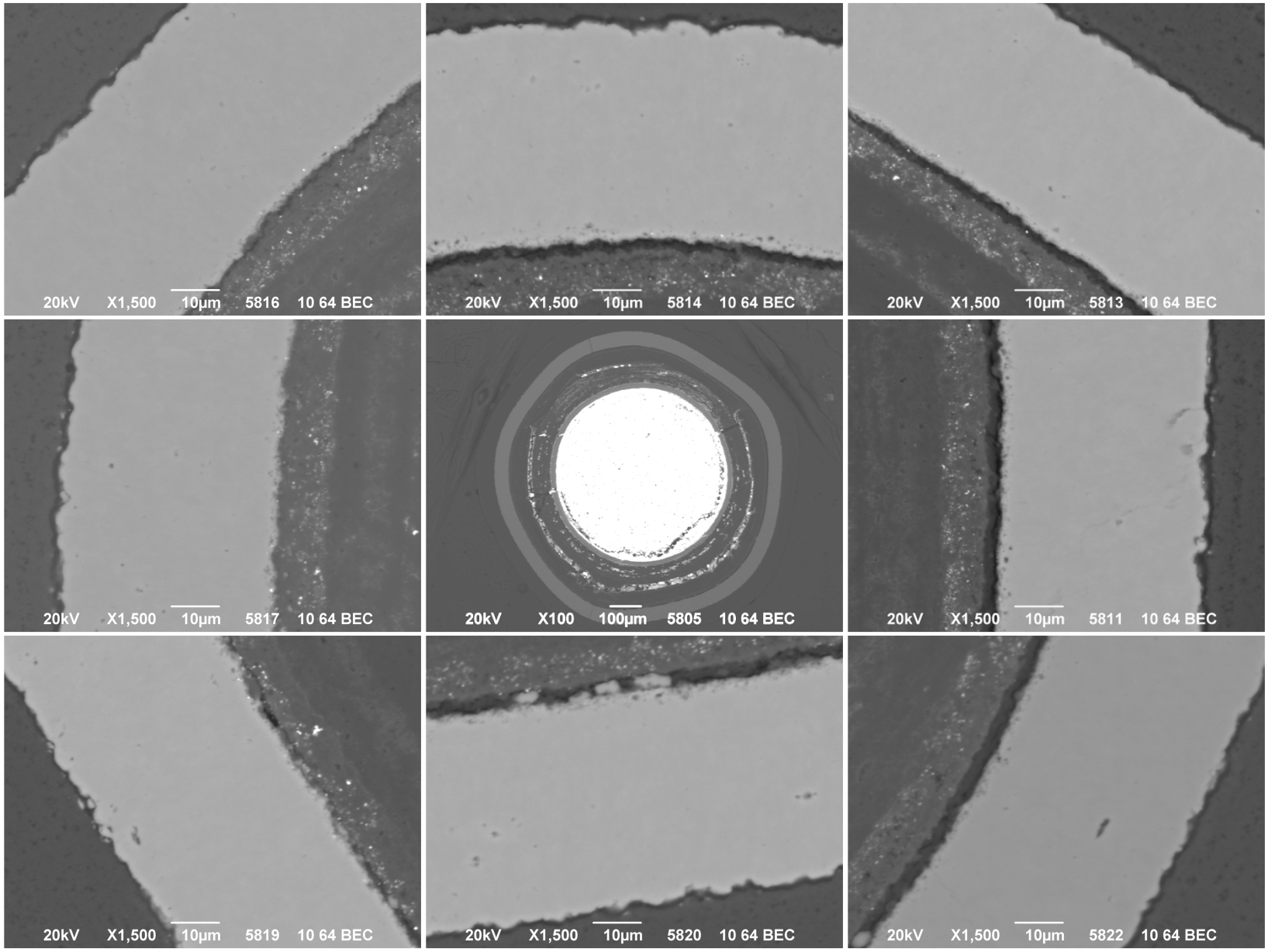

Appendix Figure D-114. 1,500× BEC micrographs of Particle 342-SP07.

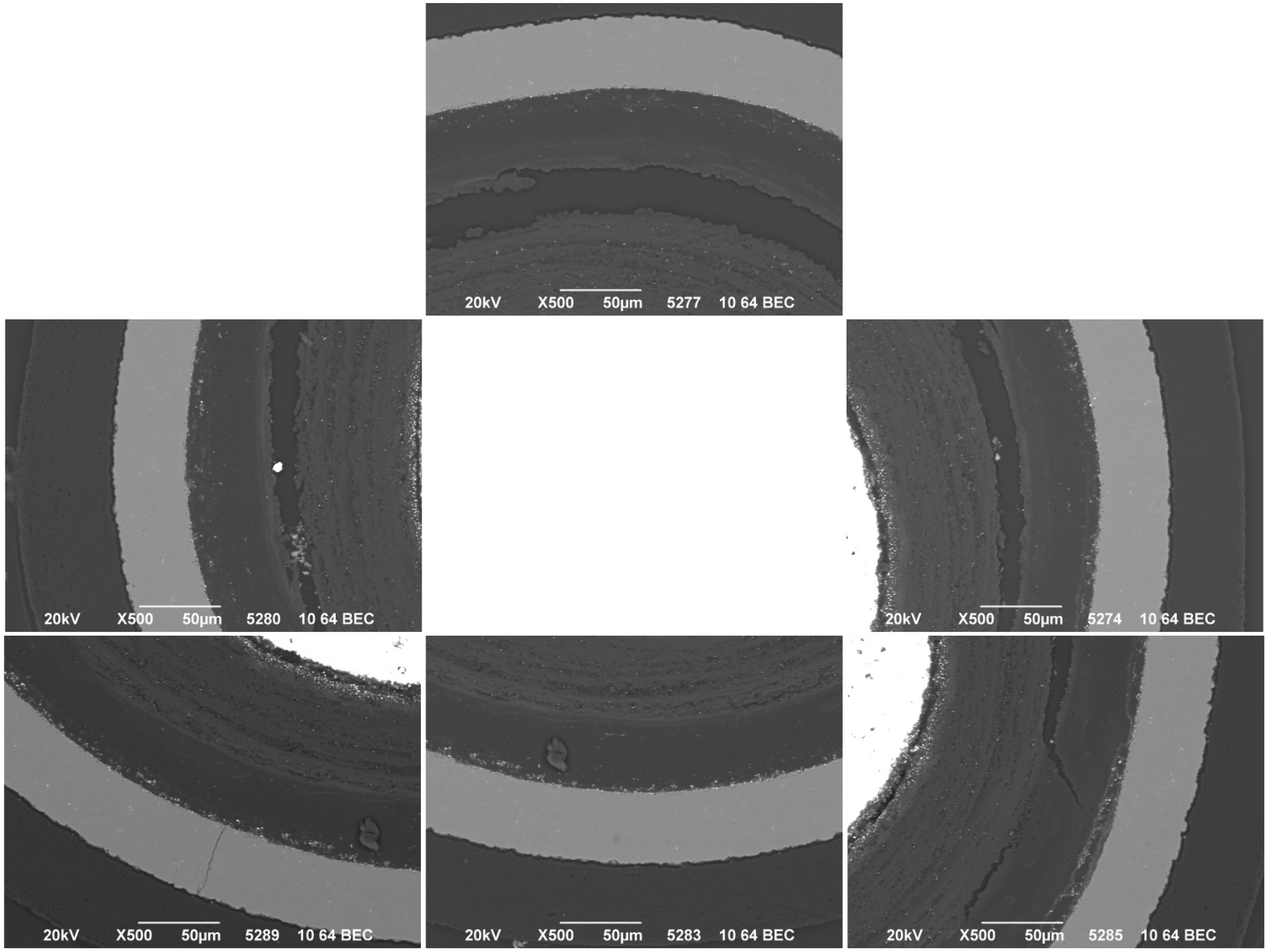

Appendix Figure D-115. 500× BEC micrographs of Particle 342-SP09.

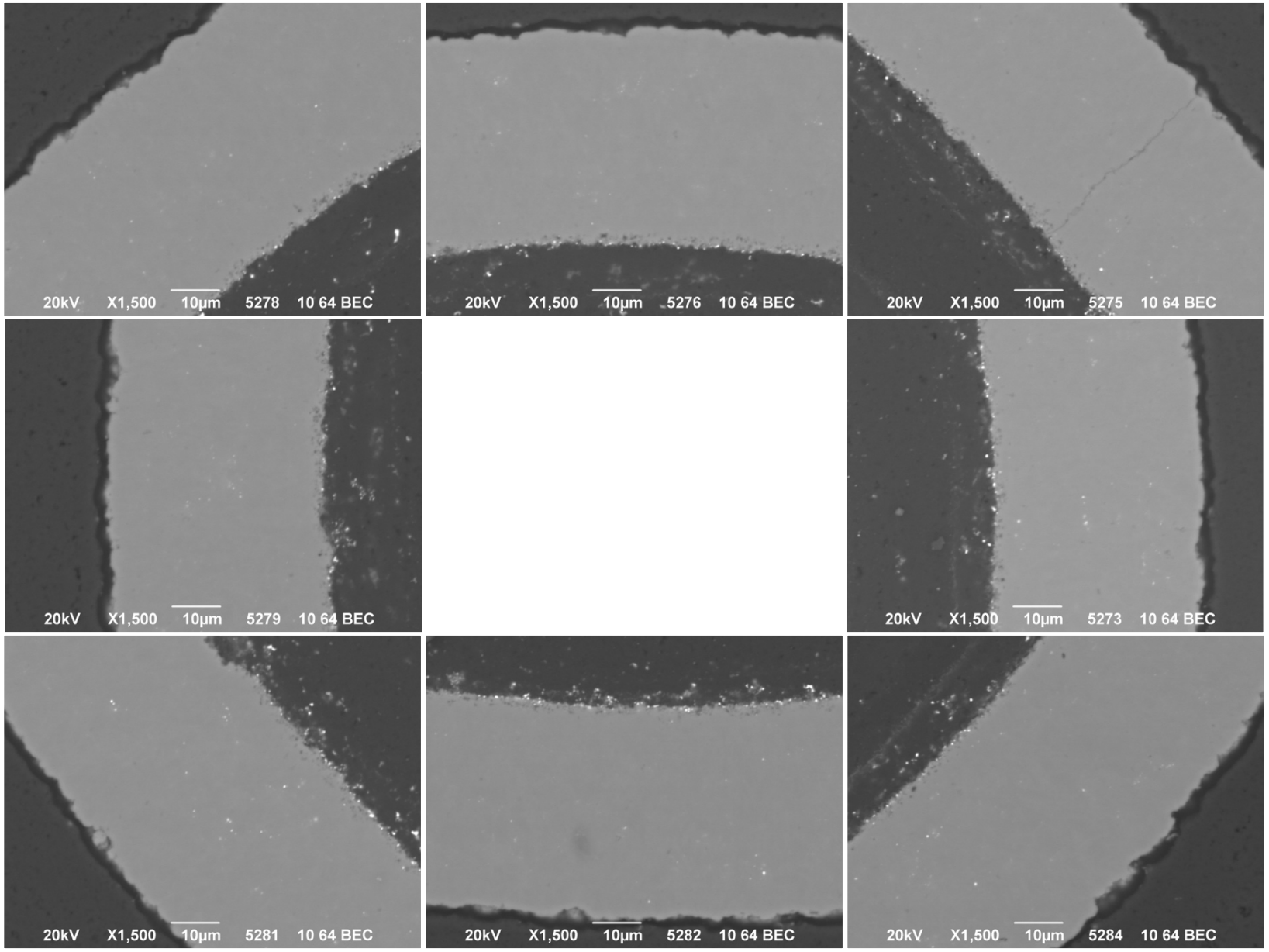

Appendix Figure D-116. 1,500× BEC micrographs of Particle 342-SP09.

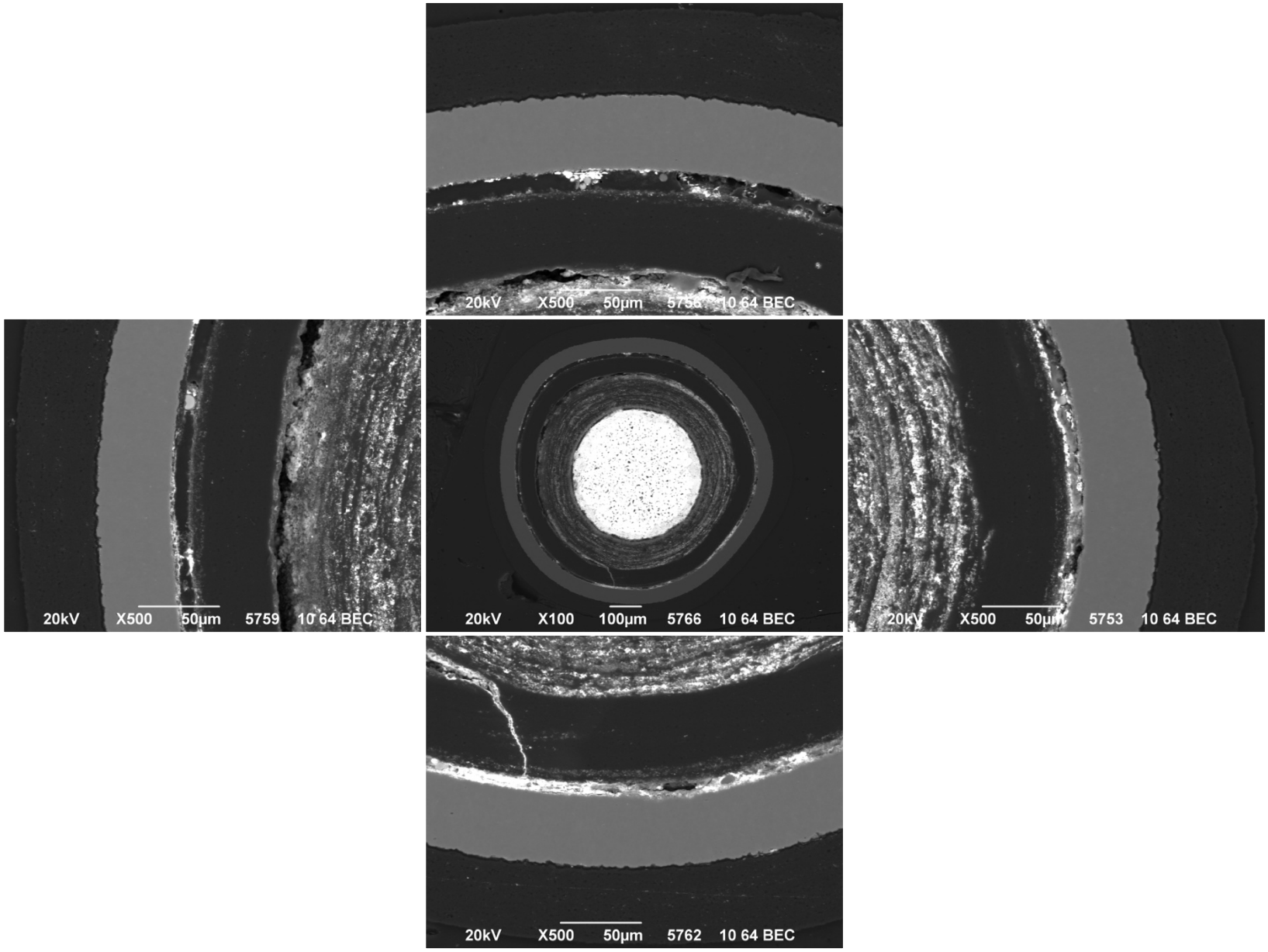

Appendix Figure D-117. 500× BEC micrographs of Particle 342-SP10.

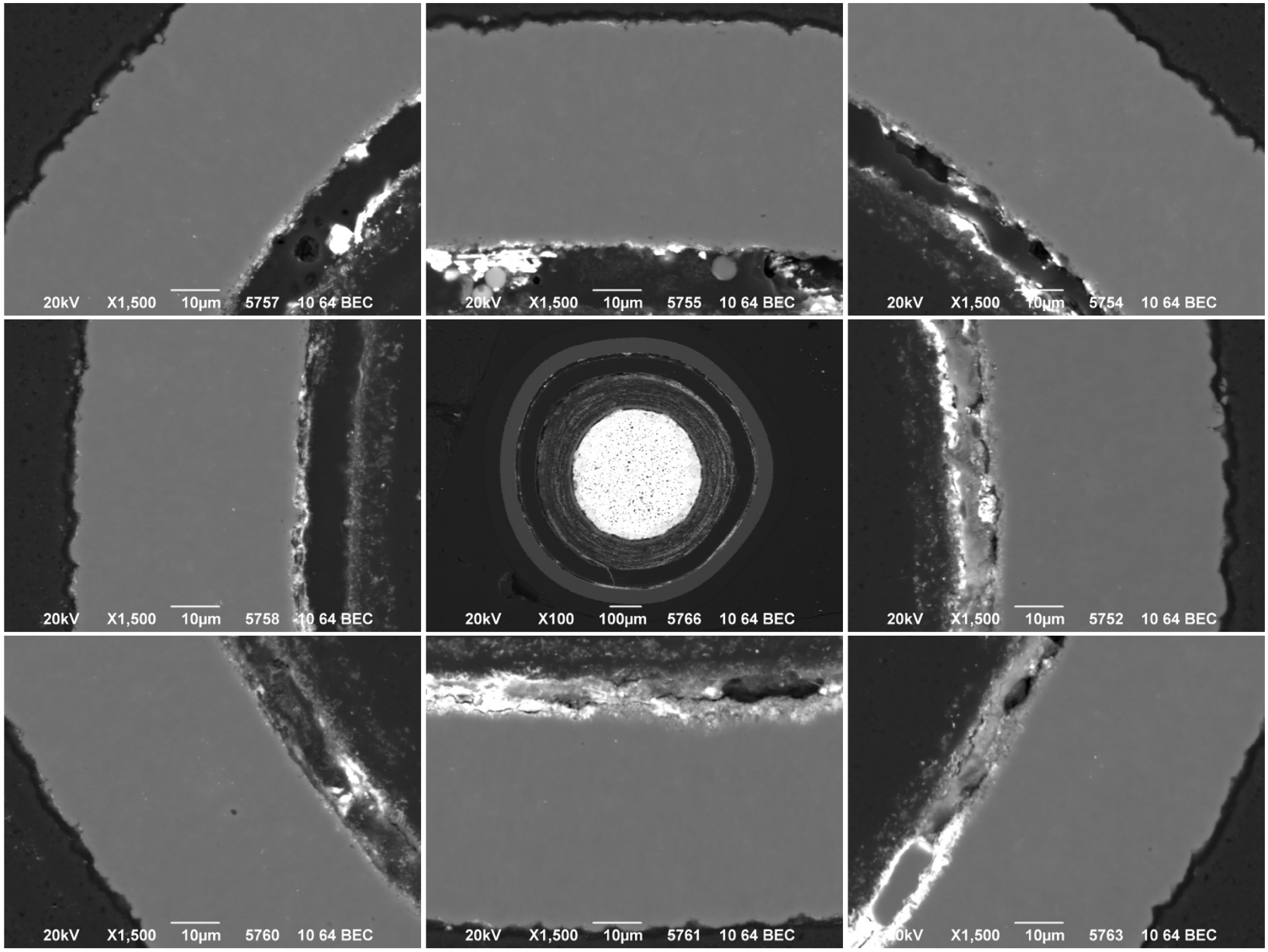

Appendix Figure D-118. 1,500× BEC micrographs of Particle 342-SP10.

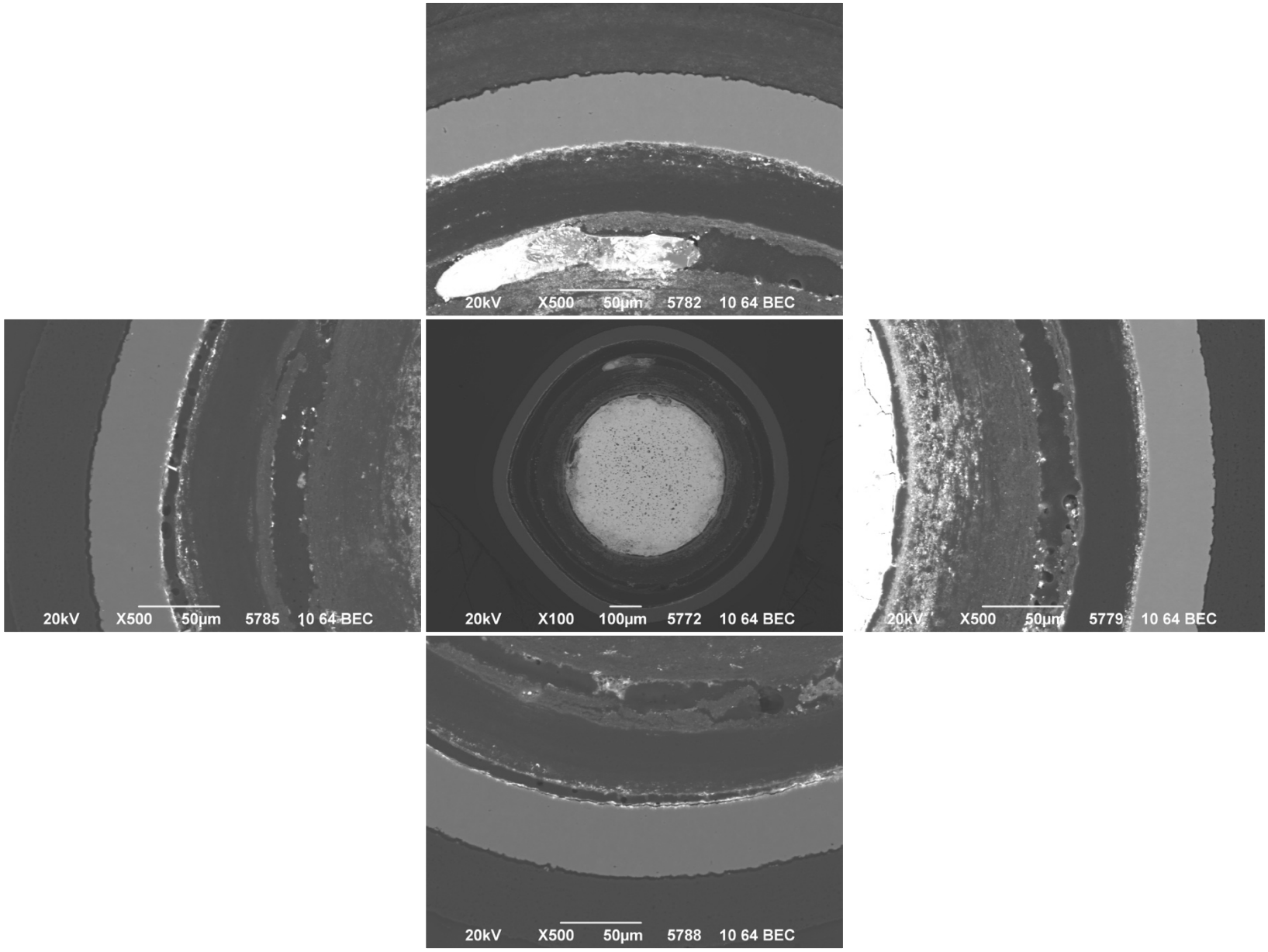

Appendix Figure D-119. 500× BEC micrographs of Particle 342-SP14.

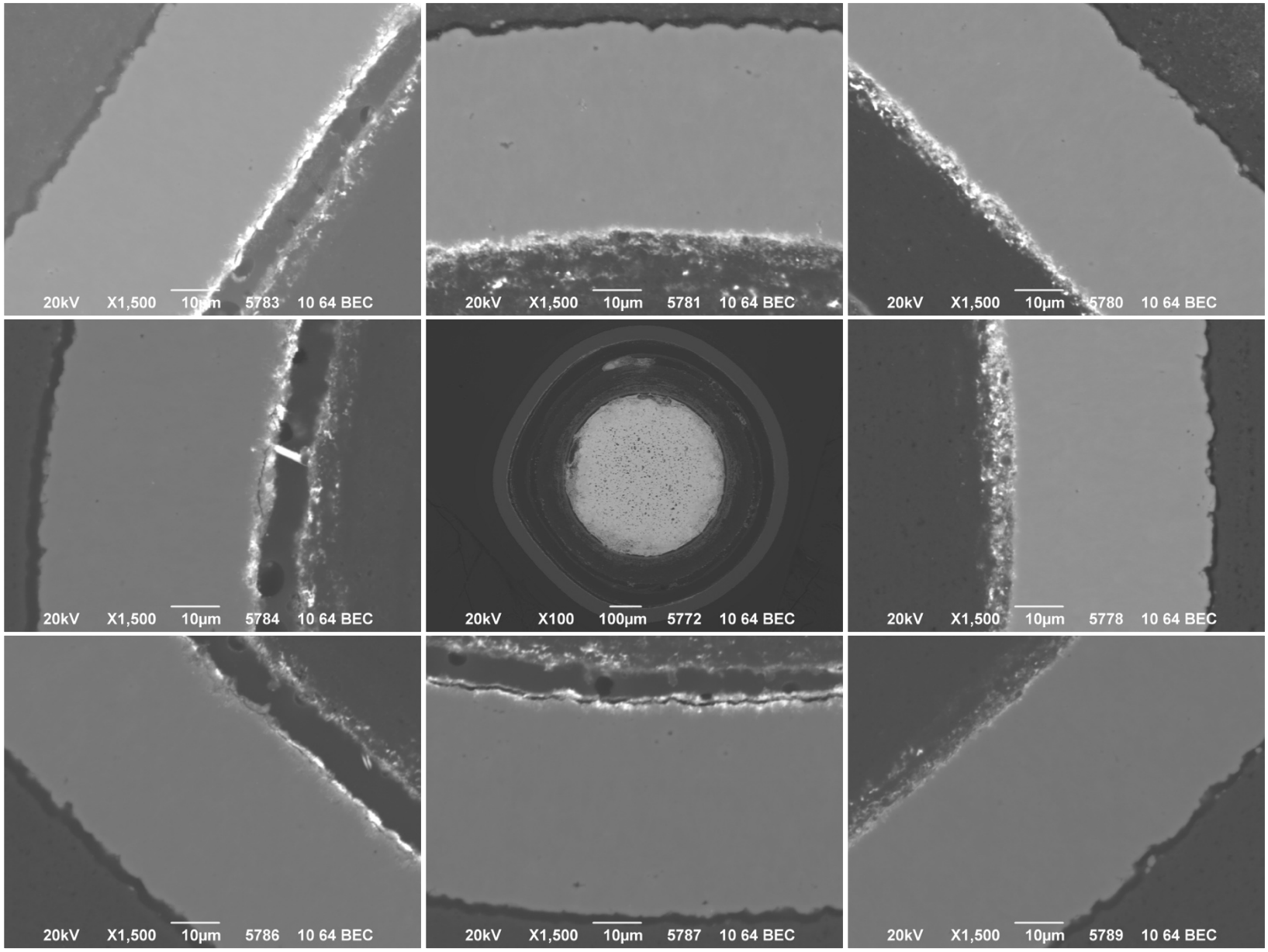

Appendix Figure D-120. 1,500× BEC micrographs of Particle 342-SP14.

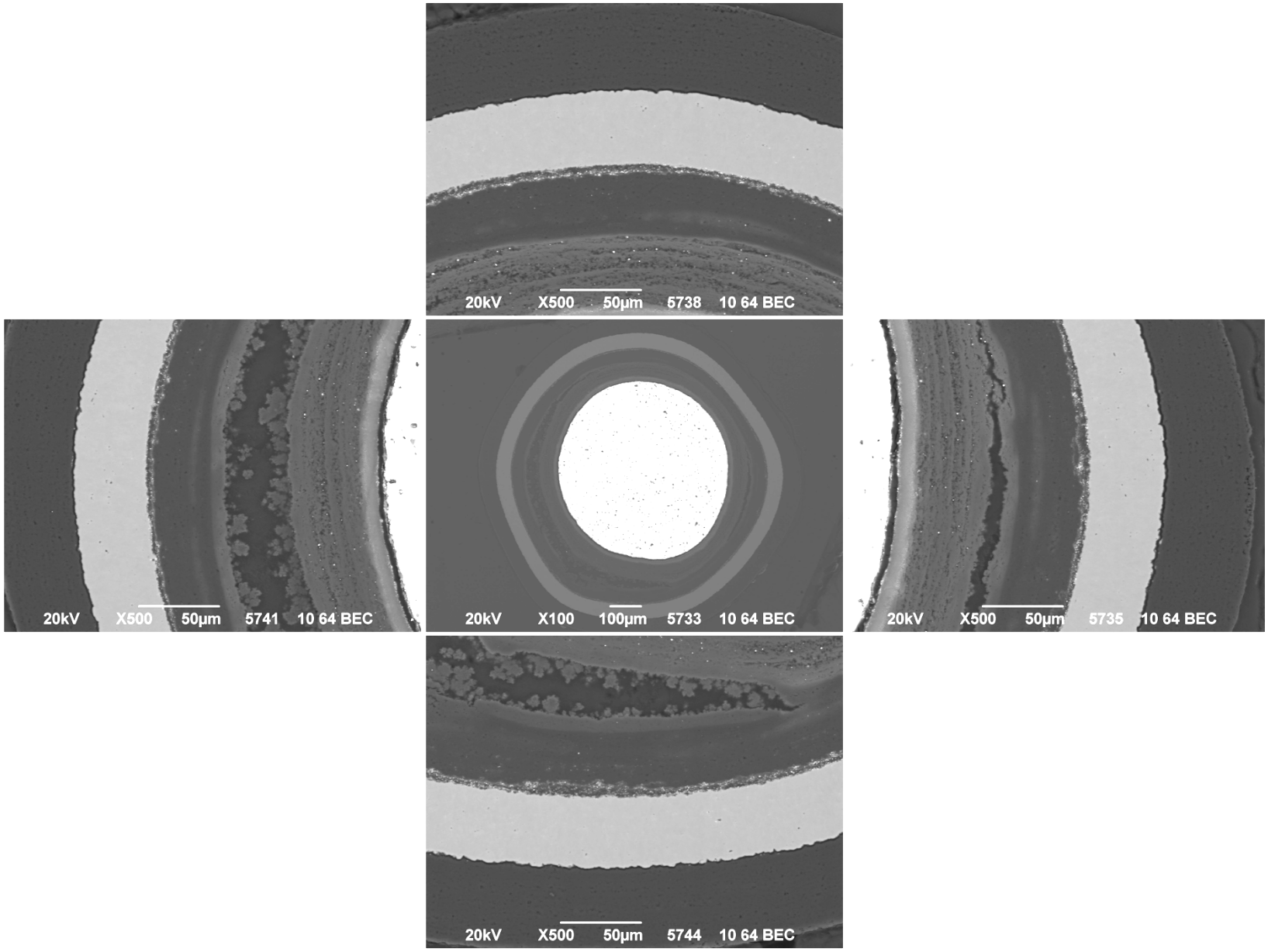

Appendix Figure D-121. 500× BEC micrographs of Particle 342-SP17.

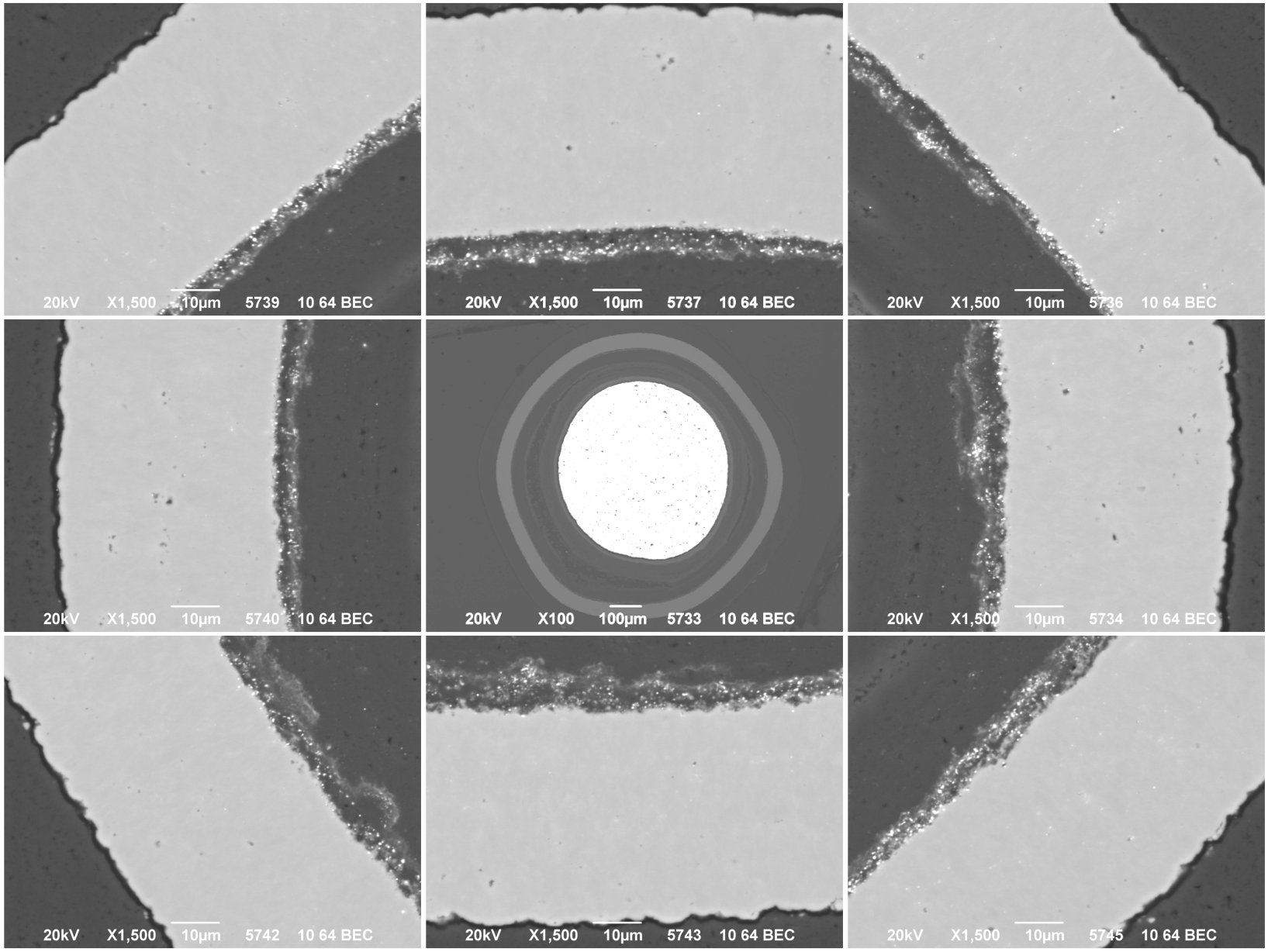

Appendix Figure D-122. 1,500× BEC micrographs of Particle 342-SP17.

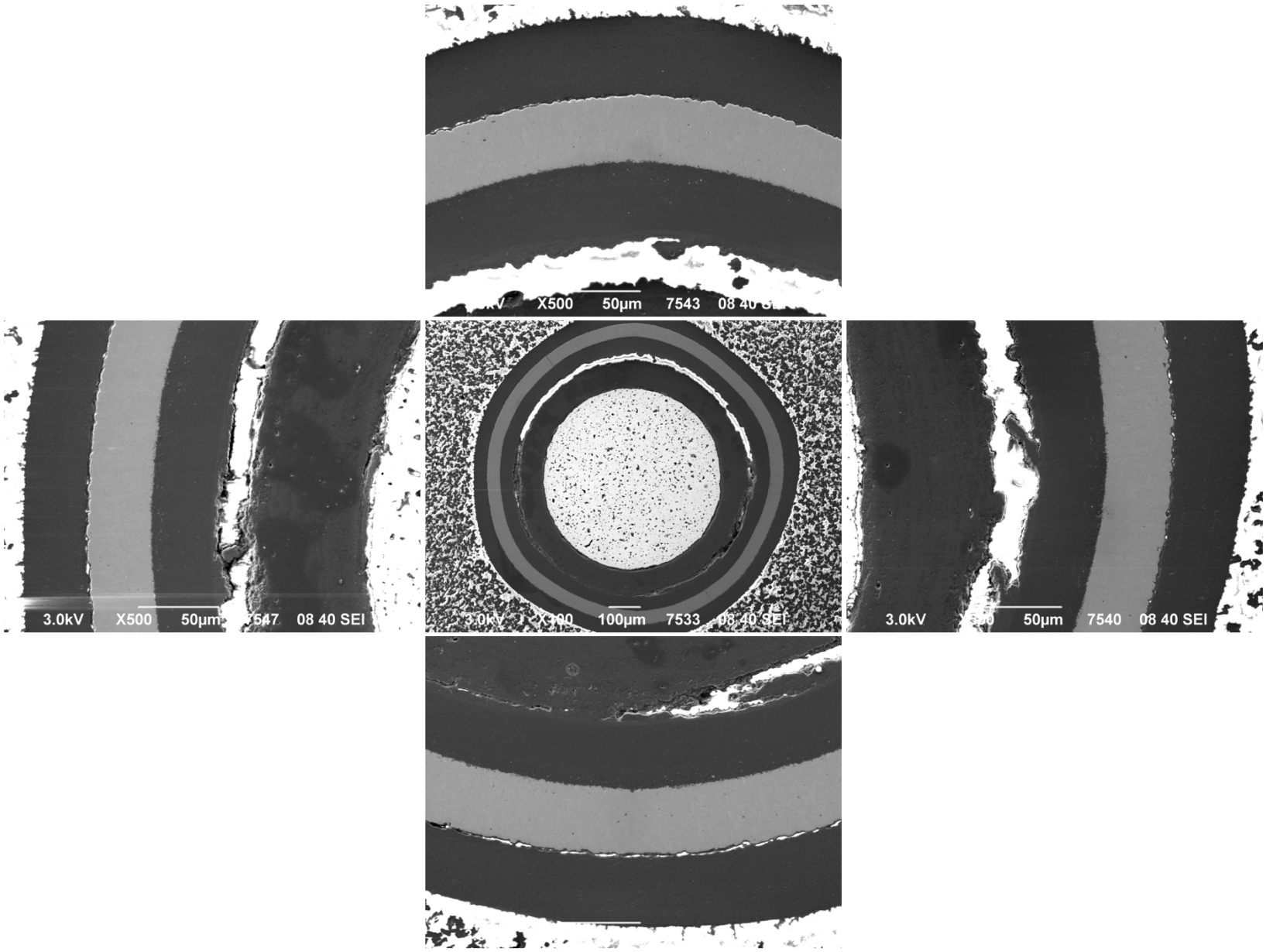

Appendix Figure D-123. 500× SEI micrographs of Particle 341-RS21.

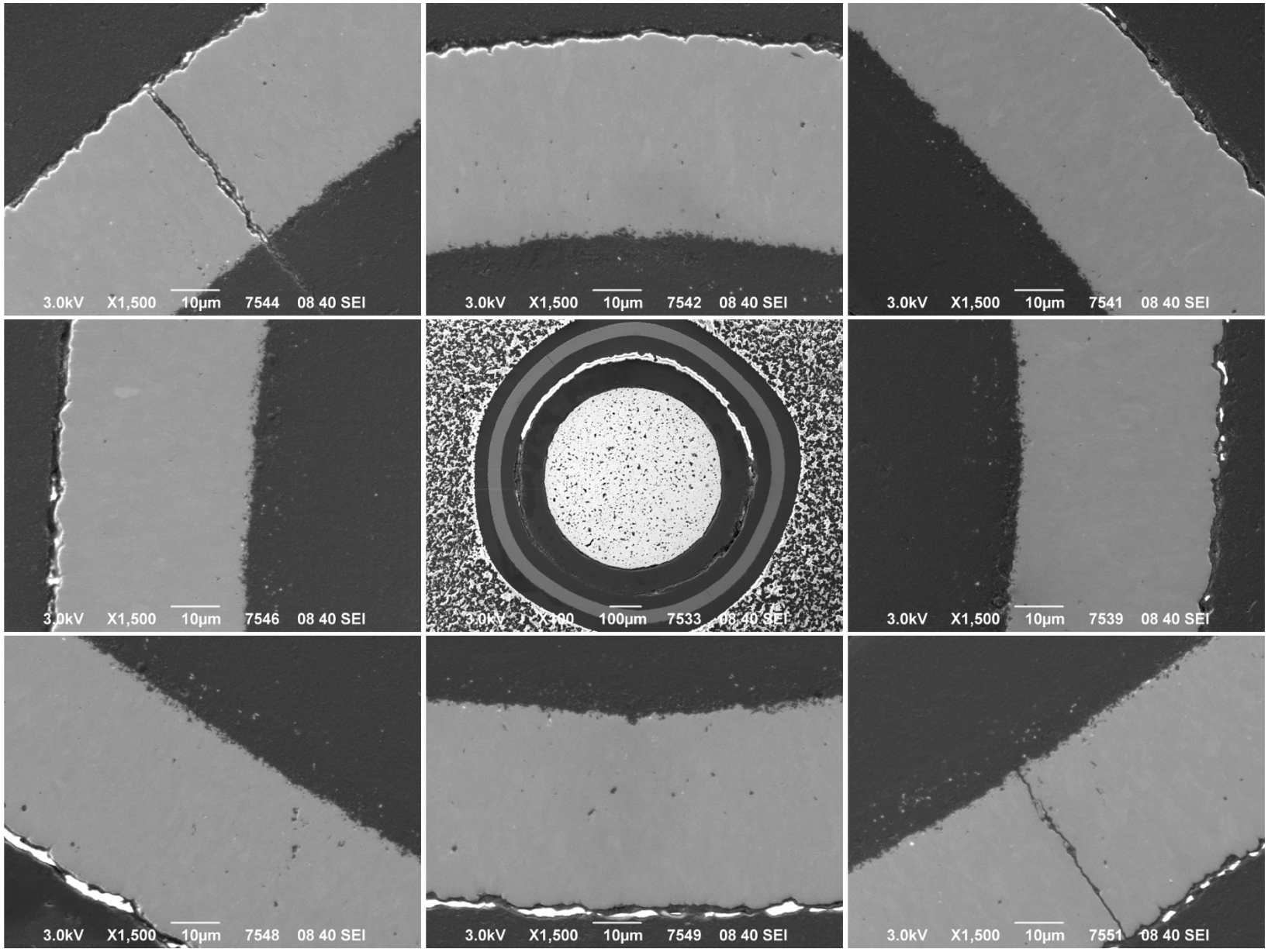

Appendix Figure D-124. 1,500× SEI micrographs of Particle 341-RS21.

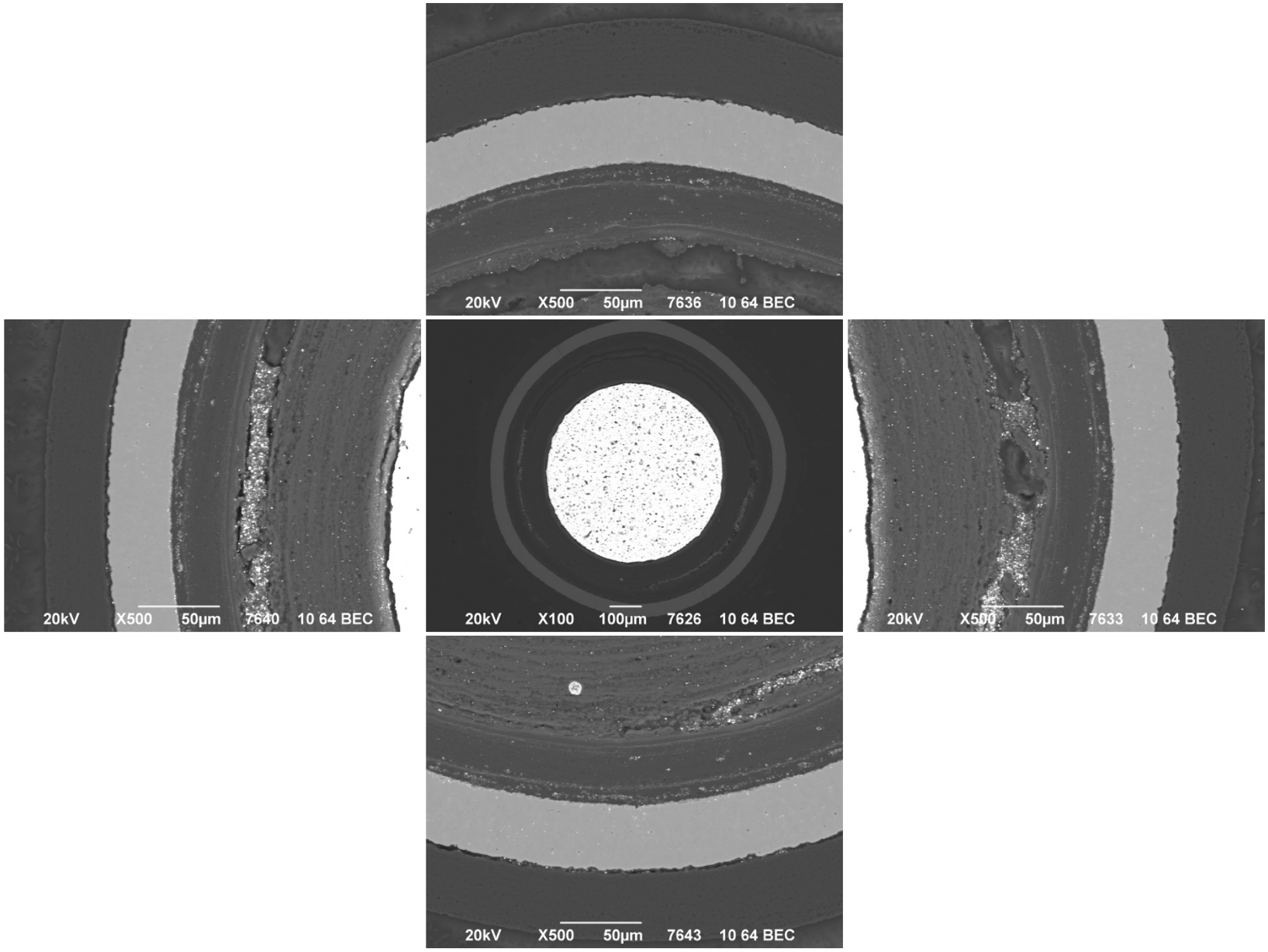

Appendix Figure D-125. 500× BEC micrographs of Particle 341-RS21.

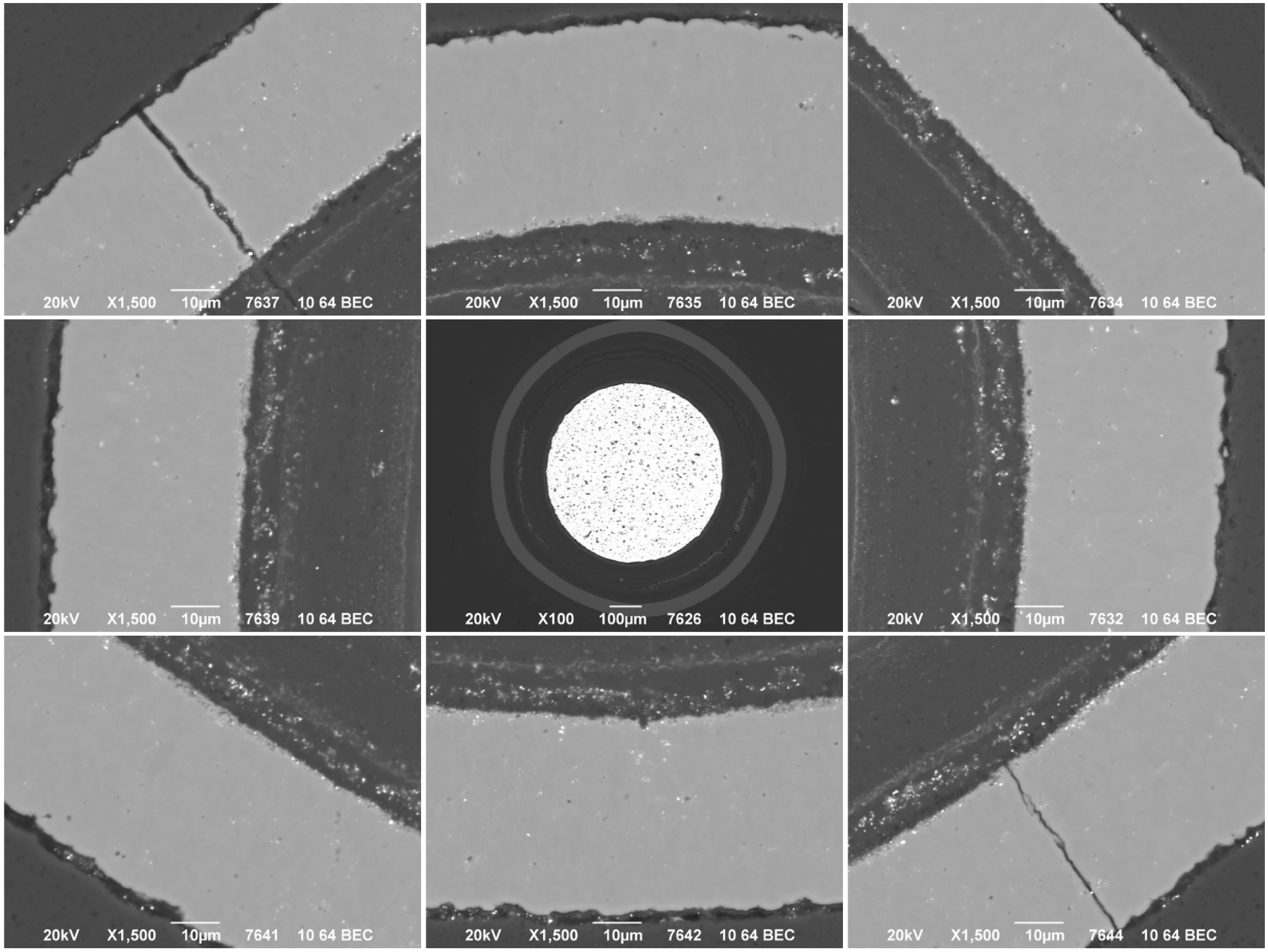

Appendix Figure D-126. 1,500× BEC micrographs of Particle 341-RS21.

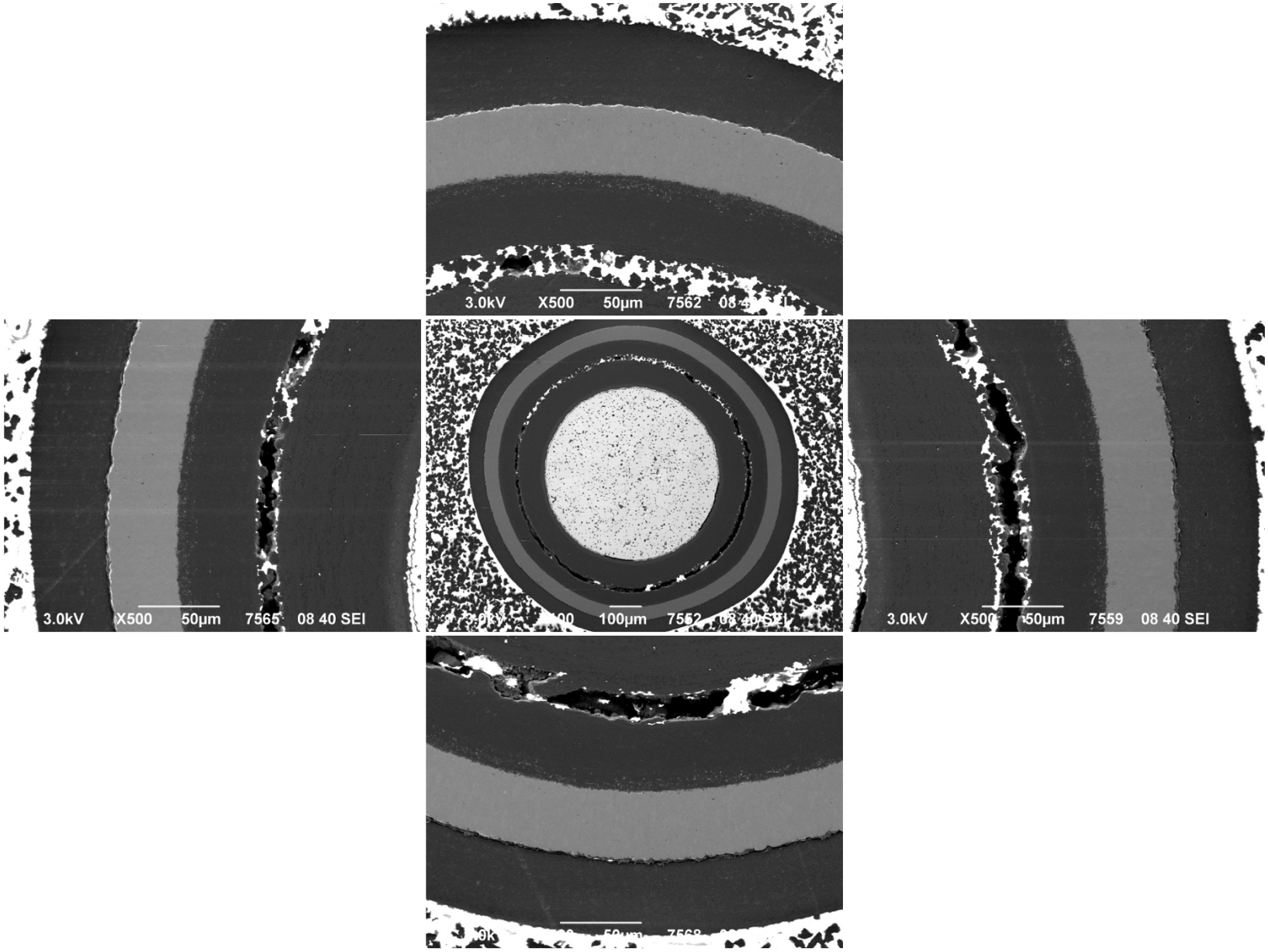

Appendix Figure D-127. 500× SEI micrographs of Particle 341-RS36.

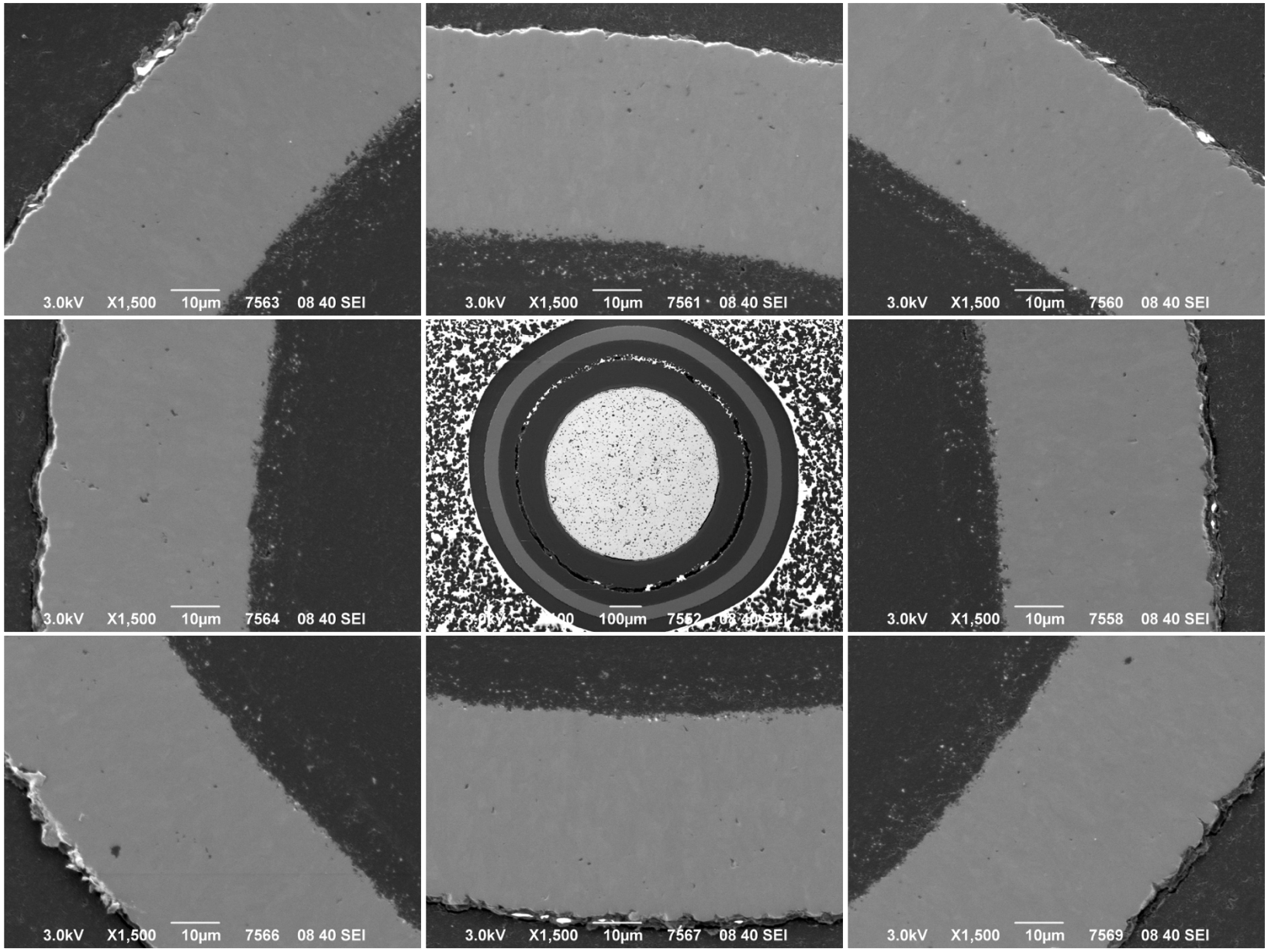

Appendix Figure D-128. 1,500× SEI micrographs of Particle 341-RS36.

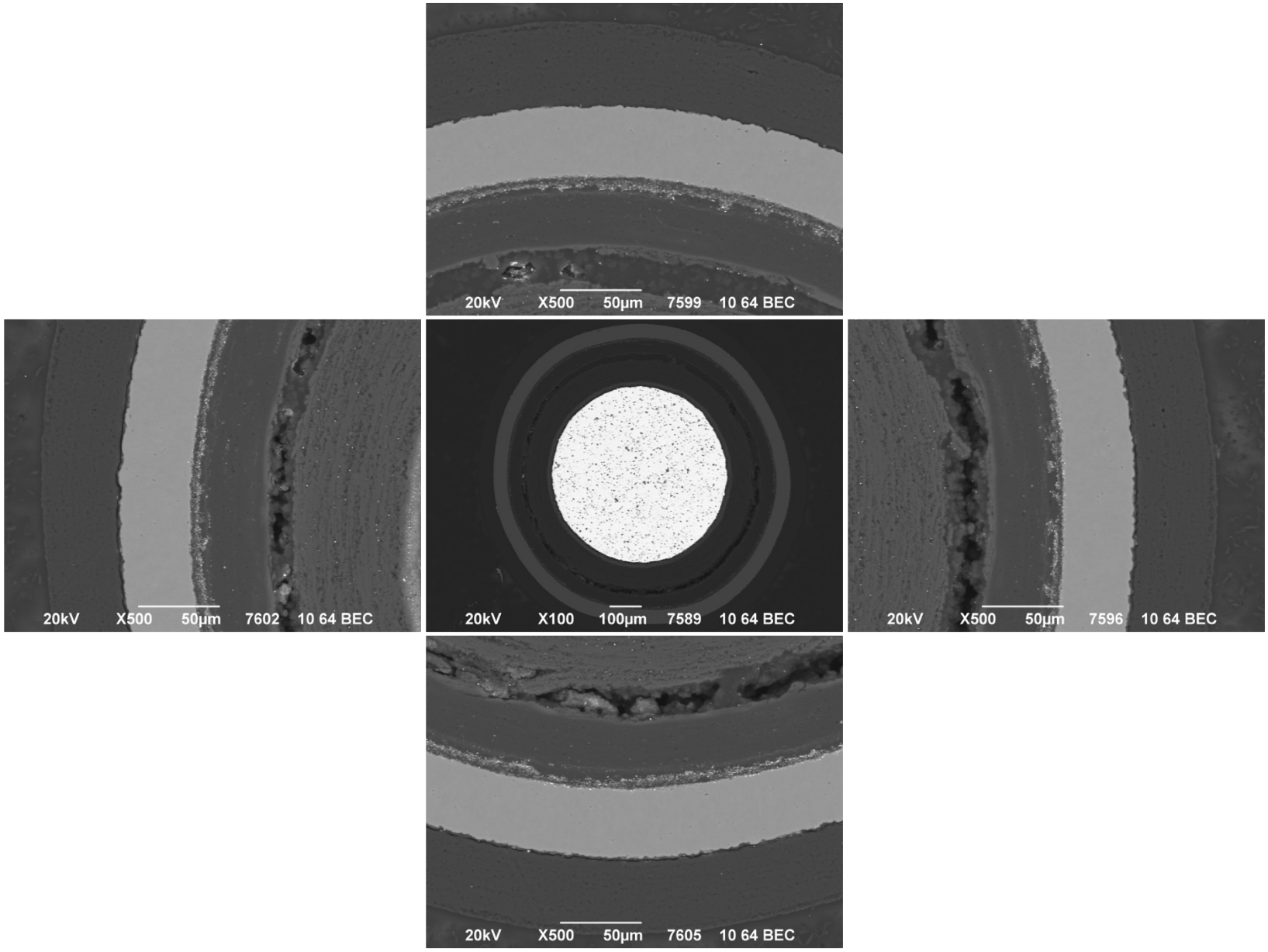

Appendix Figure D-129. 500× BEC micrographs of Particle 341-RS36.

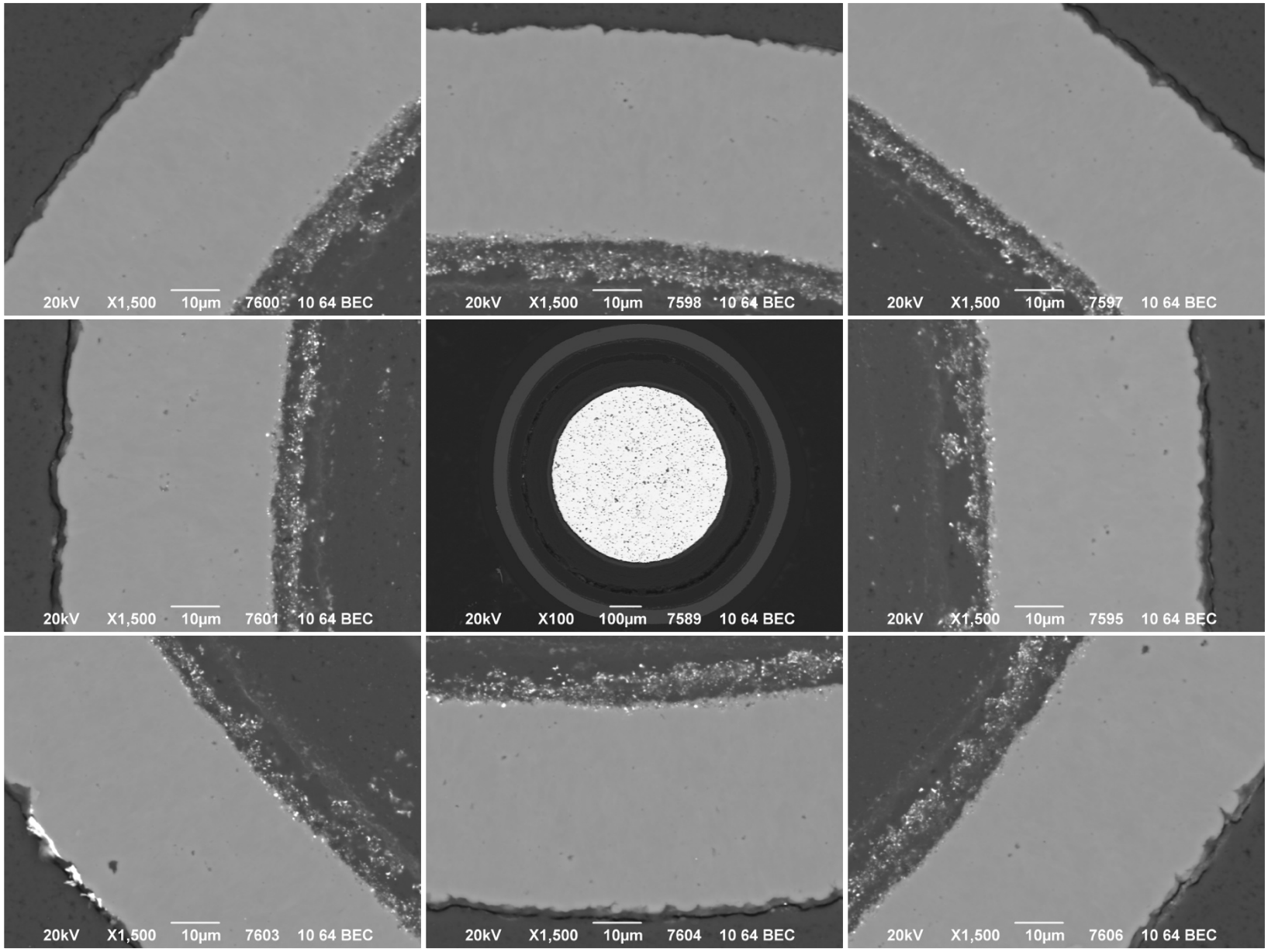

Appendix Figure D-130. 1,500× BEC micrographs of Particle 341-RS36.

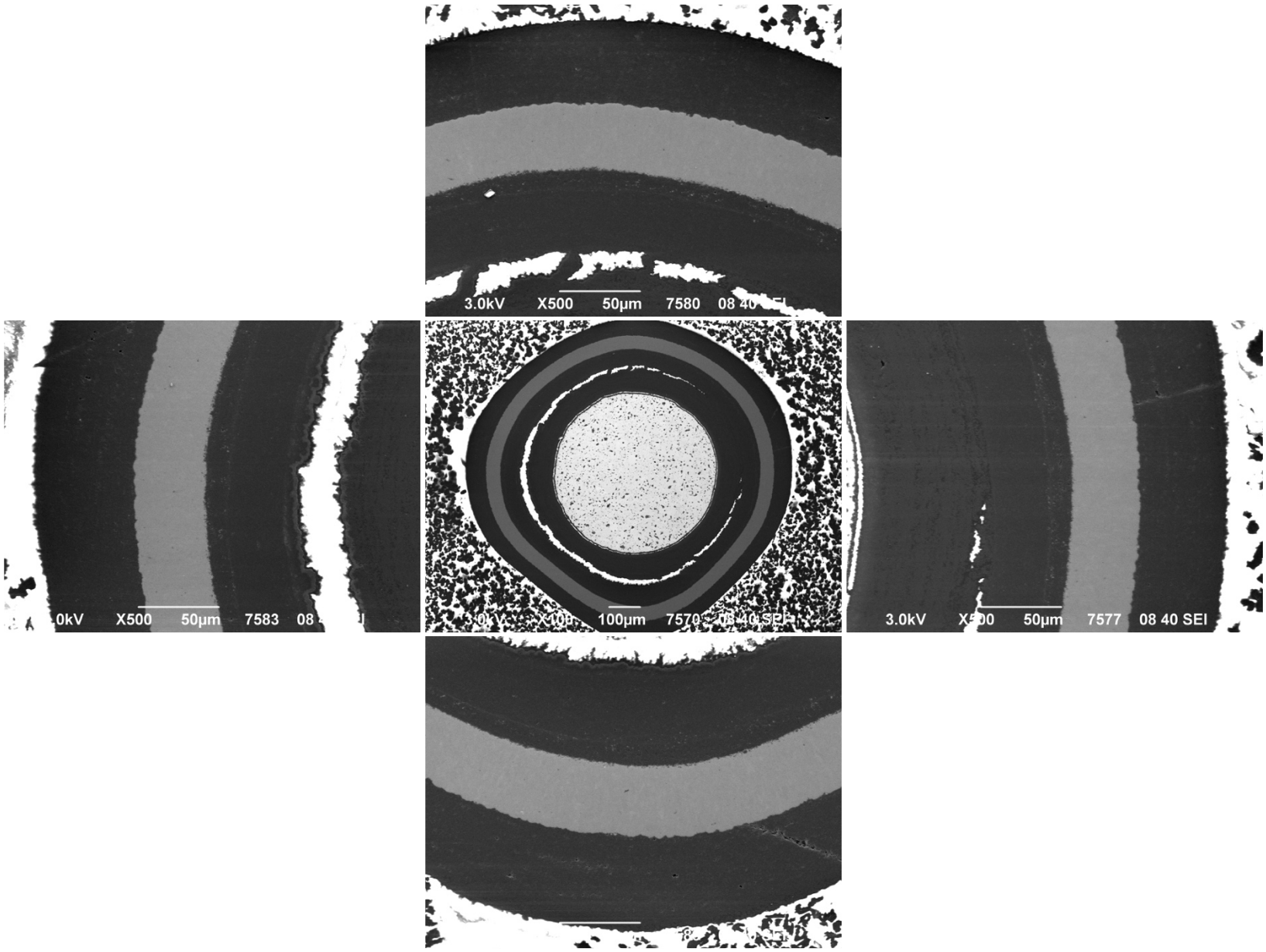

Appendix Figure D-131. 500× SEI micrographs of Particle 341-RS01.

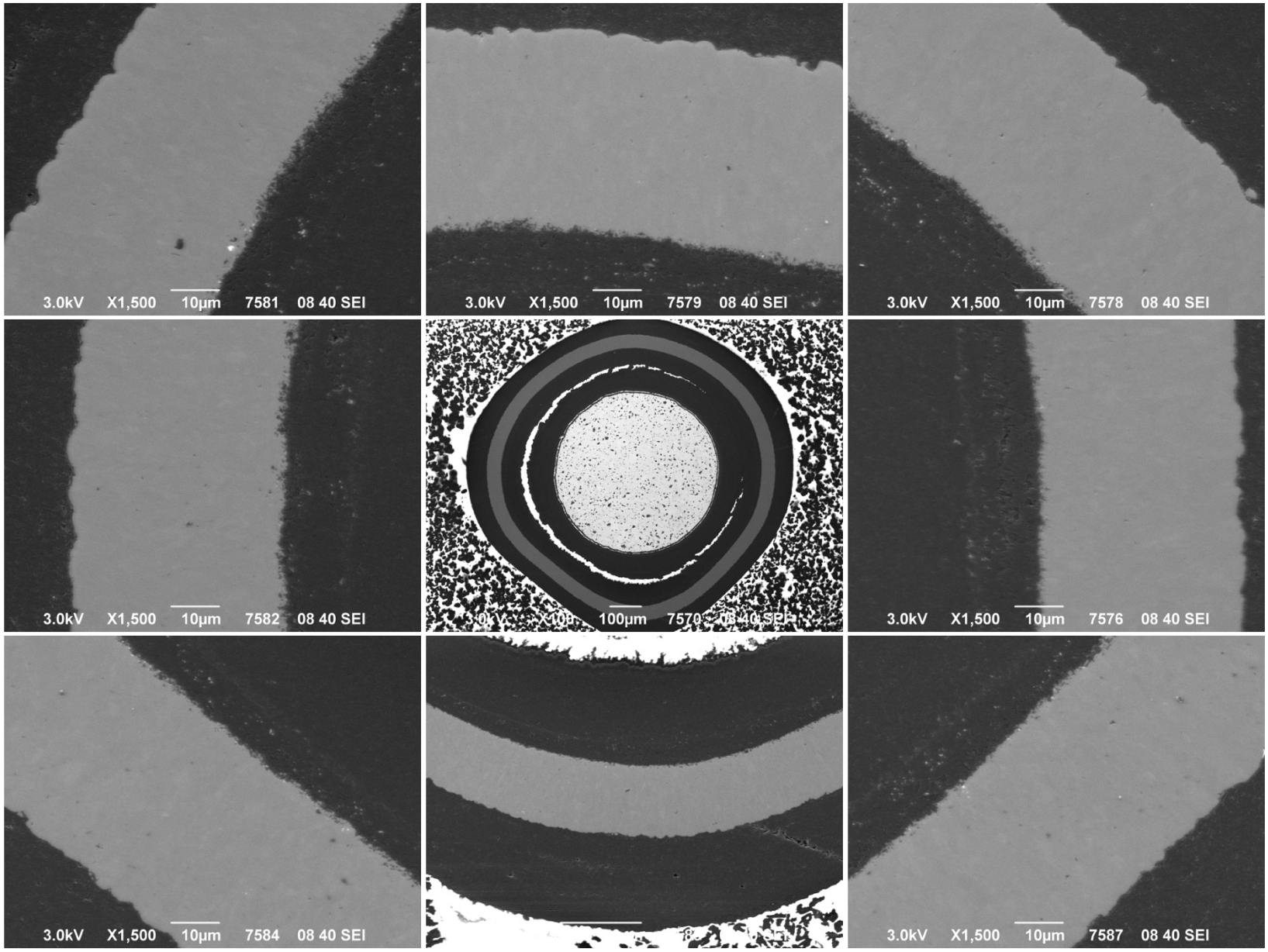

Appendix Figure D-132. 1,500× SEI micrographs of Particle 341-RS01.

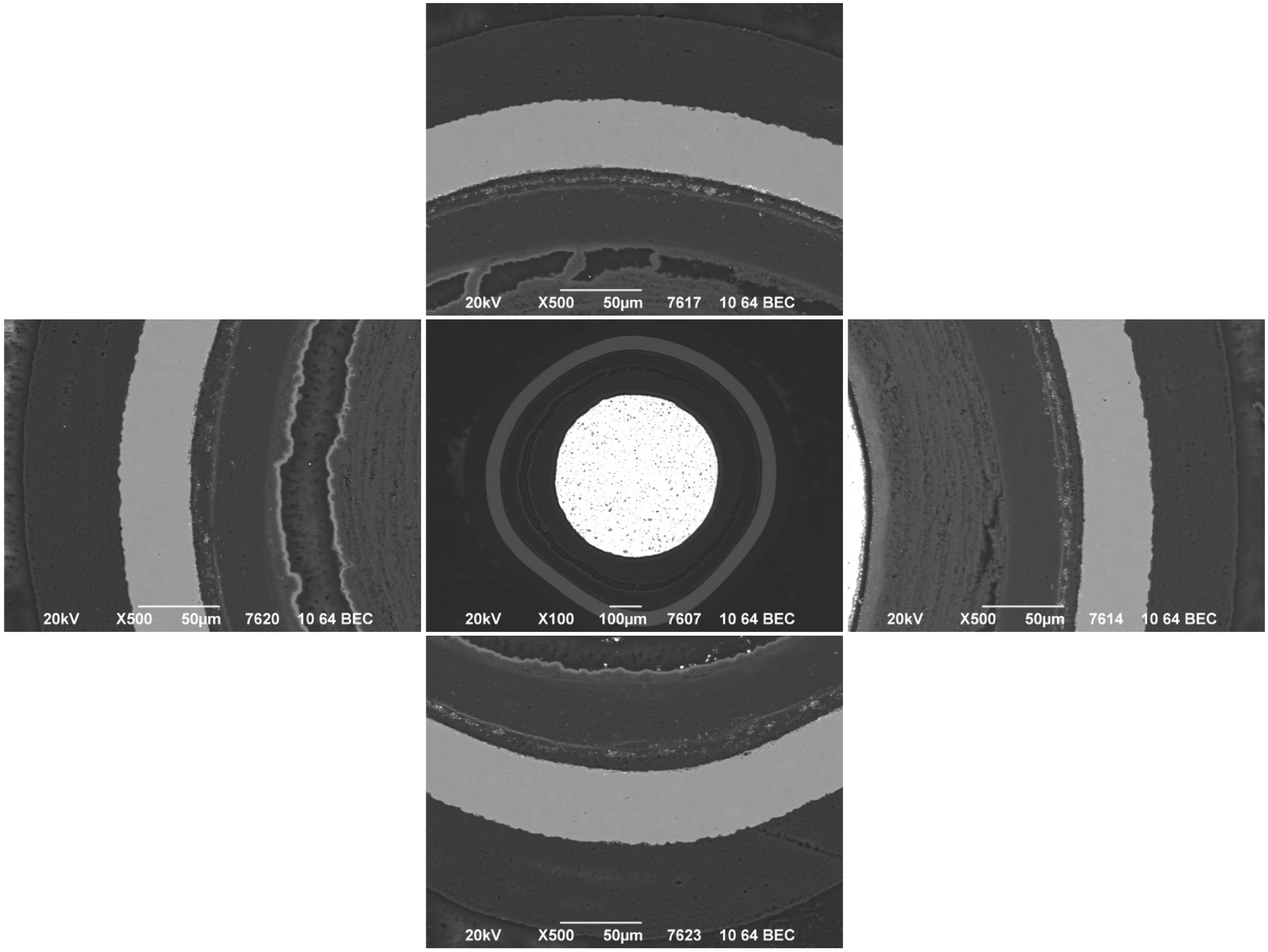

Appendix Figure D-133. 500× BEC micrographs of Particle 341-RS01.

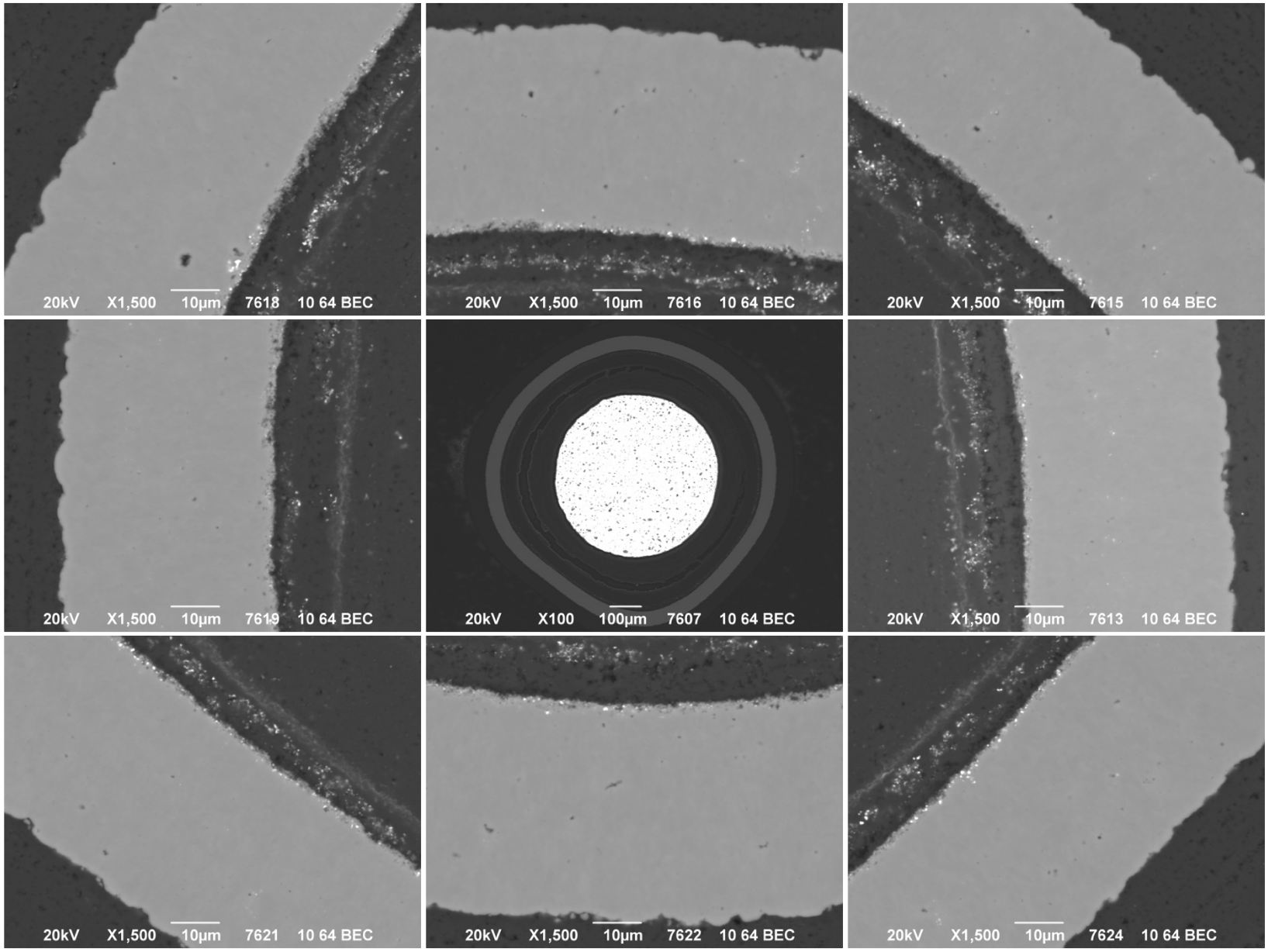

Appendix Figure D-134. 1,500× BEC micrographs of Particle 341-RS01.

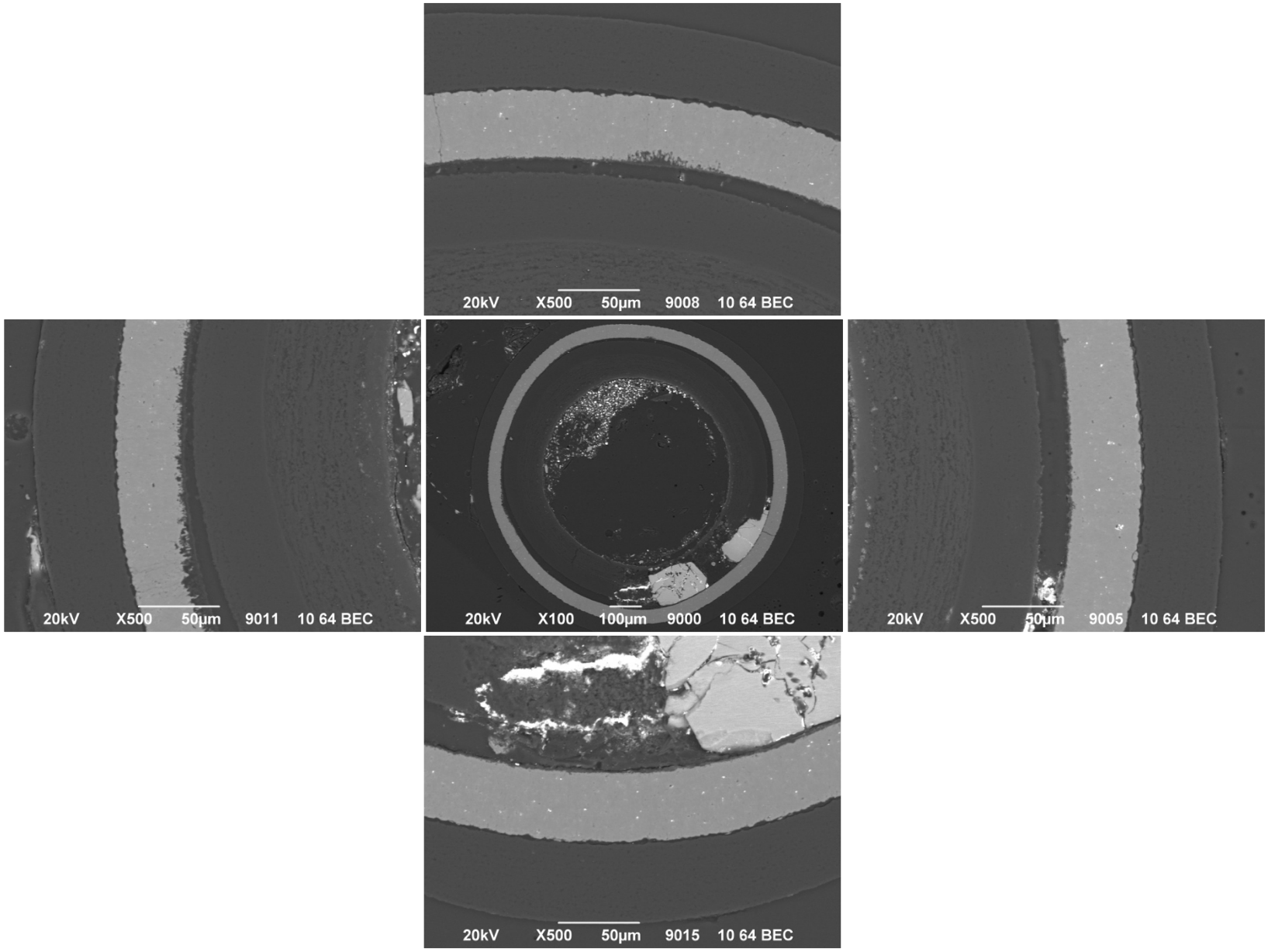

Appendix Figure D-135. 500× BEC micrographs of Particle 341-SP01.

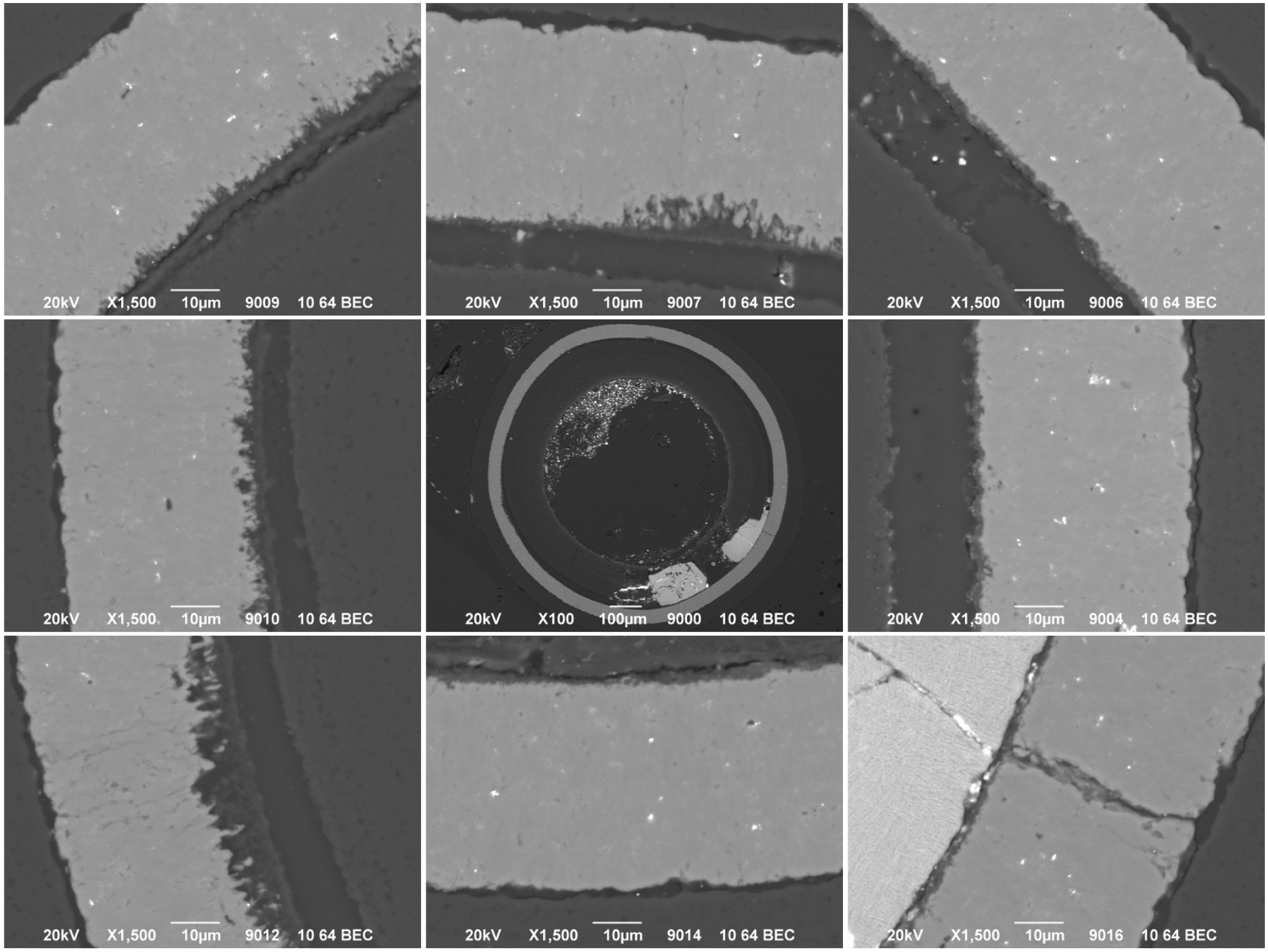

Appendix Figure D-136. 1,500× BEC micrographs of Particle 341-SP01.

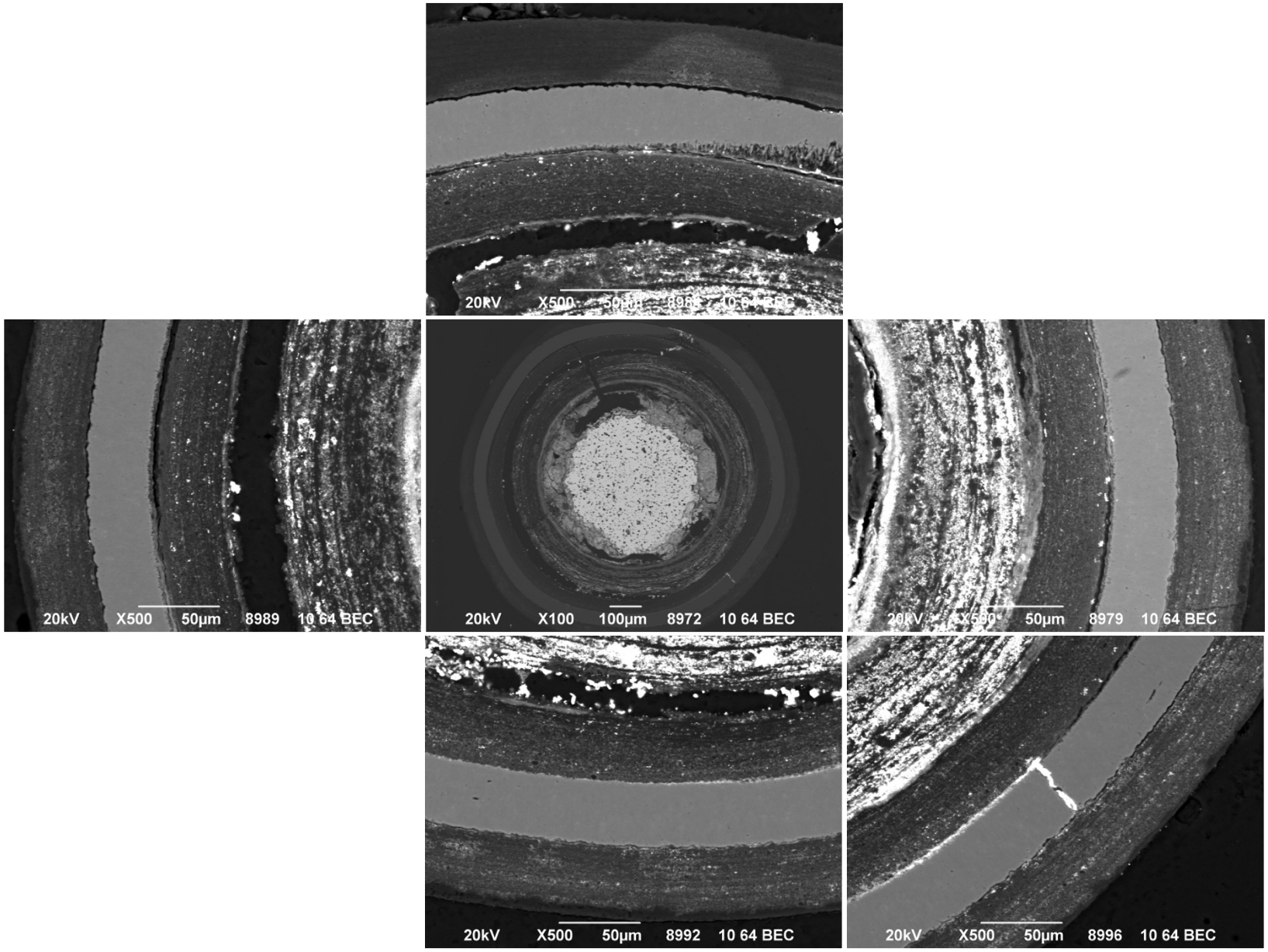

Appendix Figure D-137. 500× BEC micrographs of Particle 341-SP03.

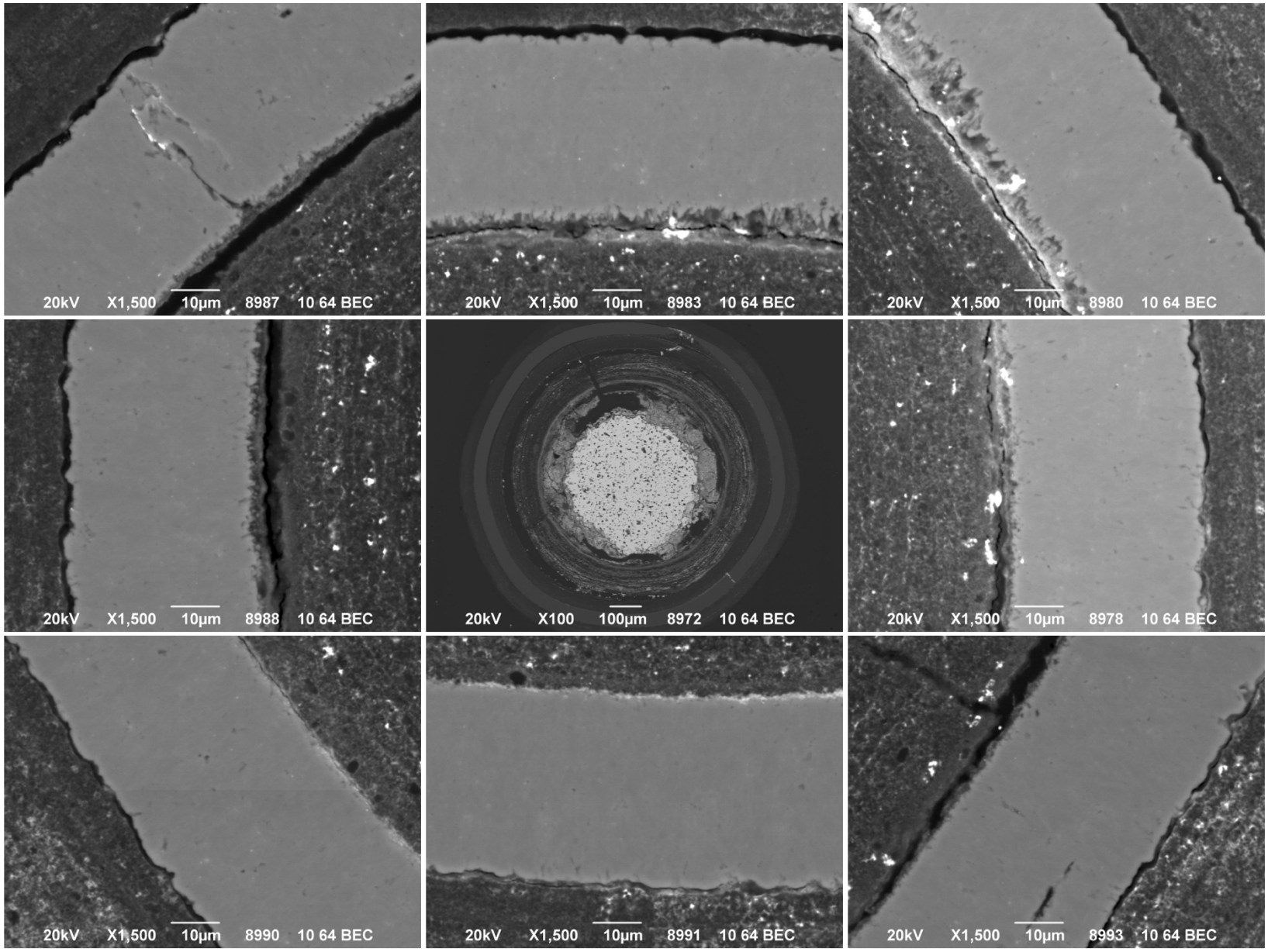

Appendix Figure D-138. 1,500× BEC micrographs of Particle 341-SP03.

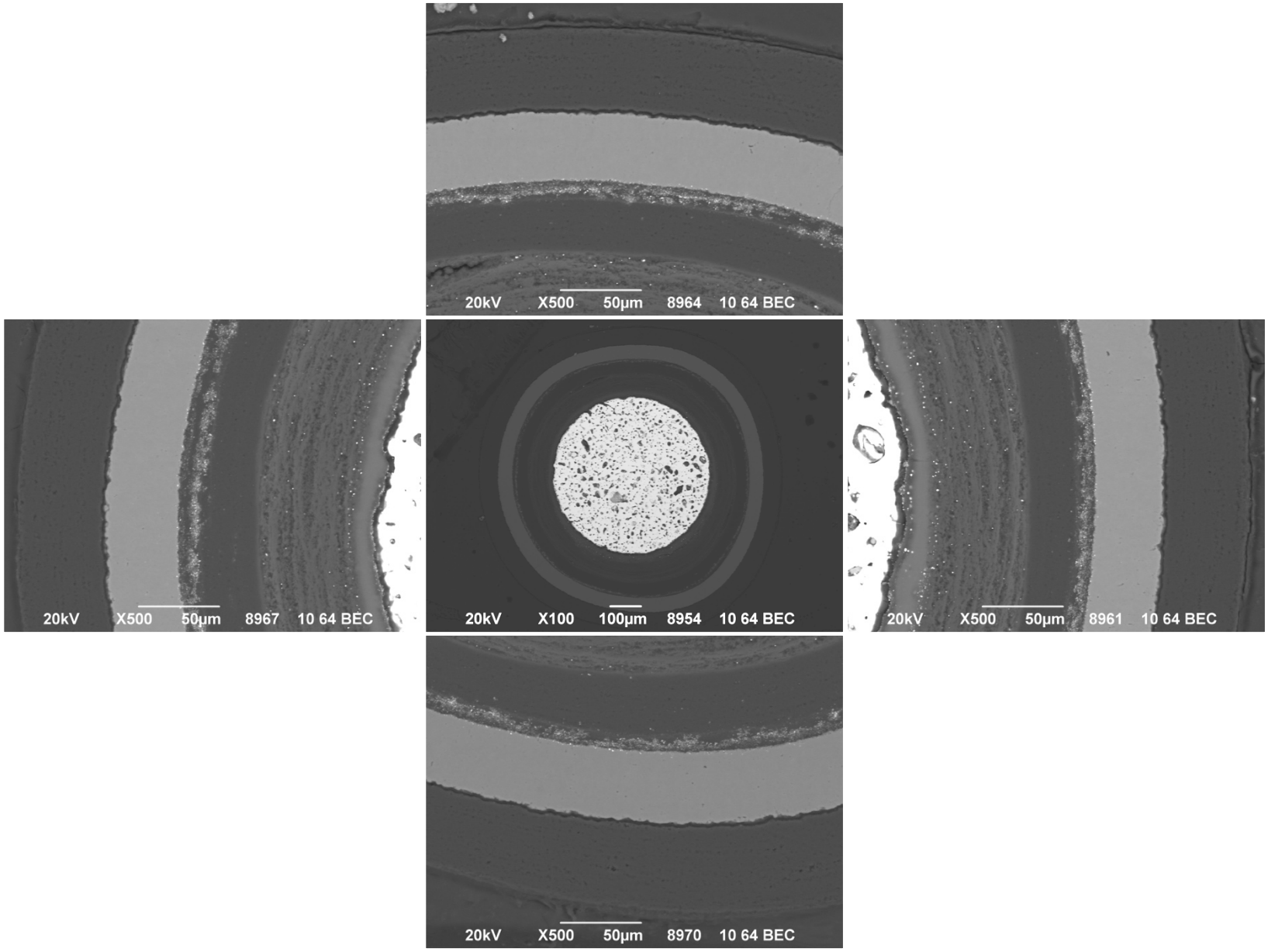

Appendix Figure D-139. 500× BEC micrographs of Particle 341-SP15.

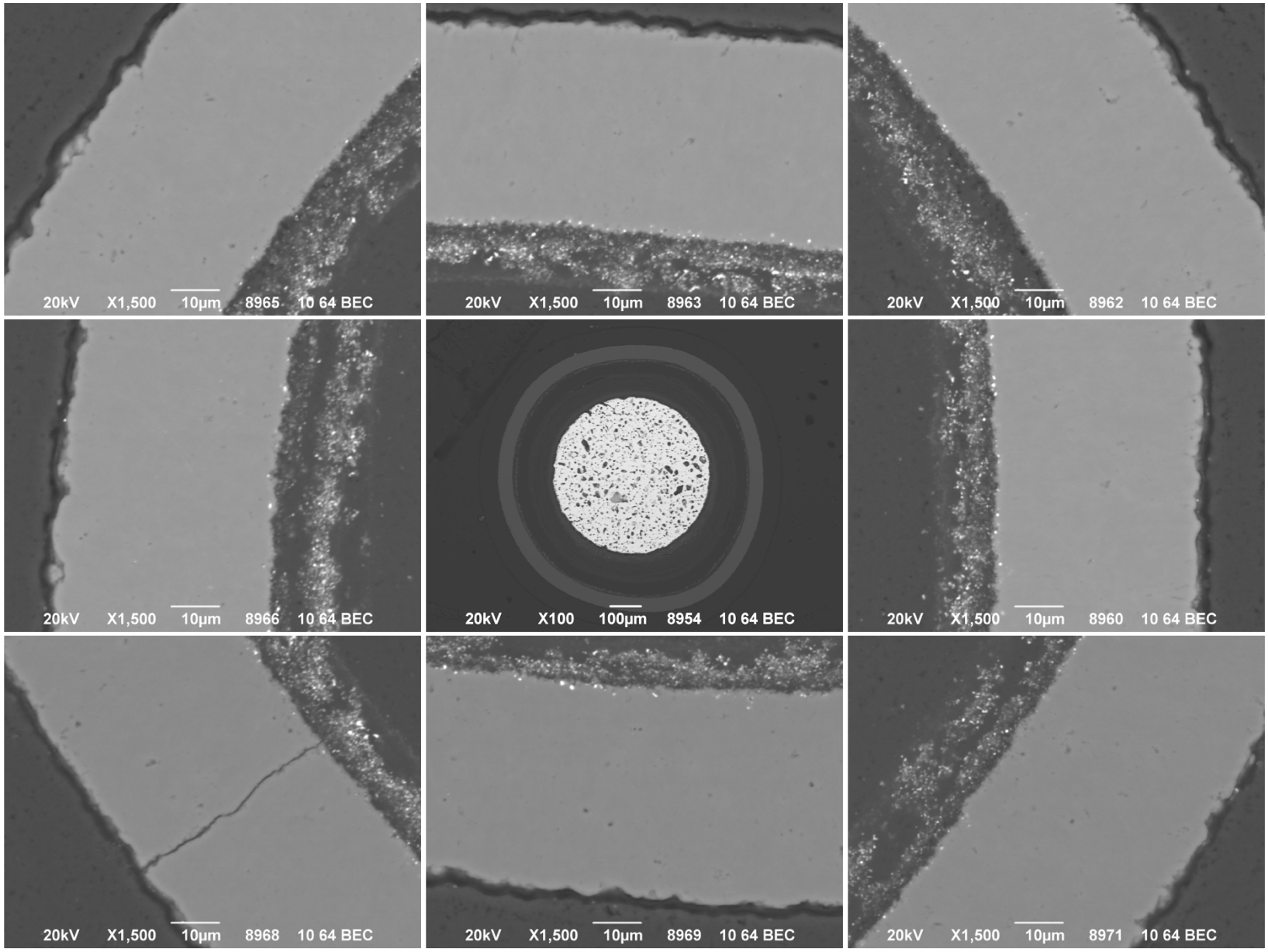

Appendix Figure D-140. 1,500× BEC micrographs of Particle 341-SP15.

APPENDIX E. CALCULATED INVENTORIES

The tables in this appendix provide the calculated inventories for select actinides and fission products (both radioisotopes and stable isotopes) that were used to calculate values reported herein (i.e., compact fraction and M/C as described in Sections 2.1 and 2.2). Calculated inventories were estimated via physics depletion calculations using the Oak Ridge Isotope Generation and Depletion (ORIGEN2) code (Croff 1983; Ludwig and Croff 2002), the Monte Carlo N-Particle Transport (MCNP) code (X-5 Monte Carlo Team 2003), and Jim Sterbentz's MCNP-ORIGEN2 coupled utility program (JMOCUP) and software extraction modules (Sterbentz 2014).

Appendix Table E-1. Calculated inventories of select actinides one year after EOL

Compact	Value	^{235}U	^{236}U	^{238}U	^{239}Pu	^{240}Pu
AGR-2 3-1-2	moles/compact	4.307E-05	5.576E-05	3.559E-03	3.743E-05	1.828E-05
AGR-2 3-1-2	µg/compact	1.012E+04	1.316E+04	8.472E+05	8.948E+03	4.388E+03
AGR-2 3-3-1	moles/compact	4.568E-05	5.574E-05	3.567E-03	3.608E-05	1.842E-05
AGR-2 3-3-1	µg/compact	1.074E+04	1.316E+04	8.491E+05	8.625E+03	4.422E+03
AGR-2 3-1-1	moles/compact	4.407E-05	5.562E-05	3.562E-03	3.731E-05	1.829E-05
AGR-2 3-1-1	µg/compact	1.036E+04	1.313E+04	8.479E+05	8.919E+03	4.391E+03
AGR-2 3-3-2	moles/compact	4.495E-05	5.588E-05	3.564E-03	3.607E-05	1.848E-05
AGR-2 3-3-2	µg/compact	1.057E+04	1.319E+04	8.484E+05	8.623E+03	4.436E+03
AGR-2 3-4-2	moles/compact	4.220E-05	5.584E-05	3.558E-03	3.749E-05	1.874E-05
AGR-2 3-4-2	µg/compact	9.919E+03	1.318E+04	8.470E+05	8.962E+03	4.499E+03
AGR-2 3-4-1	moles/compact	4.283E-05	5.574E-05	3.561E-03	3.742E-05	1.849E-05
AGR-2 3-4-1	µg/compact	1.007E+04	1.316E+04	8.477E+05	8.945E+03	4.439E+03

Appendix Table E-2. Calculated inventories of select actinides one year after EOL

Compact	Value	^{105}Pd	^{109}Ag	^{133}Cs	^{139}La	^{140}Ce
AGR-2 3-1-2	moles/compact	8.313E-06	1.837E-06	2.645E-05	2.748E-05	2.731E-05
AGR-2 3-1-2	µg/compact	8.721E+02	2.001E+02	3.515E+03	3.817E+03	3.821E+03
AGR-2 3-3-1	moles/compact	8.077E-06	1.774E-06	2.611E-05	2.702E-05	2.682E-05
AGR-2 3-3-1	µg/compact	8.473E+02	1.932E+02	3.470E+03	3.753E+03	3.752E+03
AGR-2 3-1-1	moles/compact	8.232E-06	1.810E-06	2.628E-05	2.731E-05	2.712E-05
AGR-2 3-1-1	µg/compact	8.636E+02	1.971E+02	3.493E+03	3.794E+03	3.794E+03
AGR-2 3-3-2	moles/compact	8.150E-06	1.798E-06	2.625E-05	2.717E-05	2.698E-05
AGR-2 3-3-2	µg/compact	8.550E+02	1.958E+02	3.489E+03	3.774E+03	3.775E+03
AGR-2 3-4-2	moles/compact	8.368E-06	1.852E-06	2.656E-05	2.762E-05	2.746E-05
AGR-2 3-4-2	µg/compact	8.778E+02	2.017E+02	3.530E+03	3.837E+03	3.842E+03
AGR-2 3-4-1	moles/compact	8.290E-06	1.830E-06	2.642E-05	2.747E-05	2.729E-05
AGR-2 3-4-1	µg/compact	8.697E+02	1.993E+02	3.511E+03	3.816E+03	3.818E+03

Appendix Table E-2. Calculated inventories of select actinides one year after EOL

Compact	Value	^{141}Pr	^{146}Nd	^{152}Sm	^{153}Eu	^{156}Gd
AGR-2 3-1-2	moles/compact	2.505E-05	1.712E-05	2.735E-06	2.080E-06	1.541E-06
AGR-2 3-1-2	µg/compact	3.530E+03	2.498E+03	4.155E+02	3.181E+02	2.403E+02
AGR-2 3-3-1	moles/compact	2.462E-05	1.678E-05	2.718E-06	2.010E-06	1.454E-06
AGR-2 3-3-1	µg/compact	3.469E+03	2.448E+03	4.129E+02	3.074E+02	2.267E+02
AGR-2 3-1-1	moles/compact	2.489E-05	1.699E-05	2.720E-06	2.058E-06	1.508E-06
AGR-2 3-1-1	µg/compact	3.507E+03	2.479E+03	4.132E+02	3.147E+02	2.351E+02
AGR-2 3-3-2	moles/compact	2.475E-05	1.687E-05	2.732E-06	2.030E-06	1.480E-06
AGR-2 3-3-2	µg/compact	3.487E+03	2.462E+03	4.150E+02	3.104E+02	2.308E+02
AGR-2 3-4-2	moles/compact	2.517E-05	1.723E-05	2.756E-06	2.090E-06	1.566E-06
AGR-2 3-4-2	µg/compact	3.547E+03	2.514E+03	4.187E+02	3.196E+02	2.442E+02
AGR-2 3-4-1	moles/compact	2.503E-05	1.713E-05	2.740E-06	2.072E-06	1.538E-06
AGR-2 3-4-1	µg/compact	3.527E+03	2.499E+03	4.163E+02	3.169E+02	2.398E+02

Appendix Table E-3. Calculated inventories of select radioactive fission products one day after EOL

Compact	Value	^{85}Kr	^{90}Sr	^{106}Ru	^{110m}Ag	^{125}Sb
AGR-2 3-1-2	moles/compact	8.756E-07	1.941E-05	3.384E-06	1.131E-08	1.951E-07
AGR-2 3-1-2	Bq/compact	1.077E+09	8.918E+09	4.397E+10	2.188E+08	9.355E+08
AGR-2 3-1-2	Bq/particle	6.979E+05	5.780E+06	2.850E+07	1.418E+05	6.063E+05
AGR-2 3-3-1	moles/compact	8.660E-07	1.919E-05	3.274E-06	1.092E-08	1.910E-07
AGR-2 3-3-1	Bq/compact	1.065E+09	8.817E+09	4.254E+10	2.112E+08	9.159E+08
AGR-2 3-3-1	Bq/particle	6.902E+05	5.714E+06	2.757E+07	1.369E+05	5.936E+05
AGR-2 3-1-1	moles/compact	8.712E-07	1.931E-05	3.322E-06	1.104E-08	1.928E-07
AGR-2 3-1-1	Bq/compact	1.071E+09	8.872E+09	4.317E+10	2.136E+08	9.245E+08
AGR-2 3-1-1	Bq/particle	6.944E+05	5.750E+06	2.798E+07	1.384E+05	5.992E+05
AGR-2 3-3-2	moles/compact	8.696E-07	1.925E-05	3.329E-06	1.115E-08	1.929E-07
AGR-2 3-3-2	Bq/compact	1.069E+09	8.845E+09	4.326E+10	2.157E+08	9.250E+08
AGR-2 3-3-2	Bq/particle	6.931E+05	5.732E+06	2.804E+07	1.398E+05	5.995E+05
AGR-2 3-4-2	moles/compact	8.786E-07	1.947E-05	3.410E-06	1.152E-08	1.963E-07
AGR-2 3-4-2	Bq/compact	1.080E+09	8.946E+09	4.431E+10	2.228E+08	9.413E+08
AGR-2 3-4-2	Bq/particle	7.003E+05	5.798E+06	2.872E+07	1.444E+05	6.100E+05
AGR-2 3-4-1	moles/compact	8.749E-07	1.941E-05	3.354E-06	1.130E-08	1.943E-07
AGR-2 3-4-1	Bq/compact	1.076E+09	8.918E+09	4.358E+10	2.186E+08	9.317E+08
AGR-2 3-4-1	Bq/particle	6.973E+05	5.780E+06	2.825E+07	1.417E+05	6.038E+05

Appendix Table E-3. Calculated inventories of select radioactive fission products one day after EOL

Compact	Value	^{134}Cs	^{137}Cs	^{144}Ce	^{154}Eu	^{155}Eu
AGR-2 3-1-2	moles/compact	2.307E-06	2.662E-05	5.602E-06	3.589E-07	8.756E-07
AGR-2 3-1-2	Bq/compact	1.478E+10	1.171E+10	9.499E+10	5.520E+08	1.077E+09
AGR-2 3-1-2	Bq/particle	9.576E+06	7.587E+06	6.156E+07	3.577E+05	6.979E+05
AGR-2 3-3-1	moles/compact	2.200E-06	2.616E-05	5.623E-06	3.412E-07	8.660E-07
AGR-2 3-3-1	Bq/compact	1.409E+10	1.150E+10	9.535E+10	5.247E+08	1.065E+09
AGR-2 3-3-1	Bq/particle	9.132E+06	7.456E+06	6.180E+07	3.401E+05	6.902E+05
AGR-2 3-1-1	moles/compact	2.280E-06	2.644E-05	5.550E-06	3.539E-07	8.712E-07
AGR-2 3-1-1	Bq/compact	1.460E+10	1.163E+10	9.411E+10	5.443E+08	1.071E+09
AGR-2 3-1-1	Bq/particle	9.464E+06	7.535E+06	6.099E+07	3.527E+05	6.944E+05
AGR-2 3-3-2	moles/compact	2.228E-06	2.631E-05	5.670E-06	3.453E-07	8.696E-07
AGR-2 3-3-2	Bq/compact	1.427E+10	1.157E+10	9.615E+10	5.310E+08	1.069E+09
AGR-2 3-3-2	Bq/particle	9.249E+06	7.498E+06	6.231E+07	3.442E+05	6.931E+05
AGR-2 3-4-2	moles/compact	2.330E-06	2.677E-05	5.599E-06	3.615E-07	8.786E-07
AGR-2 3-4-2	Bq/compact	1.492E+10	1.177E+10	9.494E+10	5.560E+08	1.080E+09
AGR-2 3-4-2	Bq/particle	9.672E+06	7.629E+06	6.153E+07	3.603E+05	7.003E+05
AGR-2 3-4-1	moles/compact	2.298E-06	2.660E-05	5.547E-06	3.574E-07	8.749E-07
AGR-2 3-4-1	Bq/compact	1.472E+10	1.170E+10	9.406E+10	5.497E+08	1.076E+09
AGR-2 3-4-1	Bq/particle	9.539E+06	7.581E+06	6.096E+07	3.562E+05	6.973E+05